Bio-based 3D printing and testing of a digitally designed structural element

Graduation plan for the final graduation project of the Master variant Structural Engineering and Design of the Master Architecture, Building and Planning at Eindhoven University of Technology

F.E. Pels Rijcken

Eindhoven, 19-06-2025

Title:	Bio-based 3D printing and testing of a digitally designed structural element
Subtitle:	Master Thesis
Author:	F.E. (Franka) Pels Rijcken
Student number:	0893736
E-mail:	f.e.pels.rijcken@student.tue.nl frankapr@hotmail.com
Date:	19/06/2025
Location:	Eindhoven, The Netherlands
Department:	Built Environment
Master	Architecture, Building and Planning
Master track	Structural Engineering and Design
Chair	Innovative Structural Engineering and Design
Graduation Committee:	Ir. A.P.H.W. (Arjan) Habraken Assistant Professor, Built Environment, Innovative Structural Design Dr.ir. S.P.G. (Faas) Moonen Associate Professor Built Environment, Innovative Structural Design Ir. V. (Vincent) Staat External, SID studio

Preface

I was brought up by my parent with great concern for nature and our environment. This made me aware of the impact we human have on nature. I have, therefore, always been fascinated by innovative designs that are driven by sustainability and during my University study, I learned more about this topic. Especially in my Bachelor End Project (BEP), supervised by Ir. A.P.H.W. (Arjan) Habraken, I was introduced to parametric design. I experienced that parametric design offers many possibilities to integrate structural design, robotics (automations), and improved sustainability. I therefore chose to structure my Master's degree around the topics of sustainable parametric design.
After an internship at Habraken's company, SID Studio, I decided to perform my graduation project under his supervision. The exploratory meetings for graduation topics led me to bio-based 3D printing, which integrates not only structural design, automation and sustainability, but also a hands-on approach of production and mechanical testing in the Structural Engineering and Design laboratory (SED lab).

My graduation project is part of the Resource Efficient Structural Engineering and Design (RESED) studio within the Chair of Innovative Structural Engineering and Design (ISD) at the Eindhoven University of Technology (TU/e). The project focuses on 3D printing of a digitally designed structural element using a newly developed bio-based material. This graduation project is part of the master track Structural Engineering and Design (SED) within the Master of Architecture, Building and Planning (ABP).

I would like to express my gratitude to my supervisor Ir. A.P.H.W. (Arjan) Habraken for his valuable feedback and support throughout the project. Due to the unique nature of the research, it was difficult to confine the boundaries of this project. Arjan let me free to define (and refine) my own thesis subjects. Besides that, Arjan allowed me to do the research at my own pace, for which I am especially grateful.
I would also like to thank Ir. M.T. (Matthew) Ferguson for sharing his knowledge regarding the robots and assistance during manufacturing. Furthermore, I would like to thank all staff of the SED-lab, in particular Ir. H.M. (Hans) Lamers for his help and support, especially during the long days in the lab. I would also like to thank Dr.ir. S.P.G. (Faas) Moonen, for his interest in the project and his constructive feedback.
I highly appreciated the collaboration with my research partner Ir. L. (Luc) Roex during the early phases of the project. I gained new insights by working together, brainstorming, experimenting and sharing our knowledge. All this combined made it to a successful project.
Furthermore, I would like to thank the two former Delft University of Technology (TU Delft) students, Ir. C. (Christopher) Bierach and Ir. A.A. (Alexsander) Coelho, for providing us with additional information about their graduation projects, which formed the basis of my project.
I would also like to thank Ir. C.M. (Carolina) Rangel for her very useful advice at a crucial point in the material exploration, which ultimately led to the correct mixture ratio.
Dr.ir. RJA (Richard) Gosselink of Wageningen University provided useful references to companies that supplied the necessary materials.

Finally, I would like to thank my family for the for assistance and mental support, not only during my graduation project but throughout my studies and personal life.

Franka Pels Rijcken
Eindhoven, June 19, 2025

Abstract

The aim of this research was to develop a bio-based material to be applied in a structural final element (beam). This element was designed digitally and fabricated using additive manufacturing (AM) and tested on its mechanical behaviour.

There are a variety of AM methods and this study focused on Liquid Deposition Modeling (LDM). In 2022, C. Bierach and A. Coelho, of TU Delft, developed two promising "wood-based" mixtures consisting of cellulose, lignin and a binder. The binders used were methylcellulose (MC) or wood glue, the latter not being bio-based.
The two mixtures from Bierach and Coelho (2022) were replicated and improved by adjusting the composition. For this, three different binders, MC, wood glue and a bio-glue, were investigated using various mixture compositions until a printable paste was formed. Due to poor printability and mould growth, the MC mixtures could not be used. So, only the mixtures containing wood glue and bio-glue were selected for further investigation. The best performing, i.e. reference composition, of the mixtures consisted of cellulose, lignin and Valida L,3% (fibrillated nanocellulose) combined with wood glue or bio-glue. This composition formed homogeneous and printable mixtures.

Mechanical tests were used to determine the compressive and flexural properties of these mixtures. Despite the higher strength of wood glue (particularly in compression), the bio-glue mixture was preferred because of its fully bio-based nature.
The effect of adding bentonite and flax fibres on the mechanical properties was also investigated. Both additives clearly improved the compressive properties, although the effect on the flexural properties varied depending on the material and layer orientation of the test specimen. The mixture with flax as an additive resulted in the best overall flexural properties and was selected for printing the final element.

The final element was designed and (structurally) optimised specifically for AM, using Grasshopper and GSA. This resulted in a truss-like beam with a length of 730 mm, height of 220 mm and a thickness of six layers. The print path of this element was designed specifically for the ABB IRB 1200-5/0.9 robot, with a Makita caulk gun as the end effector, the latter was use throughout this study.
During printing of the single final element, various challenges occurred. For instance, layer misalignment and a faulty connection between a wave and the top chord led to imperfections.
When the final element was subjected to a bending test, the applied force (1.65 kN) slightly exceeded the force expected from the numerical model (1.63 kN), but the measured displacement of 24.67 mm was significantly larger than expected. The aforementioned faulty connection caused the element to behave unexpectedly, i.e. due to a significant redistribution of stresses, the element failed not in the centre, but in between the centre and a support of the bottom chord.

In the end, it was concluded that a digitally designed structural element using AM can be produced with a 100% bio-based material. This material shows great potential in the building and construction industry, but additional research is needed before it can be used in (outdoor) structural applications.

Contents

Preface 2
1 Introduction 7
2 State of the art bio-based 3D printing 10
2.1 Bio-based projects and studies 10
2.2 Material selection 21
3 Material exploration 30
3.1 Materials and equipment 30
3.2 Method 32
3.3 Mixtures 35
3.4 Additive exploration 39
3.5 Discussion and conclusion 40
4 Printability exploration 43
4.1 Robot setup 43
4.2 Print parameters 45
4.3 Printed test beams 46
5 Mechanical properties 49
5.1 Test setups 49
5.2 Reference mixtures 55
5.3 Reference mixture with additives 61
5.4 Classification of the material 68
6 Final element 71
6.1 Structural optimisation 71
6.2 Print tests 73
6.3 New shape 78
6.4 Printing the final element and test beams 87
6.5 Testing 90
7 Result summary and final conclusion 105
8 Recommendations 108
9 Bibliography 111
10 Appendices 121

List of abbreviations

Abbreviation	Definition
3DCP	3d Concrete Printing
ABP	Master of Architecture, Building and Planning
AM	Additive Manufacturing
BEP	Bachelor End Project
BG	Bio-Glue
CNC	Cellulose Nanocrystals
CNF	Cellulose Nanofibrils
CO2	Carbon Dioxide
DIW	Direct Ink Writing
DOF	Degrees of Freedom
FDM	Fused Deposition Modeling
GHG	Green House Gases
ISD	Chair of Innovative Structural Engineering and Design
LDM	Liquid Deposition Modeling
MC	Methylcellulose
MCC	Microcrystalline Cellulose
PF	Phenol-Formaldehyde Resin
PLA	Polylactic Acid
PVAc	Polyvinyl Acetate Emulsion
RESED	Resource Efficient Structural Engineering and Design
RH	Relative Humidity
SED	Structural Engineering and Design
TO	Topology Optimization
TU Delft	Delft University of Technology
TU/e	Eindhoven University of Technology
UF	Urea-Formaldehyde Resin
WG	Wood Glue

INTRODUCITON

1 Introduction

Global warming is a worldwide phenomenon that poses a threat to the life as we know it. The consequences of rising global temperatures include, amongst others, rising sea levels, declining biodiversity, desertification and more frequent and more destructive natural disasters [1,2]. It is primarily caused by the increasing emissions of greenhouse gases (GHG) due to human activity. The five primary economic sectors responsible for these emissions are: energy, industry, building, transport, and AFOLU (agriculture, forestry, and other land uses) [1,3].

In response to this global crisis, the United Nations Paris Climate Accord, hereafter referred to as the Paris Agreement, was adopted in 2015 by 196 parties with the objective of addressing this persistent problem. This is a legally binding international treaty on climate change that aims to limit global warming by reducing the GHG emissions by 50% by 2030 [4]. The Netherlands signed the Paris Agreement and aims to implement a circular and bio-based economy [5].

In the Netherlands, the building industry consumes 40% of the total energy, 50% of all the raw materials, and is also responsible for 40% of the total waste production. This results in the building sector being responsible for 35% of the total carbon dioxide (CO_2) emissions in the Netherlands [5]. In response, various actions and plans have been initiated to reduce the CO_2 pollution of this sector. For example, one of the goals of the Rijksoverheid is to reduce the use of primary (raw) resources by 50% [5].

One of the possible methods to reach this goal is to maximise the use of renewable resources and to optimise the material usage during the whole lifecycle of a building. In recent years, numerous materials and technologies have been researched and developed to reduce the raw material usage, improve the sustainability of buildings, and to optimise the material usage. This study focuses on maximising the use of renewable resources and optimising the material use for a structural element. Bio-based materials originate, in whole or significant part, from renewable resources, while the most CO_2-neutral bio-based materials are made from locally sourced materials, which can be raw resources from nature or materials that are often regarded as waste [6,7]. The utilisation of bio-based materials in the building sector has the potential to lead to a significantly (ranging from 10-50%) decrease of the GHG emissions [7,8].

This study introduces a new bio-based material and utilises additive manufacturing to produce a structurally optimised beam, henceforth referred to as the final element. Additive manufacturing or three-dimensional (3D) printing is developed as an environmentally-friendly and sustainable technology capable of reducing material usage and energy consumption. In addition, it provides the freedom to design and produce unique elements due to its high level of precision and the fact that formwork is not required. This innovative technology of digital design and fabrication is gradually gaining traction within the construction industry, largely due to the numerous benefits including reduced waste production, decreased physical labour, design freedom and increased construction speed [9]. To utilise the benefits of this innovative technology, the final element is digitally designed and optimised to limit the material usage and thus reduce the potential CO_2 emissions [10].

A number of bio-based materials, such as timber, are successfully used in the construction industry. However, new bio-based materials still face many challenges, including industry and societal perceptions of their durability and reliability as a construction material [11]. Further research and experimental testing of bio-based materials is required to determine the materials and mechanical properties, and to ensure their (structural) safety.

Given the recognised impact of CO_2 emissions on the planet [1], in this study it was decided to prioritise the use of bio-based materials, rather than focusing purely on its mechanical properties.

This study is part of the Innovative Structural Engineering and Design (ISD) research field. The objective of the study is to design and fabricate a parametric structural element, made from a bio-based material using additive manufacturing. The research question is formulated as follows:

What is the structural behaviour of a digitally designed structural element (beam) made from a bio-based material using additive manufacturing?

This question is divided into seven sub-questions:

1. What kind of bio-based 3D printing is currently utilised, in scientific research or development?
2. Which bio-based mixture is best suited for additive manufacturing of a structural element?
3. What are the potential additives to improve the structural properties of the mixture?
4. What are the best print parameters for printing objects with the chosen mixtures?
5. What are the mechanical properties of the selected mixtures and what mechanical tests are needed to determine them?
6. How to digitally design a structural beam specifically for additive manufacturing with the selected mixture?
7. What is the structural behaviour of a bio-based 3D printed beam?

To answer these questions, the project has been divided into two main parts: the creation of a bio-based printable mixture and the design and testing of a final structural element. Figure 1 illustrates the individual phases of the project. The first part was executed in close collaboration with Luc Roex and consisted of a literature study, a material and printability exploration and the determination of the material's mechanical properties. The second part of the project entailed the design, printing, and testing of the final element.

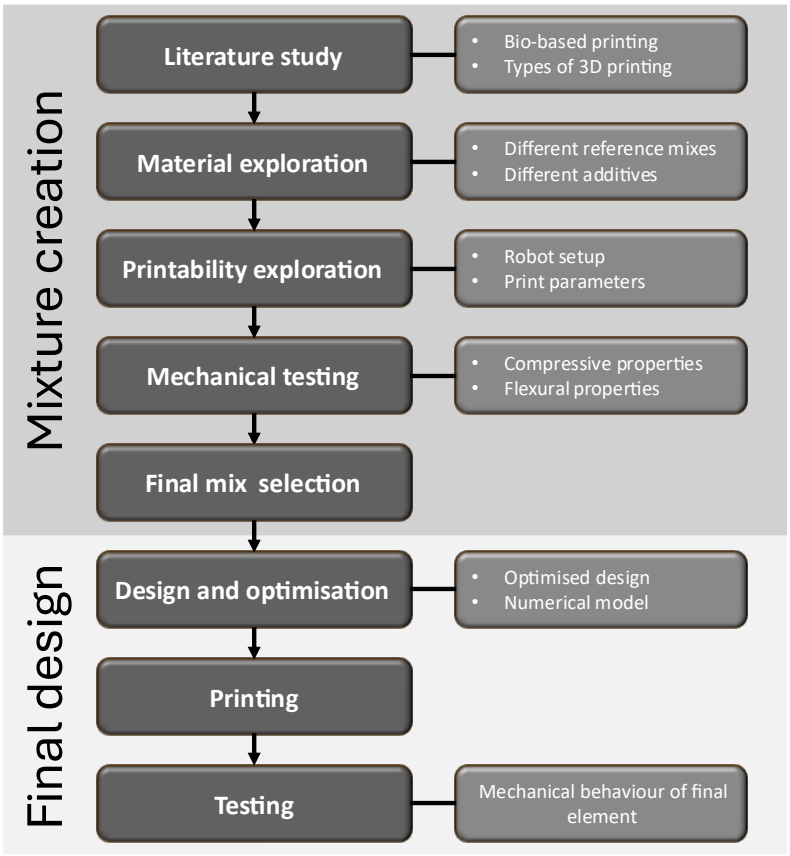


Figure 1. Phases of the graduation project.

STATE OF THE ART BIO-BASED 3D PRINTING

2 State of the art bio-based 3D printing

Additive manufacturing (AM) or 3D printing is widely utilised by a variety of industries, such as medicine, aerospace, automotive, food and military industries. AM has numerous advantages when compared to traditional manufacturing processes, including reduced production time and costs, as well as the ability and freedom to create complex parts [12]. A wide variety of materials can be used in AM, including ceramics, plastics, concrete and bio-composite materials [12]. The popularity to use bio-based materials with AM is rising in all industries. The following chapters highlight some projects and studies that have been executed based on bio-based 3D printing and address some of the AM technologies used in these projects and studies. At the end a bio-based material is selected as a reference material for this thesis, and some background information regarding this material is provided.

2.1 Bio-based projects and studies

2.1.1 Biopolymers

Polylactic acid

Polylactic acid (PLA) is a biopolymer that is frequently utilised as a filament for 3D printing using the fused deposition modelling (FDM) approach. PLA is one of the most common filaments due to its favourable properties such as versatility, sustainability and recyclability [13], and under the right circumstances it is also biodegradable [14]. PLA is manufactured from renewable feedstocks, such as food crops and waste sugars. It is commonly used in hobby printing, but is also utilised in several industries including the biomedical and health industry, electrical engineering, the automotive sector and aviation and aerospace [15]. Figure 2 and Figure 3 illustrate PLA filaments and a commonly used hobby FDM printer, respectively.



Figure 2. PLA filaments in various colours [16].



Figure 3. A FDM 3D printer (Bambu Lab) [17].

Biopolymers are compatible with a wide range of natural materials. Artist Arthur Mamou-Mani collaborated with the fashion house COS and realised a digitally designed and manufactured pavilion made from 700 3D-printed “bio-blocks” [18,19]. These “bio-blocks” are made from a mixture of recycled wood powder and a sugar-based PLA, both being fully compostable [19] and are illustrated in Figure 4.



Figure 4. Two pictures of the Conifera pavilion by Arthur Mamou-Mani and the fashion house COS [20].

Algae based polymers

Seaweed (or algae) is abundant in the marine environment, and can be harvested to create a variety of products. Moreover, its cultivation is also beneficial in preventing excessive algae blooms, which are harmful to the marine flora and fauna [21]. The following types of raw materials can be obtained [22]:

1. The fibres can be used to create a biopolymer.
2. An extracted liquid that can be used as a natural fertiliser.
3. Proteins that can substitute for animal proteins.
4. Fresh/demineralised water, which is a by-product of the cells of the seaweed

It is important to note that all materials obtained from the four streams are usable, meaning no waste is generated during the process.

Weedware© (Wierwaar in Dutch) by Studio Klarenbeek&Dros is a 3D printable product that is made from seaweed. This material is a renewable and compostable alternative to fossil fuel-based polymers [22]. Weedware© has been implemented in fashion, art, interior design and the built environment. Figure 5 to Figure 10 present examples of such products.



Figure 5. A 3D printable filament from Weedware [23].

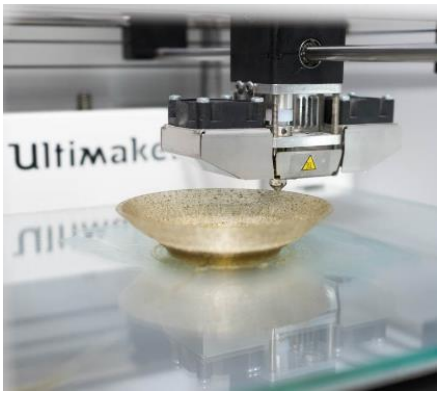




Figure 6. 3D printed objects from algae polymer created by the Algae lab, a collaboration between Klarenbeek & Dros with Atelier Luma [24]





Figure 7. In a collaboration between Iris van Herpen and Klarenbeek & Dros, van Herpen created wearable fashion items made from Weedware[25].



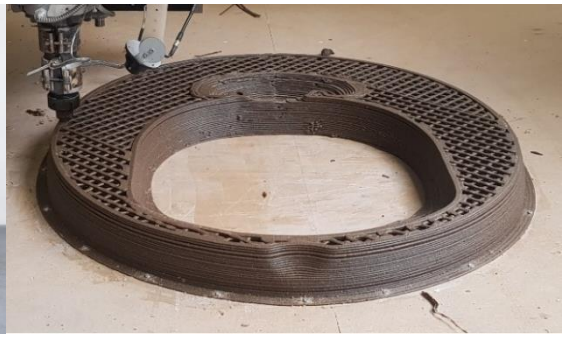


Figure 8. The iconic Peter Ghyczy's Garden Egg Chair (1967) remade and printed with algea based polymers [26,27].



Figure 9. The light Catcher printed with Weedware [22].



Figure 10. A 3D printed triangle that is part of a switchable system that can be used to cultivate green walls/roofs, made from Weedware [22].

2.1.2 Earthy materials

Soil

In 2018, the Italian 3D-printing technology developer WASP (World's Advanced Saving Project), constructed, in collaboration with RiceHouse, the Gaia house in Massa Lombarda, Italy. The house was developed to demonstrate the possibilities of 3D printing in terms of minimising environmental impact and efficient use of agricultural resources and waste [28].

The walls of the house were 3D printed on-site with a mixture of locally sourced natural materials and agricultural waste. For insulation, the vertical cavities in the wall were filled with rice husk, an agricultural waste from rice production. The composition of the mixture is provided in Table 1. According to WASP, the house is fully biodegradable, and will revert back to soil if not maintained [29]. The 30m^2 house was printed over a 10-day period and the design made excellent use of the computational design and the Crane WASP printer to create the house, with complex geometries that are difficult to replicate with traditional construction systems [28]. Figure 11 and Figure 12 present the finished Gaia house and the Crane WASP printer respectively.

Table 1. Mixture composition Gaia house [28].

Material	Content [%]
Soil (30% clay, 40% silt, 30% sand)	25
Straw chopped rice	40
Rice husk	25
Hydraulic lime	10



Figure 11. The Gaia house [29].



Figure 12. The Crane Wasp printer [28].

WASP has also collaborated with Mario Cucinella Architects to develop a progressive project named TECLA (a combination of Technology and Clay), an eco-sustainable 3D printed habitat in Massa Lombarda, Italy. The house was entirely manufactured with locally sourced materials that are reusable and recyclable [30]. The 60m^2 house was constructed on-site with multiple Crane WASP printers at the same time. This demonstrated the potential of 3D technology to optimise the construction process and minimise the material, energy and human labour usage [30,31]. The project received support from Mapei, a worldwide producer of construction materials with a high expertise on clay materials, and contributed to the development of the highly optimised printable mixture [30]. Figure 13 and Figure 14 illustrate the finished TECLA house and the Crane WASP printers respectively.



Figure 13. A realised prototype of the TECLA house [31].

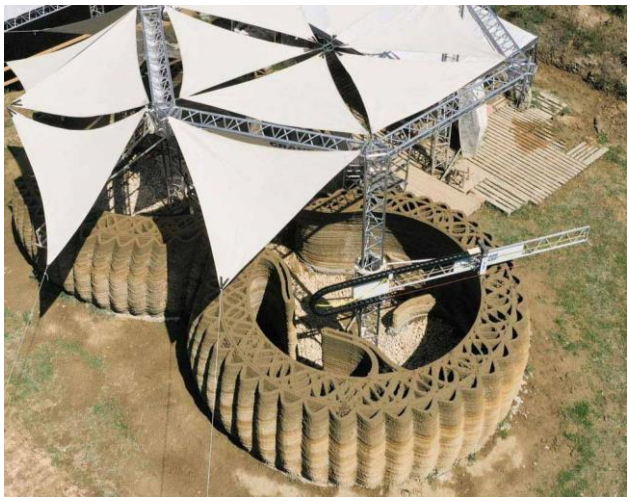


Figure 14. The two Crane Wasp printers [30].

The University of Virginia pushed the boundaries of soil printing, by using a seed-impregnated 3D-printable soil, also called “living soil”. Just after printing, a printed element (for instance a wall) looks like an ordinary raw-earth structure, however, over the course of a few days, the seeds sprout, and the element becomes covered in greenery. This method is a circular alternative to more emission-intensive building materials. The use of locally sourced soil, water and plants, ensures a low carbon footprint, or even a carbon negative footprint, with the plants removing CO_2 from the air. Depending on the plants that are used, the element can also function as a pollinator [32,33]. Figure 15 presents a wall element made of 3D printed living soil.

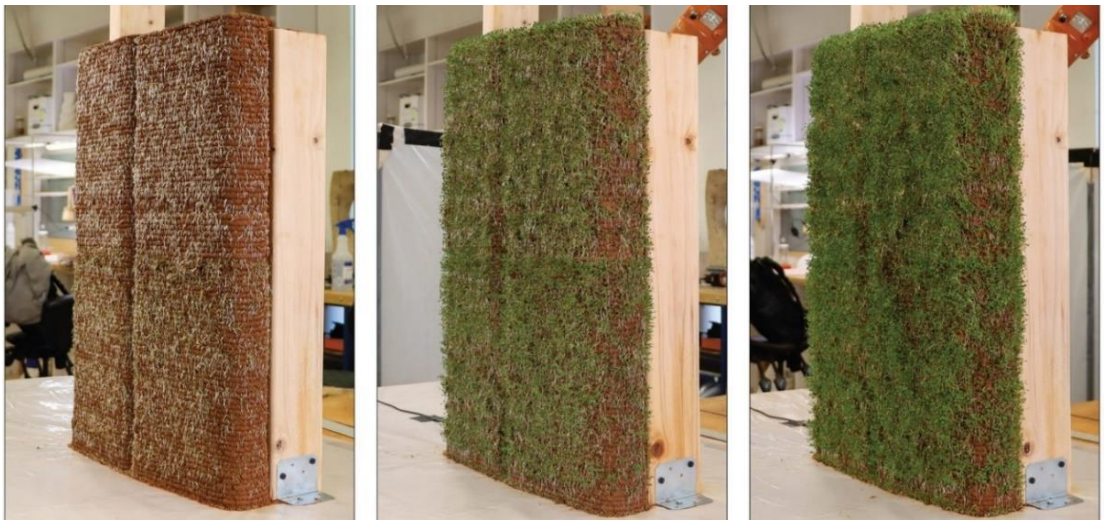


Figure 15. A 3D-printed wall element with living soil, after 48, 96 and 144 hours from left to right [33].

Sand

Bavarian manufacturer Sandhelden fabricated four 3D printed trophies made from Bavarian quartz sand, which were printed using binder jetting technology. The binder used was Furan, which is made from several renewable resources such as sugar cane, corn husks or rice hulls.

The binder jetting process allows for a high level of precision, resulting in objects that are rather fragile. A clear advantage is that this type of printing consumes little energy, and excess material can be reused to minimise waste [34]. Sandhelden uses their patented binder jetting process to create objects for several art and architecture projects, three of which are shown in Figure 16 to Figure 18.



Figure 16. 3D printed trophies made from quartz sand [34].



Figure 17."Monolith" a 3D printed sculpture made from quartz sand [35].



Figure 18. A 3D printed architectural airflow barrier made from quartz sand [36].

Like Sandhelden, Arthur Mamou-Mani also worked with sand printing. In collaboration with Precht, Mamou-Mani designed Sandwaves, a pavilion made from 3D-printed sand elements in Saudi Arabia, see Figure 19. In order to construct an ecological design, the materials were sourced locally, and the elements were produced near the site. A furan resin derived from the cellulose of pine trees and corn kernels was used as the binder [37,38].



Figure 19. The Sandwaves in Saudi Arabia by Mamou-Mani [37,38].

Clay printing

The development and application of 3D ceramic printing technologies has been pursued by a number of companies and individuals [39–41]. Internationally, clay/ceramic additive manufacturing is already used for artistic applications, but is also a subject for (ongoing) research. For example, Cristina Nan leads a research group on alternative print materials such as clay printing at the TU/e [42]. Examples of 3D-printed ceramics are presented in Figure 20 to Figure 23.



Figure 20. 3D printed clay brick wall by Virginia San Fratello [43].



Figure 21. 3D printed clay scultputre [42].



Figure 22. 3D printed ceramics by Olivier van Herpt [39].



Figure 23. 3D printed ceramic cups by Arthur Mamou-Mani [44].

2.1.3 Waste materials

Sewage water treatment residuals

The bio-circular design studio Omlab was founded in 2019 and its primary objective was researching and inventing new sustainable and ecofriendly materials for the construction, soil and biodiversity industries, with the focus on alternatives for 3D structural printing [45].

They developed a 3D printable (clay-like) paste, based on waste streams from the sewage water treatment plants in the Netherlands, called “BuildMatterial”. They filter cellulose from the wasted toilet paper and process it into Recell (recovered cellulose) with unique properties [46]. This cellulose is then mixed with calcium carbonate, water and Kaumera or alginate (see Table 2 for the exact composition). The later components are also waste materials obtained from these sewage water treatment plants that would normally be incinerated. The result after printing and curing is a breathable material that feels likes stone or ceramic, which is also ecologically friendly and biodegradable [47]. Currently, this material can be used for permanent construction indoors and temporary structures outdoors and has the strength of an aerated concrete block (C8) [48,49].

In 2021, Omlab created a toilet room from its BuildMatterial (see Figure 24). The company has also created several (temporary) structures to contribute to the biodiversity in the Netherlands, illustrated by Figure 25 and Figure 26.

Table 2. Mixture composition Omlab's BuildMatterial [47].

Material	Content [%]
Calcium carbonate	60
Cellulose	5
Kaumera or alginate	5
Water	30

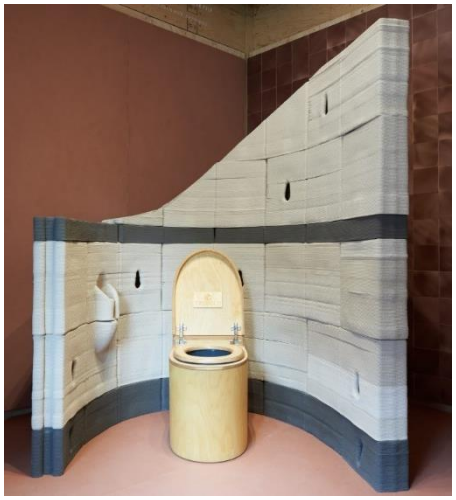


Figure 24. Omlab's toilet room at the DDW21, made from 24 blocks of their supercirculair BuildMatterial [50].



Figure 25. Vesper, a temporary bat box made from Omlab's BuildMatterial [51].



Figure 26. "Biotaludtegels" or bio-enbankment-tiles, 100% bio-circular tiles to prevent erosion [52].

2.1.4 Living organisms

In 2013, Eric Klarenbeek created the first 3D-printed element made from living fungi, utilising a mixture of water, powdered straw and mycelium (the root system of fungi) which requires a substrate in order to grow. Klarenbeek designed a chair and after printing it, the mycelium grew within the structure, creating a solid but lightweight and durable structure. After the first mushrooms started to show, the chair underwent a drying process to stop further growth of the mycelium [27,53]. Figure 27 and Figure 28 show two generations of the mycelium chair.

The production of mycelium structures does not require any heating during the printing process, thereby significantly reducing the carbon footprint, or even reaching a negative carbon footprint. Moreover, the material is fully compostable and can fertilise the soil [27,53].

In 2018, Paola Garnousset, Martin Detoeuf, and Pierre de Pingon, founded Blast Studio, with the vision of integrating nature and technology to produce innovative materials from urban waste [54]. In 2020, the company created their first mycelium element: The Lovely Waste Column (see Figure 29). The 3D-printable mixture consisted of locally wasted cardboard as a substrate, which was inoculated with mycelium. The shape of the column was digitally designed to optimise the growth of the mycelium.

The process of creating the mycelium elements is as follows: once the shape is printed, the mycelium consumes the substrate and takes over the whole element, while producing mushrooms that can be picked off and consumed. To prevent further growth, the element is then dried to kil the organisms. This solidifies the material to create a load-bearing element with insulating and fire-retardant properties. Blast studio estimates the strength of their materials to be similar to medium-density

fibreboard (MDF). Since Blast Studio's first column, the company has created more mycelium 3D printed elements, a few of which are shown in Figure 30 to Figure 32. The company's goal is to eventually print a pavilion or perhaps entire buildings with their mycelium mixture [54,55].



Figure 27. The first Mycelium Chair by Eric Klarenbeek [53].



Figure 28. The second Mycelium Chair by Eric Klarenbeek [27].



Figure 29. The Lovely Trash Column by Blast Studio [56].



Figure 30. The Blue Tree by Blast Studio [56].



Figure 31. The cabinet of Curiosities by Blast Studio [56].



Figure 32. The Op't Oog Columns (eyewear displays) by Blast Studio [56].

2.1.5 Wood printing

Many ongoing research concern different bio-based alternatives for structural 3D printing and wood printing, using raw materials from trees, is rising in popularity. In combination with different binders and additives one can create a bio-based 3D printable mixture.

In 2016, Kariz et al. [57] researched a 3D printable mixture of beech wood powder and adhesives, utilising urea–formaldehyde (UF) adhesive or a polyvinyl acetate (PVAc) adhesive as a binder. Different ratios between the adhesive and wood powder were tested based on the printability of the fresh mixture and the strength of the cured material. Figure 33 shows the printing setup during a print.
The study demonstrated that a higher percentage of wood powder resulted in a higher extrusion force compared to mixtures with a lower percentage. The bending properties of the 3D-printed blocks (150 x 30 x 8 mm) depended mostly on the adhesive. The UF adhesive resulted in higher values for the bending strength and the modulus of elasticity compared to the PVAc adhesive.
The most optimal mixture contained 15% UF adhesive (W-Leim 3000) and 85% wood powder. The 3D printed blocks had an average bending strength of 19 N/mm2 and an average modulus of elasticity of 1930 N/mm2 [57].



Figure 33. 3D printing setup of the wood powder with adhesive

In 2018, Rosenthal et al. [58] of the University of Dresden developed a 3D printable mixture utilising sawdust from beech and methylcellulose. The sawdust was ground into two different particle size ranges: smaller than 0.25 mm and between 0.25 and 0.4 mm. The methylcellulose (MC) powder was combined with water and served both as a lubricant and binder. Three different mixes were prepared, see Table 3. Towers and bending elements were printed using these mixes. Printed tower specimens are illustrated in Figure 34. The elements were tested for different (mechanical) properties and the test results for the average bending strength, modulus of elasticity, density and height shrinkage are presented in Table 4.

It was concluded that a lower wood content in the mixture resulted in higher bending strength, modulus of elasticity and density. Furthermore, utilising smaller wood particles resulted in higher bending strength, modulus of elasticity and density.

Because the 3D printed mixture consisted of 100% bio-based materials, the production was both easy and cost-effective [58].

Table 3. Sawdust mixture by Rosenthal et al. [58].

Material	**Content [%]**		
	M1	**M2**	**M3**
Water	3	4	4
Methylcellulose	77	76	74
Wood	21	21	22
Wood particle size [mm]	<0.25	<0.4	<0.25



Figure 34. Printed "tower" specimens [58].

Table 4. Mechanical properties of the sawdust mixtures by Rosenthal et al. [58].

Mixture	**Average bending strength [N/mm²]**	**Average modulus of elasticity [N/mm²]**	**Density [g/cm³]**	**Height shrinkage [%]**
M1	2.3 ± 0.4	284.8 ± 46.4	0.33 ± 0.05	17.3 ± 1.1
M2	5.1 ± 1.0	546.5 ± 109.7	0.40 ± 0.03	18.0 ± 1.3
M3	7.4 ± 1.1	733.1 ± 128.0	0.48 ± 0.03	20.0 ± 2.4

Cellulose and lignin, the two primary components of wood, are one of the most abundant organic polymers on earth. While these polymers are being utilised in many applications, for instance as additives, they have not been often combined [59]. In 2022, T. Liebrand of TU Delft [60] reported on a lignin and cellulose mixture with acetone and water. This was a promising mixture, however, acetone is not bio-based and exposure to this substance can be hazardous to the equipment or health [60,61].

Further research was conducted by master students A. Coelho and C. Bierach, who analysed and evaluated 12 different mixtures with bio-based and synthetic binders mixed with cellulose and lignin [62,63]. First, a pilot study was carried out by manual and visual testing, based on the material properties (among others: homogeneity, viscosity, adhesion, extrudability and bio-based content).
Following this, four mixtures with different binders were selected to test their strength: methylcellulose (MC), wood glue, acetone and dimethyl sulfoxide (DMSO) and their compositions are presented in Table 5. For testing the mechanical properties, moulded elements were produced and tested, the results of which are presented in Table 6. It was concluded that the wood glue mixture was the strongest and mixture with acetone was the weakest material tested. Surprisingly, the mixtures with MC and wood glue presented similar results for the flexural modulus of elasticity.
Since the mixture with MC was the only fully bio-based mixture, it was selected for further research. First, identical shaped test elements were now printed instead of moulded, using Liquid Deposition Modeling (LDM), and the same tests were performed. These results are also provided in Table 6.
Finally, two prototypes were printed with the MC mixture: a window frame (Figure 35) and a structural node (Figure 36).

Table 5. Mixtures compositions by A. Coelho and C. Bierach [62,63].

Binder type	Content of component			
	Cellulose	Lignin	Water	Binder
Methylcellulose	2.9%	29.1%	63.1%	4.9%
Wood glue	2.4%	24.4%		73.2%
Acetone	4.9%	58.3%	9.7%	27.2%
DMSO	5.8%	50.7%	14.5%	29.0%

Table 6. Mechanical properties of the mixtures by A. Coelho and C. Bierach [62,63].

Mixture	Flexural strength [N/mm²]	Flexural modulus of elasticity [kN/mm²]	Yield strength [%]	Tensile modulus of elasticity
Methylcellulose	8.59 - 10.60	0.67 - 1.05	3.21 - 4.06	0.33 - 0.56
Wood glue	20.67 - 28.89	0.64 - 0.90	3.58 - 4.81	0.30 - 0.77
Acetone	4.77 - 9.74	0.15 - 0.37	0.81 - 1.51	0.11 - 0.20
DMSO*	-	-	-	-
Methylcellulose Extruded	8.48 - 9.55	0.60 - 0.64	2.38 - 3.10	0.40 - 0.52

**) All specimens failed prematurely.*



Figure 35. 3D printed window frame [63].



Figure 36. 3D printed strucutral node [62].

2.1.6 Additive manufacturing methods

A large number of AM methods are currently available. Figure 37 provides an overview of six different AM categories with their corresponding subcategories. Table 7 further describes the major categories. Each category has its own (dis)advantages and they should therefore be carefully selected, based on the material composition and properties as well as the desired product.

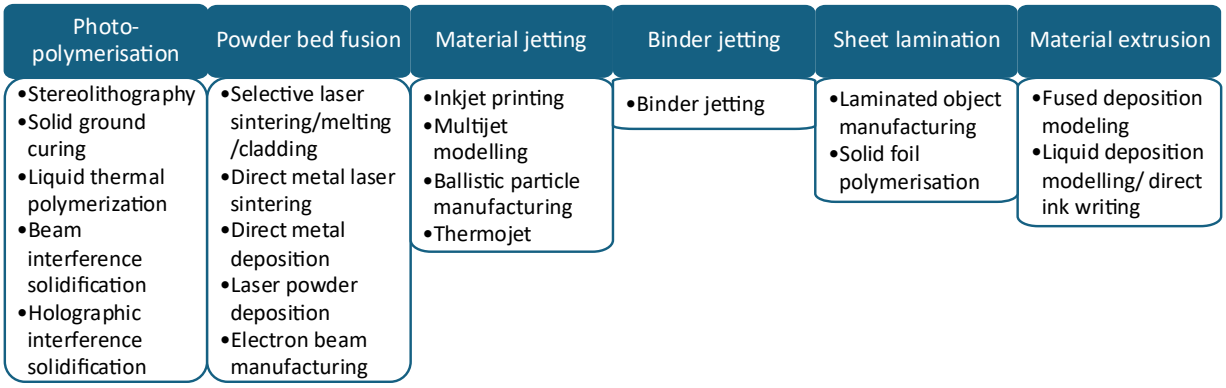


Figure 37. Methods and types of additive manufacturing processes [64,65].

Table 7. AM processes and descriptions [66].

AM process	Description
Photo- polymerisation	Liquid photopolymer in a vat is selectively cured by light-activated polymerisation.
Powder bed fusion	Thermal energy selectively fuses regions of a powder bed.
Material jetting	Droplets of build material are selectively deposited.
Binder jetting	Liquid bonding agent is selectively deposited to join powder materials.
Sheet lamination	Sheets of material are bonded to form an object.
Material extrusion	Material is selectively dispensed through a nozzle or orifice.

In the aforementioned examples of bio-based 3D printing, two categories of AM processes were utilised: material extrusion and binder jetting. Mainly, bio-based polymers were printed using fused deposition modeling (FDM). For all other materials liquid deposition modeling (LDM), or direct ink writing (DIW), method was employed, with the exception of the sand objects, for which a binder jetting process was used. These three processes are described below.

The FDM method is illustrated in Figure 38. In this process, a (thermoplastic) filament is supplied to a heated nozzle, and the filament is heated just above its melting point. After extrusion the melted material solidifies and subsequently adheres to the previous layer. This method is inexpensive and low-cost; however, the accuracy and surface quality are relatively poor compared to powder-based plastic AM processes [64].

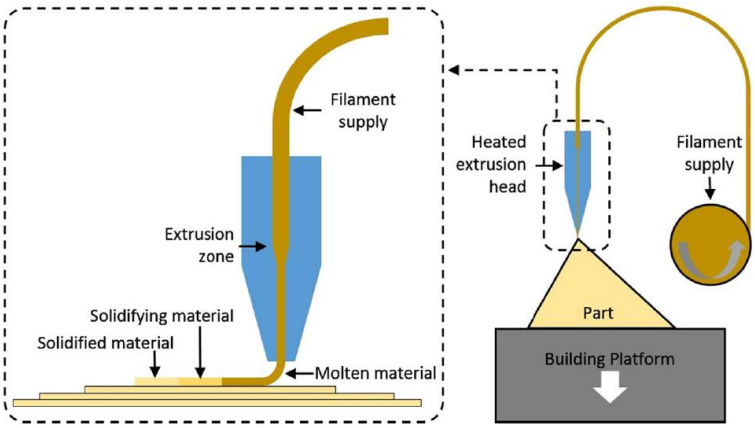


Figure 38. Schematic visualization of the FDM process [64].

LDM (Figure 39) is considered to be one of the most versatile AM methods as it enables the utilisation of a wide range of materials, provided that the material can be engineered to have the appropriate rheological properties. The material should be extrudable, self-standing and adhere to the previous layers. The exact rheological properties depend on the material utilised and the desired printed product. The material is extruded through a (small) nozzle and no additional heat is required. The pressure, flow rates, and diameter of the nozzle can be easily controlled. After extrusion, the material solidifies, either naturally or assisted by external processes such as evaporation or heat treatment [67–69].

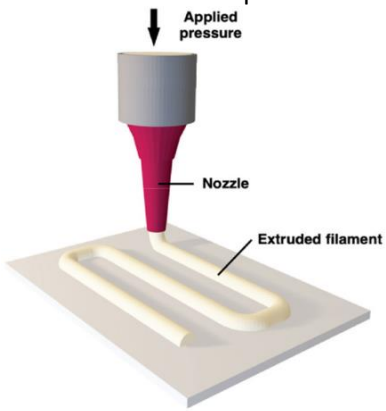


Figure 39. Schematic visualization of DIW/LDM [67]

Binder jetting is illustrated in Figure 40. In this method, small droplets of a liquid binder are carefully applied to a powder bed. When a layer is complete, the building platform moves downwards and a new thin powder layer is added on top of the previous layer and a new layer of binder can be applied [64,70].

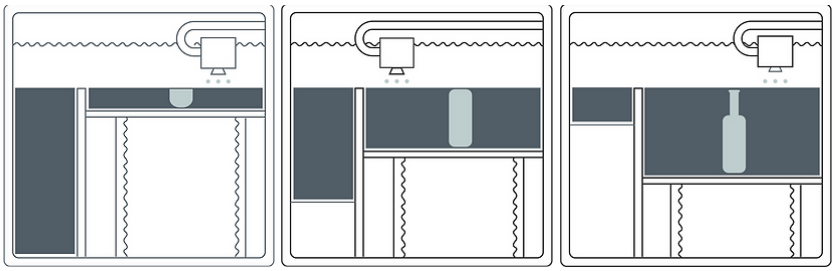


Figure 40. Schematic visualization of the binder jetting AM process [70].

In this project, the LDM method was selected for further research based on the available equipment in the structures laboratory (SED-lab) and the TU/e's knowledge regarding extrusion-based 3D printing with clay and concrete.

2.2 Material selection

Based on the aforementioned examples of bio-based 3D printing that utilised the LDM method, the following mixtures were possible options: soil/clay-based mixtures, the water treatment waste-based 'BuildMatterial' from Omlab, a mycelium-based mixture and wood-based mixtures.

Due to the scale of this research, the level of expertise and the availability of materials, it was decided to focus on wood-based printing in this research. Wood-based printing has a lot of potential for use in a variety of applications, as demonstrated by research conducted at TU Delft [62,63], however, further studies and improvements are necessary to apply it in structural elements.

It was decided to use the wood glue and methylcellulose mixtures from TU Delft as reference mixtures. Despite the wood glue mixture not being 100% bio-based, it was included due to its better mechanical properties. The mechanical properties of these mixtures could be improved by using alternative materials, binders and/or additives, which are divided into three categories: raw materials, binders and additives. Table 8 provides a list of possible (alternative) materials categorised into the three categories.

Table 8. Possible materials divided into three categories.

Raw material	Binder	Additives
Cellulose	Methylcellulose	Bentonite
Lignin	Wood glue	Natural fibres
	Bio-based glue	Wood powder

For the LDM method, a mixture should be capable of being printed using a 3D printer. Generally, printability is a measure of how suitable a mixture is for AM, however, the term is not clearly defined in literature. For the printability of a mixture with LDM, the rheological properties of a mixture are unquestionably important. These properties determine the range of structures that can be printed, the print parameters and the quality of the printed product. The following rheological properties are of importance [71]:

- Shear-thinning behaviour, to facilitate the extrusion of the mixture through different nozzles.
- Optimised yield stress and stiffness of the mixture formulation, to ensure that the shape is kept as much as possible
- Thixotropic behaviour, for a good viscosity recovery upon extrusion to avoid layer slump

Shear-thinning is a phenomenon in which the viscosity of a mixture decreases when the shear-rate is increased, causing the mixture to become more fluid and flow faster [72].
The optimised yield stress and stiffness of the mixture formulation should ensure that the mixture is capable of carrying its own weight, as well as the weight of the layers above it, i.e. it should be able to withstand all the required gravitational forces [71].
Thixotropy is defined as the decrease in viscosity of a mixture under pressure, and the immediate recovery of its viscosity when the material exits the extruder is removed [71,73].

In addition to the rheological properties, the following mixture properties are important for the printability of a mixture [62,74,75]:

- The mixture should be homogeneous prior to printing, and no air bubbles should be present during printing.
- The working life of the mixture should be long enough to print and for layers to form a bond with the subsequent layers.
- The interfacial adhesion between two printed layers is important to achieve maximum strength of the printed element.
- The printed element should retain its shape throughout the curing process, with keeping the shrinkage at a minimum.
- During the curing process the printed material should build up its mechanical (bond) strength.
- The layers should adhere properly to each other, with the printed element ideally breaking before the layers start to separate.

2.2.1 Raw materials

Cellulose

One of the raw materials of the mixture is cellulose. Cellulose, a tough and fibrous material, is the most abundant biopolymers on earth, and is generally made by plants but is also produced by some bacteria. It is an integral structural component of the plant cell walls, cellulose chains are arranged in bundles which make up the plant/tree cell wall. This suggests that cellulose has high strength and other preferable mechanical properties [76].
Cellulose has a wide variety of applications, such as being the main ingredients of paper, paper products, plant-based textiles [76]. In the 3D printing realm, cellulose and its derivatives are increasingly utilised [77], as illustrated in Figure 41 and Table 9. This increasing utilisation is due to their availability, environmentally friendliness, renewability, their low costs and high flexibility [77,78].

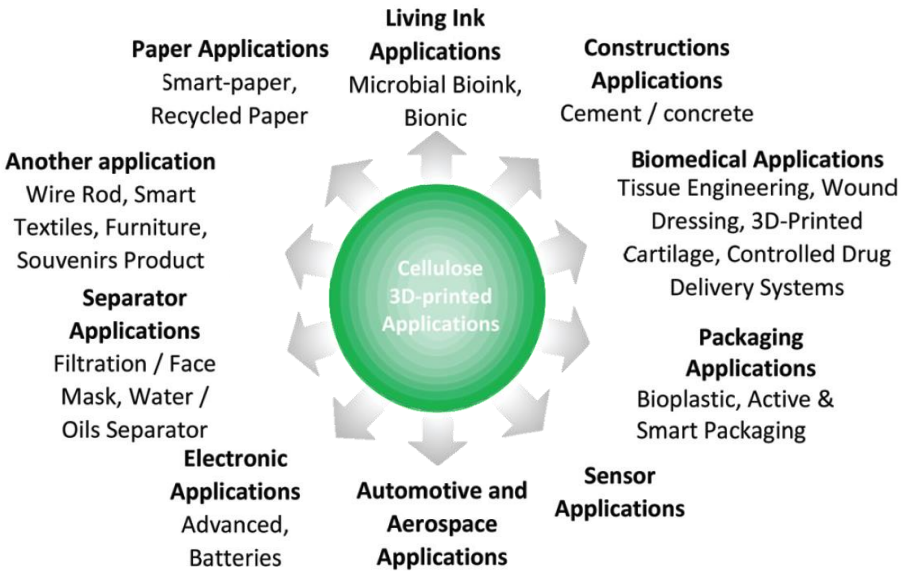


Figure 41. Application of 3D printed cellulose [77].

Table 9. Properties of cellulose and some of its derivatives as bio-feedstocks for 3D printing [78,79].

Cellulose	Derivative	Role in mixture
Cellulose		Thickening, good shear-thinning behaviour
Cellulose ethers	Methyl cellulose (MC)	Viscosity modifier, binder, stabilizer, strengthener, emulsifier, extrusion aid
	Carboxymethyl cellulose (CMC)	Viscosity thickening, thixotropic rheology, binder, sizing agent
Cellulose esters	Cellulose acetate (CA)	Enhancing viscosity, formability and glossy appearance
Nano cellulose	Cellulose nanofibrils (CNF)	Appropriate rheological properties, gel-like consistency, crosslinking to from network structure, increasing yield stress and modulus
	Cellulose nanocrystals (CNC)	Good shear-thinning, reducing viscosity and modulus modifier
Microcrystalline cellulose (MCC)		Emulsifier and thickening

Cellulose fibres are often utilised as a bio-based alternative for synthetic fibres [77]. They exhibit a relatively high tensile strength and high flexibility [80], and they have the highest specific stiffness among naturally produced materials. Due to its favourable chemical network, cellulose can bind strongly to other materials, and therefore it is often used as a reinforcing agent in 3D composites to improve the mechanical properties of the mixture [78].

Cellulose ethers are regarded as one of the most important cellulose derivatives, given that they are already produced on an industrial scale. They possess favourable properties with regard to the improvement of composite materials for 3D printing. They are frequently used as a viscosity modifier, binder, plasticiser or as a filler. They have good solubility, high chemical stability, physiological safety and good biodegradability. The ethers can often be combined with nanocellulose, other cellulose derivatives or other additives to achieve a printable mixture [78,79].

The popularity of nanocelluloses as components in 3D printable mixtures is increasing, due to their versatility and sustainability [79]. They possess a number of fascinating properties, including high strength, a high surface area, flexibility and shear-thinning behaviour. They are frequently used as a biodegradable reinforcing agent, as well as a building block or binder [78].

Microcrystalline cellulose, with a length of approximately 1 µm, is currently commercially significant. It is frequently utilised as an emulsifier, filler, rheology modifier, binder or reinforcing agent. It is sustainable, biodegradable, low-cost, lightweight and causes less damage to the equipment when compared to glass fibres, silica of carbon fibres. In additions, MCC is less expensive than CNC, and can be used to replace CNC as a reinforcing agent for 3D printed mixtures [78].

Lignin

Lignin is the other primary raw material, and it is the second most abundant biopolymer on earth after cellulose [81]. It is, like cellulose, a fundamental component of the structural cell walls of plants, and its main function is to act as a natural glue that holds the cellulose fibres together, providing rigidity and strength [82]. Lignin can be obtained inexpensively from a variety of sources, including woody biomass, energy crops, agricultural waste and the paper and pulp industry, with the latter generating the most lignin as a by-product. Historically, lignin was regarded as a low-value waste product, however, it is now considered as a valuable product, with an increasing popularity in several industries, due to its low cost, renewability, biodegradability and high carbon content [59,81,83].

The favourable properties and characteristics of lignin allow for its interaction with a variety of polymers, resulting in the production of homogeneous composites. Numerous studies have demonstrated that lignin can be applied in a wide variety of applications, including automotive components, adhesives, bioplastics, fillers, emulsifiers, reinforcing agents, and numerous others [81].

The separation of lignin from its biomass can be achieved through various processes. The end products are called technical lignin [76]. Not all types of technical lignin are suitable for 3D printing due to their different properties regarding the viscosity, shear-thinning behaviour, stiffness and rheological properties [83].

There are various methods of extracting the technical lignin from lignocellulosic materials, as illustrated in Figure 42. The two main methods are kraft pulping and sulphite pulping. Kraft pulping accounts for approximately 85% of global lignin production, with the primary application being as a fuel for heat generation, representing a low-value utilisation [83]. Sulphite pulping results in lignosulfonates or also soda lignin. Soda lignin is a widely available material with a variety of applications, including dispersants, flocculants, and additives in concrete and (bio)composites [83]. A significant difference between soda and kraft lignin is that the soda lignin is sulphur-free, has no odour and its chemical composition is closer to pure lignin [84].

In recent developments, both kraft lignin and soda lignin, have been utilised to manufacture filaments for FDM [84]. Despite the limited utilisation of technical lignins with the LDM method, studies have shown that they are well suited for the LDM method. However, further research or modifications of the lignins are required so that they can be combined with natural fibres to print composites that can substitute wood elements [85].

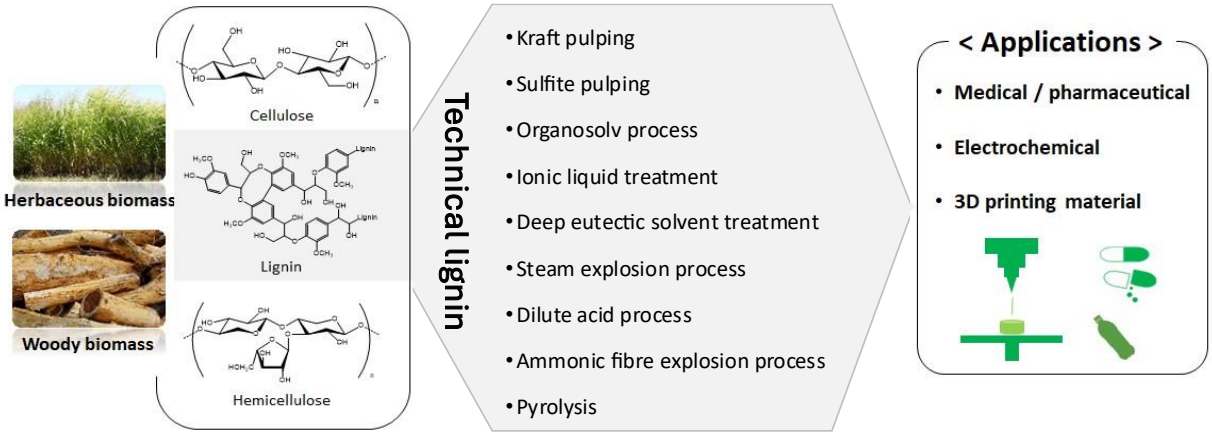


Figure 42. Processes for the extraction of technical lignins and its applications [83].

2.2.2 Binders

Methylcellulose

As previously mentioned, methylcellulose (MC) is a derivative of cellulose. It is a white tasteless powder with multiple functions, including emulsifier, adhesive, thickener and a dispersing agent. It is widely used as an additive in the food, cosmetics, textile, electronics, pharmaceutical, paper and construction industries [86–88]. Its use as a binder is extensive, with applications in electronics, clothing, paper products, fertilisers, pesticides, ceramics, animal feed and soil stabilisation [87,88]. In common households, MC is employed as wallpaper adhesive, either alone or in combination with starch [88].

One of the largest industries where MC is utilised is the construction industry. Due to its water solubility, MC is employed as an additive in cement formulations such as mortars, stuccos and plasters, improving the workability, adhesion, stability, strength and the water retention. In addition, MC improves the curing process, and it reduces the shrinkage, resulting in high viscous mixture with good adherence [88,89].

In the field of 3D printing, numerous studies have examined the impact of MC in 3D printable mixtures. A study of H. Li investigated the rheological properties of MC in a hydrogel, finding that MC significantly improved the viscosity, the shear-thinning behaviour and the thixotropic behaviour, creating an ideal 3D printable hydrogel [90]. This conclusion was also drawn by the study of N. Contessi Negrini [91].

Within the construction industry, several studies have investigated the effect of utilising MC as an additive in cementitious mixtures. Y. Zang research revealed that MC affects the rheological properties, enhancing the shear-thinning behaviour of 3D printable cement [92]. This finding was confirmed in the studies conducted by Y. Yin and P. Shoaei, demonstrating that MC (in the form of hydroxypropyl methylcellulose (HPMC)), affected the rheologic and thixotropic properties, improving the extrudability and constructability, increasing the viscosity and yield stress, and resulting in a more stable mixture with a higher printing accuracy [93,94].

As previously mentioned in Chapter 2.1.5, Rosenthal et al. investigated a 100% bio-based mixture with the use of MC as a binder with wood particles, which resulted in a smooth printable mixture [58]. In a separate study, Peeters et al. investigated a 100% biodegradable 3D printable mixture consisting of 85% sawdust, MC, water, and bentonite. This mixture was utilised to create a large vase, which, at the time, represented the biggest 3D printable object [95].

These studies demonstrate that printing with MC offers significant potential, but further investigation is necessary to explore the possibilities for a mixture with MC to be applied structurally.

Wood adhesives

The majority of wood adhesives are synthetic in nature, and they can be categorised into three main groups with a wide range of applications: urea-formaldehyde resins (UF), phenol-formaldehyde resins (PF) and polyvinyl acetate emulsion (PVAc) [96,97].

The most widely used of these are UF resins, which are extensively employed in the wood and interior construction industries. However, they have certain drawbacks including the possible release of formaldehyde, and poor water and heat resistance [96,97].

PF resins are the second largest group of wood adhesives. They have excellent weather-resistant properties and have a high bond strength and are thus commonly used for outdoor applications. However, disadvantages of PF include their colour, their hard and brittle nature after being cured, their high costs and the fact that their raw material is petroleum based [96].

PVAc emulsions are distinguished by their low-cost, non-toxic, harmless qualities and that they are a green adhesive. However, they have poor water, heat and low-temperature resistance, mechanical instability and decreased bond strength at higher temperatures [96].

The utilisation of wood adhesives in additive manufacturing has not been a subject of many investigations. However, in the study previously mentioned by Kariz et al, a 3D printable mixture was created using wood powder and a UF or PVAc adhesive as a binder. This study demonstrated that printing with a wood adhesive shows promise, however, the mechanical behaviour of the printed product depends highly on the used binder [57].

Bio-based adhesives

The majority of wood adhesives are synthetic and made from non-renewable materials, consequently, bio-based adhesives are the subject of numerous studies due to the environmental issues of the synthetic adhesives [96]. Natural adhesives are gaining popularity due to their many advantages, including availability, sustainability, renewability and some outstanding features. However, they have many disadvantages such as limited water and heat resistance, low bonding strength and a short application period [96].

Natural adhesives are derived from a wide range of natural products, including proteins, starch, lignin and tannins [96,98]. Table 10 provides a concise summary of the benefits and drawbacks of each of these natural products as adhesives. (Soy) protein, lignin and starch are commonly by-products of other industries, which makes them inexpensive to obtain and widely available. However, to achieve sufficient water resistance and the required bonding strength, modifications to the natural products are necessary [96,98].

Table 10. Comparison of different bio-based adhesives [96,98].

Biopolymer	Advantages	Disadvantages	
Lignin	Inexpensive to obtain Widely available	Highly complex structure High production cost Low moisture tolerance	Extreme low reactivity (low curing rate) Requires modification
Tannin	Relatively good adhesion High moisture tolerance Fast curing rate	Short adhesive activity Poor water resistance High viscosity	Not widely available
(Soy) protein	Inexpensive Easy to handle Widely available	High viscosity Short pot live Relatively low bond strength Poor water resistance	Sensitive to biological degradation Sensitive to temperature changes Requires modification
Starch	Inexpensive Widely available Easy to handle	Poor water resistance Poor storage stability Relatively low bond strength	Moulds easily Low reactivity High viscosity Modification or grafting required

2.2.3 Additives

An additive is a substance that is added to a mixture to improve different parameters of its properties. They can boost existing properties, suppress unwanted properties or even introduce new properties [99]. There are different functions of additives: fillers, binding agents, reinforcing agents, plasticisers, lubricants/flow promoters or multifunctional additives [100].

In this project to focus for additives is on a plasticiser, reinforcer and filler.

- A reinforcer is a substance or material that improves either or both the physical and mechanical properties of a mixture, such as resilience, toughness, and tensile strength [101].
- A plasticiser is a substance that can improve the flexibility and the workability in order to facilitate the manufacturing process, it could also have a significant effect of the mechanical properties of the hardened mixture [102,103].
- Fillers are commonly used to increase the volume or weight of a mixture, that also can change the physical (or even mechanical) properties [103,104].

In the following paragraphs three different materials will be highlighted: bentonite, natural fibres and wood powder.

Bentonite

The selection of bentonite as an additive was based on the findings of previous studies by Peeters et al. [95], C. Bierach [63] and A. Coelho [62]. Bentonite, a non-toxic type of clay, is found across the globe, including in North America, Europe and Asia. It is an economic, environmentally friendly and high-performance rheological additive, which provides excellent rheological properties such as viscosity, shear-thinning behaviour and thixotropy [105,106].

Numerous studies have investigated the effect of adding bentonite to a 3D printable cement composite. These studies demonstrated that the addition of bentonite, even in small quantities, improves the rheological behaviour of the fresh mixture, including parameters such as viscosity, thixotropy, and shape stability (buildability) of the mixture. Furthermore, it enhanced the compressive strength of the cured elements [106–108]. However, excess addition of bentonite resulted in poor extrudability and consequently led to a reduction in the compressive strength [106].
The utilisation of bentonite as an additive in wood-based 3D printable mixtures has been demonstrated to be beneficial, as demonstrated by C. Bierach and A. Coelho, who demonstrated that bentonite improved the adhesion, the stability and stiffness of the fresh mixture and cured products [62,63]. In addition, J. Peetsers demonstrated that the incorporation of bentonite as an additive in a wood-based mixture resulted in a successfully 3D printed vase [95]. Furthermore, the RISE institute in collaboration with WASP developed a wood-based 3D printable mixture in which bentonite was added to improve the elasticity and hardening properties [63].

Natural fibres

Natural fibres are an eco-friendly reinforcement, due to their abundance, renewability, availability, biodegradability and sustainability. They are also inexpensive and have a low production cost. The most common and commercially available natural fibres in the world include bamboo, cotton, jute, flax, grass, sisal, hemp and coconut and ramie [109,110]. A number of characteristics of these fibres are provided in Table 11. They are well suited in composite materials, due to their favourable properties which include low density, reasonable/acceptable mechanical properties, good strength [109,111]. However, natural fibres also possess several undesired properties, including high water absorption, low melting point, poor moisture resistance, high flammability, low thermal stability and inconsistent quality and irregular dimensions [109–111].
Numerous studies have demonstrated that the addition of natural fibres into 3D concrete printing (3DCP) mixtures results in improved mechanical properties, primarily the tensile and flexural strength [109–112]. Furthermore, in some studies, an improvement of the compressive strength was observed [111]. These fibres have demonstrated to reduce the crack width, lower the shrinkage, improve the mechanical properties and enhance the fresh and rheological characteristics [110]. However, excess addition of fibres can form a challenge in the extrusion process, leading a diminished workability and a reduced mechanical strength [110,111]
The number of studies of bio-based LDM 3D printing with natural fibres is limited in comparison to 3DCP and other additive manufacturing methods, and mainly discontinuous (short) fibres (or powders) have been investigated in composite mixtures [109,113].
Continuous (long) fibres have the potential to improve the mechanical strength more than short fibres, especially in terms of the tensile and flexural strength [113]. An example of a study in which long fibres were utilised as reinforcement is the study of A. Coelho, in which approximately 10 mm long flax fibres were added to the wood-based mixture, resulting in improved strength of the final product. The addition of flax fibres resulted in a denser and drier mixture, while maintaining the original viscosity and consistency. However, a spiralled piston was used during the extrusion process, resulting in the long fibres becoming entangled around the piston, thereby adding resistance during extrusion [62].

Table 11. Characterisation of typical plant fibres [111].

Type of fibre	Fiber Length [mm]	Diameter [µm]	Tensile strength [MPa]	Young's Modulus [GPa]
Bamboo	0.8	19.8	540–630	11–17
Coconut	200–300	500	170–275	3–26
Cotton	25–37	12–35	5.5–12.6	287–597
Flax	6–80	12.4–23.9	800–1500	60–80
Hemp	5–55	10.9–42	550–900	70
Jute	1–6	5–25	393–770	10–30
Ramie	25	155	321.5	16.7
Sisal	0.5–8	10–20	600–700	9.4–22.0

Wood powder

Wood powders, which are made by grinding sawdust/wood particles, are typically composed of particles smaller than 850 µm [114]. Sawdust is a by-product of the agricultural, wood and timber industries, and is widely available, versatile, sustainable, non-toxic and inexpensive. However, the availability and quality can vary depending on the sourcing and processing methods [115,116]. Currently, the majority of sawdust is dumped, burned or used as a low-value energy source, with only a small part being used for the fabrication of fibre/particle boards or other products [116,117].

The utilisation of wood powders is primarily as cheap fillers, which the purpose of increasing the volume of a mixture and thereby reducing the costs due to their low price [116]. Due to their favourable properties, including good thermal and acoustic insulation properties and low weight, they are often incorporated into non-load-bearing concrete or composite materials. Studies have shown that the addition of wood powder can affect physical and mechanical properties such as the viscosity, shear-thinning behaviour, flexural and tensile strength. Some studies demonstrated improvements in the properties, while other studies concluded that the wood powder had a negative effect on these properties [116–118].

The utilisation of wood powders in AM has the potential to transform this low-valued product into a valuable product due to its positive environmental impact and good properties [116]. The number of studies on bio-based LDM 3D printing with wood powders is limited compared to other additive manufacturing methods. Numerous studies have demonstrated adding wood powders to PLA filaments can reduce their cost, enhance their biodegradability and result in increased stiffness and reduced density. In some cases, improvements in tensile strength and modulus have been observed [116,119]. A range of studies have investigated the effects of varying particle sizes and different wood contents of wood powders with different AM processes, these studies are listed in Table 12.

In order to use wood powders in FDM printing, it is necessary that they are around the fine or ultrafine particle size, see Table 13, which describes the particle size classification of wood powders. Smaller particle sizes lead to significantly higher energy consumption and consequently to higher production costs, so using larger particles would be more sustainable [120]. For the LDM method, it has been demonstrated that the larger wood particles can be utilised [114], as can be seen in Table 12.

Table 12. Studies that utilised wood powder with 3D-printing technologies.

AM method	Wood type	Particle size [mm]	Wood content [wt%]	Other (main) material	Reference
FDM	Beech	0.237	50	PLA	Ayrilmis et al. [121]
	Aspen	0.014	-	PLA	Tao et al. [122]
	Poplar	0.150	0-40	Thermoplastic polyurethane (TPU)	Bi et al. [123]
	-	0.5	2.5-10	Acrylonitrile butadiene styrene (ABS)	Chawla et al. [124]
LDM/DIW	Spruce	0.8 – 2	67-85	Gypsum, methylcellulose, cement	Henke et al. [125]
	Beech	0.237	85	UF adhesive	Kariz et al. [57]
	Beech	0.250-0.4	21	Methylcellulose, water	Rosenthal et al. [58]

Table 13. Size classification of wood powder [114].

	Ultrafine	Fine	Intermediate	Course	Wood powders in 3D printing
Size range [mm]	<0.02	0.05-0.5	1-10	>10	0.014-2

Material exploration

3 Material exploration

The objective of the material exploration was firstly to gain an understanding of the interactions between the cellulose and lignin with various binders, and secondly to find the most optimal mixture compositions with the different binders. In order to achieve this, different mixture compositions were produced and assessed on their fresh and cured properties. The most promising mixtures were selected and further optimised and tested with different additives. Finally, the final reference mixtures were selected based on printability, mechanical properties and the most optimal bio-based content.

3.1 Materials and equipment

3.1.1 Materials + resources

The materials were acquired following consultations with R. Gosselink, C. Bierach and A. Coelho, and through independent research. The materials and their resources are addressed in the following paragraphs.

Cellulose

Kraft cellulose

The cellulose utilised in this project was kraft pulp derived from pine wood (softwood) supplied by StoraEnso. The pulp was supplied in the form of bleached paper, and it is prized for its sustainability, strength, and reinforcing properties. The fibres are characterised by their length, slenderness and strength, and provide excellent bonding and tensile properties [126].

Valida L, 3%

Valida is a bio-based, renewable and biodegradable material that contains fibrillated nanocellulose (CNF) and is manufactured and provided by Sappi Maastricht BV. It is used in concrete and concrete admixtures as a sustainable additive, functioning as a stabiliser, rheology and viscosity modifier. Valida L, 3% consists of 3% active fibres and 97% water. The fibres are suspended in water, forming an extensive network that results in a gel-like substance. It has a high viscosity at rest, exhibits excellent shear-thinning behaviour and is thixotropic, which improves the workability and pumpability of mixtures [127].

Lignin

The lignin employed in this study was soda lignin derived from miscanthus, which was provided by WEPA Nederland BV. Through their upgrade of their miscanthus fibre and paper production, another product stream has been made possible, namely the production of a premium circular resource: soda lignin powder [128,129].

Methylcellulose

Methocel® was the provider of the utilised methylcellulose, which is a commercial purified cellulose derivative. It is food-graded (E461) and is frequently used as an additive in food, where it functions as a thickener, stabiliser, or dispersant. Methocel dissolves in cold water and forms a gel in hot water, however, when added to cold water, it causes the material to lump together and form a heterogeneous mixture. The most effective method is to add in to 70 °C hot water [130].

Wood glue

The wood glue utilised in this project was a white PVAc wood adhesive with durability class D2 (EN 204 D2). Class D2 is moisture resistant, suitable for all types of wood, transparent when cured and suited for indoor use [131]. Two adhesive brands were used: Bison and Pattex [132,133], and after some practical investigation it was found that there was no difference in the working of these glues in the mixtures.

Bio-glue

In this study, the VA 104 adhesive from Intercol was utilised. This adhesive is based on a polyvinyl alcohol solution, which is non-toxic and one of the very few vinyl polymers that is water soluble [134]. Its biodegradability depends on the environmental conditions [135]. The adhesive is 100% biodegradable according to the supplier Intercol (S. de Jong, personal communication), therefore VA 104 is considered a bio-glue.

Bentonite

The bentonite employed in this study was a clay product in the form of a very fine powder. It was of volcanic origin, with a highly plastic characteristic, and suitable as an additive to increase the plasticity of a composite material. The bentonite was purchased via the webshop of Silex Totaal Service b.v. [136].

Flax fibres

Flax fibres were selected for use as a natural fibre additive. They have a reasonably long fibre length, and they exhibit one of the highest tensile strengths and Young's modulus of all the common natural fibres (see Table 11). The unidirectional flax tape (FLAXTAPE-200) from Eco-Technilin was utilised in this study, and fortunately this tape was already in stock at the TU/e and was originally purchased via Easy Composites EU B.V. [137]. The advantages of these fibres include a low environmental impact, low weight, high strength in the direction of the fibres and are user-friendliness. The tape could be separated into long individual strands, which were further cut into smaller strands of approximately 10 mm.

Sawdust

The sawdust utilised in this study was supplied by Ir. A. Habraken from the TU/e. Unfortunately, the type of sawdust was not specified, and it was possibly a mixture of different trees. However, it was still utilised in the material exploration to ascertain whether the addition of any type of sawdust delivered a positive result. If that was the case, sawdust with known properties could be acquired.

Figure 43 and Table 14 provide a photo and a list of all utilised materials.



Figure 43. Overview of the materials.

Table 14. Materials corresponding to the numbers in Figure 43.

	Material
1	Bentonite
2	Valida L, 3%
3	Bison wood glue
4	Lignin
5	Kraft cellulose
6	Flax fibres
7	Methylcellulose
8	Sawdust
9	Bio-glue VA104

3.1.2 Equipment

A variety of equipment was used during the material exploration phase. Figure 44 and Table 15 present the equipment. The material exploration experiments were conducted in the SED-lab at Vertigo, which is located at the TU/e campus. This laboratory is equipped with several facilities including an oven, a climate room and an industrial mixer. The oven had a substantial temperature range, enabling the mixtures to be heated to approximately 40 °C during the curing process. The climate room ensured that the temperature and the relative humidity were constant during all the curing stages, with a temperature of 20 °C and an average relative humidity (RH) of 60%. Lastly, the industrial mixer allowed larger batches of mixtures to be manufactured in later phases of the study.



Figure 44. Overview of the equipment.

Table 15. Equipment corresponding to the numbers in Figure 44.

	Materials
1	Piping bags
2	Hot plate
3	Pan
4	Scale
5	Scoops
6	Mixing bowls
7	Measuring cups
8	(Plastic) beakers
9	Pipet
10	Syringes
11	Mixer
12	Blender
13	Rubber spatulas
14	Petri dishes
15	Makita caulk gun

3.2 Method

The material exploration was executed in three distinct phases. Firstly, the mixtures from A. Coelho and C. Bierach were recreated and evaluated on their fresh and cured properties. Subsequently, the compositions and mixing processes were altered to accommodate the available materials and equipment. Finally, reference mixtures were selected for the exploration of the addition of additives and for further testing of the mechanical behaviour and strength.

Figure 45 provides an illustration of the mixture exploration process and with a brief overview of each step provided in the following paragraphs. Following an assessment of the properties of a mixture, it was determined whether the mixture could be improved. If necessary, the composition was modified, and the mixture exploration would restart with mixing. This process was repeated until a final promising mixture composition was found.

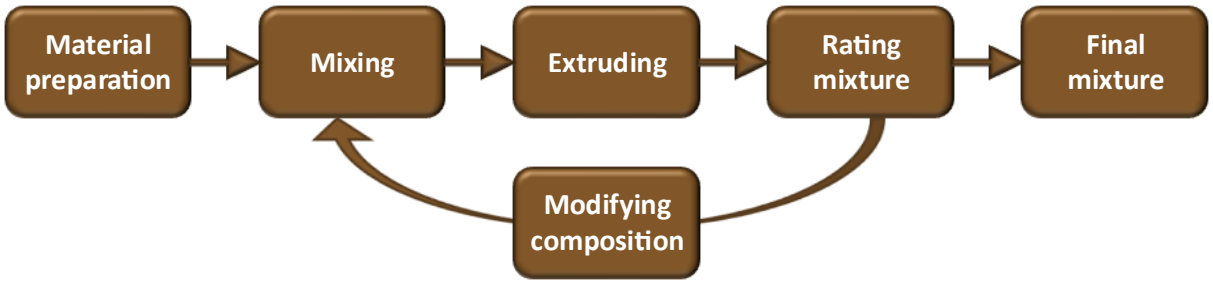


Figure 45. Mixture exploration process

Materials preparation

Prior to the production of any mixture, the materials were prepared. This process entailed cellulose pulping, weighing, heating water or cutting the flax fibres. Cellulose pulping involves separating the cellulose fibres. The large cellulose sheets were cut into smaller chips, which were then shredded in a blender until the chips of cellulose turned into a fluffy ball of separate fibres. The cellulose pulping process is illustrated in Figure 46.



Figure 46. The process of cellulose pulping, from paper sheets to separated fibres.

Mixing

The ingredients were mixed in two stages: dry mixing and wet mixing. In the process of dry mixing, the dry ingredients, cellulose fibres and lignin, were mixed together, and if required, additives were also introduced at this stage. Mixing the dry ingredients ensured that the cellulose fibres were fully separated and had full lignin coverage, which increases the bonding between the materials.

The subsequent wet mixing process involved the initial mixing of the wet ingredients, the binder, a liquid or Valida L, to form a homogenous mixture. Thereafter, the dry ingredients were added to the wet mixture and thoroughly mixed together. This procedure ensured a homogenous mixture with a uniform fibre distribution. Figure 47 to Figure 49 show the end products during the mixing process. Appendix A provides a more detailed elaboration of the mixing processes for each binder.



Figure 47. The mixed dry ingredients.



Figure 48. The mixed wet ingredients.



Figure 49. All the ingredients mixed.

Extruding

Once a mixture was manufactured and appeared to be printable, the mixture was extruded, with the printability of each mixture analysed during the process. Initially, the mixtures were manually extruded using a piping bag or a plastic syringe with a large tip diameter (Figure 50).

As more promising mixtures were manufactured, the Makita caulk gun was used to extrude the mixture, and the printability was assessed even more (Figure 51). The Makita caulk gun, designated as "Makita" in this study, was utilised to print the test and final products. More information about the Makita is elaborated in Chapter 4.



Figure 50. Manual extrusion with the plastic syringe.



Figure 51. Manual extrusion with the Makita.

Rating

A set of five criteria was developed and used to evaluate the various mixtures. The evaluation was based on manual assessment and eye observations, with the criteria divided into two groups: the fresh state and the cured state. Each individual criterion is elaborated in the following paragraphs.

Each criterion was assigned a value rating from -2 to 2, with negative values indicating poor mixture behaviour and positive values indicating good mixture behaviour. The final score of a mixture was determined by adding all the criterion values and could have a maximum value of 10. This final score was then compared to the other mixtures (compositions) and the mixtures with the highest potential were enhanced further until a final promising mixture composition was reached. Which was then subjected to mechanical testing to evaluate its mechanical behaviour.

Fresh properties

- **Homogeneity:** Homogeneity indicates a uniform distribution of materials throughout a mixture, resulting is a mixture that is characterised by a uniform colour and consistency, free from any clumps and large air bubbles.
- **Extrudability:** Extrudability is defined as the ease with which a mixture can be extruded and is primarily based on viscosity and internal adhesion. If the material is too fluid, meaning a low viscosity, the mixture will flow out the extruder without additional pressure. However, if the mixture is too dry, meaning a high viscosity, extruding the mixture will take too much force and thus will not extrude properly. The extruded materials should also form a cohesive string of material, adhering together without breaking.
- **Adhesion:** Adhesion refers to the bond between layers, which is necessary to ensure proper bond strength when the material cured. Conversely, a weak bond has a detrimental effect on the mechanical strength and behaviour of the cured material.

Cured properties

- **Failure behaviour:** The failure behaviour refers to the manner in which an element behaves prior to breaking. A manual force is applied to the extruded elements until the element breaks. There are two distinct failure behaviours: plastic and brittle failure. In the case of a plastic failure, the element undergoes deformation before breaking, whereas in the case of brittle failure, the elements abruptly break without any noticeable deformation. The object is to create a material that undergoes reasonable deformation prior to breaking, and for this to require a relatively substantial breaking force.
- **Curing time:** The term 'curing time' is used to primarily indicate the duration of the curing process, which is determined by the number of days required for a material to fully harden. In addition, factors such as the curing method, whether at room temperature or at an elevated temperature, along with the types of cover utilised, can influence the duration of the curing process. Figure 52 shows the three different cover types.



Figure 52. Different type of covers. A: plastic cover B: glass cover C: wooden cover.

3.3 Mixtures

3.3.1 Methylcellulose

First, an attempt was made to reproduce the methylcellulose mixture of A. Coelho and C. Bierach, the composition of which is provided in Table 16. After preparing the materials and equipment, the cellulose, methylcellulose and lignin were mixed and then 80 °C water was added and continuously mixed until it was a homogenous paste. Since to that the mixture was produced at a higher temperature, the mixture was cooled down in a closed container for at least 24 hours after manufacturing to ensure an optimal consistency. Various mixtures were produced, all with the same composition but different mixing and curing methods.

Figure 53 provides photos of a (extruded) methylcellulose mixture. Photo 1 shows the freshly prepared mixture. Photo 2 shows three extrusions: on the day of mixing (on the left), 24 hours later (middle one) and 48 hours after mixing (on the right). Unfortunately, the paste was not viscous enough and did not have good adhesion for an optimal extrusion. Photos 3 and 4 show the cured extrusions, 10 and 16 days after mixing, respectively. On photo 4, and even better in Figure 54, shows that mould had started to grow on the methylcellulose elements, which eventually took over the whole elements, and consequently impacted the mechanical behaviour, making them too brittle.

Table 16. TU Delft methylcellulose mixture ratio [62,63].

Materials	Content
Cellulose	2.9%
Lignin	29.1%
Water	63.1%
MC	4.9%



Figure 53. Photos of the methylcellulose mixtures: the mixture right after mixing (1), three extrusions that were produced on three consecutive days (2), the three extrusions 10 (3) and 16 (4) days after mixings



Figure 54. Mould began to grow on the extrusions made from methylcellulose.

In the end, 10 mixtures were produced and evaluated, with the overall scores shown in Table 17. More detailed information on the various mixtures, curing processes and individual scores is provided in Chapter B1 of Appendix B.

Despite modifying the mixing and curing processes, it was not possible to produce a promising mixture. The mixtures remained too viscous and with poor extrudability, homogeneity and adhesion and the cured elements simply fell apart. After several days the elements started to grow mould, attempts were made to prevent this by curing the elements in a 40 °C oven for several hours, which ensured that the elements did not become mouldy and to remained in one piece, however this resulted in the elements becoming far too brittle. In addition, where were no fibres visible when it broke, which could have burned away in the oven. Due to the poor results and the mould growth on the elements, it was decided to discontinue with the use of the methylcellulose mixtures.

Table 17. The average ratings for the methylcellulose mixtures.

Curing conditions	Fresh			Cured*		Total
	Homogeneity	Extrudability	Adhesion	Failure behaviour	Curing time	
All	-0.6	-1.2	-0.9	-2	1.5	**-2.9**
Oven	-1.2	-1.8	-1.4	-2	2	**-3.9**
Lab	-0.6	-0.9	-1	-1.9	0.9	**-3.3**

**) Average curing time was 6 days.*

3.3.2 Wood glue

Attempts were made to reproduce the wood glue mixture originally developed by A. Coelho and C. Bierach. The compositions of the attempts to reproduce the mixture are presented in Table 18, with mixtures 1, 3 and 5. After preparing the materials and equipment, the cellulose and lignin were mixed and then added to the wood glue (and water). While A. Coelho and C. Bierach previously heated the bowl during mixing, this study found no benefits to heating the wood glue. Therefore, the same composition was repeated without heating during mixing, resulting in mix 5. This showed great adhesion during extrusion and between layers, and excellent failure behaviour. With an overall score of 9 when cured at room temperature, mix 5 proved to be a promising mixture.

However, due to the high content of wood glue, only 20% of mix 5 was bio-based. Several attempts were made to increase the bio-based content while maintaining the excellent properties of the wood glue mixture. This was mainly achieved by adding Valida to the mixture and increasing the lignin content and reducing the wood glue content. This resulted in the promising mixes 18, 28 and 35, which are also given in Table 18. In addition, an attempt was made to increase the amount of cellulose fibre, however, this proved to be detrimental to the consistency and reduced the extrudability.

Table 18. Wood glue mixture compositions.

Mix	Lignin	Cellulose	Wood glue	Valida	Water	Bio-based content	Comment
1*	19.7%	2.0%	65.2%		13.1%	35%	TU Delft, water was added
3*	16.8%	2.8%	80.4%			20%	TU Delft, no water
5	16.6%	2.9%	80.5%			20%	TU Delft, without heating
18	24.2%	3.6%	48.2%	24.0%		52%	Increase bio content
28	22.7%	3.4%	45.5%	28.4%		55%	Decrease cellulose fibres
35	21.6%	2.7%	43.2%	32.5%		57%	Increase Valida content

**) Heated while mixing*

Figure 55 to Figure 57 present a series of photographs of some wood glue mixtures with different curing processes and the ratings of the promising mixes are provided Iin Table 19.
Figure 55 shows mix 1, having an average score of 8.5. The fresh mixture exhibited excellent properties, however, its cured properties could be improved. Over time, the elements initially became darker brown before gradually turning white.
Figure 56 demonstrates that the curing process in an oven did not result in excessive shrinkage. The colour of the element was found to be somewhat more 'true' brown when cured in the oven compared to the element that was cured at room temperature. However, upon evaluation, it was observed that the element cured in the oven scored significantly lower at the failure behaviour compared to the element cured at room temperature. The element had become too brittle and no fibres were visible after breaking.
As demonstrated in Figure 57, the application of a plastic cover during the curing process appeared to slow down the curing process. Whereas the elements with the wooden cover turned white after 12 days, the elements with a plastic cover turned white after 21 days.



Figure 55. Photos of wood glue mix 1: fresh extrusion (1), after two (2) and six (3) days.



Figure 56. Photos of wood glue mix 5: fresh extrusion (1) and after five days (2). Extrusions were cured in the oven for 94 hours (a) or at room temperature (b).

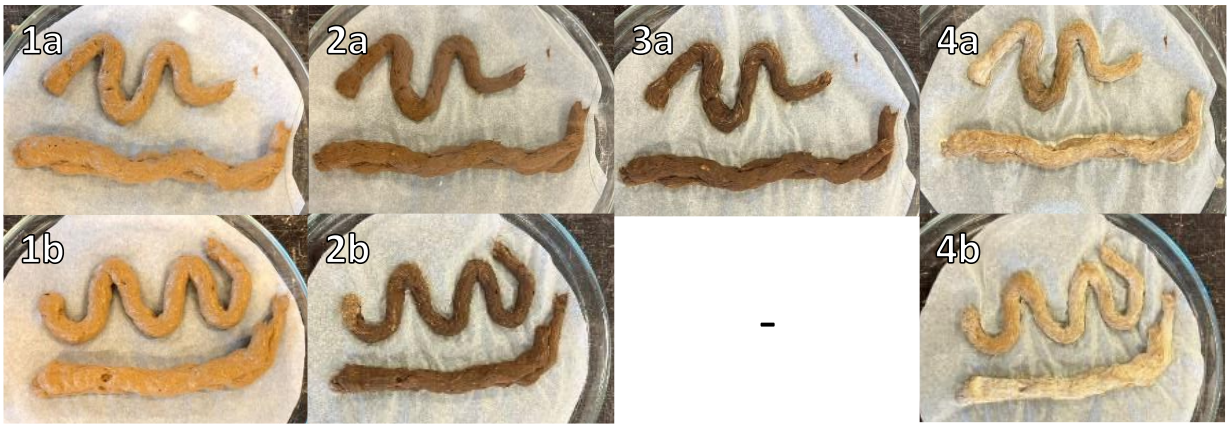


Figure 57. Photos of wood glue mix 35: fresh extrusion (1), after seven (2), 12 (3) and 21 (4) days. Extrusions were cured with a plastic cover (a) or with a wooden cover (b).

Table 19. The rating of a few selected wood glue mixtures.

Mix	Curing conditions	Fresh properties			Cured properties		Final rating
		Homogeneity	Extrudability	Adhesion	Failure behaviour	Curing time	
1	Lab	2	2	2	-2	2	8
	Lab	2	2	2	2	1	9
3	Oven	0.5	0.5	2	1	2	6
	Lab	0.5	0.5	2	2	-1	4
5	Oven	2	1.0	2	-2	2	5
	Lab	2	1.0	2	2	2	9
18	Lab	2	2.0	2	2	1.5	9.5
28	Climate room	2	2.0	2	2		8
35	Wood cover	2	2.0	2	2	2	10
	Plastic cover	2	2	2	1.7	1.5	9.2

Following a comprehensive analysis, mix 35 demonstrated the highest bio-based content, while maintaining the excellent properties that were previously observed. It was assigned an overall score of 10 and 9.2 for a wood and a plastic cover, respectively. More detailed information on all wood glue mixtures, curing processes and individual scores is provided in Chapter B2 of Appendix B.
The wood glue mixtures obtained relatively high scores for their fresh properties, with the potential to enhance their cured properties. Given these findings, it was determined that wood glue mix 35 would be utilised as the first reference mixture for further investigation.

3.3.3 Bio-glue

The experimentation with bio-glue mixtures began at a later stage than the experiments with wood glue and methylcellulose, due to issues regarding the availability of resources. The starting point for the bio-glue mix was therefore wood glue mix 16, with almost the same composition repeated for bio-glue mix 1, but with bio-glue instead of wood glue.
The mixing process of the bio-glue mixtures is identical to the mixing process of wood glue, but instead of wood glue the bio-glue is utilised. Due to the substitution of wood glue with bio-glue, this mixture is considered to be 100% bio-based. More detailed information on all bio-glue mixtures, curing processes and individual scores is provided in Chapter B3 of Appendix B.
The first attempt was a promising mixture with an overall score of 8.5. following a series of alterations and evaluations, the final composition, mix 4, was achieved with an overall score of 9 and 9.8 for a plastic cover and no cover, respectively. The compositions of mix 1 and mix 4 are provided in Table 20 and Table 21 presents their respective ratings.
As demonstrated in Figure 58, which presents mix 4, the bio-glue mixture initially transitions to a darker brown colour before gradually turning white.

The bio-glue mixtures also received relatively high scores for their fresh properties, with the potential to enhance their cured properties. In light of these findings, it was determined that bio-glue mix 4 would be employed as the second reference mixture for further investigation.

Table 20. Bio-glue mixture compositions.

Mix	Lignin	Cellulose	Bio-glue	Valida
1	27.5%	2.7%	54.8%	15.0%
4	27.8%	2.8%	41.7%	27.8%

Table 21. The rating of a few selected wood glue mixtures.

Mix	Curing conditions	Fresh properties			Cured properties		Final rating
		Homogeneity	Extrudability	Adhesion	Failure behaviour	Curing time	
1	Wooden cover	1.5	2	2	1.5	1.5	8.5
4	Plastic cover	2	2	2	2	1	9
	No cover	2	2	2	1.8	2	9.8



Figure 58. Photos of bio-glue mix 4: fresh extrusion (1), after nine (2) and fifteen (3) days. Extrusions were cured with a plastic cover (a) or with no cover (b).

3.4 Additive exploration

The exploration of the final composition of the wood- and bio-glue mixture, as well as the exploration with additives, occurred simultaneously. The available additives were bentonite, flax fibres and sawdust. The preparation of the additives consisted of several steps. The bentonite was used as is, the long flax fibres were cut into smaller strands of approximately 10 mm and the sawdust was ground to smaller pieces.

The objective of the additive exploration was to add as much of one additive as possible without changing the amount of the other materials and improving (or at least maintaining) the fresh and cured properties. Several attempts were executed with the three different additives. The quantities of each material required to produce one batch are provided in Table 22. On batch was based on the amount of material that could fit in one Makita cartridge. The reference mixtures refer to the mixture compositions determined in the previous sections, without any additives. A table with the ratios instead of quantities is provided in Chapter B4 of Appendix B.

The first significant finding was the addition of the ground sawdust, which drastically altered the materials failure behaviour, causing the cured elements to become too brittle. In addition, sawdust was added with the aim of increasing the volume of the mixture. However, the amount of sawdust that was required to achieve this would have caused the mixture to be too dry, leading to poor adhesion, extrudability and even poorer cured properties. Consequently, it was decided to eliminate sawdust from further research, as its use as an additive would no longer be a suitable option.

The addition of bentonite affected the fresh and cured properties, and depending on the amount added, it could drastically change the adhesion and the failure behaviour. However, after a series of experiments, a viable ratio of bentonite was ultimately determined. Table 22 shows two different quantities for bentonite with the bio-glue mixture: 75 and 37.5 gram, respectively 6.5% and 3.4% of the total weight of the corresponding mixture. In the exploration phase, the mixture with 6.5% bentonite was deemed optimal, however, during the printing phase (addressed in Chapter 4), this mixture was found to be too dry and had insufficient adhesion. Consequently, the amount of bentonite was reduced by half for subsequent batches, resulting in a mixture that exhibited good adhesion.
The addition of a small amount of flax appeared to have a negligible impact on the fresh properties of the mixture. However, the addition of this small amount was evident during the mixing process, as the fibres were visible everywhere. Furthermore, after the curing and breaking of the elements, the longer fibres were clearly visible inside the cracks. This is illustrated in Figure 59 and Figure 60, which show the visible fibres in a crack of a broken bio-glue element without flax and with flax, respectively.

Table 22. Final mixture quantities for one batch.

Mix		Lignin [g]	Cellulose [g]	Glue [g]	Valida [g]	Bentonite [g]	Flax [g]	Total weight [g]
Wood glue	Reference	200	25	400	300			925.0
	Bentonite	200	25	400	300	37.5		962.5
	Flax	200	25	400	300		10.0	935.0
	Bentonite + flax	200	25	400	300	37.5	10.0	972.5
Bio-glue	Reference	300	30	450	300			1080.0
	Bentonite 6.5%	300	30	450	300	75.0		1155.0
	Bentonite 3.4%	300	30	450	300	37.5		1117.5
	Flax	300	30	450	300		11.2	1091.2
	Bentonite + flax	300	30	450	300	37.5	11.2	1128.7



Figure 59. Broken bio-glue element.



Figure 60. Broken bio-glue with flax element.

3.5 Discussion and conclusion

The methylcellulose mixtures created in this study exhibited numerous shortcomings. Firstly, the fresh properties of the mixtures from TU Delft were never reached, meaning that the mixture was unsuitable for good extrusion. Secondly, when eventually extruded, the mould growth had a significantly detrimental effect on the cured elements, which made them unmanageable.
A range of different attempts were made to create a promising mixture, including methylcellulose from different (uncontaminated) containers, distilled/demi water instead of tap water, different water temperatures, different methylcellulose amounts, different oven temperatures and different covers during the curing process. Further exploration of the mixing and curing process even more could have potentially resulted in a homogeneous, extrudable 100% bio-based mixture. However, due to the time constraints of this study and the positive outcomes of the other mixtures, it was decided to discontinue the exploration of the methylcellulose mixtures.

The reasons for the colour change from brown to white has not been thoroughly investigated. One possible cause of this colour change could be the Valida, since the elements remained brown when Valida was not added. Another potential factor could be the presence of limescale in the utilised tap water. Lime often leaves a white limescale residue behind after water has evaporated, however, the utilisation of filtered water instead of tab water has not been investigated. At the end of the exploration phase with the wood glue mixture, a material called “calcium carbonate” was added to investigate its potential to prevent this colour change. However, it did not only fail to prevent the colour change, it also had a negative effect on the brittleness. Ideally, for aesthetic purposes, the elements would maintain a brown colour after the curing process, thereby resulting in more “wood-like” elements.

Although the wood glue mixture was not fully bio-based, based on its promising results, it was decided to proceed with it through the next phase. However, given that the objective of this study was to find a bio-based 3D printable material, the wood glue mixture was still included in the next stages of the study, but with the bio-glue mixture having the advantage of being bio-based.

In order to extrude the material with the Makita, it was necessary to fill its cartridge. The process of filling this cartridge was not without difficulties, especially with air bubbles trapped within the cartridge. The presence of air bubbles is detrimental to the extruding process, causing gaps in the material while extruding, and consequently resulting in poor adhesion. The possible solutions to this problem are addressed in Chapter 4.

The curing process was determined on the basis of the available material and equipment. However, it is possible that a different humidity, temperature or covering conditions could have accelerated the curing process, and limit or even eliminate any shrinkage or warping. It was concluded that curing in an oven at 40 °C is detrimental for the cured properties of an element, as they became too brittle, with no fibres visible in the cracks. Curing at room temperature meant that the elements were cured in the temperature of the large SED-lab, which is never stable due to the large size of the hall, the various activities and the possible influence of the weather outside. The climate room ensured that the temperature and humidity were constant, however, it was not investigated if these conditions were the most optimal for the curing process.
In the case of the various covers, it was observed that curing without any cover caused the element to cure too quickly, with larger (eyeballed) shrinkage and more warping of the element compared to elements that were cured with a full cover. A glass cover caused the element to cure too slowly, due to the “lack” of evaporation of the water. A wooden cover with holes and plastic cover performed almost the same, if the plastic was not fully sealed at the edges. The curing time was observed to fall in between that of a full glass cover and no cover. It was determined that, taking larger elements into consideration, the plastic film cover was selected as the optimal curing method.

Shrinkage has not been a primary focus in this exploratory phase, instead, the warping and shrinkage were visually estimated and was solely considered for the most effective curing method. The extruded elements showed signs of shrinkage in length and height, and some warping occurred during the curing process. This could have negatively effect on a larger 3D-printed element, impacting the layer bond and the final dimensions. Reducing the shrinkage and warping has not been investigated thoroughly, however, in the following phases the actual shrinkage was measured and in the final phase, the warping was addressed by adding “constraints” to the element to ensure they remained relatively flat.

Based on the material exploration two mixtures were selected as references: a wood glue and a bio glue mixture. The mechanical properties of these mixtures were determined by conducting a series of mechanical tests. Based on these test results, one mixture was selected for further investigation into the effects of the additives on the mechanical properties, see Chapter 5. However, before testing the mechanical properties, the printability was investigated and described in the following chapter.

PRINTABILITY EXPLORATION

4 Printability exploration

This chapter only presents a concise summary of the printability exploration. For a detailed elaboration of this process, please read Luc Roex's research report.

4.1 Robot setup

The robot used in this study was an ABB IRB 1200- 5/0.9, a six-axis robot with six degrees of freedom (DOF), a loading capacity of five kilograms, and a radius of 0.9 metres [138]. This robot was available in the SED-lab and was equipped with the Makita through a steel connector element. The robot with the Makita is displayed in Figure 61 and Figure 62 shows the Makita. The Makita uses a piston (push bar) to extrude material by applying pressure to the contents of the cartridge. The flow rate of the material depends on the nozzle, the speed settings of the Makita, and the material itself.

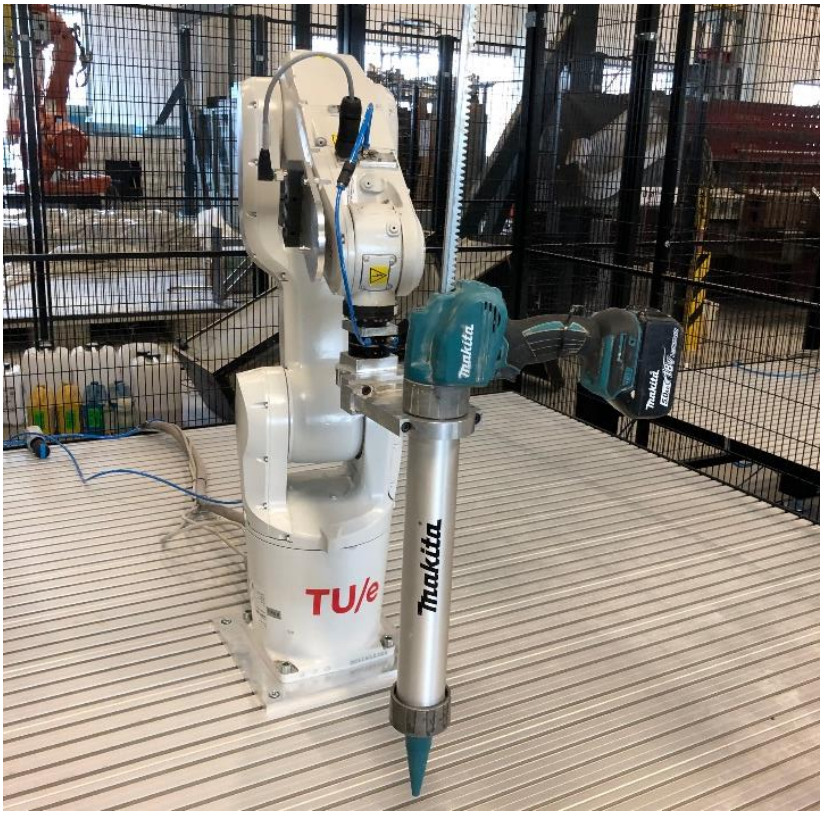


Figure 61. ABB IRB 1200- 5/0.9 with the Makita.

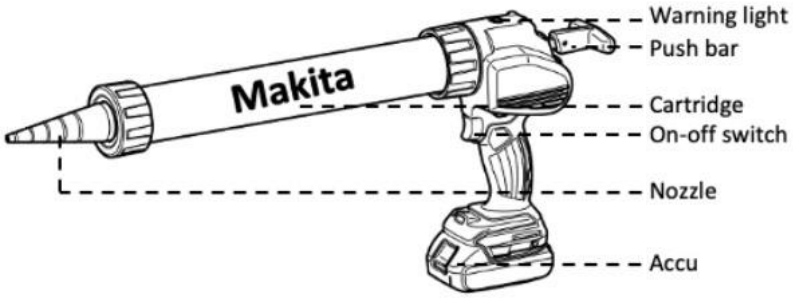


Figure 62. Makita components [139].

It is possible to attach different nozzles to the Makita. In this study, two nozzles were utilised: a rectangular nozzle and a round nozzle, both illustrated in Figure 63. The rectangular nozzle was used for the fabrication of the test beams and the round nozzle was used for the final element.

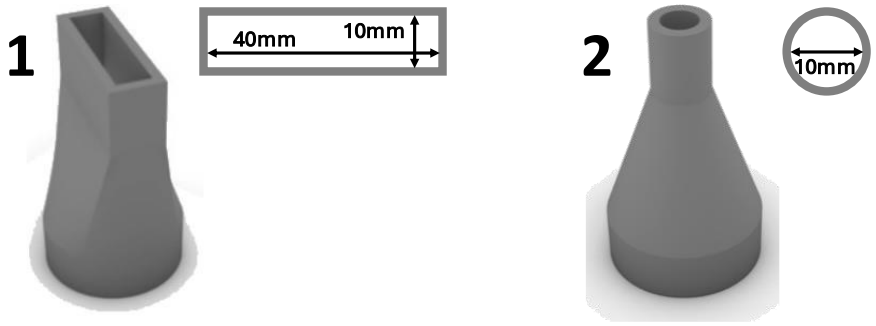


Figure 63. The rectangular nozzle (1) and the round nozzle (2).

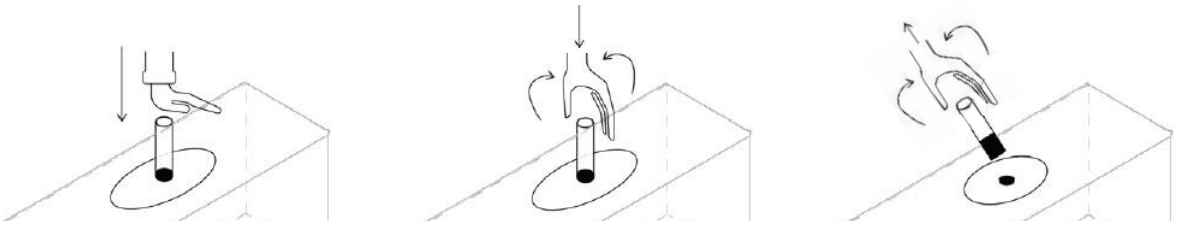
Air bubbles were frequently observed within the material and cartridge, with these air bubbles having a detrimental effect on the quality of the printed elements. In particular, large air bubbles led to gaps in the extruded material. Several processes were investigated in order to remove these air bubbles:

- The mixture was placed on a vibrating table.
- The mixture was folded like wedge clay [140].
- Using a vacuum pugmill [141].

However, due to the viscosity of the mixtures the first two options were not suitable. The mixtures were not sufficiently liquid to shake out all the air bubbles, but they were too liquid to be folded. The viscosity of the mixtures would be suitable for a vacuum pugmill, but unfortunately this was not available in the SED-lab and too expensive to purchase. Consequently, the process of filling the cartridge had to be executed in a particular manner to avoid the formation of large air bubbles within in the cartridge. The following steps describe the filling process, which is also illustrated in Figure 64:

1. Knead the mixture into a homogenous ball.
2. Press it down on a flat piece of hard plastic or a sheet of parchment paper.
3. Put the cartridge down on to material and press softly.
4. Rotate the cartridge while pressing it fully down in the material.
5. Remove the cartridge from the material while rotating still/
6. Repeat these steps until the cartridge is full.

Provided that all the print parameters were sufficiently fine-tuned, following these steps guaranteed a continuous stream of material while extruding.



Place the cartridge on top op the material and press gently

Rotate the cartridge while pressing its fully into the mixture

Remove the cartridge while rotating and repeat until cartridge is full

Figure 64. Diagram to describe how the material is inserted into the cartridge [63].

A drawback of this robot setup was that the extrusion was not controlled by the script, the Makita could only be switched on and off manually. To start a print, the Makita was activated, and the trigger was held in place with a tie-wrap, after which the robot was started directly. These actions should occur at roughly the same time, which was difficult when printing alone. Ideally, a pump would have been used to supply the robot with the mixture. Utilising a pump would allow for a continuous stream of material and the controls of the pump could be integrated into the script, thereby making the printing process more streamlined and efficient. However, the use of a pump was briefly considered but rejected due to the fact that the mixture was not sufficiently liquid, and the quantity of material required for using the pump was not feasible, which would have resulted in a significant amount of material being wasted in the pump hose, which was not deemed viable.

4.2 Print parameters

To achieve perfectly printed elements, the optimal printer settings were determined, and the print parameters that were investigated were the pressure, print speed and nozzle standoff distance.

The pressure applied by the Makita on the material within the cartridge influences the material's flow rate, which is dependent on the push bar speed. This push bar speed can be adjusted through a dial, as illustrated in Figure 65. This push bar presses the material out of the cartridge through the nozzle. The push bar speed of the Makita is henceforth called the Makita pressure, and is set to 2 until otherwise is indicated.

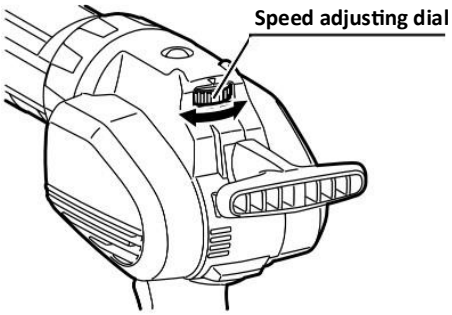


Figure 65. The speed adjusting dial of the Makita [138].

The print speed is defined as the velocity at the tip of the nozzle and has a unit of mm/s. The print speed was adjusted to the Makita pressure, with the objective of achieving a continuous stream of material. The optimal print speed was determined through a series of tests, of which an example is displayed in Figure 66. The first line was printed with a print speed of 37.5 mm/s, and after each corner this print speed decreased. A series of tests were executed for each mixture to determine the most optimal print speeds, the results of which are listed in Table 23.

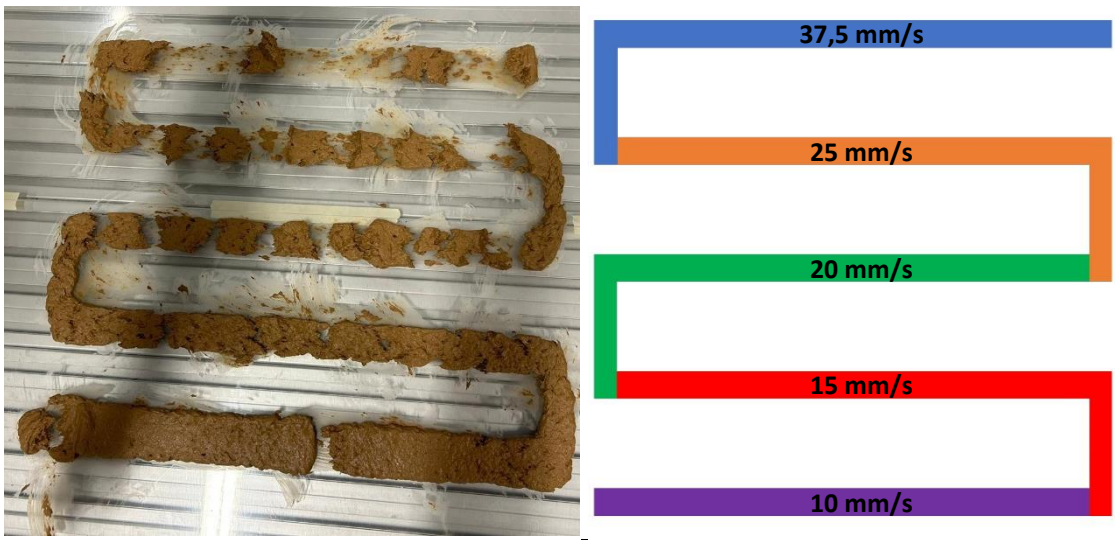


Figure 66. The result of a print speed test, with its course on the right showing the print speed per line.

Table 23. Final print speeds of the reference mixtures.

Reference mixture	Print speed [mm/s]
Wood glue	15.5
Bio glue	16.5

The nozzle standoff distance is defined as the distance between the nozzle tip and the top of the work surface, which could be the print bed or a previous layer. Following a series of tests, two different distances were selected: one for the first layer and one for the subsequent layers. The nozzle standoff distance for the first layer was 10 mm and for the subsequent layers was 9.5 mm, as demonstrated in Figure 67.

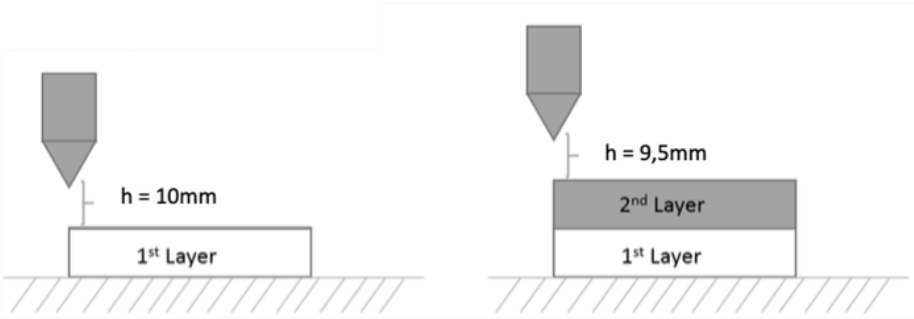


Figure 67. The nozzle standoff distances for the first and subsequent layers.

4.3 Printed test beams

The robot was controlled using a RAPID code that was implemented in Robot Studio. This RAPID code was created with the program Grasshopper and the plugin "Robot Components". Utilising this code test beams were printed with dimensions of were 250 mm in length, 40 mm in width and five layers in height. Following a series of print sessions, a total of 29 test beams were produced, 14 of which were made from the wood glue mixture and 15 from the bio glue mixture. The average curing time for the beams was 21 days, with ± 7 days with a plastic film cover, ± 7 days without a cover, and finally ± 7 days with the beams turned upside down. The test beams were stored in the climate room throughout the entire curing process. Figure 68 and Figure 69 depicts a freshly printed and a cured test beam, respectively.



Figure 68. A freshly printed test beam.



Figure 69. A cured test beam.

Subsequent to the selection of a reference mixture was selected, new test beams were produced from this reference mixture with additives. These test beams were subjected to the same curing conditions as the reference mixtures. Appendix C provides detailed information about the curing process of each individual test beam.

The dimensions of the test beams made from the selected reference mixture with additives were measured, directly after printing and, if possible, right before testing. The measured dimensions were the length, height and width. If possible, the weight was also measured right before testing. With these fresh and cured dimensions the shrinkage of each beam was determined. Table 24 shows the average shrinkage of the printed beams after curing. The exact dimensions and shrinkage per individual test beam are provided in Appendix C.

Table 24. Average shrinkage of the test beams.

Additive	Length shrinkage [%]*	Height shrinkage [%]*	Width shrinkage [%]*
Bentonite	10	18	11
Flax	7	24	11
Bentonite with flax	8	24	17

**) Compared to the original dimensions of the freshly printed element*.

Following the curing process, it was observed that the width shrinkage was uneven, with the top layers shrinking more than the bottom layers. Unfortunately, this shrinkage could not be measured due to the inability to accurately measure the width of the bottom layer when it was freshly printed. A cross-section of a cured test beam is displayed in Figure 70, which shows a trapezoid-like cross-section.

The test beams shrunk considerably during the curing process, especially the height decreased significantly more compared to the other dimensions. The fresh mixtures contained a relatively large amount of liquid, which could have caused the elements to shrink while curing, due to the evaporation of this liquid.
A potential explanation for the observed larger height shrinkage could be attributed to the relatively low strength of the fresh mixture. The weight of the layers may have caused the bottom layers to be compressed, thus resulting in a larger reduction in height compared to the other dimension.
The uneven width shrinkage may be attributed to the fact that the top layer has a larger exposed surface area compared to the other layers. This may have caused more rapid evaporation of the moisture within the layer, causing it to cure quicker and consequently shrink more than the layers that had less exposed surface area.
The right curing conditions could cause less shrinkage in the test beams. The current test beams were all cured inside the climate room. However, the removal of the plastic and turning the beams upside down did not happen at the exact same moment, which leaves small differences in the curing process, which can cause difference in the shrinkage of the beams. However, this was not further investigated because it fell outside the scope of this research

In addition to the shrinkage of the test beams, warping was also observed. This was addressed with turning the beams upside down. The warping of a test beam after ± 14 days of curing is demonstrated in Figure 71, where the ends of the beam elevated compared to the middle.



Figure 70. A cross-section of a cured beam.



Figure 71. The warping of a test beam after ± 14 days of curing.

MECHANICAL PROPERTIES

5 Mechanical properties

This chapter explores the mechanical properties of the mixtures. The compression and flexural strength are researched, and their respective moduli are determined. These mechanical properties are determined by executing compression tests and flexural tests. Figure 72 shows the specimens that are used for the tests. Only for the compression tests, test beams were cut into cubes of roughly 4x4x4 cm.

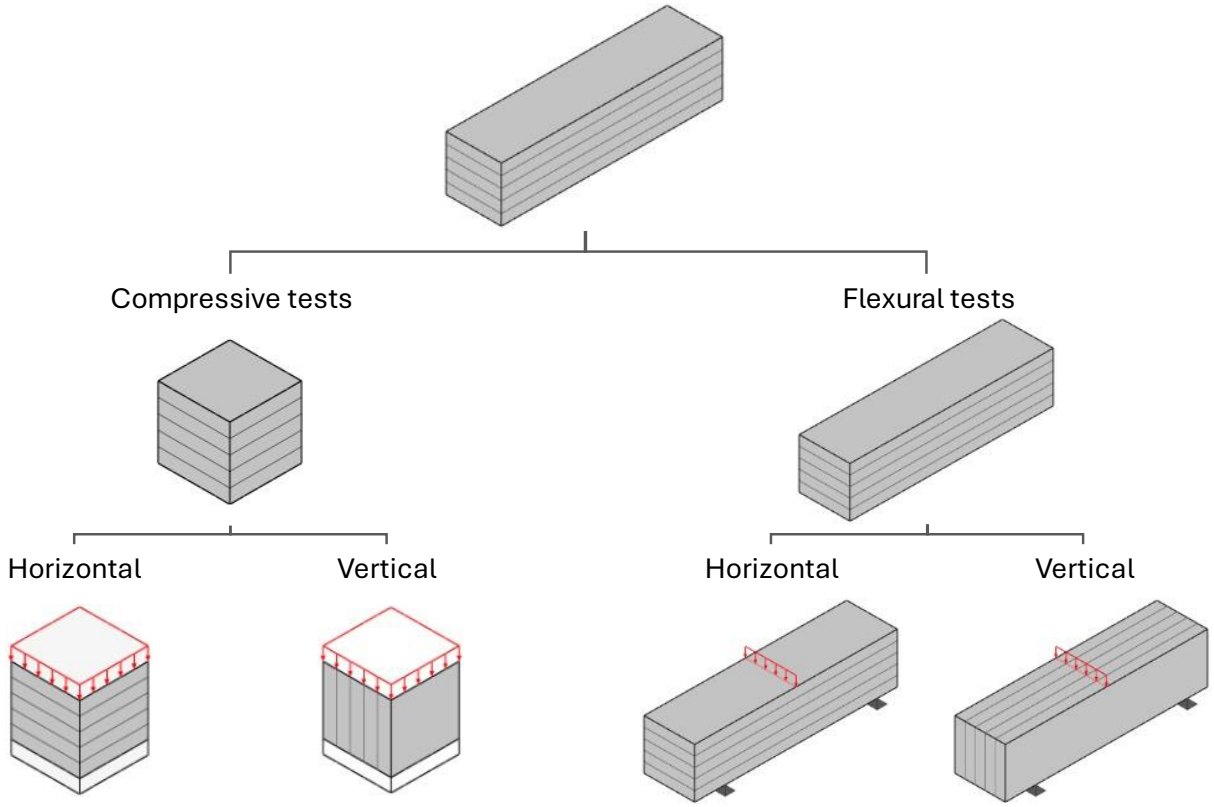


Figure 72. The different specimen orientations used for testing.

In the following sections the setup and method of both the compression and flexural tests are explained. After that, the results of the two reference mixtures are presented and discussed. On the basis of these results, one of the reference mixtures is selected for further research. After that, the impact of the additives is investigated, and the results are presented. Following the discussion, a final mixture is chosen to print the final element.

5.1 Test setups

5.1.1 Compression tests

Setup

The compression test setup was based on the standardised cement mortar test of the NEN-EN 196-1:2016 [142]. The setup consisted of a rigid steel frame (Figure 73) which was placed in the Schenck Trebel test bench with a 100 kN load cell (Figure 74).

The rigid steel frame consisted of a fixed bottom plate of 40 x 40 mm and a movable top part. The lower end of the movable part also has a plate of 40 x 40 mm connected by a hinge to the rest of the movable part. In the tests, the load is applied on the large round plate at the top of the movable part.

The specimens were placed in between the two 40 x 40 mm plates and for compression, the movable part was pushed down. This movable has a limited displacement of 14.5 mm as otherwise the load acts on the whole steel frame. Therefore, if a specimen had not enough height to be compressed within this frame, small plates were added to the bottom plate to ensure that the full specimen would be compressed.



Figure 73. The rigid steel frame of the compression test setup.

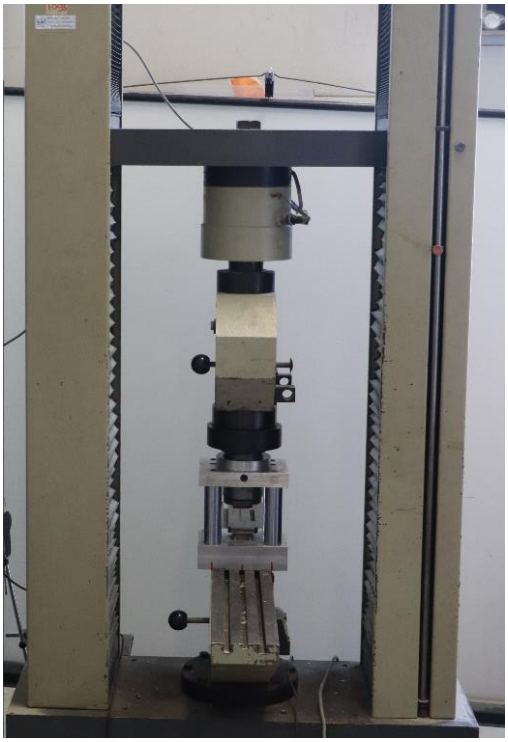


Figure 74. The rigid steel frame in the Schenck Trebel test bench with a 100kN load cell.

Specimens of roughly 40 x 40 x 40 mm were used, and they were tested with two different layer orientations, as mentioned in the beginning of Chapter 5.
The test was displacement controlled with a speed of 2 mm/min, and the vertical displacement and force applied on the specimen were measured. These values were then used to calculate the compressive strength (f_c), the compressive strain and the compression modulus (E_c).

Figure 75 and Figure 76 show the crack patterns that occur in the compression specimens. The crack patterns in the specimens with a horizontal layer orientation are similar to the crack patterns of cement mortar compression cubes [143]. The cracks of the specimens with a vertical layer orientation ultimately result in separation of the layers.

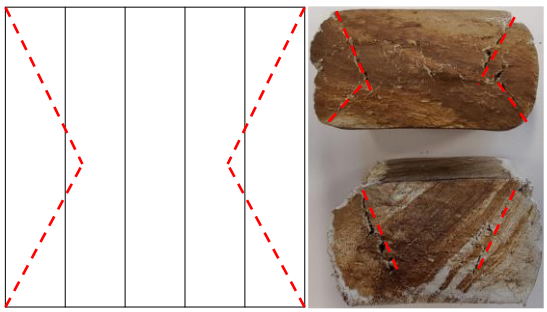


Figure 75. The crack pattern of the compression specimens with a horizontal layer orientation. With on the left a simplified drawing of the crack pattern and on the right two cracked specimens.

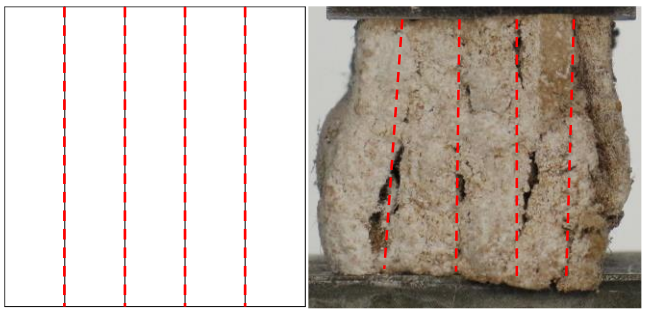


Figure 76. Crack pattern of the compression specimens with a vertical layer orientation. With on the left a simplified drawing of the crack pattern and on the right a cracked specimen.

Test cycles

The compression test consisted of three cycles, each being repeated three times (sub-cycles). In Table 25, each sub-cycle with its corresponding desired displacement is given. Between each sub-cycle the pressure was fully released for one minute, in order to allow the specimen to bounce back if possible. After this minute, the pressure was increased again until the desired displacement was reached.

Table 25. The nine different sub-cycles and the displacement that was reached at the end of each cycle.

Cycle	Displacement [mm]	Cycle	Displacement [mm]	Cycle	Displacement [mm]
1.1	4	**2.1**	8	**3.1**	12
1.2	4	**2.2**	8	**3.2**	12
1.3	4	**2.3**	8	**3.3**	12

Compressive stresses, strains and compression modulus

The compressive stresses are calculated with equation 1, and the strains with equation 2.

$$f_c = \frac{F}{A} \qquad 1$$

In which: f_c = *compressive stress [MPa]*
F = *force [N]*
A = *Cross-sectional area [mm²]*

$$\varepsilon = \frac{h}{\Delta h} \qquad 2$$

In which: ε = *strain [-]*
h = *height of uncompressed specimen [mm]*
Δh = *height difference = displacement [mm]*

The compressive strength (f_c) is calculated at the end of cycle 1.1. The compressive strength is the calculation strength that is utilised in the calculations in Chapter 6. The ultimate compressive stress (f_{cu}) is the maximum stress reached during the test. This maximum stress occurs usually at the end of cycle 3.1, but it might also appear earlier during the test.

Through the values of cycle 1.1 a linear trendline is generated with excel, the slope of this trendline indicates the compression modulus (E_c). The R^2 value indicates the fitness of the trendline with the actual graph. The closer the R^2 value is to 1.0, the more accurate the trendline predicts the values of cycle 1.1. Figure 77 shows an example of a stress-strain diagram of a compression test.

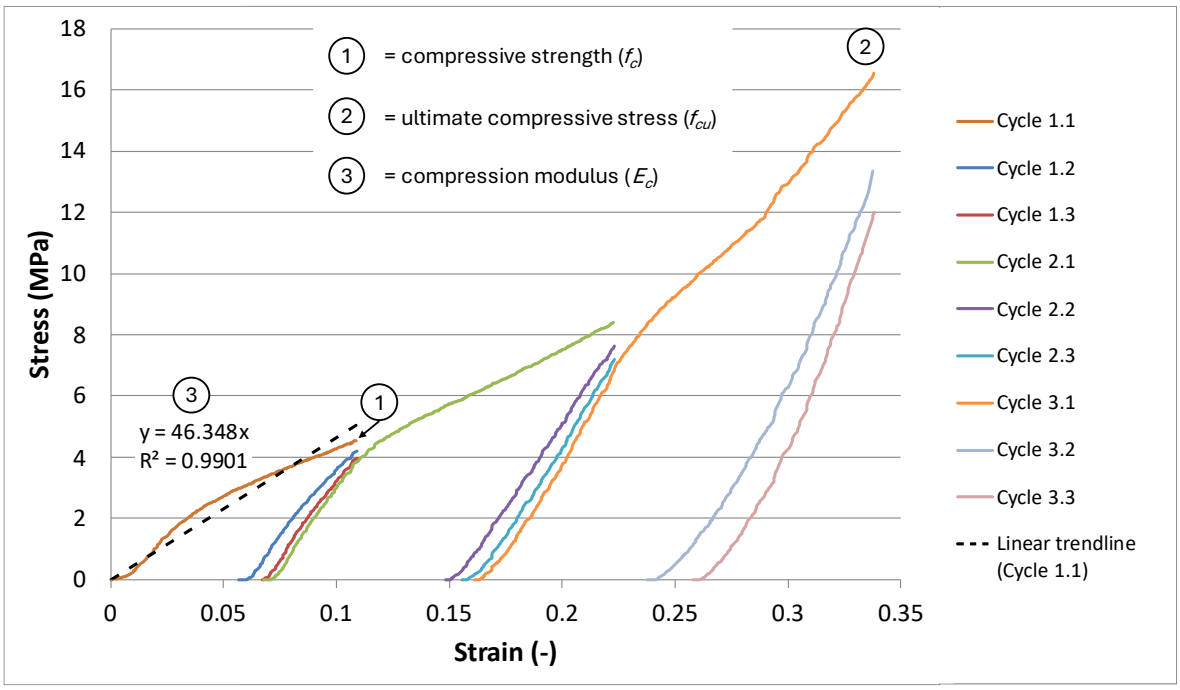


Figure 77. Example of a stress-strain graph of a compression test.

5.1.2 Flexural tests

Setup

The flexural tests were three-point bending tests based on the standardised cement mortar test of the NEN-EN 196-1:2016 [142]. The standardised tests have a span of 100 mm. In this research, however, the span is increased to 220 mm to ensure that the specimens are actually subjected to bending and to minimise the shear stresses. Figure 78 depicts a mechanical scheme of this test. And Figure 79 shows the test setup in an Schenck Trebel test bench with a 100 kN load cell.

The dimensions of a printed test beam were roughly 40 x 40 x 250 mm, and they were tested with two different layer orientations, as mentioned in the beginning of Chapter 5.

The test was displacement controlled with a speed of 3 mm/min, and the vertical displacement and force applied on the specimen were measured. These values were then used to calculate the flexural strength (f_b), the flexural strain and the flexural modulus (E_b).

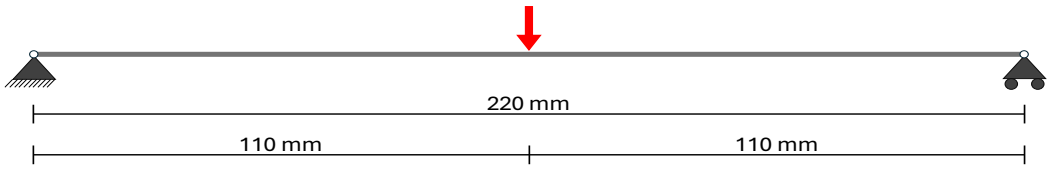


Figure 78. Mechanical scheme of the flexural tests.



Figure 79. Test setup of the three-point bending tests in the Schenck Trebel test bench with a 100kN load cell.

Analysis different support conditions

The tests were unintentionally executed with two hinges instead of one roller and one hinge. To check whether the different support conditions significantly affected the stress levels of the specimen, a numerical analysis in GSA was executed. For this analysis only the maximum displacement and the maximum compressive and tensile stresses were taken into account. It was concluded that these values did not differ significantly. Therefore, the tests were considered similar to tests with one hinge and one roller. For more a more details analysis, see Chapter D1 in Appendix D.

Flexural stresses (tensile stresses)

The stresses at the bottom of the specimen at any point during the flexural tests are calculated with equation 3. These specific stresses are always tensile stresses. The calculation of the second moment of inertia will be addressed in the following paragraph.

$$f_b = \frac{M * z}{I} \qquad 3$$

In which: f_b = *flexural stress i.e. tensile stress [MPa]*
M = *moment in the middle of the specimen [Nmm]*
z = *the distance between the line of gravity and the bottom of the specimen [mm]*
I = *second moment of inertia [mm^4]*

The ultimate tensile stress (f_{bu}) is the maximum stress that is reached during the test. The tensile strength (f_b) is calculated at the end of the linear part of the graph. The tensile strength is the calculation strength that is utilised in the calculations in Chapter 6. Figure 80 shows an example of a stress-strain diagram of a flexural test.

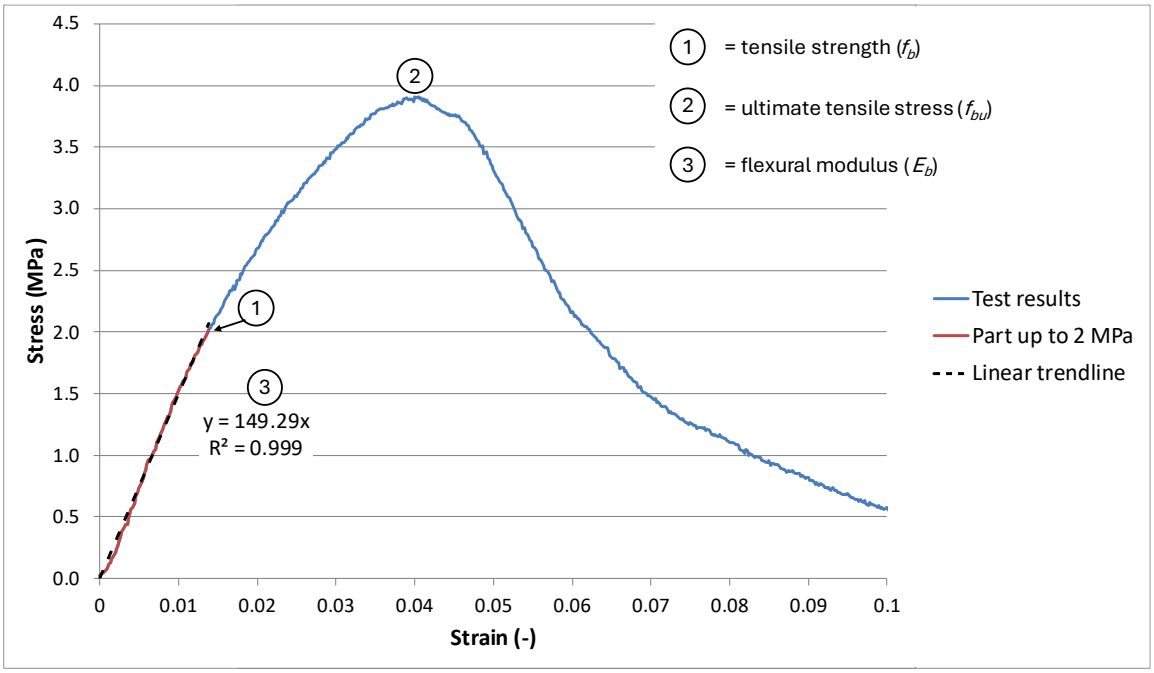


Figure 80. Example of a stress-strain graph of a flexural test in which the specimen cracked.

Flexural modulus

In order to calculate the flexural modulus, it was necessary to consider only the tests which resulted in a cracked specimen. Figure 81 shows an example of an uncracked and a cracked specimen, the crack always occurred in the middle of the specimen, right under the load location. For this, only the linear part of the graph is taken, see the red part in Figure 80. Through this red part a linear trendline is generated with excel and the slope of this trendline equals the flexural modulus (E_b). The R^2 value indicates the fitness of the trendline with the actual graph. The closer the R^2 value is to 1.0, the more accurate the trendline predicts the values of this part.

For the flexural modulus of the reference mixtures, the linear part of the graph ended around 2 MPa. But for the reference mixture with additives the linear part went up to 3 MPa.



Figure 81. Two examples of an uncracked (left) and a cracked (right) specimen at the end of a flexural test.

Second moment of inertia

The specimens were supposed to have a squared cross-section, but due to the shrinkage difference, the cross-section resembled a more trapezoid. The differences in the second moment of inertias between the two cross-sections were investigated, this is elaborated in Chapter D2 of Appendix D. And it was concluded that the use of a trapezoidal cross-section was more accurate.

The calculation of the second moment of inertia (I_y) with a trapezoid cross-section was not straight forward. The cross-section was divided into three parts, as illustrated in Figure 82. This shows three parts of the cross-section with the following assumptions:

- All the layers of the specimen adhere perfectly to each other, creating one solid cross-section.
- The cross-section of the specimen is a perfect trapezium, meaning that it has at least two parallel sides.
- The trapezium is symmetrical meaning:
    - A is a perfect rectangle.
    - Triangles B and C are right-angled triangles.
    - The dimensions of triangles B and C are the same.

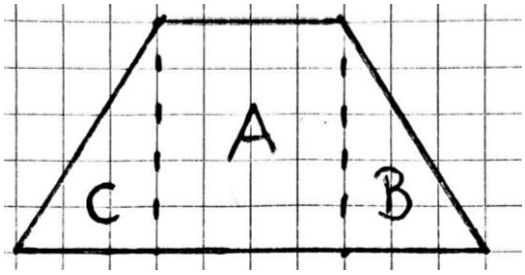


Figure 82. Trapezium divided into three parts: A, B and C.

The second moment of inertia for the specimens in both orientations was calculated with equation 4. The derivation of this equation for both orientations can be found in Chapter D2 of Appendix D. The results of this calculation were verified with an online calculation tool [144].

$$Iy = Iy_a + ((Z_{a1})^2 * A_a) + Iy_b + ((Z_{b1})^2 * A_b) + Iy_c + ((Z_{c1})^2 * A_c) \quad 4$$

In which:
Iy = the second moment of area the complete cross section "i" [mm^4
Iyi = the second moment of area of partial cross section "i" [mm^4]
Z_{i1} = the distance between the line of gravity of partial cross section "i" and the line of gravity of the complete cross section [mm]
A_i = *the area of partial cross section "i" [mm^2]*

Strain calculation

Due to the trapezoidal shape of the specimen, the maximum strain calculation in the bottom of the specimen is calculated with equation 5. Its derivation is elaborated in Chapter D3 of Appendix D.

$$\varepsilon = \frac{12 * D * z}{L^2} \quad 5$$

In which:
ε = strain [-]
D = displacement [mm]
z = distance from the neutral axis to the bottom fibres [mm]
L = span [mm]

5.2 Reference mixtures

5.2.1 Results and discussions

5.2.1.1 Compression tests

This section presents the results of the compression tests of the wood glue and bio-glue mixtures. Henceforth, wood glue and bio-glue will be referred to as WG and BG, respectively.

The dimensions of each tested compression cube can be found in Chapter E1 of Appendix E. And each test is elaborated individually in Chapter E2 in Appendix E.

Figure 83 and Figure 84 display the stress-strain graphs of the WG and BG tests with the layers in the horizontal orientation respectively.

Figure 85 and Figure 86 display the stress-strain graphs of the WG and BG tests with the layers in the vertical orientation respectively.

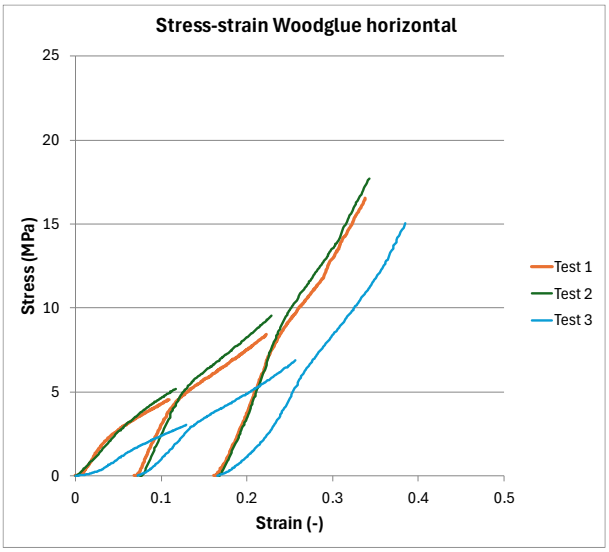


Figure 83. The stress-strain graph of the wood glue compression tests with a horizontal layer orientation.

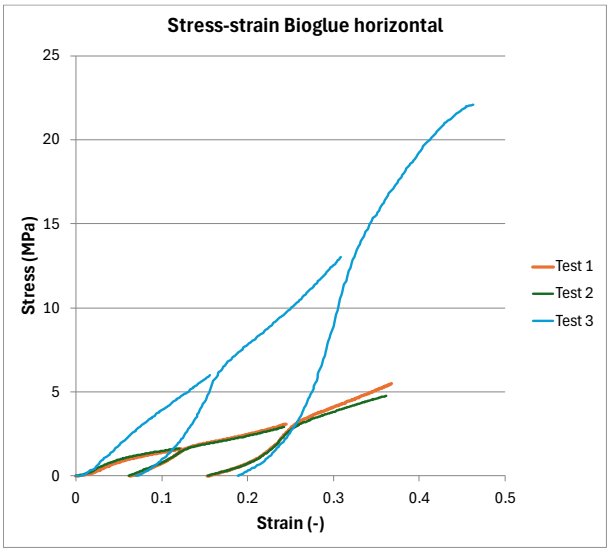


Figure 84. The stress-strain graph of the bio-glue compression tests with a horizontal layer orientation.

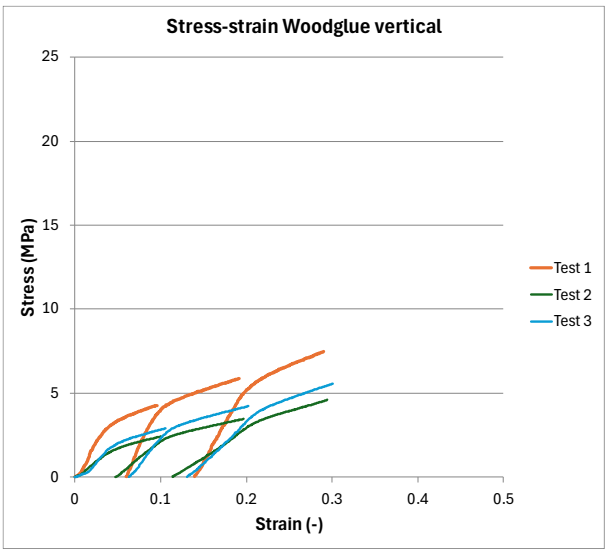


Figure 85. The stress-strain graph of the wood glue compression tests in the vertical orientation.

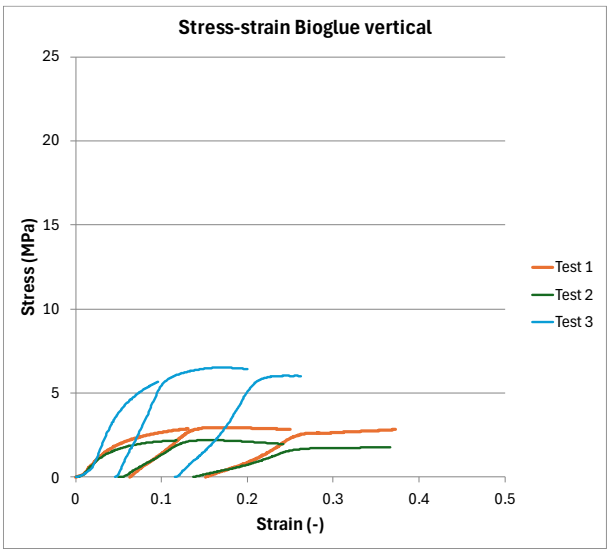


Figure 86. The stress-strain graph of the bio-glue compression tests in the vertical orientation.

Table 26 presents the average results of the WG and BG tests with both layer orientations. The compressive mechanical properties of both mixtures and both orientations are presented in Table 27. The outliers (both test 3 in Figure 84 and Figure 86) were not included to obtain the results presented in both tables below.

Table 26. Compression test results of the wood glue and bio-glue mixtures in both layer orientations.

Glue type	Days cured		Peak force [kN]		Peak stress [MPa]		Stress cycle 1.1 [MPa]	
	Horizontal	Vertical	Horizontal	Vertical	Horizontal	Vertical	Horizontal	Vertical
Wood glue	42.3	41.7	23.85	7.12	16.38	5.87	4.24	3.18
Bio-glue	36	36	8.13	4.21	5.13	2.57	1.63	2.52

Table 27. The compressive mechanical properties of the wood glue and bio-glue mixtures in both layer orientations.

Glue type	Ultimate compressive stress [MPa]		Compressive strength f_c [MPa]		Compression modulus E_c [MPa]	
	Horizontal	Vertical	Horizontal	Vertical	Horizontal	Vertical
Wood glue	16.38	5.87	4.24	3.18	38.36	32.92
Bio-glue	5.13	2.57	1.63	2.52	14.12	20.17

The compressive mechanical properties (Table 27) are summarized as follows:

- The WG-mixture resulted in higher values for the compressive mechanical properties in comparison to the BG-mixture.
- The WG tests with the horizontal layer orientation resulted in higher values for the compressive mechanical properties in comparison to the vertical layer orientation tests.
- The BG tests with the horizontal layer orientation resulted in a higher value for the ultimate compressive stress and lower values for the compressive strength and compression modulus in comparison to the vertical layer orientation tests.

5.2.1.2 Discussion compression tests

As a consequence of the uneven shrinkage of the printed test beams, the compression specimens were not perfect cubes. The dimensions were measured at different points and the averages calculated in order to determine the cross-sectional area and the height. This could mean that the calculated stresses and strain could differ from the real stresses and strains. However, these possible differences are not further discussed.

The imperfections of the cubes caused some cubes to have different heights at the edges of the specimens. This means that before the whole specimen was compressed, the plate of the rigid frame already pressed down on a small part. Causing low pressure to develop before the whole cross-sectional area was utilized, after that the pressure significantly increased. This behaviour influenced the test results, which is demonstrated in WG test 3 with a horizontal layer orientation. This behaviour directly impacts the strain, which subsequently affects the compression modulus by reducing its value in comparison to the tests where this did not occur.

The three different displacements for the three cycles were taken so that each specimen would have roughly the same strain in the cycles. However, the displacements were based on a perfect cube with a height of 40 mm. As earlier mentioned, the test beams did not have the same shrinkage, meaning that the heights differed between the specimens. Also, the heights between the specimens with the horizontal and vertical layer orientation differed significantly.
Different heights, but the same displacements means that the strains at the end of each were not identical between the tests. This could affect the stresses at the end of each cycle. However, for simplicity, the stresses are taken at the end of each cycle and are directly compared to each other.

To get more reliable results for the compression tests, specimens of exactly the same size should be used. However, due to the nature of the used materials and the printing and curing processes, this was hard to achieve. A possible solution to this, is to cut the specimens to exactly the same size. However, this would mean that the outer layers of some specimens would be thinner others, or in the worst-case scenario, a layer could be removed entirely if a specimen had to be cut smaller than its original size.

It is clear from Table 26 that the maximum force of the horizontal tests is significantly higher than with the vertical tests. This was expected, as with the vertical test the layers separate, leading to a reduced stiffness and subsequently to a lower maximum force (and thus a lower ultimate compressive stress) compared to the horizontal layer orientation.

Irrespective of the layer orientation, BG test 3 had significant higher stress result than the other two tests. These differences might be explained by the difference in curing times (43 days for tests 3 and 36 days for tests 1 and 2). A longer curing time could mean a higher compressive strength, but the effect of the length of the curing time on the mechanical properties was not investigated because it fell outside the scope of this research. Due to the considerable differences in the results, tests 3 of both layer orientations were considered outliers and they were excluded from the calculation of the averages and mechanical properties.

In almost all compression tests, cycles 1.1 were not 100% linear, in particular not with the test with a vertical layer orientation. The lowest R^2 values of the linear trendlines were 0.9554 and 0.8575 for the horizontal and vertical layer orientation, respectively. This means that the compression moduli did not accurately describes cycles 1.1. However, developing a more accurate calculation of the compression modulus fell outside the scope of this research. Therefore, the values of the compression moduli of Table 27 were used for further comparisons and calculations.

It was expected that the tests with a horizontal layer orientation would have overall higher values of the mechanical properties due to the difference in crack patterns and failure behaviour. However, the results of the BG test did not meet these expectations, which could indicate that the bond strength between the layers is higher with the BG-mixture compared to the WG-mixture. However, researching this hypothesis fell outside the scope of the research.

5.2.1.3 Flexural tests

This section presents the results of the flexural tests of the WG and BG mixtures.
The dimensions of each tested specimen can be found in Chapter F1 of Appendix F. And each test is elaborated individually in Chapter F2 of Appendix F.
Figure 87 and Figure 88 display the stress-strain graphs of the WG and BG tests with the layers in the horizontal orientation respectively.
Figure 89 and Figure 90 display the stress-strain graphs of the WG and BG tests with the layers in the vertical orientation respectively.

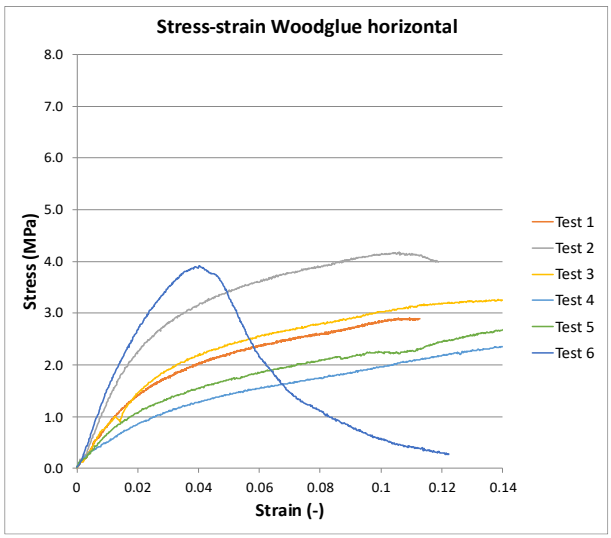


Figure 87. The stress-strain graph of the wood glue flexural tests in the horizontal orientation.

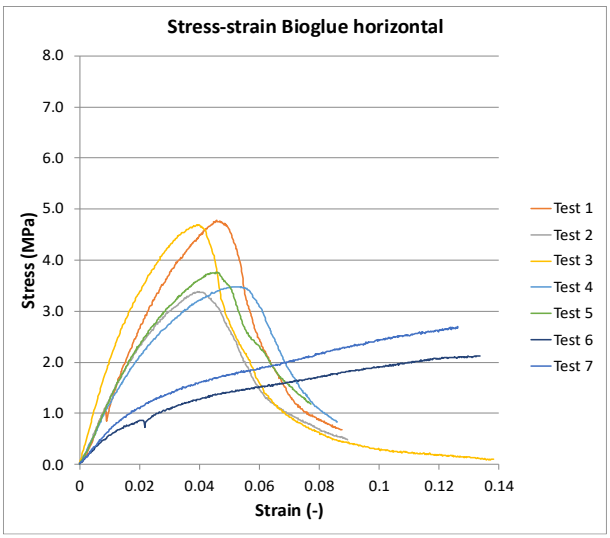


Figure 88. The stress-strain graph of the bio-glue flexural tests in the horizontal orientation.

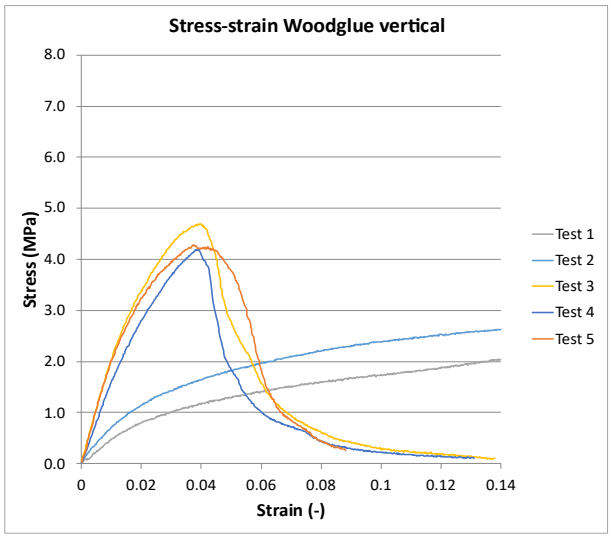


Figure 89. The stress-strain graph of the wood glue flexural tests in the vertical orientation.

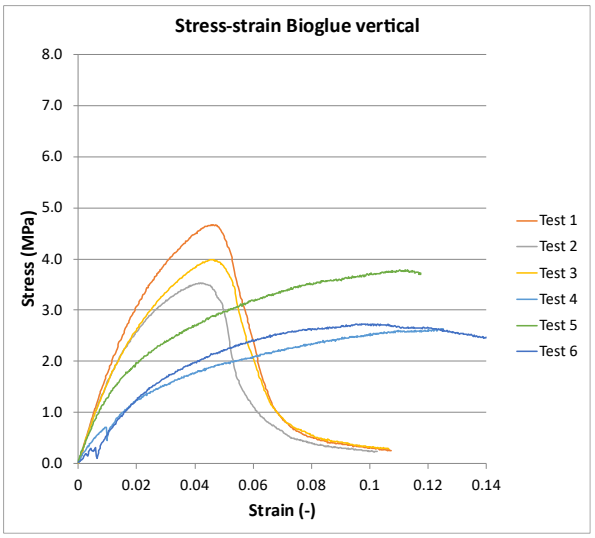


Figure 90. The stress-strain graph of the bio-glue flexural tests in the vertical orientation.

Table 28 presents the average results of the WG and BG tests with both layer orientations.
The flexural mechanical properties of both mixtures and both orientations are presented in Table 29.
The specimens that did not crack during the tests are disregarded in these averages. Only the following tests were included to obtain the results presented in both tables below:

- Figure 87, test 1.
- Figure 88, test 1, 2, 3, 4 and 5.
- Figure 89, test 3, 4 and 5.
- Figure 90, test 1, 2, and 3.

Table 28. Flexural test results of the wood glue and bio-glue mixtures in both layer orientations.

Glue type	Days cured		Peak force [kN]		Displacement* [mm]		Stress* [MPa]		Strain* [-]	
	Hor	Vert	Hor	Vert	Hor	Vert	Hor	Vert	Hor	Vert
Wood glue	38	36	0.43	0.58	10.76	8.37	3.91	4.70	0.040	0.039
Bio-glue	41.2	41	0.53	0.75	11.36	8.58	3.86	4.28	0.046	0.048

**) These values are determined/calculated at the moment of peak force*

Table 29. The flexural mechanical properties of the wood glue and bio-glue mixtures in both layer orientations.

Glue type	Ultimate tensile stress [MPa]		Tensile strength f_b [MPa]		Flexural modulus E_b [MPa]	
	Horizontal	Vertical	Horizontal	Vertical	Horizontal	Vertical
Wood glue	3.91	4.70	2.02	2.01	149.29	212.60
Bio-glue	3.86	4.28	2.02	2.01	124.05	166.70

The flexural mechanical properties (Table 29) are summarized as follows:

- The WG-mixture resulted in higher values for the flexural mechanical properties in comparison to the BG-mixture, with the same value for the tensile strength.
- With both mixtures, the tests with the vertical layer orientation resulted in higher values for the flexural mechanical properties in comparison to the horizontal layer orientation tests, with the same value for the tensile strength.

5.2.1.4 Discussion flexural test results

The analysis of the two different support conditions mentioned in 5.1.2 concluded that the different support conditions had a negligible impact on the stresses. As a result, despite the tests being executed with two hinges, they were calculated with one hinge and one roller. However, with a numerical analysis all the conditions are perfect. During the tests in the SED-lab, these conditions were never that perfect and several imperfections and uncertainties could have played a significant role. For example, imperfections in the specimen, cross-section, and GSA settings that were unknown and kept on the GSA default settings. So probably during the actual tests there could have been a large difference between the two different support conditions.

In order to obtain a reliable determination of the mechanical properties, it is recommended that at least three specimens need to be tested. However, only one test was used to determine the flexural mechanical properties of the WG-mixture with a horizontal layer orientation. In spite that Table 29 does not give an accurate representation of the flexural mechanical properties of this mixture, this test result had to be used in further comparisons.

In order to calculate the second moment of inertia (see Chapter 5.1.2), it was assumed that the five layers adhere perfectly together and form a perfect solid trapezium-shaped cross-section. However, this bond strength between the layers might not be perfect, but investigating the bond strength fell outside the scope of this research.
The bond strength impacts the mechanical behaviour of the specimens. This means that the aforementioned assumption may have overestimated the calculated second moment of inertia, and therefore leading to an overestimation of the calculated stresses and strengths, particularly with regard to the horizontal layer orientation.

In all flexural tests the R^2 values of the linear trendlines exceeded 0.99, meaning that the slope accurately describes the first part of the graph.

5.2.2 Summary and conclusion reference mixtures

All compression and flexural tests showed that for both layer orientations, the WG-mixture resulted in a higher value for the mechanical properties compared to the BG-mixture, except for the tensile strength, which was the same value for both mixtures.
It can be concluded that the WG-mixture is considerably stronger in compression and somewhat stronger in bending in comparison to the BG-mixture.

The WG compression tests with a horizontal layer orientation resulted in higher values for the mechanical properties compared to the vertical layer orientation. Conclusively, the WG-mixture is stronger in compression when the specimens have a horizontal layer orientation compared to a vertical layer orientation.
The BG compression test did not result in the highest ultimate compressive stress with the vertical layer orientation. The other mechanical properties necessary for the future calculations were higher. It was therefore concluded that the BG-mixture is stronger in compression when the specimens have a vertical layer orientation compared to a horizontal layer orientation.

For both mixtures, all flexural tests with a vertical layer orientation yielded higher values for the mechanical properties. Therefore, it can be concluded that the printed specimens are stronger in bending when they have a vertical layer orientation compared to a horizontal layer orientation.

The test results would indicate that the WG-mixture is the optimal choice to proceed with. However, as the one of the most significant objectives of this research was to develop a bio-based printable mixture, the bio-based content of each mixture was considered a crucial factor in the selection of the mixture.
The bio-based content of the WG-mixture is 57%, while the bio-based content of the BG-mixture is 100% (see Chapter 3.3.2). For further experimentation, the BG-mixture was therefore selected and will hereafter be referred to as the reference mixture.

5.3 Reference mixture with additives

This chapter presents an investigation of the mechanical properties of the reference mixture with the different additives referenced in Chapter 3.4, namely, bentonite, flax and a combination of bentonite and flax. The mixtures with the additives will henceforth be referred to as the ”additive” mixture, i.e. the bentonite, flax and bentonite+flax mixture, respectively. Furthermore, due to the varying bentonite contents, the bentonite mixture is divided into the bentonite 6.5% and bentonite 3.4% mixture.

5.3.1 Results and discussions

5.3.1.1 Compression test results

This section presents the results of the compression tests of the reference mixture with additives.
The dimensions of each tested compression cube can be found in Chapter E1 of Appendix E. And each test is elaborated individually in Chapter E3 in Appendix E.
The figures below show the stress-strain graphs of the bentonite tests (Figure 91 and Figure 92), the flax tests (Figure 93 and Figure 94) and the bentonite+flax tests (Figure 95 and Figure 96). The left and right figures represent the horizontal and vertical layer orientation respectively.

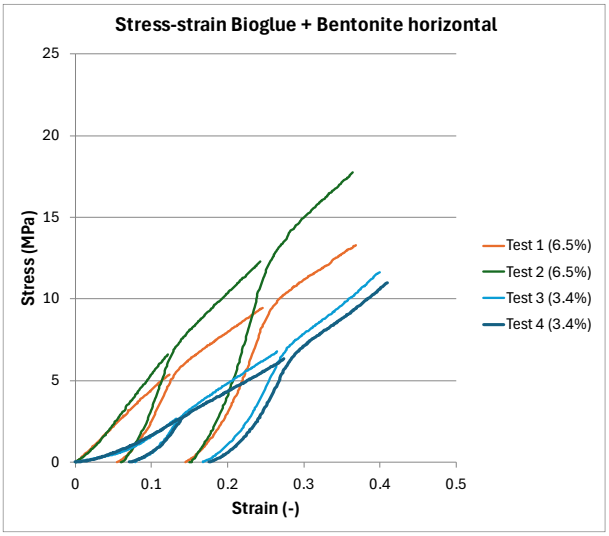


Figure 91. The stress-strain graph of the bentonite compression tests in the horizontal orientation.

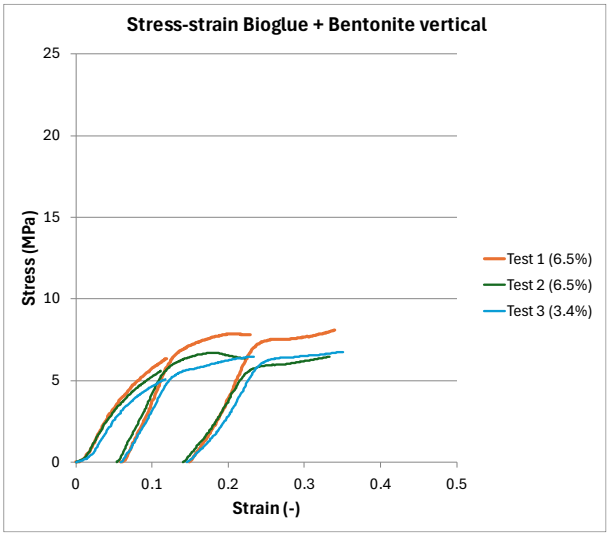


Figure 92. The stress-strain graph of the bentonite compression tests in the vertical orientation.

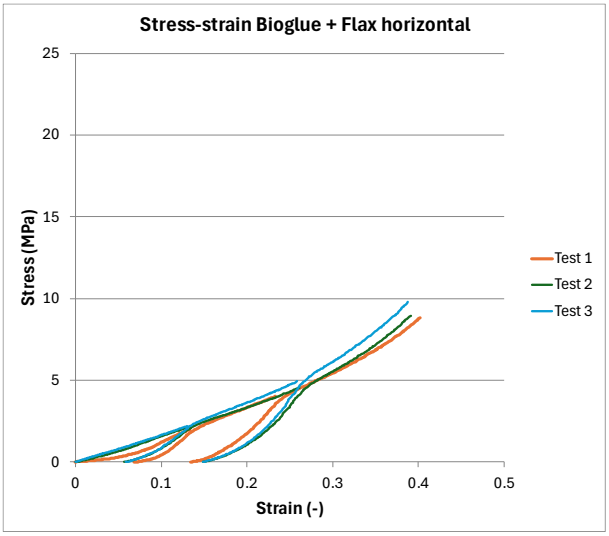


Figure 93. The stress-strain graph of the flax compression tests in the horizontal orientation.

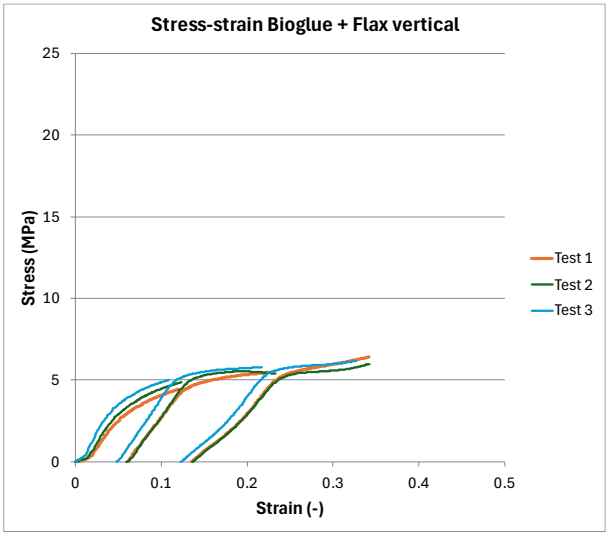


Figure 94. The stress-strain graph of the flax compression tests in the vertical orientation.

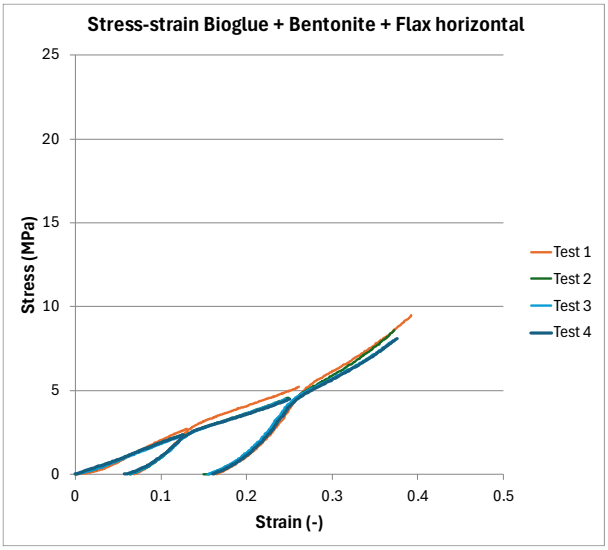


Figure 95. The stress-strain graph of the bentonite+flax compression tests in the horizontal orientation.

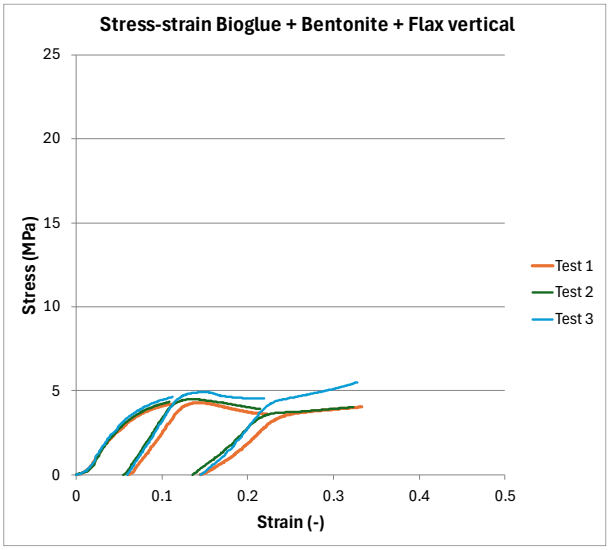


Figure 96. The stress-strain graph of the bentonite+flax compression tests in the vertical orientation.

Table 30 and Table 31 present test results and compressive mechanical properties of the reference mixture with additives respectively.

Table 30. Compression test results of the reference mixture with additives in both layer orientations.

Additive	Days cured		Peak force [kN]		Peak stress* [MPa]		Stress cycle 1.1 [MPa]	
	Horizontal	Vertical	Horizontal	Vertical	Horizontal	Vertical	Horizontal	Vertical
-	36	36	8.13	4.21	5.13	2.57	1.63	2.52
Bentonite 6.5%	36	35	23.74	10.47	15.52	7.38	5.95	5.96
Bentonite 3.4%	34	34	17.47	8.10	11.31	6.76	2.67	5.07
Flax	35	34.7	14.07	7.29	9.17	6.19	2.11	4.77
Bentonite + flax	31	31	12.81	5.89	8.53	4.75	2.43	4.38

**) These values are determined/calculated at the moment of peak force*

Table 31. The compressive mechanical properties of the reference mixture with additives in both layer orientations.

Additive	Ultimate compressive stress [MPa]		Compressive strength f_c [MPa]		Compression modulus E_c [MPa]	
	Horizontal	Vertical	Horizontal	Vertical	Horizontal	Vertical
-	5.13	2.57	1.63	2.52	14.12	20.17
Bentonite 6.5%	15.52	7.38	5.95	5.96	50.98	56.47
Bentonite 3.4%	11.31	6.76	2.67	5.07	19.83	49.49
Flax	9.17	6.19	2.11	4.77	16.19	44.52
Bentonite + flax	8.53	4.75	2.43	4.38	20.29	44.80

The compressive mechanical properties (Table 31) are summarized as follows:

- All additives improved the compressive mechanical properties of the reference mixture.
- The bentonite 6.5% mixture resulted in the highest values for all properties.
- The bentonite 3.4% mixture resulted in the second-highest values for all properties, with the exception of the compression modulus for a horizontal layer orientation.
- The compression modulus of the bentonite 3.4% mixture and the bentonite+flax mixture resulted in an equally high value of roughly 20 MPa.
- The horizontal layer orientation tests resulted in higher values for the ultimate compressive stress, but resulted in lower values for the compressive strength and compression modulus when compared to the vertical layer orientation tests.

5.3.1.2 Discussion compression tests

The general comments on the imperfections of the compression cubes due to the uneven shrinkage, as outlined in the beginning of Chapter 5.2.1.2, do also apply here.

As expected from the literature, the addition of bentonite resulted in the enhancement of the stiffness of the reference mixture, supported by the increased values for the compression moduli with all the mixtures that contain bentonite (Table 31). Also, the values for the ultimate compressive stress and compressive strength are higher compared to the reference mixture. In addition, the bentonite 6.5% mixture increased the compressive mechanical properties significantly more than the 3.4% mixture.

The relative increases of compressive mechanical properties of the bentonite 6.5% mixture compared to the reference mixture, are larger with the horizontal layer orientation compared to the vertical layer orientation. In case of the other additives, the opposite was observed.
With the vertical layer orientation, the stiffness of the specimen largely depends on the bond strength between the layers, because the layers want to separate under pressure. During printing, the bentonite 6.5% mixture adhered less well, which made printing more challenging and resulted in an uneven extrusion of the test beams. This observed reduced adhesion is likely to have had a negative impact on the bond strength, thereby counteracting the enhancement of material stiffness with the vertical layer orientation. Due to its poor printability, the bentonite 6.5% mixture was therefore excluded from further investigation.

When the batches for the additives mixtures were produced, no new control (reference) mixture was created and results from previous tests were used for comparison. It is possible that, due to the biological nature of the materials, their properties changed over time, which could have a negative effect on the mixture. The most optimal scenario would have been to simultaneously produce a “new” reference and additive mixtures, which would increase the reliability of the investigation on the impact of the additives.

5.3.1.3 Flexural test results

This section presents the results of the flexural tests of the reference mixture with additives.
The dimensions of each tested specimen can be found in Chapter F1 of Appendix F. And each test is elaborated individually in Chapter F3 of Appendix F.
The figures below show the stress-strain graphs of the bentonite tests (Figure 97 and Figure 98), the flax tests (Figure 99 and Figure 100) and the bentonite+flax tests (Figure 101 and Figure 102). The left and right figures represent the horizontal and vertical layer orientation respectively.

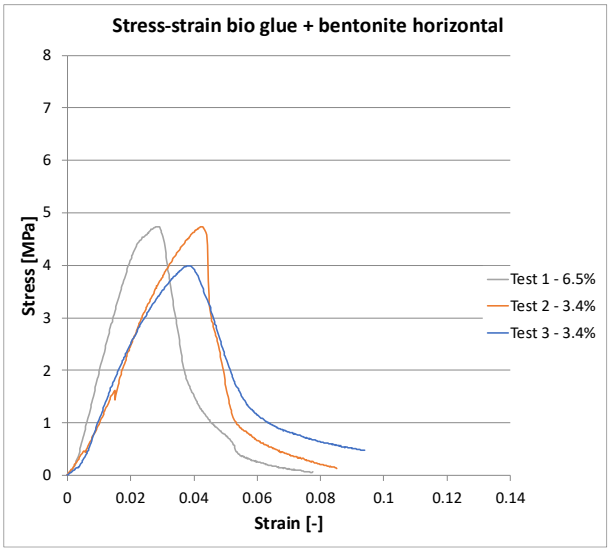


Figure 97. The stress-strain graph of the bentonite flexural tests in the horizontal orientation.

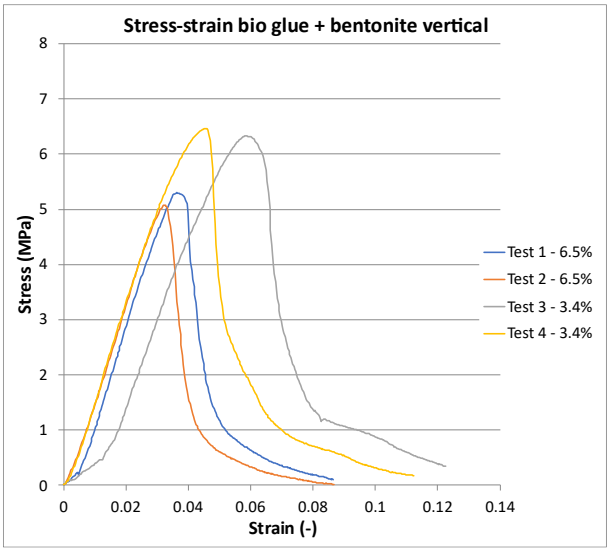


Figure 98. The stress-strain graph of the bentonite flexural tests in the vertical orientation.

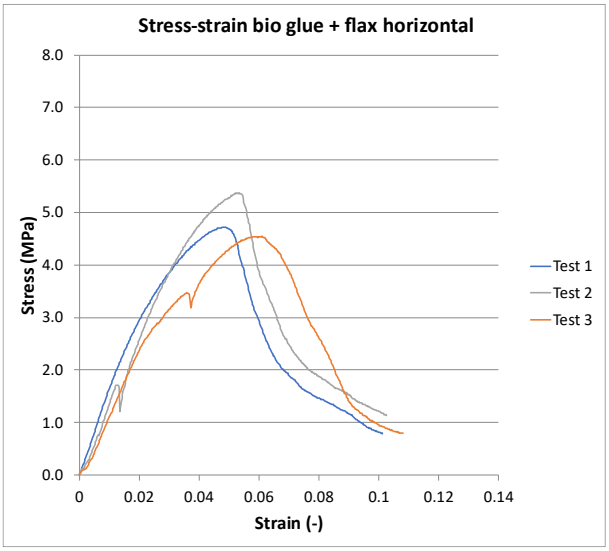


Figure 99. The stress-strain graph of the flax flexural tests in the horizontal orientation.

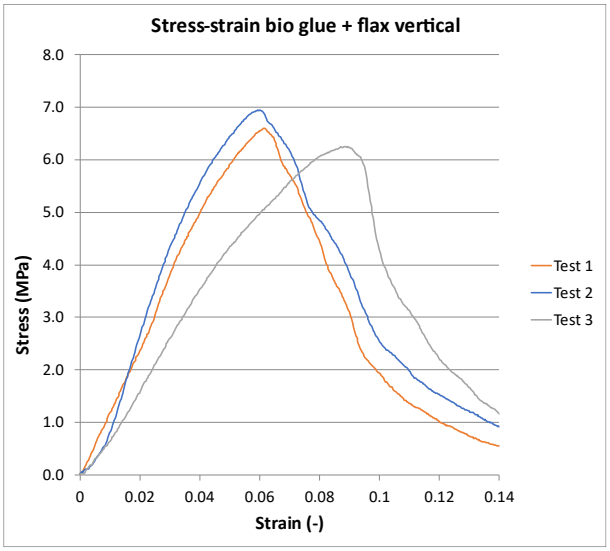


Figure 100. The stress-strain graph of the flax flexural tests in the vertical orientation.

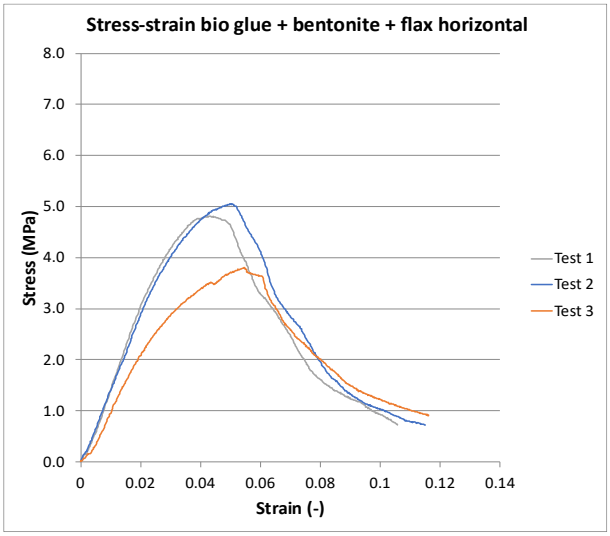


Figure 101. The stress-strain graph of the bentonite+flax flexural tests in the horizontal orientation.

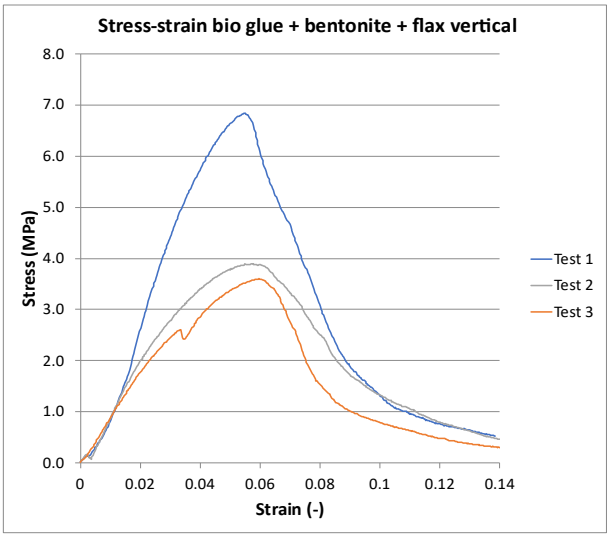


Figure 102. The stress-strain graph of the bentonite+flax flexural tests in the vertical orientation.

Table 32 presents the average results of the reference mixture with additives with both layer orientations. The flexural mechanical properties of both mixtures and both orientations are presented in Table 33.

Table 32. Flexural test results of the reference mixture with additives in both layer orientations.

Additive	Days cured		Peak force [kN]		Displacement* [mm]		Stress* [MPa]		Strain* [-]	
	Hor	Vert	Hor	Vert	Hor	Vert	Hor	Vert	Hor	Vert
-	41.2	41	0.53	0.75	11.36	8.58	3.86	4.28	0.046	0.048
Bentonite 6.5%	50	50	0.71	1.09	6.80	5.90	4.74	5.19	0.029	0.034
Bentonite 3.4%	48	48	0.73	1.15	9.46	8.38	4.37	6.40	0.040	0.052
Flax	49	49.7	0.82	1.25	12.76	11.48	4.88	6.60	0.056	0.070
Bentonite + flax	42.3	37.7	0.68	0.82	11.56	9.80	4.54	4.74	0.048	0.055

**) These values are determined/calculated at the moment of peak force*

Table 33. The flexural mechanical properties of the reference mixture with additives in both layer orientations.

Additive	Ultimate tensile stress [MPa]		Tensile strength f_b [MPa]		Flexural modulus E_b [MPa]	
	Horizontal	Vertical	Horizontal	Vertical	Horizontal	Vertical
-	3.86	4.28	2.02	2.01	124.05	166.70
Bentonite 6.5%	4.74	5.19	3.03	3.04	194.61	140.34
Bentonite 3.4%	4.37	6.40	3.01	3.03	118.94	117.11
Flax	4.88	6.60	3.02	3.03	128.86	106.53
Bentonite + flax	4.54	4.74	3.02	3.02	129.68	95.30

The flexural mechanical properties (Table 33) are summarized as follows:

- All additives increased the ultimate tensile stress and the tensile strength of the reference mixture, irrespective of the layer orientation.
- The flax mixture resulted in the highest values for the ultimate tensile stress.
- The tensile strength of all the additive mixtures is the same, irrespective of the layer orientation.
- The horizontal layer orientation resulted in lower values for the ultimate tensile stress, but resulted in higher values for the flexural modulus in comparison to the vertical layer orientation tests.
- The flexural modulus in the horizontal layer orientation showed the highest value with the bentonite 6.5% mixture, which was approximately 1.6 times higher than the reference mixture.

The flax mixture and the bentonite+flax mixture resulted in the second-highest value of roughly 129 MPa

- For the vertical layer orientation, all additives decreased the flexural modulus of the reference mixture. Of the mixtures with additives, the bentonite 6.5% mixture resulted in the highest value and the bentonite 3.4% mixture resulted in the second highest value.
- The flexural moduli of the bentonite 3.4% of both layer orientations resulted in an equally high values of roughly 118 MP.

5.3.1.4 Discussion flexural tests

Figure 102 depicts that the peak stress of bentonite+flax test 1 is substantially higher than that of tests 2 and 3. The difference between these tests is that the specimen of test 1 was tested 47 days after printing, whereas the specimens of tests 2 and 3 were tested only 33 days after printing, this is a difference of 14 days. The same can be observed with the bentonite+flax with the horizontal layer orientation tests in shown Figure 101. However, the differences between the peak stresses are less significant than in the vertical orientation. The curing time for the specimens of test 1 and 2 was 47 days, while the curing time of the specimen of test 3 was 33 days.
The specimens with a shorter curing time resulted in lower peak stresses than those with a longer curing time, irrespective of the layer orientation. This suggests that the curing time may have a significant impact on the mechanical behaviour. However, as previously stated, the effect of the length of the curing time on the mechanical properties was not investigated because it fell outside the scope of this research. In spite of the considerable differences in the results of the tests, all bentonite+flax tests were included when calculating the flexural mechanical properties.

As a result of the additives a higher tensile strength was observed, which is illustrated by the longer linear part of the graphs, i.e. it reached 3 MPa compared to the 2 MPa of the reference mixture. This could be attributed to the higher peak stresses reached during the tests compared to the reference mixture.

The bentonite 6.5% supported the hypothesis that bentonite increases the stiffness, but only in the horizontal layer orientation. As mentioned earlier, due to its poor printability, the bentonite 6.5% mixture was excluded from further investigation and comparisons. Interestingly, apart from the reference mixture, with bentonite 6.5% the highest flexural moduli were obtained.

The test with a horizontal layer orientation with mixtures that contain flax, resulted in the highest ultimate stress and flexural modulus. This demonstrated that the flax fibres affected the mechanical behaviour of the specimens, with the long flax fibres spanning the small cracks of the specimens, as previously demonstrated in Figure 60. This reinforced the specimen and improved the tensile strength of the reference mix, which is in line with the literature mentioned in Chapter 2.2.3.
However, this is not the case for the tests with the vertical layer orientation. The flax mixture resulted in the highest ultimate stress, while the bentonite+flax mixture resulted in the lowest ultimate stress. One possible explanation for this lower tensile strength is the shorter curing time of the specimens compared to the other mixtures.

In most flexural tests with additives, the R^2 values of the linear trendlines exceeded 0.99, indicating that the slope accurately describes the part of the graph up to 3 MPa. However, this was not the case for following tests:

- Bentonite test 1 with a horizontal layer orientation.
- Bentonite test 1 and 3 with a vertical layer orientation.
- Flax test 2 with a vertical layer orientation.
- Bentonite+flax test 1 with a vertical layer orientation.

The trendlines of these four tests appear to be fairly linear, as demonstrated by a minimum R^2 value of 0.94. Additionally, they all resulted in an underestimation of the flexural modulus, indicating that the actual specimen may have been stiffer than the trendline predicts. However, all the calculated flexural moduli were incorporated with the calculation of the mechanical properties, and any possible under- or overestimations were excluded from further discussion of the results.

It was not anticipated that the flexural modulus would decrease with the vertical layer orientation when additives were added to the reference mixture. The cause of this decrease was not investigated, but there are some possible explanations:

- The additives could have a negative effect on the bond strength between layers. However, if this would be the case, it would have also impacted the flexural modulus with the horizontal orientation.
- The other reason might have been the lack of a "new" reference mixture for adequate comparison as explained previously.

5.3.2 Conclusion bio-glue with additives

This section deals with the selection of the best additive for the final element. For a better understanding, relevant data from Table 31 and Table 33 are combined below in Table 34.

Table 34. Mechanical properties of the mixtures with additives with a vertical layer orientation.

Additive	Ultimate compressive stress [MPa]	Compressive strength f_c [MPa]	Compression modulus E_c [MPa]	Ultimate tensile stress [MPa]	Tensile strength f_b [MPa]	Flexural modulus E_b [MPa]
Bentonite 3.4%	6.76	5.07	49.49	6.40	3.03	117.11
Flax	6.19	4.77	44.52	6.60	3.03	106.53
Bentonite + flax	4.75	4.38	44.80	4.74	3.02	95.30

The final element will be subjected to bending, therefore the test results of the flexural tests were more important in the selection than the results of the compression tests.
First the bentonite+flax mixture was eliminated as it had the lowest values for most of the mechanical properties compared to the other two additives.
The bentonite 3.4% has the highest values for the majority of the mechanical properties, except for the ultimate tensile stress and the tensile strength (which are roughly the same value as for the flax mixture).
The mixture with only flax had the highest ultimate tensile stress and a medium-high flexural modulus compared to the other additives. These high values for the tensile and flexural mechanical properties led to the conclusion that the mixture with flax fibres was the optimal choice for the production of the final element.

5.4 Classification of the material

Figure 103 presents a bubble chart that classifies different families of building materials. The vertical axis shows the Young's modulus and the horizontal axis shows the density, both on a logarithmic scale [145]. In order to classify the bio-glue with flax mixture, the Young's modulus and the density are needed. The density is calculated from the cured dimensions and weight of the test beams given in Chapter C3 of Appendix C. The average density of bio-glue with flax beams was 923.73 kg/m^3 (0.92 Mg/m^3). The Young's modulus is equal to the tensile or compression modulus [146]. So, for the bio-glue with flax mixture with a vertical layer orientation, the compression modulus of 44.52 MPa (44.52*10^{-3} GPa) was used.

The values for the density and Young's modulus are indicated with the red lines in Figure 103. This places the bio-glue with flax mixture in the top of the elastomer family. When plotting the other additive mixtures in this figure, it can be observed that they all fall within the elastomer's family.

An elastomer is characterized by its elasticity and viscosity. Elastomers have a low Young's modulus, leading to large deformations before failure [147]. This was also the case with the bio-glue with flax specimens. However, this is often an undesired property in a structural building material. Figure 103 clearly demonstrates that the mixture is considerably less strong than conventional building materials such as wood, concrete or steel.

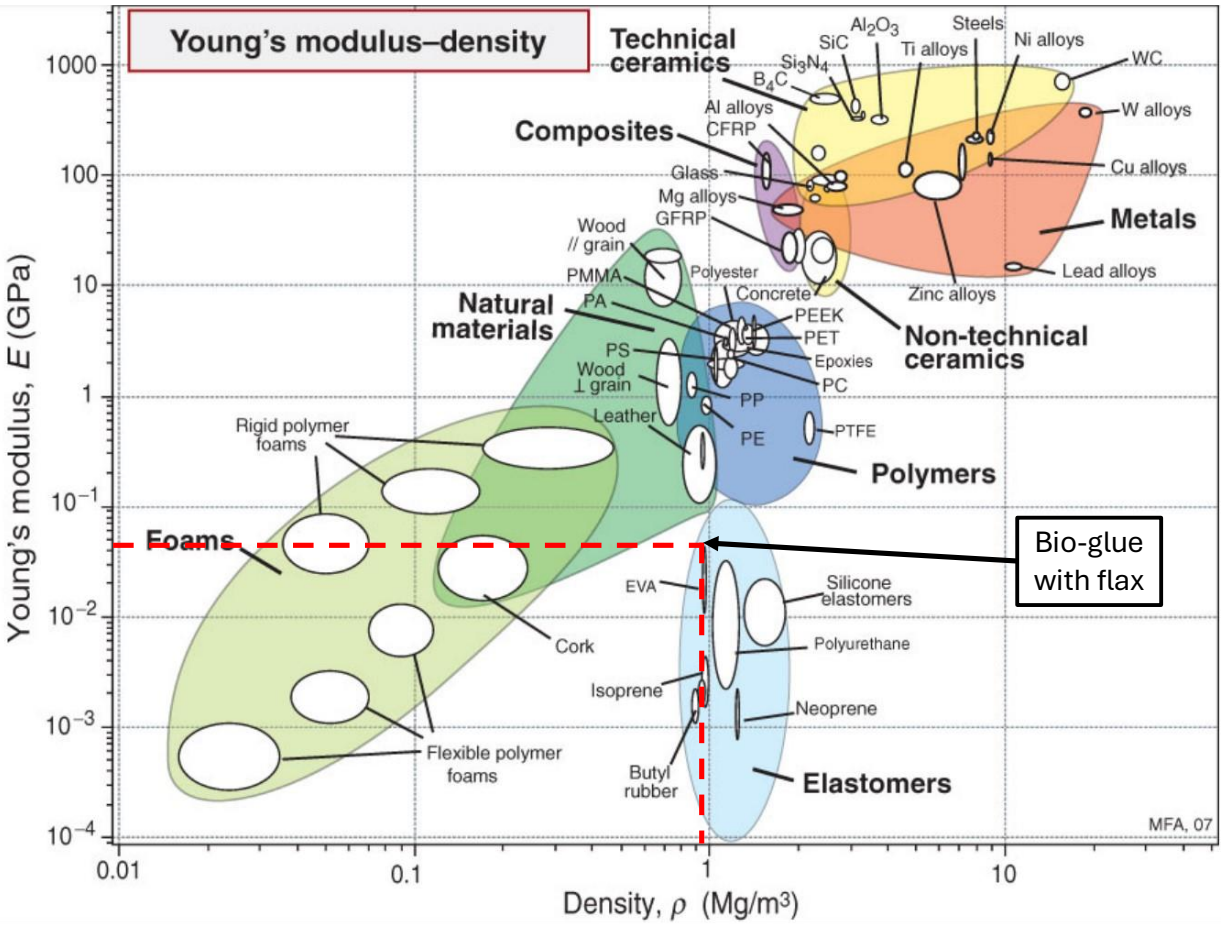


Figure 103. A bubble chart of material families. With on the vertical axis the Young's modulus and on the horizontal axis the density, both on logarithmic scales [145].

Table 35 presents the mechanical properties of various wood species, (3D printed) wood composites, 3D printed concrete and the bio-glue with flax mixture. It is evident that the bio-glue with flax mixture has a significantly lower flexural modulus compared to the other materials. The values for the strengths are also relatively low compared to the other materials, yet it demonstrates that its strengths are comparable or higher to that of certain wood species in their weak direction (perpendicular to the grain).
Both Figure 103 and Table 35 demonstrate that the current bio-glue with flax mixture is considerably less strong than conventional and comparable building materials, including wood, concrete, steel, wood composites and 3D printed concrete. Its flexural strength is comparable to that some of the 3D printed wood composites and is higher than that of 3D printed concrete. However, its flexural modulus is particularly low, which renders it currently unsuitable for use as a building material.

Table 35. Mechanical properties comparison

Material	Flexural strength (tension) [MPa]	Flexural modulus [MPa]	Compressive strength [MPa]	Reference
Bio-glue with flax	6.60	106.53	6.19	[this study]
Beech (American)	86.2 / 7.0 *	9500	50.3 / 7.0 *	[148]
Oak (Overcup)	77.9 / 6.5 *	9800	42.7 / 5.6 *	[148]
Pine (Eastern White)	73.1 / 2.1 *	8500	33.1 / 3.0 *	[148]
Spruce (Engelmann)	84.8 / 2.4 *	8900	30.9 / 2.8 *	[148]
Particleboard		2760 – 4140		[148]
MDF		3590		[148]
OSB		4410 – 6280		[148]
Plywood		6960 - 8550		[148]
Glulam		9000 - 14500		[148]
Wood plastic		1530 - 4230	11.7 – 61.2	[148]
Pla + Lignin (40wt%)		1930		[84]
Wood Powder + Glue		3000 - 3940		[114]
FLAM!		260		[149]
15% wood powder 1 UF	19	1930		[57]
17.5% wood powder 1 UF	18	2002		[57]
Methylcellulose - moulded	8.59 - 10.60	670 - 1050		[62,63]
Methylcellulose - printed	8.48 - 9.55	600 - 640		[62,63]
Wood glue - moulded	20.67 - 28.89	640 - 900		[62,63]
89 w% wood sawdust MC	2.3 ± 0.4	284.8 ± 46.4		[58]
84.5 w% wood sawdust MC	5.1 ± 1.0	546.5 ± 109.7		[58]
85.5 w% wood sawdust MC	7.4 ± 1.1	733.1 ± 128.0		[58]
3D printed concrete	3 - 3.6		± 30	[150]
3D printed concrete cube			11.3	[151]
3D printed concrete prism			17.51	[151]

**) These data represent "Parallel to grain / perpendicular to grain"*

FINAL ELEMENT

6 Final element

6.1 Structural optimisation

6.1.1 Optimisation methods

With structural optimisation, a structure is altered to support the loads in the best way, but the "best way" has to be defined before execution. For example, the structure needs to be as light or as stiff as possible, or characteristics need to be maximised or minimised. To limit the number of solutions, constraints are necessary. These constraints can include parameters such as stresses, displacements, critical loads and/or the weight and the size of a structure [152].

There are three different methods to tackle structural optimisation [152,153] (visualized in Figure 104):

a) Size optimisation: the structural thickness of a certain cross-section is adjusted, depending on the stresses that occur in the cross-section. This is also referred to as cross-section optimisation.
b) Shape optimisation: the optimal shape is derived while keeping the boundary conditions the same.
c) Topology optimisation: the material usage is optimised. The structure can be altered in such a way that the topology changes. This involves the removal of material that is not needed and retains material in locations where stresses occur.

The difference between topology optimisation (TO) and the other methods, is that with TO a completely new structural layout is generated from an initial volume, while the other methods need an initial design before execution. TO is often conducted during the design process and involves the distribution of material within the constraints and boundaries of the structure [153].

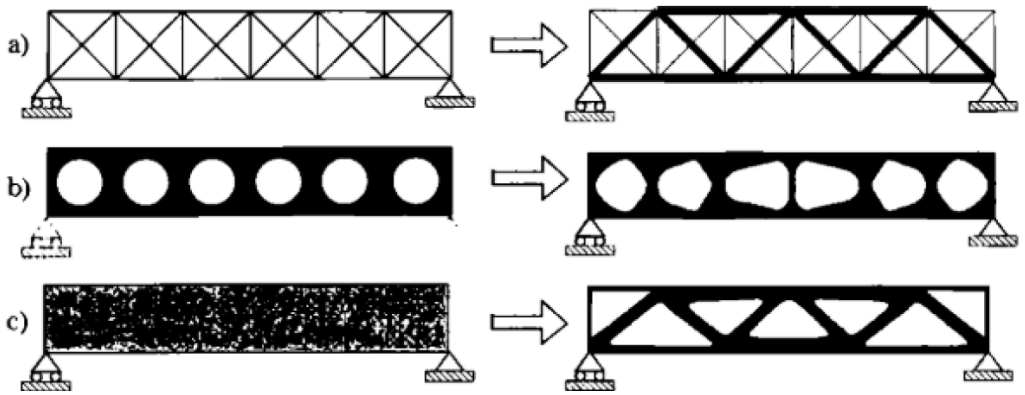


Figure 104. Examples of optimisation methods: a) Size Optimisation b) Shape Optimisation c) Topology Optimisation [153].

The final element of this project is a beam, subjected to one load in the middle and supported by two hinges, one of which contains a roller. Figure 105 depicts the mechanical scheme and the element before optimisation. Table 36 presents a list with some of the available programs or Grasshopper plugins that are suitable for the execution of TO. Following a quick analysis of these programs and plugins, it was decided that Grasshopper with the plugin Karamba3D was the best choice for optimisation, as it was the most up-to-date. Moreover, a licence for this plugin had previously been acquired. Karamba3D is developed by Karamba, which is a finite element program that can be used to analyse structures [154].

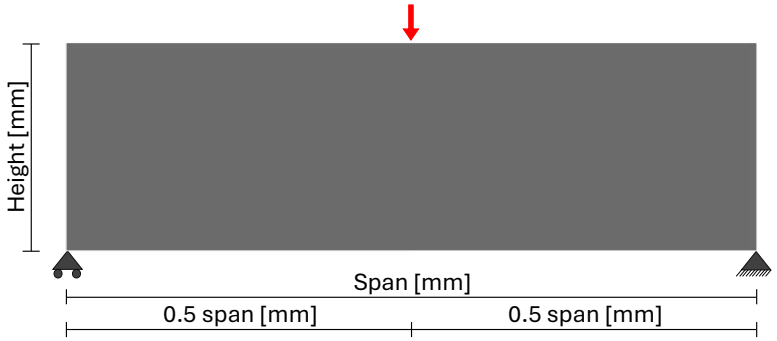


Figure 105. The mechanical scheme of the final element before optimisation.

Table 36. A comparison of available topology optimisations programs and tools [153].

Program/ Plugin	Environment	Accessibility	Dimension
Millipede	Grasshopper	Free	2D&3D
TopOpt	Grasshopper	Free	2D
Topos	Grasshopper	Free	3D
Ameba	Grasshopper	Commercial	2D&3D
Karamba3D	Grasshopper	Commercial	Discrete 3D
BESO 3D RMIT	Python	Free	2D&3D
Ansys	Stand-alone program	Commercial	2D&3D
Altair Optistruct	Stand-alone program	Commercial	3D
Topostruct	Stand-alone program	Commercial	2D&3D
Autodesk Fusion 360	Stand-alone program	Commercial	3D
Tosca	Abaqus	Commercial	2D&3D

6.1.2 Grasshopper script

The element of Figure 105 was recreated and optimisation was executed. The goal was to minimise the amount of material, while the strength and displacement results needed to be within their respective limits. This chapter provides a quick overview of the TO process and the accompanying assumptions, boundaries and model variables. Appendix G provides an in-depth elaboration of the Grasshopper script and the TO process.

Assumptions:

- Each layer has a hardened height of 5 mm.
- Each layer is perfectly printed right on top of the layer beneath.
- The layers and paths adhere perfectly together, they form one coherent element.

Constraints:

- $\sigma_{tensile,max} \leq 3.0$ MPa
- $\sigma_{compressive,max} \leq 4.77$ MPa
- The maximum deflection in the middle of the beam is span/250.

Model variables:

- The length (span) ranged from 0.5 m to 1.2 m.
- The height ranged from 0.2 m to 0.4 m.
- The number of layers ranged from 2 to 6 layers (thickness ranges from 10 mm to 30 mm).

In order to reduce the calculation time and ensure a fully symmetrical final element, only half the beam was simulated. The corresponding mechanical scheme is displayed in Figure 106. Table 37 provides the converted material properties that were used as input for the model. A non-linear calculation was executed and the "BESO for Shells" component was used to execute the topology optimisation.

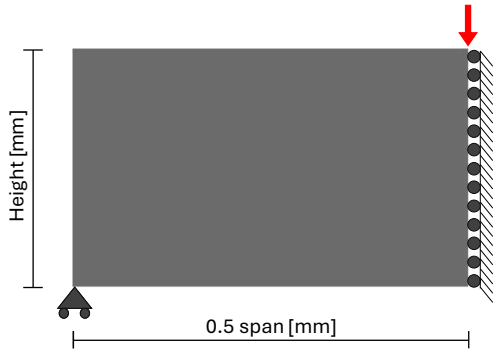


Figure 106. The mechanical scheme of only half the element.

Table 37. Material properties resulted from flexural tests using the BG with flax in vertical layer orientation.

Modulus	106.53	MPa	10.653	kN/cm^2
Specific weight	923.73	kg/m^3	9.061	kN/m^3
Tensile strength	3.00	MPa	0.300	kN/cm^2
Compressive strength	-4.65	MPa	-0.465	kN/cm^2

Figure 107 gives a result of the TO with the variables input given in Table 38. For details regarding the specific inputs of the Grasshopper components please refer to Appendix G.
The following step is to generate the print path (this process is also explained in Appendix G). Prior to this, a series of print tests were conducted to investigate the printability of “sharp” corners and to determine the print overlap between two paths. These print tests are elaborated in the next chapter.

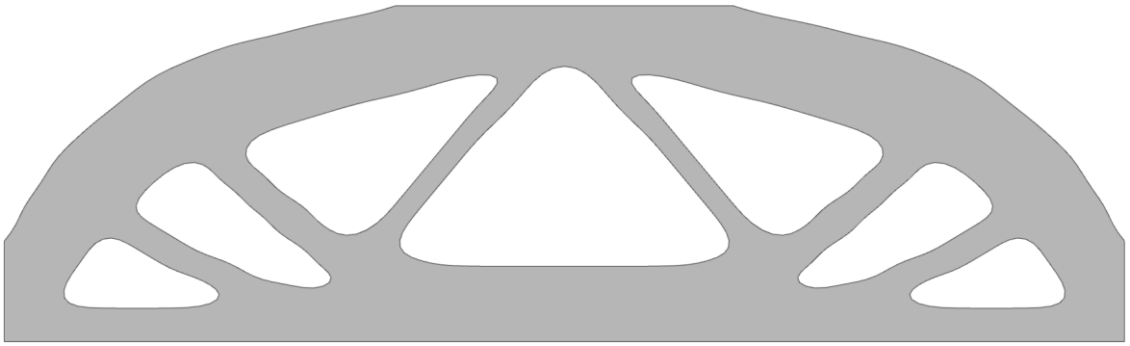


Figure 107. The result of the topology optimisation.

Table 38. Input of the model variables.

Input whole model		
Length	1000	mm
Height	300	mm
Thickness	10	mm
Load	0.01	kN

6.2 Print tests

This chapter presents an overview of the print tests. For more details, see Appendix H, which provides additional information and the corresponding Grasshopper scripts and RAPID codes. The following print tests with BG with flax mixture were executed:

- Determination of the print speed settings.
- A full cartridge print to determine the path length of one full cartridge.
- 180 degrees corner print test (Figure 108).
- The adhesion/overlap test between two paths next to each other (Figure 108).
- The adhesion/overlap test between a corner and another path (Figure 109).



Figure 108. Two print paths next to each other with a 180-degree turn at the end. The thick red line indicates the location of the overlap, and the thin red line indicates the 180-degree turn.

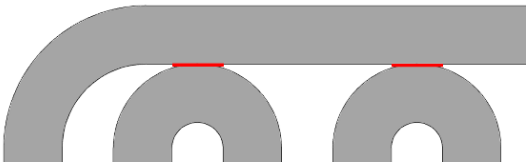


Figure 109. A part of the corner adhesion/overlap print path. The red lines indicating the location of the adhesion/overlap between corners and a straight path.

6.2.1 Print speed test

The first test was to determine the optimal Makita pressure and robot speed. For the BG with bentonite mixture, from the study of L. Roex [139], the Makita pressure was set to 1, and the robot speeds was set at 20 mm/min. These settings were used as starting points for the determination of the optimal settings for the BG with flax mixture.
As expected, these settings were not optimal for this mixture. This could be attributed to the high fibre content, compared to the bentonite mixture, which likely increased the resistance during the extrusion process. A Makita pressure of 1.1 and a robot speed of 13 mm/min, resulted in a consistent extrusion of BG with flax mixture.

6.2.2 Full cartridge print

Once the optimal speed settings were determined, the full cartridge print test was conducted and the result is shown in Figure 110. This test was conducted with one full cartridge and the Makita pressure set to 1.2 and a robot speed of 13 mm/min. The calculated print length was around 4.2 metres, and the average path width of 19.6 mm was determined.

The reason for increasing the Makita pressure to 1.2 was that the material did not come out smoothly at the start of this test. With this higher pressure, a more consistent flow was obtained. However, the path width increased gradually as the test progressed, as shown in Figure 110. The actual reason for this is unknown, but the possible explanations are addressed in Chapter 6.2.4.



Figure 110. One full cartridge print, with Makita on 1.2 and the robot on 13 mm/min.

6.2.3 Corner and adhesion tests

Subsequently, the adhesion test objects were printed. The ideal overlap between two paths was determined based on four prints with an increasing overlap, and Figure 111 shows the freshly printed objects. Due to the shrinkage of the material, the optimal overlap was determined after the elements had cured, which are presented in Figure 112. The first three prints showed some gaps between the two paths, particularly when the objects were turned over. The fourth print did not show any gaps between the two paths. The fourth print had a simulated overlap of -2.0 mm, but due to the varying path width, an actual overlap of -3.0 mm with the earlier mentioned speed settings.

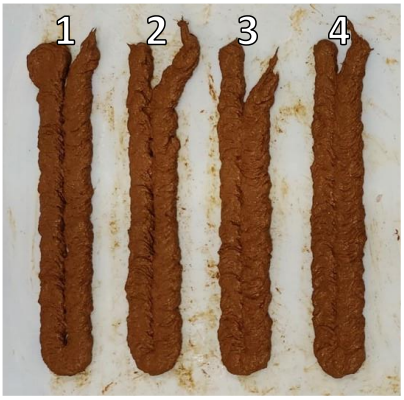


Figure 111. Freshly printed path-adhesion-test objects. With increasing overlap from 1 to 4.

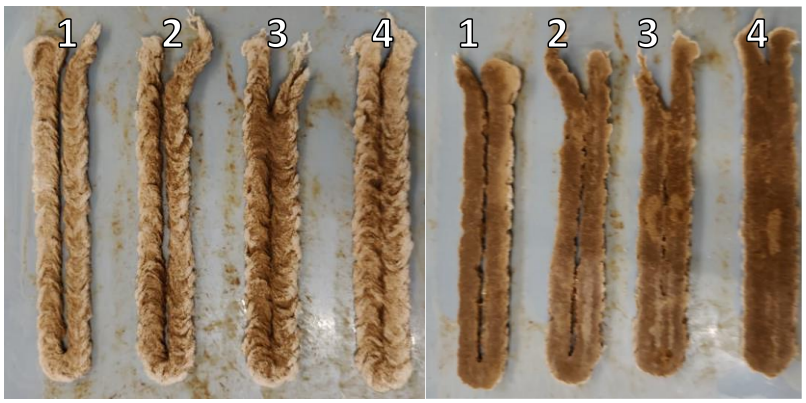


Figure 112. Cured path-adhesion-test objects. With increasing overlap from print 1 to 4, top view on the right and the bottom view on the left

The simulated overlap value of -2.0 mm and a layer width of 18 mm were used to print the corner adhesion test, the simulation of this print path is presented in Figure 113. This path was designed to investigate the impact of the print order on the corners. The freshly printed results are presented in Figure 114. The print was simulated with a path width of 18 mm, however, the actual path width was a quite a bit larger with an average path width of 22.5 mm. Due to the varying path width, the actual overlap was -6.5 mm.

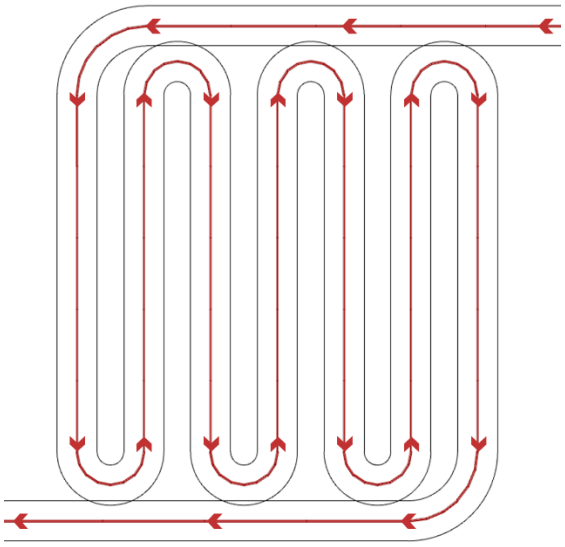


Figure 113. The print path (red line) of the corner adhesion test. The black lines indicate the outside of the paths, and the arrows indicate the print direction.

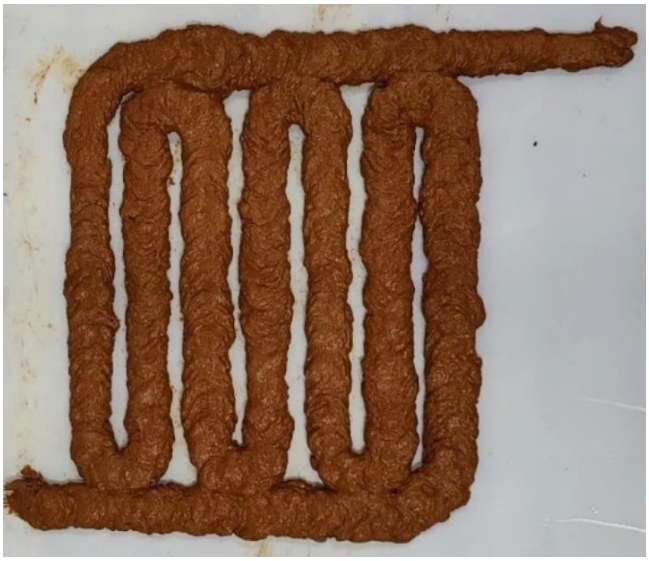


Figure 114. Freshly printed corner adhesion test print.

Figure 115 shows the cured results of the corner adhesion test. Five of the six corners exhibit sufficient adhesion to the respective straight line. Figure 116 provides a photo of the bottom of the cured print and a close-up of the corner that displays a lack of adhesion to the straight line. At this particular corner, both the path widths of the straight line and the corner itself are smaller than the rest of the printed object. Table 39 presents the path widths and the actual overlap of this corner.



Figure 115. Cured corner-adhesion-test print.

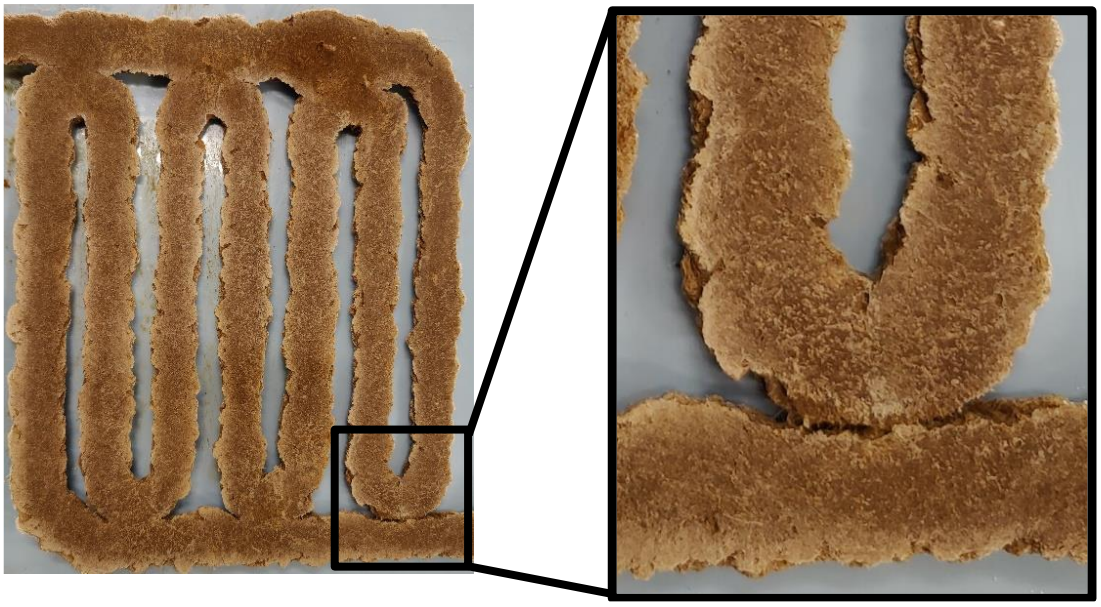


Figure 116. A close up of the bottom of cured corner adhesion test print, of the corner that shows gaps.

Table 39. Actual overlap in the corner that resulted in no adhesion.

Simulated C.T.C distance [mm]	Corner path width [mm]	Straight path width [mm]	Actual overlap [mm]
16	19	18	-2.5

6.2.4 Discussion and conclusion of the print tests

The print tests show that the path width is not a constant value and can exhibit significant variation during the printing process. This variation could cause complications when printing complex elements. It could result in weak adhesion between adjacent paths or could cause sagging when stacking layers. The three most likely explanations for the varying path width are discussed below:

- The mixture is not homogeneous.

  The mixture with flax fibres contains a relatively high number of different fibres (flax and cellulose) which could clump together, thereby potentially clogging the nozzle. This clogging could in turn lead to less material being extruded, and hence a smaller path width. Furthermore, a clogged nozzle may result in an increase in pressure. When the pressure inside the cartridge is too high, too much material will eventually burst out the nozzle, leading to a larger path width.

- There is a difference in resistance during printing.

  The resistance of the material within a cartridge is likely to be higher when the cartridge is completely filled in comparison to the resistance when the cartridge is less full.

  Due to the higher resistance when the cartridge is full, the material could expand, causing even more resistance. This causes less material to be extruded, leading to a smaller path width. When the amount of material in the cartridge decreases during printing, the total resistance also decreases. This could cause more material to be extruded, leading to larger path widths. However, this explanation only explains the phenomenon that occurred while printing the full cartridge print (Figure 50). At the start of this print, the path width is significantly less compared to the path width at the end of this print and the path width gradually increases while the amount of material in the cartridge gradually decreases.

- A cartridge is damaged.

  One of the cartridges was damaged on the inside, causing much more material to stick to the inside compared to the other two cartridges that were used. This could have caused differences in the resistance between the cartridge and the material, potentially influencing

the flow rate at which the material was extruded during printing and resulting in fluctuations in the path width.

In order to achieve a consistent path width during printing, it was necessary to eliminate the damaged cartridge. The next step was to test whether a higher Makita pressure causes a more consistent path width and if so, then a new print speed test needs to be executed with the higher Makita pressure. This is addressed in Chapter 6.4.

From the analysis of the best overlap value, two different values were calculated: -3.0 mm and -6.5 mm. However, the fourth path adhesions test and the corner adhesion test had one value in common, which was the C.T.C. distance of 16 mm. So instead of designing with a certain overlap, the C.T.C. distance value is kept at 16 mm in future prints.

6.2.5 Lignin shortage

Upon completion of the final print tests, the amount of lignin became short and, unfortunately, this specific material could not be ordered again. Earlier during the project, a second order of lignin was received, however the colour of this batch was different, as illustrated in Figure 117. Furthermore, the prepared mixtures had a different consistency and turned out to be much more sticky and this resulted in unmanageable and unprintable mixtures.

The supplier, company WEPA, stated that the second order of lignin originated from the same large container as the first order. However, the lignin affected the workability of the mixtures significantly, and therefore, only the remaining material from the first order was used.
The remaining lignin was ± 1740 gram, which was sufficient for ± 5.5 print batches (see Chapter 3.4 for the print batches), which could fill approximately eight cartridges. The necessary test elements require two or three cartridges, meaning that the size of the final element was limited to five of six cartridges.



Figure 117. Photo two piles of lignin. The first order on the left and the second order the right.

6.3 New shape

As a consequence of the lignin shortage, a new design for the final element was created. This design needed to be simple and includes some of the tested connections from Chapter 6.2.
In order to prevent interruptions at critical points, one cartridge should be utilized to print one layer. This meant that 4.0 meter was the maximum print length, resulting in an element of five layers. However, if less than 4.0 meters is printed, at least six layers can be realized.
Figure 118 shows a hand-drawn sketch of the new design, which is a variation of a truss: it consists of a top and bottom chord and diagonals. This design was recreated using Grasshopper, shown in Figure 119, and the script for this design can be found in Appendix I. The output of the script was a line model that could be transferred to GSA, where a numerical calculation was executed to determine the maximum displacement and stresses.
The final design was created in a number of steps. First, four different outer shapes were compared, and the optimal shape was selected. Then three different infills were compared and the best one was selected. These are addressed in sections 6.3.1 and 6.3.2, respectively. Finally, the dimensions and the cross-section were optimised based on the slenderness, lateral torsional buckling and print length.

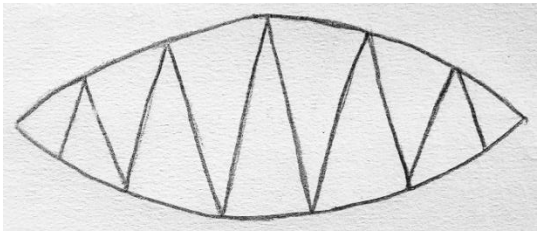


Figure 118. Hand drawn sketch of the idea of the new shape.

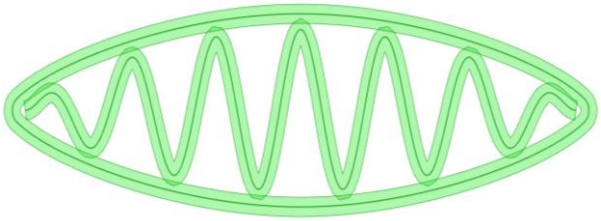


Figure 119. The design created in Grasshopper.

6.3.1 Outer shape

6.3.1.1 The four different shapes

Figure 120 shows the four designs, which differed only differ in outer shape, i.e. all other variables were identical, and their corresponding mechanical schemes. The infill waves were based on a sinusoidal function and followed the outer shape.
The mechanical schemes were simplified: the centre lines of the outer shape and the infill overlap where the waves meet the outer shape. In reality, however, these centre lines do not overlap, creating eccentricity within these nodes, as illustrated in Figure 121. This eccentricity was disregarded in this analysis, but will be taken into account in further analyses.
Each shape is 800 mm long, 240 mm high and is constructed of four layers. The shape is supported by a hinge and a hinged roller. The span between the supports is 780 mm and a load is applied in the centre at the top of the element.

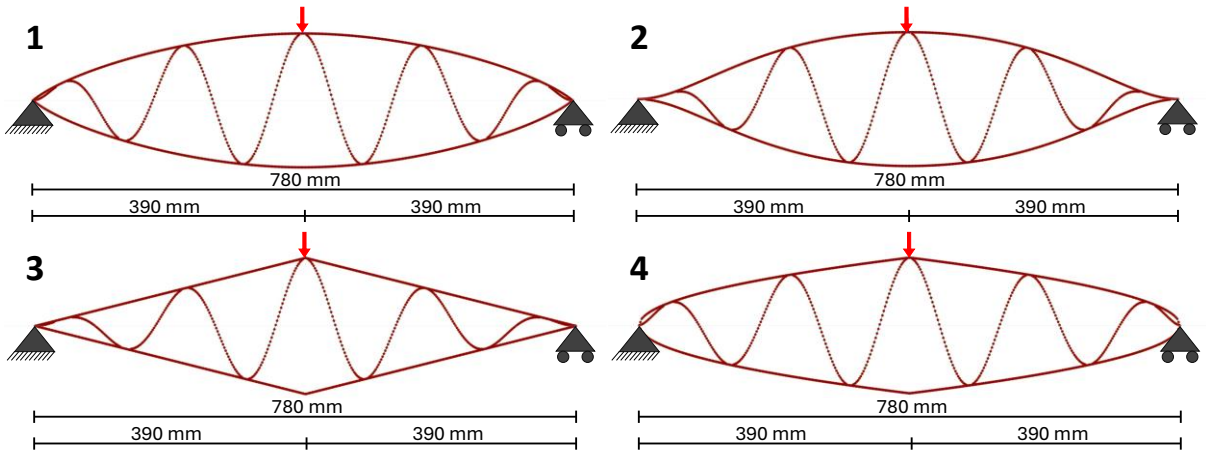


Figure 120. Mechanical schemes of shape 1, 2, 3 and 4.

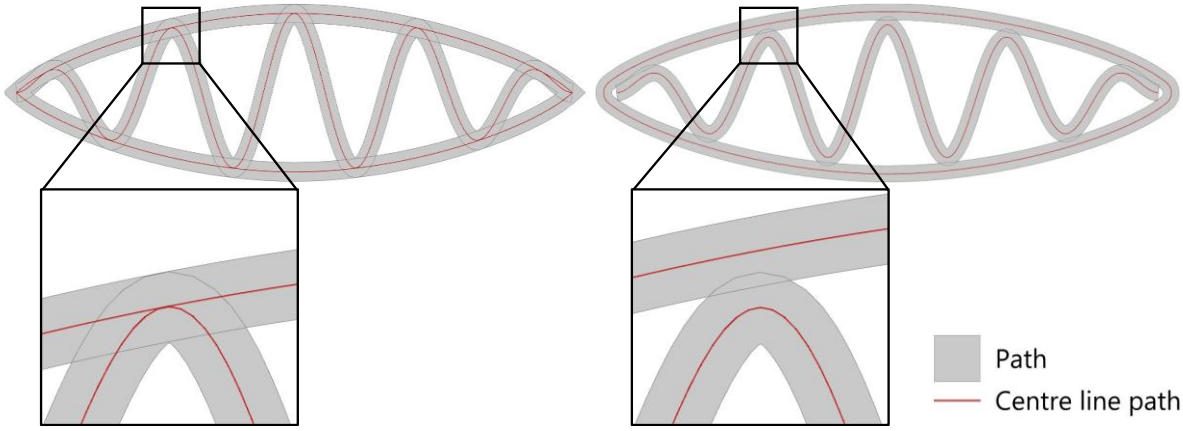


Figure 121. Details of the simplified design (on the left) and the design with eccentricity in the nodes (on the right).

6.3.1.2 Material and element properties in GSA

Using GSA, numerical models were created. The geometric properties of the cross-section are listed in Table 40. Figure 122 shows the four shapes with the selected cross-section. The following assumptions were made:

- Each layer has a constant width.
- Each layer has a constant hardened height of 5mm.
- Every layer has the same dimensions.
- Each layer is perfectly printed right on top of the layer beneath, the cross-section is thus a perfect square.

Table 40. Geometric properties of the cross-section.

Name	Width [mm]	Height [mm]	A [cm²]	I_{yy} [cm⁴]
4 layers	20	20	4.00	1.33

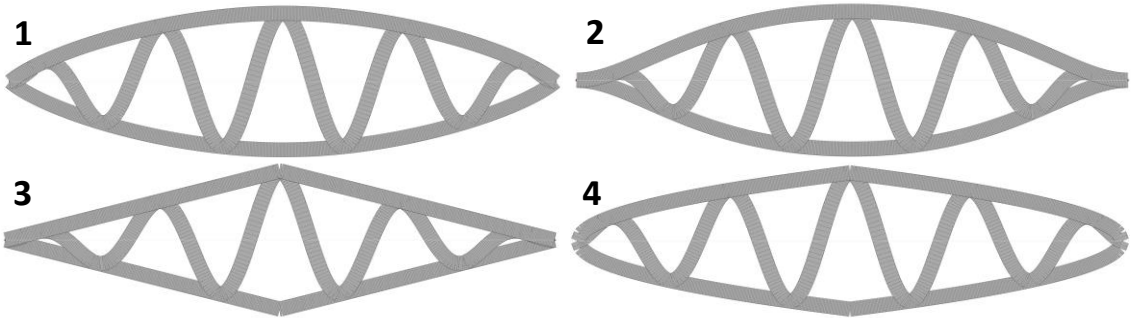


Figure 122. The four shapes in GSA with a cross-section of 20x20mm.

Two different types of loads were applied to the element: a gravity load, representing the self-weight of the structure and an applied load, a point load of 0.1 kN.

The material properties of the element are listed in Table 41. It was assumed that the material was elastic isotropic, and that the flexural modulus and the elastic modulus of the material were equal. Following a sensitivity analysis of the shear modulus and the Poisson's ratio, it was concluded that default values of GSA could be used (see Chapter J1 of Appendix J for details of this analysis).

Table 41. Material properties.

Elastic modulus (E)	106.5	MPa
Density (ρ)	923.7	kg/m³
Shear modulus (G) ($E/2\,(1+\nu)$)	40.97	MPa
Poisson's ratio (ν)	0.30	

6.3.1.3 Type of analysis and the required output of GSA

Large displacements could occur, due to the low E-modulus. Such displacements may influence the stress distribution within the element. Therefore, a non-linear analysis was conducted to take this stress redistribution into account when analysing the structure [155]. And the nodal displacement in the z-direction (U_z) was required as the first output.

The second output were the combined stresses. The equations for these stresses are provided by equations 6 and 7 [155]. Due to the loading conditions, the flexural stresses in the y-direction of the cross-section are zero. Consequently, the combined stresses consist only of the axial stresses and the flexural stresses in the z-direction.

$$C_1 = A + |B_y| + |B_z| \qquad C_1 = A + |B_z| \tag{6}$$

$$C_2 = A - |B_y| - |B_z| \qquad C_2 = A - |B_z| \tag{7}$$

In which: C_i = *the maximum and minimum combined stresses [MPa]*
A = *the axial stress [MPa]*
B_z = *the flexural stress in the z direction [MPa] (see equation 8)*
$B_y = 0$ = *the flexural stress in the y-direction [MPa]*

$$B_z = \frac{M_{zz}}{I_{zz}} D_y \tag{8}$$

In which: B_z = *the flexural stresses [MPa]*
M_{zz} = *the flexural moment [Nmm]*
I_{zz} = *the second moment of area the cross section [mm^4]*
D_z = *the distance between the line of gravity and the outer fibres of the cross section [mm]*

6.3.1.4 Results and conclusion outer shape

This section discusses the analysis results of the four shapes. For detailed results see figure J1 to figure J12 in Appendix J. Table 42 presents the maximum values of the outputs for each shape, with the overall largest displacement and largest stresses highlighted. The selection of the optimal outer shape was based on an elimination process, with shape 3 being the first to be eliminated due to its largest displacement and highest tensile stresses. This resulted in the values presented in Table 43. It is clear from this table that now shape 2 has the largest displacement and the highest compressive stresses and was therefore eliminated, which resulted in the values presented in Table 44.

Table 42. Maximum results of each shape analysis.

Outer shape	U_z	Maximum combined stresses*	
		C1	C2
	[mm]	[MPa]	[MPa]
1	2.509	0.5629	-0.7508
2	3.493	0.5925	-0.8111**
3	4.428**	1.1010**	-0.5785
4	2.769	0.7133	-0.6019

**) Positive values represent tensile stresses, and the negative values represent the compression stresses.*
***) Highest result for the specified parameter is highlighted in red.*

The values presented in Table 44 show that shape 4 exhibited the highest tensile stresses and the largest displacement, while shape 1 had the highest compressive stresses. As the tensile stresses were the most decisive, please refer to, see Table 34 in Chapter 5.3.2 for explanation. This ultimately led to the elimination of shape 4, and consequently, shape 1 was selected as the most optimal outer shape.

Table 43. Maximum values for analyses of shape 1, 2 and 4.

Outer shape	U_z	Maximum combined stresses*	
		C1	C2
	[mm]	[MPa]	[MPa]
1	2.509	0.5629	-0.7508
2	3.493**	0.5925	-0.8111**
4	2.769	0.7133**	-0.6019

**) Positive values represent tensile stresses, and the negative values represent the compression stresses*
***) Highest result for the specified parameter is highlighted in red.*

Table 44. Maximum values for the analyses of shape 1 and 4.

Outer shape	U_z	Maximum combined stresses*	
		C1	C2
	[mm]	[MPa]	[MPa]
1	2.509	0.5629	-0.7508**
4	2.769**	0.7133**	-0.6019

**) Positive values represent tensile stresses, and the negative values represent the compression stresses*
***) Highest result for the specified parameter is highlighted in red.*

6.3.2 Infill

The next step in designing the final element was to determine the best infill. Three different infills were analysed: a wave-like infill with three, five or seven peaks at the top. These three elements are referred to as 3-waves, 5-waves and 7-waves, respectively.
These elements had the same properties as mentioned in Chapter 6.3.1.2 and the same type of analysis was executed as stated in Chapter 6.3.1.3.

6.3.2.1 The three different infills

In the previous step, the eccentricity was disregarded, although it might have significantly impacted the stress distribution. In order to include this eccentricity at the nodes, it was necessary to connect the two centre lines of the outer shape and the infill, see Figure 123. In GSA, these connections were created as follows: first, the element was created with only the infill and the outer shape (panel 1). At the places where the cross-sections overlapped, connection elements were created, and to prevent shear in these connection elements, the connection consisted of a few straight elements with diagonals in between (panel 2). These connection elements had the same properties as the rest of the element (panel 3). Using this connection, all the forces that occur in these nodes could be transferred, without any peak stresses occurring in the additional connection elements.

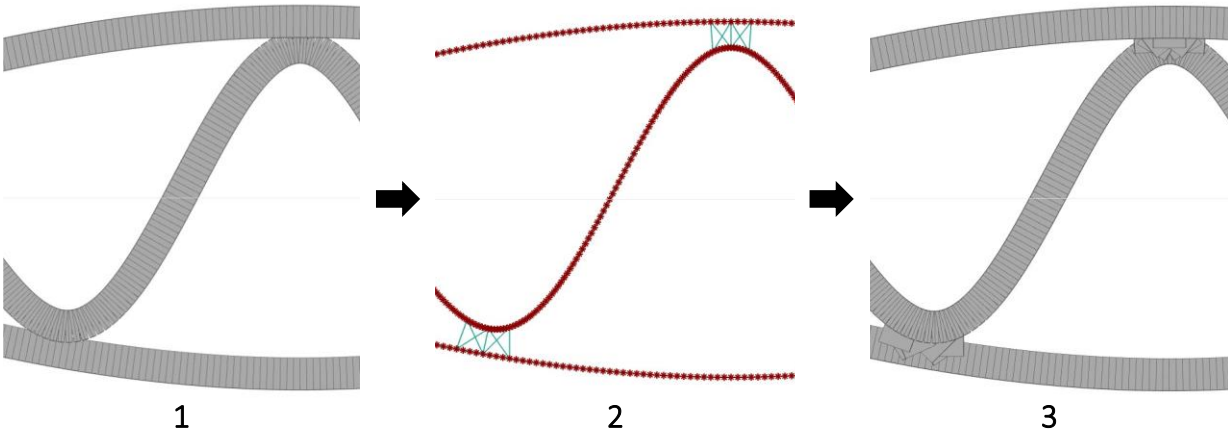


Figure 123. Creating a connection between the infill and the outer shape.

This method of connecting the outer shape and infill was applied on the three different infill variants, as illustrated in Figure 124, which shows the three different infills and their corresponding mechanical schemes.

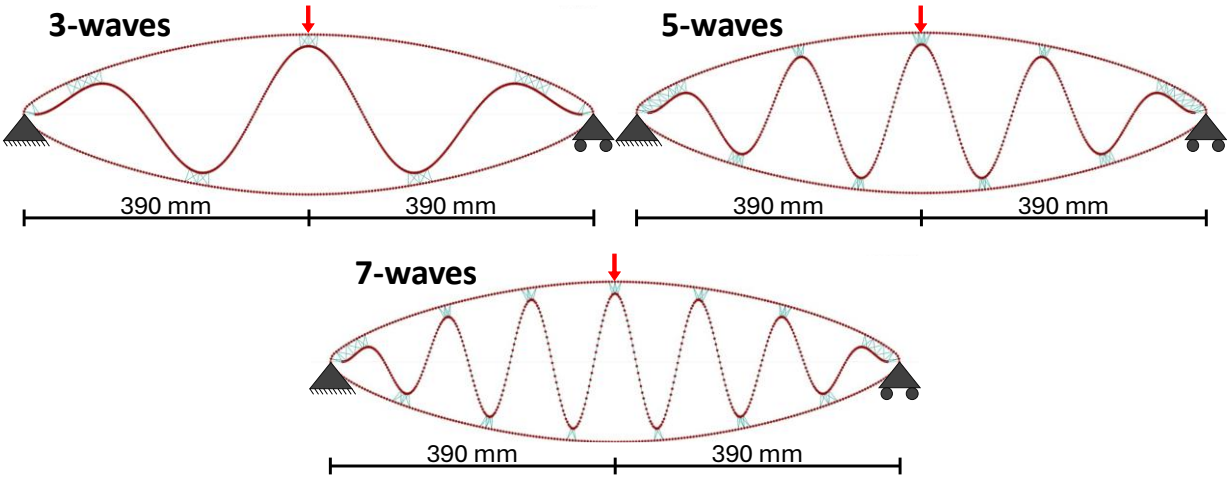


Figure 124. Mechanical schemes of the different infill variants.

6.3.2.2 Results and conclusion

This section discusses the analysis results of the three different infills, with Table 45 presenting the maximum values of the output for each shape. It is evident that the 7-waves element has the smallest displacement and the lowest stresses. Consequently, the 7-waves was therefore selected as the most optimal infill. Detailed results of the individual analyses are provided in figures J13 to J21 in Appendix J.

Table 45. Maximum values for the results for each infill.

Number of waves	U_z	Maximum combined stresses*	
		C1	C2
	[mm]	[MPa]	[MPa]
3	2.629**	0.7194**	-0.5772**
5	2.131	0.4507	-0.4335
7	2.113	0.3746	-0.4277

**) Positive values represent tensile stresses, and the negative values represent the compression stresses*
***) Highest result for the specified parameter is highlighted in red.*

6.3.3 Print path

Once the final shape was determined, the print path was designed. In order to prevent weak points in the element that could be caused by replacing an empty cartridge halfway a layer, it was decided that a single layer should be printed with one cartridge. Thus, a print path for one single layer was designed, with an adjustable height to be able print all the layers. To prevent the accumulation of material, the print path was designed without crossing itself. The start and end points were strategically located "outside" the element, ensuring that the replacement of a cartridge and the continuation of printing would not result in interruptions within a layer, thereby preventing the creation weak points in the element. Furthermore, this ensured that the extrusion functioned properly before reaching the main part. Following the curing of the element, these "outside" parts were sawn off. The print path is illustrated in Figure 125. It is acknowledged that the best method of printing an element is to print all the layers in one setting. However, this was not possible, due to the limitations of the current printer setup.

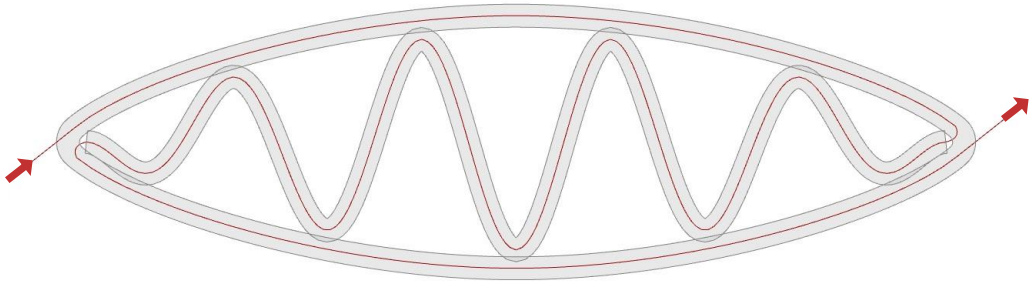


Figure 125. The print path for one layer of the final element. The grey part is the final shape, and the red line is the centre line.

6.3.4 Optimised dimensions and test setup selection

6.3.4.1 Optimisation of dimensions of the final element

The dimensions of the final element used in previous chapters, were determined by the maximum dimensions that could be printed and tested in the SED-lab, rather than on structural functionality. It was noted that the height and width of the beam (20 mm by 240 mm) resulted in a relatively slender cross-section, and with a length of 800 mm, this created a slender beam, which is disadvantageous for the mechanical behaviour of the element. Therefore, an optimisation was conducted to determine the most optimal dimensions. For this, the Galapagos component in Grasshopper, with the previously created script, was used (Figure 126). Further information regarding this optimisation part of the script can be found in Figure I5 in Appendix I.

This component can determine the most optimal solution for a given design and requires two different kinds of input: genomes and a fitness value. Genomes are variables (i.e. number sliders) that can alter the design, whilst a fitness value is the result of a calculation and can be either maximised or minimised. The Galapagos component adjusts the number sliders to modify the fitness value, thereby combining different variable values to determine the optimal solution. It uses evolutionary algorithms based on natural selection to find the best solution. This method begins with values for the genomes to create the first generation, and only the fittest members survive. The genomes of these fittest members are used to create the next generation, and this process is repeated until Galapagos stops when the outcome cannot be further improved [156].

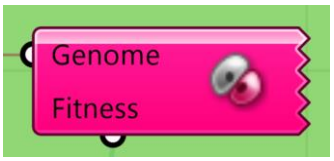


Figure 126. The Galapagos component in Grasshopper, with two different inputs: genomes and a fitness value.

In this study, the genomes were the element length, height and the number of layers (i.e. element width). The calculation of the fitness value consisted of three parts: the print length, the effective slenderness and the width-height ratio of the element. These are described in the following paragraphs.

The desired print length was set to 3.4 m, guaranteeing that the element would be sufficiently large so that it could be tested, while ensuring that there was enough material to print the whole element and some extra tests beams.

It is essential to ensure that the slenderness of the beam is kept at a minimum, in order to prevent unfavourable deformations. A slender beam, characterised by a large depth-to-width ratio and a relatively long unsupported span that is subjected to bending, is prone to lateral torsional buckling [157]. This phenomenon is caused by the relatively high compressive forces in the top of the beam, as illustrated in Figure 127.

The effective slenderness ratio was calculated using the formula provided in equation 9. To avoid lateral torsional buckling, the effective slenderness ratio needed to be minimised and therefore a maximum of 225 was applied [158].

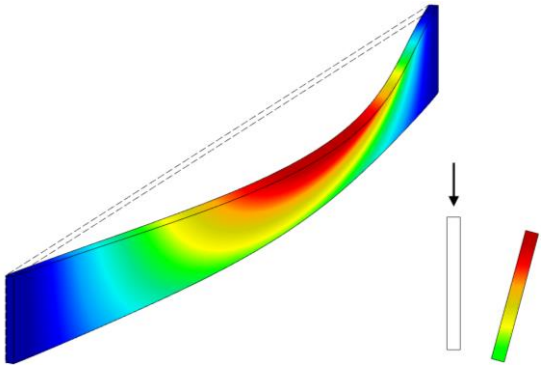


Figure 127. Lateral torsional Buckling of Single-Span Beam [159].

$$\lambda_{ef} = L_{ef} * \frac{h}{b^2} < 225 \qquad 9$$

In which: λ_{ef} *= effective slenderness ratio [-]*
L_{ef} *= effective span [mm]*
h = height in the middle of the beam [mm]
b = beam width [mm]

In addition to the effective slenderness of the beam, the width-to-height ratio of the element can significantly influence its stiffness. Although the width and the height of the element already feature in equation 9, an additional check was implemented. The width-height ratio was calculated using equation 10, and the result should fall between 6 and 8.

$$width/height\ ratio = 6 < \frac{h}{b} < 8 \qquad 10$$

In which: *h = height in the middle of the beam [mm]*
b = beam width [mm]

The results of the optimisation process are presented in Table 46 and Figure 128. It is clear from the side views that the optimised dimensions have resulted in a more stocky beam, which is less prone to lateral torsional buckling.

Table 46. Calculation results before and after optimisation.

	Effective slenderness ratio [-]	**Width-height ratio [-]**	**Print length [mm]**
Before	480	12	3773.8
After	178.44	7.33	3426.3

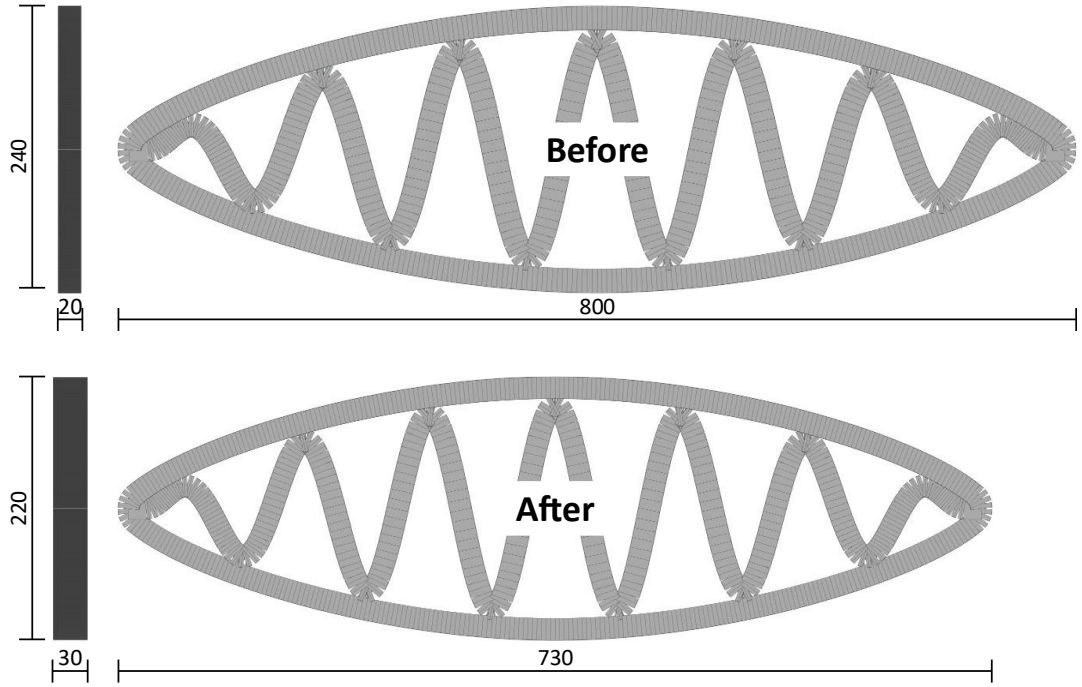


Figure 128. A side and front view of the final shape with the dimensions before and after the optimisation (in millimetres).

6.3.4.2 Different supports and loading conditions

After the optimisation process, different setups were investigated. Figure 129 and Figure 130 present two different setups: setup 1 and setup 2. Figure 131 shows the names used in this study to identity parts of the element.

The primary difference between the setups, is in the positioning and size of the supports. In order to prevent local stress peaks, the supports should cover a larger area in order to distribute the stresses

In Setup 1 the supports are positioned at a point where the first valley meets the bottom chord. The connections between the infill and the chords may be considered a weak point due to the manufacturing process, placing the supports at these points could therefore result in even higher local peak stresses.

Setup 2 involves a 180-degree rotation of the element (i.e. it is flipped upside down) and two (half) loads are applied at the two middle tops. The supports are positioned where the waves and the bottom chord converge, where more material is located compared to setup 1, due to the two paths being adjacent to each other. This could potentially result in less high local peak stresses compared to setup 2, which would be a favourable outcome.

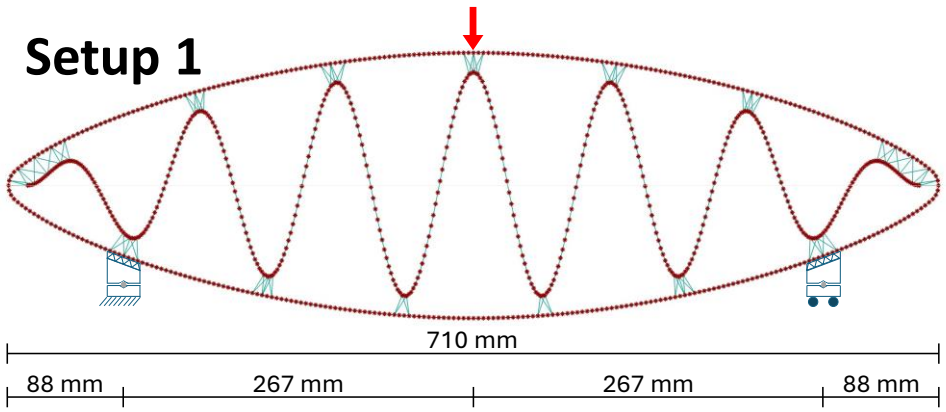


Figure 129. Mechanical scheme of setup 1.

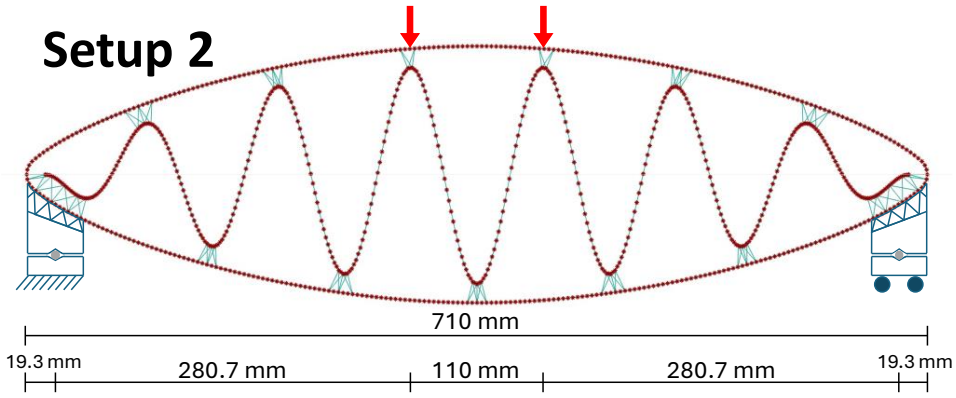


Figure 130. Mechanical scheme of setup 2.

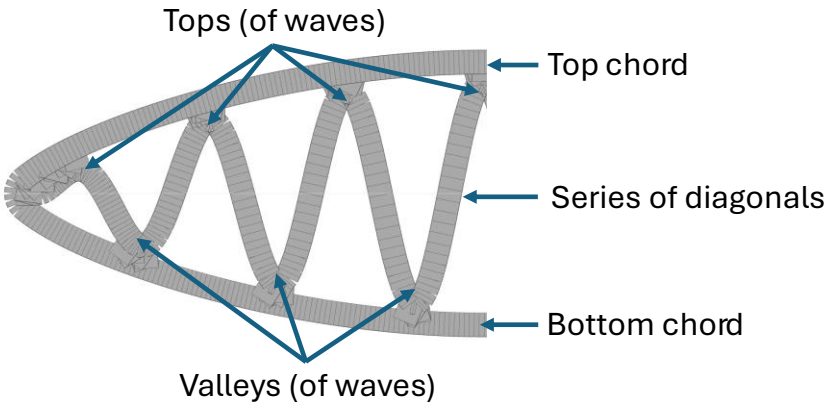


Figure 131. Naming conventions of parts of the element.

The optimisation process led to the geometric properties presented in Table 47 and the same cross-sectional assumptions as in Chapter 6.3.1.2 were adopted. And the total applied load for each setup is 0.1 kN. In the case of setup 2, this is divided over the two loads, resulting in two loads of 0.5 kN.

Table 47. Geometric properties of the cross-section in GSA.

Name	Width [mm]	Height [mm]	A [cm²]	I_{yy} [cm⁴]
6 layers	30	20	6.00	2.00

A comparative analysis was conducted on the results of setups 1 and 2 (see Table 48). The differences between the two setups were considered negligible due to the minimal differences observed. This was attributed to the fact that the self-weight of the element was relatively large compared to the applied load of 0.1 kN. Consequently, the total applied force was increased to 1 kN, and the structures were analysed once more. The results of these analyses are presented in Table 49. For more detailed analyses, see Figures J22 to J33 of Appendix J.

Table 48. Maximum values for the results of setups 1 and 2, with an applied load 0.1 kN.

Setup	U_z	Maximum combined stresses*	
		C1	C2
	[mm]	[MPa]	[MPa]
1	0.8074	0.1813	-0.2335
2	0.8612	0.1848	-0.2771

**) Positive values represent tensile stresses, and the negative values represent the compression stresses*

Table 49. The results of setups 1 and 2, with an applied load 1 kN.

Setup	U_z	Maximum combined stresses*	
		C1	C2
	[mm]	[MPa]	[MPa]
1	7.540	1.770	-2.225
2	7.670	1.694	-2.335

**) Positive values represent tensile stresses, and the negative values represent the compression stresses*

It is clear from the presented data, that setup 2 exhibited the largest displacement and the highest compressive stresses, while setup 1 exhibited the largest tensile stresses. As previously mentioned in Chapter 5, the material was less strong in tension than in compression. Therefore, the lowest tensile stress was an important argument to select setup 2 as the final test setup. Furthermore, setup 2 utilised a larger part of the element to transfer the load to the supports, whereas with setup 1 the outer parts of the element were not utilised for the load transfer.

6.4 Printing the final element and test beams

6.4.1 Final prints

For the sake of clarity, the final prints were done with the same mixture ratio as the previously made test beams with BG with flax (see Chapter 3.4). This final mixture is from now on referred to as the 'second' mixture, whereas the original mixture is referred to as the 'first' mixture.

In order to ensure a more consistent path width during the printing process, a series of additional extra print tests were conducted, during which certain print settings were adjusted. The Makita pressure was increased to 2 and a new print speed was explored and for a more detailed elaboration of this new print test, see Chapter K1.1 of Appendix K. The new print speed was 32.5 mm/s with the Makita pressure set to 2 with an average fresh print path of 18.7 mm.

Once the new print speed had been determined, the final element was printed, and the freshly printed element is presented in Figure 132. Upon completion of the final element print, the remaining material was used to print five test beams (Figure 133).
During the printing process of the final element, (significant) misalignments between the layers occurred. This was due to the fresh layers having a lower height than expected, resulting in that the predetermined nozzle standoff distance was incorrect (the fresh layer height was assumed to be equal to that of the final prints made by L. Roex [139]). With the final three layers, this was addressed by manually adjusting the nozzle standoff distance before printing a new layer. However, this misalignment caused many imperfections in the element, some of which were fixed by gently pushing some material back to its original place, but some could not be easily corrected. After the final element was fully printed and was set aside, a part of the final element fell over (Figure 134). This part was gently put back by hand (Figure 135).
An elaborate description of the printing processes of all the prints can be found in chapters K1.2 and K1.3 of Appendix K.



Figure 132. Freshly printed final element.

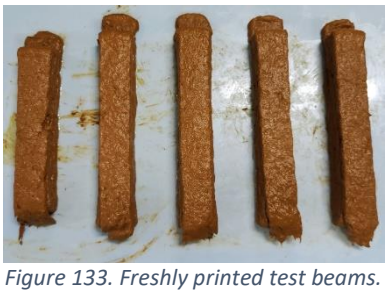


Figure 133. Freshly printed test beams.



Figure 134. Part of the freshly printed final element that fell down.



Figure 135. Part of the element that had fallen down but was pushed back up again.

The freshly printed final element and the test beams were placed in the climate room until the tests were performed. The curing conditions were the same as those described in Chapter 4.3, except that now weights were added on top of the elements to prevent warping. The curing process took 40 days, and the cured final element and test beams are presented in Figure 136 and Figure 137. A detailed description of the whole curing process is provided in Chapter K2 of Appendix K.



Figure 136. Cured final element.



Figure 137. Cured test beams

During the curing process the elements shrunk substantially, which was calculated using the fresh and cured dimensions of the final element and test beams. For the test beams, the length, height and width were measured, while for the final element, only the height was measured. Table 50 and Table 51 present the average shrinkage results for the final element and the test beam, respectively. See Chapter K3 and K4 of Appendix K for more details.

Table 50. Average shrinkage of the height of the final element.

Fresh height [mm]	Cured height [mm]	Shrinkage [%]*
36.5	27.4	25

**) Compared to the original dimensions of the freshly printed element.*

Table 51. Average shrinkage of the test beams.

Length [%]*	Height [%]*	Width [%]*
4	32	10

**) Compared to the original dimensions of the freshly printed element.*

6.4.2 Discussion

The issues with the misalignment of the layer of the final element arose around the third layer. The best way to deal with this would have been to remove all the printed layers and reprint from the start or to start over with a new batch on another day. However, reprinting would have cost a lot of time to recalibrate the robot and reprint the element, which was not possible due to the closure of SED-lab at the end of the day. To start another day was also not possible, because almost all of the leftover lignin had been used to produce the final batch. This meant that, despite the print containing multiple inaccuracies, it had to suffice as the final element.

The main issue encountered during printing of the final element, was that the assumed height of the fresh layer was less than expected. This could have several reasons:

- The combination of the print speed and Makita pressure settings caused the layers to have different dimensions compared to the print settings of L. Roex [139].
- The final mixture of L. Roex [139] contained bentonite instead of flax fibres. Bentonite gives the mixture more stiffness, resulting in a better shape retention leading to a larger fresh height compared with the mixture with flax fibres

In some layers, it was observed that not all the waves were connected to the chords, which could be attributed to the misalignment of the layers. It is also possible that, in some areas, the path width was smaller than expected, resulting in insufficient overlap between the paths to ensure a connection. This was, however, not considered to be a significant problem during printing, due to following reasons:

- In other layers, the waves and chords were able to connect at the points where a faulty layer did not connect properly.
- The weight of the printed layer(s) could have compressed a previously printed layer, causing the path to widen slightly and enabling a connection between the wave and the chord.
- These disconnections were not observed in the first and the sixth layer.

Although this was not of great concern, it should be kept in mind during the analysis of the test results.

The curing conditions of the first and second test beams differed, i.e. weight were only used for the second test beams. As a result of the weights, the height shrinkage of the second test beams was increased (32% reduction compared to a 24% reduction of the first test beams). This resulted in more compact beams, and thus a higher density was observed.
The curing time of the first test beams was 33 and 50 days, for the compression and flexural specimens, respectively, whereas the second test beams had a curing time of 40 days for both the compression and flexural specimens. It is essential to consider the difference in curing time when analysing the test results, because the curing time can significantly impact the mechanical behaviour (as discussed in Chapter 5.3.2).

Concerning the height shrinkage, the difference between the final element and the test beams could be explained by the use of different weights. For the final element, random pieces of metal that were lying around in the SED-lab were used, whereas those for the test beams were kept almost the same, which resulted in almost the same pressure on each beam (g/mm^2). However, determining the actual pressure on the final element was difficult, as the surface area could not be determined exactly. Therefore, it may well be possible that the overall pressure on the final element was less than that on the test beams, causing the final element to be less compressed and thus have less height reduction.

The shape of the cured final element is not perfect symmetrical. Imperfections such as the chords not being perfect arcs (and others mentioned previously), should be kept in mind when making the test setup. Assembling the test setup with tolerances for these imperfections is essential.

6.5 Testing

6.5.1 Numerical model in GSA (expected results)

6.5.1.1 Mesh model

To verify the test results of the final element, a mesh with 2D elements was generated using Grasshopper and transferred to GSA. Figure 138 and Figure 139 present the mechanical scheme of the element and its mesh, respectively. This mesh represents the nodes where the waves and the chords meet more accurately than the line models used with 1D elements (as in previous GSA models, see Chapter 6.3), and the eccentricity in the nodes is now fully taken into account. The mesh is fully symmetrical and consists mostly of squares, which have a greater accuracy than the triangular elements [155].

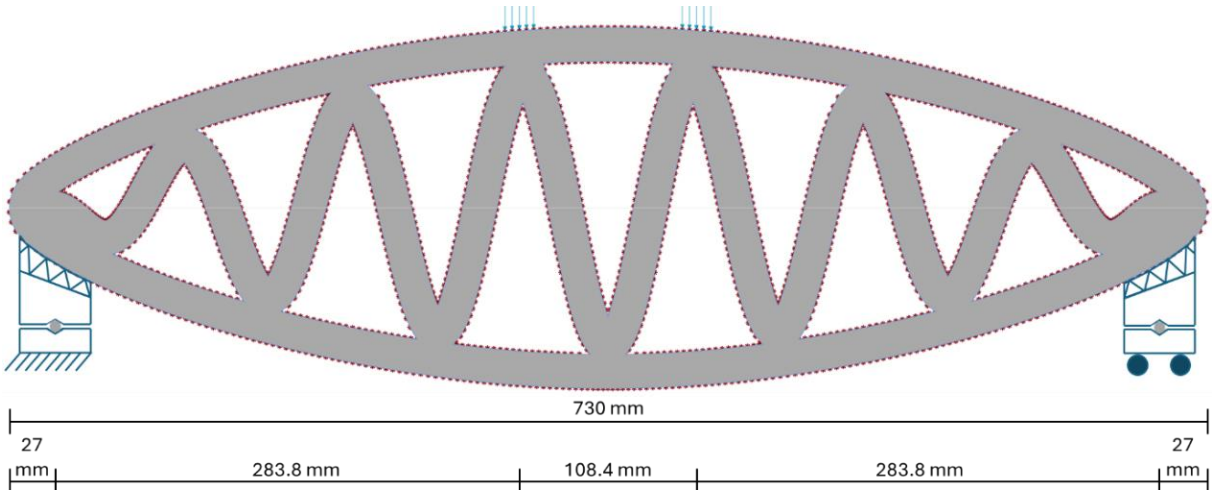


Figure 138. Mechanical scheme of the final mesh model in GSA.

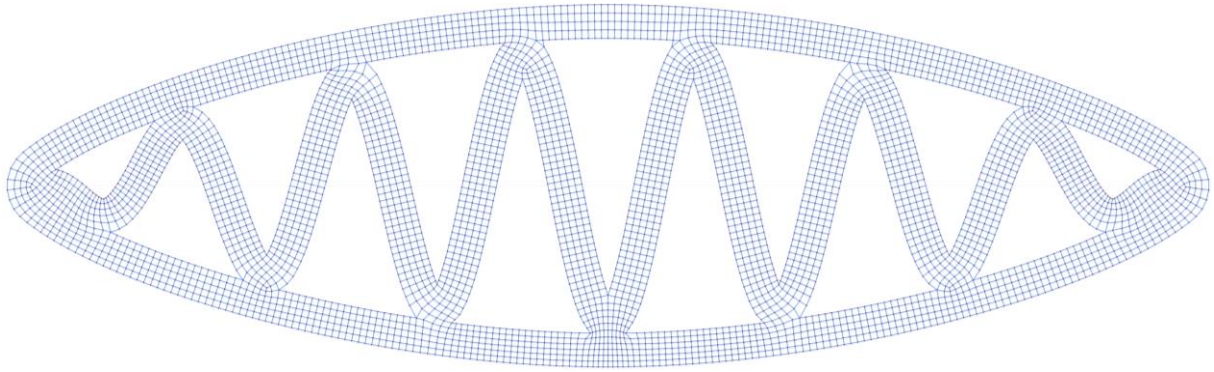


Figure 139. The mesh of the final mesh model in GSA.

To verify the accuracy of the mesh model, the same conditions and properties as those of setup 2 in Chapter 6.3.4.2 were applied and the results of the GSA analysis were compared with results of setup 2. The comparison confirmed that the mesh model accurately simulated the final element, which was, therefore, used in further analyses. For a more detailed analysis, see Chapter J5.1 of Appendix J.

Next, the final dimensions of the cross-section listed in Table 52, were applied to the mesh model. These final dimensions were based on the dimensions of the cured final element. The following assumptions for the mesh model were made for the geometric properties in GSA:

- Each layer had a constant width of 20.4 mm.
- All layers had the same dimensions.
- Each layer was perfectly printed right on top of the layer beneath, resulting in a perfect rectangular the cross-section.

- The layers and paths adhered perfectly together, forming a coherent element.
- The height of the element was constant over the whole element, with a height of 27.4 mm.

The material properties are listed in Table 53. The density was based on the second test beams described in Chapter 6.4, and for more information see Chapter K4 of Appendix K.

Table 52. Cross-sectional properties.

Name	Width [mm]	Height [mm]	A [cm²]	I_{yy} [cm⁴]
Mesh	27.4	20.4	5.59	1.94

Table 53. Material properties in GSA.

Elastic modulus (E)	106.5	MPa
Density (ρ)	1106.6	kg/m³
Shear modulus (G) ($E/2\,(1+v)$)	40.97	MPa
Poisson's ratio (v)	0.30	-

6.5.1.2 GSA analysis

In a 2D element in GSA there are six different stress components, as illustrated by Figure 140: three direct stresses (σ_{xx}, σ_{yy}, σ_{zz}) and three shear stresses (τ_{xy}, τ_{yz}, τ_{zx}). In GSA, there are two different kinds of stress results: projected stresses and derived stresses.

The projected stresses can be projected either on the global coordinate system or on the local coordinate system of each individual element.

The derived stresses allow for the selection of the principal stresses, whereby the stresses are rotated in such a way that there are no shear stresses. This approach ensures that the principal stresses are only direct stresses (tensile and compressive), with the principal axes representing the flow of these stresses [155,160].

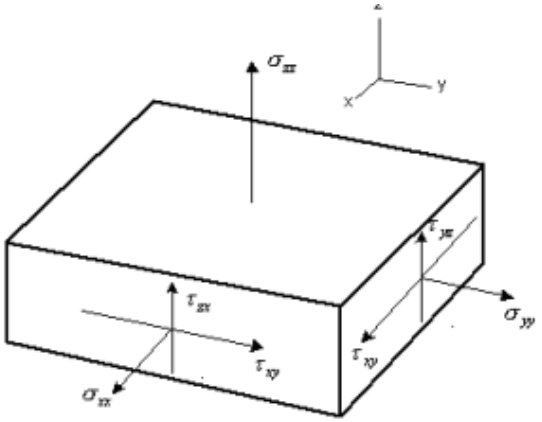


Figure 140. 2D element stress sign convention [160].

Unfortunately, due to the configuration of the mesh, the local axes of all the individual elements had the same orientation as the axes of the global coordinate system. Therefore, the projected stress results were considered useless. So, the principal stresses of the element were used for the analysis, and Figure 141 shows the orientations of these principal stresses.

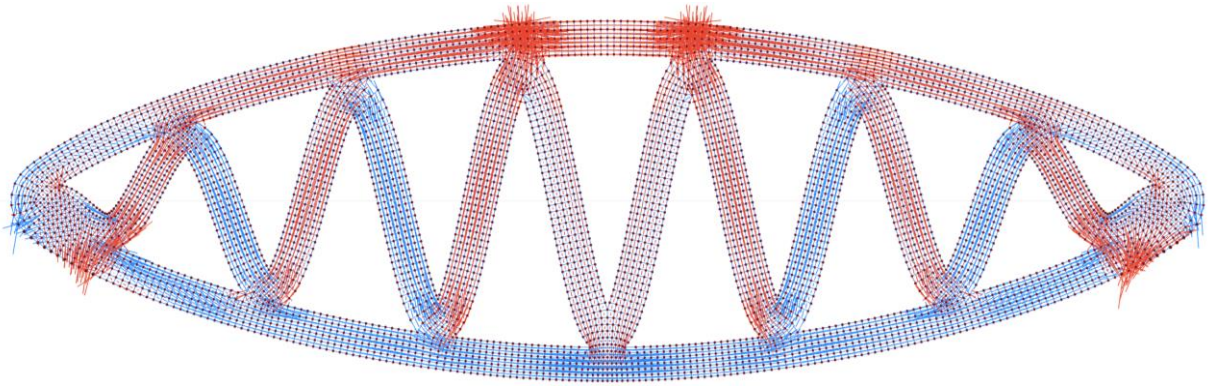


Figure 141. The orientation of the principal stresses. Red lines indicate compressive stresses, and blue lines tensile stresses.

To determine the failure load of the element, a trial-and-error analysis was conducted with the results presented in Table 54. The failure load resulted in the maximum tensile stresses in the bottom chord reaching the tensile strength of 3 MPa. The fifth attempt resulted in a value of 3 MPa for the tensile stresses in the bottom chord, with a corresponding applied load of 1.63 kN.

Table 54. Failure load of the final element.

Attempts	Applied load [kN]	Tensile stresses in bottom chord [MPa]	Displacement in bottom chord [mm]
1	1.00	1.841	-8.042
2	2.00	3.691	-16.09
3	1.60	2.948	-12.85
4	1.62	2.985	-13.02
5	1.63	3.003	-13.10

Table 55 presents the GSA analysis results using an applied load of 1.63 kN. Please, see Chapter J5.2 of Appendix J for full elaboration of results including the local peak stresses.

Table 55. Maximum values for the results with the applied load of 1.63 kN.

Model	U_z	Principal stresses*		
	Bottom chord [mm]	Tensile [MPa]	Compressive [MPa]	Tension in bottom chord [mm]
Mesh model without local peak stresses	13.10	3.00	-2.93	3.00

**) Positive values represent tensile stresses, and the negative values represent the compression stresses*

The maximum tensile stresses of 3.00 MPa and occurred in the middle of the bottom chord, while the maximum compressive stresses of 2.93 MPa occurred at the top chord close to the load locations. These stresses equalled or were below than the material's strength (refer to Table 34 for the material's strength), indicating that the final element can easily reach 1.63 kN with ease before breaking, since the 3.00 MPa is the "save" tensile strength and not the ultimate stress.

6.5.2 Tests setup

Three types of tests were carried out: compression, flexural and the final element test. The general test setups for the compression and flexural tests were the same as described in Chapter 5.1. For now, only the vertical layer orientation was tested and instead of the Schenck Trebel test bench an Instron electromechanical universal testing machine with a load cell of 250 kN was used. For the flexural tests, a LVDT (Linear Variable Differential Transformer) sensor was placed at the midpoint of the bottom of a specimen to measure the displacement at the bottom. Figure 142 and Figure 143 present the compression and the flexural test setups, respectively. These tests were displacement controlled with a speed of 2 mm/min. And the vertical displacement and the force applied on the specimen were measured. These values were then used to calculate the compressive strength (f_c), the compressive strain and the compression modulus (E_c).



Figure 142. The compression test setup placed in the Instron electromechanical universal testing machine.

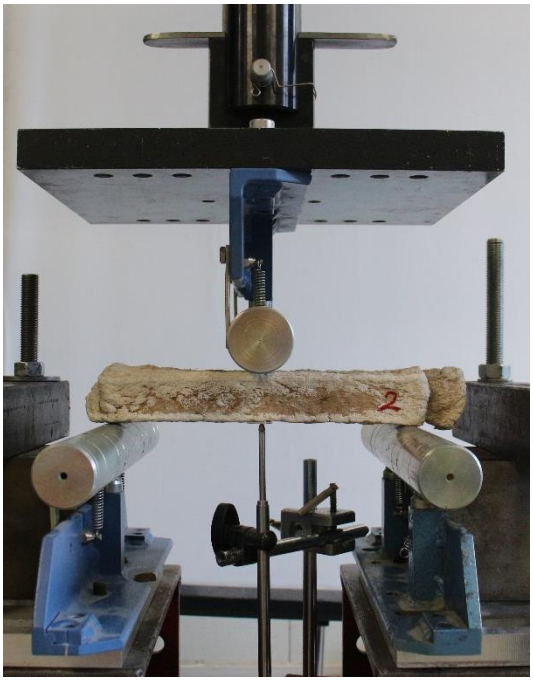


Figure 143. The flexural test setup placed in the Instron machine, with a LVDT sensor at the midpoint of the bottom.

Figure 144 shows the final element test setup. The load was applied to the top chord and distributed over two rollers, which were attached to a plate that was able to rotate slightly. This enabled the rollers to continuously be in contact with the element, resulting in an evenly distributed load on the element.
The element was supported on both sides by two U-shaped wooden blocks (see Figure 145), with two layers of foam between the wood and the element to compensate for the imperfections of the element preventing high local stresses. On top of each wooden block, two L-shaped plates were attached to prevent the element from tipping over or turning sideways. These plates were not in contact with the element, but only touched the element when tipping over.
Perpendicular to the cutout for the element, the wooden blocks had a cylindrical cutout at the bottom, allowing them to be placed perfectly on top of two bars. This allowed free rotation around the bars, thereby creating a hinged connection on both sides. The bar on the right could move slightly in the vertical direction and acted as a hinge on a roller, whereas the bar on the left had a fixed position and functioned only as a hinged support.
This setup was installed in the Instron electromechanical universal testing machine, which was equipped with a load cell of 5 kN. The test was displacement controlled with a speed of 1 mm/min. The vertical displacement at the middle of the bottom chord and force applied on the specimen were measured, by the LVDT sensor and the machine respectively.

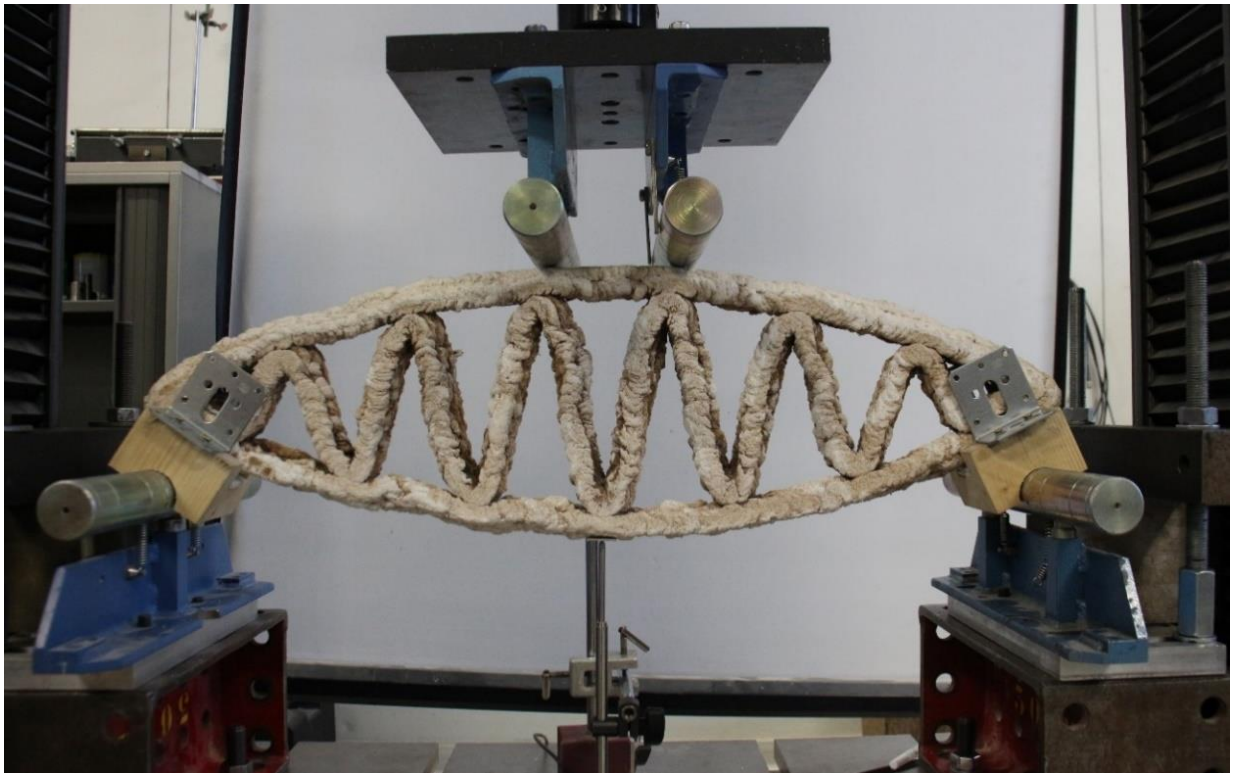


Figure 144. Final element test setup up.

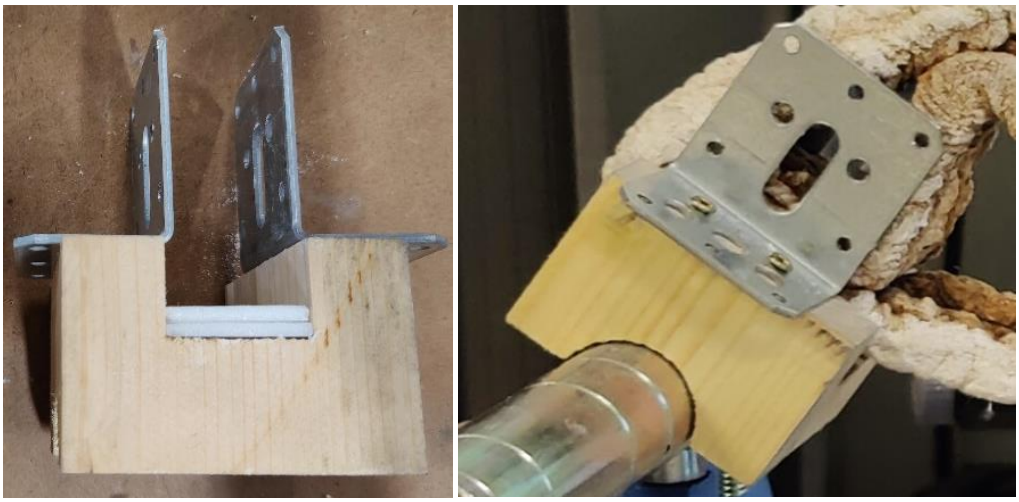


Figure 145. Two different views of a wooden U-shaped block with two L-shaped plates on top. The left photo shows the side view which shows two layers of foam at the bottom of the cutout. The right photo shows the front view with the circular cutout placed on top of the roller.

6.5.3 Results and discussion

In this section, the different tests are evaluated. For the compression and flexural tests, the results of the second mixture are also compared to the previously obtained results of the first mixture of Chapter 5.3. Please note, that this only concerns results of vertical layer orientation tests. And at last, the results of the final element test are presented.

6.5.3.1 Compression tests

Figure 146 displays the stress-strain graphs of all the second compression tests and Table 56 lists the results of each individual test of the second mixture. For more details see Chapter L1.1 in Appendix L.

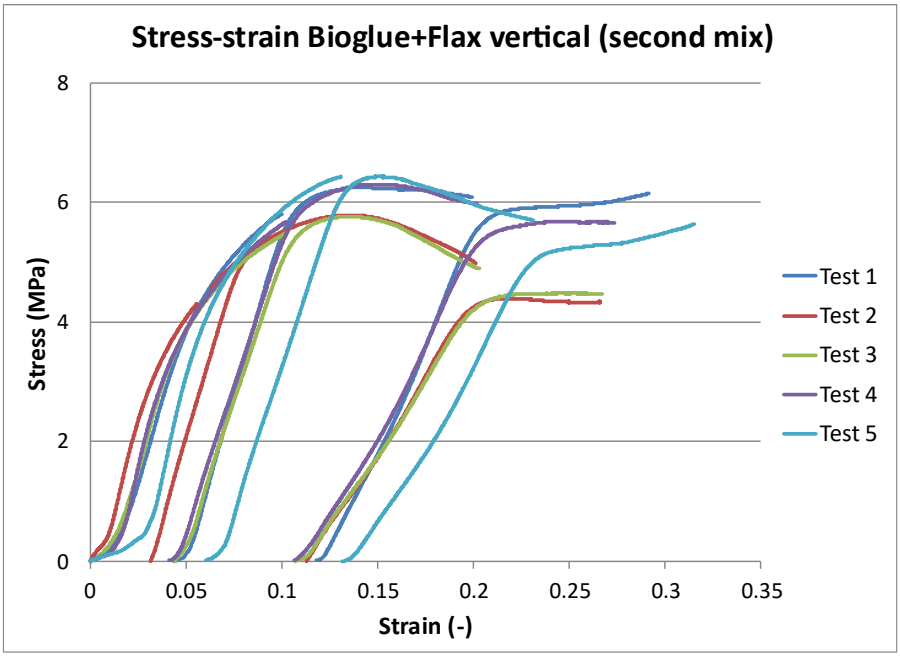


Figure 146. The stress-strain diagram of the compression tests with the second mixture.

Table 56. Compression test results and compressive mechanical properties of the second mixture.

Test	Cross-sectional area [mm²]	Peak force [kN]	Peak stress* [Mpa]	Compressive strength f_c [Mpa]	Compression modulus E_c [Mpa]
1	849.00	5.31	6.26	5.81	67.83
2	878.16	5.08	5.79	4.99	71.24
3	834.34	4.81	5.77	5.49	60.70
4	945.66	5.96	6.30	5.68	63.12
5	876.80	5.64	6.43	6.43	61.06
Average**	876.45	5.43	6.19	5.85	63.18

**) These values are determined/calculated at the moment of peak force.*
***) Result of test 2 were excluded (see text).*

Test 2 was executed poorly. Initially, the applied force in cycle 1.1 was released prematurely, and after applying the force again it was released prematurely again. The displacement did not reach the desired value, which resulted in a lower compressive strength and a higher compression modulus compared to the other four tests. Due to the fact that test 2 was poorly executed and exhibit a significant difference in results, it was excluded when the average results were calculated. Consequently, the results of test 2 were excluded from any subsequent discussions.

The first part of test 5 demonstrates a larger displacement in comparison to the other tests. However, the remainder of the test progresses is a similar manner to the other tests, and thus test 5 is included in the averages and further comparisons.

As illustrated in Table 56, the maximum values for the compressive strength (cycle 1.1) of the four tests are relatively close, with a range of 5.49 MPa to 6.43 MPa. However, after cycle 1.1, the differences between the tests becomes larger. Test 3 has a much lower peak in cycles 2.1 and 3.1 compared to tests 1, 4 and 5. However, this difference is disregarded as only cycle 1.1 is utilised to calculate the compressive strength and the compression modulus.

Figure 147 shows a boxplot graph of the compressive strengths of each cycle for the first and second mixtures. And Table 57 gives the average results of the first and second mixture. The latter data show that, apart from a longer curing time, the specimens of the second mixture have a significantly lower average peak force, a higher compressive strength and a higher compression modulus compared to the first mixture. Notably, the ultimate compressive stress of both mixtures is the same, which is explained by the smaller cross-sectional area of the more compact specimens of the second mixture.

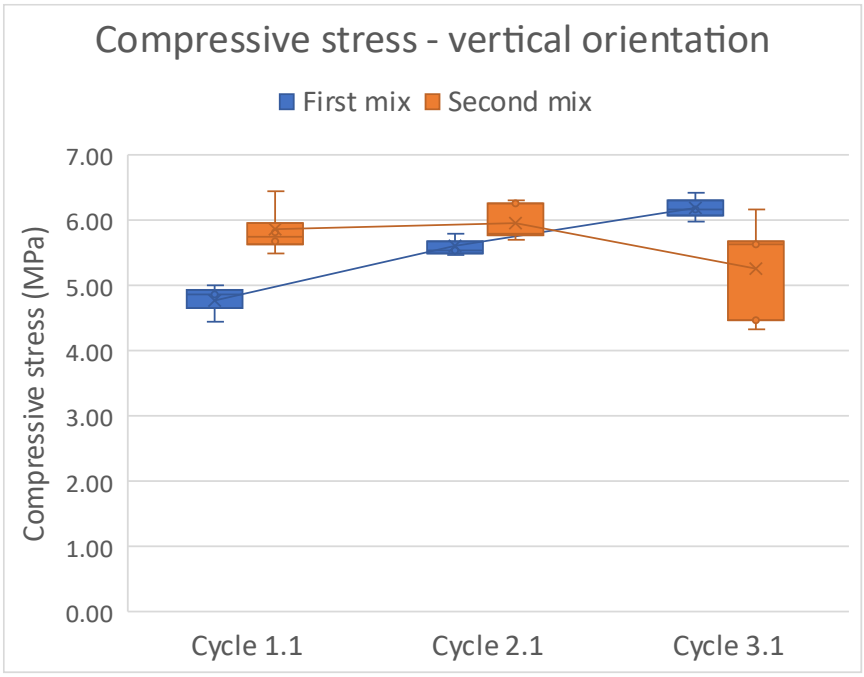


Figure 147. A boxplot graph of the compressive stresses of cycle 1, 2 and 3 of the first and second mixture.

Table 57. Compression test results and compressive mechanical properties of the first and second mixture.

Test	Days cured	Peak force [kN]	Ultimate compressive stress * [MPa]	Compressive strength f_c [MPa]	Compression modulus E_c [MPa]
First mix	34.7	7.29	6.19	4.77	44.52
Second mix	40	5.43	6.19	5.85	63.18

**) These values are determined/calculated at the moment of peak force.*

The second and the first mixtures consisted of the same ratios of ingredients, therefore, it was expected that the tests would produce similar results. However, a higher compressive strength and compression modulus were observed in the second mixture compared to the first mixture. This might be explained as follows:

- The curing time of the specimens of the second mixture was longer than that of the first mixture. And as previously mentioned in Chapter 5, a longer curing time could result in stronger and stiffer specimens.
- The weights that were applied during the curing process, which resulted in more compact specimens, which likely strengthened the bond between the layers compared to the first specimens that cured without additional weights. This stronger bond between the layers could have increased the specimen's stiffness and as a consequence a higher compression modulus.

6.5.3.2 Flexural test

Figure 148 displays the stress-strain graph of the second flexural tests and Table 58 lists the results of each individual test. For more details see Chapter L1.2 in Appendix L.

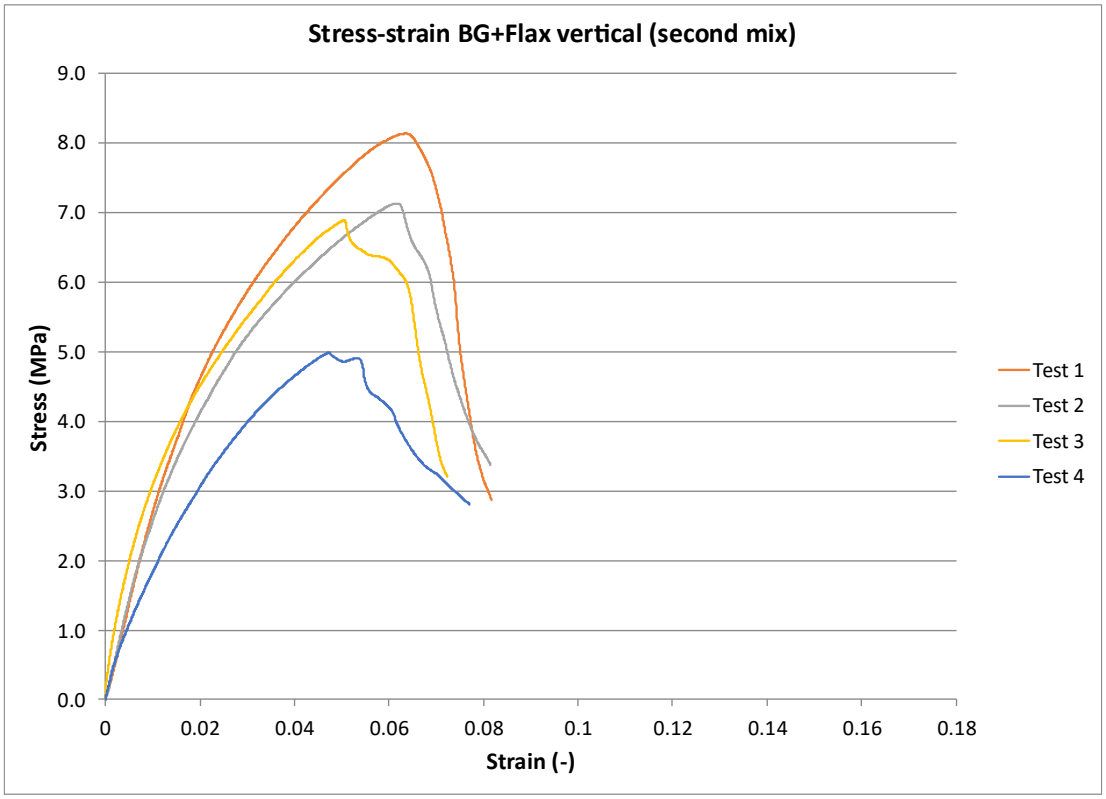


Figure 148. The stress-strain diagram of the four flexural tests with the second mixture.

Table 58. Flexural tests results of the second mixture.

Test	Cross-sectional area [mm2]	Force [kN]	Displacement* [mm]	Stress* [MPa]	Strain* [-]	Flexural modulus [MPa]
1	865.1	0.69	14.21	8.13	0.064	271.11
2	903.1	0.70	13.88	7.13	0.062	262.38
3	918.8	0.66	11.38	6.89	0.050	361.99
4	1098.7	0.57	9.64	4.98	0.047	170.58
Average	946.43	0.66	12.28	6.78	0.056	266.52

**) These values are determined/calculated at the moment of peak force.*

As anticipated, the second flexural tests developed as expected. Initially, the force increased, and when the first crack appeared at the bottom of the specimen, the force decreased gradually as the crack grew. Test four resulted in a significantly lower stress value at the moment of peak force and a significantly lower flexural modulus compared to the other three tests. Despite these differences, all test results were included in all the calculated averages and further comparisons.

Table 59 presents the average results of the first and second mixture. These data show that the specimens of the second mixture had a shorter curing time, a higher ultimate tensile stress and a higher flexural modulus compared to the specimens of the first mixture. The tensile strength was however the same.

Table 59. Flexural test results and flexural mechanical properties of the second mixture.

Test	Days cured	Strain*	Ultimate tensile stress [MPa]	Tensile strength f_b [MPa]	Flexural modulus E_b [MPa]
First mix	49.7	0.070	6.60	3.03	106.53
Second mix	40	0.056	6.78	3.00	266.52

**) These values are determined/calculated at the moment of peak force.*

The second and the first mixtures consisted of the same ratios of ingredients, therefore, it was expected that the tests would produce similar results. However, this was only found to be the case for the tensile strength. The flexural modulus of the specimens of the second mixture is significantly larger compared to that of the first mixture, whereas the ultimate stress is relatively similar. The reason for the larger flexural modulus of the second mixture is the lower strain exhibited by the second mixture.

It was expected that a longer curing time should result in a higher strength and modulus, but the curing time of the specimens of the second mixture was almost ten days shorter than those of the first mixture, however, higher ultimate tensile stress and flexural modulus were observed with the specimens of the second mixture. This might be due to the applied weights having a larger impact on the mechanical properties than expected. Possible other factors that may have influenced the properties, are:

- Another test machine was used for the specimens of the second mixture, which may have caused the test setup to be slightly different.
- The quality of the raw materials used for the second mixture and first mixture may have not been the same:
    - For the second mixture, a new batch of glue had to be ordered.
    - Some materials were in store already before the production of the first mixture and might have been slightly outdated (somewhat deteriorated) when utilised for the second mixture.
    - It concerns bio-based materials, characterised by naturally occurring differences

6.5.3.3 Final element test

Figure 149 shows the force-displacement graph of the final element test and Figure 150 shows three photos at different moments of the test. In addition to the results presented and discussed below, Chapter L2 in Appendix L provides extra information.

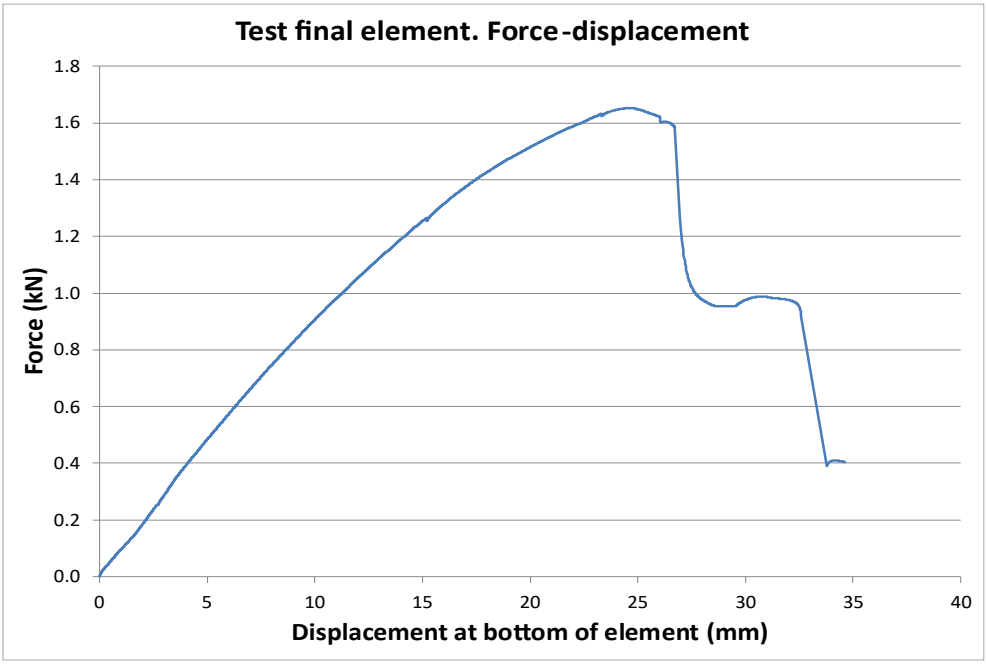


Figure 149. The force-displacement graph of the final element test.

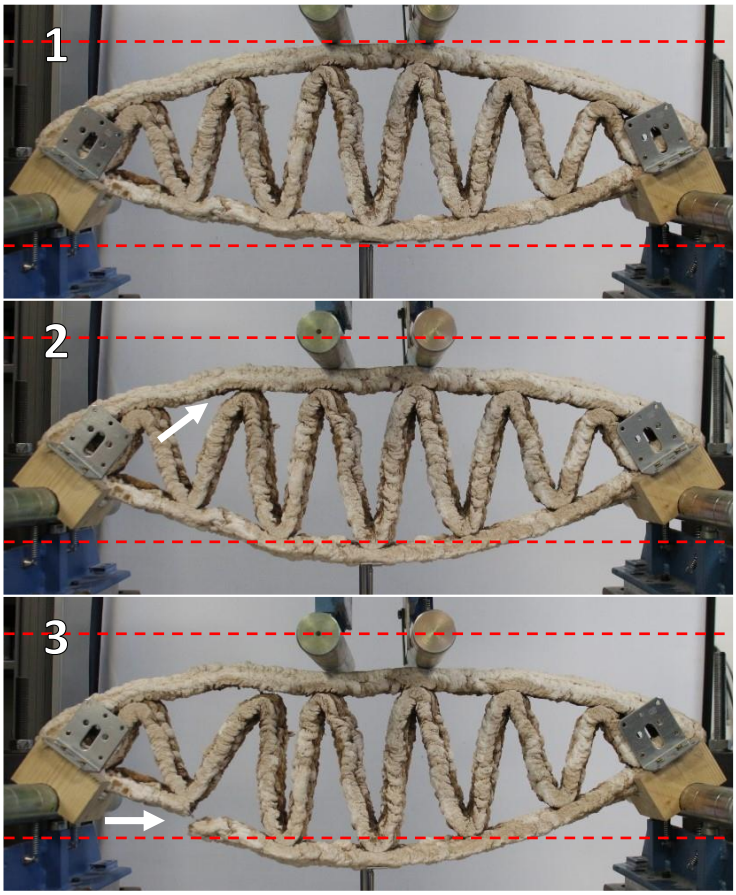


Figure 150. Photos taken during the test, with the red lines indicating the original position of the top and bottom chord. 1) At the start of the test. 2) During the test. 3) At the end of the test.

The graph in Figure 149 is relatively linear up to 0.8 kN, after which the slope gradually decreased until the peak force of 1.65 kN was reached. At this moment the accompanying displacement amounted to 24.67 mm.
After this, a wave disconnected from the top chord, which is illustrated in photo 2 in Figure 150. This disconnection led to a significant drop in force (from 1.6 kN to 0.95 kN). The disconnected site of the wave will henceforth be referred to as “top 2”. Following this first drop, the test speed was increased to 2 mm/min, which resulted in a minor increase in force. The reason for increasing the test speed, was that apparently nothing happened after the first drop except for an increasing displacement with the same load.
Shortly after the speed adjustment, a second significant drop in force (from 0.95 kN to 0.4 kN) occurred when the bottom chord fully broke right beside a valley, as illustrated in photo 3. The test was then stopped. The valley where the element broke at the bottom chord will henceforth be referred to as “valley 2”.

The expected force obtained with the numerical model in GSA was 1.63 kN, which was slightly exceeded with the final element test. However, the element behaved not as expected, with the disconnection of top 2 and the breakage of the bottom chord next to valley 2, instead of breaking in the middle of the bottom chord. Furthermore, the measured displacement was significantly higher than expected: 24.67 mm vs 13.10 mm respectively.
In the GSA model, the following assumptions were made: the path width was constant, each layer had the same dimensions, and the layers laid perfectly on top of each other. However, this was not the case with the real element, as was mentioned in Chapter 6.4. There were many imperfections in the element, especially with the connections between the chords and the waves. The layers did not lay perfectly on

top of each other and the path width was not constant, resulting in some inadequate connections between the paths.
The final assumption was that the layers and paths adhered perfectly to each other, however, this was not tested. Only the overlap was determined to connect two different paths, but testing bond strength between the paths fell outside the scope of this project.
Furthermore, the element in the GSA model was perfectly symmetrical with perfect dimensions. However, the printed element was far from perfect and not perfectly symmetrical due to the many imperfections. This alone can cause discrepancies between the results of the GSA analysis and the tested results.
The material properties used in GSA may have been different from the actual properties of the final element:

- The flexural modulus was used as the elastic modulus in GSA, but these properties may be different in reality. The elastic modulus has a significant effect on the mechanical behaviour, especially the displacements. However, testing this fell outside the scope of this project.
- The flexural modulus of the first mixture was (106.53 MPa) utilised, instead of that of the final mixture (266.52 MPa). However, a higher modulus would result in a smaller displacement and the actual displacement was already larger than the predicted displacement.
- Testing the shear modulus fell outside the scope of this project, thus, the shear modulus was assumed to be the default value of GSA. The sensitivity analysis of Chapter 6.3.1.2 concluded that changing the shear modulus did not have a significant impact on the behaviour of the model. However, this was tested on a different model version with a different applied load, and researching this for the mesh model fell outside the scope of this project.
- The density was based on the beams made from the same mixture, but due to the different print settings and the different weights that were put on top, the density of the final element may have been different than the density of the beams. A different density would have affected the self-weight of the GSA model, and this would have affected the mechanical behaviour and influenced the results.

In addition, the support conditions differed between the actual test setup and the GSA model. The supports in the GSA model were simulated as closely as possible to the test model, but there were differences:

- In GSA, the right support had no limit to its movement from left to right, whereas the right support of the test setup could only move slightly.
- The supported part of the element in the test setup could rotate a bit more than the supported part in the GSA model. In the GSA model, several points were constrained to move in the z-direction but could rotate around their individual y-axes. However, in the test, the supports had only one axes of rotation (around the roller), meaning that the supported parts of the element had a slightly more moving freedom than in the GSA model. This extra movement freedom may have contributed to the larger displacement compared to the GSA model.

Figure 151 compares the results of the final element test and that of GSA non-linear analysis, with both graphs plotted up to an applied force of 1.65 kN. The GSA graph has a constant slope up to 1.65 kN, with a value of 0.1243 kN/mm. The final element test graph has a slope of 0.0947 kN/mm up to 0.8 kN.

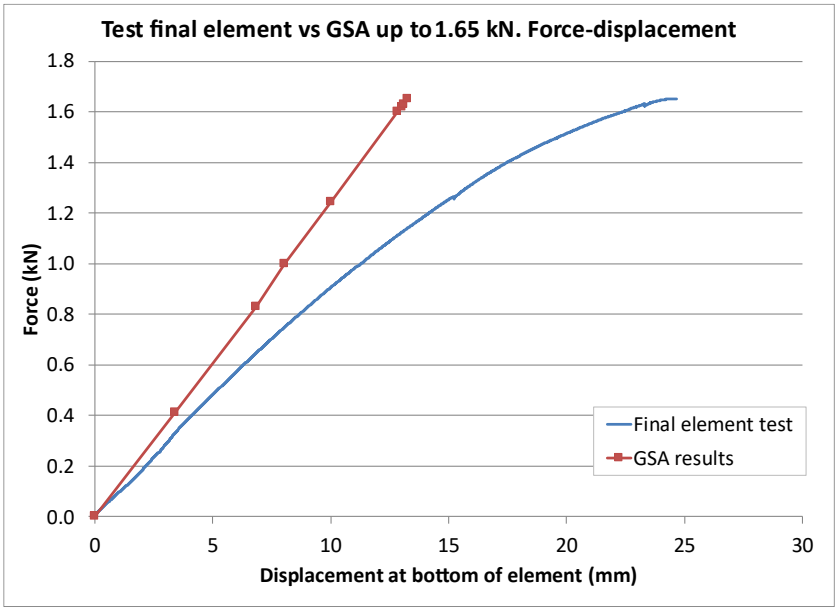


Figure 151. Force-displacement graphs of the GSA analysis and the final element test.

The GSA results are linear, despite being analysed with a non-linear analysis. Investigating the reasons for this linear behaviour in GSA, however, fell outside the scope of this project.
The final element test graph becomes gradually less steep in comparison to the GSA graph. This is likely due to the fact that the GSA model is a perfectly shaped solid model without imperfections, in contrast to the final element with its many imperfections.

The faulty connection at top 2 most likely had a considerable impact on the structural behaviour of the element. Ideally, multiple final elements should have been tested to verify the behaviour of the final element. However, due to the practical reasons (lignin shortage), this was impossible. In addition, the location of the bottom chord's fracture was unexpected. There are several reasons why the final element broke at this particular spot:

- The material falling over after printing at this spot could have made it weaker than the rest of the bottom chord (see Chapter 6.4.1).
- Following the disconnection of top 2, the stresses may have redistributed, resulting in a stress peak at that particular location.
- Or a combination of being both a weaker spot and a stress peak location.

6.5.4 Verification of the failure behaviour

In this section, a new GSA model without a connection between top 2 and the top chord, referred to as the “broken wave” model (Figure 152), was used to verify the failure behaviour of the final element. This model was analysed with an applied force of 1 kN, which was the maximum force measured prior to the second drop in Figure 149, which corresponded to the moment the bottom chord broke. The analysis focused on the two parts of the element, as illustrated below (Figure 153). A detailed elaboration of this analysis provided in Chapter J5.3 of Appendix J.

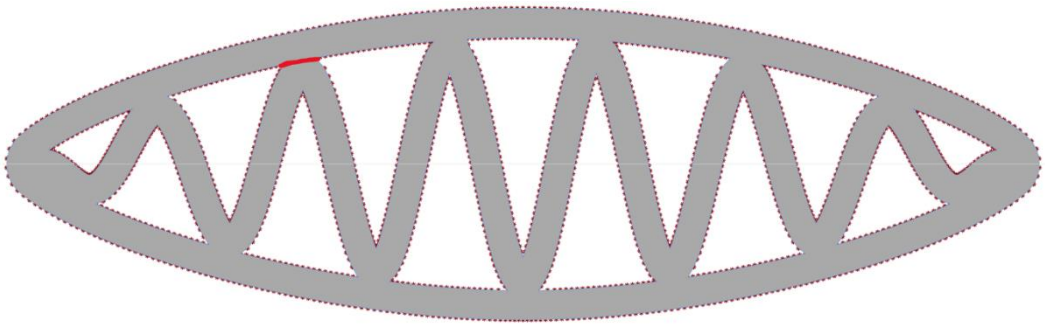


Figure 152. The “broken wave” model in GSA. The red line indicates where the model was split.

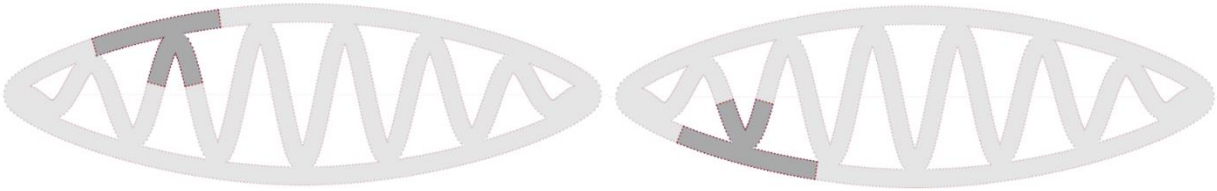


Figure 153. The GSA model with the darker grey highlighted part being top 2 in the left model and valley 2 in the right model.

These parts were analysed separately for both the “broken wave” model and the intact model. The results for the top part are presented in Figure 154, while the results for the bottom part are presented in Figure 155. Table 60 presents the maximum results of the compressive stresses in the top chord and the tensile stresses in the bottom chord.

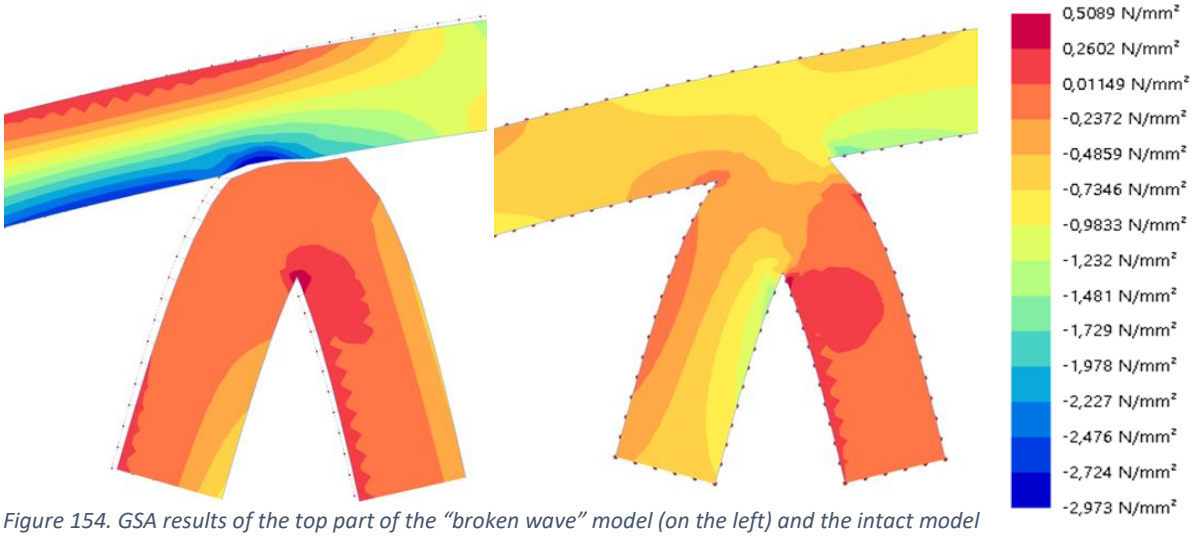


Figure 154. GSA results of the top part of the “broken wave” model (on the left) and the intact model (on the right).

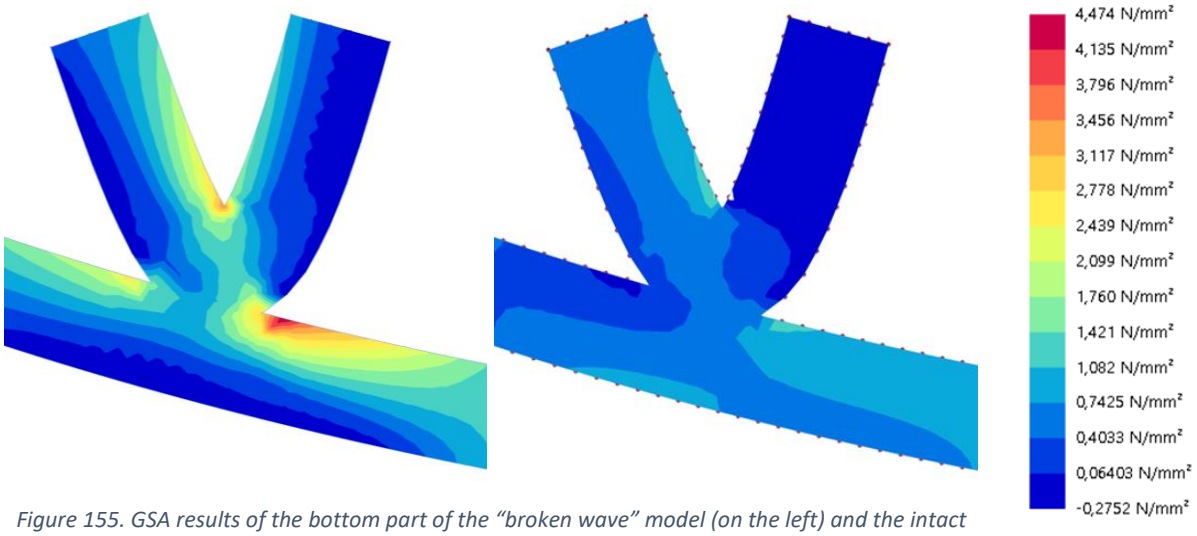


Figure 155. GSA results of the bottom part of the "broken wave" model (on the left) and the intact model (on the right).

Table 60. Results of the GSA analysis of both models.

Model	Compressive stresses in top chord* [MPa]	Tensile stresses in bottom chord** [MPa]
Intact model	-1.785	1.475
"Broken wave" model	-2.973	4.474

**) These stresses occur in the top chord right above wave.*
***) These stresses occur right next to valley.*

Compared to the intact model, the "broken wave" model distributed the stresses significantly different. It resulted in higher compressive stresses in the top chord and higher tensile stresses in the bottom chord. Here the high local peak stresses that occur are clearly visible as a red spot on the right of valley 2 in Figure 155.
During the test it was observed that the top chord buckled upwards, eventually causing the wave to become completely detached from the top chord. This could be attributed to higher compressive stresses in the top chord, which was confirmed by the "broken wave" model which showed higher compressive stresses than the intact model.
The tensile stresses in the bottom chord are three times the stresses recorded in the intact model, which could indicate that the actual stresses during the test were significantly higher than expected, and may even have exceeded the tensile strength, causing the element to break at this particular point.

In should be noted that the results presented in Table 60 may not be representative of the actual stresses in the final element following the disconnection of top 2. This is due to the fact that the actual displacement of the final element at the moment of breaking was significantly larger due to the progression of the test. It is possible that this large displacement has resulted in higher stress values for the same load.

The "broken wave" GSA model confirmed the behaviour of the final element during the test, thereby demonstrating the importance of a good connection between different paths. For this particular shape, a faulty connection between a wave and the top chord had a substantial impact on the stress distribution within the element. Resulting in a rapid increase in the tensile stresses at an unexpected spot, to levels much higher than expected, explaining the observed failure behaviour of the element during the test.

CONCLUSION

7 Result summary and final conclusion

For this thesis, a new bio-based material was developed to create a digitally designed structural element using additive manufacturing. To achieve this, a series of sub-questions were addressed and these are presented below together with the answers.

1. **What kind of bio-based 3D printing is currently utilised in scientific research or development?**

Currently, numerous studies, companies and individuals are investigating additive manufacturing using bio-based materials. A number of these are already (commercially) available, including PLA, wood composites, sand mixtures, clay, mycelium, and 'BuildMatterial' by Omlab. These existing materials use different types of additive manufacturing such as FDM, LDM and binder jetting. Alternatives using LDM, such as soils, clays, and wood-based mixtures are still under investigation.

2. **Which bio-based mixture is best suited for additive manufacturing of a structural element?**

With regards to LDM, the wood-based mixtures developed at TU Delft showed promising results in terms of their mechanical properties and printability. This concerns mixtures based on cellulose and lignin in combination with a binder. When using a bio-glue as binder instead of a wood glue, such a mixture can be fully bio-based. Given the scale of this research, the level of expertise and the availability of materials, it was concluded that these mixtures were selected as the reference mixtures for this study.

3. **What are the potential additives to improve the structural properties of the mixture?**

Bentonite and flax fibres showed the greatest potential for enhancing the mechanical properties. The addition of bentonite significantly improved the compressive strength and the stiffness of the mixture. And the flax fibres significantly increased the resistance of tensile stresses of the material.

4. **What are the best print parameters for printing objects with the chosen mixtures?**

In this study, the ABB IRB 1200-5/0.9 robot was used with a Makita caulk gun as the extruder. For the test beams, a rectangular nozzle of 40x10 mm was used while for the final element, a round nozzle with a diameter of 10 mm was used. The print speed depended on the mixture type and nozzle size. For the final element, the print speed was set at 32.5 mm/s, with the Makita pressure set to 2. This approach sufficed for this project, so no further adjustments were made to the robot setup.

5. **What are the mechanical properties of the selected mixtures and what mechanical tests are needed to determine them?**

Compression and a three-point bending tests were performed to determine the compressive and flexural properties of these mixtures. Specimens for both tests were tested with two different layer orientations: horizontal and vertical.
The bio-glue with flax mixture, with the layers in a vertical layer orientation, had a compressive strength of 4.77 MPa and a compression modulus of 44.52 MPa. The tensile strength was 3 MPa and the flexural modulus was 106.53 MPa.

6. **How to digitally design a structural beam specifically for additive manufacturing (AM) with the selected mixture?**

A truss-like beam was created with a length of 730 mm, height of 220 mm and a thickness of six layers. The beam was designed using Grasshopper, a parametric design program, with a focus on the feasibility for manufacturing using AM. A range of outer shapes and infills were analysed using GSA, and based on their structural behaviour, the most optimal design was selected. Afterwards, the beam dimensions were further optimized using Galapagos.

7. **What is the structural behaviour of a bio-based 3D printed beam**?

The final element reached a peak force of 1.65 kN. The failure behaviour was different from the numerical model in GSA. A faulty connection, between top 2 and the top chord, resulted in a significant redistribution of stresses, causing the element to break in between the centre and a support of the bottom chord.

The primary research question (repeated below) can be answered from the conclusions to the sub-questions.

What is the structural behaviour of a digitally designed structural element (a beam) made from a bio-based material using additive manufacturing?

The objective of digitally designing a structural beam, that was optimised for AM, was successfully completed. Despite several challenges during the printing process, including layer misalignment and a faulty connection between a wave and the top chord, the final element was successfully subjected to a flexural test. After an extra numerical verification, the structural behaviour was validated.

In conclusion, it is possible to produce a digitally designed structural element using AM with a newly developed 100% bio-based material consisting of lignin, cellulose, bio-glue, Valida L,3% and flax fibres. This material demonstrates great potential for the building industry, as its mechanical properties, such as compressive and tensile strength, are comparable to those of other low-strength materials already in use. In terms of sustainability, the material can be produced with locally sourced materials and it is a great advantage that the material can be reused in the event of a failed print (unlike with 3DCP).
At the moment, the investigated material is clearly not suitable for structural applications. The material's current strength and stiffness are not yet structurally safe and further investigation is needed to improve its properties.

RECOMMENDATIONS

8 Recommendations

This study is a continuation of the Master's thesis projects "Wood-based printing" by TU Delft students C. Bierach and A. Coelho. Significant progress in this project was made in the development of wood-based mixtures and the knowledge of their printability and structural behaviour. However, more research is needed before such mixtures can be used in structural applications. Below, recommendations for further research are proposed, based on the results in this study.

Mould growth on the methylcellulose mixtures

Without applying additional heat, all of the MC mixtures eventually grew mould. The TU Delft students also observed mould growth on their material. This was only observed with the methylcellulose mixtures and various unsuccessful attempts were made to prevent the mould growth. For instance, by using MC from different containers or different types of covers during the curing process. However, this issue was not further addressed in this study, as the wood glue and bio-glue mixtures were not affected by mould and performed very well. It might be worthwhile to explore the use of a (degradable) fungicide in the MC mixtures.

Mixture composition

The final (reference) mixtures were effective and resulted in promising printed elements, it was however not clear why these mixtures performed so well, but further investigation was beyond the scope of this project. Furthermore, a material expert, to overcome students' lack of expertise, was not consulted. And so, the mixture compositions were based on the knowledge of the TU Delft students, a literature study and a trial-and-error mixture exploration. Selection of other materials and additive combinations may resolve some of the issues encountered during curing, printing and testing. Additionally, the mechanical properties of the material were by far not structurally sound, so exploring alternatives for certain materials and additives, for example plasticisers or other reinforcing agents, might improve this mixture. As the mixture composition also influences the consistency, one could develop a mixture type having a consistency suitable for printing with a pump instead of the Makita.

Fresh material properties

In this study, the properties of the fresh mixture were not investigated, although, these properties are of significance in the context of additive manufacturing. Properties such as the poisson's ratio, the fresh strength and adhesion can have a significant impact on the printability of a material. An investigation should be carried out to determine the fresh properties.

Time between mixing and printing

The time between mixing and printing fluctuated, which might have affected the material and mechanical properties. Furthermore, the material was reused for later prints when a print failed, which could also have influenced the material properties. In order to determine the optimal time between mixing and printing, and to gain more information on the consequences of reusing the material, additional studies are required.

Air bubbles

The presence of air bubbles during the printing process highly affected the quality of a printed element. Filling the cartridge as described in 4.1 removed the large air bubbles, but small air bubbles were still present in the cartridge. It should be investigated how to adjust the mixture ratio or the extrusion process (e.g. using a pump) to obtain an air bubble free extrusion and a high-quality print.

Colour changes during the curing process
The fresh mixture had a brown colour, but after curing a white “powder” formed on the surface, which may be caused by the Valida or the presence of lime in the tap water. It would be interesting to explore how this colour change could be prevented, and a printed element would retain its “wood-like” colour after the curing process.

Curing conditions
The curing conditions were based on the available equipment of the SED-lab. And with the second mixture, weights were added to the printed elements during the curing process, which prevented much of the warping. However, more research is needed to determine the optimal curing conditions, for example applying heat or a different cover. An additional study might be helpful to determine the effect of extended curing time on the mechanical properties and but also the optimal curing time.

Shrinkage
The shrinkage of the printed elements was significant, which could cause problems when printing larger elements. Further investigation is required to determine effective methods of limiting, or even eliminating, shrinkage. Potential solutions include altering the curing conditions or adding other additives.

Sample sizes
The sample sizes for the mechanical test were limited due to time constraints and material availability. Further investigation using larger sample sizes to more accurately determine the mechanical properties is recommended.

Mechanical and material properties
This study exclusively investigated certain compressive and flexural properties of the cured material. To be able to use this material in a structural setting, more research is needed into the mechanical properties, e.g. elasticity, tensile strength, creep, toughness, etc.
In addition, to be able to use this material in an outdoor environment, it is essential to investigate properties such as material degradation, oxidation, fire safety, moisture and UV resistance.

Bond strength
The bond strength between the layers was not investigated in this study. In the field of additive manufacturing, the bond strength is a critical factor and can significantly influence the structural behaviour of a printed element. Further mechanical tests to determine this bond strength are therefore recommended

BIBLIOGRAPHY

9 Bibliography

[1] United Nations. What Is Climate Change? [Internet]. Climate Fast Facts. [cited 2023 Jan 12]. Available from: https://www.un.org/en/climatechange/climate-fast-facts

[2] Nukusheva A, Ilyassova G, Rustembekova D, Zhamiyeva R, Arenova L. Global warming problem faced by the international community: international legal aspect. Int Environ Agreem. 2021;21(2):219–33.

[3] Lamb WF, Wiedmann T, Pongratz J, Andrew R, Crippa M, Olivier JGJ, et al. A review of trends and drivers of greenhouse gas emissions by sector from 1990 to 2018. Environmental Research Letters. 2021;16(7):073005.

[4] United Nations Framework Convention on Climate Change. What is the Paris Agreement? [Internet]. United Nations. 2015 [cited 2023 Jan 12]. Available from: https://unfccc.int/process-and-meetings/the-paris-agreement/the-paris-agreement

[5] Ministerie van Infrastructuur en Waterstaat. Nederland circulair in 2050 [Internet]. 2016 [cited 2022 Dec 13]. Available from: https://www.rijksoverheid.nl/onderwerpen/circulaire-economie/documenten/rapporten/2016/09/14/bijlage-1-nederland-circulair-in-2050

[6] Rural Business-Cooperative Service. Biobased Markets Program [Internet]. Department of Agriculture. 2024 [cited 2025 Mar 18]. Available from: https://www.federalregister.gov/documents/2024/12/09/2024-28431/biobased-markets-program#page-97465

[7] Yadav M, Agarwal M. Biobased building materials for sustainable future: An overview. Mater Today Proc. 2021;43:2895–902.

[8] Keena N, Raugei M, Lokko M ling, Aly Etman M, Achnani V, Reck BK, et al. A Life-Cycle Approach to Investigate the Potential of Novel Biobased Construction Materials toward a Circular Built Environment. Energies (Basel) [Internet]. 2022;15(19). Available from: https://www.mdpi.com/1996-1073/15/19/7239

[9] Wang D, Zhang T, Guo X, Ling D, Hu L, Jiang G. The potential of 3D printing in facilitating carbon neutrality. Journal of Environmental Sciences. 2023;130:85–91.

[10] Liu H, Li B, Tang W. Manufacturing oriented topology optimization of 3D structures for carbon emission reduction in casting process. J Clean Prod. 2019;225:755–70.

[11] Dams B, Maskell D, Shea A, Allen S, Cascione V, Walker P. Upscaling bio-based construction: challenges and opportunities. Building Research & Information. 2023;51(7):764–82.

[12] Zhai X, Jin L, Jiang J. A survey of additive manufacturing reviews . Materials Science in Additive Manufacturing. 2022;1(4):21.

[13] BCN3D. The most popular 3D printing materials in FDM and their properties [Internet]. 2022 [cited 2023 Jan 31]. Available from: https://www.bcn3d.com/the-most-popular-3d-printing-materials-in-fdm-and-their-properties/

[14] McKeown P, Jones MD. The Chemical Recycling of PLA: A Review. Sustainable Chemistry. 2020;1(1):1–22.

[15] Tümer EH, Erbil HY. Extrusion-Based 3D Printing Applications of PLA Composites: A Review. Coatings. 2021;11(4).

[16] Polygenis T. A Comprehensive Guide to PLA Melting Point and How it Influences 3D Printing [Internet]. Wevolver. 2023 [cited 2025 Feb 7]. Available from: https://www.wevolver.com/article/pla-melting-point

[17] BambuLab. Bambu Lab X1 Series [Internet]. Bambu Lab. 2025 [cited 2025 Feb 7]. Available from: https://bambulab.com/en-eu/x1

[18] Mamou-Mani Ltd. Conifera [Internet]. 2019 [cited 2025 Jan 20]. Available from: https://mamou-mani.com/project/cos/

[19] Fab.Pub. Biomaterials [Internet]. [cited 2025 Jan 20]. Available from: https://fabpub.com/pages/biomaterials
[20] Cosentino. Conifera [Internet]. [cited 2025 Jan 20]. Available from: https://www.cosentino.com/nl-nl/blog/conifera/
[21] Sellner KG, Doucette GJ, Kirkpatrick GJ. Harmful algal blooms: causes, impacts and detection. J Ind Microbiol Biotechnol. 2003;30(7):383–406.
[22] Klarenbeek E, Dros M. Weedware© [Internet]. 2022 [cited 2023 Feb 2]. Available from: http://weedware.org/
[23] Klaarenbeek E, Dros M. Seaweed Cycle for The Breakdown Economy Museum Boijmans Van Beuningen [Internet]. 2022 [cited 2023 Feb 2]. Available from: https://www.ericklarenbeek.com/
[24] Morris A. Dutch designers convert algae into bioplastic for 3D printing. Dezeen [Internet]. 2017 Dec 4 [cited 2023 Feb 2]; Available from: https://www.dezeen.com/2017/12/04/dutch-designers-eric-klarenbeek-maartje-dros-convert-algae-biopolymer-3d-printing-good-design-bad-world/
[25] Herpen I van. Inside the atelier ~ 'Meta Morphism' [Internet]. 2022 [cited 2023 Feb 2]. Available from: https://www.youtube.com/watch?v=S3JPiT6ZXn8&t=20s
[26] GHYCZY. Algae Egg Chair [Internet]. 2022 [cited 2025 Jan 20]. Available from: https://ghyczy.com/algae-egg-chair/
[27] Klarenbeek E, Dros M. .unusual [Internet]. 2025 [cited 2025 Jan 20]. Available from: https://www.dotunusual.com/
[28] Chiusoli A. The first 3D printed House with earth | Gaia [Internet]. WASP. 2018 [cited 2025 Jan 20]. Available from: https://www.3dwasp.com/en/3d-printed-house-gaia/
[29] Jordahn S. 3D-printed Gaia house is made from biodegradable materials. Dezeen [Internet]. 2019 Feb 27 [cited 2023 Feb 2]; Available from: https://www.dezeen.com/2019/02/27/gaia-wasp-3d-printed-house-biodegradable-video/
[30] WASP. TECLA [Internet]. 2021 [cited 2025 Jan 20]. Available from: https://www.3dwasp.com/en/3d-printed-house-tecla/
[31] Parkes J. Tecla house 3D-printed from locally sourced clay. Dezeen [Internet]. 2021 Apr 23 [cited 2023 Feb 2]; Available from: https://www.dezeen.com/2021/04/23/mario-cucinella-architects-wasp-3d-printed-housing/
[32] Emre M. University of Virginia 3D-prints living structures that can grow plants. Parametric Architecture [Internet]. 2022 Nov 22 [cited 2025 Jan 20]; Available from: https://parametric-architecture.com/university-of-virginia-3d-prints-living-structures-that-can-grow-plants/?srsltid=AfmBOopx_DGGu99soCNMMF4d-2D4a12WvoFKJvKi517-aBwS-6eyxXE3
[33] Aouf RS. University of Virginia 3D-prints living soil walls that sprout greenery. Dezeen [Internet]. 2022 Sep 5 [cited 2023 Feb 2]; Available from: https://www.dezeen.com/2022/09/05/university-of-virginia-3d-printed-soil-seed-walls/
[34] Skrebels A. Sandhelden and Archisource 3D print sand trophies for drawing competition. Dezeen [Internet]. 2022 Mar 10 [cited 2023 Feb 2]; Available from: https://www.dezeen.com/2022/03/10/3d-printed-quartz-sand-trophies-archisource-sandhelden/
[35] Sandhelden, Grossman J. Monolith [Internet]. 2024 [cited 2025 Jan 20]. Available from: https://www.sandhelden.de/projects/james-grossman/monolith
[36] Sandhelden, Mitchell M. Airflow Barrier [Internet]. 2022 [cited 2025 Jan 20]. Available from: https://www.sandhelden.de/projects/mark-mitchell/airflow-barrier
[37] Mamou-Mani Ltd. The Sandwaves [Internet]. 2019 [cited 2025 Jan 20]. Available from: https://mamou-mani.com/project/sandwaves/

[38] Crook L. Chris Precht and Arthur Mamou-Mani use sand to 3D print pavilion in Saudi Arabia. Dezeen [Internet]. 2020 Jan 20 [cited 2023 Feb 2]; Available from: https://www.dezeen.com/2020/01/20/sandwaves-precht-arthur-mamou-mani-pavilion-saudi-arabia/
[39] Herpt O van. 3D Printing Ceramics [Internet]. 2024 [cited 2025 Jan 20]. Available from: https://oliviervanherpt.com/3d-printing-ceramics/
[40] WASP. WASP Clay [Internet]. 2025 [cited 2025 Jan 20]. Available from: https://www.3dwasp.com/en/ceramic-3d-printing-wasp-clay/
[41] 3D Potter. Pioneering innovative technology with clay & Cement [Internet]. 2025 [cited 2025 Jan 20]. Available from: https://3dpotter.com/
[42] TU/e. 3D Clay Printing [Internet]. TU/e. 2025 [cited 2025 Jan 20]. Available from: https://www.tue.nl/en/research/research-groups/structural-engineering-and-design/roasd/3d-clay-printing
[43] Severi A. A Wall of 3D Printed Ceramic Bricks. WASP. 2024 Sep 13;
[44] Finney A. Arthur Mamou-Mani creates 3D-printed cups for Trame's latest collection. Dezeen [Internet]. 2022 Mar 2 [cited 2023 Feb 2]; Available from: https://www.dezeen.com/2022/03/02/trame-alhambra-rug-ceramic-design-arthur-mamou-mani/
[45] Looze H, Uffelen M van. Wij zijn Omlab [Internet]. 2022 [cited 2025 Jan 20]. Available from: https://www.omlab.nl/wij-zijn-omlab/
[46] Recell. Recell [Internet]. 2025 [cited 2025 Jan 20]. Available from: https://recell.eu/nl/
[47] The Exploded View. Printed building elements from the water treatment plant [Internet]. The Exploded View Beyond Building. 2021 [cited 2023 Feb 2]. Available from: https://theexplodedview.com/materialbb/printed-building-elements-from-the-water-treatment-plant/
[48] Omlab. Let's make #3dcp a lot more sustainable! [Internet]. 2021 [cited 2025 Jan 20]. Available from: https://www.omlab.nl/lets-make-3dcp-a-lot-more-sustainable/
[49] Buildmatterial 0.8 [Internet]. MaterialDistrict. 2022 [cited 2025 Jan 20]. Available from: https://materialdistrict.com/material/buildmatterial-0-8/
[50] Omlab. Omlab x The Exploded View Beyond Building [Internet]. 2023 [cited 2025 Jan 27]. Available from: https://www.omlab.nl/omlab-x-the-exploded-view-beyond-building/
[51] Omlab. Vesper [Internet]. 2024 [cited 2025 Jan 27]. Available from: https://www.omlab.nl/en/vesper/
[52] Omlab. Bioslopetile [Internet]. 2024 [cited 2025 Jan 27]. Available from: https://www.omlab.nl/en/bioslopetile/
[53] Fairs M. Mycelium Chair by Eric Klarenbeek is 3D-printed with living fungus. Dezeen [Internet]. 2013 Oct 20 [cited 2023 Feb 2]; Available from: https://www.dezeen.com/2013/10/20/mycelium-chair-by-eric-klarenbeek-is-3d-printed-with-living-fungus/
[54] Blast studio. Blast studio [Internet]. 2025 [cited 2025 Jan 27]. Available from: https://blast-studio.com/
[55] Hahn J. Blast Studio 3D prints column from mycelium to make 'architecture that could feed people'. Dezeen [Internet]. 2022 Jan 18 [cited 2023 Feb 2]; Available from: https://www.dezeen.com/2022/01/18/blast-studio-tree-column-mycelium-design/?li_source=LI&li_medium=rhs_block_1
[56] Blast studio. Portfolio [Internet]. 2025 [cited 2025 Jan 20]. Available from: https://blast-studio.com/blogs/portfolio

[57] Kariz M, Sernek M, Kuzman MK. Use of wood powder and adhesive as a mixture for 3D printing. European Journal of Wood and Wood Products. 2016 Nov 4;74(1):123–6.
[58] Rosenthal M, Henneberger C, Gutkes A, Bues CT. Liquid Deposition Modeling: a promising approach for 3D printing of wood. European Journal of Wood and Wood Products. 2018;76(2):797–9.
[59] Zarna C, Opedal MT, Echtermeyer AT, Chinga-Carrasco G. Reinforcement ability of lignocellulosic components in biocomposites and their 3D printed applications – A review. Composites Part C: Open Access. 2021;6.
[60] Liebrand TRH. 3D printed fiber reinforced lignin. [Delft]: Delft University of Technology; 2018.
[61] Johanson G. Acetone. In: Patty's Toxicology. 2023. p. 1–18.
[62] Coelho AA. Cellulose & Lignin in Additive Manufacturing: Potential and challenges in the fabrication of structural nodes for free-form building envelope structures. [Delft]: Delft University of Technology; 2022.
[63] Bierach C. Wood-based 3d printing: Potential & limitation to 3D print a window frame with pure cellulose & lignin. [Delft]: Delft University of Technology; 2022.
[64] Bikas H, Stavropoulos P, Chryssolouris G. Additive manufacturing methods and modelling approaches: a critical review. The International Journal of Advanced Manufacturing Technology. 2016;83(1):389–405.
[65] Applied engineering. 7 Types of Additive Manufacturing [Internet]. 2021 [cited 2025 Jan 21]. Available from: https://www.appliedengineering.com/blog/2021/1/22/7-types-of-additive-manufacturing
[66] Shah P, Racasan R, Bills P. Comparison of different additive manufacturing methods using computed tomography. Case Studies in Nondestructive Testing and Evaluation. 2016;6:69–78.
[67] Saadi MASR, Maguire A, Pottackal NT, Thakur MSH, Ikram MMd, Hart AJ, et al. Direct Ink Writing: A 3D Printing Technology for Diverse Materials. Advanced Materials. 2022 Mar 4;34(28).
[68] Tagliaferri S, Panagiotopoulos A, Mattevi C. Direct ink writing of energy materials. Mater Adv. 2021;2(2):540–63.
[69] Mondal D, Willett TL. Chapter 23 - Three-dimensional printable nanocomposite biomaterials as bone scaffolds and grafts. In: Gupta RK, Nguyen TA, editors. Smart Multifunctional Nano-inks. Elsevier; 2023. p. 579–94.
[70] Sandhelden. Our technology [Internet]. 2025 [cited 2025 Jan 21]. Available from: https://www.sandhelden.de/about
[71] Bouzidi K, Chaussy D, Gandini A, Bongiovanni R, Beneventi D. 3D printable fully biomass-based composite using poly(furfuryl alcohol) as binder and cellulose as a filler. Carbohydr Polym. 2022;293:4848–65.
[72] Guillopé C. Non-Newtonian Fluids. In: Françoise JP, Naber GL, Tsun TS, editors. Encyclopedia of Mathematical Physics. Oxford: Academic Press; 2006. p. 560–7.
[73] Cullen PJ. Chapter 3 - Fluid Rheology in Novel Thermal and Non-Thermal Processes. In: Cullen PJ, Tiwari BK, Valdramidis VP, editors. Novel Thermal and Non-Thermal Technologies for Fluid Foods. San Diego: Academic Press; 2012. p. 35–61.
[74] Elahee GMF, Cheng X, Rong L, Xu MW, Souza L, Advincula RC, et al. On the cogent formulation of an elastomeric silicone ink material for direct ink write (DIW) 3D printing. Polym Eng Sci. 2024 Jun 1;64(6):2476–90.
[75] Walker S, Lingle E, Troxler N, Wallin T, Healy K, Mengüç Y, et al. Predicting interfacial layer adhesion strength in 3D printable silicone. Addit Manuf. 2021;47.
[76] Brigham C. Chapter 3.22 - Biopolymers: Biodegradable Alternatives to Traditional Plastics. In: Török B, Dransfield T, editors. Green Chemistry. Elsevier; 2018. p. 753–70.

[77] Firmanda A, Syamsu K, Sari YW, Cabral J, Pletzer D, Mahadik B, et al. 3D printed cellulose based product applications. Mater Chem Front. 2022 Feb 7;6(3):254–79.
[78] Dai L, Cheng T, Duan C, Zhao W, Zhang W, Zou X, et al. 3D printing using plant-derived cellulose and its derivatives: A review. Carbohydr Polym. 2019 Jan 1;203:71–86.
[79] Yang J, An X, Liu L, Tang S, Cao H, Xu Q, et al. Cellulose, hemicellulose, lignin, and their derivatives as multi-components of bio-based feedstocks for 3D printing. Carbohydr Polym. 2020 Dec 15;250.
[80] Gauss C, Pickering KL, Muthe LP. The use of cellulose in bio-derived formulations for 3D/4D printing: A review. Composites Part C: Open Access. 2021;4.
[81] Agustiany EA, Rasyidur Ridho M, Rahmi D. N. M, Madyaratri EW, Falah F, Lubis MAR, et al. Recent developments in lignin modification and its application in lignin-based green composites: A review. Polym Compos. 2022 Aug;43(8):4848–65.
[82] Mili M, Hashmi SAR, Ather M, Hada V, Markandeya N, Kamble S, et al. Novel lignin as natural-biodegradable binder for various sectors—A review. J Appl Polym Sci. 2022 Apr 15;139(15).
[83] Yu O, Kim KH. Lignin to materials: A focused review on recent novel lignin applications. Applied Sciences. 2020 Jul 3;10(13):4626–42.
[84] Tanase-Opedal M, Espinosa E, Rodríguez A, Chinga-Carrasco G. Lignin: A Biopolymer from Forestry Biomass for Biocomposites and 3D Printing. Materials. 2019;12(18).
[85] Ebers LS, Arya A, Bowland CC, Glasser WG, Chmely SC, Naskar AK, et al. 3D printing of lignin: Challenges, opportunities and roads onward. Biopolymers. 2021 Jun 1;112(6).
[86] Hao L, Li Y, Gong P, Xiong W. Chapter 8 - Material, Process and Business Development for 3D Chocolate Printing. In: Godoi FC, Bhandari BR, Prakash S, Zhang M, editors. Fundamentals of 3D Food Printing and Applications. Academic Press; 2019. p. 207–55.
[87] Lee T, Camp CP, Kim B, Kim M. Environmentally Friendly Methylcellulose Blend Binder for Hydrophobic Dust Control. ACS Appl Polym Mater. 2022 Jan 28;4(2):1512–22.
[88] Grover JA. Chapter 18 - Methylcellulose And Its Derivatives. In: WHISTLER ROYL, BEMILLER JN, editors. Industrial Gums (Third Edition). London: Academic Press; 1993. p. 475–504.
[89] de Carvalho Oliveira G, Filho GR, Vieira JG, De Assunção RMN, da Silva Meireles C, Cerqueira DA, et al. Synthesis and application of methylcellulose extracted from waste newspaper in CPV-ARI Portland cement mortars. J Appl Polym Sci. 2010 Nov 5;118(3):1380–5.
[90] Li H, Tan YJ, Leong KF, Li L. 3D Bioprinting of Highly Thixotropic Alginate/Methylcellulose Hydrogel with Strong Interface Bonding. ACS Appl Mater Interfaces. 2017 Jun 14;9(23):20086–97.
[91] Contessi Negrini N, Bonetti L, Contili L, Farè S. 3D printing of methylcellulose-based hydrogels. Bioprinting. 2018;10.
[92] Zhang Y, Jiang Z, Zhu Y, Zhang J, Ren Q, Huang T. Effects of redispersible polymer powders on the structural build-up of 3D printing cement paste with and without hydroxypropyl methylcellulose. Constr Build Mater. 2021;267.
[93] Yin Y, Huang J, Wang T, Yang R, Hu H, Manuka M, et al. Effect of Hydroxypropyl methyl cellulose (HPMC) on rheology and printability of the first printed layer of cement activated slag-based 3D printing concrete. Constr Build Mater. 2023;405.
[94] Shoaei P, Gallantree-Smith H, Martínez Pacheco V, Pamies R, Kjøniksen AL, Pilehvar S. Comparative analysis of 3D printing of Portland cement mortars with hydroxypropyl methylcellulose and microfibrillated cellulose as viscosity modifying agents. Mater Des. 2024;244:113124.
[95] Peeters J, van der Veen R, Helgers R, Långström O, Bambi M, Papworth N, et al. Resisting Plastics for Ambiguous Results. In: Proceedings of the 4th Biennial Research Through Design Conference. Delft and Rotterdam; 2019.

[96] Zhao L feng, Liu Y, Xu Z dong, Zhang Y zhuo, Zhao F, Zhang S bao. State of research and trends in development of wood adhesives. For Stud China. 2011;13(4):321–6.
[97] Frihart C. Introduction to Special Issue: Wood Adhesives: Past, Present, and Future. For Prod J. 2015 Mar 1;65:4–8.
[98] Hemmilä V, Adamopoulos S, Karlsson O, Kumar A. Development of sustainable bio-adhesives for engineered wood panels–A Review. RSC Adv. 2017;7(61):38604–30.
[99] Braun J. Additives. In: Lubricants and Lubrication. 2017. p. 117–52.
[100] Brydson JA. Additives for Plastics. In: Brydson JA, editor. Plastics Materials (Seventh Edition). Oxford: Butterworth-Heinemann; 1999. p. 124–57.
[101] Merriam-Webster.com Dictionary. Reinforcing agent [Internet]. 2025 [cited 2025 Feb 3]. Available from: https://www.merriam-webster.com/dictionary/reinforcing%20agent
[102] Ebnesajjad S. Effect of Chemicals on Plastics. In: Baur E, Ruhrberg K, Woishnis W, editors. Chemical Resistance of Engineering Thermoplastics [Internet]. William Andrew Publishing; 2016. p. 27–41. Available from: https://www.sciencedirect.com/science/article/pii/B9780323473576000222
[103] Thomas EW, Todd JE. Additives. In: Beadle JD, editor. Plastics Forming. London: Macmillan Education UK; 1971. p. 15–28.
[104] BioPowder. Fillers, Binders & Carriers [Internet]. 2022 [cited 2022 Dec 1]. Available from: https://www.bio-powder.com/en/fillers-binders-carriers/
[105] Zhuang G, Li Q, Zhang Z, Bergaya F, Yuan P. Chapter 2 - Application of bentonite in water-based drilling fluids. In: Zhuang G, Yuan P, editors. Developments in Clay Science. Elsevier; 2024. p. 21–53.
[106] Chen M, Liu B, Li L, Cao L, Huang Y, Wang S, et al. Rheological parameters, thixotropy and creep of 3D-printed calcium sulfoaluminate cement composites modified by bentonite. Compos B Eng. 2020 Apr 1;186.
[107] Robayo-Salazar R, Muñoz MA, Vargas A, Mejía de Gutiérrez R. Effects of incorporating bentonite, metakaolin, microsilica, and calcium carbonate on the rheological properties of portland cement-based 3D printing inks. Constr Build Mater. 2024;445.
[108] Zhao Z, Chen M, Zhong X, Huang Y, Yang L, Zhao P, et al. Effects of bentonite, diatomite and metakaolin on the rheological behavior of 3D printed magnesium potassium phosphate cement composites. Addit Manuf. 2021;46.
[109] Jiang L, Peng X, Walczyk D. 3D printing of biofiber-reinforced composites and their mechanical properties: a review. Rapid Prototyp J. 2020 Jun 4;26:1113–29.
[110] Dias JP, Brandão F, Figueiredo B, Cruz P. The potential of natural fiber reinforcement in 3D printed concrete: a review. In: DigitalConcrete 2024 - 4th RILEM International Conference on Concrete and Digital Fabrication. Munich, Germany; 2024.
[111] Lu Y, Xiao J, Li Y. 3D printing recycled concrete incorporating plant fibres: A comprehensive review. Constr Build Mater. 2024;425.
[112] Luhar S, Suntharalingam T, Navaratnam S, Luhar I, Thamboo J, Poologanathan K, et al. Sustainable and Renewable Bio-Based Natural Fibres and Its Application for 3D Printed Concrete: A Review. Sustainability. 2020;12(24).
[113] Le Duigou A, Correa D, Ueda M, Matsuzaki R, Castro M. A review of 3D and 4D printing of natural fibre biocomposites. Mater Des. 2020;194.
[114] Das AK, Agar DA, Rudolfsson M, Larsson SH. A review on wood powders in 3D printing: processes, properties and potential applications. Journal of Materials Research and Technology. 2021;15:241–55.
[115] Olaiya BC, Lawan MM, Olonade KA. Utilization of sawdust composites in construction—a review. SN Appl Sci. 2023;5(5):140.

[116] Krapež Tomec D, Kariž M. Use of Wood in Additive Manufacturing: Review and Future Prospects. Polymers (Basel). 2022;14(6).
[117] Mwango A, Kambole C. Engineering characteristics and potential increased utilisation of sawdust composites in construction—A review. Journal of Building Construction and Planning Research. 2019;7(3):59–88.
[118] Trifol J, Jayaprakash S, Baniasadi H, Ajdary R, Kretzschmar N, Rojas OJ, et al. 3D-Printed Thermoset Biocomposites Based on Forest Residues by Delayed Extrusion of Cold Masterbatch (DECMA). ACS Sustain Chem Eng. 2021 Oct 18;9(41):13979–87.
[119] Kong M, Qin Z, Zhang P, Xie G, Wang H, Wang J, et al. Study on modified poplar wood powder/polylactic acid high toughness green 3D printing composites. Int J Biol Macromol. 2023;228:311–22.
[120] Mayer-Laigle C, Rajaonarivony RK, Blanc N, Rouau X. Comminution of Dry Lignocellulosic Biomass: Part II. Technologies, Improvement of Milling Performances, and Security Issues. Bioengineering. 2018;5(3).
[121] Nadir Ayrilmis MK, Kuzman MK. Effect of wood flour content on surface properties of 3D printed materials produced from wood flour/PLA filament. International Journal of Polymer Analysis and Characterization. 2019;24(7):659–66.
[122] Tao Y, Pan L, Liu D, Li P. A case study: Mechanical modeling optimization of cellular structure fabricated using wood flour-filled polylactic acid composites with fused deposition modeling. Compos Struct. 2019;216:360–5.
[123] Bi H, Ren Z, Guo R, Xu M, Song Y. Fabrication of flexible wood flour/thermoplastic polyurethane elastomer composites using fused deposition molding. Ind Crops Prod. 2018;122:76–84.
[124] Chawla K, Singh J, Singh R. On recyclability of thermosetting polymer and wood dust as reinforcement in secondary recycled ABS for nonstructural engineering applications. Journal of Thermoplastic Composite Materials. 2022;35(7):913–37.
[125] Henke K, Treml S. Wood based bulk material in 3D printing processes for applications in construction. European Journal of Wood and Wood Products. 2013;71(1):139–41.
[126] StoraEnso. Pulp for paper, board and tissue [Internet]. 2025 [cited 2025 Feb 10]. Available from: https://www.storaenso.com/en/products/market-pulp/pulp-for-paper-board-and-tissue
[127] Sappi. Valida [Internet]. 2025 [cited 2025 Feb 10]. Available from: https://www.sappi.com/nl/valida-home
[128] Rijksdienst voor Ondernemend Nederland. Black Elephant: downstream processing of Black Liquor [Internet]. 2022 Aug [cited 2025 Feb 10]. Available from: https://projecten.topsectorenergie.nl/projecten/black-elephant-downstream-processing-of-black-liquor-34555
[129] Hoof E van. Why Miscanthus. In: Miscanthus Society 11th International Meeting. 2022.
[130] Special Ingredients Ltd. Methocel - Methylcellulose [Internet]. Special Ingredient Europe. 2025 [cited 2025 Feb 10]. Available from: https://specialingredientseurope.com/nl/products/methyl-cellulose-e461
[131] NEN-EN. Classification of thermoplastic wood adhesives for non-structural applications. In: NEN-EN 204:2016 en. 2016.
[132] Pattex. PATTEX Classic [Internet]. Henkel Nederland B.V. 2025 [cited 2025 Feb 10]. Available from: https://www.pattex.nl/products/central-pdp.html/pattex-classic/SAP_0201FTP03EI1.html
[133] Bison. Bison PVAC Wood Adhesive D2 [Internet]. Bolton Adhesives. 2025 [cited 2025 Feb 10]. Available from: https://www.bison.net/en-en/products/bison-wood-glue-bottle-750-g-multi-language

[134] Chiellini E, Corti A, D'Antone S, Solaro R. Biodegradation of poly (vinyl alcohol) based materials. Prog Polym Sci. 2003;28(6):963–1014.
[135] Ben Halima N. Poly(vinyl alcohol): review of its promising applications and insights into biodegradation. RSC Adv. 2016;6(46):39823–32.
[136] Silex. GS 4104 Bentoniet [Internet]. Silex Totaal Service b.v. 2025 [cited 2025 Feb 11]. Available from: https://www.silexshop.nl/product/gs-4104-bentoniet/
[137] Easy Composites. 200g Unidirectional Flax Fibre Tape (600mm) [Internet]. Easy Composites Ltd. 2025 [cited 2025 Feb 11]. Available from: https://www.easycomposites.co.uk/200g-unidirectional-flax-fibre-tape
[138] ABB. IRB1200-datasheet. Robotics. 2023.
[139] Roex LMJ. Structural performance of a three dimensional bio-based parametric structural element, through additive manufacturing. [Eindhoven]: Eindhoven University of Technology; 2023.
[140] Jeni Hansen-Gard. How to Wedge Clay Properly [Internet]. The American Ceramic Society. 2024 [cited 2025 Mar 12]. Available from: https://ceramicartsnetwork.org/daily/article/How-to-Wedge-Clay-Properly
[141] UNi-CROWN CO. LTD. The Importance of Vacuum Deairing Pug Mill in Clay Processing [Internet]. 2023 [cited 2025 Mar 12]. Available from: https://unicrown-tw.com/en/importance-of-pugmill-in-clay-processing/
[142] NEN-EN. Methods of testing cement : part 1 : determination of strength. In: NEN-EN 196-1:2016 [Internet]. British Standard; 2016 [cited 2024 Aug 8]. p. 33. Available from: https://www.academia.edu/43087671/Methods_of_testing_cement_Part_1_Determination_of_strength
[143] BS EN 12390-3:2002. Compressive strength of test specimens. In: Testing hardened concrete. 2002.
[144] Lemonis ME. Moment of Inertia of a Trapezoid [Internet]. 2020 [cited 2023 Sep 8]. Available from: https://calcresource.com/author_minas-lemonis.html
[145] Mackay S. Materials: Engineering, Science, Processing and Design. Proceedings of the Institution of Civil Engineers - Construction Materials. 2011;164(4):215.
[146] Team Xometry. Flexural Modulus: Definition, Calculation, and Importance [Internet]. 2023 [cited 2023 Dec 12]. Available from: https://www.xometry.com/resources/3d-printing/flexural-modulus/#:~:text=Flexural%20modulus%20refers%20to%20a,when%20in%20tension%20or%20compression.
[147] De SK, White JR. Rubber Technologist's Handbook. Vol. 1. Rapra Technology Limited; 2001.
[148] Ross RJ, USDA Forest Service. FPLaboratory. Wood handbook : wood as an engineering material. 2010.
[149] Sanandiya ND, Vijay Y, Dimopoulou M, Dritsas S, Fernandez JG. Large-scale additive manufacturing with bioinspired cellulosic materials. Sci Rep. 2018;8(1):8642.
[150] Wolfs RJM, Bos FP, Salet TAM. Hardened properties of 3D printed concrete: The influence of process parameters on interlayer adhesion. Cem Concr Res. 2019;119:132–40.
[151] Pan Z, Si D, Tao J, Xiao J. Compressive behavior of 3D printed concrete with different printing paths and concrete ages. Case Studies in Construction Materials. 2023;18:e01949.
[152] Christensen PW, Klarbring A. An Introduction to Structural Optimization [Internet]. Gladwell GML, editor. Vol. 153. Springer; 2009. Available from: www.springer.com/series/6557
[153] Selmi M, İlerisoy ZY. A Comparative Study of Different Grasshopper Plugins for Topology Optimization in Architectural Design. 2022 Sep 1;
[154] Preisinger C. Linking Structure and Parametric Geometry. Lobe G, Tam M, editors. Vol. 83, Architectural Design. 2013. 110–113 p.

[155] Oasys. Oasys GSA Help Guide [Internet]. 2017 [cited 2024 Apr 9]. Available from: https://www.oasys-software.com/wp-content/uploads/2018/04/gsa9.0_manual.pdf
[156] Rutten D. Evolutionary Principles applied to Problem Solving [Internet]. 2010 [cited 2024 Jul 16]. Available from: https://www.grasshopper3d.com/profiles/blogs/evolutionary-principles
[157] Xiao Q, Doudak G, Mohareb M. Numerical and experimental investigation of lateral torsional buckling of wood beams. Eng Struct. 2017;151:85–92.
[158] Kuhn B. Torsion Design of Glulam Beams [Internet]. Dlubal Structural Analysis and Design Software. 2017 [cited 2024 Jun 3]. Available from: https://www.dlubal.com/en/support-and-learning/support/knowledge-base/001410
[159] Rehm G. Lateral-Torsional Buckling in Timber Construction | Theory [Internet]. Dlubal Structural Analysis and Design Software. 2024 [cited 2024 Jun 18]. Available from: https://www.dlubal.com/en/support-and-learning/support/knowledge-base/001625
[160] Oasys. Oasys GSA Theory [Internet]. 2022 [cited 2024 Apr 9]. Available from: https://www.oasys-software.com/wp-content/uploads/2018/04/gsa9.0_manual.pdf

Appendices

10 Appendices

Appendix A – Mix processes

Appendix B – Mixture evaluations

Appendix C – Test beam information

Appendix D – Extra information for the flexural tests

Appendix E – Compression tests

Appendix F – Flexural tests

Appendix G – Topology optimisation

Appendix H – Printability exploration with the bio glue with flax mixture

Appendix I – Script new shape

Appendix J – Numerical models GSA

Appendix K – Final prints

Appendix L – Final testing

Appendix A – Mix processes

Bio-based 3D printing and testing of a digitally designed structural element

F.E. Pels Rijcken

Eindhoven, 19-06-2025

Contents

A.1 Methylcellulose mixing process 1
A.2 Wood glue mixing process 1
A.3 Bio-glue mixing process 1
A.4 Additive mixing process 1

A.1 Methylcellulose mixing process

The following mixing process was utilised for the fabrication of the methylcellulose mixtures:

1. Cut the cellulose paper into smaller pieces and shred them in a blender until the fibres are separated (cellulose fluff).
2. Mix the methylcellulose, lignin and cellulose fluff together until all the cellulose fibres are covered with methylcellulose and lignin.
3. Heat water to 80 °C
4. Add the methylcellulose, lignin and cellulose to the heated water while continuously mixing. Mix until it is a homogeneous paste.
5. Let the mixture cool down to room temperature.
6. When cooled down, the mixture should be set aside in a closed container for at least 24 hours until it has reached the optimal consistency.

A.2 Wood glue mixing process

The following mixing process was utilised for the fabrication of the final wood glue mixtures:

1. Cut the cellulose paper into smaller pieces and shred them in a blender until the fibres are separated (cellulose fluff).
2. Mix the lignin and cellulose fluff together until all the cellulose fibres are covered with lignin.
3. Mix the wood glue and Valida L, 3% together until all Valida is fully incorporated in the wood glue.
4. Add the lignin and cellulose to the wood glue and Valida mixture and mix until a homogeneous paste is achieved.

A.3 Bio-glue mixing process

The following mixing process was utilised for the fabrication of the final bio-glue mixtures:

1. Cut the cellulose paper into smaller pieces and shred them in a blender until the fibres are separated (cellulose fluff).
2. Mix the lignin and cellulose fluff together until all the cellulose fibres are covered with lignin.
3. Mix the bio-glue and Valida L, 3% together until all Valida is fully incorporated in the wood glue.
4. Add the lignin and cellulose to the bio-glue and Valida mixture and mix until a homogeneous paste is achieved.

A.4 Additive mixing process

The following mixing process was utilised for the final wood/bio-glue mixtures containing additives, with the steps for the additives being underlined. The recipes for all the additives were combined into one recipe, one or more additive could be excluded depending on the goal of the mixture.

1. Cut the cellulose paper into smaller pieces and shred them in a blender until the fibres are separated (cellulose fluff).
2. Cut the flax fibres into small strands of approximately 10 mm
3. Grind the sawdust into smaller particles
4. Mix the lignin, cellulose fluff together until all the cellulose fibres are covered with lignin.
5. Add the bentonite, flax fibres and ground sawdust to the lignin and cellulose and mix until they are fully integrated.
6. Mix the glue and Valida L, 3% together until all Valida is fully incorporated in the wood glue.
7. Add the lignin and cellulose to the glue and Valida mixture and mix until a homogeneous paste is achieved.

Appendix B – Mixture evaluations

Bio-based 3D printing and testing of a digitally designed structural element

F.E. Pels Rijcken

Eindhoven, 19-06-2025

Contents

B.1 Methylcellulose 1
B.2 Wood glue 3
B.3 Bio-glue 8
B.4 Final mixes 9

B.1 Methylcellulose

Table B1 presents the various compositions of the methylcellulose mixtures.
Table B2 presents the mix- and extrusion-dates, and where applicable, the number of hours a mixture was cured in the oven.
Table B3 displays the number of days that a certain mixture had been cured before testing, and Table B4 provides the individual ratings of each methylcellulose mixture.

Table B1. Compositions of the methylcellulose mixtures.

Mix	Lignin [g]	Cellulose [g]	Methylcellulose [g]	Water [g]	Bentonite [g]	Total weight [g]
1	60.3	6.1	10.5	110.8		187.7
2	30.0	2.9	5.0	65.6		103.6
3	30.1	3.1	5.0	65.1		103.3
4	30.8	3.0	5.2	67.3	1.1	107.4
5	30.2	3.0	5.1	66.5	6.1	111.0
6	30.9	3.0	10.1	67.0		111.0
7	30.0	3.1	5.1	66.4		104.6
8	29.9	3.0	5.0	67.2		105.2
9	30.1	3.0	5.0	66.6		104.6
10	40.1	3.0	5.0	66.4		114.6

Table B2. Mixing dates, extrusion dates, and time in the oven where applicable.

Mix	Mix date [date]	Extrusion dates [date]			Time in oven [hours]
		1	2	3	
1	07/02/2023	07/02/2023	08/02/2023	09/02/2023	-
2	08/02/2023	09/02/2023	10/02/2023	-	-
3	13/02/2023	14/02/2023	-	-	67:11
4	13/02/2023	14/02/2023	-	-	67:11
5	13/02/2023	13/02/2023	14/02/2023	-	67:11
6	06/03/2023	07/03/2023	-	-	23:13
7	06/03/2023	07/03/2023	-	-	23:13
8	06/03/2023	07/03/2023	-	-	23:13
9	06/03/2023	07/03/2023	-	-	23:13
10	06/03/2023	07/03/2023	-	-	23:13

Table B3. Number of curing days.

Mix	Hardened state tested [date]	Days cured [date]		
		1	2	3
1	17/02/2023	10	9	8
2	17/02/2023	8	7	-
3	17/02/2023	3	-	-
4	17/02/2023	3	-	-
5	17/02/2023	4	3	-
6	13/03/2023	6	-	-
7	13/03/2023	6	-	-
8	13/03/2023	6	-	-
9	13/03/2023	6	-	-
10	13/03/2023	6	-	-

Table B4. Methylcellulose mixture ratings.

Mix	Curing conditions	Fresh			Hardened		
		Homogeneity	Extrudability	Adhesion	Failure behaviour	Curing time	Final rating
1	Lab[1]	1	-1	0	-2	-2	**-2.5**
	Lab[2]	1	1	0	-2	-2	**-0.5**
2	Lab	1	1	1	-2		**1**
3[3]	Oven		-2		-2	2	**-2**
	Lab		-2				**-2**
4	Oven[1]	1	-1.8	1	-2	2	**0.2**
	Oven[2]	1	-0.5	1	-2	2	**1.5**
5	Oven	1	0.5	0		2	**1.5**
6	Oven	-2	-1	-2	-2	2	**-5**
	Lab	-2	-1	-2	-2	2	**-5**
7	Oven	-1	-1	-1	-1.9	2	**-2.9**
	Lab	-1	-1	-1	-1.9	2	**-2.9**
8	Oven	-1	-2	-2	-1.9	2	**-4.9**
	Lab	-1	-2	-2	-1.9	2	**-4.9**
9	Oven	-2	-2	-2	-1.9	2	**-5.9**
	Lab	-2	-2	-2	-1.7	2	**-5.7**
10	Oven	-2	-2	-2	-2	2	**-6**
	Lab	-2	-2	-2	-2	2	**-6**

[1] Extruded with a syringe

[2] extruded with a piping bag

[3] too bad to give a rating

B.2 Wood glue

Table B5 and Table B6 present the various compositions of the wood glue mixtures, and the bio-based vs non biobased content of each individual mixture, respectively.

Table B7 presents the mix- and extrusion-dates, number of curing days and, where applicable, the number of hours a mixture was cured in the oven.

Table B8 and Table B9 provide the individual ratings of each wood glue mixture.

Table B5. Ratio of the wood glue mixes.

Mix	Lignin [g]	Cellulose [g]	Wood glue [g]	Valida [g]	Water [g]	Bentonite [g]	Flax [g]	Saw dust [g]	Total weight [g]
1	30.3	3.0	100.2		20.1				153.6
2[1]	30.3	3.0	173.0		14.0				220.3
3[1]	12.6	2.1	60.4						75.1
4	60.4	2.0	60.2	68.1					188.7
5	12.5	2.2	60.5						75.2
6	12.6	2.2	60.4		1.5	2.1			78.8
7	12.6	2.1	60.0	5.6					80.3
8	12.6	2.1	60.7	5.2		2.2			82.8
9	12.7	2.1	60.1	5.3		5.1			85.3
10	12.5	2.1	60.8					3.0	78.4
11	12.5	2.1	60.0				0.5		75.1
12	12.5	2.0	60.0					5.0	79.5
13	12.6	2.0	60.0				1.0		75.6
14	20.0	2.0	60.0	6.2					88.2
15	20.1	2.1	50.1	10.2					82.5
16	20.0	2.1	40.2	15.6					77.9
17	20.1	3.0	30.1	20.3					73.5
18	20.1	3.0	40.1	20.0					83.2
19	20.1	3.0	40.2	20.3		5.0			88.6
20	25.0	2.0	39.9	14.9	7.9				89.7
21	20.1	2.0	40.0	15.5				3.0	80.6
22	20.1	3.0	40.0	20.7				3.0	86.8
23	20.1	3.0	40.4	20.0			1.0		84.5
24	60.1	9.0	120.0	60.3					249.4
25	60.0	9.0	120.0	60.1					249.1
26	20.1	3.0	40.0		16.5				79.6
27	60.0	9.0	120.0	59.9		15.0			263.9
28	40.0	6.0	80.0	50.0					176.0
29	40.0	6.0	80.0	50.0		7.9			183.9
30	40.0	6.0	80.1	50.0		8.0			184.1
31	40.0	6.0	80.0	50.0					176.0
32	40.0	6.0	90.0	60.0					196.0
33	40.0	6.0	80.1	60.1					186.2
34	40.0	4.0	80.1	59.9					184.0
35	40.0	5.0	80.0	60.1					185.1
36	40.0	5.0	80.1	60.0		7.5			192.6
37	40.0	5.0	80.0	59.9		7.5	2.0		194.4
38	40.0	5.0	80.0	60.0					185.0
39	240.0	30.0	480.0	360.0					1110.0
40	40.0	5.0	80.0	60.1		10.0			195.1
41	40.0	5.0	80.0	60.0		12.0			197.0
42	40.0	5.0	80.0	60.0				8.6	193.6
43	200.0	25.0	400.0	300.0					925.0
44	40.0	5.0	80.1	60.0					185.1

[1] Heated while mixing

Table B6. Wood glue mixtures and their bio-based/wood glue percentages

Mix		Wood glue [%]	Bio-based [%]
1	Try mix ratios of TU Delft	65%	35%
2[1]	Try mix ratios of TU Delft	79%	21%
3[1]	TU Delft with more lignin	80%	20%
4	Try Valida for the first time	32%	68%
5	Retry mix 3	80%	20%
6	Mix 5 + water + bentonite	77%	23%
7	Mix 5 + Valida	75%	25%
8	Mix 5 + Valida + bentonite	73%	27%
9	Mix 5 + Valida + more bentonite	70%	30%
10	Mix 5 + sawdust	78%	22%
11	Mix 5 + flax fibres	80%	20%
12	Mix 5 + more sawdust	75%	25%
13	Mix 5 + more flax fibres	79%	21%
14	Ratio 1:3 lignin:WG	68%	32%
15	Ratio 1:2.5 lignin:WG	61%	39%
16	Ratio 1:2 lignin:WG	52%	48%
17	Ratio 1:1.5 lignin:WG + more Valida + cellulose	41%	59%
18	Ratio 1:2 lignin:WG + more Valida + cellulose	48%	52%
19	Mix 18 + bentonite	45%	55%
20	Ratio 1:1.6 lignin:WG	44%	56%
21	Mix 16 + saw dust	50%	50%
22	Mix 18 + saw dust	46%	54%
23	Mix 18 + flax fibres	48%	52%
24	Mix 18 for caulking gun	48%	52%
25	Mix 18 for caulking gun	48%	52%
26	Mix 18 with water instead of Valida	50%	50%
27	Mix 18 for caulking gun with bentonite	45%	55%
28	More Valida	45%	55%
29	More Valida + bentonite	44%	56%
30	Mix 29 with vibrating table	44%	56%
31	Mix 28 with vibrating table	45%	55%
32	Mix 28 with more Valida + more wood glue	46%	54%
33	Mix 28 with small diameter caulking gun (1mm)	43%	57%
34	Mix 28 with less cellulose diameter caulking gun (7mm)	44%	56%
35	Mix 28 with less cellulose	43%	57%
36	Mix 35 with bentonite	42%	58%
37	Mix 35 with bentonite and flax fibres	41%	59%
38	Mix 35 with other brand wood glue	43%	57%
39	Mix 35 printing test batch	43%	57%
40	Mix 35 with more bentonite	41%	59%
41	Mix 35 with even more bentonite	41%	59%
42	Mix 35 with sawdust	41%	59%
43	Mix 35 printing test batch	43%	57%
44	Reference mix with calcium carbonate (100 gram)	43%	57%

[1] Heated while mixing

Table B7. Mix and test dates of the wood glue mixtures.

Mix	Mix date	Time in oven	No oven		Oven	
			Hardened state tested	Days cured	Hardened state tested	Days cured
	[date]	[hours]	[date]		[date]	
1	07/02/2023		17/02/2023	10	17/02/2023	10
2	13/02/2023	90:20	23/02/2023	10	17/02/2023	4
3	14/02/2023	69:46	27/02/2023	13	17/02/2023	3
4	14/02/2023	67:55	27/02/2023	13	17/02/2023	3
5	23/02/2023	94:38	28/02/2023	5	27/02/2023	4
6	23/02/2023	93:03	27/02/2023	4	27/02/2023	4
7	23/02/2023	92:10	28/02/2023	5	27/02/2023	4
8	27/02/2023	24:05	06/03/2023	7	06/03/2023	7
9	27/02/2023	23:56	06/03/2023	7	06/03/2023	7
10	28/02/2023	24:21	06/03/2023	6	06/03/2023	6
11	28/02/2023	23:45	06/03/2023	6	06/03/2023	6
12	28/02/2023	23:45	06/03/2023	6	06/03/2023	6
13	28/02/2023	23:45	06/03/2023	6	06/03/2023	6
14	07/03/2023	-	13/03/2023	6		
15	07/03/2023	-	13/03/2023	6		
16	07/03/2023	-	13/03/2023	6		
17	08/03/2023	-	16/03/2023	8		
18	08/03/2023	-	16/03/2023	8		
19	08/03/2023	-	16/03/2023	8		
20	08/03/2023	-	16/03/2023	8		
21	13/03/2023	186:19	21/03/2023	8		
22	13/03/2023	186:19	21/03/2023	8		
23	13/03/2023	185:44	21/03/2023	8		
24	14/03/2023	166:16	30/03/2023	16	21/03/2023	7
25	14/03/2023	163:13	30/03/2023	16		
26	16/03/2023	118:51	21/03/2023	5	21/03/2023	5
27	16/03/2023	116:03	04/04/2023	19		
28	16/03/2023	115:45	24/04/2023	39		
29	17/03/2023	-	04/04/2023	18		
30	21/03/2023	-	04/04/2023	14		
31	21/03/2023	-	04/04/2023	14		
32	21/03/2023	-	13/04/2023	23		
33	23/03/2023	-	13/04/2023	21		
34	23/03/2023	-	13/04/2023	21		
35	23/03/2023	-	13/04/2023	21		
36	28/03/2023	-	13/04/2023	16		
37	30/03/2023	-	24/04/2023	25		
38	30/03/2023	-	24/04/2023	25		
39	06/04/2023	-	-	-		
40	11/04/2023	-	24/04/2023	13		
41	11/04/2023	-	24/04/2023	13		
42	11/04/2023	-	24/04/2023	13		
43	13/04/2023	-	-	-		
44	19/04/2023	-	24/04/2023	5		

Table B8. Wood glue mixture ratings part 1.

Mix	Curing conditions	Fresh			Hardened		
		Homogeneity	Extrudability	Adhesion	Failure behaviour	Curing time	Final rating
1	Lab	2	2	2	-2	2	8
	Lab	2	2	2	2	1	9
2	Oven	2	1	2	0	2	7
	Lab	2	1	2	0	2	7
3	Oven	0.5	0.5	2	1	2	6
	Lab	0.5	0.5	2	2	-1	4
4	Oven	2	2	1.5	-2	2	5.5
	Lab	2	2	1.5	-2	-1	2.5
5	Oven	2	1	2	-2	2	5
	Lab	2	1	2	2	2	9
6	Oven	2	-0.5	2	-1.9	2	3.6
	Lab	2	-0.5	2	1.5	2	7
7	Oven	1.8	0	2	-2	2	3.8
	Lab	1.8	0	2	1.8	2	7.6
8	Oven	2	2	1	0	2	7
	Lab	2	2	1	1	2	8
9	Oven	2	1.8	2	1.7	2	9.5
	Lab	2	1.8	2	2	2	9.8
10	Oven	2	1.7	2	-1	2	6.7
	Lab	2	1.7	2	1.9	2	9.6
11	Oven	2	1.7	2	0.5	2	8.2
	Lab	2	1.7	2	1.5	2	9.2
12	Oven	-2	-3	0	-1.5	2	-4.5
	Lab	-2	-3	0	-1.8	2	-4.8
13	Oven	1.8	1.5	2	1.5	2	8.8
	Lab	1.8	1.5	2	2	2	9.3
14	Lab	1.7	2	1	0.2	2	6.9
15	Lab	2	1.8	2	-1	2	6.8
16	Lab	2	2	2	0.5	2	8.5
17	Lab	2	1.8	2	-0.5	1.5	6.8
18	Lab	2	2	2	2	1.5	9.5
19	Lab	2	1.8	2	-0.5	1.5	6.8
20	Lab	2	1.6	2	-1	1.5	6.1
21	Climate room	2	1.8	0.5	-1.5	2	4.8
	Lab	2	1.8	0.5	-1.3	2	5
22	Climate room	2	2	1.5	-2	2	5.5
	Lab	2	2	1.5	-2	2	5.5

Table B9. Wood glue mixture ratings part 2.

Mix	Curing conditions	Fresh			Hardened		
		Homogeneity	Extrudability	Adhesion	Failure behaviour	Curing time	Final rating
23	Climate room	2	2	2	0.5	2	8.5
	Lab	2	2	2	1	2	9
24	Climate room	1	1.8	2	1.5	2	8.3
	Lab	1	1.8	2	1	1	6.8
	Oven	1	1.8	2	-2	2	4.8
25	Climate room	0.5	1.8	2	2	1	7.3
	Lab	0.5	1.8	2	1	1	6.3
26	Oven	1.8	2	1.8	0.5	2	8.1
	Lab	1.8	2	1.8	-0.5	2	7.1
27	Climate room	1.8	-2	-2			-2.2
	Lab	1.8	-2	-2			-2.2
28	Climate room	2	2	2	2		8
29	Lab	2	2	2	2	1	9
30	Climate room	2	2	2	0.5	1	7.5
	Lab	2	2	2	2	1.2	9.2
32	Climate room	2	2	2.1	2	0.5	8.6
33*	Wood cover	2	2	2	2	1.5	9.5
	Glass cover	2	2	2	0.5	0.5	7
34*	Wood cover	2	2	2	1.5	2	9.5
	Glass cover	2	2	2	2	0.5	8.5
35*	Wood cover	2	2	2	2	2	10
	Plastic cover	2	2	2	1.7	0.5	8.2
36*	Wood cover	2	2	2	1.8	1.5	9.3
37*	Plastic cover	1.8	2	2	2	1.5	9.3
38*	Plastic cover	2	2	2	2	1.5	9.5
39*	-	-	-	-	-	-	-
40*	Plastic cover	2	2	2	2	2	10
41*	Plastic cover	2	2	2	1	2	9
42*	Plastic cover	2	2	2	1.5	2	9.5
43*	-	-	-	-	-	-	0
44*	Plastic cover	2	2	2	-1	2	7
	No cover	2	2	2	-1	2	7

* These samples were cured in the climate room; these tests would determine what cover would be the best

B.3 Bio-glue

Table B10 present the various compositions of the bio-glue mixtures.
Table B11 presents the mix- and extrusion-dates, number of curing days and, where applicable, the number of hours a mixture was cured in the oven.
Table B12 provides the individual ratings of each bio-glue mixture.

Table B10. Ratio of the bio-glue mixes

Mix	Lignin [g]	Cellulose [g]	Bio-glue [g]	Valida [g]	Bentonite [g]	Flax [g]	Saw dust [g]	Total weight [g]
1	20.1	2.0	40.1	11.0				73.20
2	20.1	2.0	30.0	21.1				73.20
3	20.0	2.0	30.5		2.0			54.50
4	40.0	4.0	60.0	40.0				144.00
5	40.0	4.0	60.3	40.3	5.0			149.60
6	40.0	4.0	60.0	40.0	10.0			154.00

Table B11. Mix and test dates.

Mix	Mix date [date]	Time in oven [hours]	Cover Hardened state tested [date]	Cover Days cured	No cover Hardened state tested [date]	No cover Days cured
1	28/03/2023		13/04/2023	16		
2	28/03/2023	90:20	13/04/2023	16		
3	30/03/2023	69:46	13/04/2023	14		
4	04/04/2023	67:55	24/04/2023	20	13/04/2023	9
5	04/04/2023	94:38	24/04/2023	20	13/04/2023	9
6	11/04/2023	-	24/04/2023	13		

Table B12. Bio-glue mixture ratings.

Mix	Curing conditions*	Fresh Homogeneity	Fresh Extrudability	Fresh Adhesion	Hardened Failure behaviour	Hardened Curing time	Hardened Final rating
1	Wooden cover	1.5	2	2	1.5	1.5	8.5
2	Plastic cover	2	2	2	1.6	1.5	9.1
3	Plastic cover	2	2	1.5	-2	1.5	5
4	Plastic cover	2	2	2	2	1	9
	No cover	2	2	2	1.8	2	9.8
5	Plastic cover	2	2	2	-0.5	1	6.5
	No cover	2	2	2	-0.2	2	7.8
6	Plastic cover	2	2	2	1	2	9

* All samples were cured in the climate room; these tests would determine what cover would be the best

B.4 Final mixes

Table B13 presents the final quantities for one batch for both the reference mixtures and the mixtures with additives. Table B14 presents the final mixture ratios for both the reference mixtures and the mixtures with additives.

Table B13. Final mixture quantities for one batch.

	Mix	Lignin [g]	Cellulose [g]	Glue [g]	Valida [g]	Bentonite [g]	Flax [g]	Total weight [g]
Wood glue	Reference	200	25	400	300			925.0
	Bentonite	200	25	400	300	37.5		962.5
	Flax	200	25	400	300		10.0	935.0
	Bentonite + flax	200	25	400	300	37.5	10.0	972.5
Bio-glue	Reference	300	30	450	300			1080.0
	~~Bentonite bad~~	~~300~~	~~30~~	~~450~~	~~300~~	~~75.0~~		~~1155.0~~
	Bentonite good	300	30	450	300	37.5		1117.5
	Flax	300	30	450	300		11.2	1091.2
	Bentonite + flax	300	30	450	300	37.5	11.2	1128.7

Table B14. Final mixture ratios.

	Mix	Lignin [-]	Cellulose [-]	Glue [-]	Valida [-]	Bentonite [-]	Flax [-]
Wood glue	Reference	8	1	16	12		
	Bentonite	8	1	16	12	1.5	
	Flax	8	1	16	12		0.4
	Bentonite + flax	8	1	16	12	1.5	0.4
Bio-glue	Reference	10	1	15	10		
	Bentonite 6.5%	10	1	15	10	2.5	
	Bentonite 3.4%	10	1	15	10	1.3	
	Flax	10	1	15	10		0.4
	Bentonite + flax	10	1	15	10	1.3	0.4

Appendix C – Test beam information

Bio-based 3D printing and testing of a digitally designed structural element



F.E. Pels Rijcken

Eindhoven, 19-06-2025

Contents

C.1 Batch information 1
C.2 Beam information 2
C.3 Fresh and cured dimensions of the test beams with bio-glue and additives 5
C.4 Shrinkage 8

C.1 Batch information

The test beams were printed on multiple days. The set of beams printed on the same day from the same mix are called batches. These batches and their information are listed in Table C1.

Table C1. Batch information

	Batch nr.	Date	Nr. of beams	Notes
Wood glue	1	19-04-2023	1	
	2	02-05-2023	4	
	3	08-05-2023	5	
	4	09-05-2023	4	
Bio-glue	1	26-04-2023	1	
	2	03-05-2023	3	
	3	04-05-2023	6	
	4	10-05-2023	5	
Bio-glue with bentonite	1	26-06-2023	4	6.5% bentonite
	2	28-06-2023	5	3.4% bentonite
Bio-glue with flax	1	27-06-2023	6	
	2	28-06-2023	2	
Bio-glue with bentonite and flax	1	30-06-2023	3	
	2	14-07-2023	5	

C.2 Beam information

Table C2 to Table C6 give information about each test beam. This includes the robot settings; the important dates and what type of test is performed with a test beam.

Table C2. Important information of the wood glue elements.

Wood glue							
Print	**Print speed [mm/s]**	**Dimension in Grass-hopper [mm]**	**Printed [date]**	**Plastic removed [date]**	**Turned upside down [date]**	**Tested [date]**	**Test**
1*	14.5	250 x 40 x 5 layers	2-05-2023	9-05-2023	24-5-2023	13-06-2023	Bending horizontal 1mm/min
2*	14.5	250 x 40 x 5 layers	2-05-2023	9-05-2023	24-5-2023	13-06-2023	Bending horizontal 3mm/min
3*	14.5	250 x 40 x 5 layers	2-05-2023	9-05-2023	24-5-2023	13-06-2023	Bending horizontal 3mm/min
4*	14.5	160 x 40 x 5 layers	2-05-2023	9-05-2023	24-5-2023	16-06-2023	Compression 2 elements Test 1. Vertical 2 mm/min Test 2. Horizontal 2 mm/min
5**	15.5	238 x 40 x 5 layers	8-05-2023	17-05-2023	24-5-2023	14-06-2023	Bending horizontal 3mm/min
6**	15.5	238 x 40 x 5 layers	8-05-2023	17-05-2023	24-5-2023	14-06-2023	Bending horizontal 3mm/min
7**	15.5	238 x 40 x 5 layers	8-05-2023	17-05-2023	24-5-2023	14-06-2023	Bending vertical 3mm/min
8**	15.5	238 x 40 x 5 layers	8-05-2023	17-05-2023	24-5-2023	14-06-2023	Bending vertical 3mm/min
9**	15.5	110 x 40 x 5 layers	8-05-2023	17-05-2023	24-5-2023	16-06-2023	Compression 1 element Test 1. Vertical 2 mm/min
10**	15.5	238 x 40 x 5 layers	9-05-2023	17-05-2023	24-5-2023	14-06-2023	Bending vertical 3mm/min
11**	15.5	238 x 40 x 5 layers	9-05-2023	17-05-2023	24-5-2023	14-06-2023	Bending vertical 3mm/min
12**	15.5	238 x 40 x 5 layers	9-05-2023	17-05-2023	24-5-2023	14-06-2023	Bending vertical 3mm/min
13**	15.5	238 x 40 x 5 layers	9-05-2023	17-05-2023	24-5-2023	16-06-2023	Bending horizontal 3mm/min
14* ***(Reserve)***		210 x 40 x 6 layers	19-04-2023	26-4-2023	24-5-2023	30-05-2023	Compression 3 elements Test 1. Vertical 1 mm/min Test 2. Horizontal 2 mm/min Test 3. Horizontal 2 mm/min

**) Pattex wood glue*
***) Bison wood glue*

Table C3. Important information of the bio-glue elements.

Bio-glue							
Print	**Print speed [mm/s]**	**Dimension in Grass-hopper [mm]**	**Printed [date]**	**Plastic removed [date]**	**Turned upside down [date]**	**Tested [date]**	**Test**
1	16.5	250 x 40 x 5 layers	3-05-2023	10-05-2023	26-5-2023	13-06-2023	Bending horizontal 3mm/min
2	16.5	250 x 40 x 5 layers	3-05-2023	10-05-2023	26-5-2023	13-06-2023	Bending horizontal 3mm/min
3	16.5	250 x 40 x 5 layers	3-05-2023	10-05-2023	26-5-2023	14-06-2023	Bending horizontal 3mm/min
4	16.5	250 x 40 x 5 layers	4-05-2023	11-05-2023	26-5-2023	14-06-2023	Bending horizontal 3mm/min
5	16.5	250 x 40 x 5 layers	4-05-2023	11-05-2023	26-5-2023	14-06-2023	Bending horizontal 3mm/min
6	16.5	250 x 40 x 5 layers	4-05-2023	11-05-2023	26-5-2023	14-06-2023	Bending vertical 3mm/min
7	16.5	250 x 40 x 5 layers	4-05-2023	11-05-2023	26-5-2023	14-06-2023	Bending vertical 3mm/min
8	16.5	250 x 40 x 5 layers	4-05-2023	11-05-2023	26-5-2023	14-06-2023	Bending vertical 3mm/min
9	16.5	200 x 40 x 5 layers	4-05-2023	11-05-2023	24-5-2023	16-06-2023	Compression 2 elements Test 1. Vertical 2 mm/min Test 2. Horizontal 2 mm/min
10	16.5	250 x 40 x 5 layers	10-05-2023	17-05-2023	30-05-2023	14-06-2023	Bending vertical 3mm/min
11	16.5	250 x 40 x 5 layers	10-05-2023	17-05-2023	30-05-2023	14-06-2023	Bending vertical 3mm/min
12	16.5	250 x 40 x 5 layers	10-05-2023	17-05-2023	30-05-2023	16-06-2023	Bending horizontal 3mm/min
13	16.5	250 x 40 x 5 layers	10-05-2023	17-05-2023	30-05-2023	16-06-2023	Bending vertical 3mm/min
14	16.5	250 x 40 x 5 layers	10-05-2023	17-05-2023	30-05-2023	16-06-2023	Bending horizontal 3mm/min
15 ***(Reserve)***	16.5		26-4-23	3-05-2023		30-05-2023	Compression 5 elements: Test 1. Horizontal 1 mm/min Test 2. Horizontal 2 mm/min Test 3. Vertical 1 mm/min Test 4. Vertical 2 mm/min Test 5. Failed

Table C4. Important information of the bio-glue with bentonite elements.

Bio-glue with bentonite							
Print	**Print speed [mm/s]**	**Dimension in Grass-hopper [mm]**	**Printed [date]**	**Plastic removed [date]**	**Turned upside down [date]**	**Tested [date]**	**Test**
1*	15.5	250 x 40 x 5 layers	26-6-2023	3-07-2023	14-07-2023	15-08-2023	Bending horizontal 3mm/min
2*	15.5	250 x 40 x 5 layers	26-6-2023	3-07-2023	14-07-2023	15-08-2023	Bending vertical 3mm/min
3*	15.5	250 x 40 x 5 layers	26-6-2023	3-07-2023	14-07-2023	15-08-2023	Bending vertical 3mm/min
4*	15.5	250 x 40 x 5 layers	26-6-2023	3-07-2023	14-07-2023	01-8-2023	Compression 4 elements Test 1. Vertical 2 mm/min Test 2. Vertical 2 mm/min Test 3. Horizontal 2 mm/min Test 4. Horizontal 2 mm/min
5**	19	250 x 40 x 5 layers	28-6-2023	5-07-2023	14-07-2023	15-08-2023	Bending horizontal 3mm/min
6**	19	250 x 40 x 5 layers	28-6-2023	5-07-2023	14-07-2023	15-08-2023	Bending horizontal 3mm/min
7**	19	250 x 40 x 5 layers	28-6-2023	5-07-2023	14-07-2023	15-08-2023	Bending vertical 3mm/min
8**	19	250 x 40 x 5 layers	28-6-2023	5-07-2023	14-07-2023	15-08-2023	Bending vertical 3mm/min
9**	19	100 x 40 x 5 layers	28-6-2023	5-07-2023	14-07-2023	01-08-2023	Compression 3 elements Test 1. Vertical 2 mm/min Test 2. Horizontal 2 mm/min Test 3. Horizontal 2 mm/min

**) 6.5% bentonite*
***) 3.4% bentonite*

Table C5. Important information of the bio-glue with flax elements.

Bio-glue with flax							
Print	**Print speed [mm/s]**	**Dimension in Grass-hopper [mm]**	**Printed [date]**	**Plastic removed [date]**	**Turned upside down [date]**	**Tested [date]**	**Test**
1	18.5	250 x 40 x 5 layers	27-6-2023	4-07-2023	14-07-2023	15-08-2023	Bending horizontal 3mm/min
2	18.5	250 x 40 x 5 layers	27-6-2023	4-07-2023	14-07-2023	15-08-2023	Bending horizontal 3mm/min
3	18.5	250 x 40 x 5 layers	27-6-2023	4-07-2023	14-07-2023	15-08-2023	Bending horizontal 3mm/min
4	18.5	250 x 40 x 5 layers	27-6-2023	4-07-2023	14-07-2023	16-08-2023	Bending vertical 3mm/min
5	18.5	250 x 40 x 5 layers	27-6-2023	4-07-2023	14-07-2023	16-08-2023	Bending vertical 3mm/min
6	18.5	200 x 40 x 5 layers	27-6-2023	4-07-2023	14-07-2023	01-08-2023	Compression 5 elements Test 1. Vertical 2 mm/min Test 2. Vertical 2 mm/min Test 3. Horizontal 2 mm/min Test 4. Horizontal 2 mm/min Test 5. Horizontal 2 mm/min
7	18.5	250 x 40 x 5 layers	28-6-2023	5-07-2023	14-07-2023	16-08-2023	Bending vertical 3mm/min
8	18.5	50 x 40 x 5 layers	28-6-2023	5-07-2023	14-07-2023	01-08-2023	Compression 1 element Test 1. Vertical 2 mm/min

Table C6. Important information of the bio-glue with bentonite and flax elements.

Bio-glue with bentonite and flax							
Print	**Print speed [mm/s]**	**Dimension in Grass-hopper [mm]**	**Printed [date]**	**Plastic removed [date]**	**Turned upside down [date]**	**Tested [date]**	**Test**
1	18,5	250 x 40 x 5 layers	30-6-2023	6-07-2023	14-07-2023	16-08-2023	Bending horizontal 3mm/min
2	18,5	250 x 40 x 5 layers	30-6-2023	6-07-2023	14-07-2023	16-08-2023	Bending vertical 3mm/min
3	18,5	250 x 40 x 5 layers	30-6-2023	6-07-2023	14-07-2023	16-08-2023	Bending horizontal 3mm/min
4	18,5	250 x 40 x 5 layers	14-07-2023	21-07-2023	8-09-2023	16-08-2023	Bending horizontal 3mm/min
5	18,5	250 x 40 x 5 layers	14-07-2023	21-07-2023	8-09-2023	16-08-2023	Bending vertical 3mm/min
6	18,5	250 x 40 x 5 layers	14-07-2023	21-07-2023	8-09-2023	16-08-2023	Bending vertical 3mm/min
7	18,5	250 x 40 x 5 layers	14-07-2023	21-07-2023	8-09-2023	14-08-2023	Compression 4 elements Test 1. Vertical 2 mm/min Test 2. Vertical 2 mm/min Test 3. Horizontal 2 mm/min Test 4. Horizontal 2 mm/min
8	18,5	200 x 40 x 5 layers	14-07-2023	21-07-2023	8-09-2023	14-08-2023	Compression 3 elements Test 1. Vertical 2 mm/min Test 2. Vertical 2 mm/min Test 3. Horizontal 2 mm/min

C.3 Fresh and cured dimensions of the test beams with bio-glue and additives

Table C7 to Table C12 present the dimensions of the test beams made from bio-glue with additives. The dimensions are measured when the beams were freshly printed and after the curing process was completed. Unfortunately, some dimensions of the freshly printed and cured test beams were not measured because they were used for the compression tests.

Table C13 displays the volume, weight and density of each beam. The average density is 1106.6E-3 g/cm^3 = 1106.6 kg/m^3.

Table C7. Dimensions of freshly printed bio-glue elements with bentonite.

Bio-glue with bentonite					
Beam	**Length [cm]**	**Left [cm]**	**Height Middle [cm]**	**Right [cm]**	**Width middle top [cm]**
1	29.0	4.1	4.1	4.1	4.5
2	29.0	4.5	4.6	4.4	4.5
3	29.5	4.1	4.7	4.4	4.5
4	28.5	4.2	4.5	4.3	4.5
5	29.3	3.7	4.2	4.0	4.5
6	29.0	3.9	4.1	4.0	4.5
7	29.1	3.9	4.1	4.1	4.5
8	28.6	3.8	4.4	4.1	4.5
9	13.5	3.9	4.3	4.1	4.6

Table C8. Dimensions of cured printed bio-glue elements with bentonite.

Bio-glue with bentonite					
Beam	**Length**	**Height**			**Width middle top**
		Left	**Middle**	**Right**	
	[cm]	**[cm]**	**[cm]**	**[cm]**	**[cm]**
1	26.0	3.4	3.4	3.4	3.7
2	25.5	3.6	3.8	3.4	4.1
3	26.1	3.6	3.7	3.7	4.2
4	-	-	-	-	-
5	26.1	3.2	3.4	3.3	4.0
6	26.5	3.2	3.5	3.2	4.1
7	26.2	3.2	3.3	3.3	3.9
8	26.2	3.1	3.3	3.2	3.9
9	-	-	-	-	-

Table C9. Dimensions of freshly printed bio-glue elements with flax.

Bio-glue with flax					
Beam	**Length**	**Height**			**Width middle top**
		Left	**Middle**	**Right**	
	[cm]	**[cm]**	**[cm]**	**[cm]**	**[cm]**
1	28.5	4.5	4.7	4.5	4.5
2	28.6	4.5	4.7	4.4	4.5
3	28.6	4.3	4.6	4.3	4.5
4	28.7	4.3	4.5	4.4	4.5
5	28.7	4.5	4.6	4.5	4.5
6	23.3	4.2	4.5	4.2	4.5
7	29.2	4.1	4.7	4.3	4.5
8	7.5	3.8	3.9	4.0	4.5

Table C10. Dimensions of cured printed bio-glue elements with flax.

Bio-glue with flax					
Beam	**Length**	**Height**			**Width middle top**
		Left	**Middle**	**Right**	
	[cm]	**[cm]**	**[cm]**	**[cm]**	**[cm]**
1	26.6	3.5	3.6	3.4	4.1
2	26.5	3.3	3.4	3.3	3.9
3	27.0	3.5	3.6	3.4	4.0
4	26.5	3.1	3.5	3.3	4.0
5	26.5	3.2	3.3	3.3	4.1
6	-	-	-	-	-
7	26.5	3.3	3.4	3.3	4.0
8	-	-	-	-	-

Table C11. Dimensions of freshly printed bio-glue elements with bentonite and flax.

Bio-glue with bentonite and flax					
Beam	**Length**	**Height**			**Width middle top**
		Left	**Middle**	**Right**	
	[cm]	**[cm]**	**[cm]**	**[cm]**	**[cm]**
1	28.5	4.1	4.5	4.6	4.4
2	28.0	4.1	4.6	4.5	4.5
3	28.0	4.1	4.4	4.3	4.6
4	-	-	-	-	-
5	-	-	-	-	-
6	-	-	-	-	-
7	-	-	-	-	-
8	-	-	-	-	-

Table C12. Dimensions of cured printed bio-glue elements with bentonite and flax.

Bio-glue with bentonite and flax					
Beam	**Length**	**Height**			**Width middle top**
		Left	**Middle**	**Right**	
	[cm]	**[cm]**	**[cm]**	**[cm]**	**[cm]**
1	26.2	3.2	3.4	3.2	3.9
2	25.8	3.1	3.5	3.2	3.4
3	25.7	3.2	3.4	3.4	3.9
4	26.3	3.2	3.3	3.2	3.9
5	26.6	3.5	3.5	3.5	4.1
6	26.7	3.4	3.6	3.2	4.2
7	-	-	-	-	-
8	-	-	-	-	-

Table C13. Volume, weight and density of the cured bio-glue with bentonite beams and their averages.

Bio-glue with bentonite			
Beam	**Volume**	**Weight**	**Density**
	[cm³]	**[g]**	**[gr/cm³]**
1	327.08	371.8	1136.72 E-3
2	376.38	387.9	1030.61 E-3
3	401.94	382.3	951.14 E-3
4	-	-	-
5	344.52	343.9	998.20 E-3
6	358.55	344.8	961.66 E-3
7	333.79	337.6	1011.42 E-3
8	326.98	338.4	1034.94 E-3
9	-	-	-
Averages	327.08	371.8	1017.81 E-3

Table C14. Volume, weight and density of the cured bio-glue with flax beams and their averages.

Bio-glue with flax			
Beam	**Volume**	**Weight**	**Density**
	[cm³]	**[g]**	**[gr/cm³]**
1	381.71	335.5	878.94 E-3
2	344.50	322.7	936.72 E-3
3	378.00	315.4	834.39 E-3
4	349.80	325.5	930.53 E-3
5	354.92	339.8	957.39 E-3
6	-	-	-
7	353.33	354.9	1004.43 E-3
8	-	-	-
Averages	360.38	332.30	923.73 E-3

Table C15. Volume, weight and density of the cured bio-glue with bentonite and flax beams and their averages.

Bio-glue with bentonite and flax			
Beam	**Volume**	**Weight**	**Density**
	[cm³]	**[g]**	**[gr/cm³]**
1	333.79	330.4	989.85 E-3
2	286.55	318.5	1111.49 E-3
3	334.10	326.5	977.25 E-3
4	331.64	295.3	890.42 E-3
5	381.71	328.3	860.08 E-3
6	381.28	318.1	834.30 E-3
7	-	-	-
8	-	-	-
Averages	341.51	319.52	943.90 E-3

C.4 Shrinkage

Table C16 to Table C18 provides the shrinkage of each test beam. The shrinkage is calculated as the difference in dimension; in absolute value [mm] and in percentage [%] compared to the freshly printed dimension. And
Table C19 presents the average shrinkage.

Table C16. Shrinkage of the beams with bio-glue with bentonite.

Bio-glue with bentonite							
		Shrinkage					
Beam	Curing time	Length		Height		Width at the top	
	[days]	[cm]	[%]*	[cm]	[%]*	[cm]	[%]*
1	50	3	10%	0.7	17%	0.8	18%
2	50	3.5	12%	0.9	20%	0.4	9%
3	50	3.4	12%	0.7	16%	0.3	7%
4	36	-	-	-	-	-	-
5	48	3.2	11%	0.7	17%	0.5	11%
6	48	2.5	9%	0.7	18%	0.4	9%
7	48	2.9	10%	0.8	19%	0.6	13%
8	48	2.4	8%	0.9	22%	0.6	13%
9	34	-	-	-	-	-	-

**) Shrinkage compared to the original dimension of the freshly printed beam.*

Table C17. Shrinkage of the beams with bio-glue with flax.

Bio-glue with flax							
		Shrinkage					
Beam	Curing time	Length		Height		Width at the top	
	[days]	[cm]	[%]*	[cm]	[%]*	[cm]	[%]*
1	49	1.9	7%	1.1	23%	0.4	9%
2	49	2.1	7%	1.2	26%	0.6	13%
3	49	1.6	6%	0.9	20%	0.5	11%
4	50	2.2	8%	1.1	25%	0.5	11%
5	50	2.2	8%	1.3	28%	0.4	9%
6	35	-	-	-	-	-	-
7	49	2.7	9%	1.0	23%	0.5	11%
8	34	-	-	-	-	-	-

**) Shrinkage compared to the original dimension of the freshly printed beam.*

Table C18. Shrinkage of the beams with bio-glue with bentonite and flax.

Bio-glue with bentonite and flax							
		Shrinkage					
Beam	Curing time	Length		Height		Width at the top	
	[days]	[cm]	[%]*	[cm]	[%]*	[cm]	[%]*
1	47	2.3	8%	1.1	26%	0.5	11%
2	47	2.2	8%	1.1	26%	1.1	24%
3	47	2.3	8%	0.9	22%	0.7	15%
4	33	-	-	-	-	-	-
5	33	-	-	-	-	-	-
6	33	-	-	-	-	-	-
7	31	-	-	-	-	-	-
8	31	-	-	-	-	-	-

**) Shrinkage compared to the original dimension of the freshly printed beam.*

Table C19. Average shrinkage per additive.

	Length	Height	Width middle top
	[%]	[%]	[%]
Bentonite	10%	18%	11%
Flax	7%	24%	11%

Bentonite and flax	8%	24%	17%

Appendix D – Extra information for the flexural tests

Bio-based 3D printing and testing of a digitally designed structural element



F.E. Pels Rijcken

Eindhoven, 19-06-2025

List of symbols

Chapter D.2

A	=	*partial cross section a*
B	=	*partial cross section b*
C	=	*partial cross section c*
h	=	*the total height of the complete cross section*
h_n	=	*the height of a part of the cross-section*
b	=	*the total width of the complete cross section*
b_n		*the width of a part of the cross-section*
A_i	=	*the area of partial cross section "i".*
Z_i	=	*the distance between the line of gravity of a partial cross section "i" and the line y'*
Z_{grav}	=	*the distance between the line of gravity of the complete cross section and the line y'*
Z_{i1}	=	*the distance between the line of gravity of partial cross section "i" (z_i) and the line of gravity of the complete cross section (z_{grav})*
Iy_i	=	*the second moment of area of partial cross section "i", with respect to the line of gravity y' of the partial cross section*
Iy	=	*the second moment of area of the complete cross section*

Chapter D.3

ε	=	*strain*
z	=	*distance to the neutral axis*
ρ	=	*radius of the curvature*
κ	=	*curvature*
M	=	*bending moment in the middle of the beam*
EI	=	*bending stiffness (or flexural stiffness) of the beam*
D	=	*displacement in the middle of the beam*
F	=	*point load in the middle of the beam*
L	=	*span between the supports*

Contents

D.1 GSA analysis 1
D.2 Second moment of area of a trapezium shaped cross-section 3
D.2.1.1 Horizontal layer orientation 3
D.2.1.2 Vertical layer orientation 6
D.2.1.3 Difference between the calculation methods of the second moment of inertia 9
D.2.1.4 Discussion and conclusion 10
D.3 Strain derivation 11
Bibliography 13

D.1 GSA analysis

To check whether the support conditions make a significant difference in the stress levels of the beam, a GSA analysis was carried out. For this analysis, the first flax tests were recreated, and a trapezoidal cross-section was used. The dimensions of flax horizontal 1 and flax vertical 1 were used for the horizontal and vertical analysis respectively, see Figure D1. Table D1 lists the properties of the setup and the applied load.

The results of tests were used for the material properties in GSA, which are listed in Figure D3 and Figure D4, for the horizontal and vertical orientation. All the material properties that were unknown were kept at the default settings of GSA.

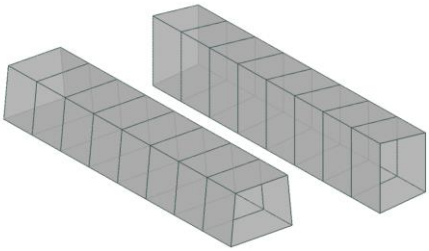


Figure D1. The trapezoidal beams in GSA.

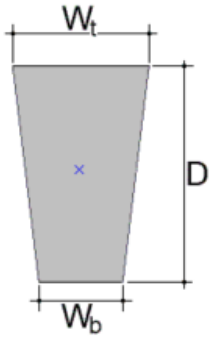


Figure D2. The cross-sectional dimensions in GSA.

Table D1. Properties of the setup and beams in the GSA analysis.

		Horizontal	Vertical
L	**[mm]**	220	220
W_t	**[mm]**	47	47
W_b	**[mm]**	41	40
D	**[mm]**	36	35
Point load	**[kN]**	0.83	1.23

	A	B	E	H
Material	Name	Material Model	Young's Modulus	Density
			[N/mm²]	[kg/m³]
Defaults	Material #	Elastic Isotropic	2,05e+005	7850
1	Flax horizontal	Elastic Isotropic	132,53	923,73

Figure D3. Material properties in GSA for the horizontal analysis.

	A	B	E	H
Material	Name	Material Model	Young's Modulus	Density
			[N/mm²]	[kg/m³]
Defaults	Material #	Elastic Isotropic	2,05e+005	7850
1	Flax	Elastic Isotropic	106,53	923,73

Figure D4. Material properties in GSA for the vertical analysis.

Figure D5 displays the mechanical schemes of both beams with different support conditions. The beam was divided into eight equal parts and the load was applied in the middle of the beam. Additionally, the self-weight of the beam was applied, see Figure D6 for the loads applied on the beam with the horizontal orientation.

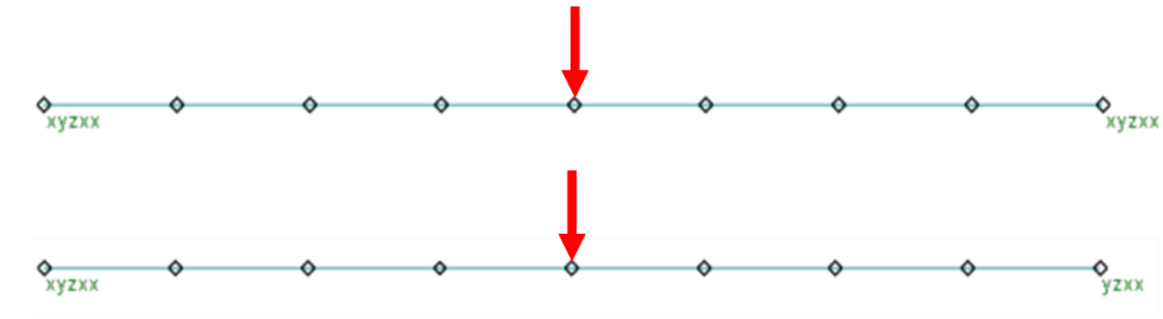


Figure D5. The mechanical schemes of the beams in GSA. The mechanical scheme with two hinges as supports (on the top) and a hinge and a roller support (on the bottom).

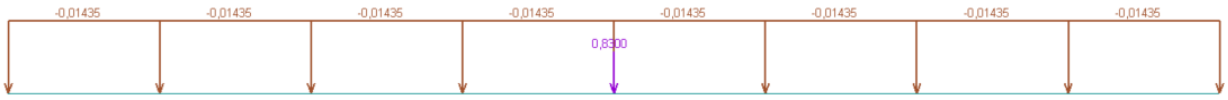


Figure D6. The loadings on the beam with the horizontal orientation in GSA. Brown: the deadweight of the beam. Purple: the applied load of 0.83 kN.

Table D2 and Table D3 present the results of the GSA analyses for both orientations. Both the displacement (U_z) and the maximum stresses (C_1 and C_2) were slightly larger with the one hinge and one roller compared to the setup with two hinges.

Table D2. GSA results of the beam in horizontal orientation.

		Combined stresses	
Support conditions	**U_z**	**C_1**	**C_2**
	[mm]	**[N/mm²]**	**[N/mm²]**
Two hinges	-7.53	4.65	-4.17
Hinge + roller	-8.11	4.70	-4.91

Table D3. GSA results of the beam in vertical orientation.

		Combined stresses	
Support conditions	**U_z**	**C_1**	**C_2**
	[mm]	**[N/mm²]**	**[N/mm²]**
Two hinges	-9.49	6.42	-5.53
Hinge + roller	-10.53	6.57	-6.54

D.2 Second moment of area of a trapezium shaped cross-section

The calculation of the second moment of a trapezium shaped cross-section is done in several steps. First, the cross-section was divided into three separate partial cross-sections (see Figure D7). Secondly, a few assumptions are made:

- The cross-section of the beam is a perfect trapezium, meaning that it has at least two parallel sides.
- The trapezium is symmetrical meaning:
  - A is a perfect rectangle.
  - Triangles B and C are right-angled triangles.
  - The dimensions of triangles B and C are the same.

In the following chapters the calculations of the second moment of area for the vertical and horizontal layer orientations are elaborated.

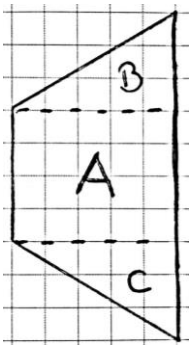


Figure D7. Trapezium divided into three parts: A, B and C.

D.2.1.1 Horizontal layer orientation

Figure D8 shows the naming conventions for the dimensions of the trapezium with a horizontal layer orientation. With the height and width of the cross-section, the centre of gravity was determined. Figure D9 shows the dimensions that are needed to calculate the centre of gravity with respect to the line y' (Z_{grav}). Table D4 to Table D7 give the formulas to calculate Z_{grav}.

The next step was to determine the second moment of area of each part of the cross-section (Iy_i). The dimensions that are necessary for this step are shown in Figure D10. Table D8 to Table D11 give the formulas to calculate the Iy_i.

Finally, equation 1 was used to calculate the second moment of area of the complete cross-section (Iy).

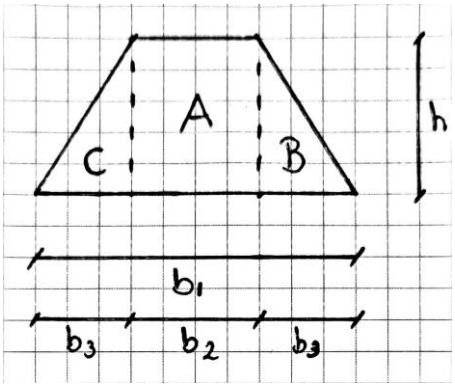


Figure D8. The important dimensions of the trapezium in horizontal orientation.

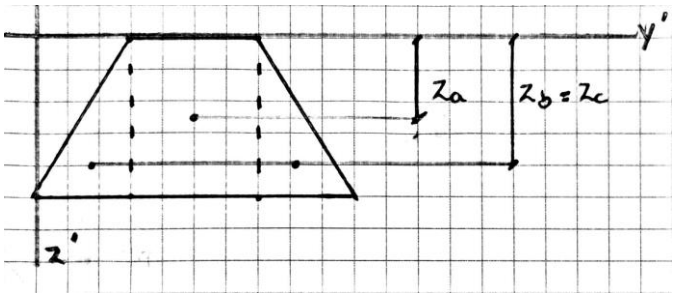


Figure D9. The necessary dimensions to calculate the line of gravity of the cross-section.

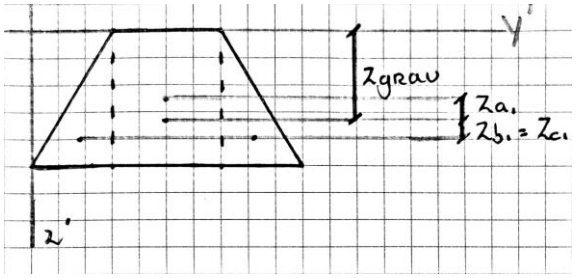


Figure D10. The necessary dimensions to calculate the second moment of area of the cross-section.

Table D4. Dimensions of the trapezium.

Dimensions trapezium		
h		mm
b_1		mm
b_2		mm
b_3	$0.5(b_1-b_2)$	mm

Table D5. Properties of part A of the trapezium.

Square A		
A_a	b_2*h	mm^2
Z_a	$0.5b_1$	mm

Table D6. Properties of part B of the trapezium.

Triangle B		
A_b	$0.5(b_3*h)$	mm^2
Z_b	(2/3)h	mm

Table D7. Properties of part C of the trapezium.

Triangle C		
A_c	$0.5(b_3*h)$	mm^2
Z_c	(2/3)h	mm

Table D8. Formulas for the calculation of the line of gravity of the complete cross section relative to the y' axis.

Line of gravity		
Z_{grav}	$(Z_aA_a+Z_bA_b+Z_cA_c)/(A_{tot})$	mm
A_{tot}	$A_a+A_b+A_c$	mm^2

Table D9. Second moment of area of square A, with respect to the line of gravity of the complete cross section.

Square A		
Iy_a	$(1/12)* b_2*h^3$	mm^4
Z_{a1}	$Z_{grav}-Z_a$	mm

Table D10. Second moment of area of triangle C, with respect to the line of gravity of the complete cross section.

Triangle B		
Iy_b	$(1/36)* b_3*h^3$	mm^4
Z_{b1}	Z_b-Z_{grav}	mm

Table D11. Second moment of area of triangle C, with respect to the line of gravity of the complete cross section.

Triangle C		
Iy_c	$(1/36)* b_3*h^3$	mm^4
Z_{c1}	Z_c-Z_{grav}	mm

$$Iy = Iy_a + ((Z_{a1})^2 * A_a) + Iy_b + ((Z_{b1})^2 * A_b) + Iy_c + ((Z_{c1})^2 * A_c) \quad (1)$$

Where: *Iy = the second moment of area the complete cross section "i" [mm^4] for the horizontal orientation*

Iyi = the second moment of area of partial cross section "i" [mm^4]

Z_{i1} = the distance between the line of gravity of partial cross section "i" and the line of gravity of the complete cross section [mm]

A_i = *the area of partial cross section "i" [mm^2]*

Figure D11 shows a screenshot of the template for the beams with a vertical layer orientation in excel. This template is used in the excel files of the bending test results. Only the values for b_1, b_2 and h are needed to calculate the second moment of area, which is then used to calculate the stress in the beam. For verification the results for Iy are compared to the results of the online tool [1]. If this difference is insignificant (difference<1), the calculation has been executed well. The online tool is shown in Figure D12.

Dimensions					Centre of gravity			
h		15	mm		Z_{grav}	$(Z_aA_a+Z_bA_b+Z_cA_c)/(A_{tot})$	7.86	mm
b_1		20	mm					
b_2		15	mm		A_{tot}	$A_a+A_b+A_c$	262.5	mm^2
b_3	$0.5(b_1-b_2)$	2.5	mm			$Z_aA_a+Z_bA_b+Z_cA_c$	2062.5	mm^3
Square A					**Seond moment of area**			
A_a	b_2*h	225	mm^2		**Iy**	$\mathbf{Iy_a+((Z_{a1})^2*A_a)+Iy_b+((Z_{b1})^2*A_b)+Iy_c+((Zc_1)^2*A_c)}$	**4888.39**	**mm^4**
Z_a	0.5h	7.5	mm					
					Iy_a	$(1/12)*b_2*h^3$	4218.750	mm^4
Triangle B					Z_{a1}	$Z_{grav}-Z_a$	0.357	mm
A_b	$0.5(b_3*h)$	18.75	mm^2			$(Z_{a1})^2*A_a$	28.699	mm^4
Z_b	(2/3)*h	10	mm					
					Iy_b	$(1/36)*b_3*h^3$	234.375	mm^4
Triangle C					Z_{b1}	Z_b-Z_{grav}	2.143	mm
A_c	$0.5(b_3*h)$	18.75	mm^2			$(Z_{b1})^2*A_b$	86.097	mm^4
Z_c	(2/3)*h	10	mm					
					Iy_c	$(1/36)*b_3*h^3$	234.375	mm^4
					Z_{c1}	Z_c-Z_{grav}	2.143	mm
						$(Z_{c1})^2*A_c$	86.097	mm^4
Check					**Chek with online**			
B1>B2	TRUE				b	b_1	20	mm
B1=B2+2*B3	TRUE				a	b_2	15	mm
Ab=Ac	TRUE				h	h	15	mm
Zb=Zc	TRUE							
Zb1=Zc1	TRUE				Iy		**4888.39**	**mm^4**
Iyb=Iyc	TRUE							
					Difference between online and self calculated		0.0029	

Figure D11. Screenshot of the excel template for the second moment of area for the beams with a horizontal layer orientation.

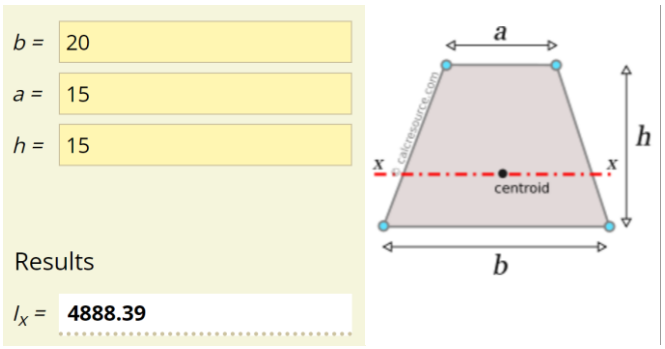


Figure D12. Online tool to calculate the second moment of area of a trapezoid [1]*. Used for the check of the beams with a horizontal layer orientation.*

D.2.1.2 Vertical layer orientation

Figure D13 shows the naming conventions for the dimensions of the trapezium with a vertical layer orientation. With the height and width of the cross-section, the centre of gravity was determined. Figure D14 shows the dimensions that are needed to calculate the centre of gravity with respect to the line y' (Z_{grav}). Table D13 to Table D16 give the formulas and equations to calculate Z_{grav}.

The next step was to determine the second moment of area of each part of the cross-section (Iy_i). The dimensions that are necessary for this step are shown in Figure D15. Table D17 to Table D19 give the formulas to calculate the Iy_i.

Lastly, to calculate the second moment of area of the complete cross-section (Iy), equation 2 was used.

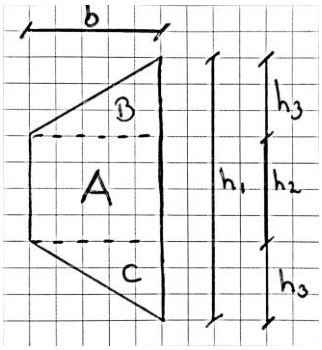


Figure D13. The important dimensions of the trapezium in vertical orientation.

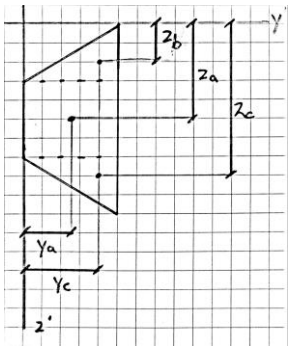


Figure D14. The necessary dimensions to calculate the line of gravity of the cross-section.

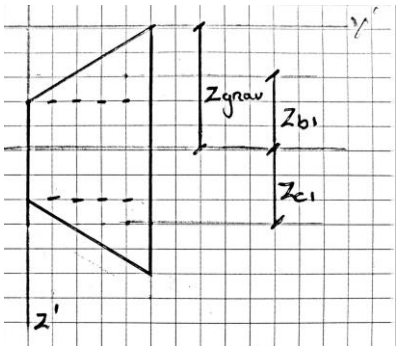


Figure D15. The necessary dimensions to calculate the second moment of area of the cross-section.

Table D12. Dimensions of the trapezium.

Dimensions trapezium		
h_1		mm
h_2		mm
h_3	$0.5(h_1-h_2)$	mm
b		mm

Table D13. Properties of part A of the trapezium.

Square A		
A_a	h_2*b	mm^2
Z_a	$0.5h_1$	mm

Table D14. Properties of part B of the trapezium.

Triangle B		
A_b	$0.5(h_3*b)$	mm^2
Z_b	$(h_1-h_2)/3$	mm

Table D15. Properties of part C of the trapezium.

Triangle C		
A_c	$0.5(h_3*b)$	mm^2
Z_c	$h_1-((h_1-h_2)/3)$	mm

Table D16. Formulas for the calculation of the line of gravity of the complete cross section relative to the y' axis.

Line of gravity		
Z_{grav}	$(Z_aA_a+Z_bA_b+Z_cA_c)/(A_{tot})$	mm
A_{tot}	$A_a+A_b+A_c$	mm^2

Table D17. Second moment of area of square A, with respect to the line of gravity of the complete cross section.

Square A		
Iy_a	$(1/12)*b*(h_2)^3$	mm^4
Z_{a1}	$Z_{grav}-Z_a$	mm

Table D18. Second moment of area of triangle C, with respect to the line of gravity of the complete cross section.

Triangle B		
Iy_b	$(1/36)*b*(h_3)^3$	mm^4
Z_{b1}	$Z_{grav}-Z_b$	mm

Table D19. Second moment of area of triangle C, with respect to the line of gravity of the complete cross section.

Triangle C		
Iy_c	$(1/36)*b*(h_3)^3$	mm^4
Z_{c1}	Z_c-Z_{grav}	mm

$$Iy = Iy_a + ((Z_{a1})^2 * A_a) + Iy_b + ((Z_{b1})^2 * A_b) + Iy_c + ((Z_{c1})^2 * A_c) \qquad 2$$

Where: *Iy = the second moment of area the complete cross section "i" [mm^4] for the vertical orientation*
Iyi = the second moment of area of partial cross section "i" [mm^4]
Z_{i1} = the distance between the line of gravity of partial cross section "i" and the line of gravity of the complete cross section [mm]
A_i = *the area of partial cross section "i" [mm^2]*

Figure D16 shows a screenshot of the template for the beams with a vertical layer orientation in excel. This template is used in the excel files of the bending test results. Only the values for h_1, h_2 and b are needed to calculate the second moment of area, which is then used to calculate the stress in the beam. For verification the results for Iy are compared to the results of the online tool [1]. If this difference is insignificant (difference<1), the calculation has been executed well. The online tool is shown in Figure D17.

Dimensions					**Line of gravity**			
h_1		20	mm		Z_{grav}	$(Z_aA_a+Z_bA_b+Z_cA_c)/(A_{tot})$	10	mm
h_2		15	mm					
h_3	$0.5(h_1-h_2)$	2.5	mm		A_{tot}	$A_a+A_b+A_c$	262.5	mm^2
b		15	mm			$Z_aA_a+Z_bA_b+Z_cA_c$	2625	mm^3
Square A					**Second moment of area**			
A_a	h_2*b	225	mm^2		**Iy**	**$Iy_a+((Z_{a1})^2*A_a)+Iy_b+((Z_{b1})^2*A_b)+Iy_c+((Zc_1)^2*A_c)$**	**6835.94**	**mm^4**
Z_a	$0.5h_1$	10	mm					
					Iy_a	$(1/12)*b*(h_2)^3$	4218.75	mm^4
Triangle B					Z_{a1}	$Z_{grav}-Z_a$	0	mm
A_b	$0.5(h_3*b)$	18.75	mm^2			$(Z_{a1})^2*A_a$	0	mm^4
Z_b	$(h_1-h_2)/3$	1.66667	mm					
					Iy_b	$(1/36)*b*(h_3)^3$	6.51042	mm^4
Triangle C					Z_{b1}	$Z_{grav}-Z_b$	8.33333	mm
A_c	$0.5(h_3*b)$	18.75	mm^2			$(Z_{b1})^2*A_b$	1302.08	mm^4
Z_c	$h_1-((h_1-h_2)/3)$	18.3333	mm					
					Iy_c	$(1/36)*b*(h_3)^3$	6.51042	mm^4
					Z_{c1}	Z_c-Z_{grav}	8.33333	mm
						$(Z_{c1})^2*A_c$	1302.08	mm^4
Check					**Check with online**			
H1>H2	TRUE				b	h_1	20	mm
H1=H2+2*H3	TRUE				a	h_2	15	mm
Ab=Ac	TRUE				h	b	15	mm
H1=Zb+Zc	TRUE				b1	h_3	2.5	mm
Zgrav=0.5H1	TRUE							
Iyb=Iyc	TRUE				Iy		**6835.94**	**mm^4**
Zb1=Zc1	TRUE							
					Difference between online and self calculated		-0.0025	

Figure D16. Screenshot of the excel template for the second moment of area for the beams with a vertical layer orientation.

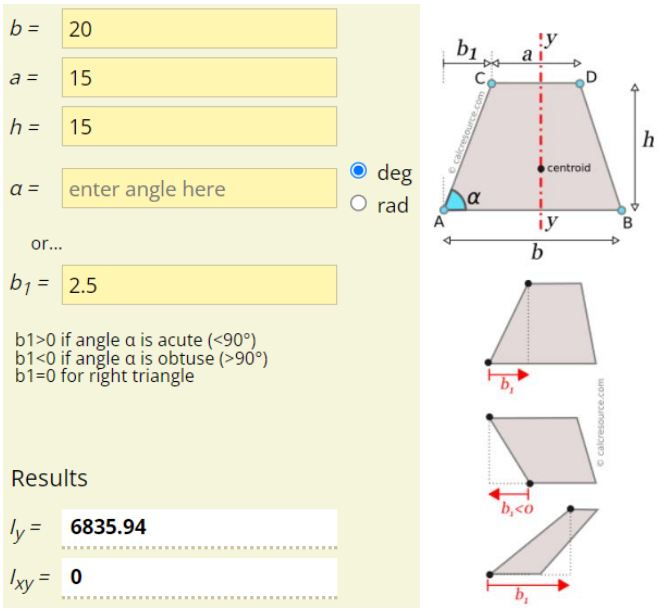


Figure D17. Online tool to calculate the second moment of area of a trapezoid [1]*. Used for the check of the beams with a vertical layer orientation.*

D.2.1.3 Difference between the calculation methods of the second moment of inertia

Table D20 and Table D21 provide the results of three different ways of calculating the second moment of inertia. The first column shows the second moment of inertia if the cross-section was squared, calculated with equation 3. The second column is the second moment of inertia calculated with the online tool a with a trapezoid cross-section and the third column is calculated with the equations 1 or 2. Additionally, the differences between a squared and trapezoid cross-section were calculated (see column 1 and 5). Column 6 lists the differences between the squared and the trapezoid second moment of inertia in percentages. A minus in front of the number indicates that the calculation with the squared cross-section gave an overestimation of the actual second moment of inertia.

$$Iy = \frac{1}{12} * b * h^3 \qquad 3$$

Where: *Iy = the second moment of area the complete cross section "i" [mm^4*
Iyi = the second moment of area of partial cross section "i" [mm^4]
Z_{i1} = the distance between the line of gravity of partial cross section "i" and the line of gravity of the complete cross section [mm]
A_i = *the area of partial cross section "i" [mm^2]*

Table D20. Results for the second moment of area for the beams in horizontal orientation.

		Square	Trapezium		Difference		
			Internet	Self-calculated	Self vs internet	Self vs square	
		[mm⁴]	[mm⁴]	[mm⁴]			
Bio-glue	1	90614.3	90155.2	90155.2	-0.02	-459.11	-0.51%
	2	125779.5	125566.0	125565.6	-0.41	-213.91	-0.17%
	3	137564.0	137330.0	137330.0	0.05	-233.95	-0.17%
	4	144114.7	143718.0	143717.7	-0.34	-397.01	-0.28%
	5	116053.3	115919.0	115919.5	0.48	-133.86	-0.12%
	6	135770.8	135489.0	135488.8	-0.24	-282.07	-0.21%
	7	101034.7	100813.0	100813.3	0.26	-221.41	-0.22%
Wood glue	1	124462.7	124003.0	124003.0	-0.03	-459.70	-0.37%
	2	95579.5	95316.2	95316.2	-0.05	-263.30	-0.28%
	3	144703.1	144108.0	144107.6	-0.36	-595.49	-0.41%
	4	159408.0	158902.0	158902.2	0.24	-505.76	-0.32%
	5	132197.9	132069.0	132069.2	0.16	-128.75	-0.10%
	6	87750.0	87576.9	87576.9	0.02	-173.08	-0.20%
Flax	1	171072.0	170807.0	170806.9	-0.09	-265.09	-0.15%
	2	142477.0	141969.0	141968.8	-0.24	-508.24	-0.36%
	3	169128.0	168763.0	168763.0	0.03	-364.97	-0.22%
Bentonite	1	135926.3	135394.0	135393.6	-0.40	-532.73	-0.39%
	2	145752.3	145256.0	145255.5	-0.49	-496.82	-0.34%
	3	162567.7	162038.0	162037.7	-0.34	-530.05	-0.33%
Bentonite + Flax	1	140839.3	140433.0	140433.1	0.09	-406.24	-0.29%
	2	139201.7	138887.0	138887.0	-0.02	-314.69	-0.23%
	3	124282.1	124132.0	124131.8	-0.21	-150.34	-0.12%

Table D21. Results for the second moment of area for the beams in vertical orientation.

		Square	Trapezium		Difference		
			Internet	Self-calculated	Self vs internet	Self vs square	
		[mm⁴]	[mm⁴]	[mm⁴]			
Bio-glue	**1**	193573.7	194276.0	194276.2	0.20	702.47	0.36%
	2	223899.7	224179.0	224178.6	-0.35	278.91	0.12%
	3	228582.6	229695.0	229695.3	0.25	1112.63	0.49%
	4	108086.0	108180.0	108179.5	-0.50	93.50	0.09%
	5	88681.0	88702.0	88702.0	-0.02	20.99	0.02%
	6	140625.0	141250.0	141250.0	0.00	625.00	0.44%
Flax	**1**	240079.2	241633.0	241633.4	0.44	1554.22	0.65%
	2	259040.0	261574.0	261573.8	-0.19	2533.78	0.98%
	3	258187.5	261375.0	261375.0	0.00	3187.50	1.23%
Bentonite	**1**	260657.4	261518.0	261518.4	0.38	860.94	0.33%
	2	280968.8	282218.0	282217.5	-0.50	1248.75	0.44%
	3	242333.1	246035.0	246034.9	-0.06	3701.84	1.53%
	4	242333.1	246035.0	246034.9	-0.06	3701.84	1.53%
Bentonite + Flax	**1**	186666.7	190867.0	190866.7	-0.33	4200.00	2.25%
	2	231895.4	232397.0	232397.1	0.08	501.67	0.22%
	3	246938.6	247232.0	247232.3	0.25	293.63	0.12%

D.2.1.4 Discussion and conclusion

Horizontal

With the horizontal beams, a squared cross-section is an overestimation of the second moment of inertia. With a trapezium cross-section the line of gravity is positioned lower compared to a squared cross-section. Both cross-sections have the same height, which means that the stresses at the bottom with a trapezium cross-section are lower than with a squared cross-section.

This was confirmed when the stresses were calculated with a trapezium cross-section and its associated second moment of inertia. The stresses were indeed lower with a trapezium cross-section.

Larger differences between the squared cross-section and the trapezium cross-section were caused by a larger difference between the shorter and longer width. With the squared cross-section the average width was used as width, which caused larger differences with the Ix when the trapezium cross-section was used.

Vertical

A simplified squared cross-section was an underestimation of the second moment of inertia with the layer orientation vertical. With the squared cross-section, the average height was used, leading to a smaller distance "z" with the squared cross-section than with the trapezium cross-section. A larger "z" means that the stresses in the outer "fibres" are larger. Meaning that a trapezium cross-section had higher stresses than with a squared cross-section.

Larger differences between the squared cross-section and the trapezium cross-section are caused by a larger difference between the shorter and longer height. With the squared the average height was used as height, which caused larger differences with the Ix when the trapezium cross-section was used.

D.3 Strain derivation

This chapter gives the derivation of the strain equation.

It starts with equation 4, the strain calculation:

$$\varepsilon = \frac{z}{\rho} \qquad 4$$

From beam theory follows equation 5:

$$\kappa = \frac{1}{\rho} = \frac{M}{EI} \Rightarrow \rho = \frac{EI}{M} \qquad 5$$

Substituting equation 5 into 4, leads equation 6 for the strain:

$$\varepsilon = \frac{zM}{EI} \qquad 6$$

The displacement in the middle of a simply supported beam with a centre load is be calculated with equation 7:

$$D = \frac{FL^3}{48EI} \qquad 7$$

Dividing both sides of equation 7 by ε and substituting equation 6 lead to equation 8 for the strain:

$$\frac{D}{\varepsilon} = \frac{FL^3}{\varepsilon 48EI} = \frac{FL^3EI}{48EIzM} = \frac{FL^3}{48zM} \Rightarrow \varepsilon = \frac{48DzM}{FL^3} \qquad 8$$

The load is in the middle of the beam, leading to a moment of M=FL/4, substituting this into equation 8 leads to the equation 9 for the strain:

$$\varepsilon = \frac{48DzFL}{4FL^3} = \frac{12Dz}{L^2} \qquad 9$$

The beam fails at the part that is under tension, meaning that the strain needs to be calculated in the bottom fibres, leading to equation 10:

$$\varepsilon = \frac{12 * D * z}{L^2} \qquad 10$$

Where:
ε = strain [-]
D = displacement [mm]
z = distance from the neutral axis to the bottom fibres [mm]
L = span [mm]

According to ASTM D790-10 the maximum strain in a three-point bending test is calculated with equation 11 [2]. However, this equation is only valid for a rectangular cross-section.

$$\varepsilon = \frac{6 * D * h}{L^2} \qquad 11$$

Where: *ε = strain [-]*
D = displacement [mm]
h = height cross-section [mm]
L = span [mm]

The main difference between equations 10 and 11 is that instead of the height of the beam (h), the distance from the neutral axis to the fibres at the bottom of the beam (z) is used. Additionally, the factor "6" is replaced by "12".
With a perfect rectangle, h=2*z applies, substituting that into equation 10 gives equation 11. However, with a trapezoid cross-section in the horizontal layer orientation (illustrated in Figure D10), the centre of gravity is not halfway the height, but a bit below the middle of the height, causing *h≠2z*. But with the vertical layer orientation the centre of gravity is halfway the height (*h=2z*).
This means that for the vertical layer orientation there is no difference between the results of equation 10 and 11. But for the vertical layer orientation only equation 10 should be used.

Bibliography

[1] Lemonis ME. Moment of Inertia of a Trapezoid [Internet]. 2020 [cited 2023 Sep 8]. Available from: https://calcresource.com/author_minas-lemonis.html

[2] ASTM international. Standard Test Methods for Flexural Properties of Unreinforced and Reinforced Plastics and Electrical Insulating Materials. 2016;

Appendix E – Compression tests

Bio-based 3D printing and testing of a digitally designed structural element



F.E. Pels Rijcken

Eindhoven, 19-06-2025

Contents

E.1 Dimensions of the compression specimens 1
E.2 Reference mixes 3
E.2.1 Wood glue 3
E.2.1.1 Horizontal layer orientation 3
E.2.1.2 Vertical layer orientation 7
E.2.2 Bio-glue 11
E.2.2.1 Horizontal layer orientation 11
E.2.2.2 Vertical layer orientation 15
E.2.3 Summary wood glue and bio-glue bending test results 19
E.3 Results bio-glue with additives 20
E.3.1 Bio-glue with bentonite 20
E.3.1.1 Horizontal layer orientation 20
E.3.1.2 Vertical layer orientation 25
E.3.2 Bio-glue with flax 29
E.3.2.1 Horizontal layer orientation 29
E.3.2.2 Vertical layer orientation 33
E.3.3 Bio-glue with bentonite and flax 37
E.3.3.1 Horizontal layer orientation 37
E.3.3.2 Vertical layer orientation 42
E.3.4 Summary bio-glue with additives bending test results 46

E.1 Dimensions of the compression specimens

Figure E1 shows a simplified version of a compression cube. Each cube is measured at fifteen different spots. The width and the depth were measured at six locations, see Figure E2 and Figure E3. The height was measured at three locations, see Figure E4. The average cross-sectional area and the average height were used for the stress-strain calculations of the compression test.

Table E1 to Table E5 give the average cross-sections and the average heights of each cube for the wood glue, bio-glue and bio-glue with additives tests.

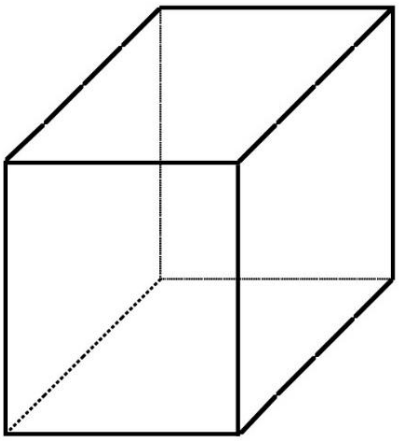


Figure E1. A simplified version of a compression cube.

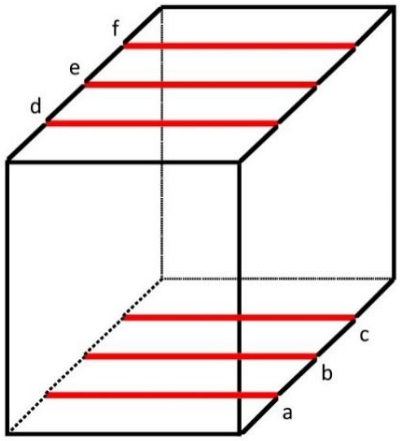


Figure E2. A simplified version of a compression cube with the red lines indicating the six locations at which the width of the cube is measured.

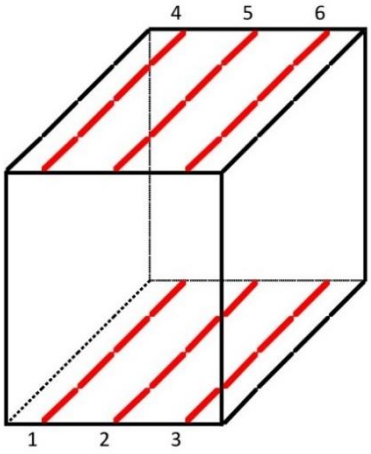


Figure E3. A simplified version of a compression cube with the red lines indicating the six locations at which the depth of the cube is measured.

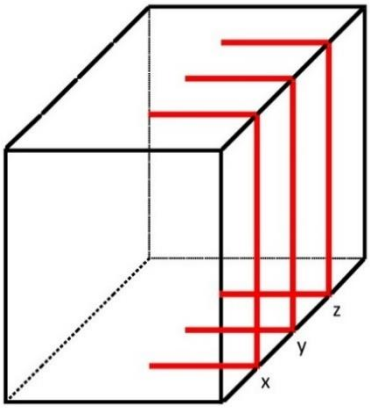


Figure E4. A simplified version of a compression cube with the red lines indicating the three locations at which the height of the cube is measured.

Table E1. Dimensions of the wood glue compression cubes of both layer orientations.

Layer orientation	Test	Cross-sectional area [mm²]	Height [mm]
Horizontal	1	1503.08	34.80
	2	1387.03	35.35
	3	1484.18	31.37
Vertical	1	1328.78	40.50
	2	1137.66	41.33
	3	1120.23	40.76

Table E2. Dimensions of the bio-glue compression cubes of both layer orientations.

Layer orientation	Test	Cross-sectional area [mm²]	Height [mm]
Horizontal	1	1551.84	32.64
	2	1625.17	33.53
	3	1539.20	26.29
Vertical	1	1562.60	32.31
	2	1733.62	32.01
	3	1026.67	42.03

Table E3. Dimensions of the bio-glue with bentonite compression cubes of both layer orientations.

Layer orientation	Test	Cross-sectional area [mm²]	Height [mm]
Horizontal	1	1561.56	32.70
	2	1506.25	32.93
	3	1509.47	30.22
	4	1581.34	29.32
Vertical	1	1382.67	36.38
	2	1460.69	36.15
	3	1199.15	34.32

Table E4. Dimensions of the bio-glue with flax compression cubes of both layer orientations.

Layer orientation	Test	Cross-sectional area [mm²]	Height [mm]
Horizontal	1	1460.61	29.98
	2	1571.23	30.73
	3	1564.19	31.03
Vertical	1	1216.18	36.10
	2	1205.52	36.45
	3	1115.43	36.75

Table E5. Dimensions of the bio-glue with bentonite and flax compression cubes of both layer orientations.

Layer orientation	Test	Cross-sectional area [mm²]	Height [mm]
Horizontal	1	1503.79	30.53
	2	1502.62	32.57
	3	1499.19	32.58
	4	1498.31	31.97
Vertical	1	1297.92	36.18
	2	1248.68	37.20
	3	1185.31	37.10

E.2 Reference mixes

E.2.1 Wood glue

E.2.1.1 Horizontal layer orientation

Figure E5 to Figure E13 show three wood glue tests with a horizontal layer orientation. Each test is accompanied with four photos during the test and two different graphs: the force-displacement and the stress-strain graph.

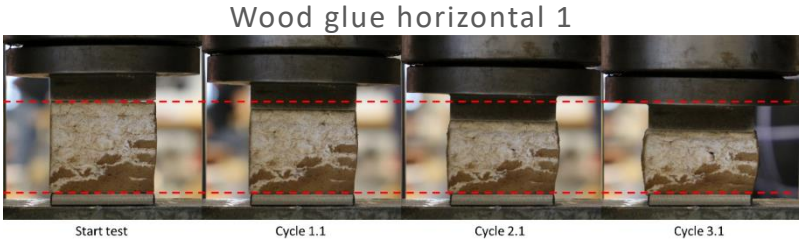


Figure E5. Four photos of compression test 1. One at the start of the test and one at the end of each cycle.



Figure E6. The force-displacement graph of compression test 1.

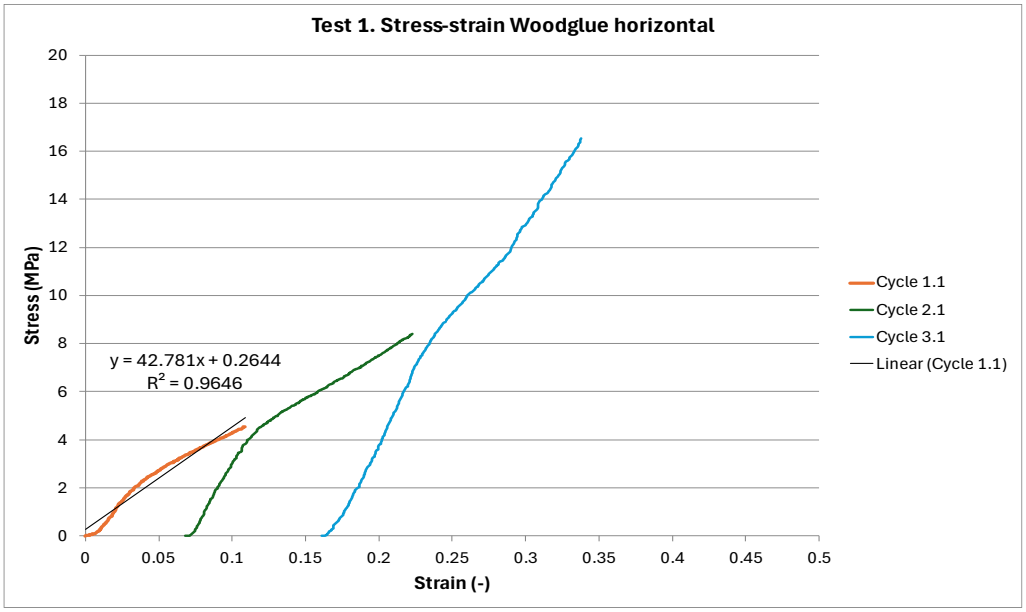


Figure E7. The stress-strain diagram of the three different cycles of compression test 1.

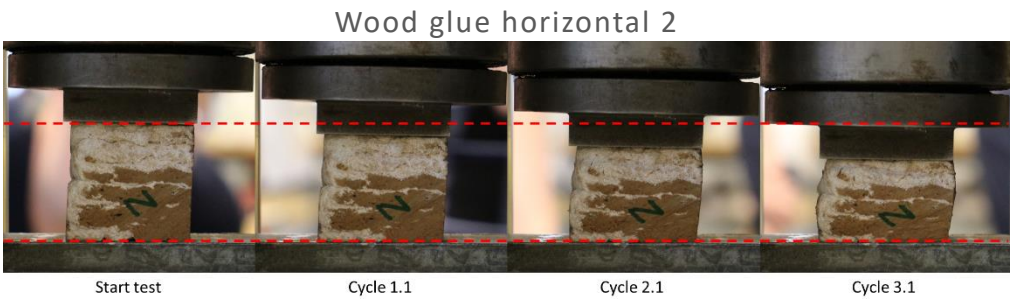


Figure E8. Four photos of compression test 2. One at the start of the test and one at the end of each cycle.



Figure E9. The force-displacement graph of compression test 2.

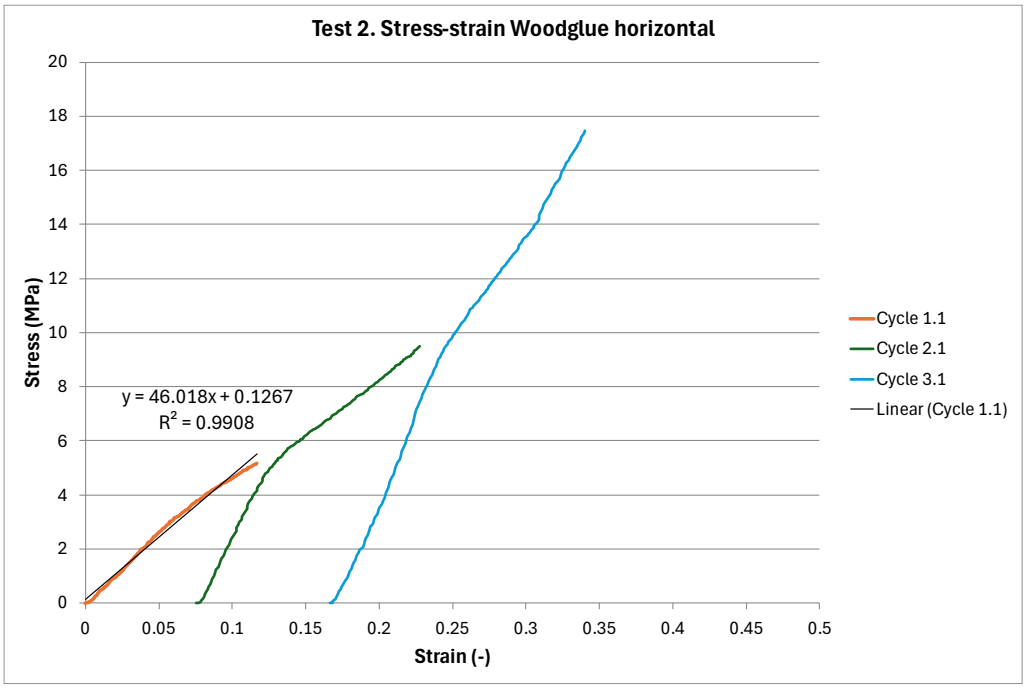


Figure E10. The stress-strain diagram of the three different cycles of compression test 2.

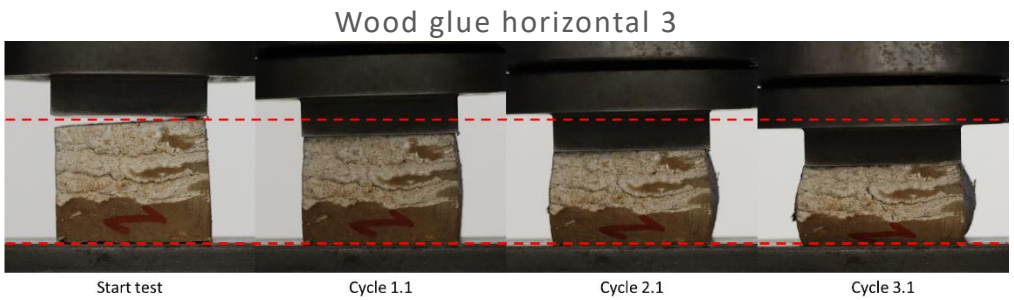


Figure E11. Four photos of compression test 3. One at the start of the test and one at the end of each cycle.

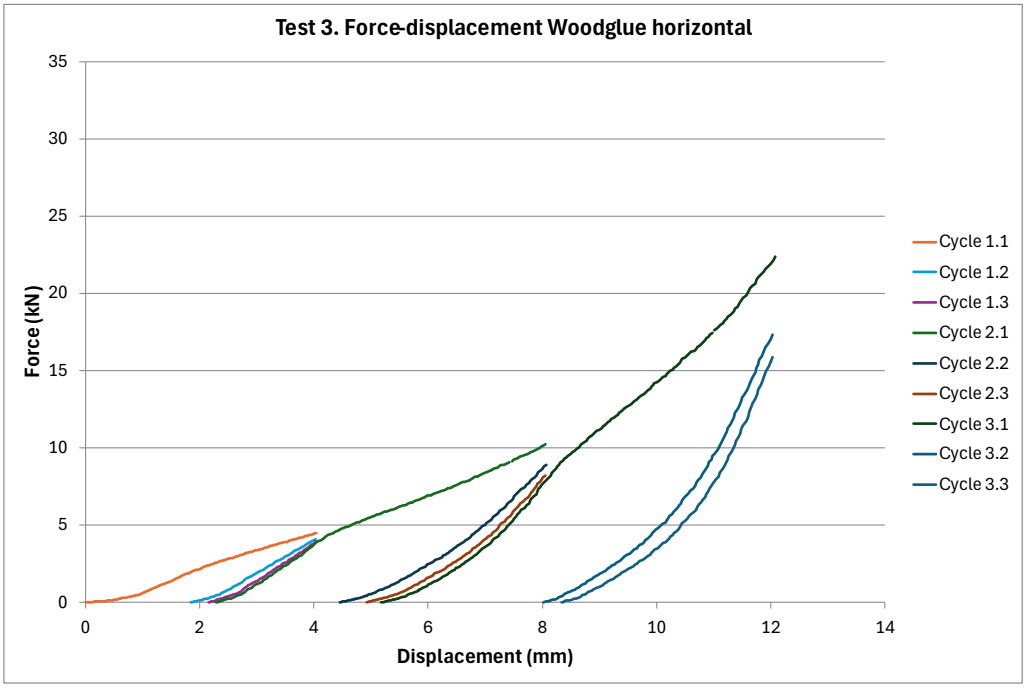


Figure E12. The force-displacement graph of compression test 3.

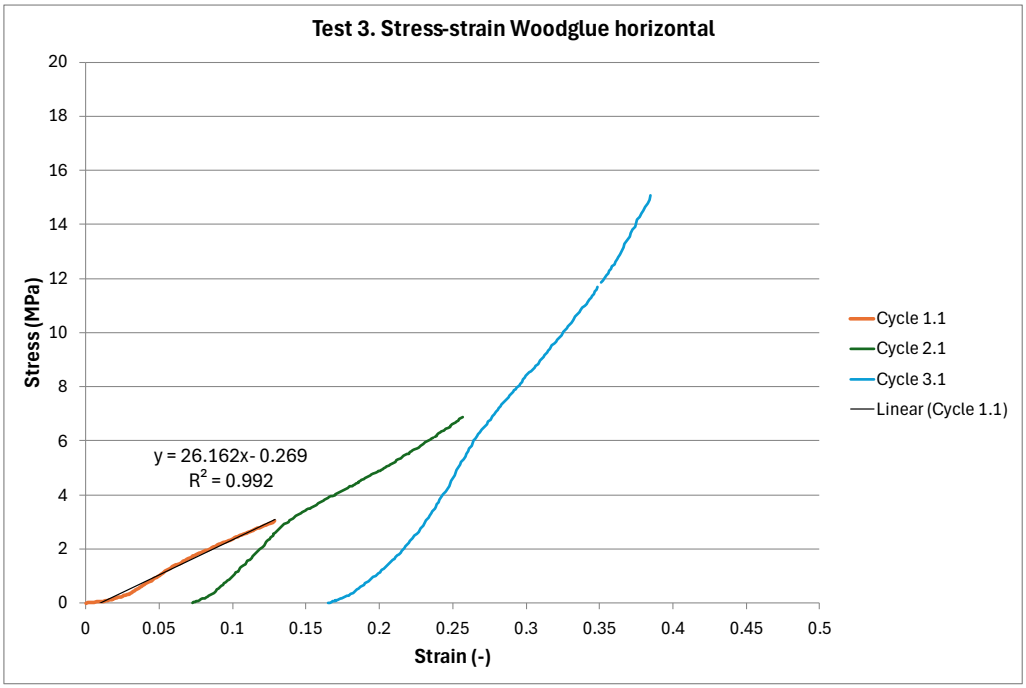


Figure E13. The stress-strain diagram of the three different cycles of compression test 3.

Figure E14 and Figure E15 present all three wood glue tests together in a force-displacement and a stress-strain graph.

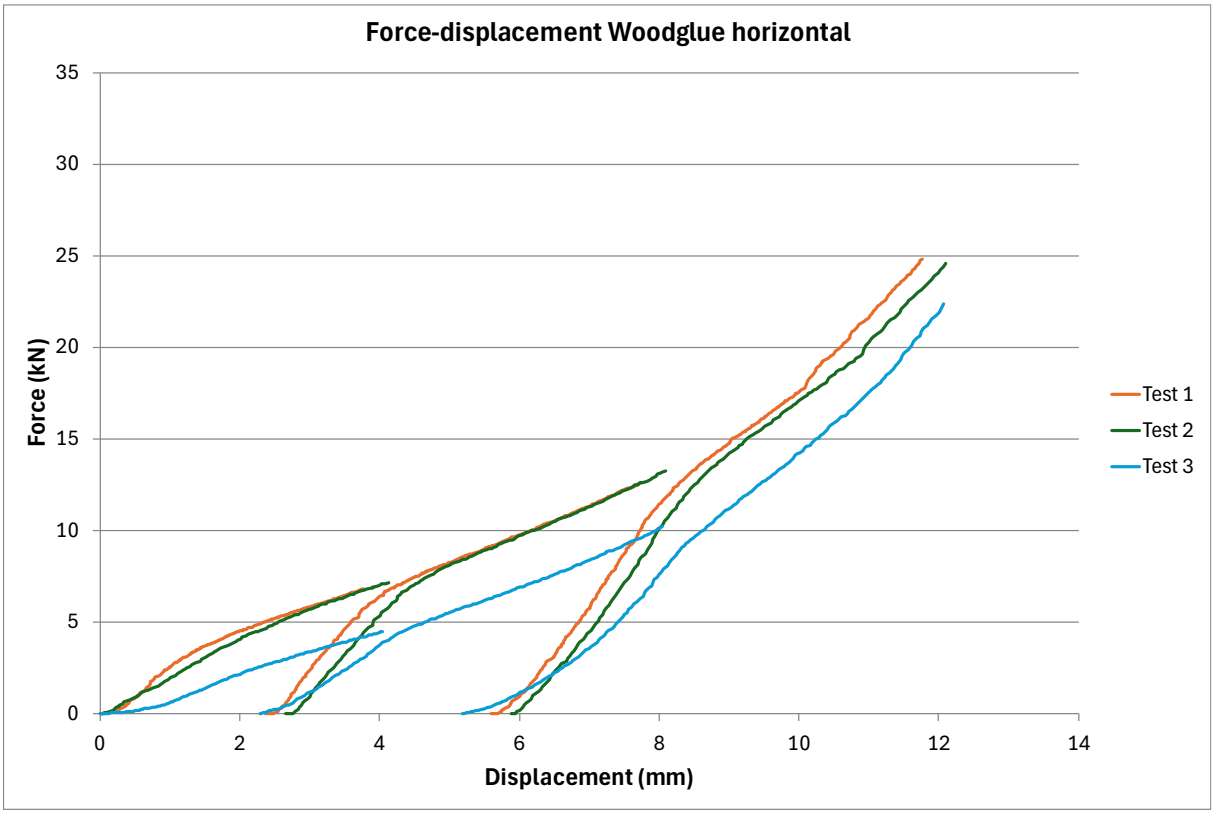


Figure E14. The force-displacement graph of all the wood glue compression tests in the horizontal orientation.



Figure E15. The stress-strain graph of all the wood glue compression tests in the horizontal orientation.

E.2.1.2 Vertical layer orientation

Figure E16 to Figure E24 show three wood glue tests with a vertical layer orientation. Each test is accompanied with four photos during the test and two different graphs: the force-displacement and the stress-strain graph.

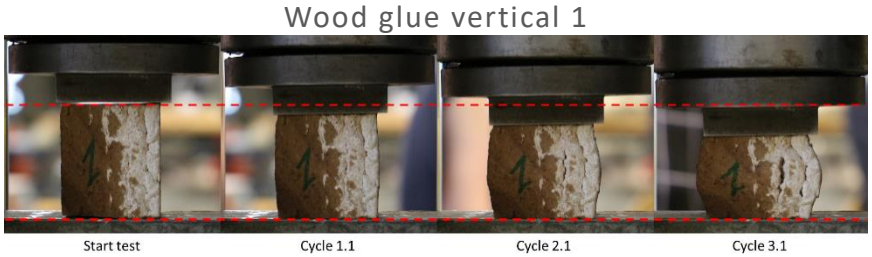


Figure E16. Four photos of compression test 1. One at the start of the test and one at the end of each cycle.

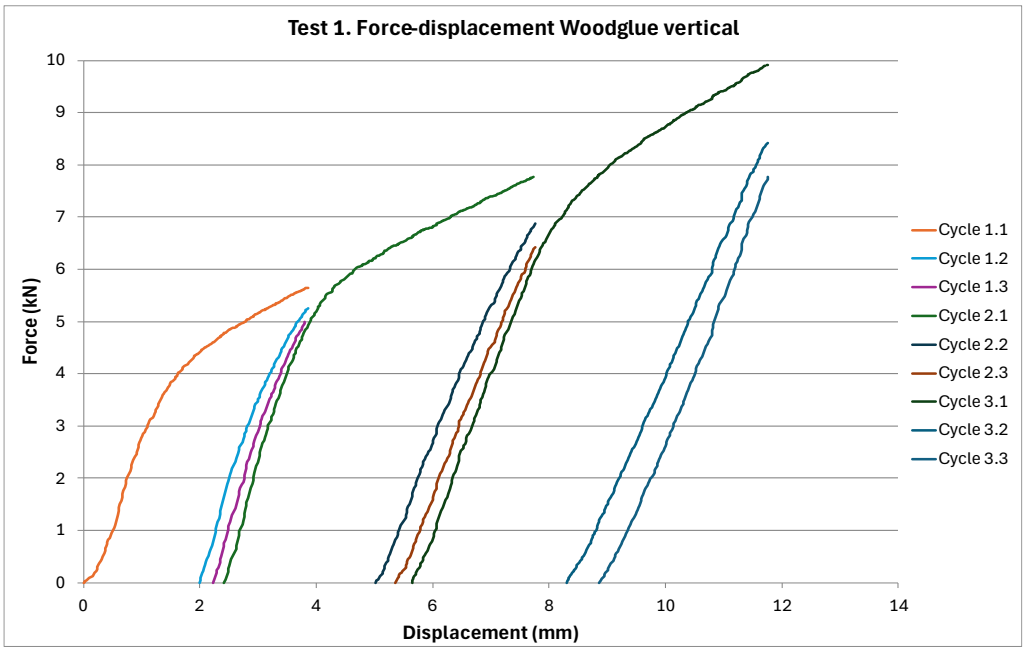


Figure E17. The force-displacement graph of compression test 1.

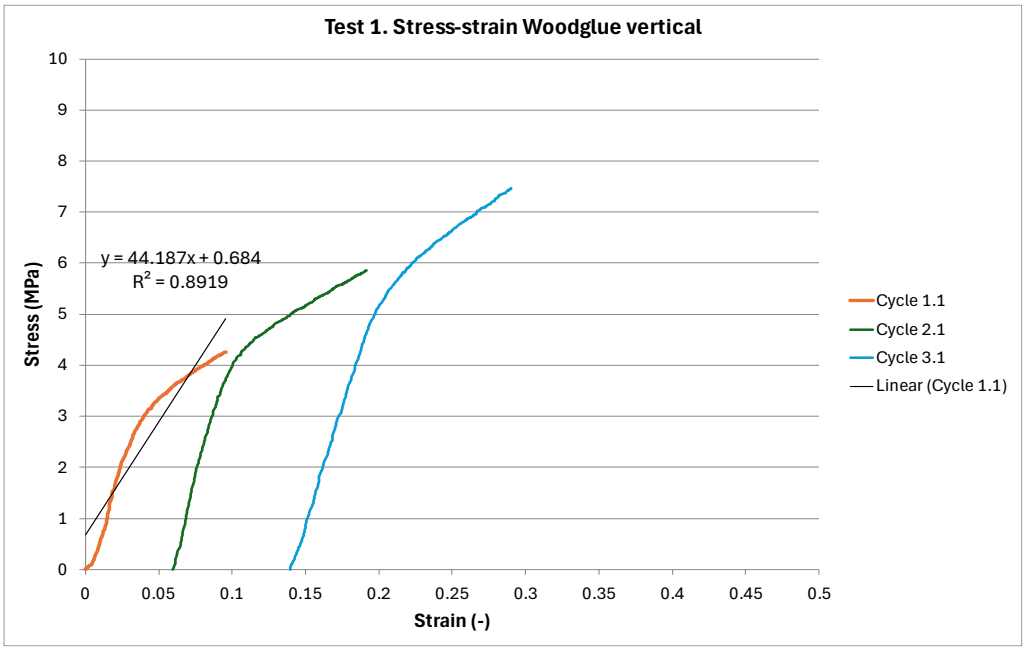


Figure E18. The stress-strain diagram of the three different cycles of compression test 1.

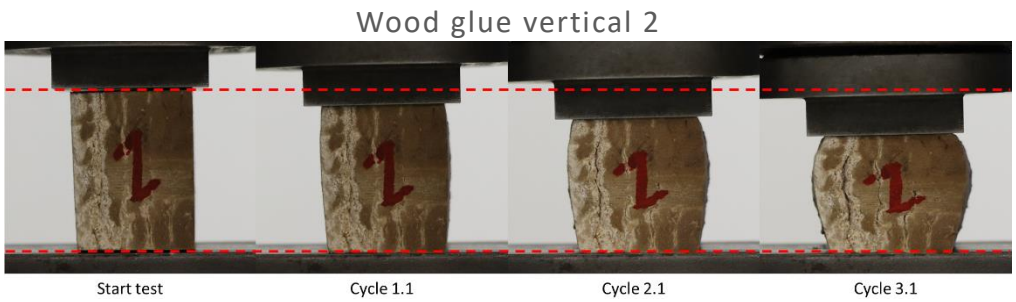


Figure E19. Four photos of compression test 2. One at the start of the test and one at the end of each cycle.



Figure E20. The force-displacement graph of compression test 2.

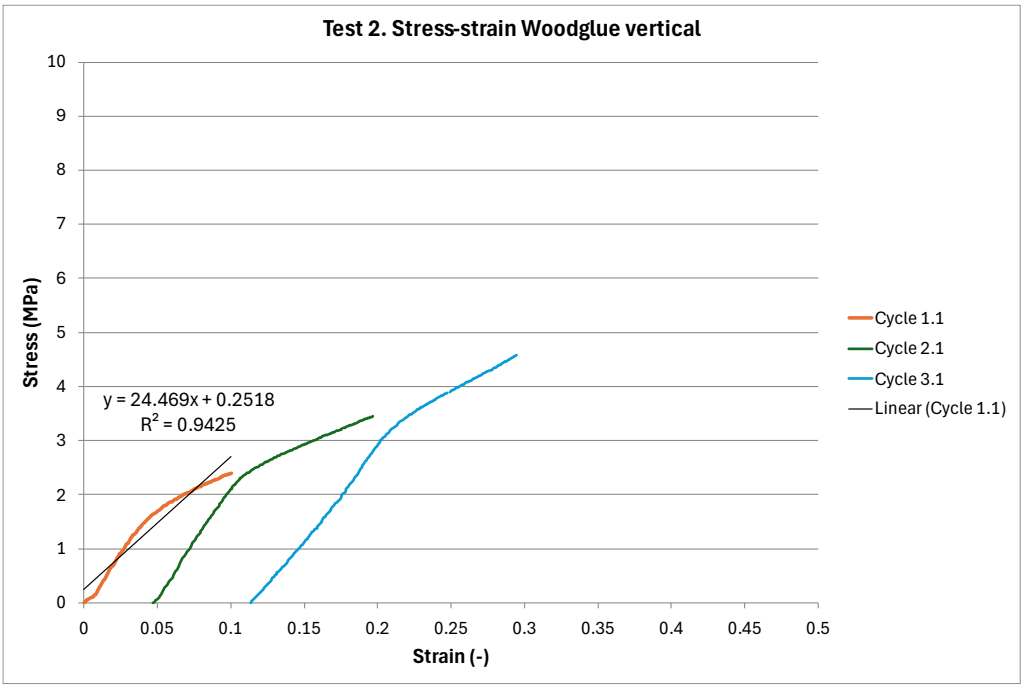


Figure E21. The stress-strain diagram of the three different cycles of compression test 2.

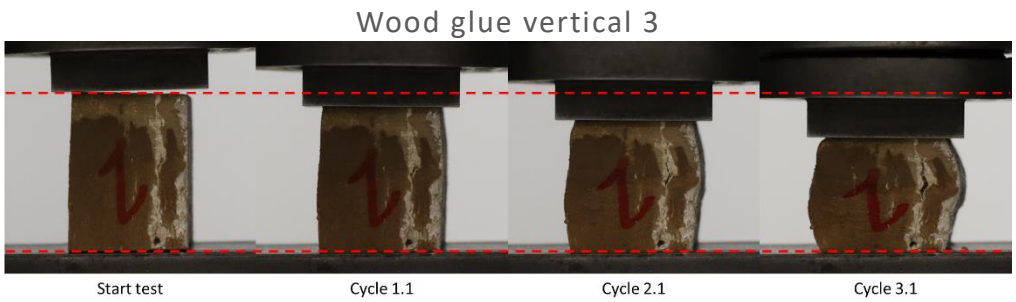


Figure E22. Four photos of compression test 3. One at the start of the test and one at the end of each cycle.



Figure E23. The force-displacement graph of compression test 3.

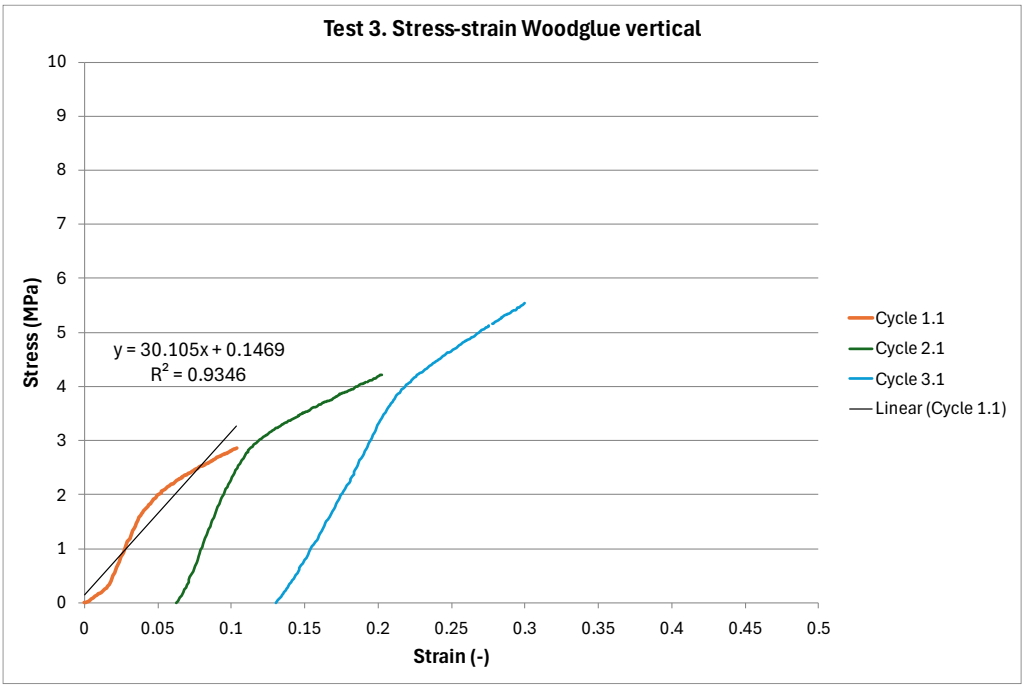


Figure E24. The stress-strain diagram of the three different cycles of compression test 3.

Figure E25 and Figure E26 present all three wood glue tests together in a force-displacement and a stress-strain graph.

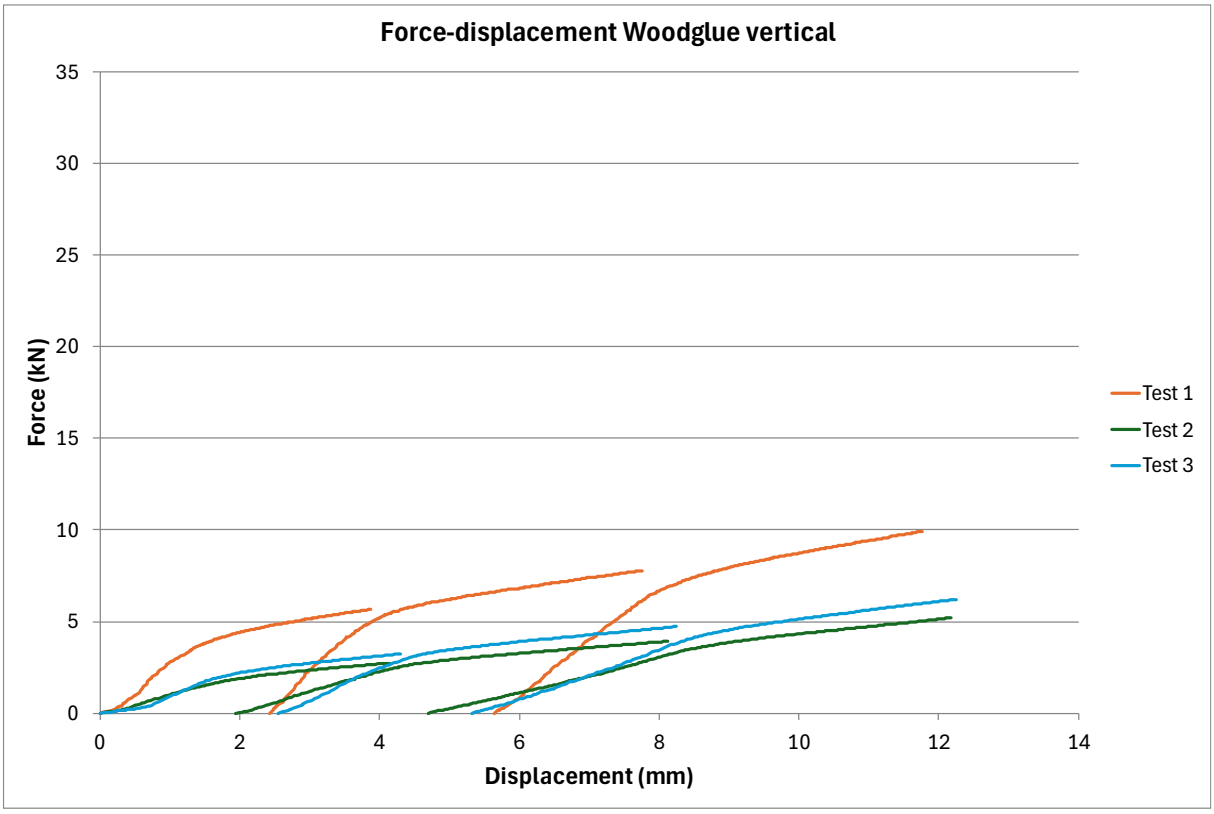


Figure E25. The force-displacement graph of all the wood glue compression tests in the vertical orientation.

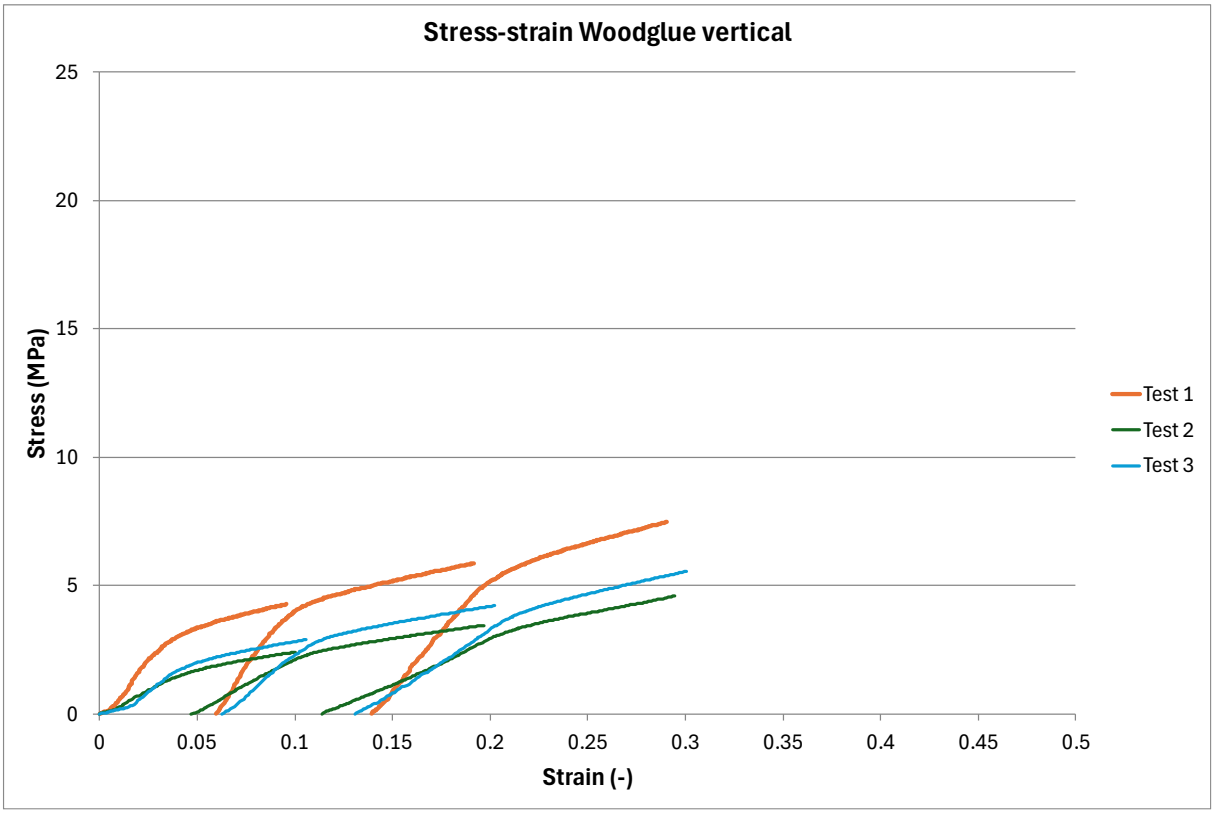


Figure E26. The stress-strain graph of all the wood glue compression tests in the vertical orientation.

E.2.2 Bio-glue

E.2.2.1 Horizontal layer orientation

Figure E27 to Figure E35 show three bio-glue tests with a horizontal layer orientation. Each test is accompanied with four photos during the test and two different graphs: the force-displacement and the stress-strain graph.

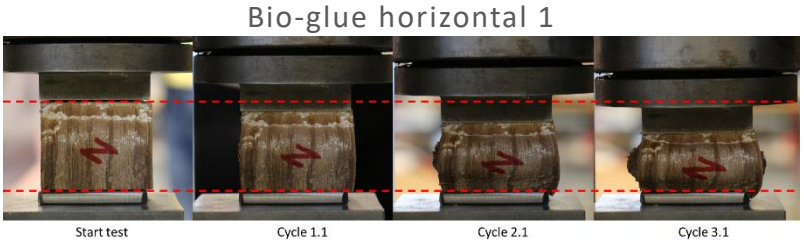


Figure E27. Four photos of compression test 1. One at the start of the test and one at the end of each cycle.

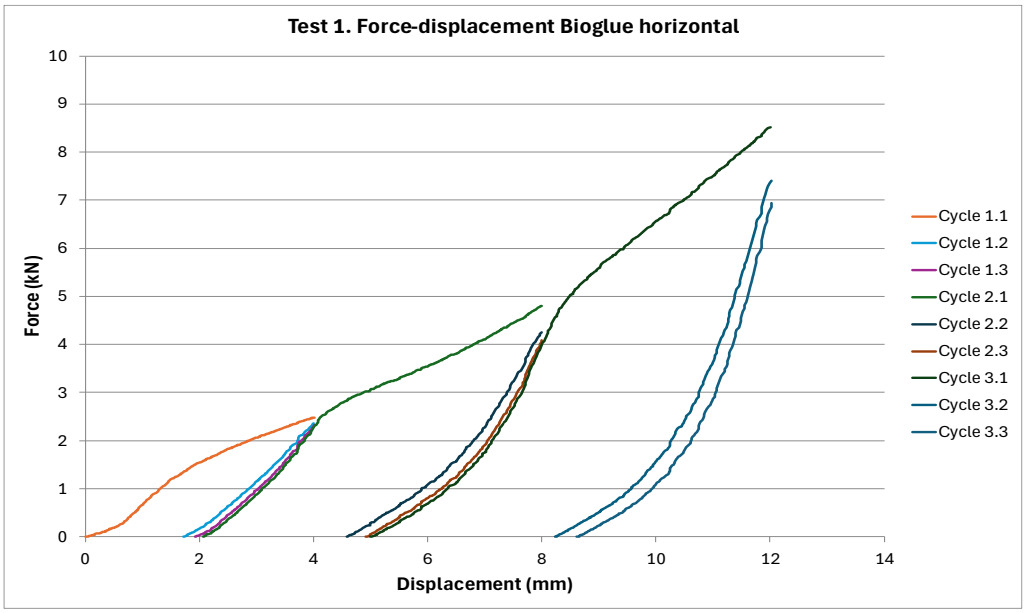


Figure E28. The force-displacement graph of compression test 1.

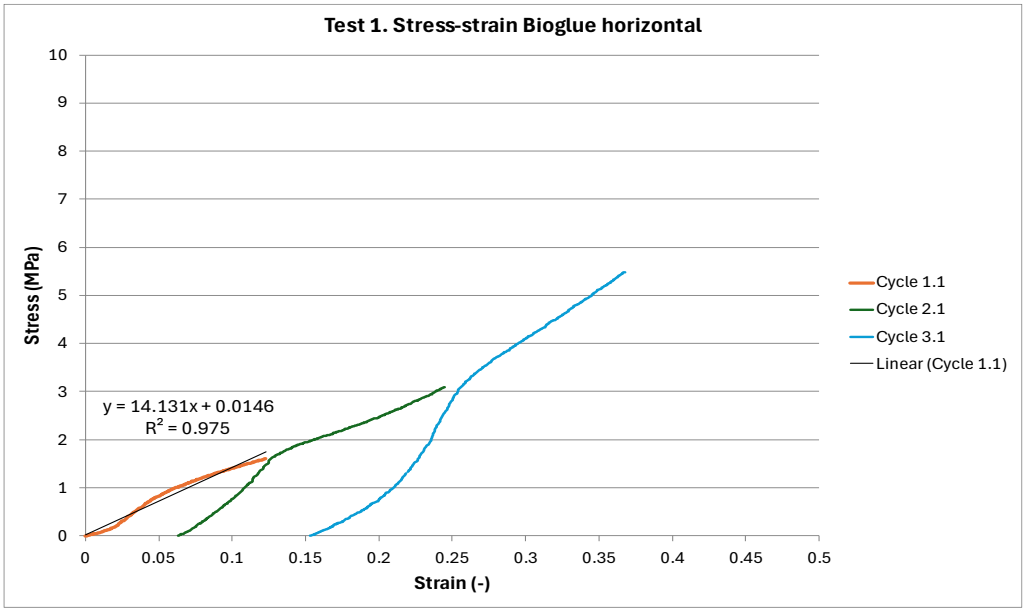


Figure E29. The stress-strain diagram of the three different cycles of compression test 1.

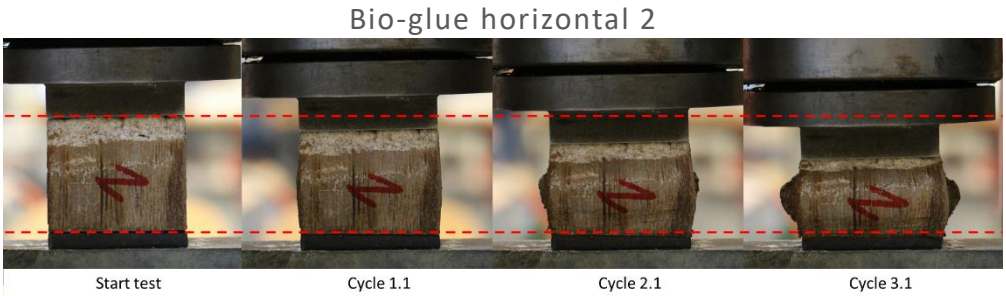


Figure E30. Four photos of compression test 2. One at the start of the test and one at the end of each cycle.

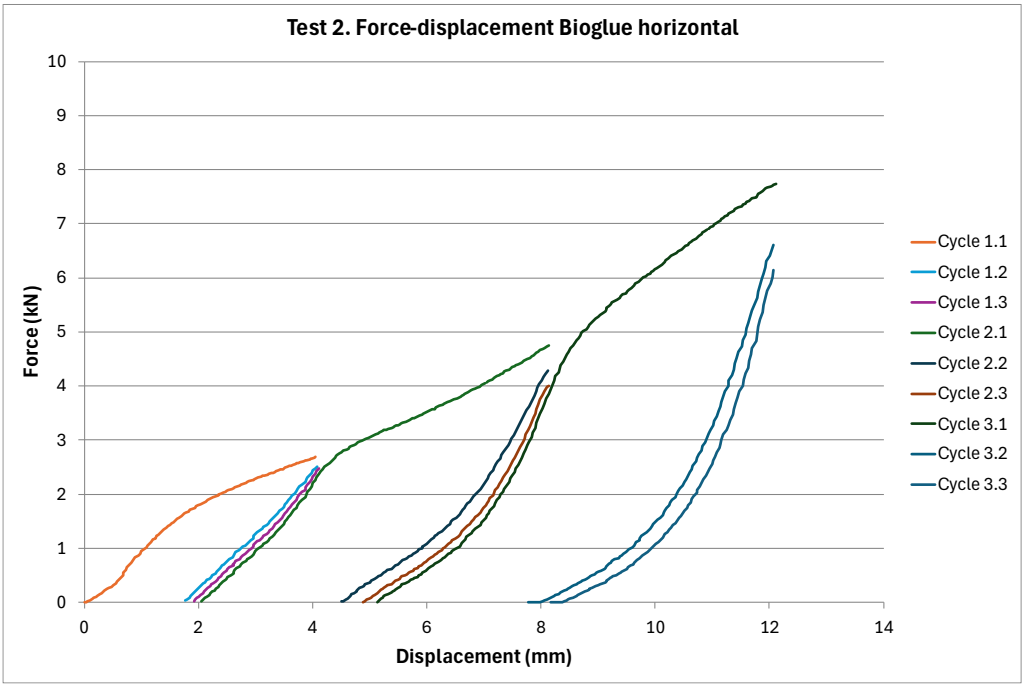


Figure E31. The force-displacement graph of compression test 2.

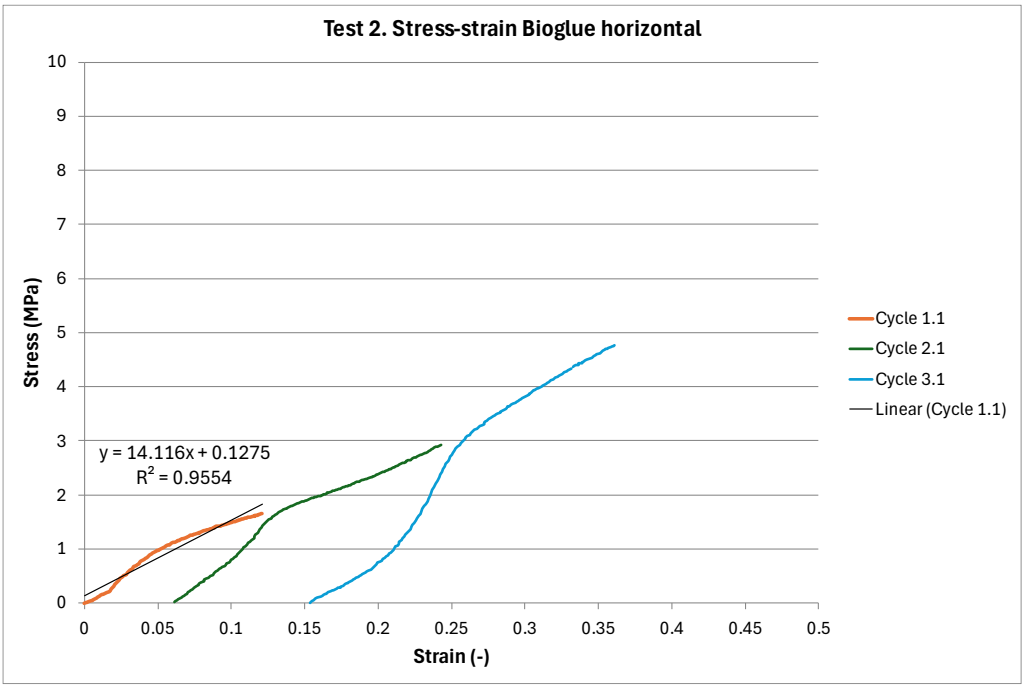


Figure E32. The stress-strain diagram of the three different cycles of compression test 2.

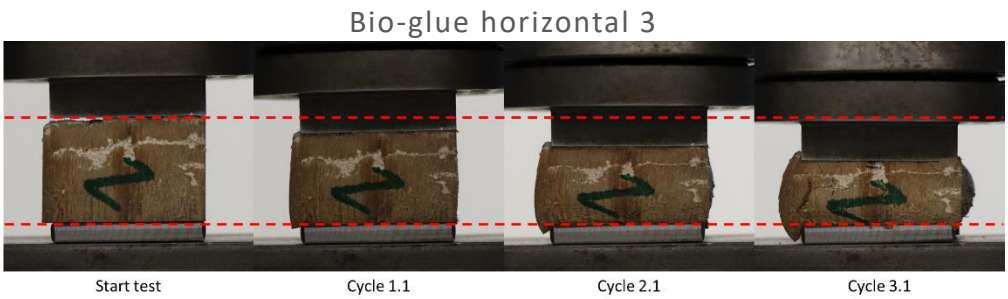


Figure E33. Four photos of compression test 3. One at the start of the test and one at the end of each cycle.

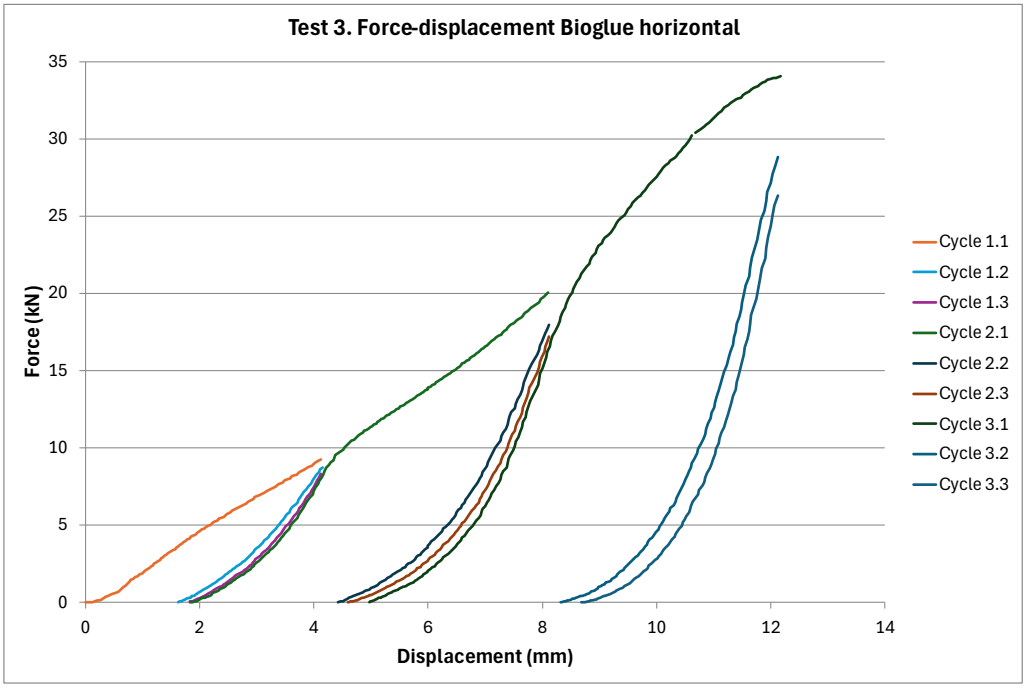


Figure E34. The force-displacement graph of compression test 3.

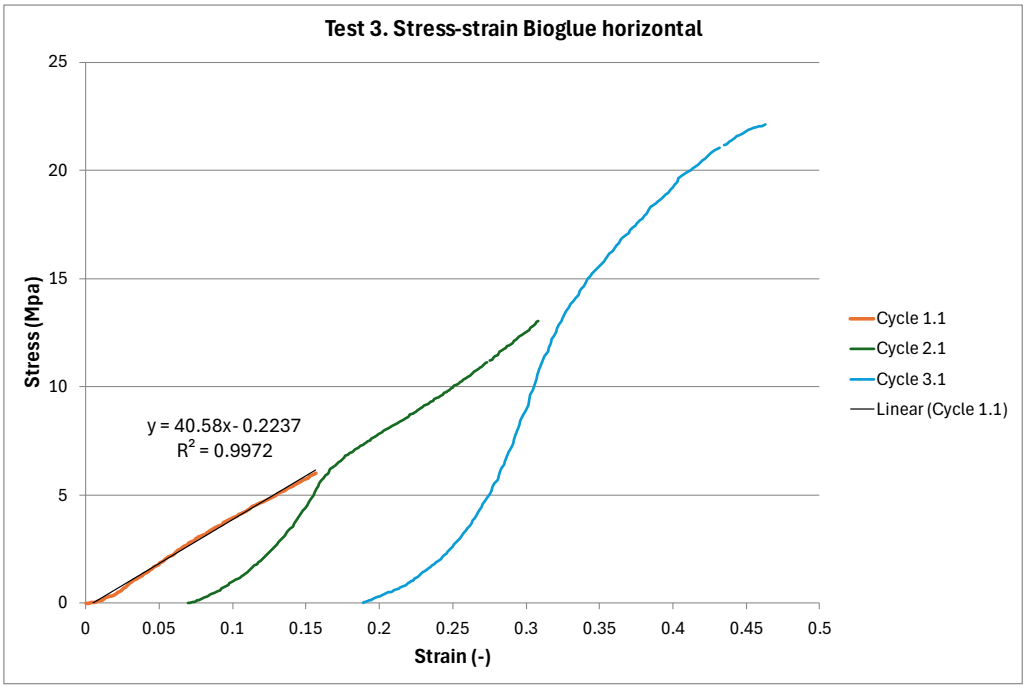


Figure E35. The stress-strain diagram of the three different cycles of compression test 3.

Figure E36 and Figure E37 present all three bio-glue tests together in a force-displacement and a stress-strain graph.

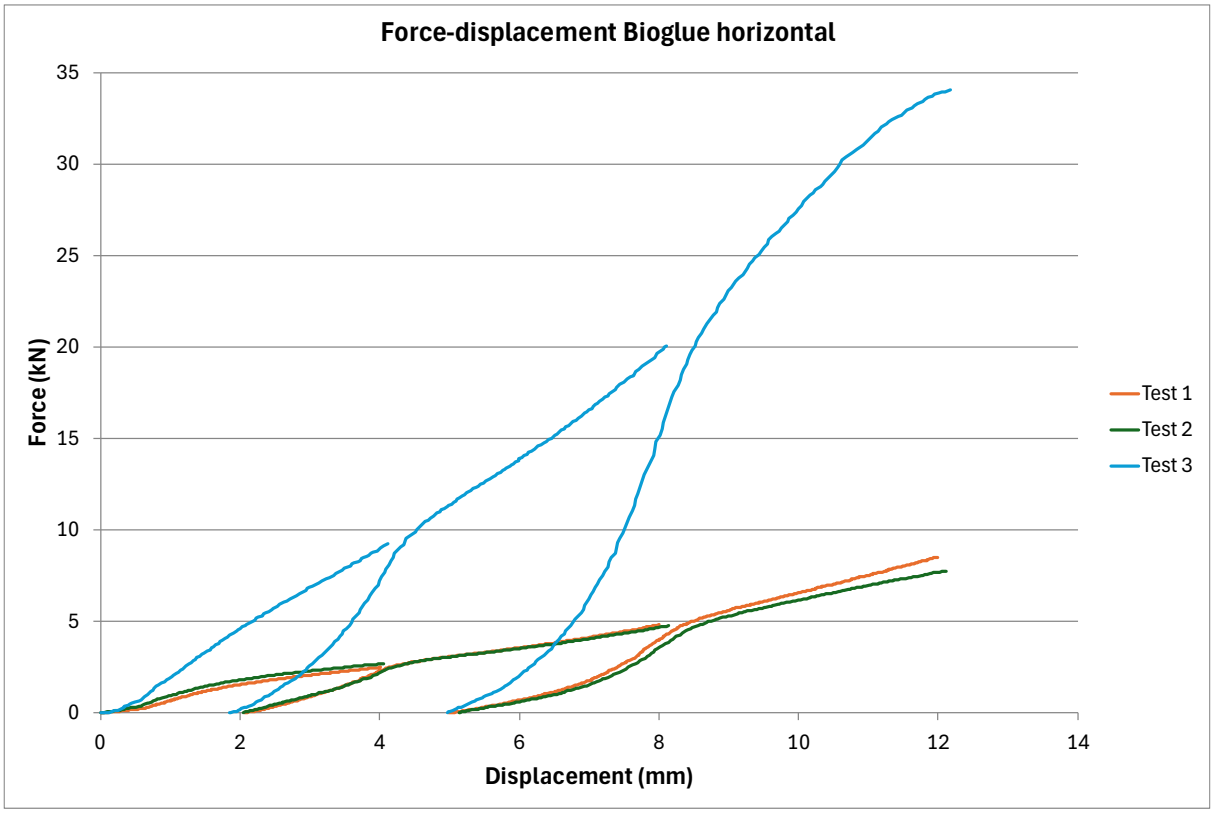


Figure E36. The force-displacement graph of all the bio-glue compression tests in the vertical orientation.

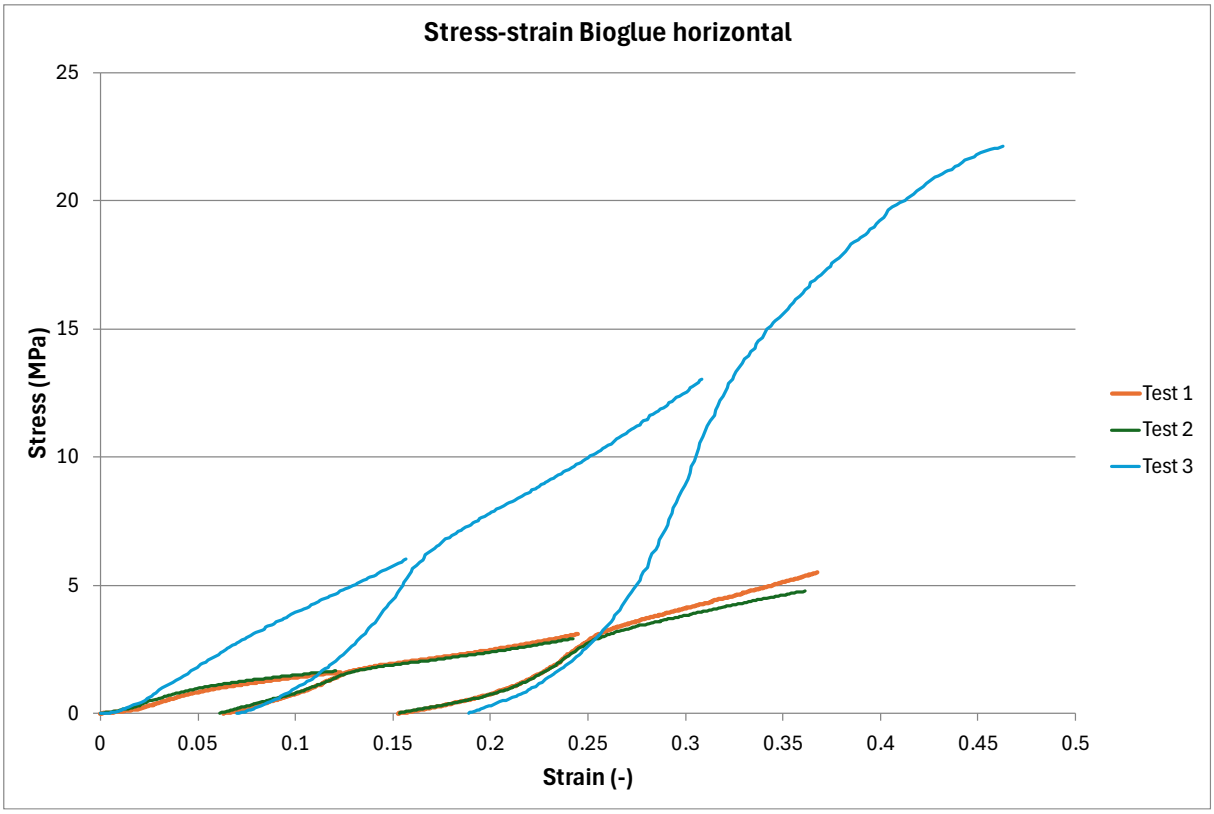


Figure E37. The stress-strain graph of all the bio-glue compression tests in the vertical orientation.

E.2.2.2 Vertical layer orientation

Figure E38 to Figure E46 show three bio-glue tests with a vertical layer orientation. Each test is accompanied with four photos during the test and two different graphs: the force-displacement and the stress-strain graph.

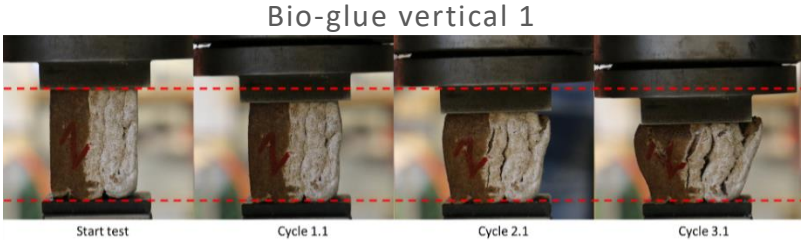


Figure E38. Four photos of compression test 1. One at the start of the test and one at the end of each cycle.

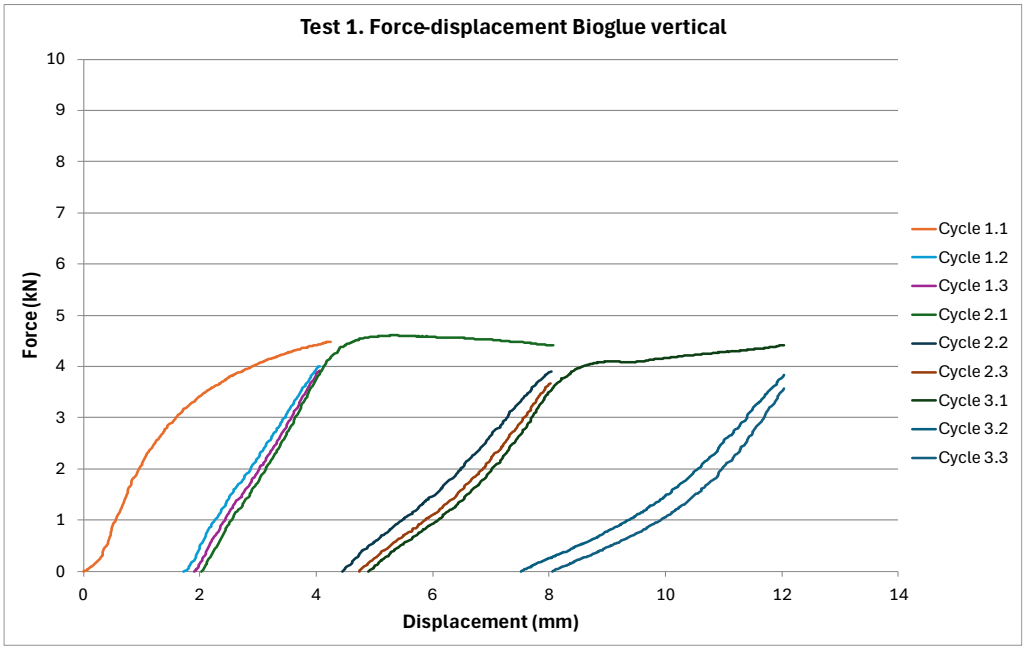


Figure E39. The force-displacement graph of compression test 1.

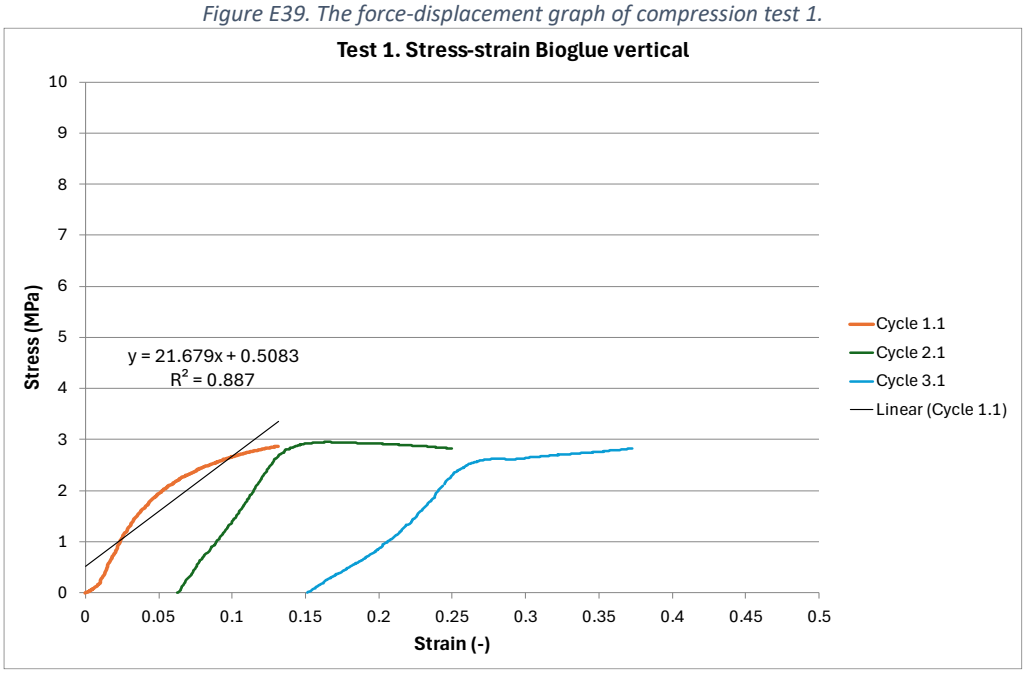


Figure E40. The stress-strain diagram of the three different cycles of compression test 1.

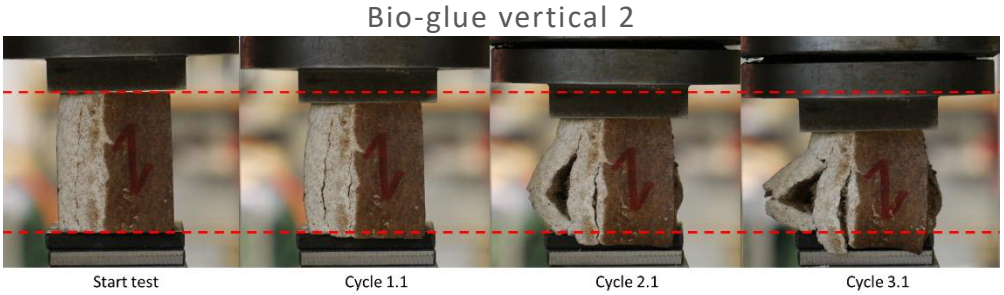


Figure E41. Four photos of compression test 2. One at the start of the test and one at the end of each cycle.

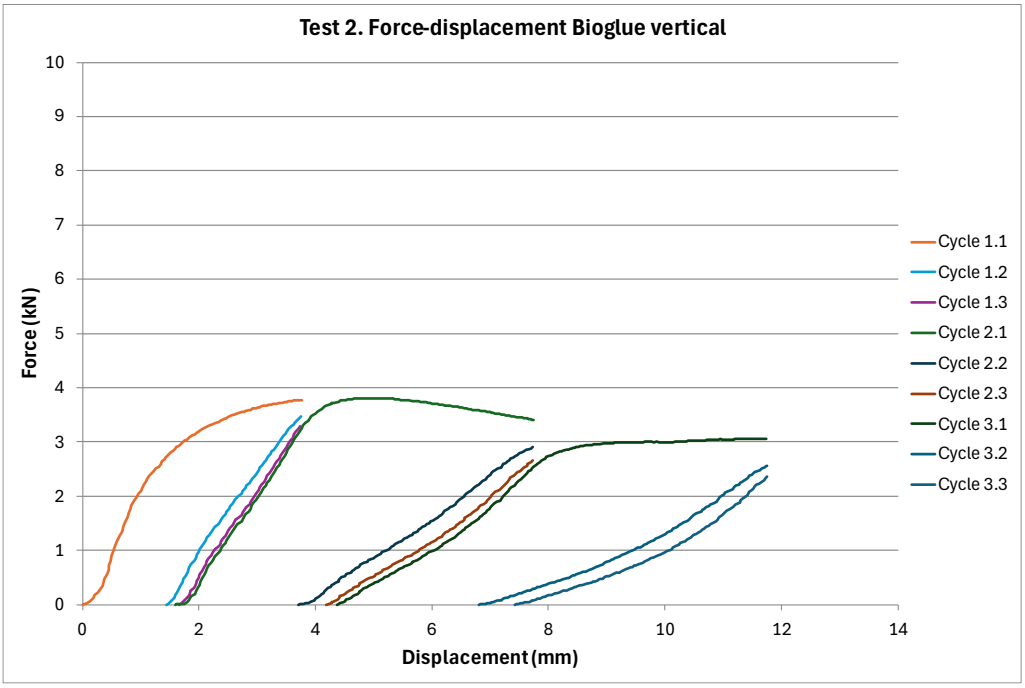


Figure E42. The force-displacement graph of compression test 2.

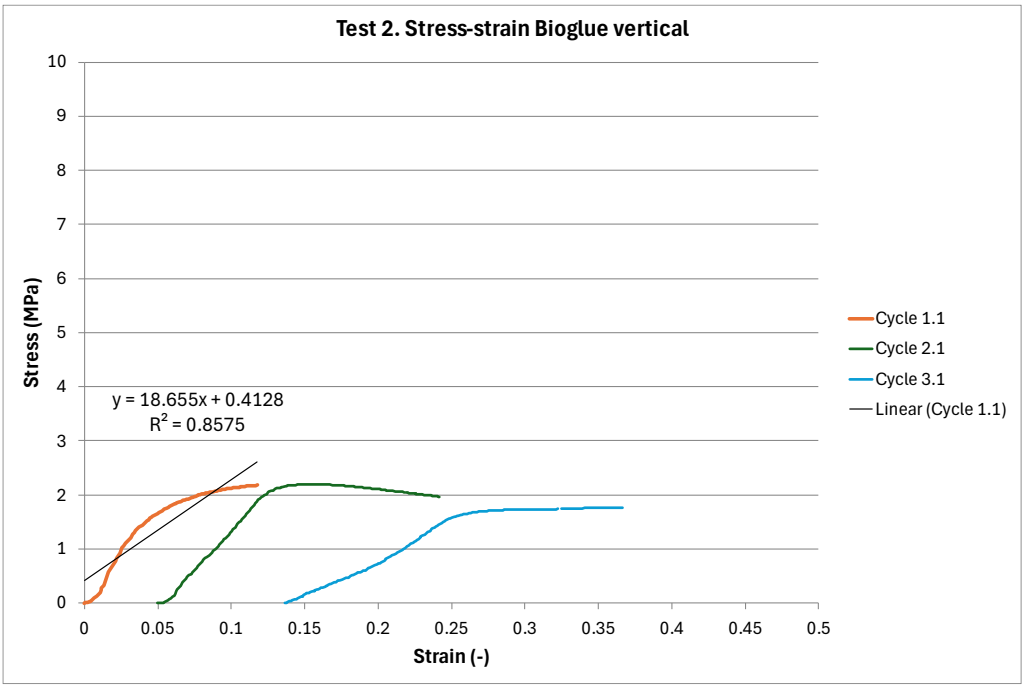


Figure E43. The stress-strain diagram of the three different cycles of compression test 2.

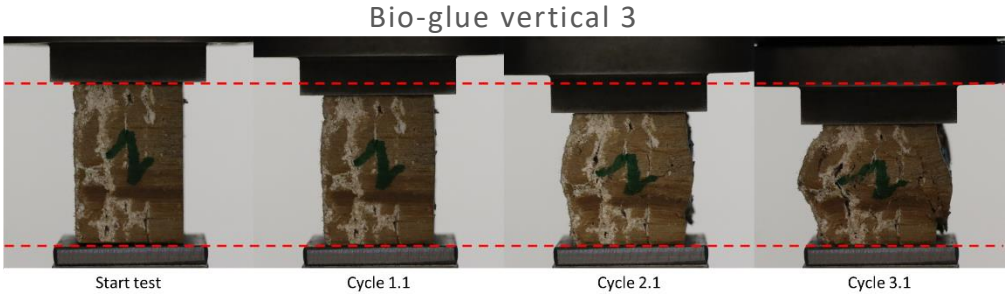


Figure E44. Four photos of compression test 3. One at the start of the test and one at the end of each cycle.

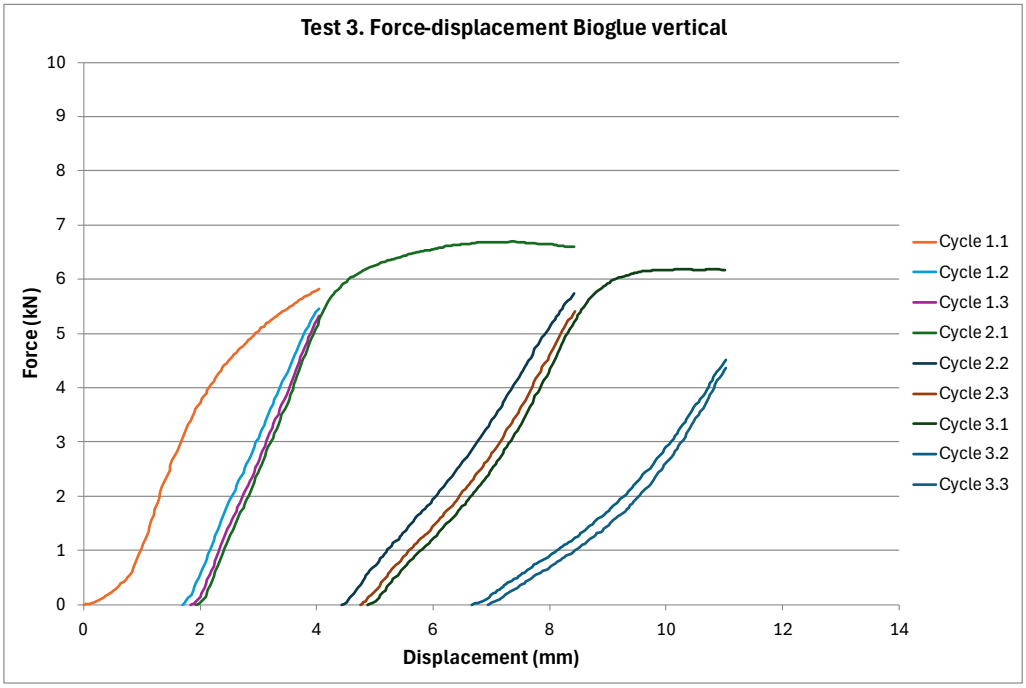


Figure E45. The force-displacement graph of compression test 3.

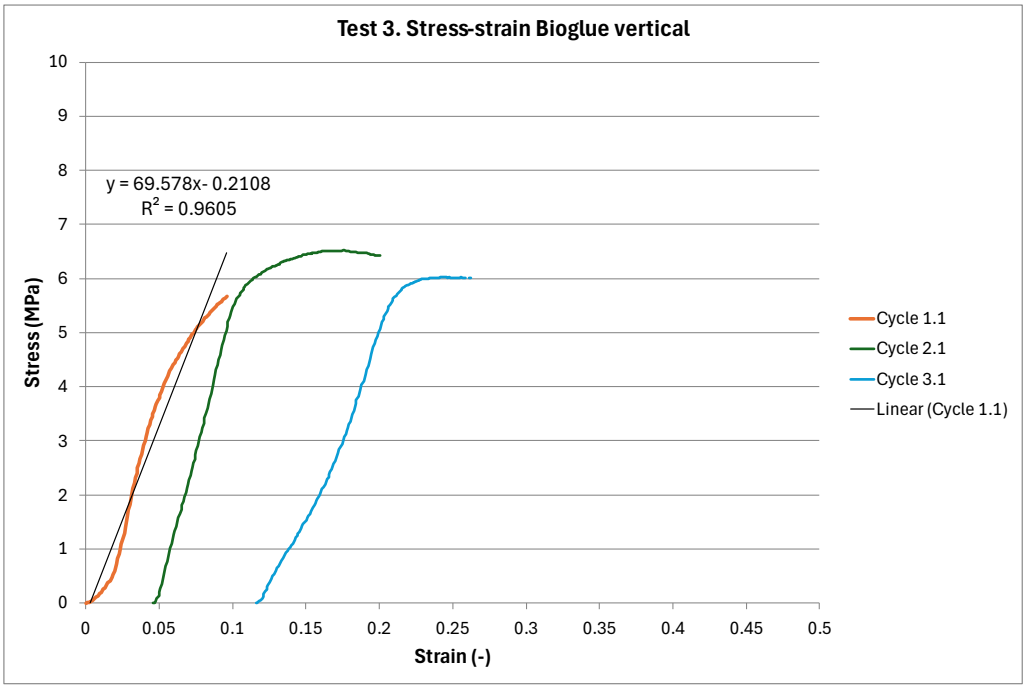


Figure E46. The stress-strain diagram of the three different cycles of compression test 3.

Figure E47 and Figure E48 present all three bio glue tests together in a force-displacement and a stress-strain graph.

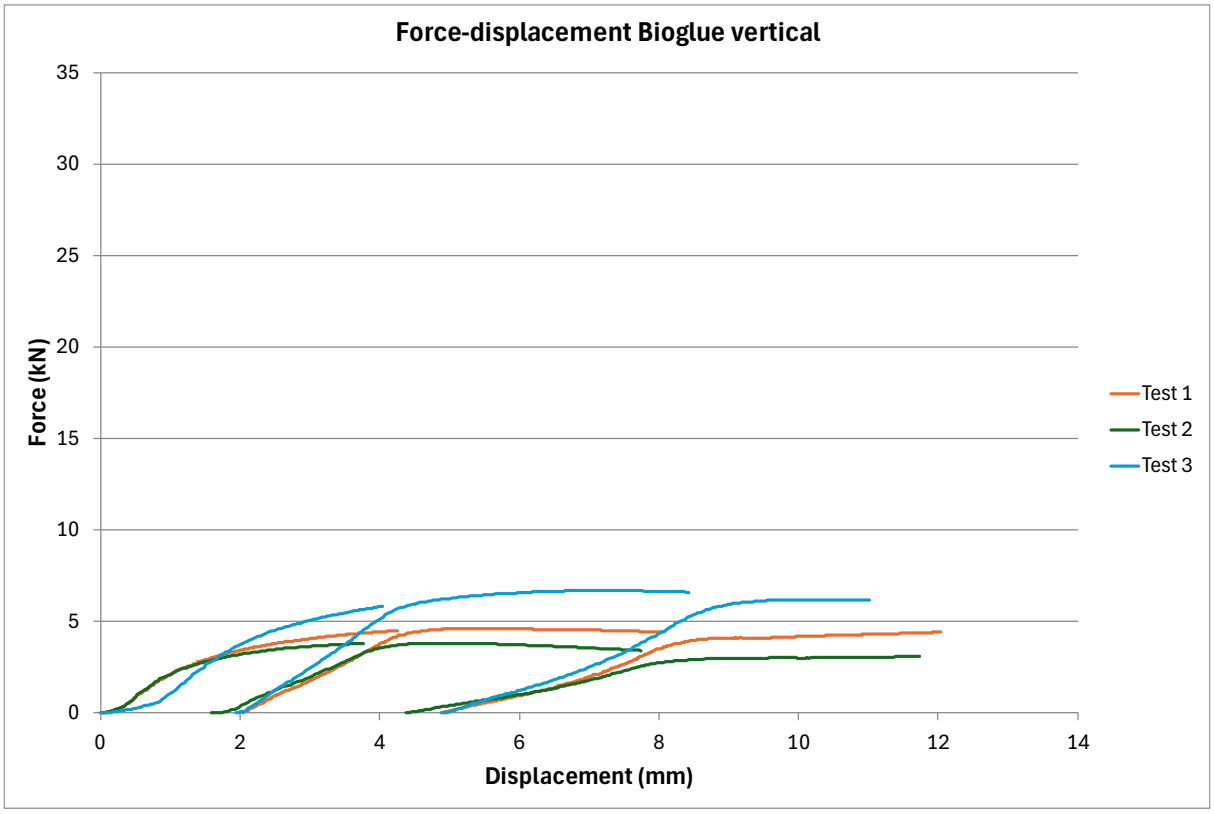


Figure E47. The force-displacement graph of all the bio-glue compression tests in the vertical orientation.

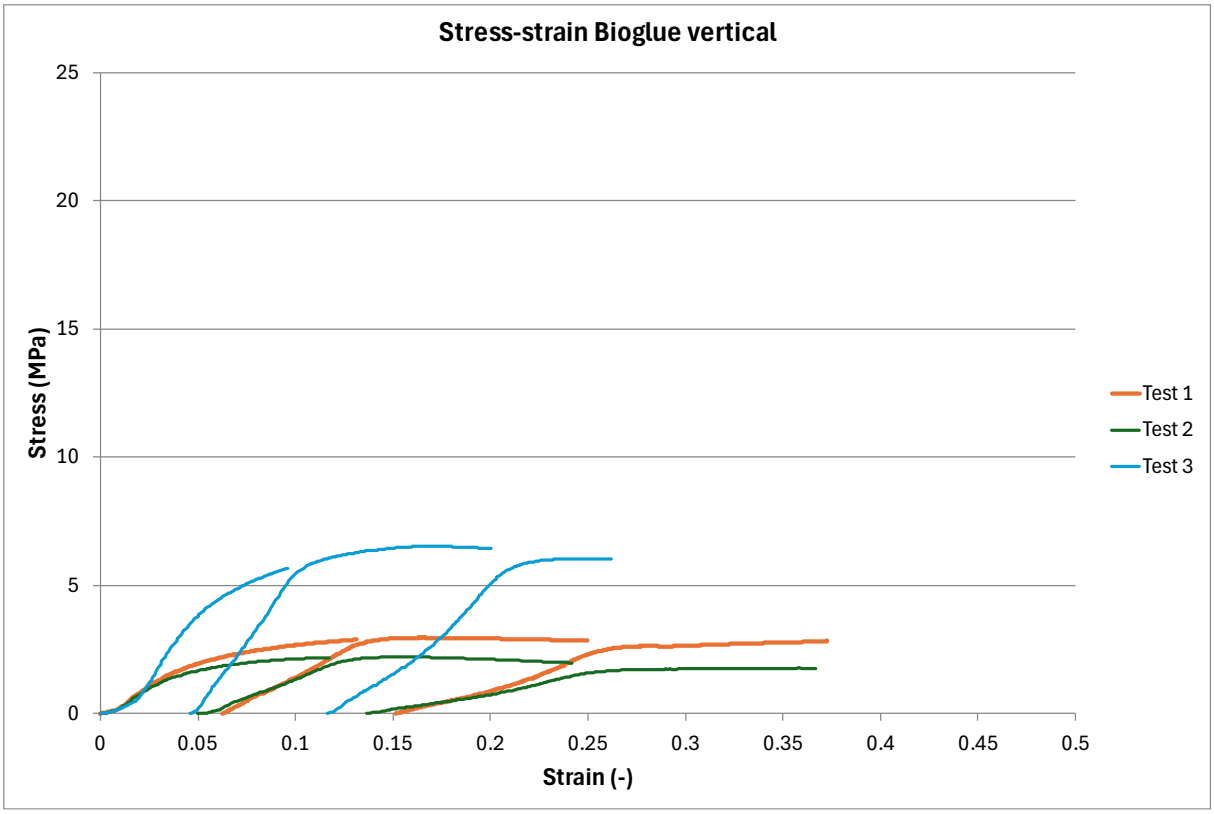


Figure E48. The stress-strain graph of all the bio-glue compression tests in the vertical orientation.

E.2.3 Summary wood glue and bio-glue bending test results

Table E6 and Table E7 present the results of cycles 1.1, 2.1 and 3.1 of the wood glue tests for both the horizontal and vertical layer orientations respectively.

Table E8 and Table E9 present the results of cycles 1.1, 2.1 and 3.1 of the bio-glue tests for both the horizontal and vertical layer orientations respectively.

Table E6. The results of the three compression tests with the wood glue mix with the horizontal layer orientation.

Test	Days cured	Cycle 1.1			Cycle 2.1			Cycle 3.1		
		Force [kN]	Stress [Mpa]	Strain [-]	Force [kN]	Stress [Mpa]	Strain [-]	Force [kN]	Stress [Mpa]	Strain [-]
1	41	6.82	4.54	0.11	12.63	8.40	0.22	24.84	16.53	0.34
2	41	7.16	5.16	0.12	13.26	9.56	0.23	24.56	17.71	0.34
3	45	4.49	3.03	0.13	10.21	6.88	0.26	22.14	14.92	0.38

Table E7. The results of the three compression tests with the wood glue mix with the vertical layer orientation.

Test	Days cured	Cycle 1.1			Cycle 2.1			Cycle 3.1		
		Force [kN]	Stress [Mpa]	Strain [-]	Force [kN]	Stress [Mpa]	Strain [-]	Force [kN]	Stress [Mpa]	Strain [-]
1	41	5.66	4.26	0.10	7.78	5.85	0.19	9.92	7.46	0.29
2	41	2.72	2.39	0.10	3.92	3.45	0.20	5.21	4.58	0.29
3	45	3.23	2.89	0.11	4.72	4.22	0.20	6.22	5.55	0.30

Table E8. The results of the three compression tests with the bio-glue mix with the horizontal layer orientation.

Test	Days cured	Cycle 1.1			Cycle 2.1			Cycle 3.1		
		Force [kN]	Stress [Mpa]	Strain [-]	Force [kN]	Stress [Mpa]	Strain [-]	Force [kN]	Stress [Mpa]	Strain [-]
1	41	2.48	1.60	0.12	4.80	3.10	0.24	8.51	5.49	0.37
2	41	2.69	1.65	0.12	4.75	2.92	0.24	7.74	4.77	0.36
3	45	9.25	6.01	0.16	20.08	13.04	0.31	34.03	22.11	0.46

Table E9. The results of the three compression tests with the bio-glue mix with the vertical layer orientation.

Test	Days cured	Cycle 1.1			Cycle 2.1			Cycle 3.1		
		Force [kN]	Stress [Mpa]	Strain [-]	Force [kN]	Stress [Mpa]	Strain [-]	Force [kN]	Stress [Mpa]	Strain [-]
1	41	4.49	2.87	0.13	4.61	2.95	0.17	4.42	2.83	0.37
2	41	3.77	2.18	0.12	3.81	2.20	0.16	3.06	1.76	0.37
3	45	5.81	5.66	0.10	6.69	6.52	0.18	6.17	6.01	0.26

E.3 Results bio-glue with additives

E.3.1 Bio-glue with bentonite

E.3.1.1 Horizontal layer orientation

Figure E49 to Figure E60 show four bio-glue with bentonite tests with a horizontal layer orientation. Each test is accompanied with four photos during the test and two different graphs: the force-displacement and the stress-strain graph.

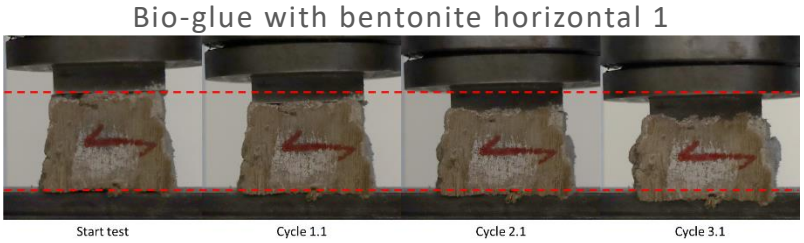


Figure E49. Four photos of compression test 1. One at the start of the test and one at the end of each cycle.

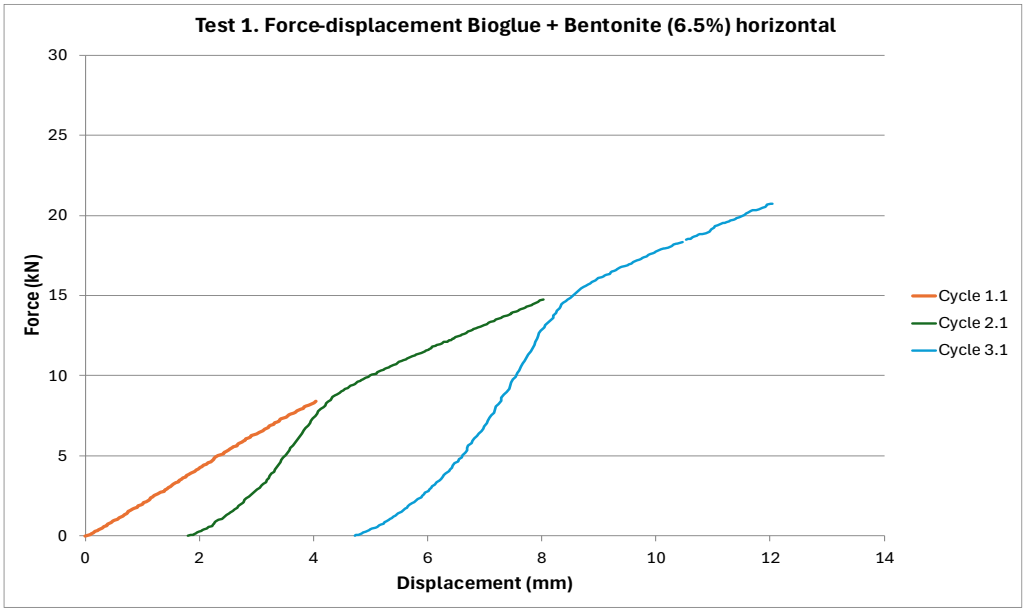


Figure E50. The force-displacement graph of compression test 1.

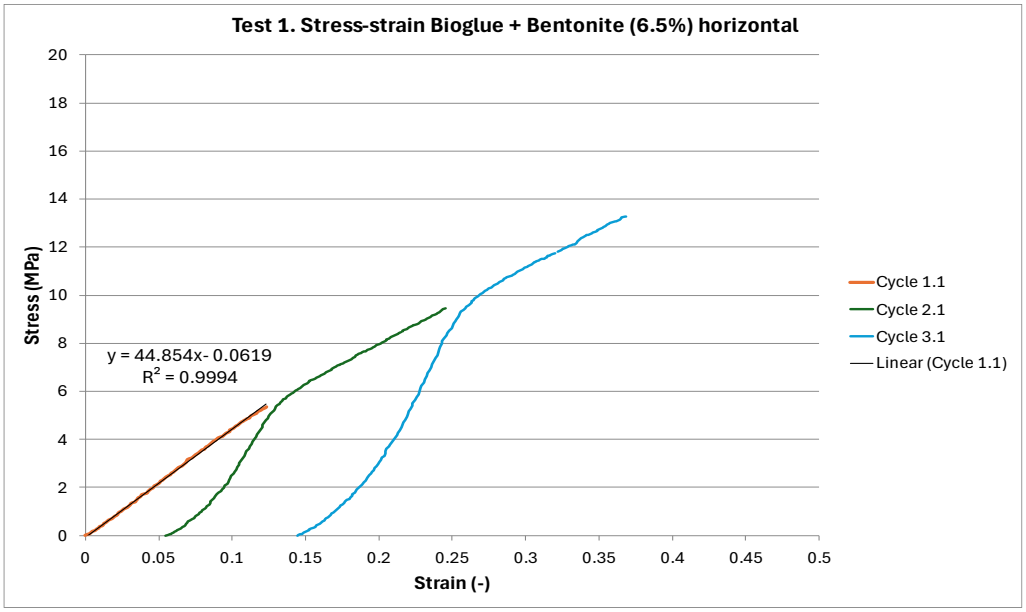


Figure E51. The stress-strain diagram of the three different cycles of compression test 1.

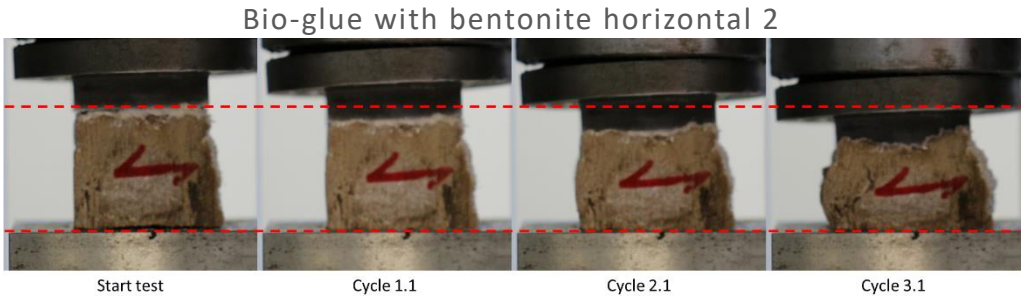


Figure E52. Four photos of compression test 2. One at the start of the test and one at the end of each cycle.

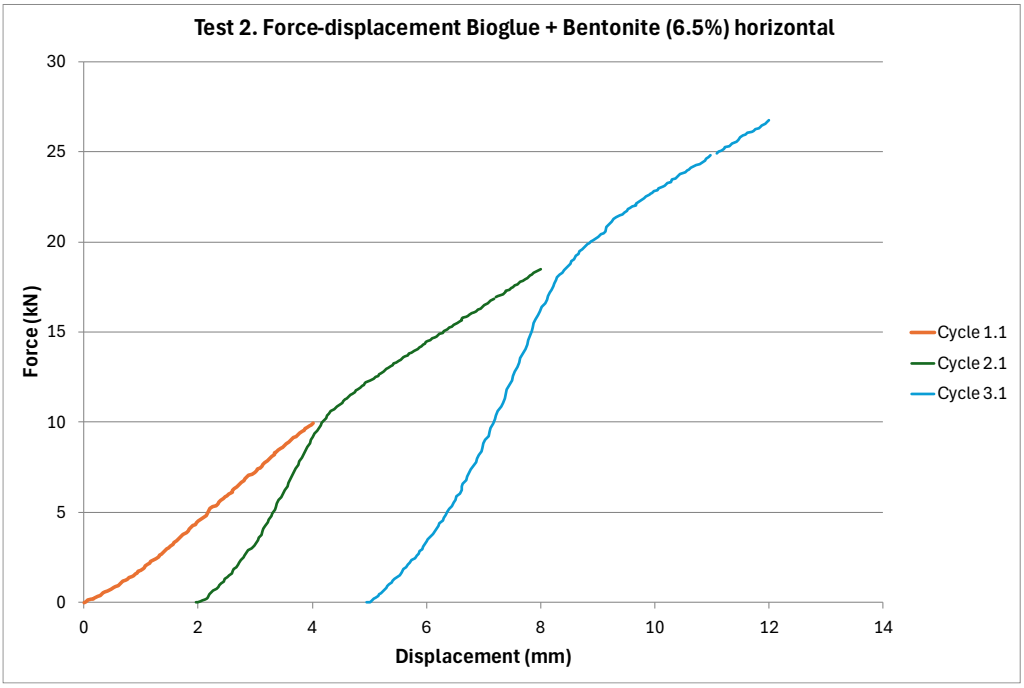


Figure E53. The force-displacement graph of compression test 2.

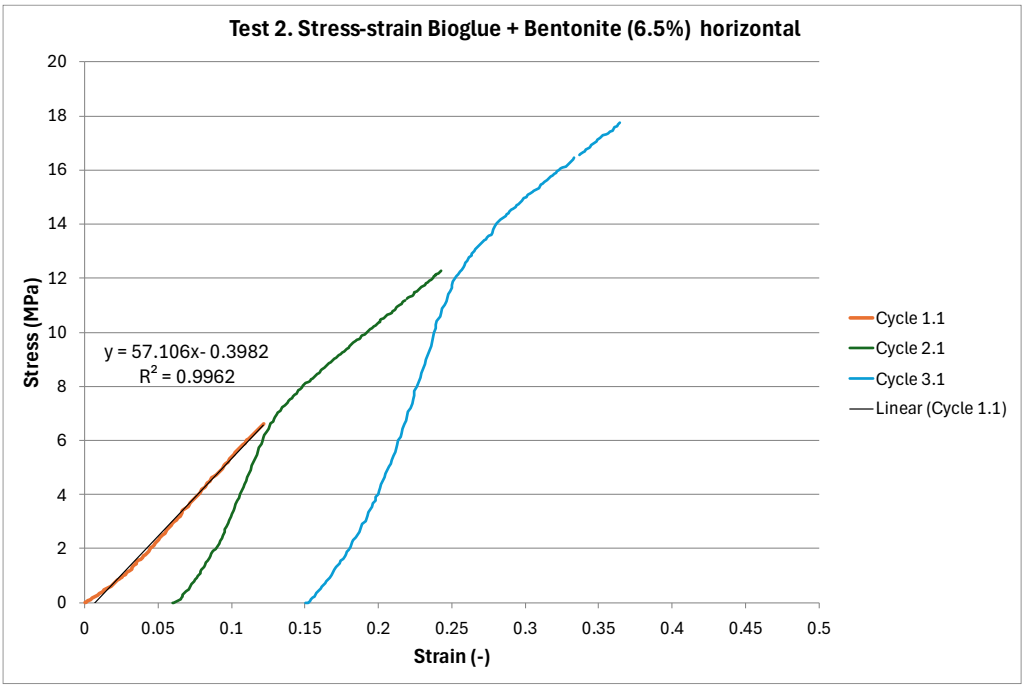


Figure E54. The stress-strain diagram of the three different cycles of compression test 2.

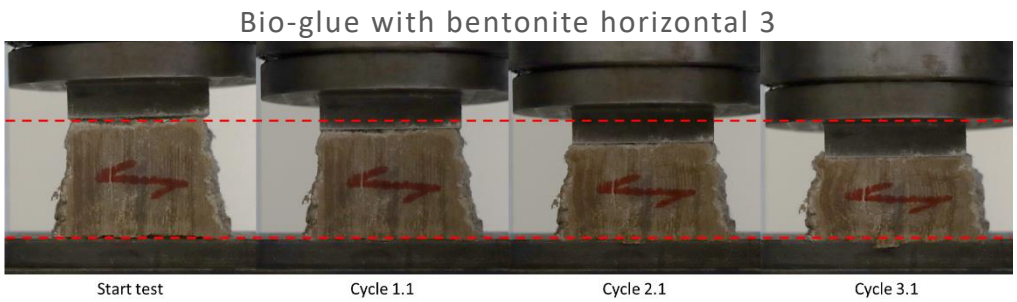


Figure E55. Four photos of compression test 3. One at the start of the test and one at the end of each cycle.

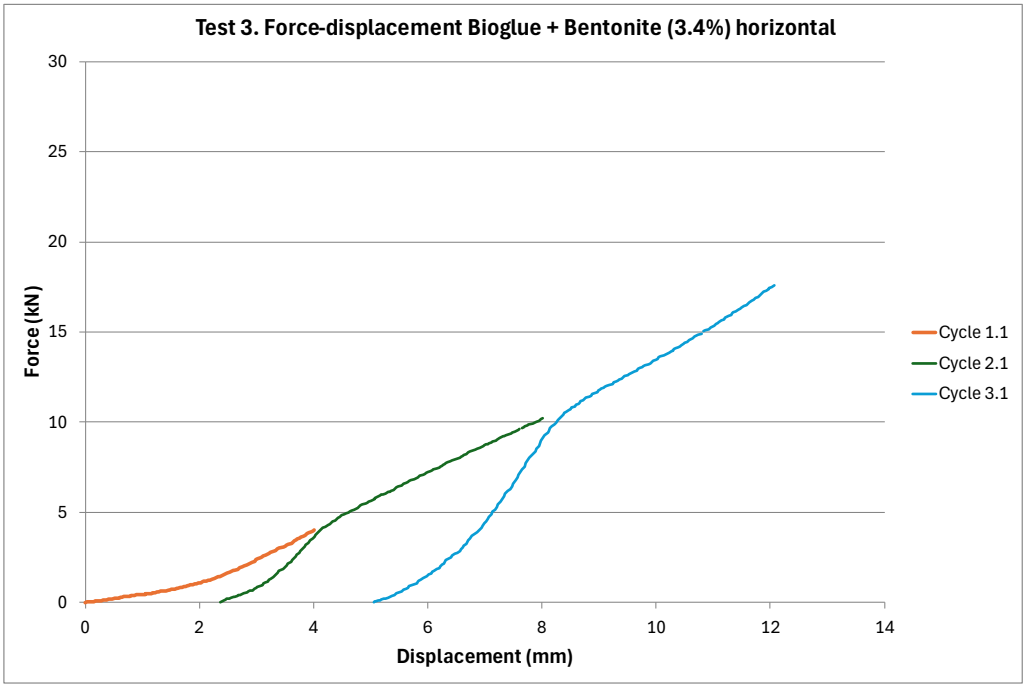


Figure E56. The force-displacement graph of compression test 3.

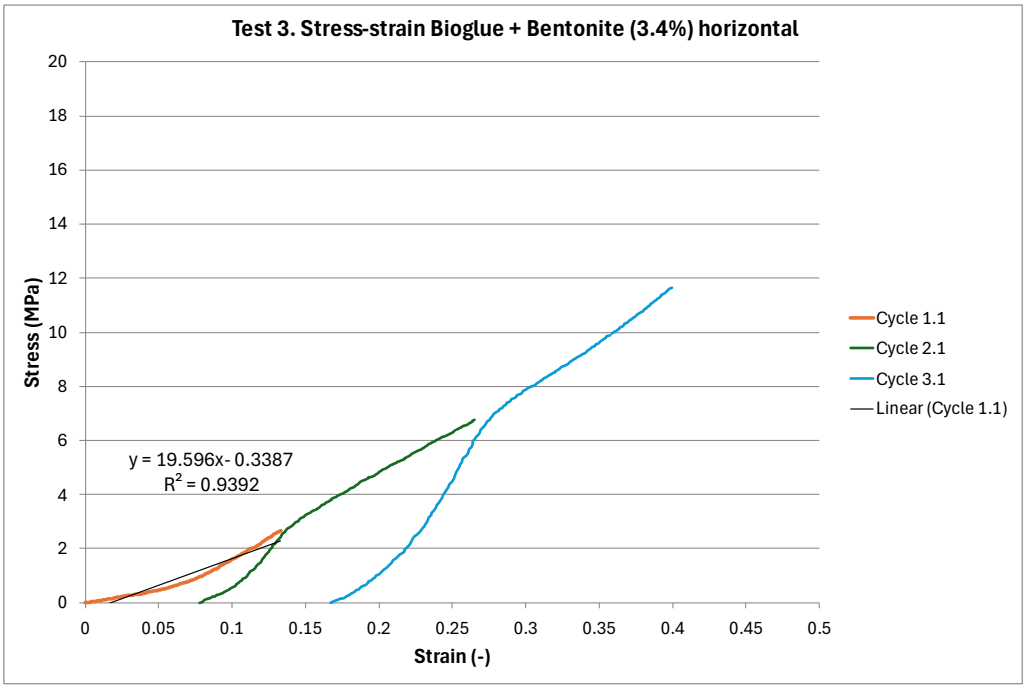


Figure E57. The stress-strain diagram of the three different cycles of compression test 3.



Figure E58. Four photos of compression test 4. One at the start of the test and one at the end of each cycle.

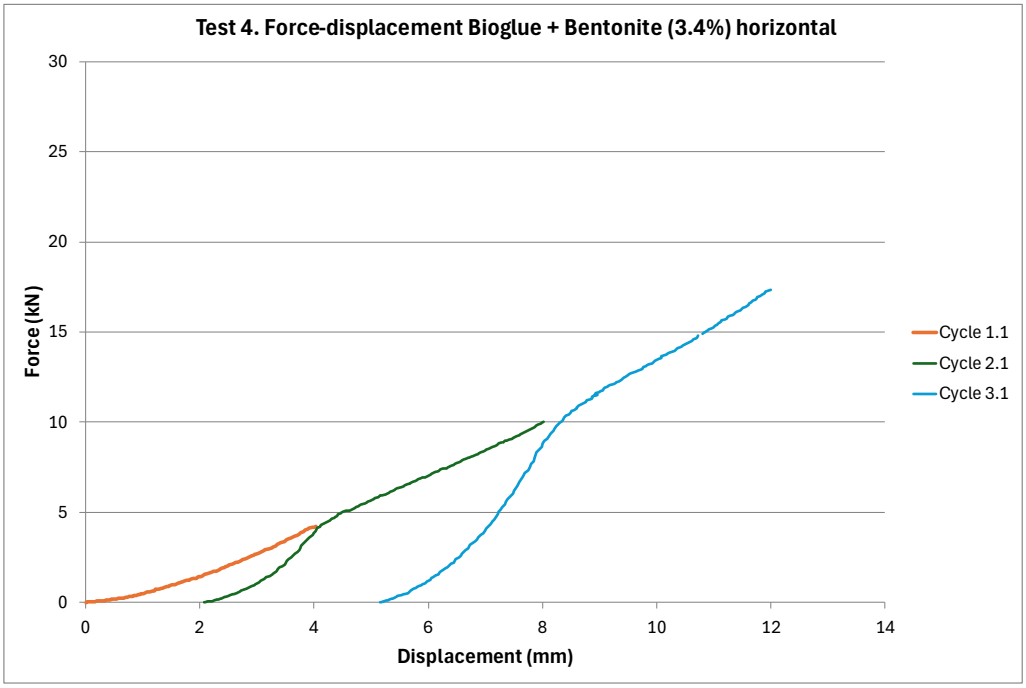


Figure E59. The force-displacement graph of compression test 4.

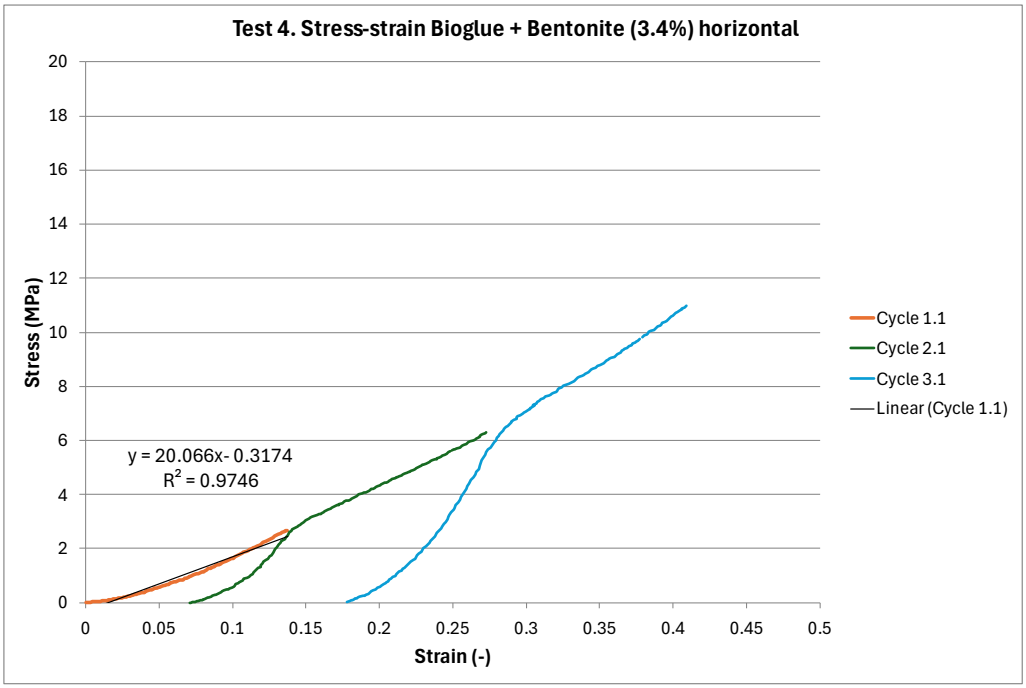


Figure E60. The stress-strain diagram of the three different cycles of compression test 4.

Figure E61 and Figure E62 present all four bio-glue with bentonite tests together in a force-displacement and a stress-strain graph.

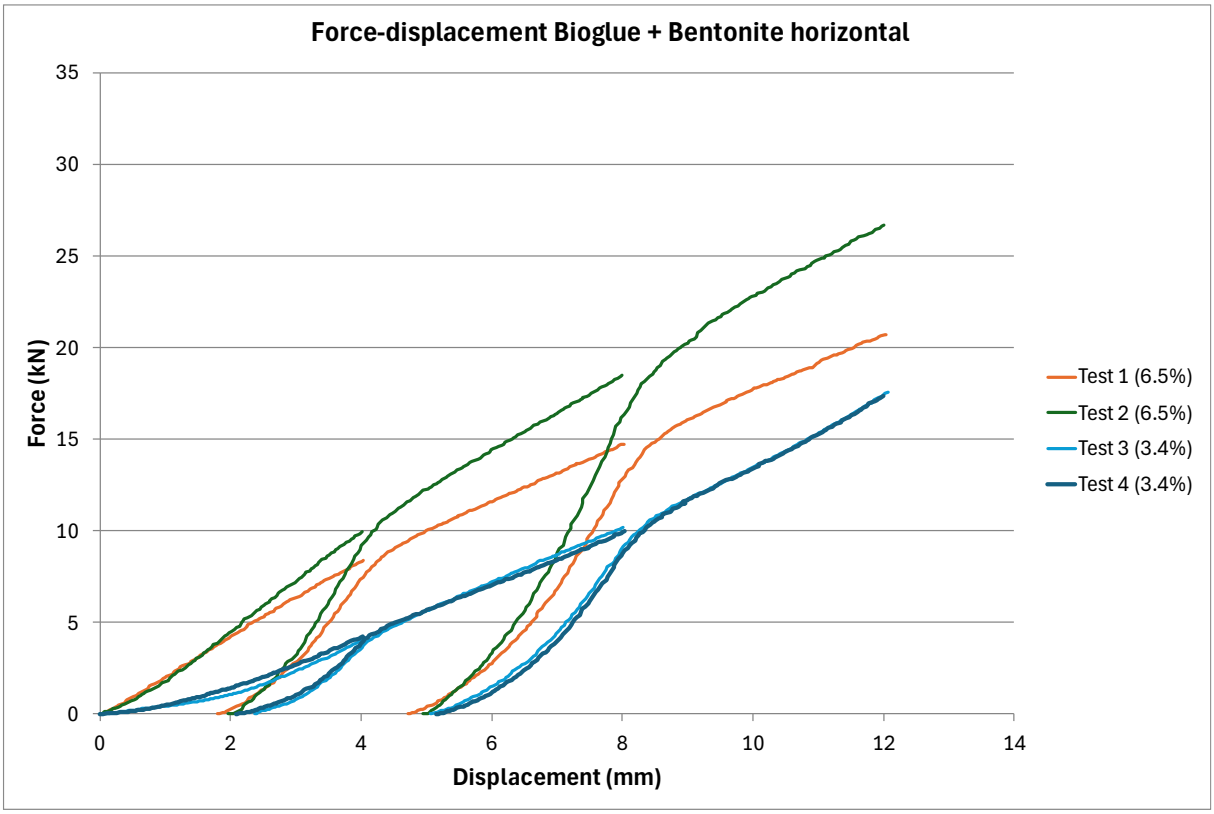


Figure E61. The force-displacement graph of all the bio-glue with bentonite compression tests in the vertical orientation.

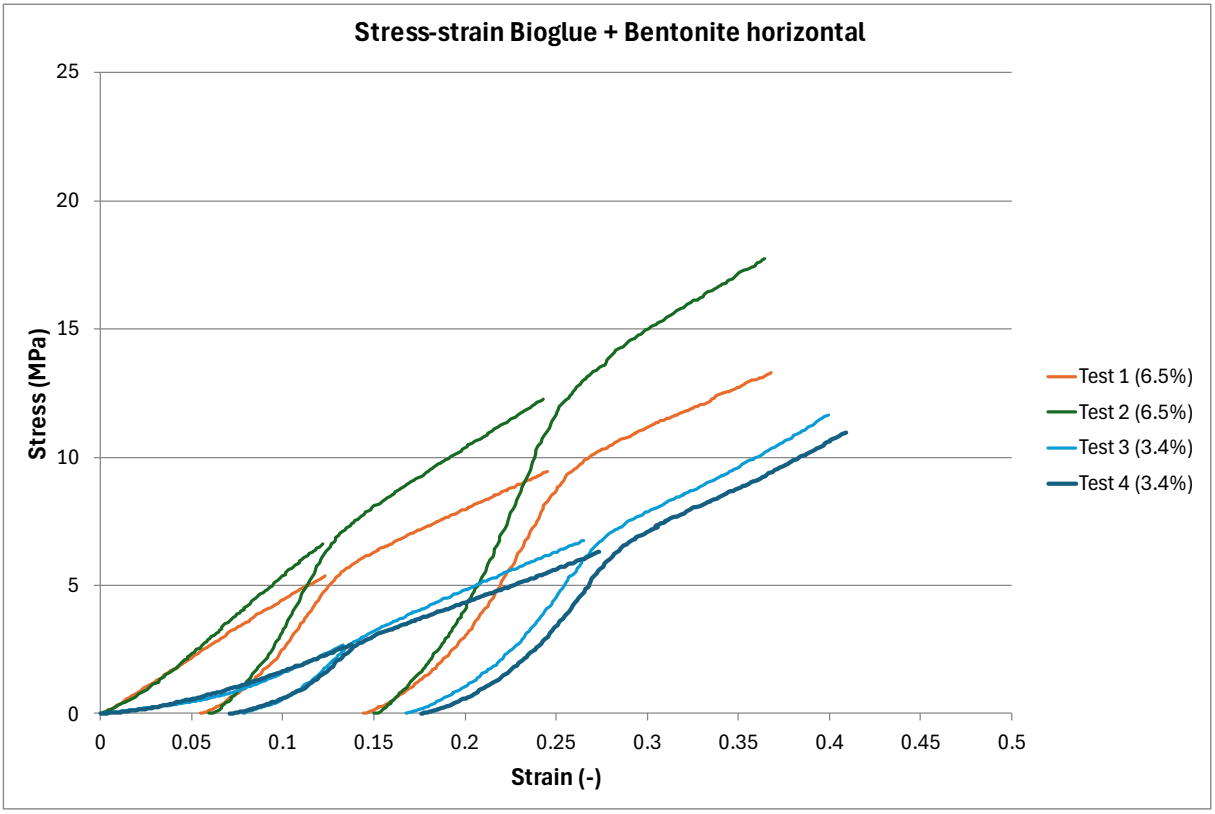


Figure E62. The stress-strain graph of all the bio-glue with bentonite compression tests in the vertical orientation.

E.3.1.2 Vertical layer orientation

Figure E63 to Figure E71 show three bio-glue with bentonite tests with a vertical layer orientation. Each test is accompanied with four photos during the test and two different graphs: the force-displacement and the stress-strain graph.

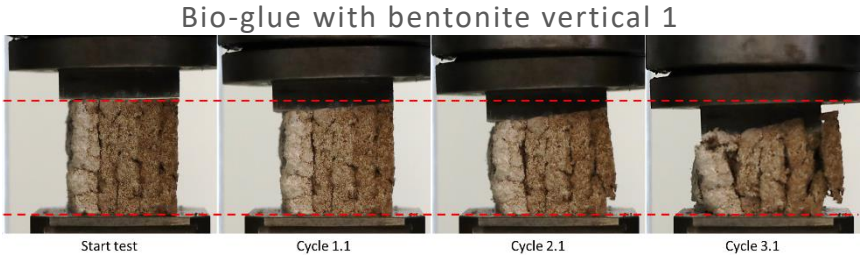


Figure E63. Four photos of compression test 1. One at the start of the test and one at the end of each cycle.

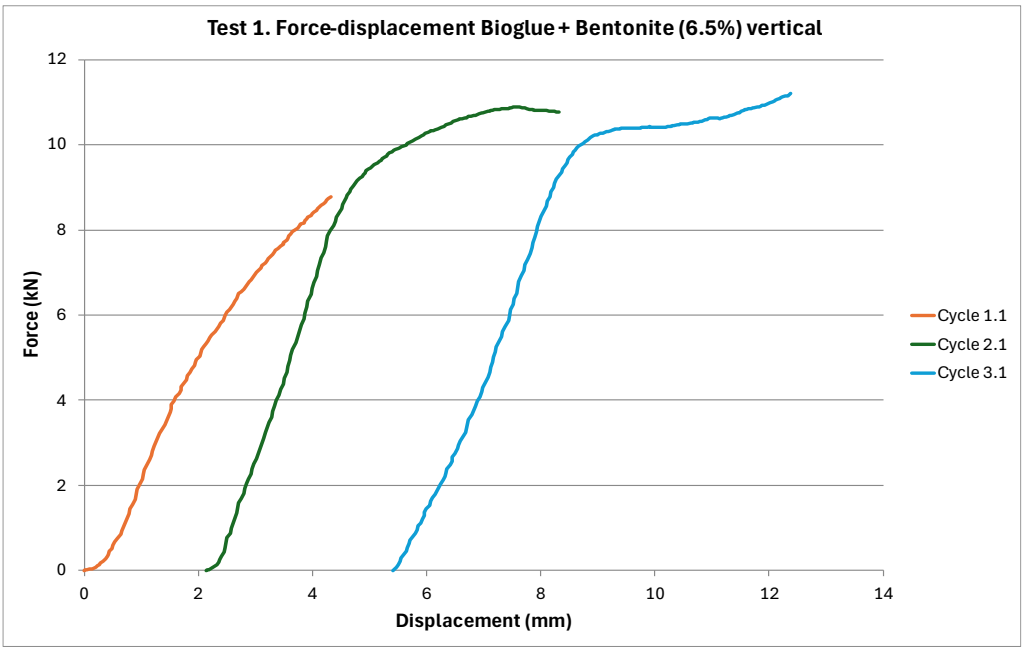


Figure E64. The force-displacement graph of compression test 1.

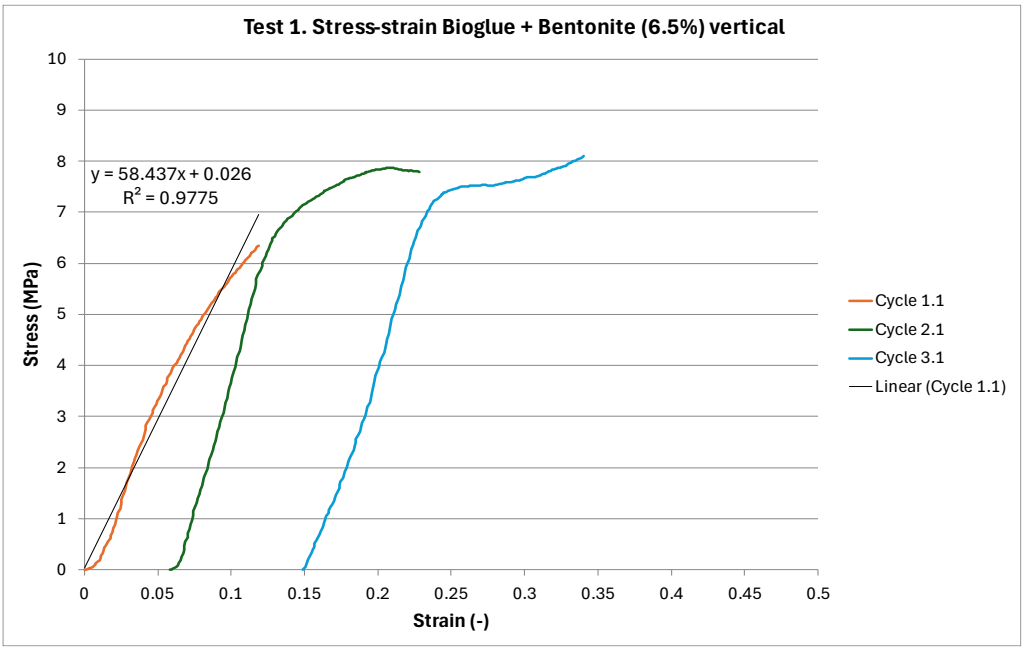


Figure E65. The stress-strain diagram of the three different cycles of compression test 1.

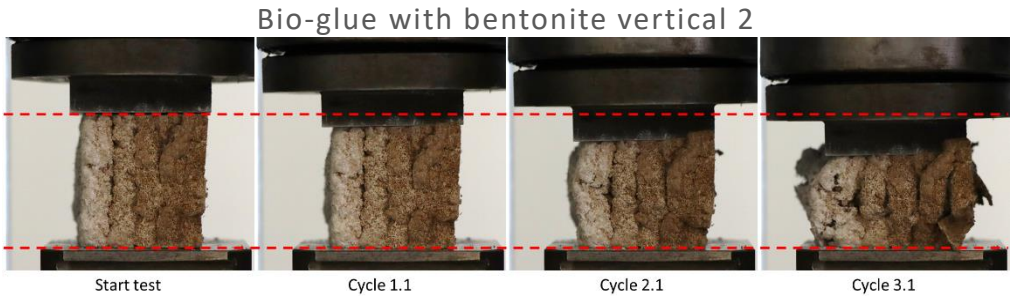


Figure E66. Four photos of compression test 2. One at the start of the test and one at the end of each cycle.

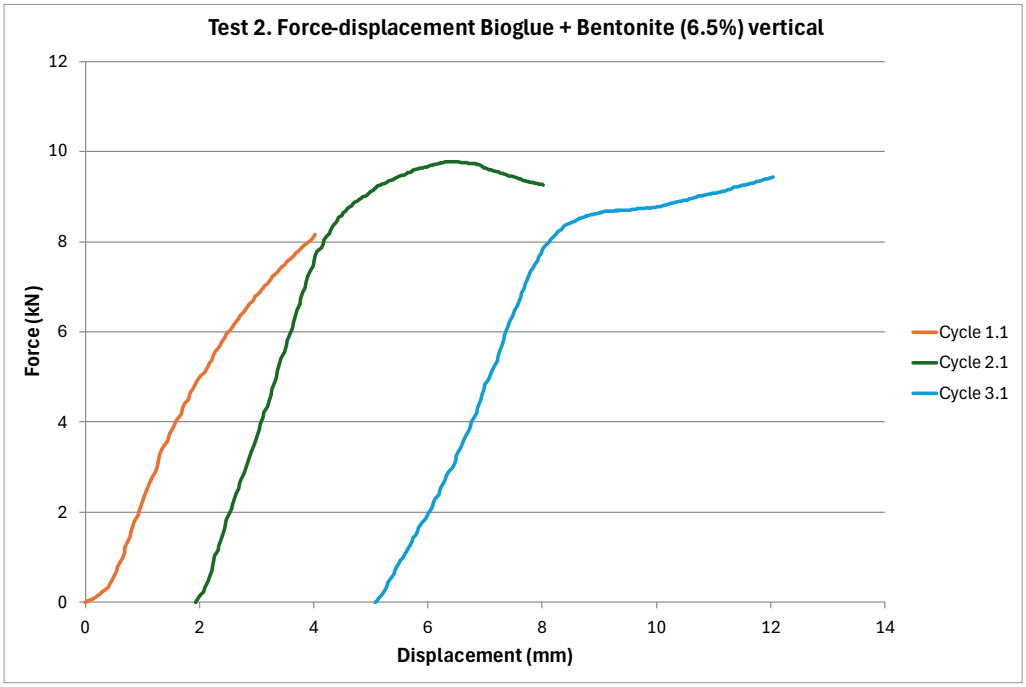


Figure E67. The force-displacement graph of compression test 2.

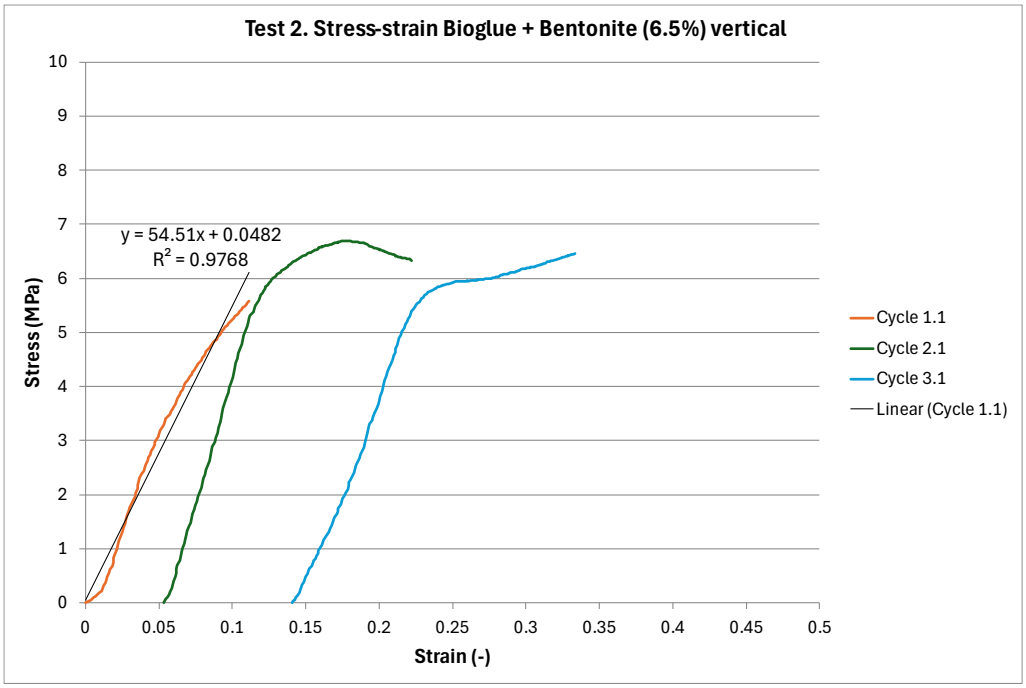


Figure E68. The stress-strain diagram of the three different cycles of compression test 2.

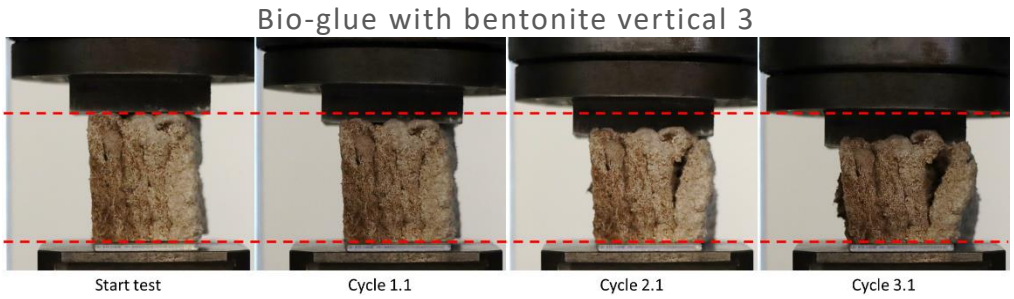


Figure E69. Four photos of compression test 3. One at the start of the test and one at the end of each cycle.

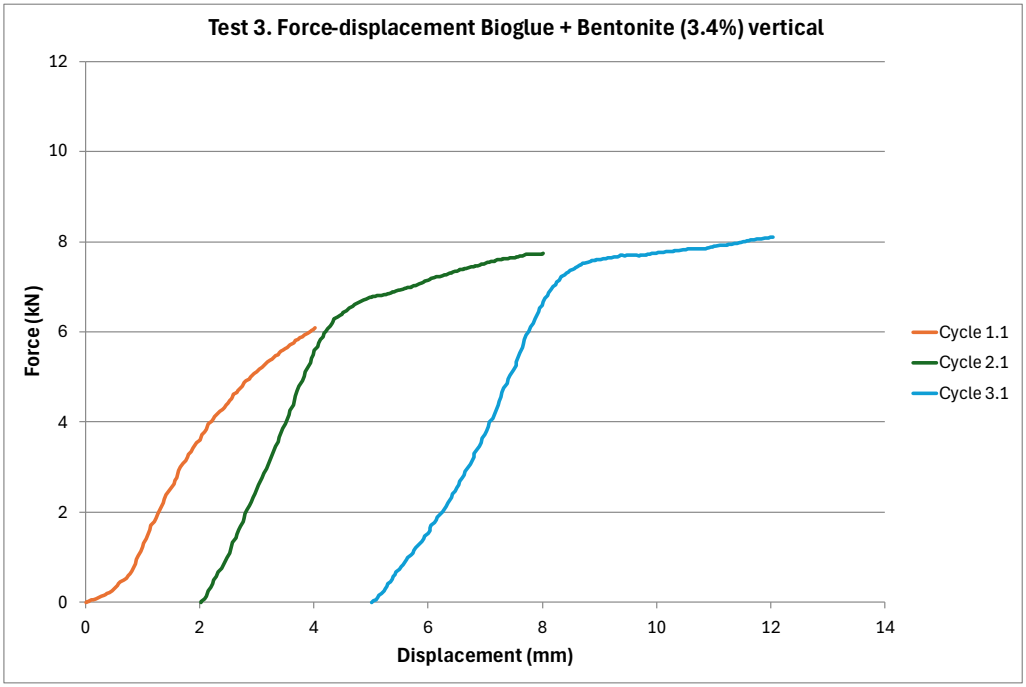


Figure E70. The force-displacement graph of compression test 3.

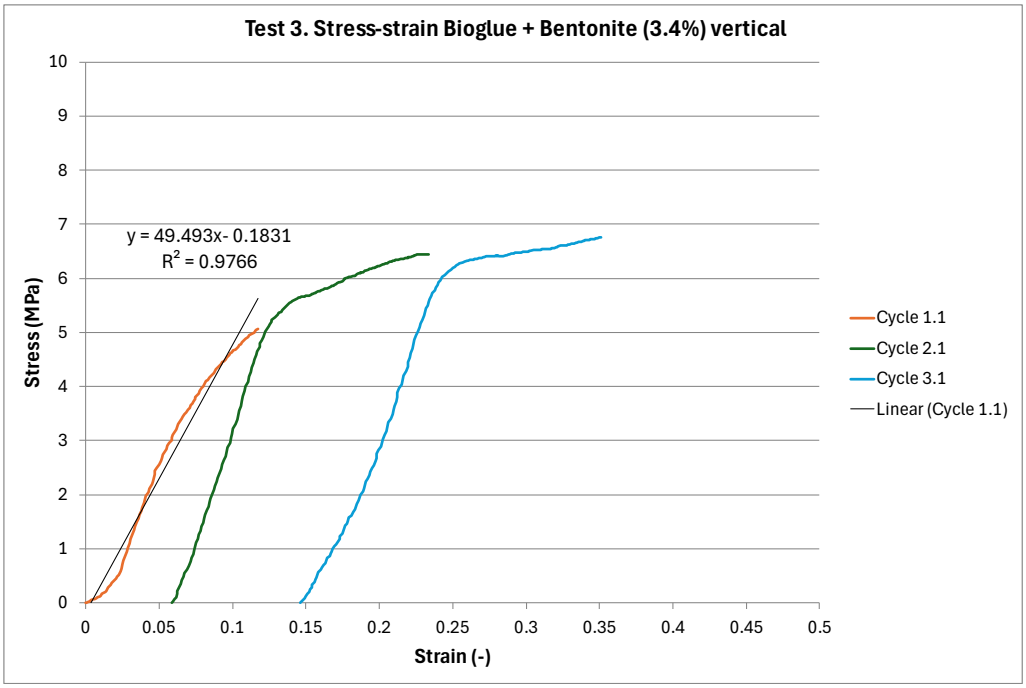


Figure E71. The stress-strain diagram of the three different cycles of compression test 3.

Figure E72 and Figure E73 present all three bio-glue with bentonite tests together in a force-displacement and a stress-strain graph.

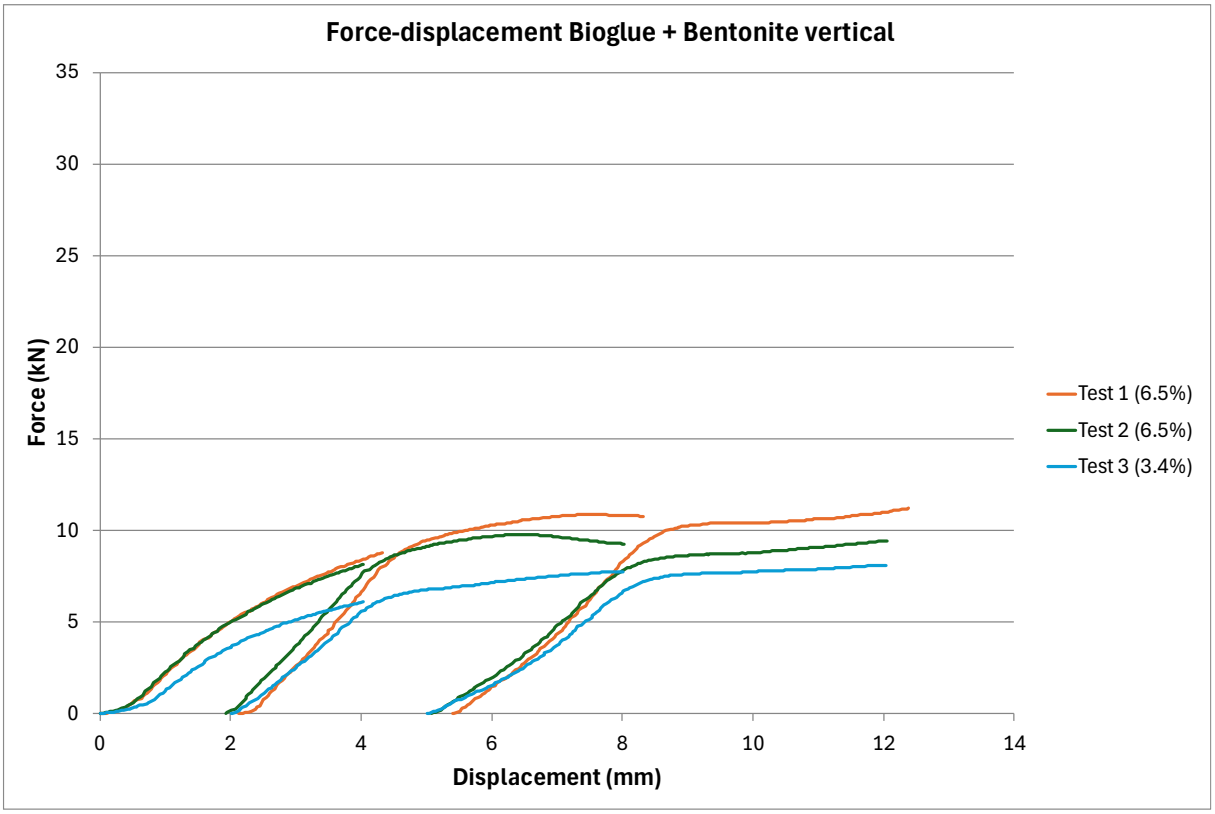


Figure E72. The force-displacement graph of all the bio-glue with bentonite compression tests in the vertical orientation.

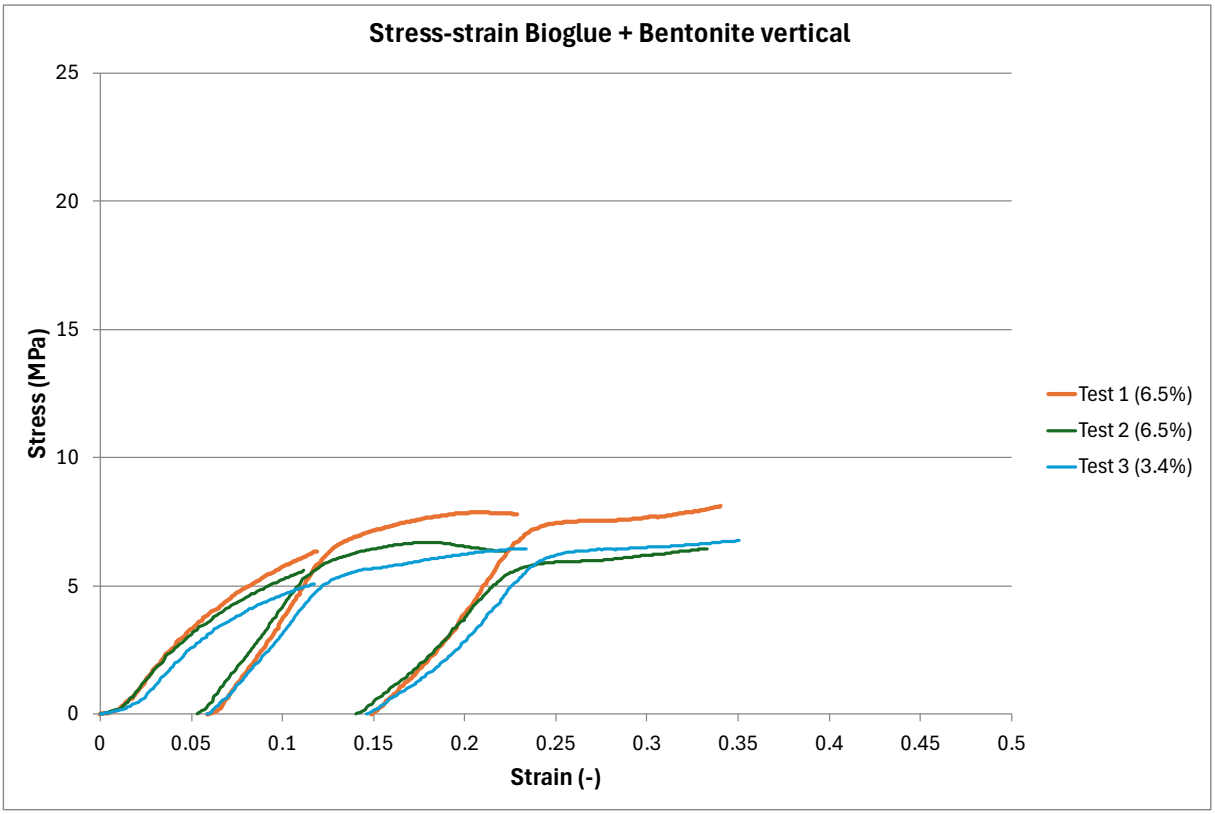


Figure E73. The stress-strain graph of all the bio-glue with bentonite compression tests in the vertical orientation.

E.3.2 Bio-glue with flax

E.3.2.1 Horizontal layer orientation

Figure E74 to Figure E82 show four bio-glue with flax tests with a horizontal layer orientation. Each test is accompanied with four photos during the test and two different graphs: the force-displacement and the stress-strain graph.

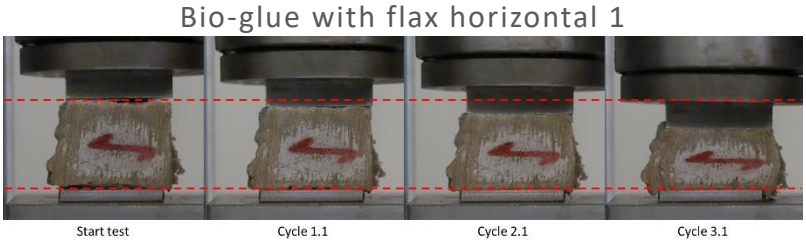


Figure E74. Four photos of compression test 1. One at the start of the test and one at the end of each cycle.

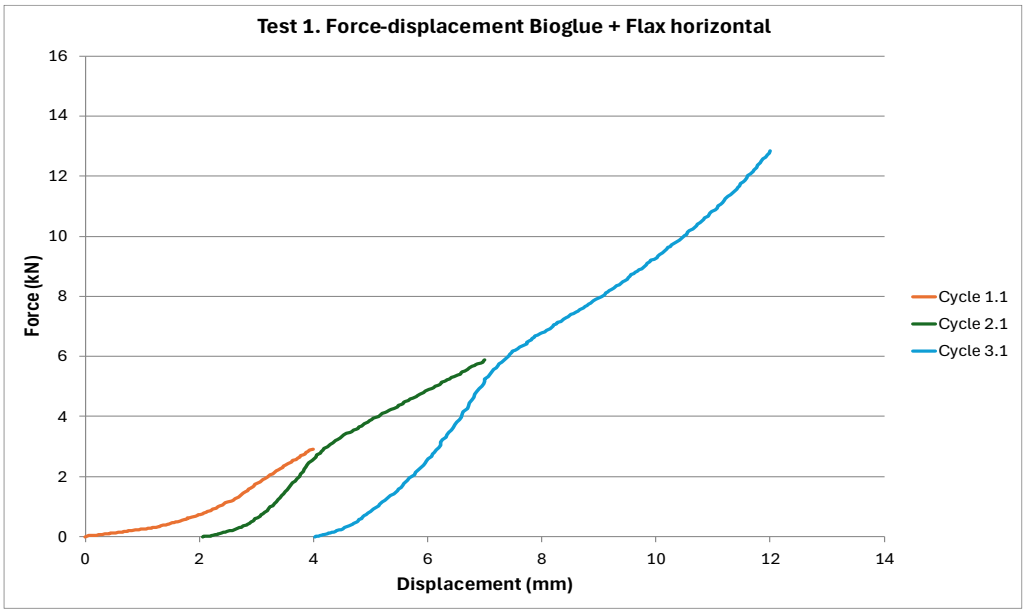


Figure E75. The force-displacement graph of compression test 1.

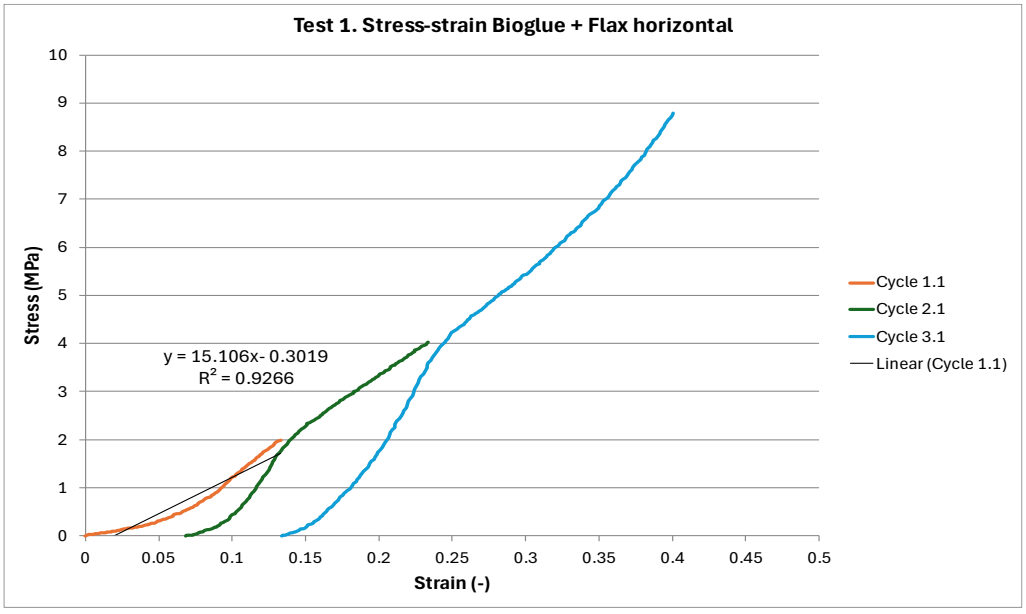


Figure E76. The stress-strain diagram of the three different cycles of compression test 1.

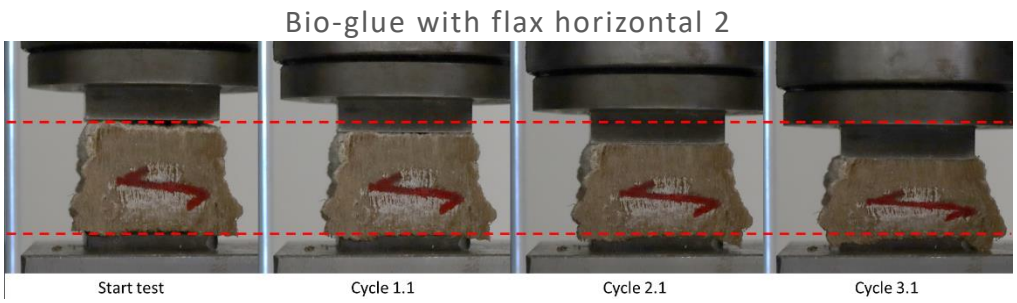


Figure E77. Four photos of compression test 2. One at the start of the test and one at the end of each cycle.

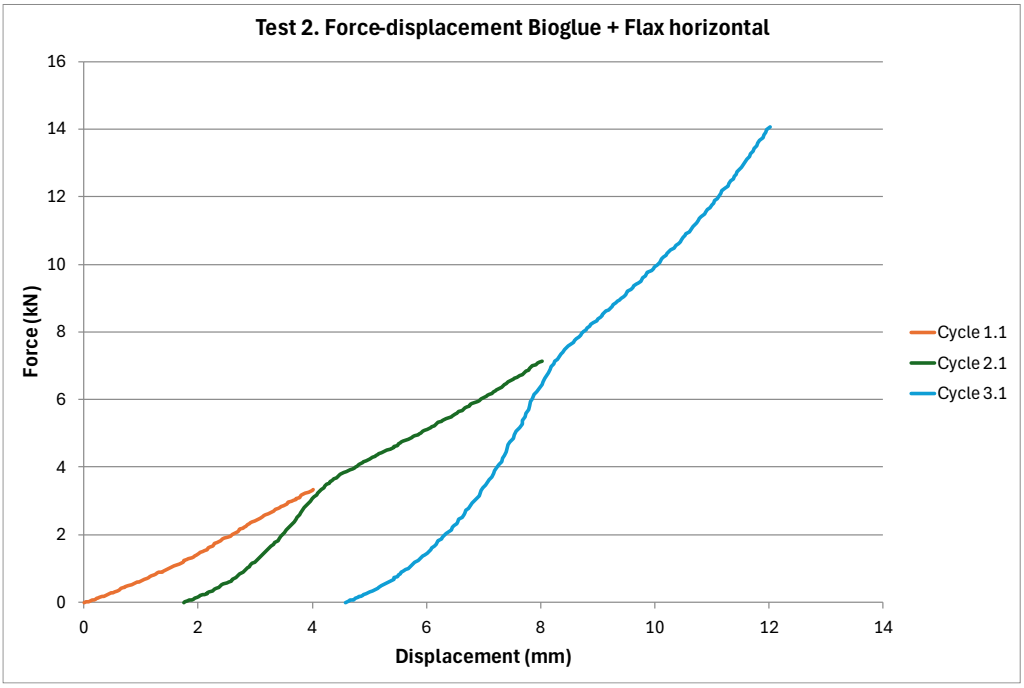


Figure E78. The force-displacement graph of compression test 2.

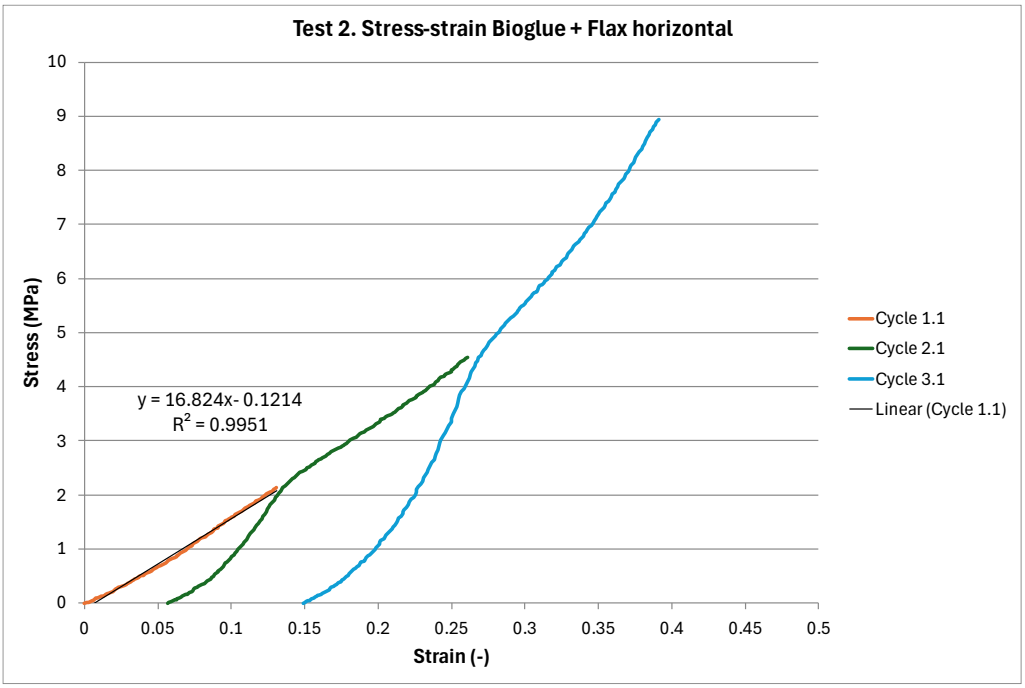


Figure E79. The stress-strain diagram of the three different cycles of compression test 2.

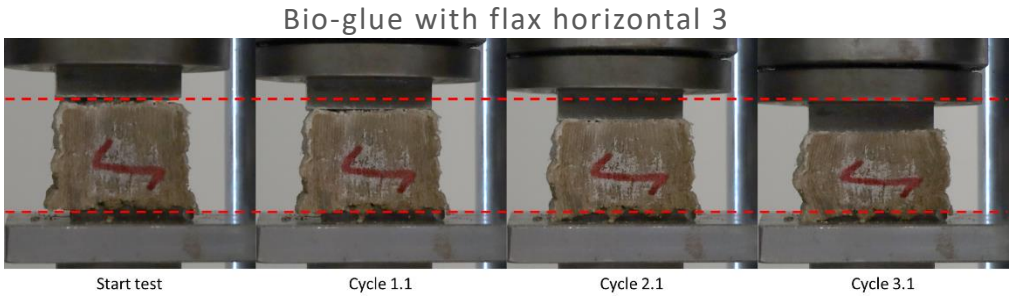


Figure E80. Four photos of compression test 3. One at the start of the test and one at the end of each cycle.

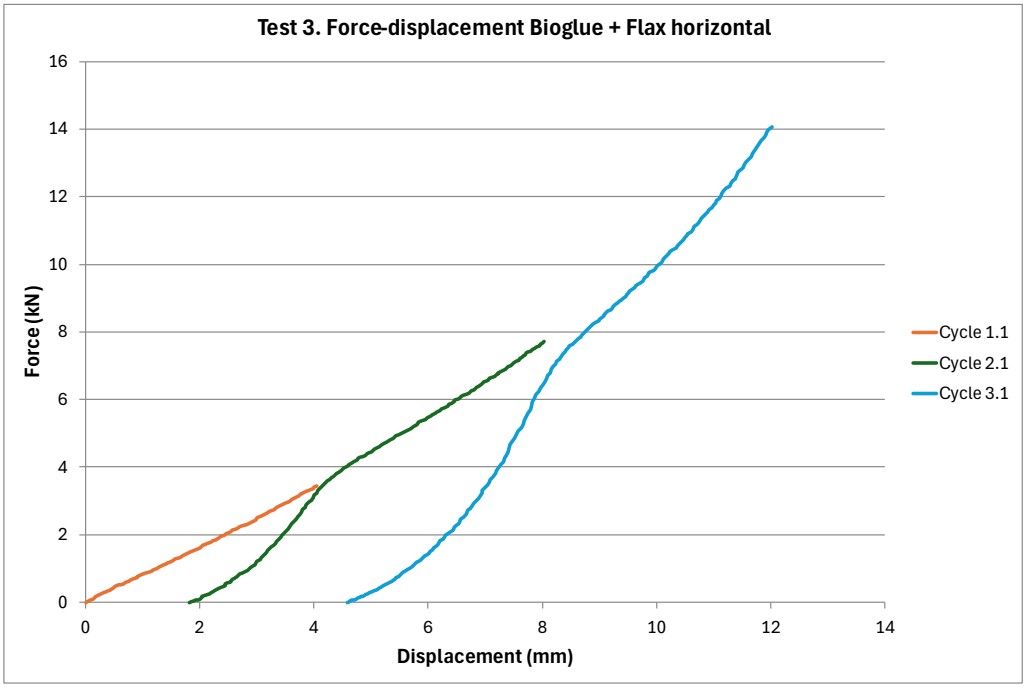


Figure E81. The force-displacement graph of compression test 3.

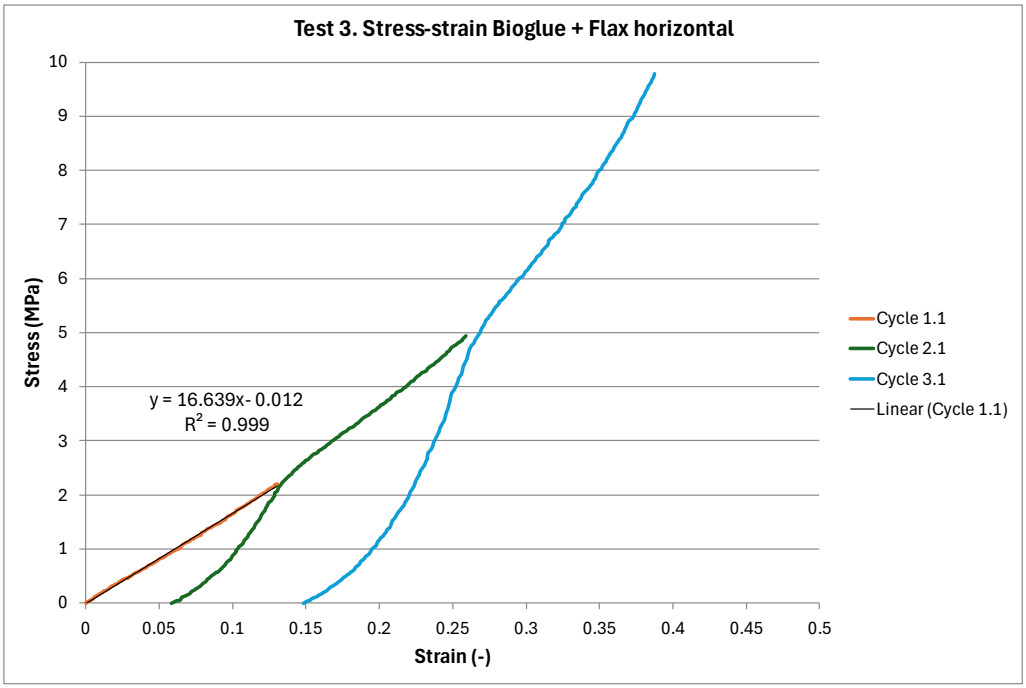


Figure E82. The stress-strain diagram of the three different cycles of compression test 3.

Figure E83 and Figure E84 present all bio-glue with flax three tests together in a force-displacement and a stress-strain graph.

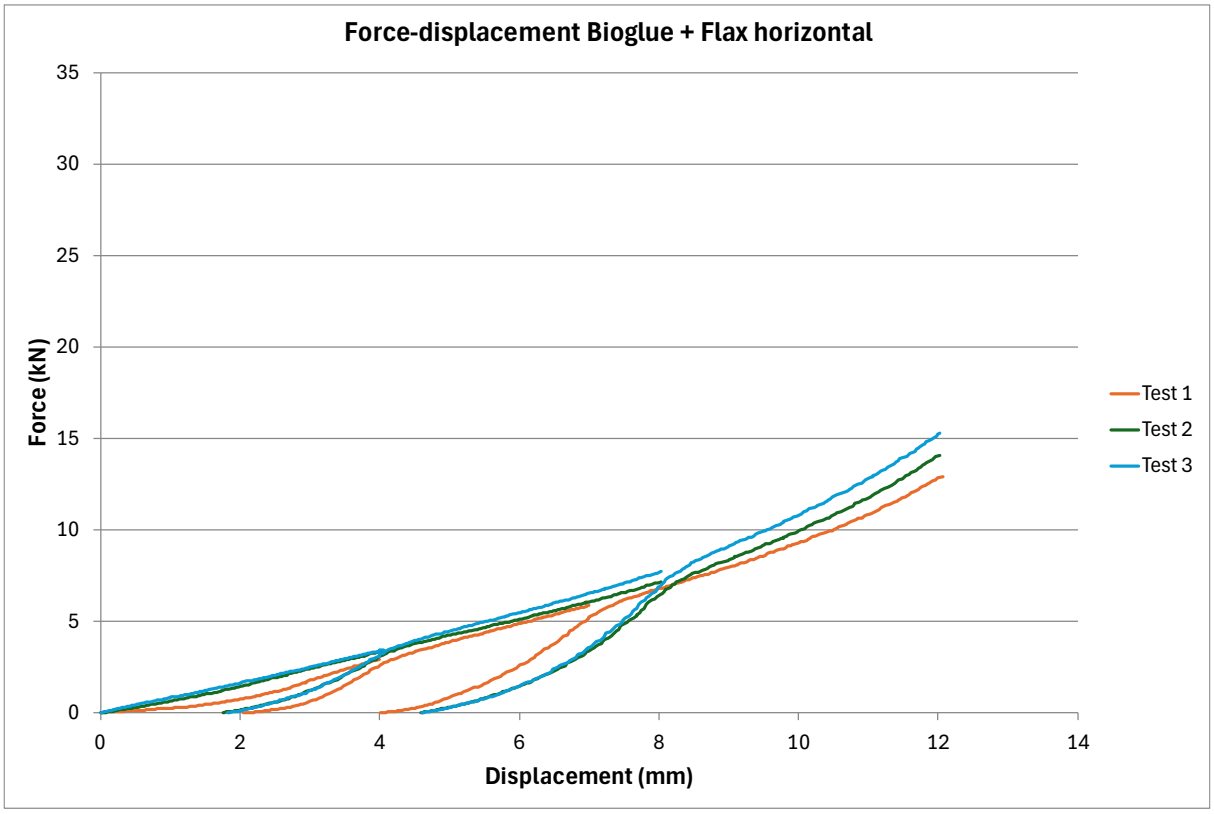


Figure E83. The force-displacement graph of all the bio-glue with flax compression tests in the vertical orientation.

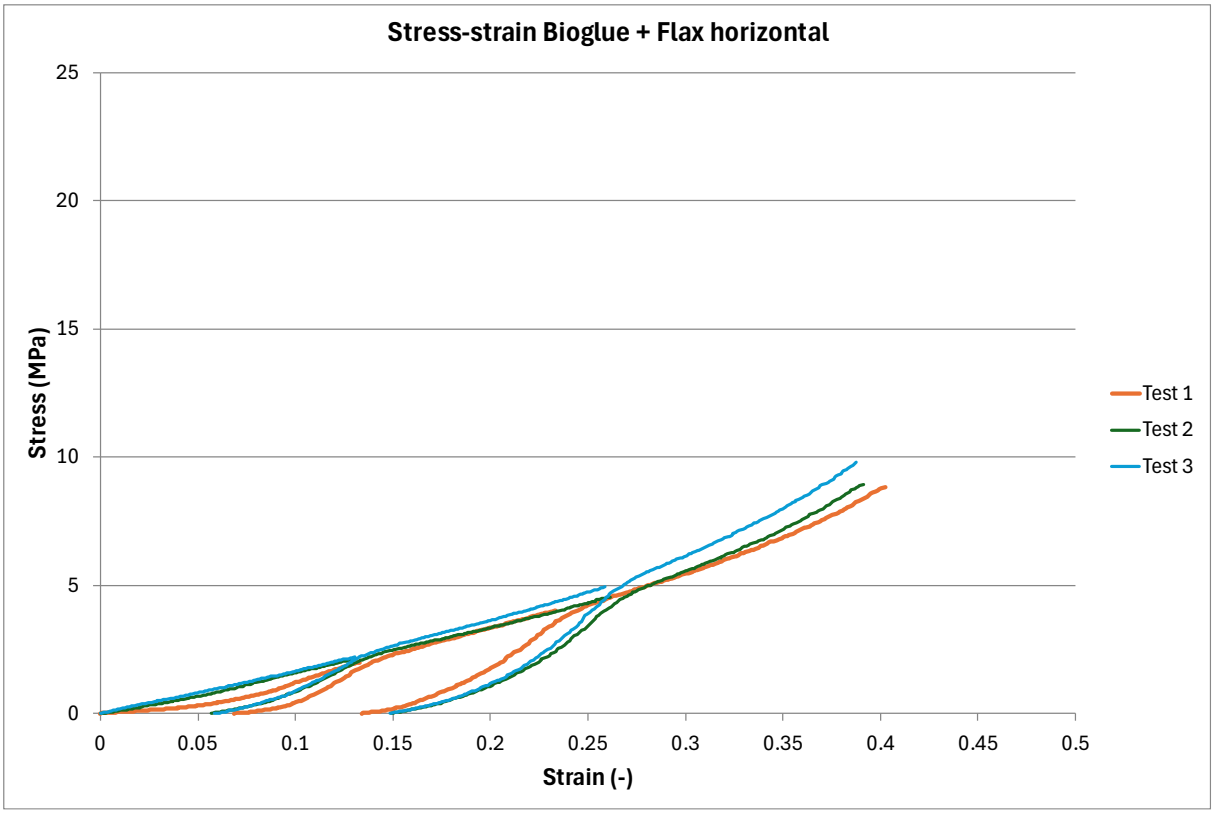


Figure E84. The stress-strain graph of all the bio-glue with flax compression tests in the vertical orientation.

E.3.2.2 Vertical layer orientation

Figure E85 to Figure E93 show three bio-glue with flax tests with a vertical layer orientation. Each test is accompanied with four photos during the test and two different graphs: the force-displacement and the stress-strain graph.

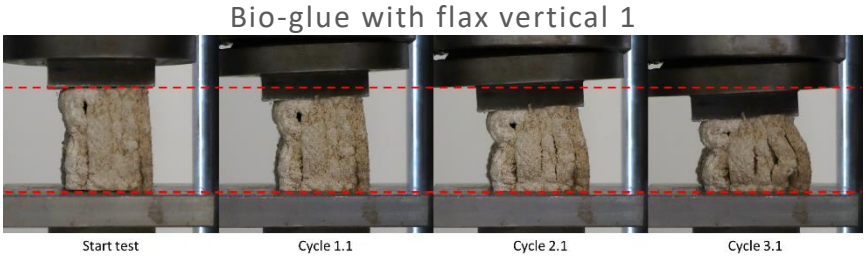


Figure E85. Four photos of compression test 1. One at the start of the test and one at the end of each cycle.

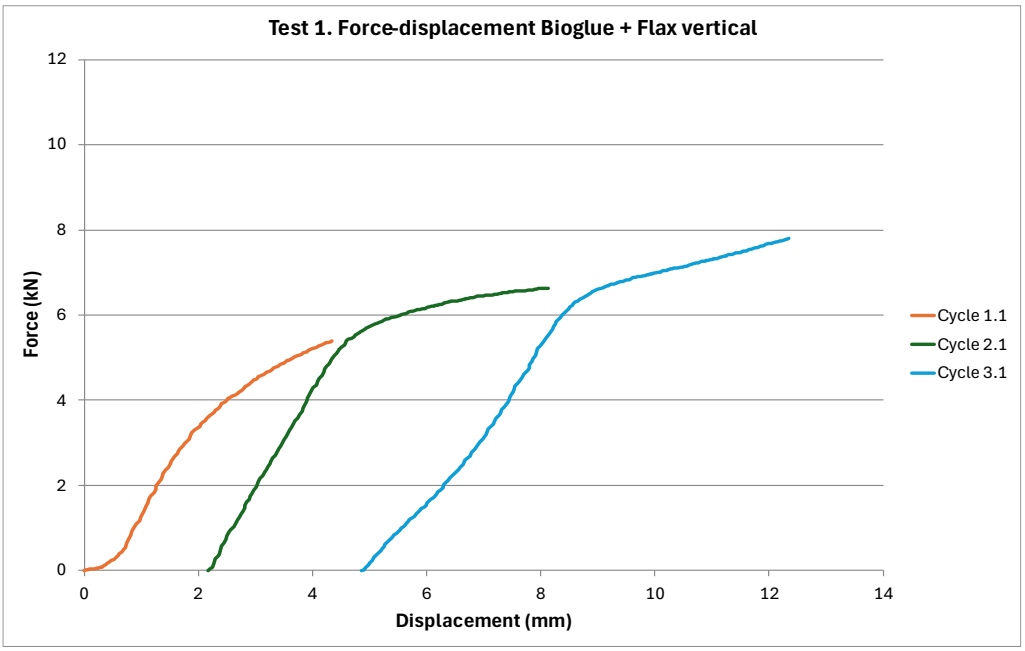


Figure E86. The force-displacement graph of compression test 1.

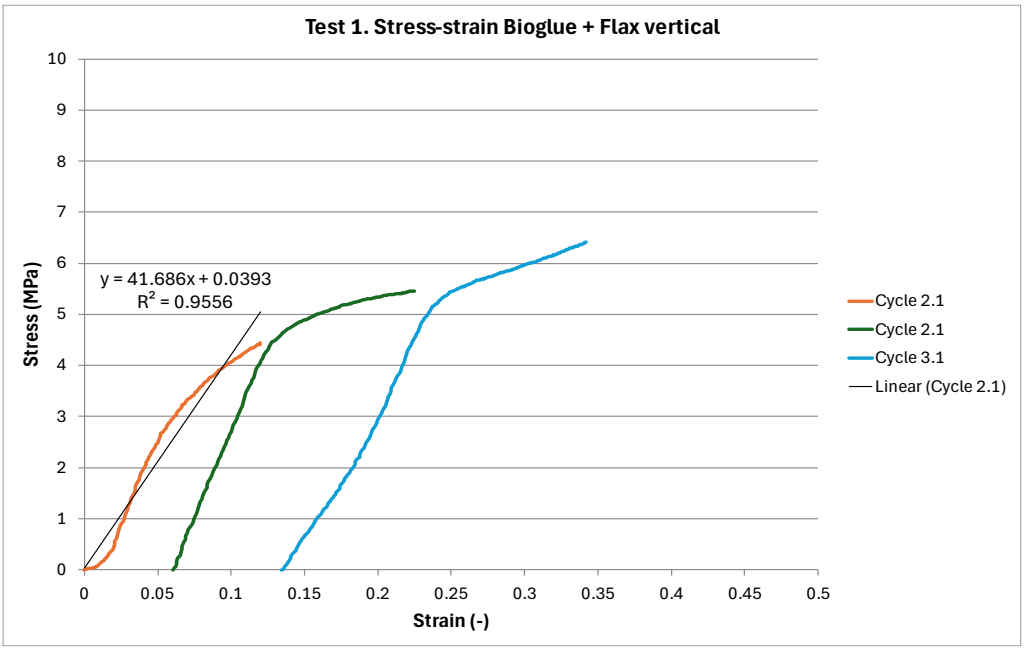


Figure E87. The stress-strain diagram of the three different cycles of compression test 1.

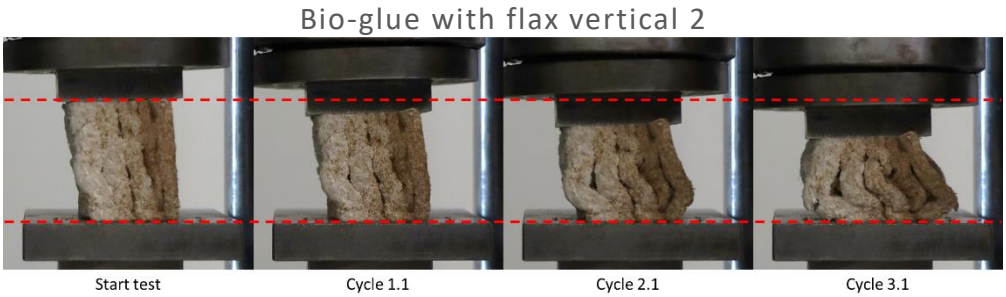


Figure E88. Four photos of compression test 2. One at the start of the test and one at the end of each cycle.

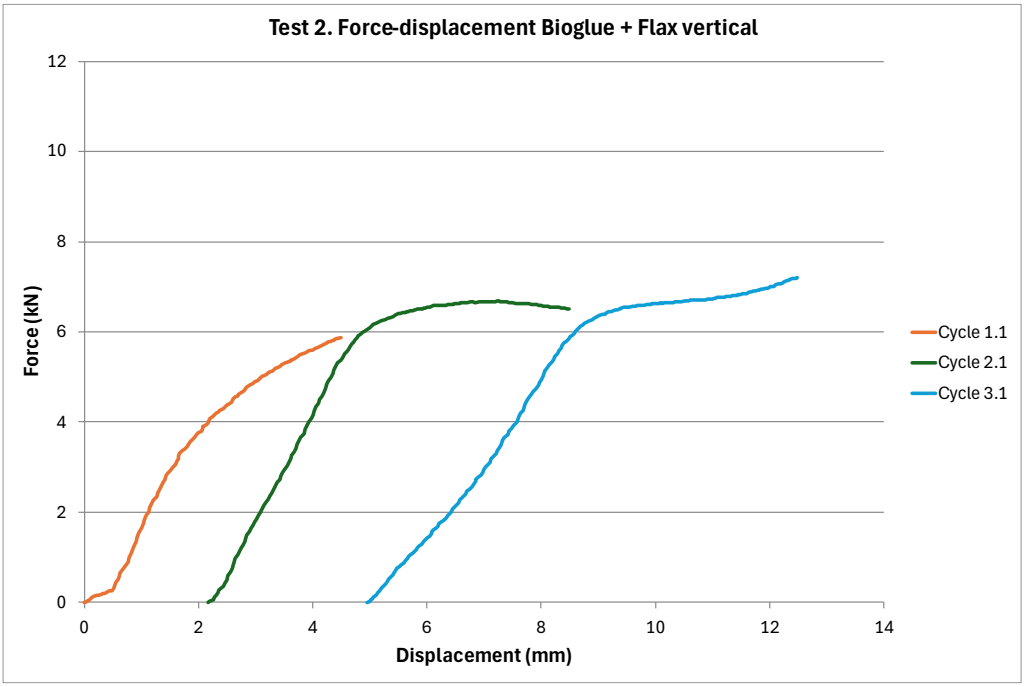


Figure E89. The force-displacement graph of compression test 2.

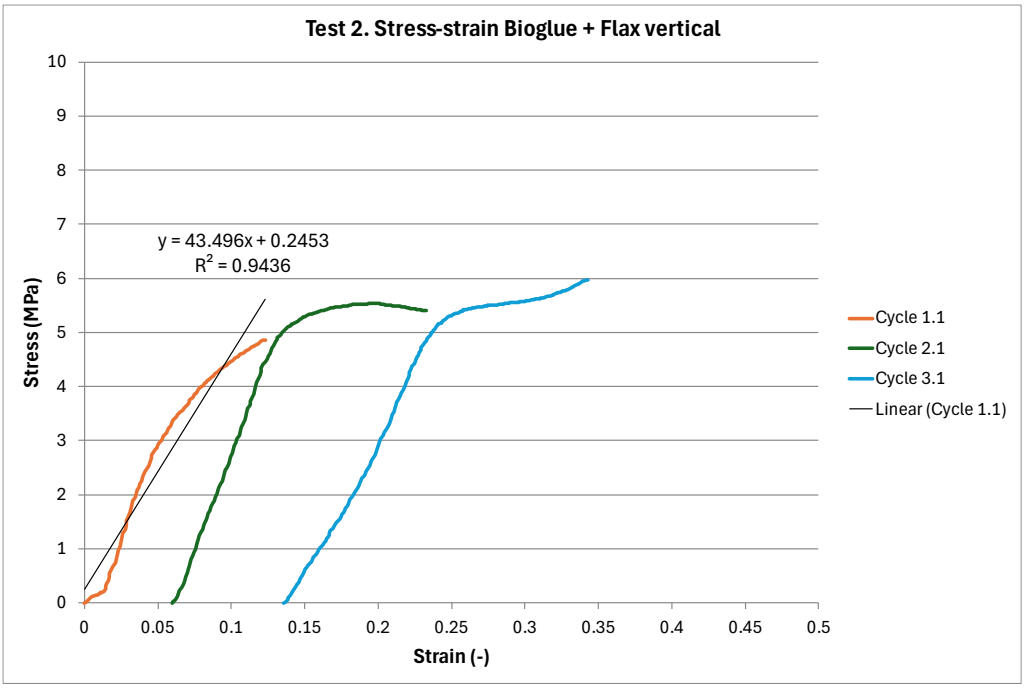


Figure E90. The stress-strain diagram of the three different cycles of compression test 2.

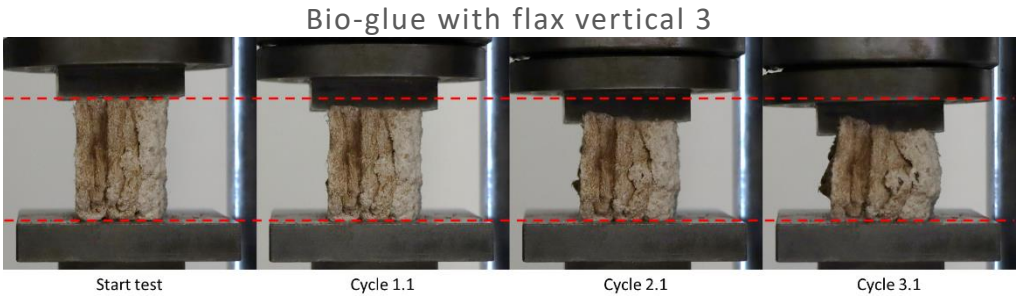


Figure E91. Four photos of compression test 3. One at the start of the test and one at the end of each cycle.

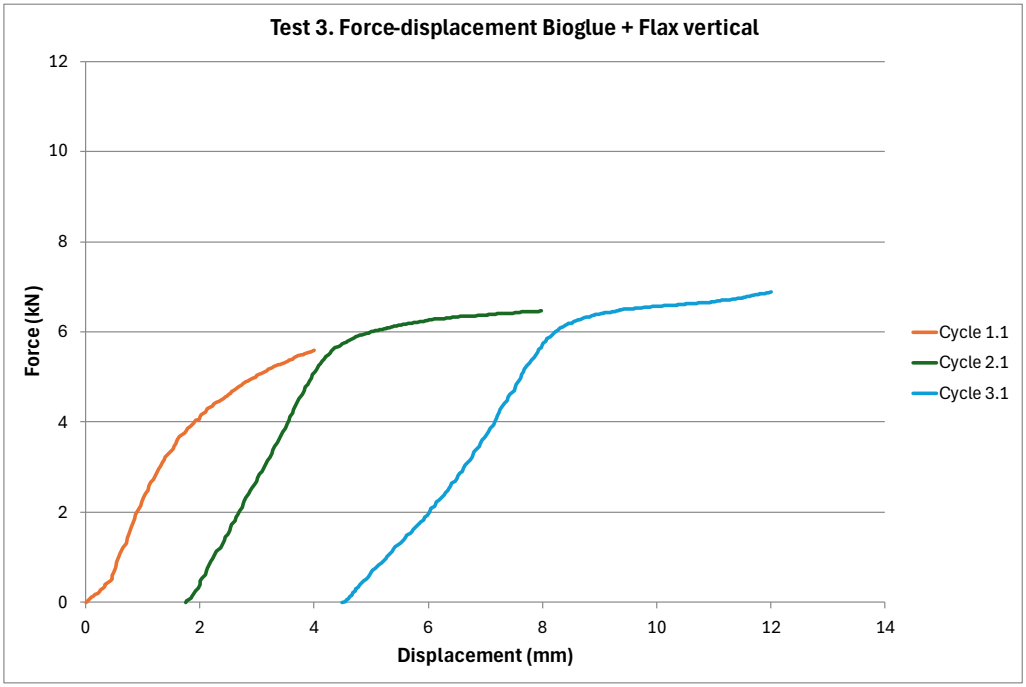


Figure E92. The force-displacement graph of compression test 3.

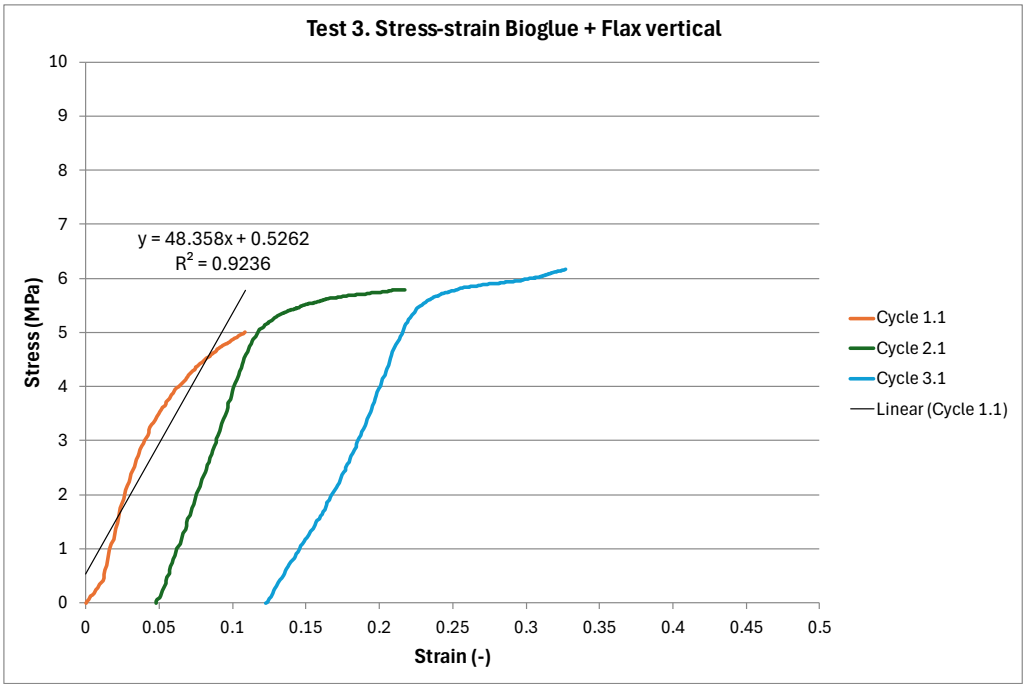


Figure E93. The stress-strain diagram of the three different cycles of compression test 3.

Figure E94 and Figure E95 present all three bio-glue with flax tests together in a force-displacement and a stress-strain graph.

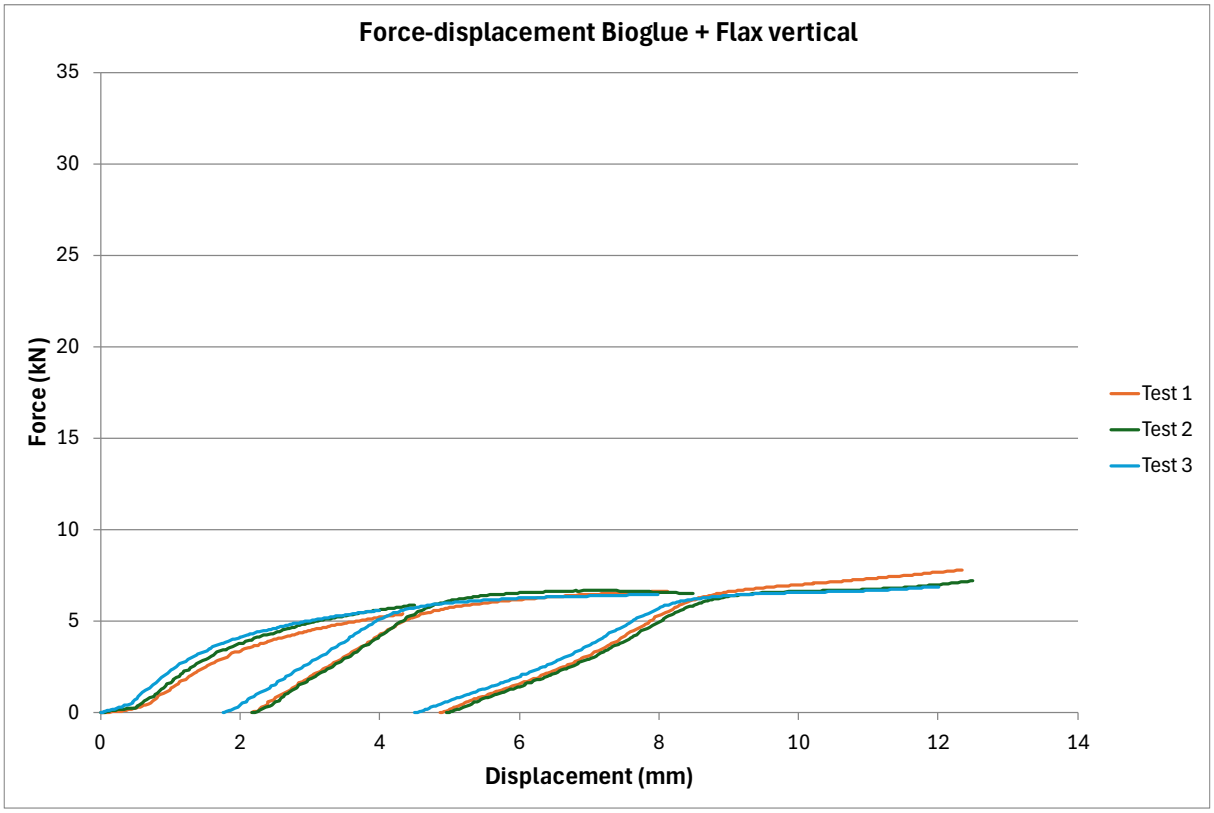


Figure E94. The force-displacement graph of all the bio-glue with flax compression tests in the vertical orientation.

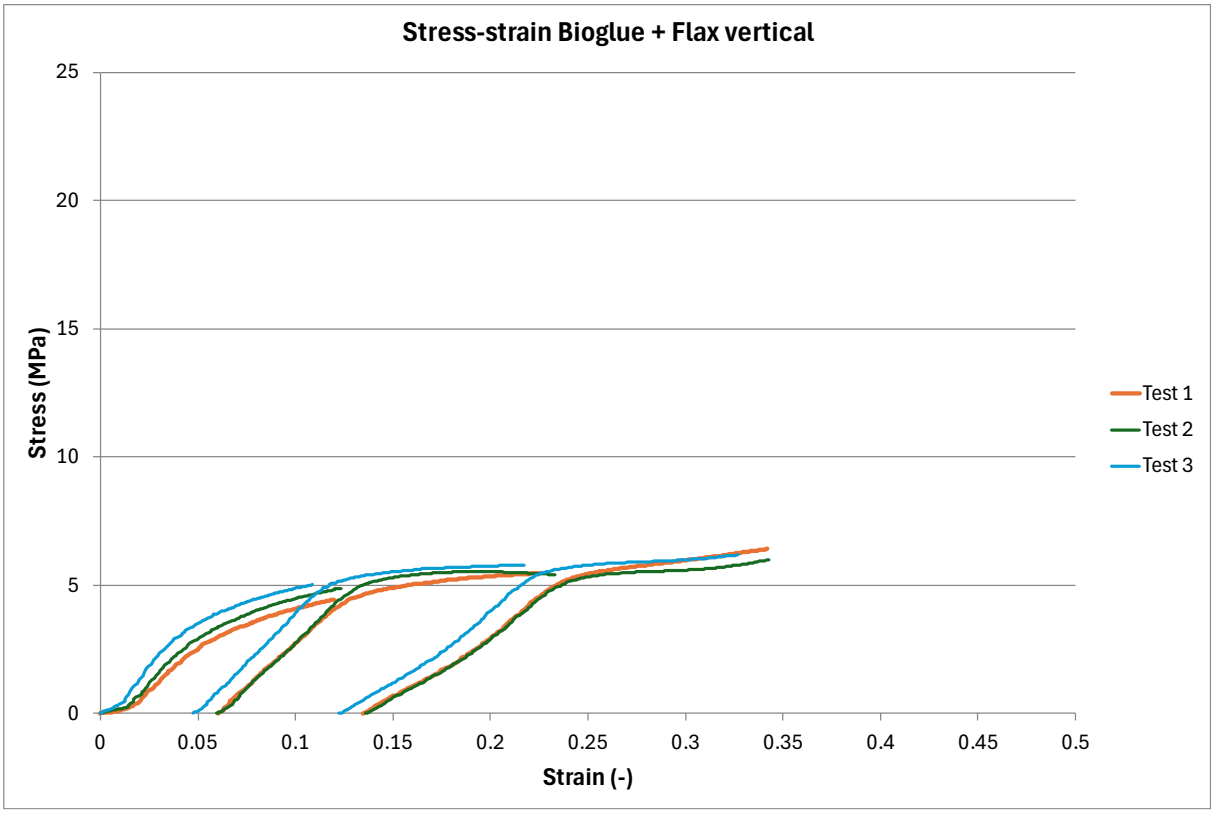


Figure E95. The stress-strain graph of all the bio-glue with flax compression tests in the vertical orientation.

E.3.3 Bio-glue with bentonite and flax

E.3.3.1 Horizontal layer orientation

Figure E96 to Figure E107 show four bio-glue with bentonite and flax tests with a horizontal layer orientation. Each test is accompanied with four photos during the test and two different graphs: the force-displacement and the stress-strain graph.

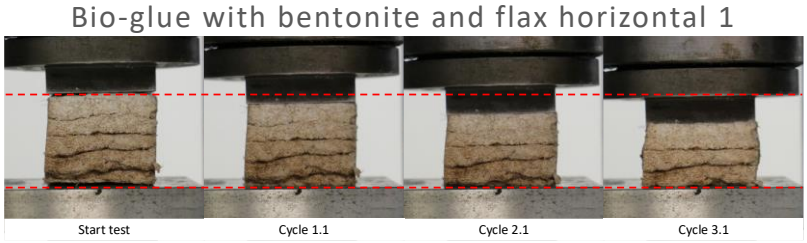


Figure E96. Four photos of compression test 1. One at the start of the test and one at the end of each cycle.

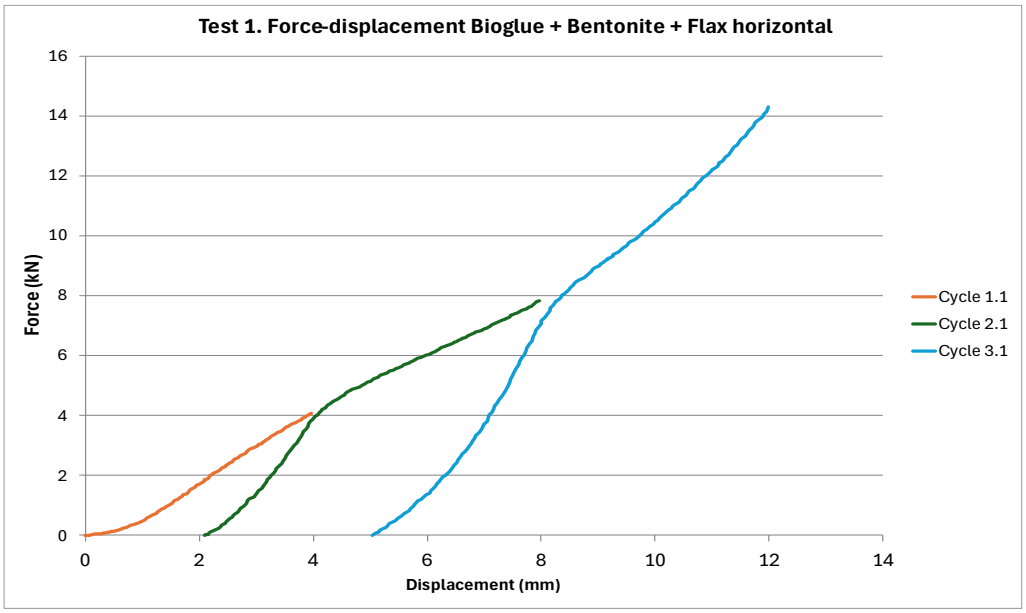


Figure E97. The force-displacement graph of compression test 1.

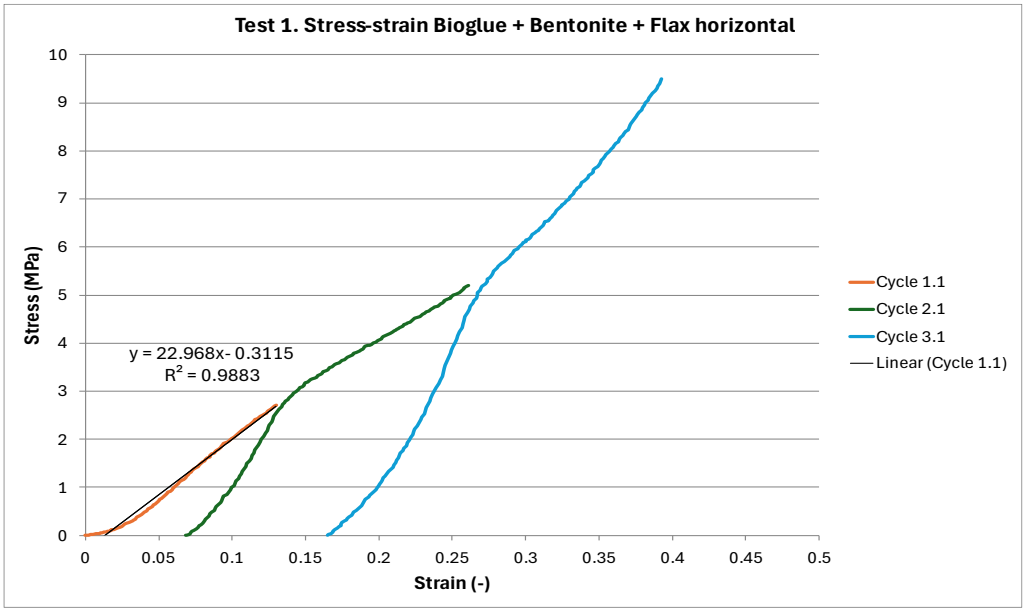


Figure E98. The stress-strain diagram of the three different cycles of compression test 1.

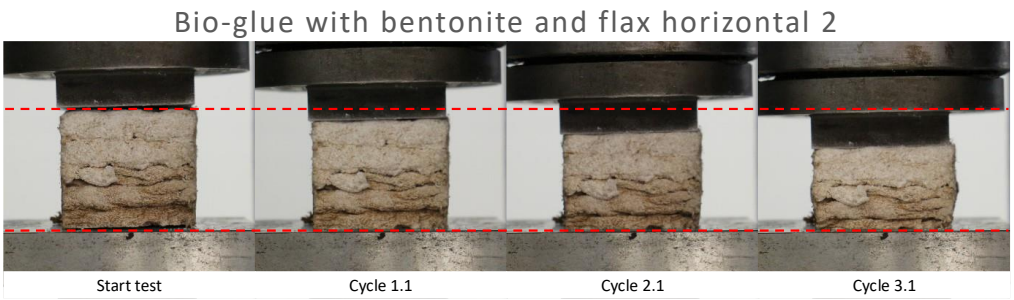


Figure E99. Four photos of compression test 2. One at the start of the test and one at the end of each cycle.

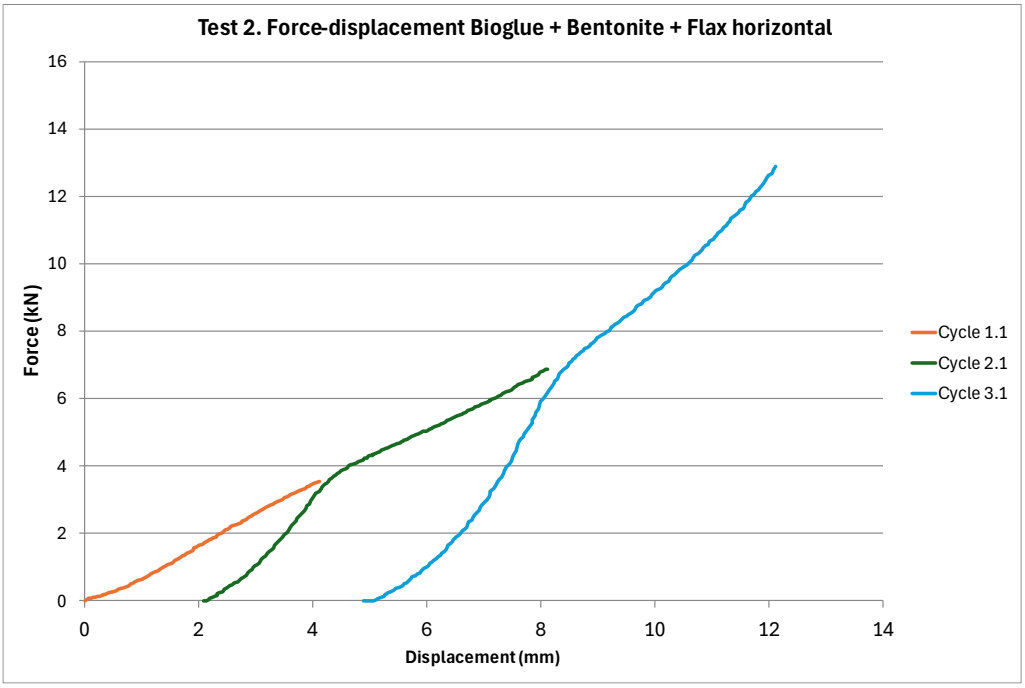


Figure E100. The force-displacement graph of compression test 2.

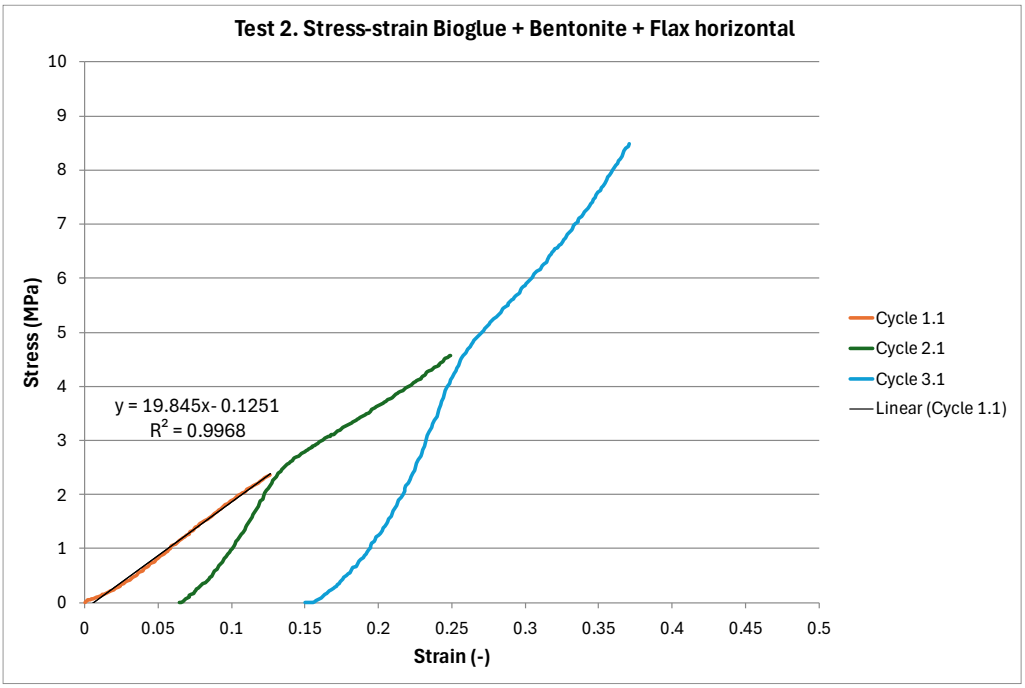


Figure E101. The stress-strain diagram of the three different cycles of compression test 2.

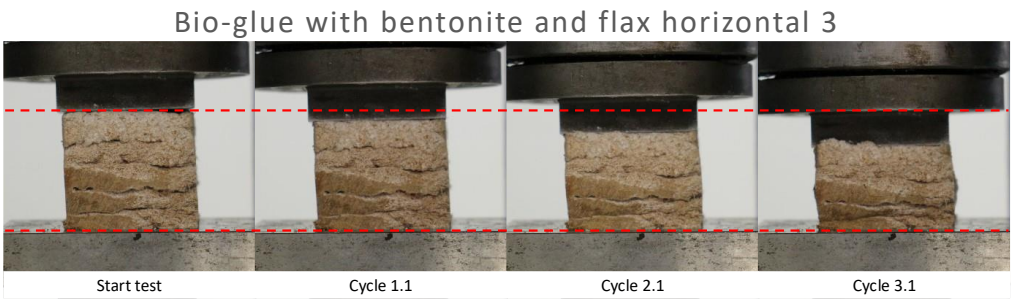


Figure E102. Four photos of compression test 3. One at the start of the test and one at the end of each cycle.

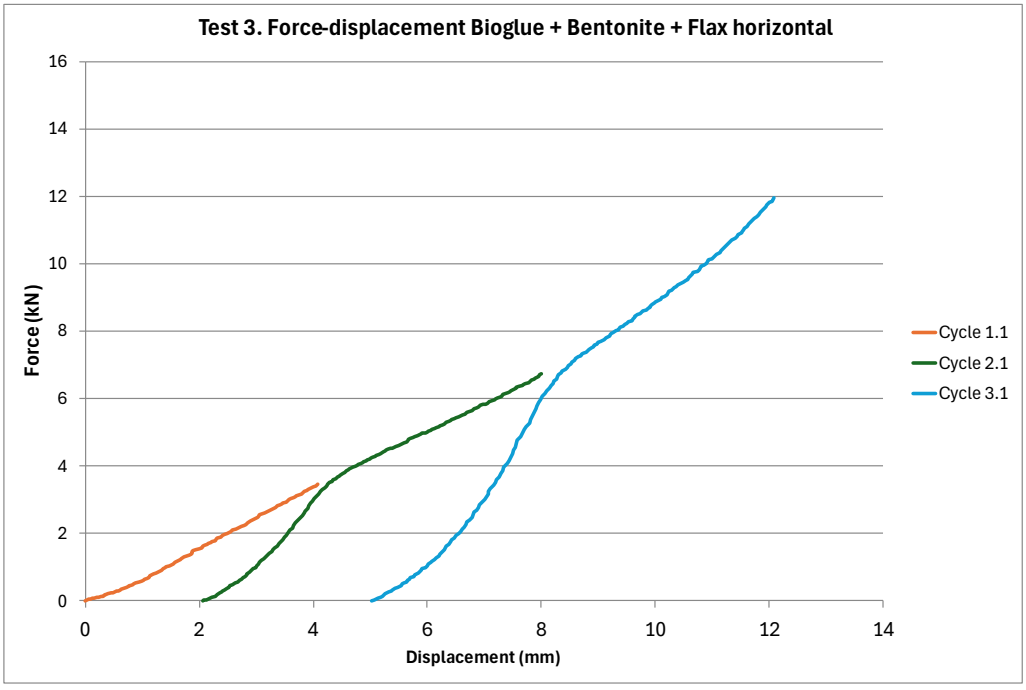


Figure E103. The force-displacement graph of compression test 3.

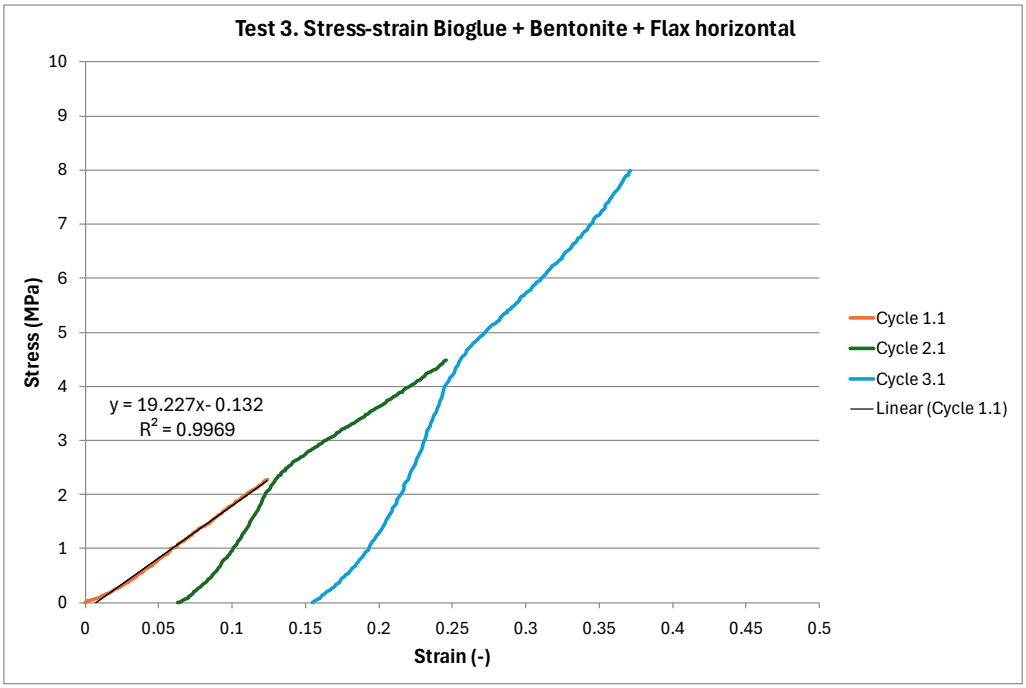


Figure E104. The stress-strain diagram of the three different cycles of compression test 3.

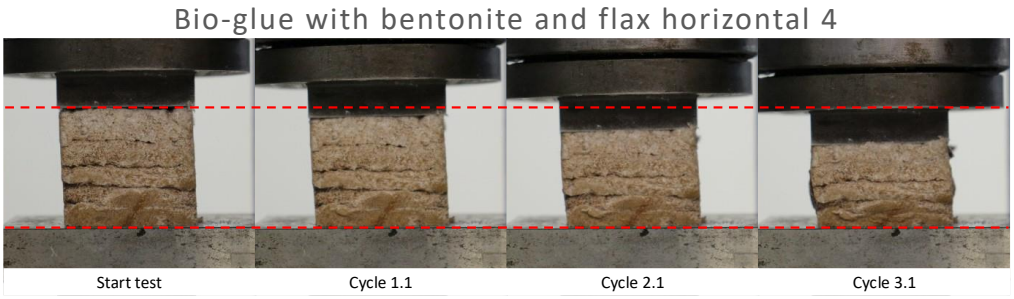


Figure E105. Four photos of compression test 4. One at the start of the test and one at the end of each cycle.

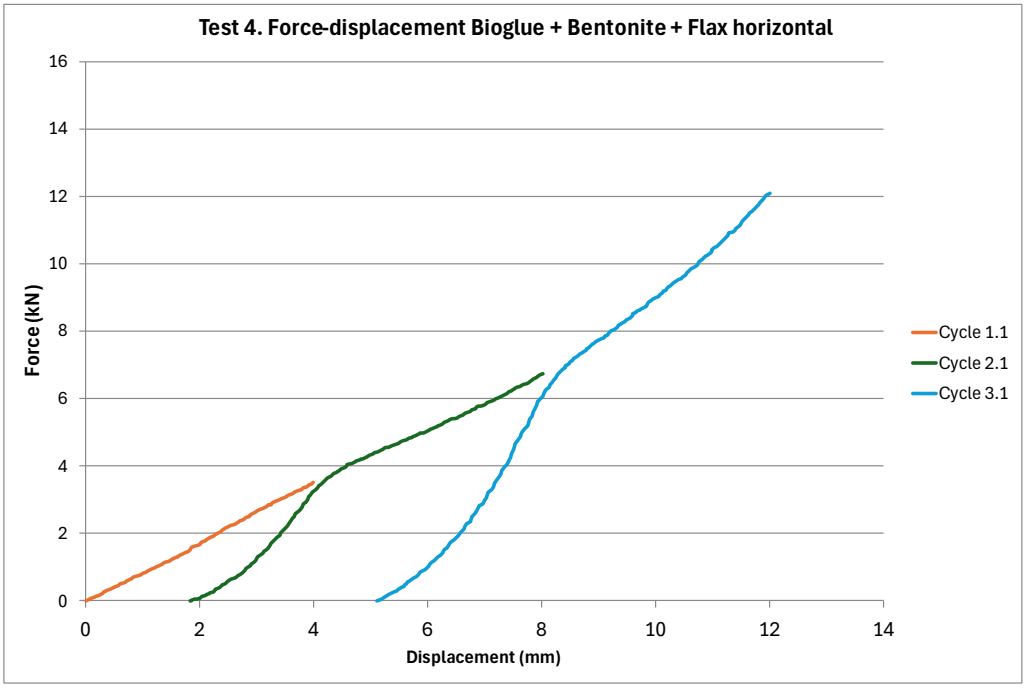


Figure E106. The force-displacement graph of compression test 4.

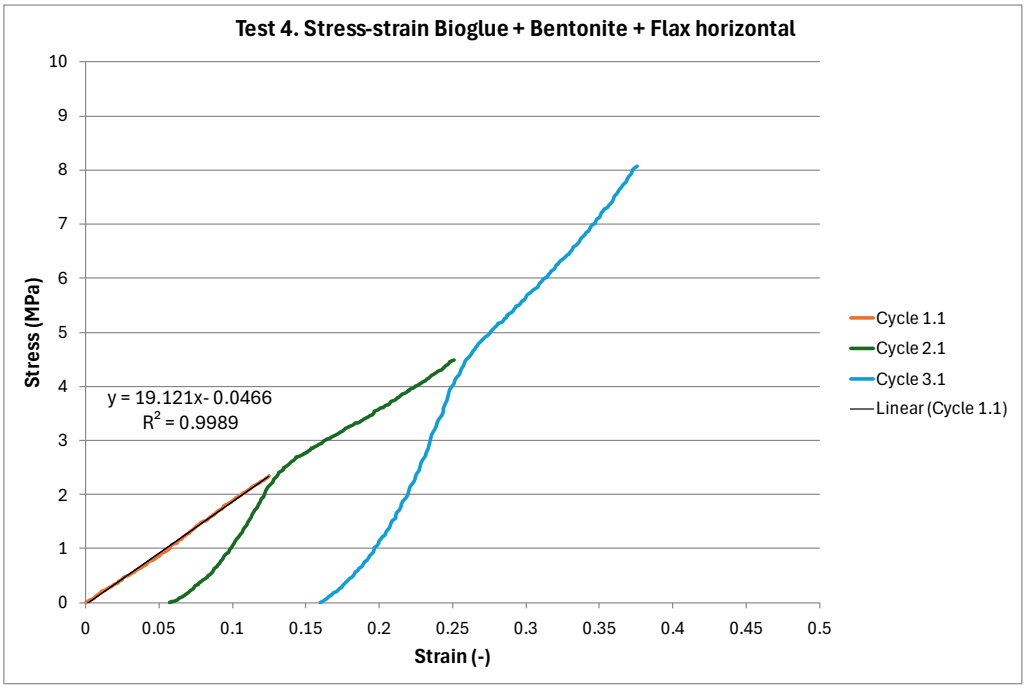


Figure E107. The stress-strain diagram of the three different cycles of compression test 4.

Figure E108 and Figure E109 present all the bio-glue with bentonite and flax compression tests together in a force-displacement and a stress-strain graph.

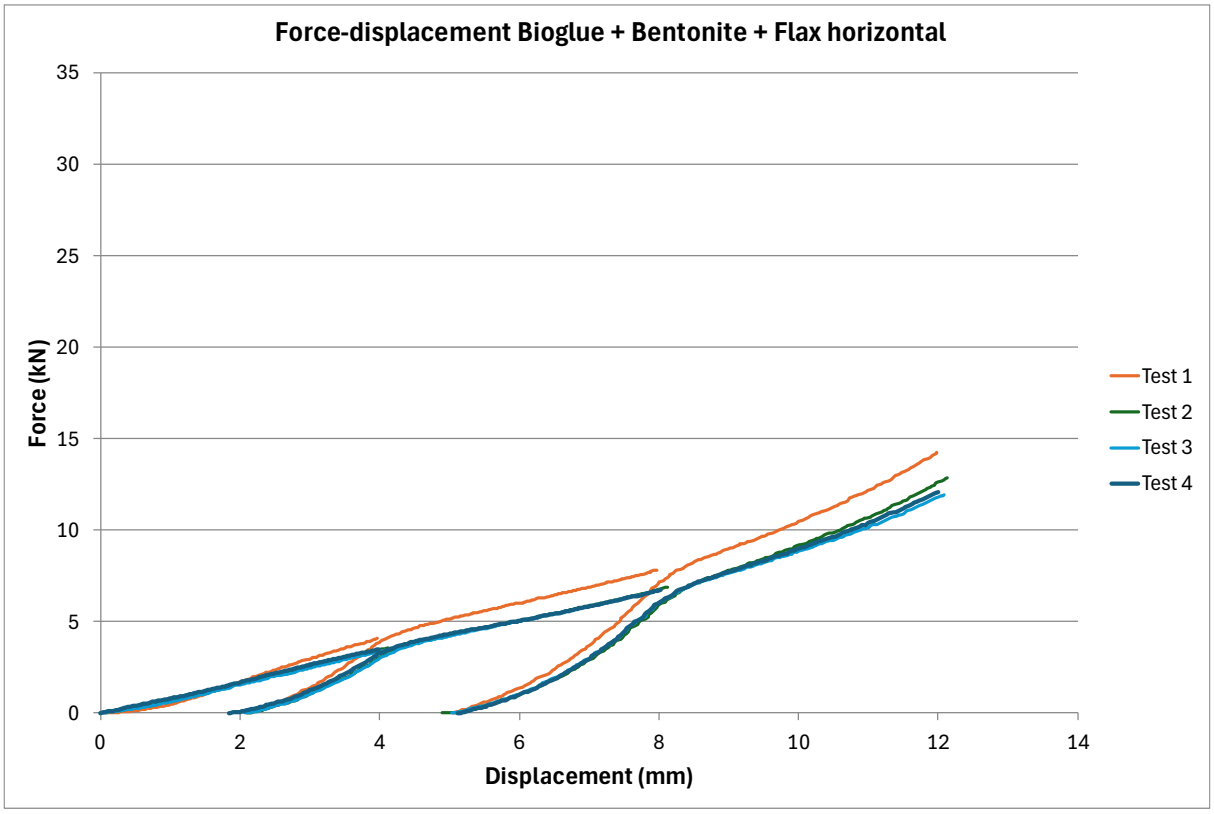


Figure E108. The force-displacement graph of all the bio-glue with bentonite and flax compression tests in the vertical orientation.

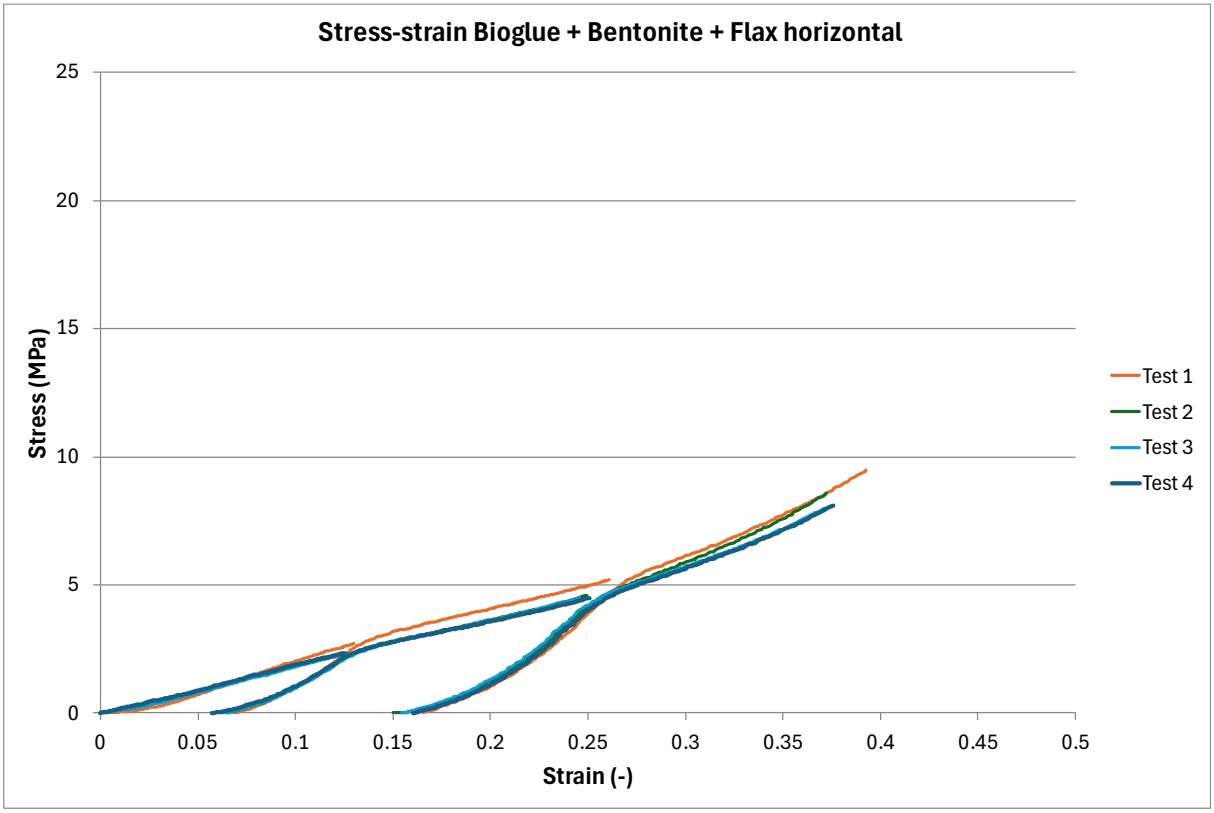


Figure E109. The stress-strain graph of all the bio-glue with bentonite and flax compression tests in the vertical orientation.

E.3.3.2 Vertical layer orientation

Figure E110 to Figure E118 show three bio-glue with bentonite and flax tests with a vertical layer orientation. Each test is accompanied with four photos during the test and two different graphs: the force-displacement and the stress-strain graph.

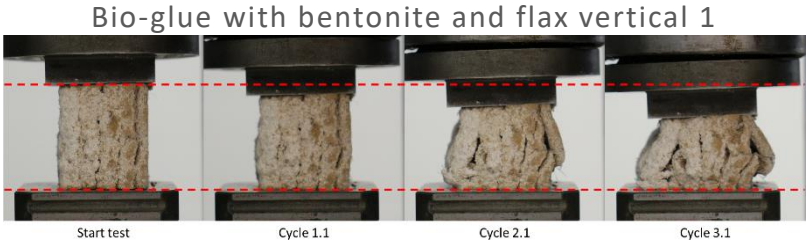


Figure E110. Four photos of compression test 1. One at the start of the test and one at the end of each cycle.

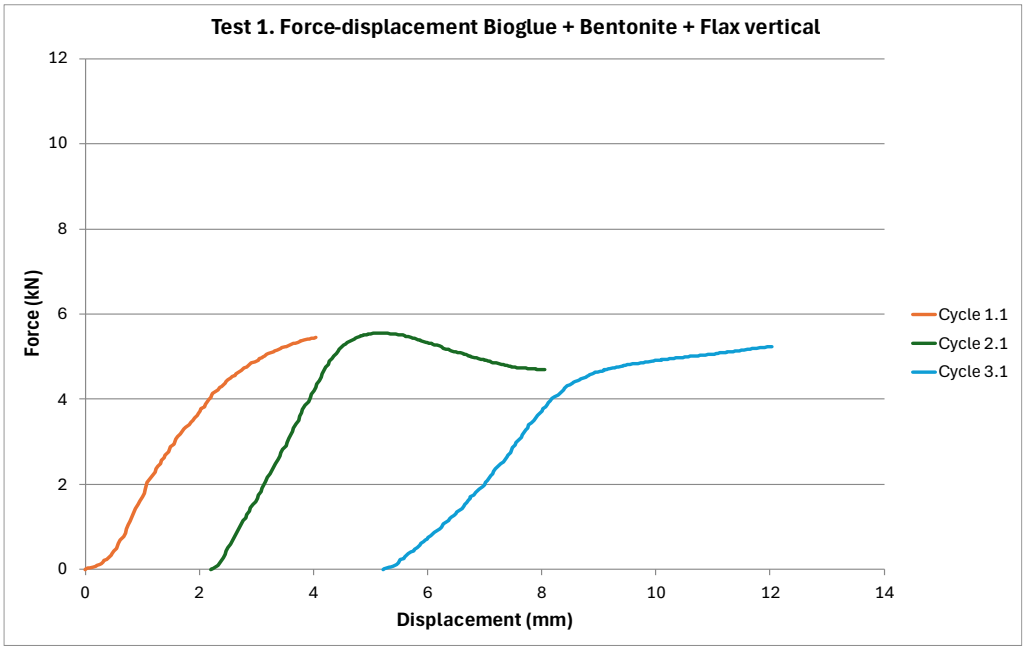


Figure E111. The force-displacement graph of compression test 1.

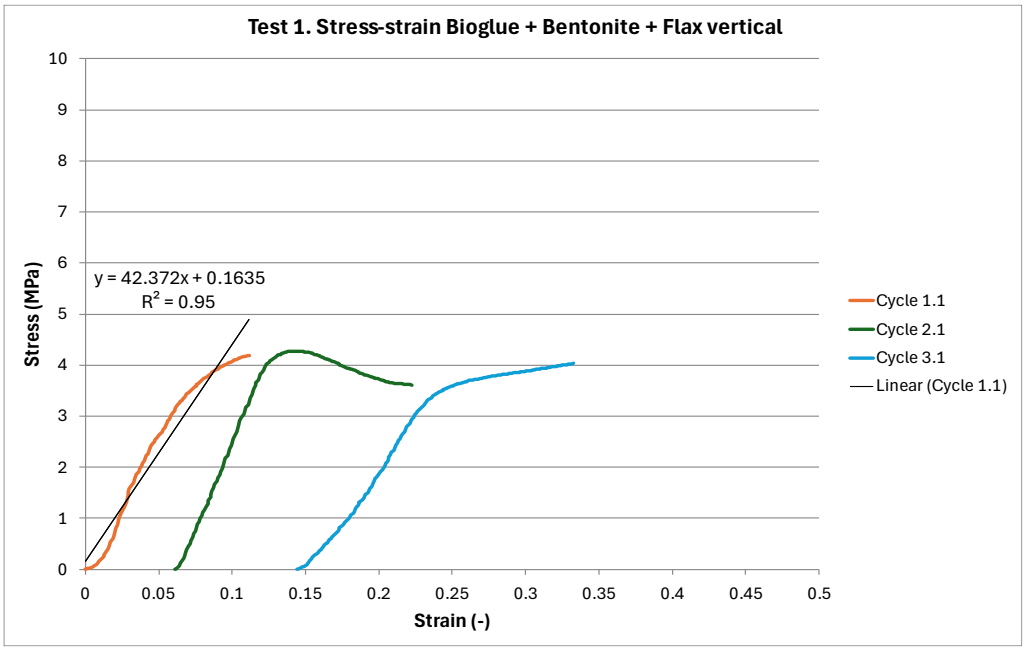


Figure E112. The stress-strain diagram of the three different cycles of compression test 1.

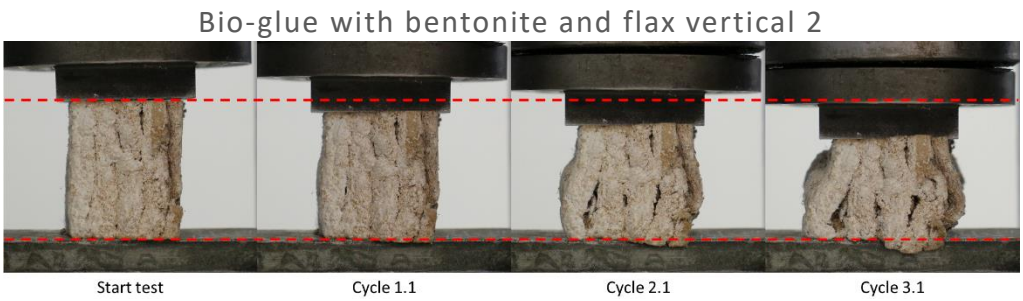


Figure E113. Four photos of compression test 2. One at the start of the test and one at the end of each cycle.

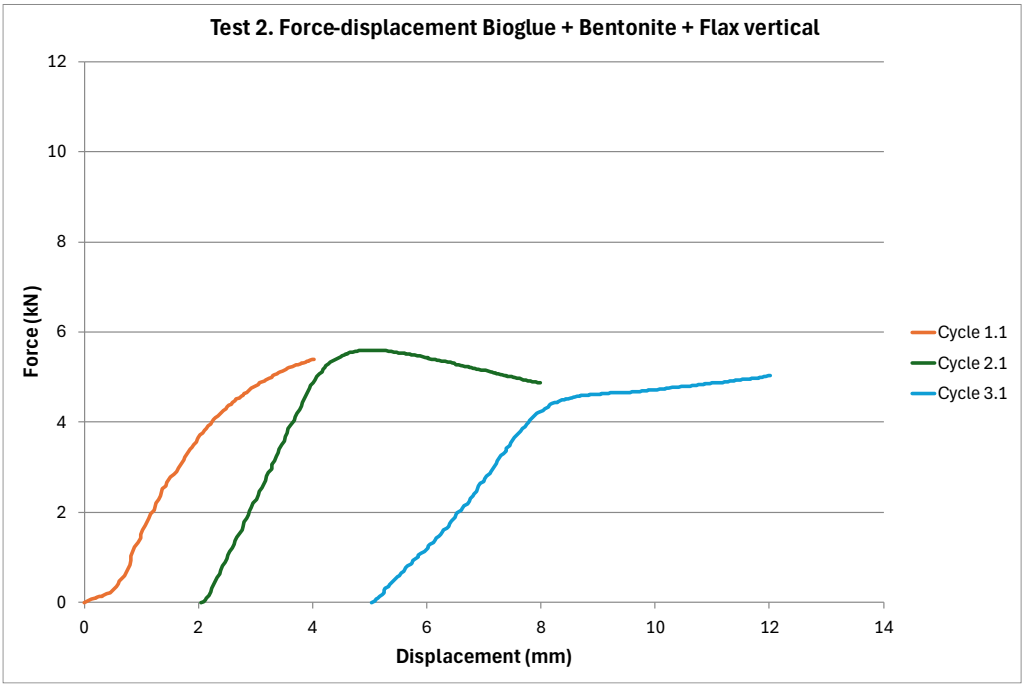


Figure E114. The force-displacement graph of compression test 2.

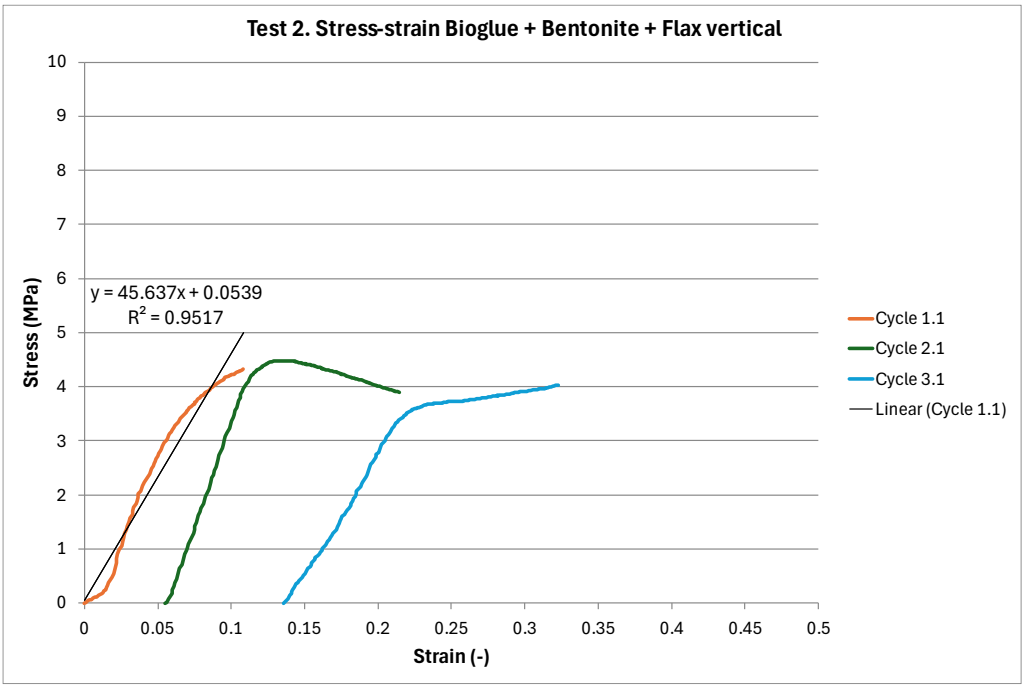


Figure E115. The stress-strain diagram of the three different cycles of compression test 2.

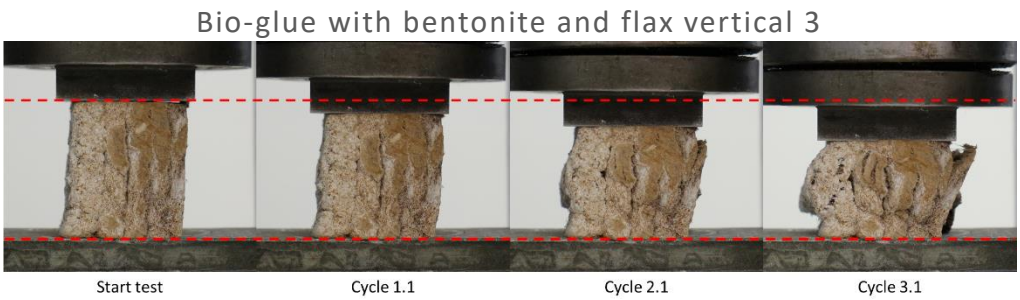


Figure E116. Four photos of compression test 3. One at the start of the test and one at the end of each cycle.

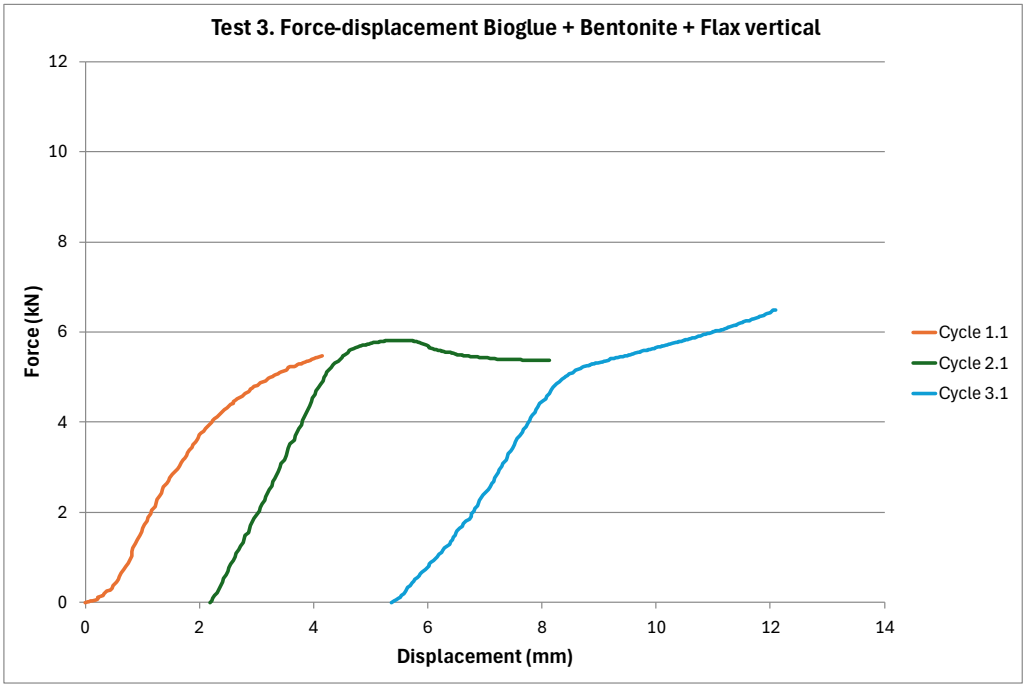


Figure E117. The force-displacement graph of compression test 3.

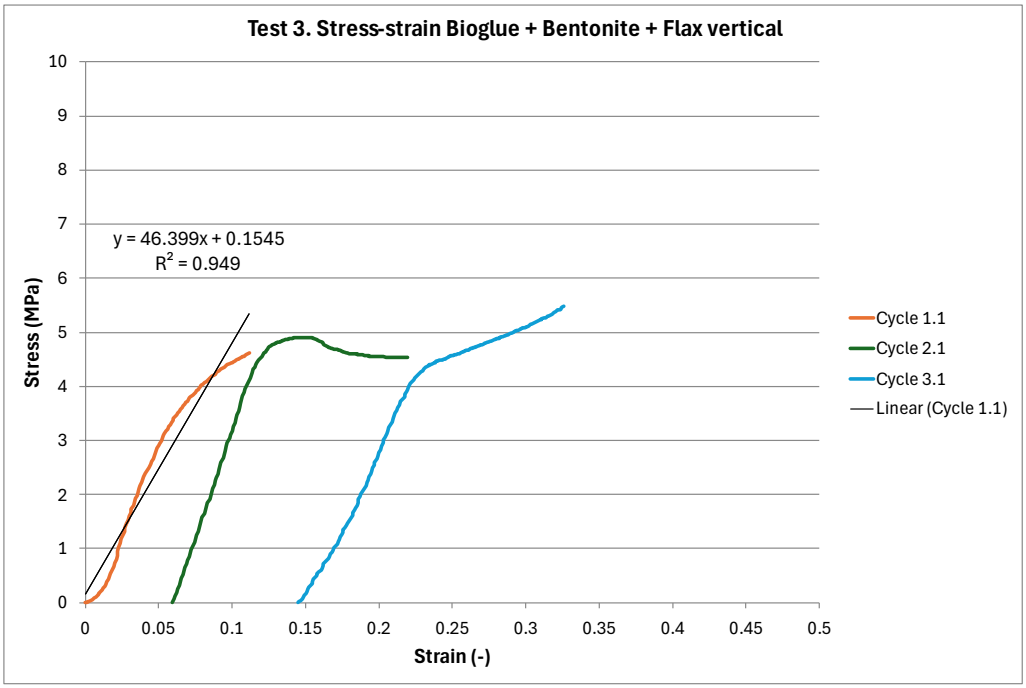


Figure E118. The stress-strain diagram of the three different cycles of compression test 3.

Figure E119 and Figure E120 present all bio-glue with bentonite and flax tests together in a force-displacement and a stress-strain graph.

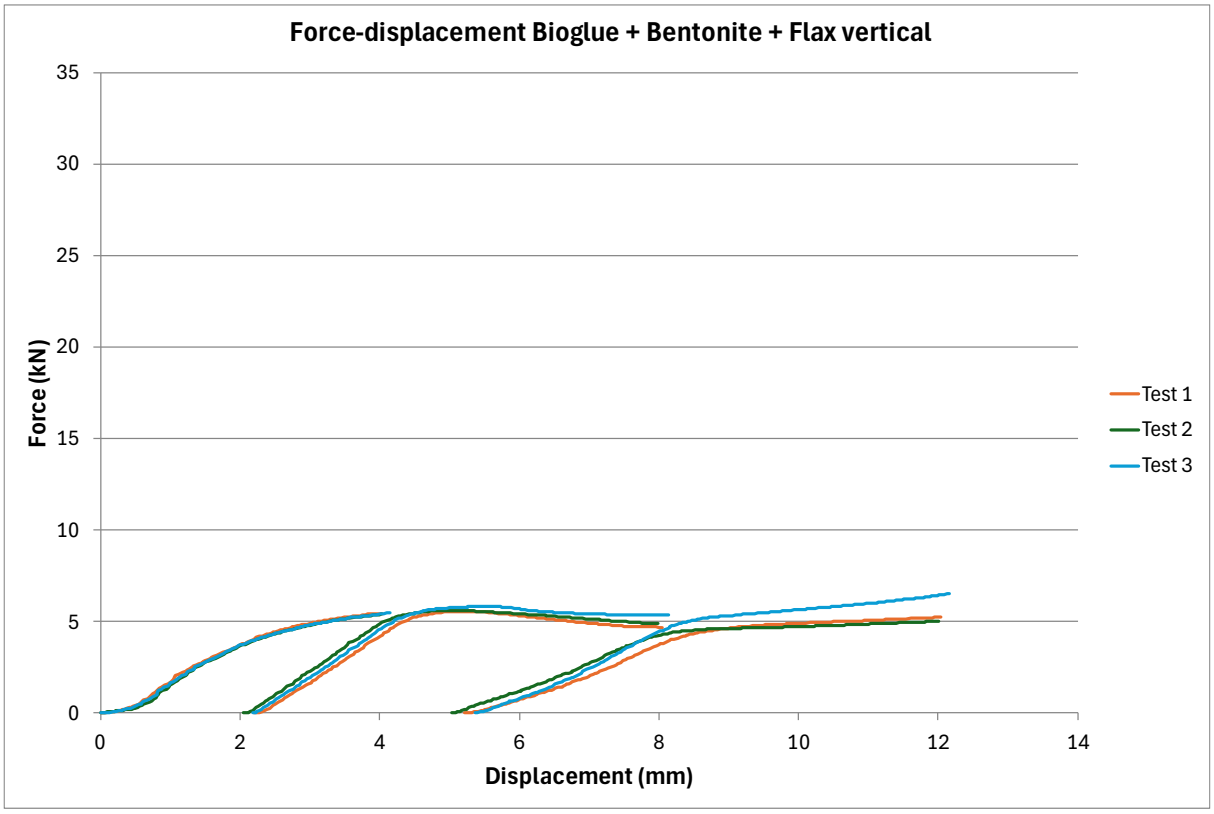


Figure E119. The force-displacement graph of all the bio-glue with bentonite and flax compression tests in the vertical orientation.

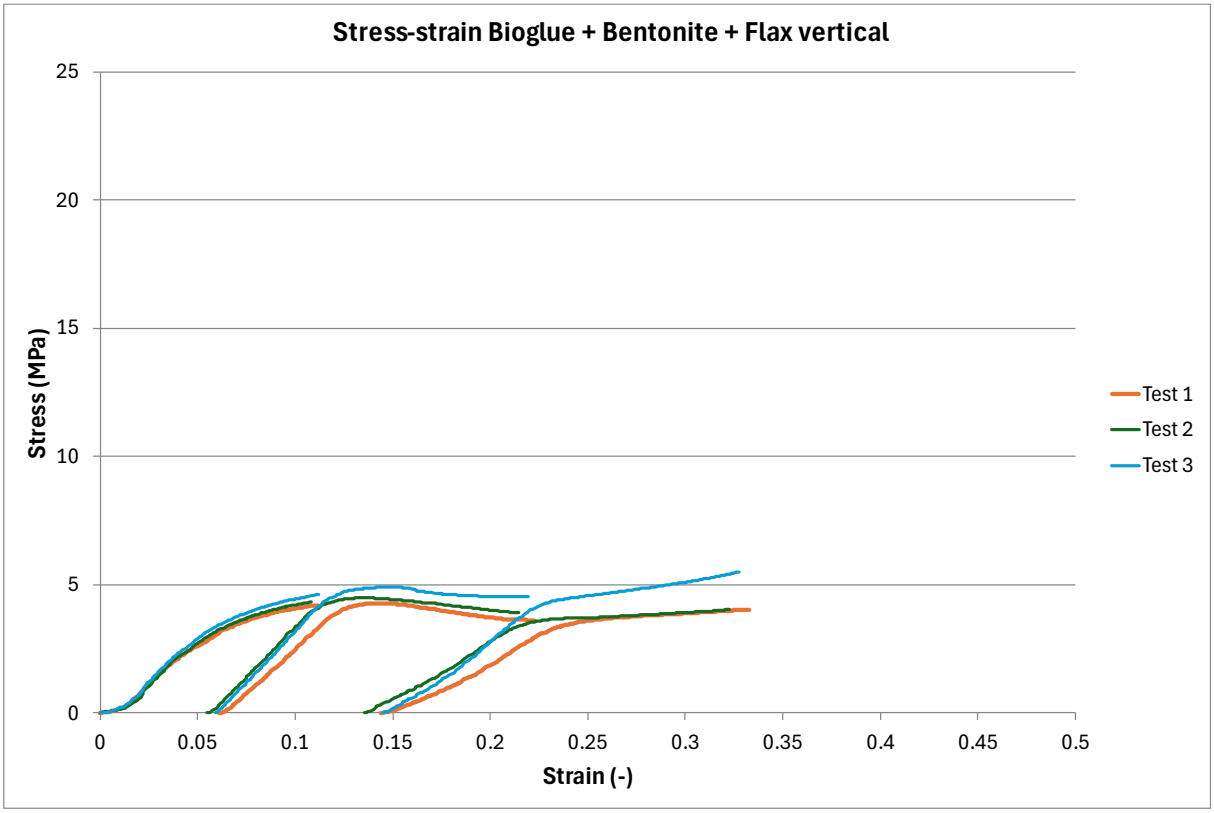


Figure E120. The stress-strain graph of all the bio-glue with bentonite and flax compression tests in the vertical orientation.

E.3.4 Summary bio-glue with additives bending test results

Table E10 and Table E11 present the results of the cycles 1.1, 2.1 and 3.1 of the bio-glue with bentonite tests are displayed for both the horizontal and vertical layer orientations respectively.

Table E10. The results of the four compression tests with the bio-glue with bentonite mix with the horizontal layer orientation.

Test	Days cured	Cycle 1.1			Cycle 2.1			Cycle 3.1		
		Force [kN]	Stress [Mpa]	Strain [-]	Force [kN]	Stress [Mpa]	Strain [-]	Force [kN]	Stress [Mpa]	Strain [-]
1	36	8.37	5.36	0.12	14.75	9.44	0.25	20.74	13.28	0.37
2	36	9.86	6.55	0.12	18.48	12.27	0.24	26.73	17.75	0.36
3	34	4.03	2.67	0.13	10.20	6.76	0.27	17.58	11.65	0.40
4	34	4.23	2.68	0.14	10.00	6.33	0.27	17.36	10.97	0.41

Table E11. The results of the three compression tests with the bio-glue with bentonite mix with the vertical layer orientation.

Test	Days cured	Cycle 1.1			Cycle 2.1			Cycle 3.1		
		Force [kN]	Stress [Mpa]	Strain [-]	Force [kN]	Stress [Mpa]	Strain [-]	Force [kN]	Stress [Mpa]	Strain [-]
1	35	8.77	6.34	0.12	10.89	7.87	0.21	11.16	8.07	0.34
2	35	8.16	5.59	0.11	9.78	6.69	0.18	9.43	6.46	0.33
3	34	6.08	5.07	0.12	7.73	6.45	0.23	8.10	6.76	0.35

Table E12 and Table E13 present the results of the cycles 1.1, 2.1 and 3.1 of the bio-glue with flax tests are displayed for both the horizontal and vertical layer orientations respectively.

Table E12. The results of the three compression tests with the bio-glue with flax mix with the horizontal layer orientation.

Test	Days cured	Cycle 1.1			Cycle 2.1			Cycle 3.1		
		Force [kN]	Stress [Mpa]	Strain [-]	Force [kN]	Stress [Mpa]	Strain [-]	Force [kN]	Stress [Mpa]	Strain [-]
1	35	2.91	1.99	0.13	5.87	4.02	0.23	12.84	8.79	0.40
2	35	3.35	2.13	0.13	7.14	4.54	0.26	14.06	8.95	0.39
3	35	3.43	2.20	0.13	7.72	4.94	0.26	15.30	9.78	0.39

Table E13. The results of the three compression tests with the bio-glue with flax mix with the vertical layer orientation.

Test	Days cured	Cycle 1.1			Cycle 2.1			Cycle 3.1		
		Force [kN]	Stress [Mpa]	Strain [-]	Force [kN]	Stress [Mpa]	Strain [-]	Force [kN]	Stress [Mpa]	Strain [-]
1	35	5.39	4.43	0.12	6.63	5.45	0.23	7.80	6.41	0.34
2	35	5.86	4.86	0.12	6.68	5.54	0.20	7.20	5.98	0.34
3	34	5.58	5.01	0.11	6.46	5.79	0.22	6.88	6.17	0.33

Table E14 and Table E15 provide the results of the cycles 1.1, 2.1 and 3.1 of the bio-glue with bentonite and flax tests are displayed for both the horizontal and vertical layer orientations respectively.

Table E14. The results of the four compression tests with the bio-glue with bentonite and flax mix with the horizontal layer orientation.

Test	Days cured	Cycle 1.1			Cycle 2.1			Cycle 3.1		
		Force [kN]	Stress [Mpa]	Strain [-]	Force [kN]	Stress [Mpa]	Strain [-]	Force [kN]	Stress [Mpa]	Strain [-]
1	31	4.09	2.72	0.13	7.82	5.20	0.26	14.29	9.50	0.39
2	31	3.55	2.36	0.13	6.86	4.57	0.25	12.88	8.57	0.37
3	31	3.45	2.30	0.13	6.73	4.49	0.25	11.97	7.98	0.37
4	31	3.50	2.34	0.12	6.73	4.49	0.25	12.10	8.08	0.38

Table E15. The results of the three compression tests with the bio-glue with bentonite and flax mix with the vertical layer orientation.

Test	Days cured	Cycle 1.1			Cycle 2.1			Cycle 3.1		
		Force [kN]	Stress [Mpa]	Strain [-]	Force [kN]	Stress [Mpa]	Strain [-]	Force [kN]	Stress [Mpa]	Strain [-]
1	31	5.44	4.19	0.11	5.55	4.28	0.14	5.23	4.03	0.33
2	31	5.40	4.32	0.11	5.60	4.48	0.14	5.04	4.03	0.32
3	31	5.47	4.61	0.11	5.81	4.90	0.15	6.52	5.50	0.33

Appendix F – Flexural tests

Bio-based 3D printing and testing of a digitally designed structural element



F.E. Pels Rijcken

Eindhoven, 19-06-2025

Contents

F.1 Dimensional properties of the beams 1
F.2 Results reference mixes 4
F.2.1 Wood glue 4
F.2.1.1 Horizontal layer orientation 4
F.2.1.2 Vertical layer orientation 11
F.2.2 Bio-glue 17
F.2.2.1 Horizontal layer orientation 17
F.2.2.2 Vertical layer orientation 25
F.2.3 Summary wood glue and bio-glue flexural test results 32
F.3 Results bio-glue with additives 33
F.3.1 Bio-glue with bentonite 33
F.3.1.1 Horizontal layer orientation 33
F.3.1.2 Vertical layer orientation 37
F.3.2 Bio-glue with flax 42
F.3.2.1 Horizontal layer orientation 42
F.3.2.2 Vertical layer orientation 46
F.3.3 Bio-glue with bentonite and flax 50
F.3.3.1 Horizontal layer orientation 50
F.3.3.2 Vertical layer orientation 54
F.3.4 Summary bio-glue + additives flexural test results 58

F.1 Dimensional properties of the beams

Table F1 to Table F10 give the relevant dimensions for the beams that are tested in bending. The beams are separated by material and the layer orientation.

Table F1. Wood glue beam dimensions for the horizontal layer orientation.

Beam	Length	Height			Width	
		Left	Middle	Right	Top	bottom
	[cm]	[cm]	[cm]	[cm]	[cm]	[cm]
1	25.5	3.2	3.4	3.4	3.4	4.2
2	25.5	3.2	3.1	3.3	3.5	4.2
3	26.0	3.3	3.5	3.4	3.6	4.5
5	24.2	3.6	3.6	3.8	3.7	4.5
6	24.0	3.4	3.5	3.5	3.5	3.9
13	25.5	2.9	3	3	3.6	4.2

Table F2. Wood glue beam dimensions after sawing and sanding for the vertical layer orientation. These beams were sawn and sanded to the cross-section was rectangular.

Beam	Length	Height			Width	
		Left	Middle	Right	Top	bottom
	[cm]	[cm]	[cm]	[cm]	[cm]	[cm]
7	24.2	3.6	3.6	3.6	3.5	3.5
8	23.6	4.0	4.0	4.0	3.3	3.5
10	24.8	3.8	3.8	3.7	2.9	2.7
11	25.1	4.1	4.0	4.0	2.9	3.0
12	25.1	3.6	3.6	3.7	2.9	2.8

Table F3. Bio-glue beam dimensions for the horizontal layer orientation.

Beam	Length	Height			Width	
		Left	Middle	Right	Top	bottom
	[cm]	[cm]	[cm]	[cm]	[cm]	[cm]
1	25.5	3	3.1	3	3.2	4.1
2	26.0	3.1	3.3	3	3.9	4.5
3	25.6	3.2	3.4	3	3.9	4.5
4	26.7	3.2	3.4	3.5	4	4.8
5	26.6	3.3	3.2	3.1	4	4.5
12	24.0	3.4	3.5	3.3	3.5	4.1
14	23.7	3.1	3.2	3.2	3.4	4.0

Table F4. Bio-glue beam dimensions after sawing and sanding for the vertical layer orientation. The first row of the height is the height on the larger side and the second row is the height on the smallest side, since the cross-section is a trapezoid.

Beam	Length	Height			Width	
		Left	Middle	Right	Top	bottom
	[cm]	[cm]	[cm]	[cm]	[cm]	[cm]
6	26.5	4.2 3.9	4.4 3.9	4.5 4.0	3.3	3.2
7	26.5	4.2 3.9	4.4 4.1	4.4 3.9	3.5	3.5
8	26.6	4.6 4.1	4.6 4.0	4.5 3.9	3.5	3.4
10	23.8	3.5 3.4	3.5 3.3	3.5 3.2	3.2	3.4
11	23.7	3.4 3.3	3.3 3.2	3.3 3.0	3.2	3.0
13	23.3		4 3.5		3.2	3.2

Table F5. Bio-glue with bentonite beam dimensions for the horizontal layer orientation.

Beam	Length	Height			Width	
		Left	Middle	Right	Top	bottom
	[cm]	[cm]	[cm]	[cm]	[cm]	[cm]
1	26.0	3.4	3.4	3.4	3.7	4.6
5	26.1	3.2	3.4	3.3	4.0	4.9
6	26.5	3.2	3.5	3.2	4.1	5.0

Table F6. Bio-glue with bentonite beam dimensions for the vertical layer orientation. The first row of the height is the height on the larger side and the second row is the height on the smallest side, since the cross-section is a trapezoid.

Beam	Length	Height			Width
		Left	Middle	Right	
	[cm]	[cm]	[cm]	[cm]	[cm]
2	25.5	4.5	4.6	4.6	3.8
		4.1	4.1	4.1	
3	26.1	4.8	4.8	4.7	3.7
		4.2	4.2	4.1	
7	26.2	4.9	5.0	4.8	3.3
		4.1	3.9	4.0	
8	26.2	5.0	5.0	4.9	3.3
		4.0	3.9	3.9	

Table F7. Bio-glue with flax beam dimensions for the horizontal layer orientation.

Beam	Length	Height			Width	
		Left	Middle	Right	Top	bottom
	[cm]	[cm]	[cm]	[cm]	[cm]	[cm]
1	26.6	3.5	3.6	3.4	4.1	4.7
2	2.65	3.3	3.4	3.3	3.9	4.8
3	27	3.5	3.6	3.4	4.0	4.7

Table F8. Bio-glue with flax beam dimensions for the vertical layer orientation. The first row of the height is the height on the larger side and the second row is the height on the smallest side, since the cross-section is a trapezoid.

Beam	Length	Height			Width
		Left	Middle	Right	
	[cm]	[cm]	[cm]	[cm]	[cm]
2	26.5	4.8	4.7	4.5	3.5
		4.0	4.0	4.1	
7	26.5	4.9	5.0	4.8	3.3
		3.7	4.1	4.1	
8	26.5	5.0	5.0	4.7	3.4
		3.8	4.0	4.0	

Table F9. Bio-glue with bentonite and flax beam dimensions for the horizontal layer orientation.

Beam	Length	Height			Width	
		Left	Middle	Right	Top	bottom
	[cm]	[cm]	[cm]	[cm]	[cm]	[cm]
1	26.2	3.2	3.4	3.2	3.9	4.7
2	25.7	3.2	3.4	3.4	3.9	4.6
3	26.3	3.2	3.3	3.2	3.9	4.4

Table F10. Bio-glue with bentonite and flax beam dimensions for the vertical layer orientation. The first row of the height is the height on the larger side and the second row is the height on the smallest side, since the cross-section is a trapezoid.

Beam	Length [cm]	Height Left [cm]	Height Middle [cm]	Height Right [cm]	Width [cm]
2	25.8	4.5 3.4	4.6 3.4	4.4 3.3	3.5
7	26.6	4.8 4.0	4.5 4.1	4.5 4.0	3.5
8	26.7	4.8 3.9	4.5 4.2	4.1 4.0	3.6

F.2 Results reference mixes

F.2.1 Wood glue

F.2.1.1 Horizontal layer orientation

In Figure F1 to Figure F18 show six wood glue tests with a horizontal layer orientation. Each test is accompanied with four photos during the test and two different graphs: the force-displacement and the stress-strain graph.

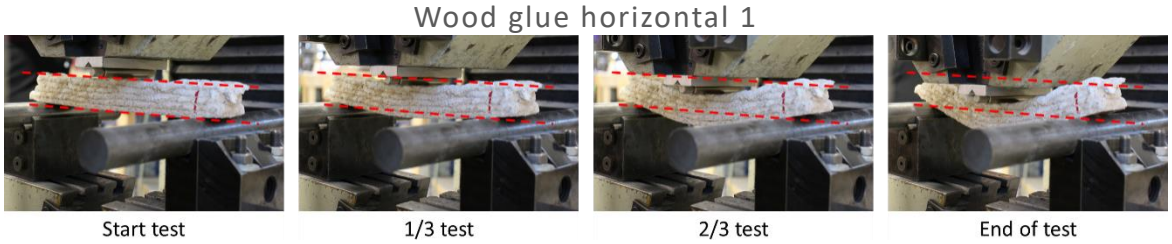


Figure F1. Four photos of process of the flexural test wood glue horizontal 1. The red lines indicate the original position of the beam at the start of the test.

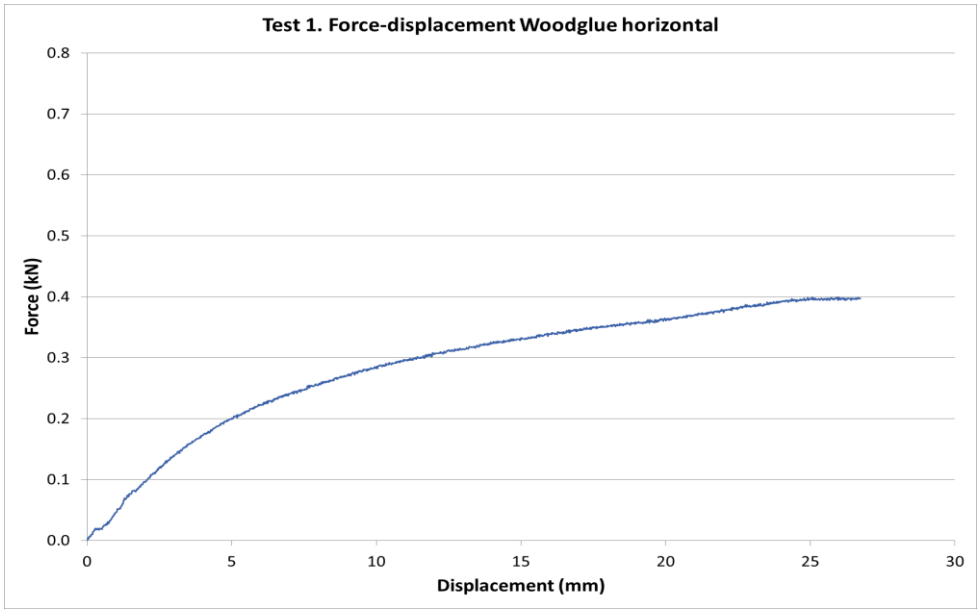


Figure F2. The force-displacement graph of flexural test wood glue horizontal 1.

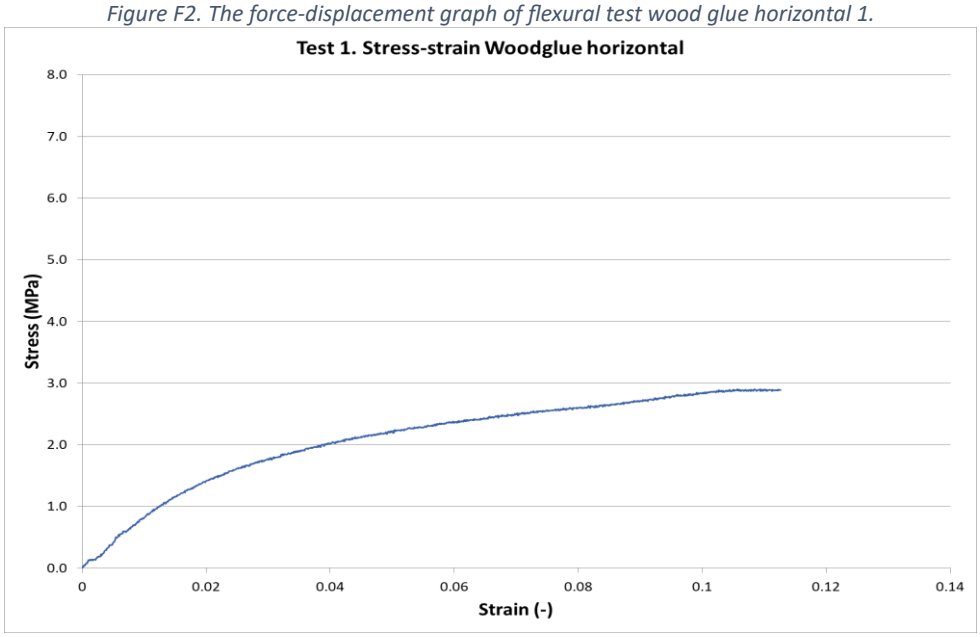


Figure F3. The stress-strain diagram of flexural test wood glue horizontal 1.

Wood glue horizontal 2

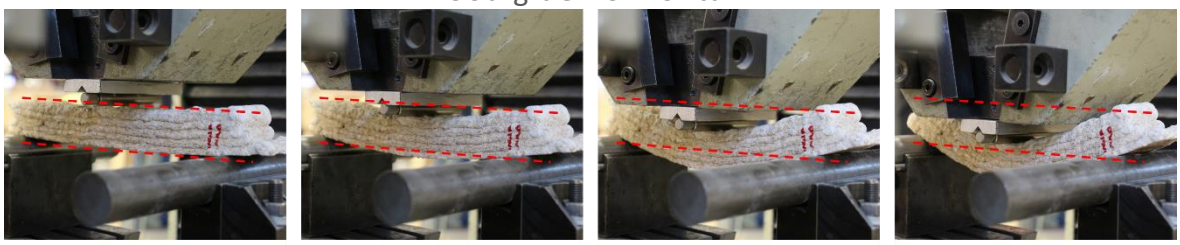


Figure F4. Four photos of the flexural test wood glue horizontal 2. The red lines indicate the original position of the beam at the start of the test.



Figure F5. The force-displacement graph of flexural test wood glue horizontal 2.

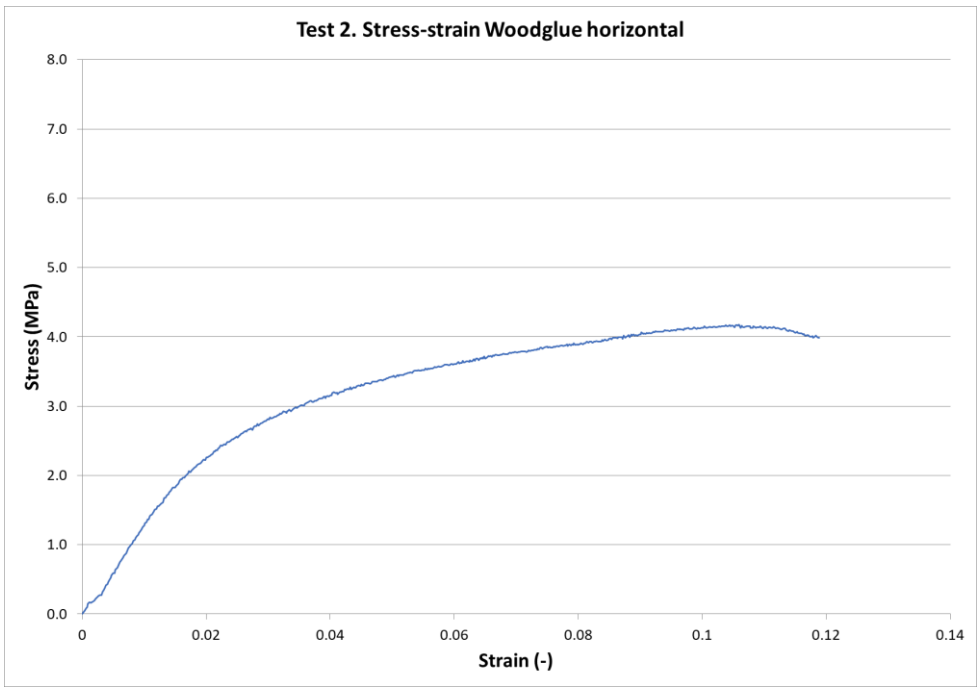


Figure F6. The stress-strain diagram of flexural test wood glue horizontal 2.

Wood glue horizontal 3

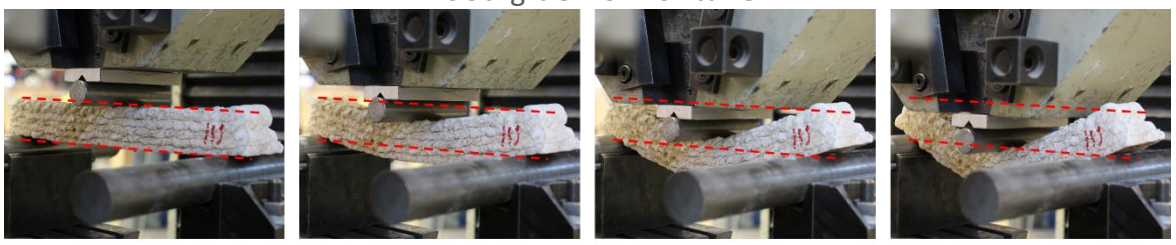


Figure F7. Four photos of the flexural test wood glue horizontal 3. The red lines indicate the original position of the beam at the start of the test.

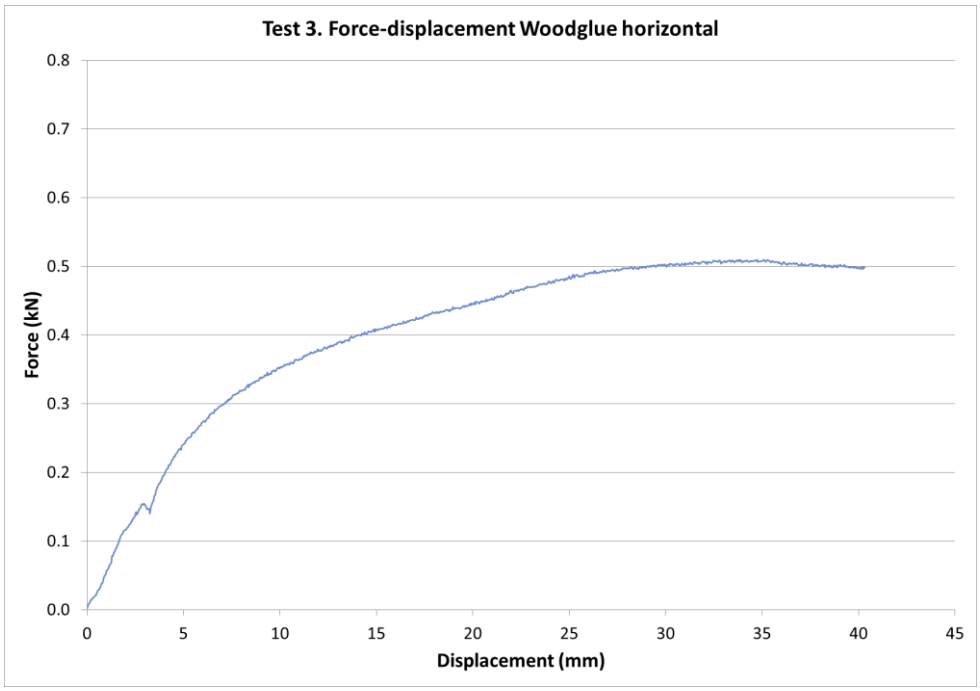


Figure F8. The force-displacement graph of flexural test wood glue horizontal 3.

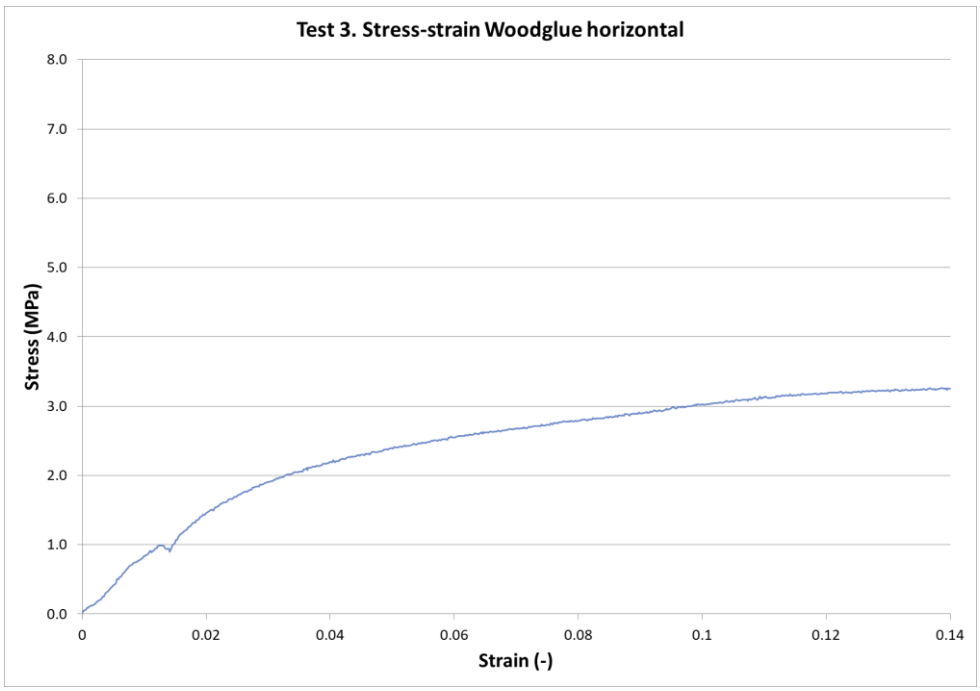


Figure F9. The stress-strain diagram of flexural test wood glue horizontal 3.

Wood glue horizontal 4

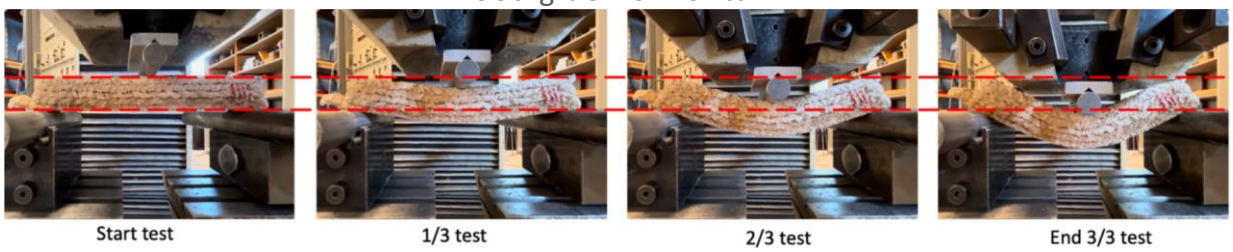


Figure F10. Four photos of the flexural test wood glue horizontal 4. The red lines indicate the original position of the beam at the start of the test.

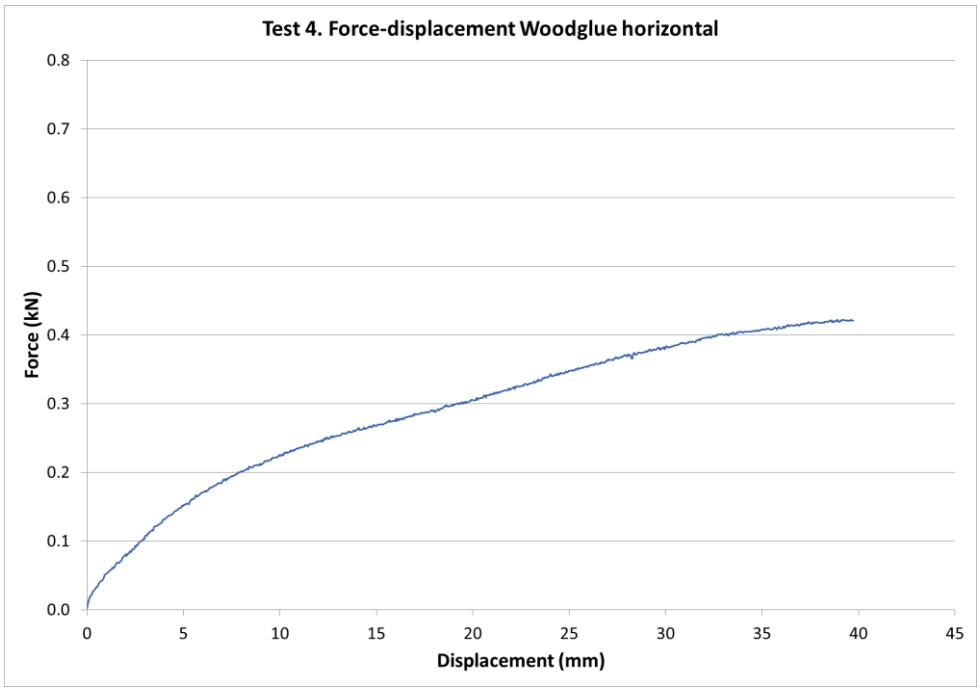


Figure F11. The force-displacement graph of flexural test wood glue horizontal 4.

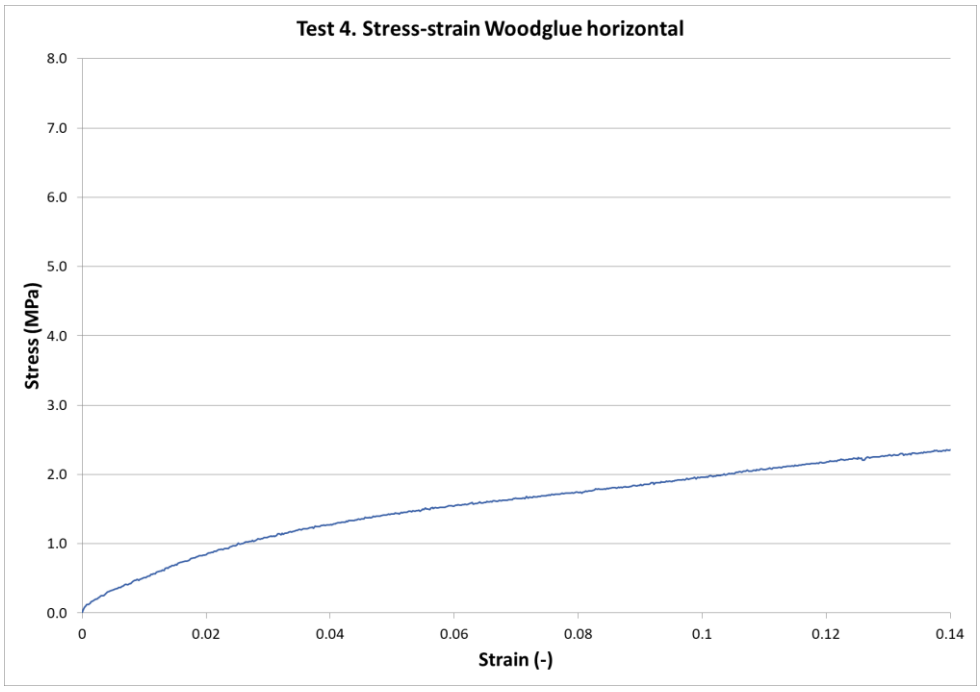


Figure F12. The stress-strain diagram of flexural test wood glue horizontal 4.

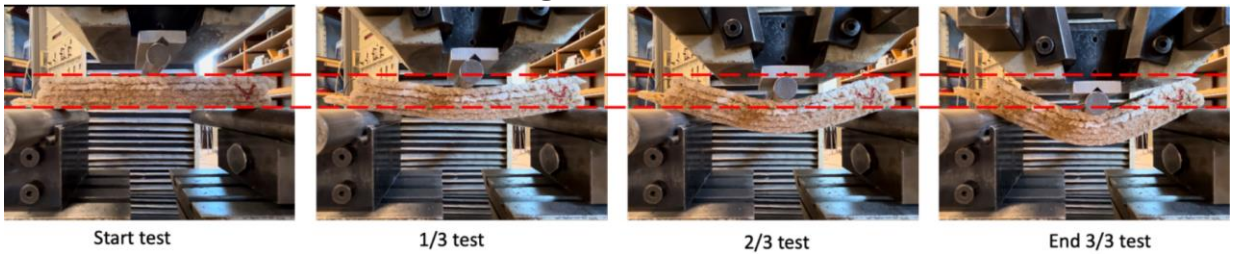


Figure F13. Four photos of the flexural test wood glue horizontal 5. The red lines indicate the original position of the beam at the start of the test.

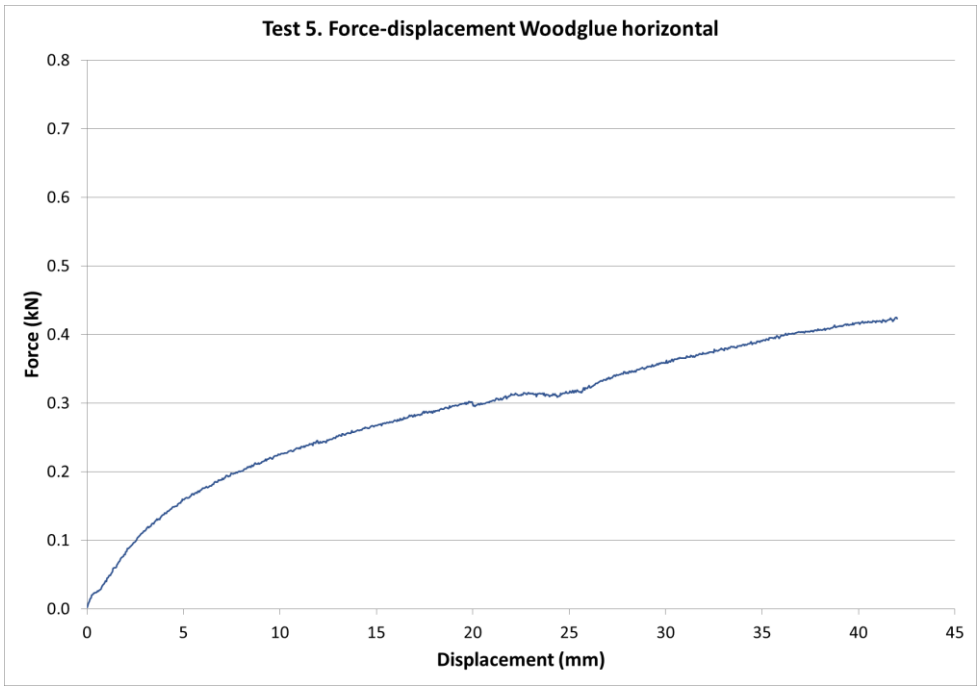


Figure F14. The force-displacement graph of flexural test wood glue horizontal 5.

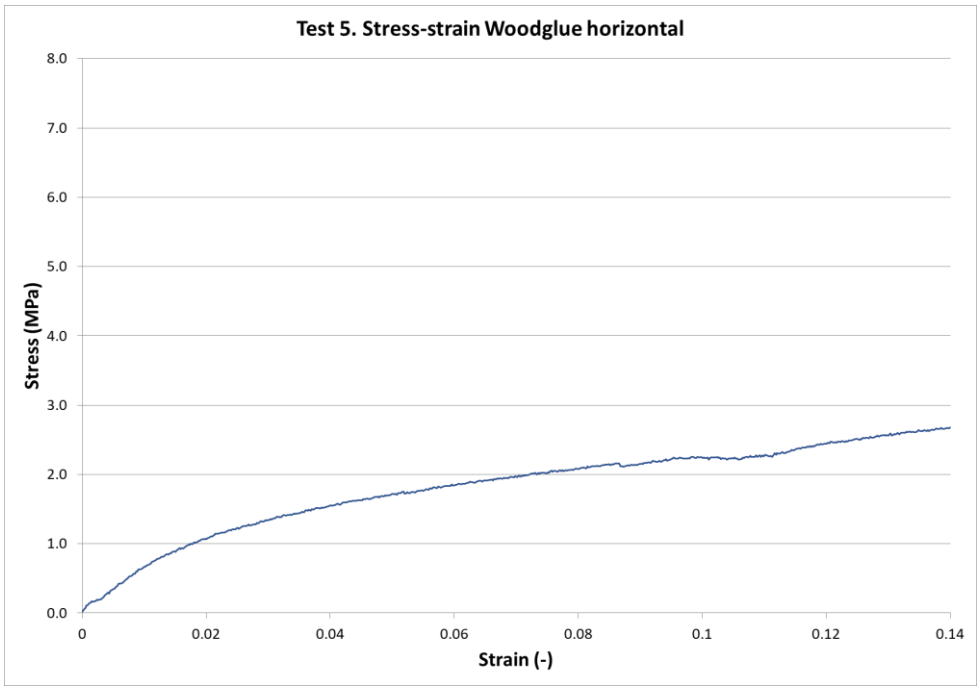


Figure F15. The stress-strain diagram of flexural test wood glue horizontal 5.

Wood glue horizontal 6

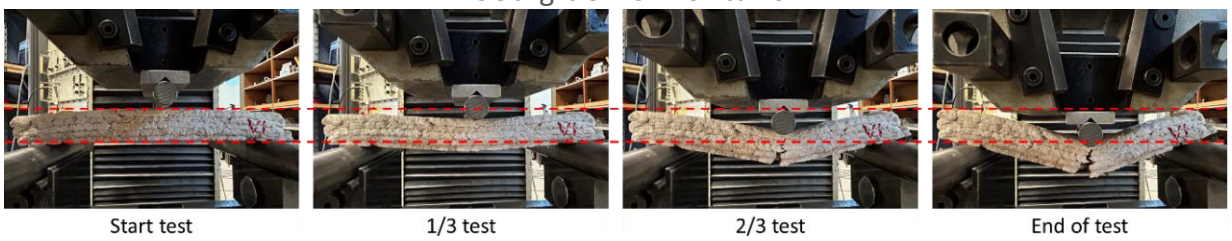


Figure F16. Four photos of the flexural test wood glue horizontal 6. The red lines indicate the original position of the beam at the start of the test.

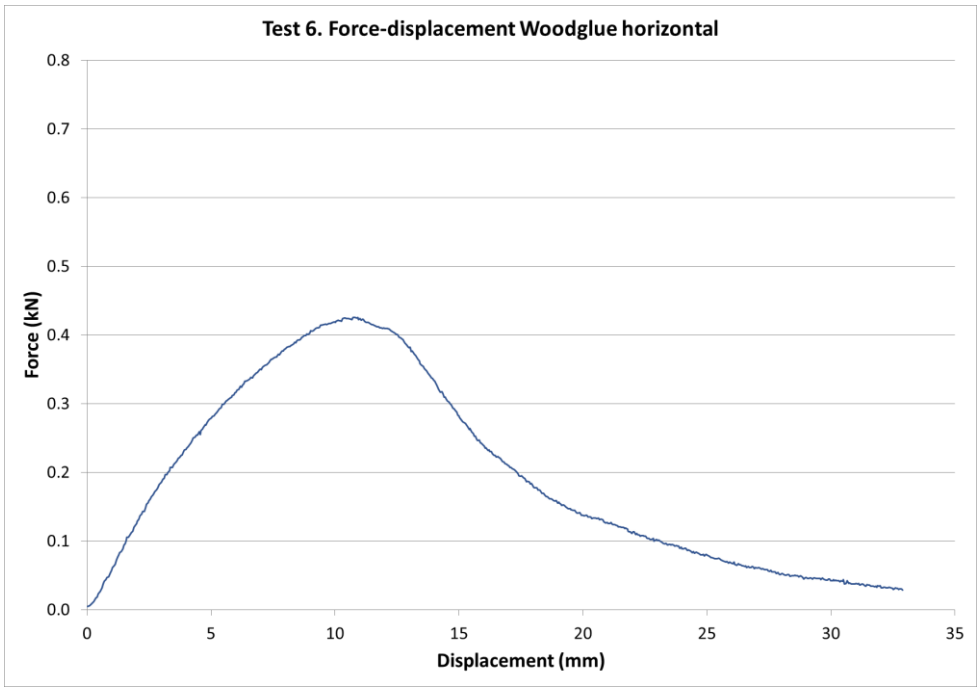


Figure F17. The force-displacement graph of flexural test wood glue horizontal 6.

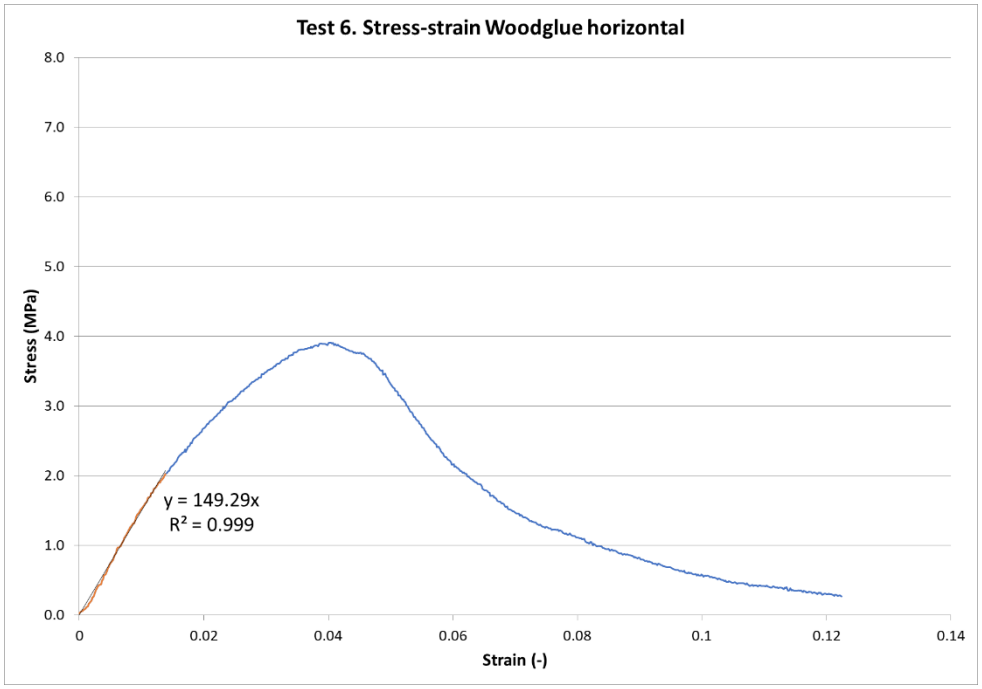


Figure F18. The stress-strain diagram of flexural test wood glue horizontal 6.

Figure F19 and Figure F20 present all six wood glue tests together in a force-displacement and a stress-strain graph.



Figure F19. The force-displacement graph of all the wood glue flexural tests in the horizontal orientation.

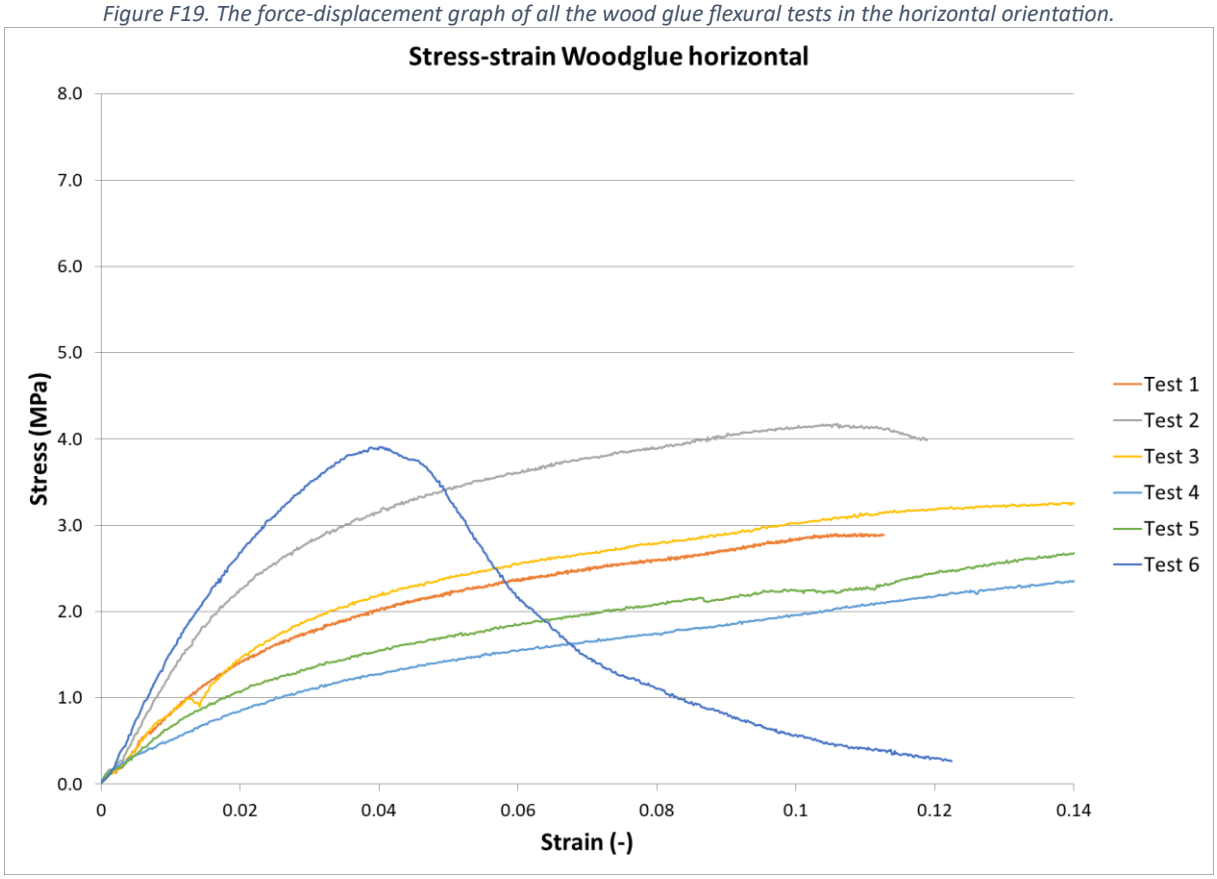


Figure F20. The stress-strain graph of all the wood glue flexural tests in the horizontal orientation.

F.2.1.2 Vertical layer orientation

Figure F21 to Figure F35 show five wood glue tests with a vertical layer orientation. Each test is accompanied with four photos during the test and two different graphs: the force-displacement and the stress-strain graph.

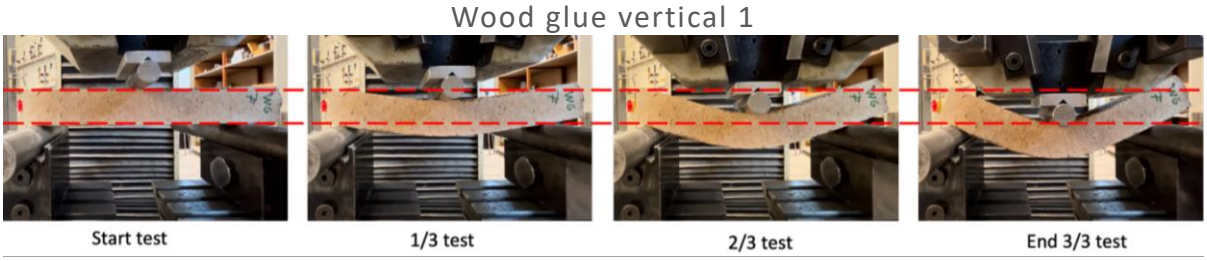


Figure F21. Four photos of the flexural test wood glue vertical 1. The red lines indicate the original position of the beam at the start of the test.

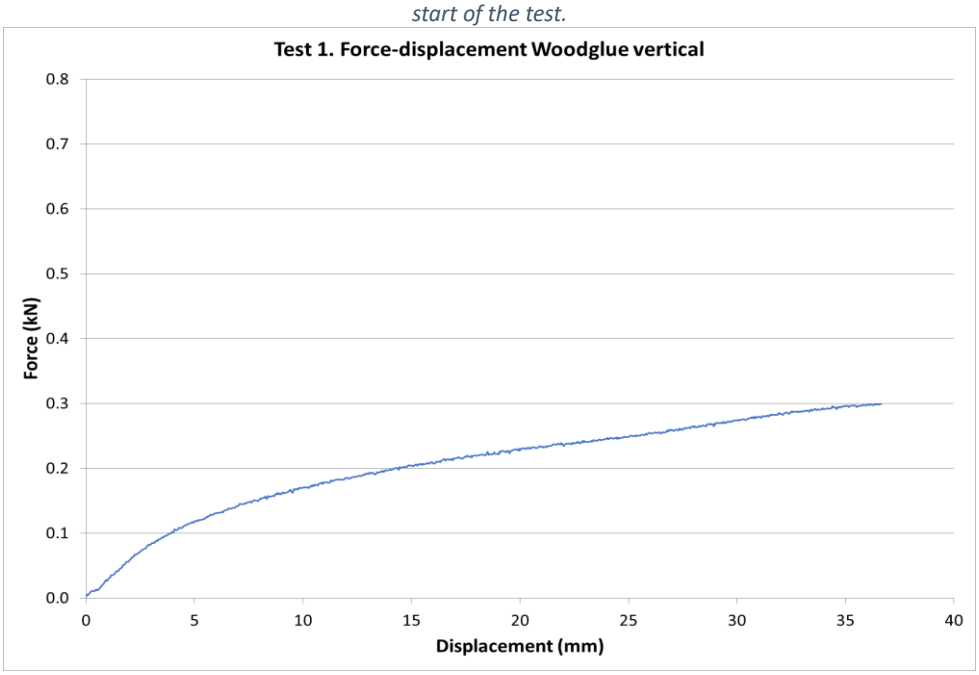


Figure F22. The force-displacement graph of flexural test wood glue vertical 1.

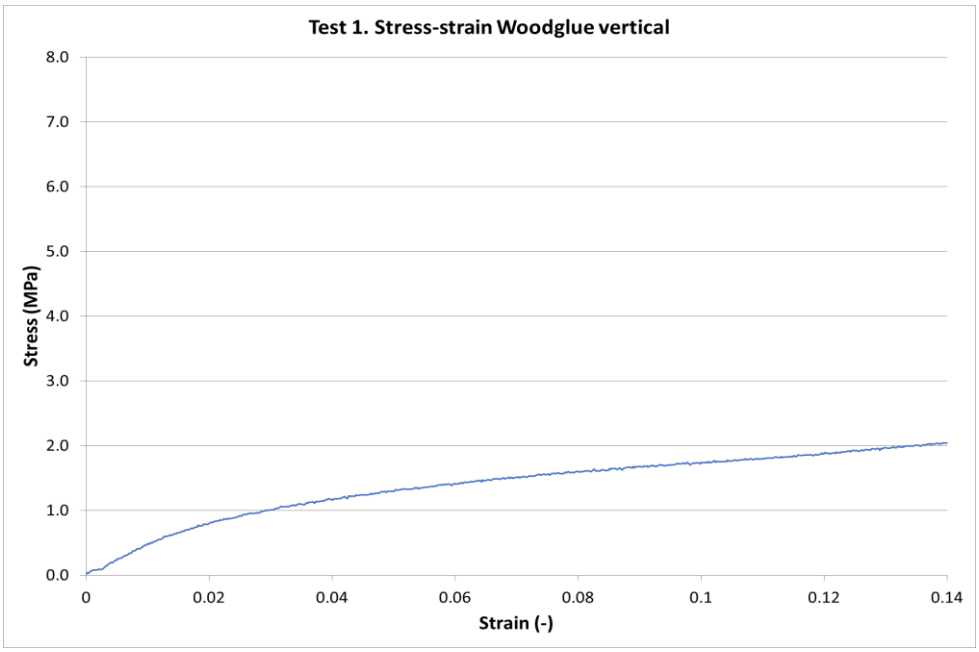


Figure F23. The stress-strain diagram of flexural test wood glue vertical 1.

Wood glue vertical 2

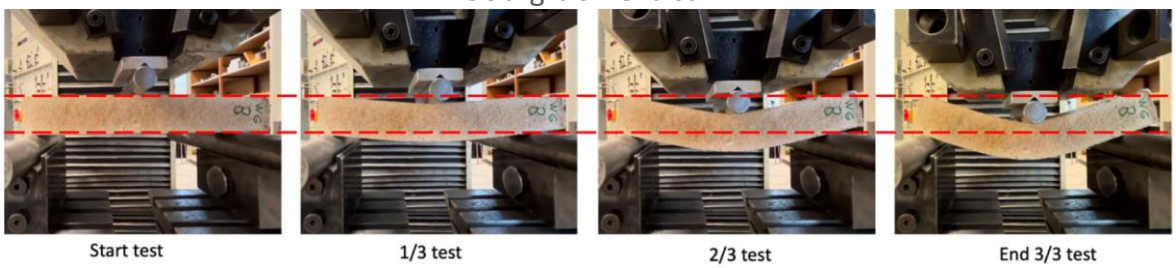


Figure F24. Four photos of the flexural test wood glue vertical 2. The red lines indicate the original position of the beam at the start of the test.



Figure F25. The force-displacement graph of flexural test wood glue vertical 2.

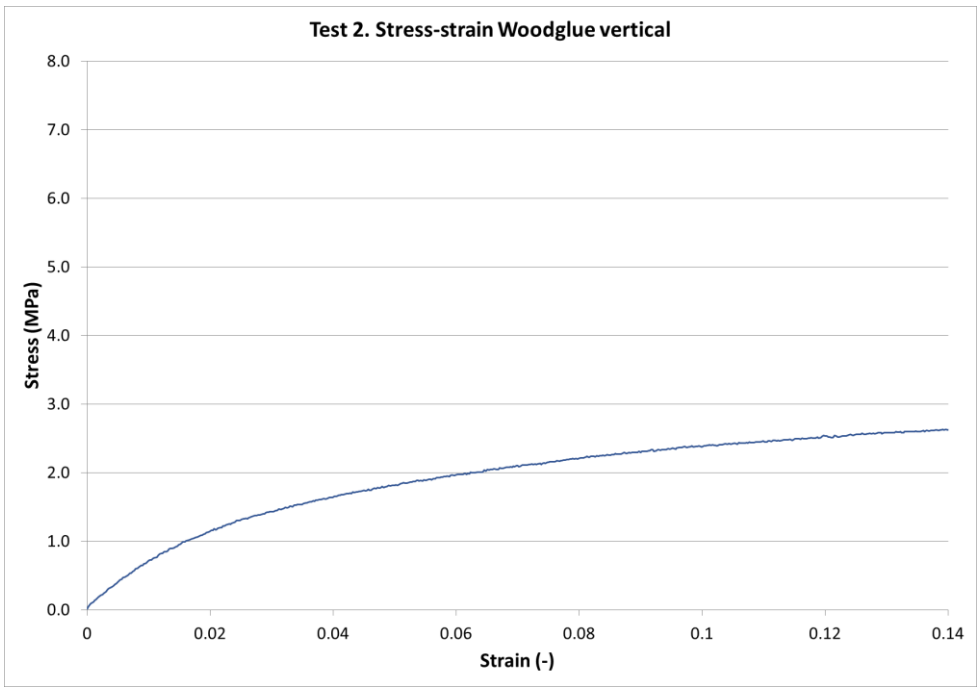


Figure F26. The stress-strain diagram of flexural test wood glue vertical 2.

Wood glue vertical 3

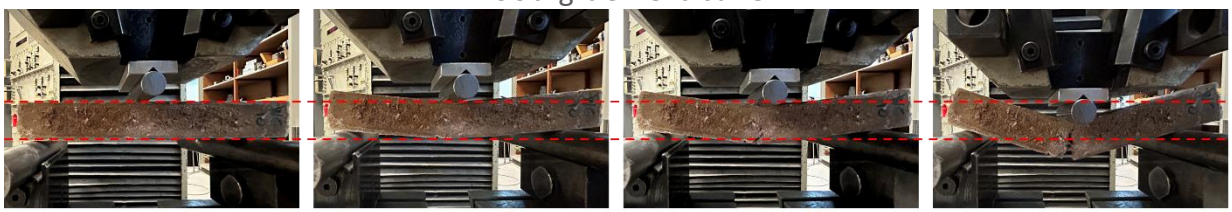


Figure F27. Four photos of the flexural test wood glue vertical 3. The red lines indicate the original position of the beam at the start of the test.



Figure F28. The force-displacement graph of flexural test wood glue vertical 3.

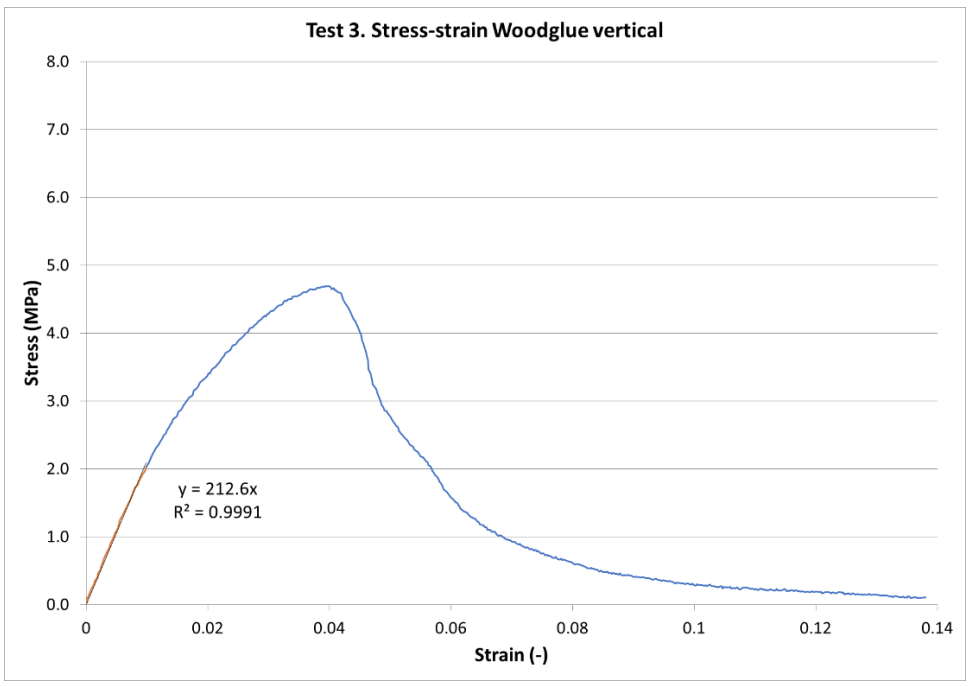


Figure F29. The stress-strain diagram of flexural test wood glue vertical 3.

Wood glue vertical 4



Figure F30. Four photos of the flexural test wood glue vertical 4. The red lines indicate the original position of the beam at the start of the test.



Figure F31. The force-displacement graph of flexural test wood glue vertical 4.

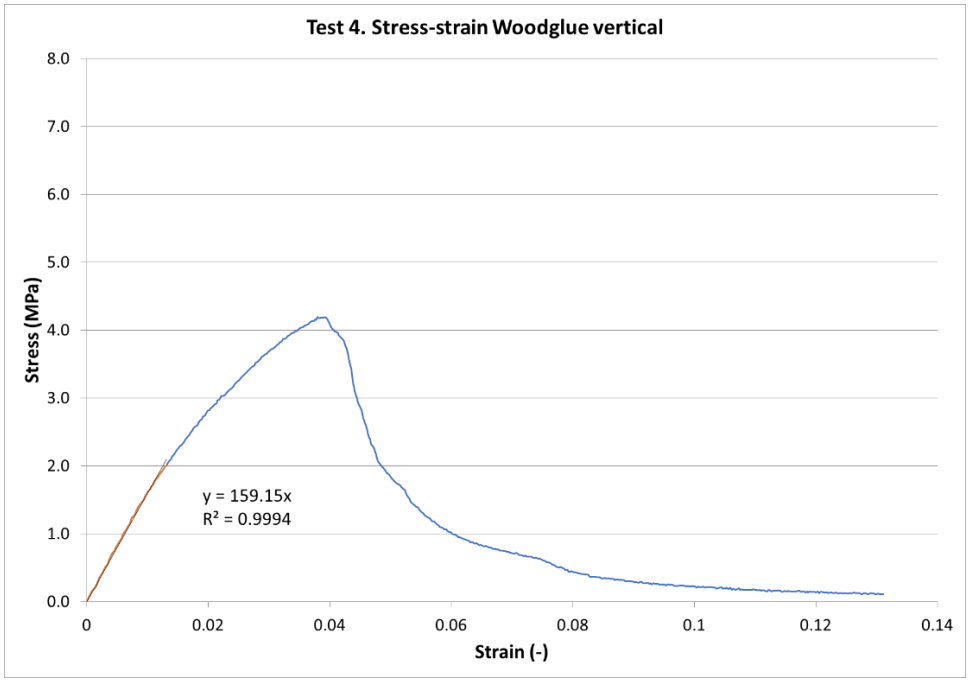


Figure F32. The stress-strain diagram of flexural test wood glue vertical 4.

Wood glue vertical 5

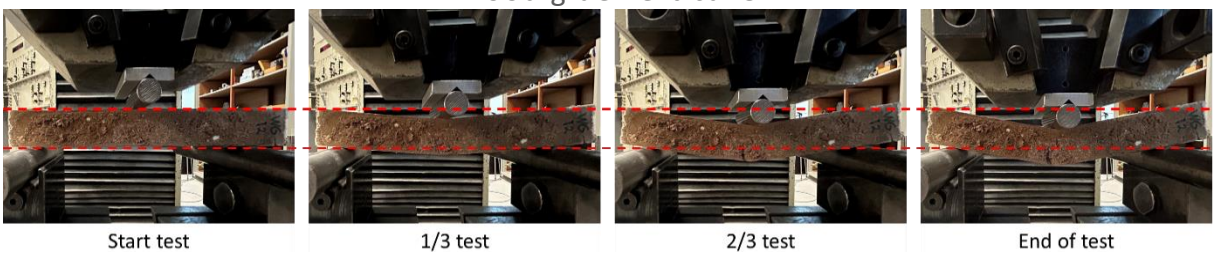


Figure F33. Four photos of the flexural test wood glue vertical 5. The red lines indicate the original position of the beam at the start of the test.



Figure F34. The force-displacement graph of flexural test wood glue vertical 5.

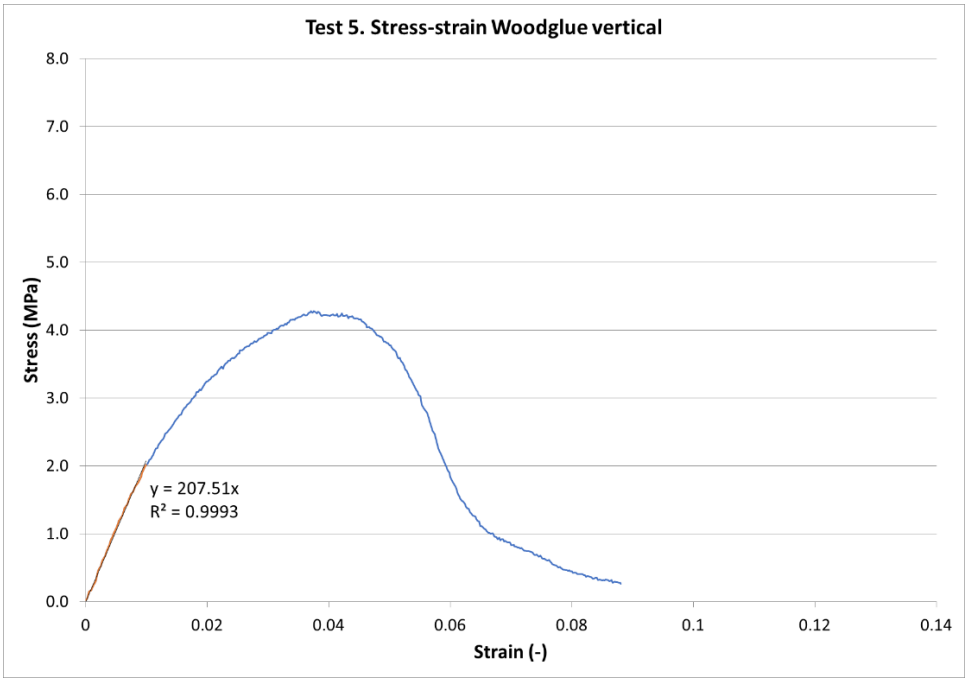


Figure F35. The stress-strain diagram of flexural test wood glue vertical 5. With the orange line indicating the path to 2 MPa. Through the red part a linear trendline is generated with excel, the slope of this linear trendline indicate the flexural modulus.

Figure F36 and Figure F37 present all five wood glue tests together in a force-displacement and a stress-strain graph.

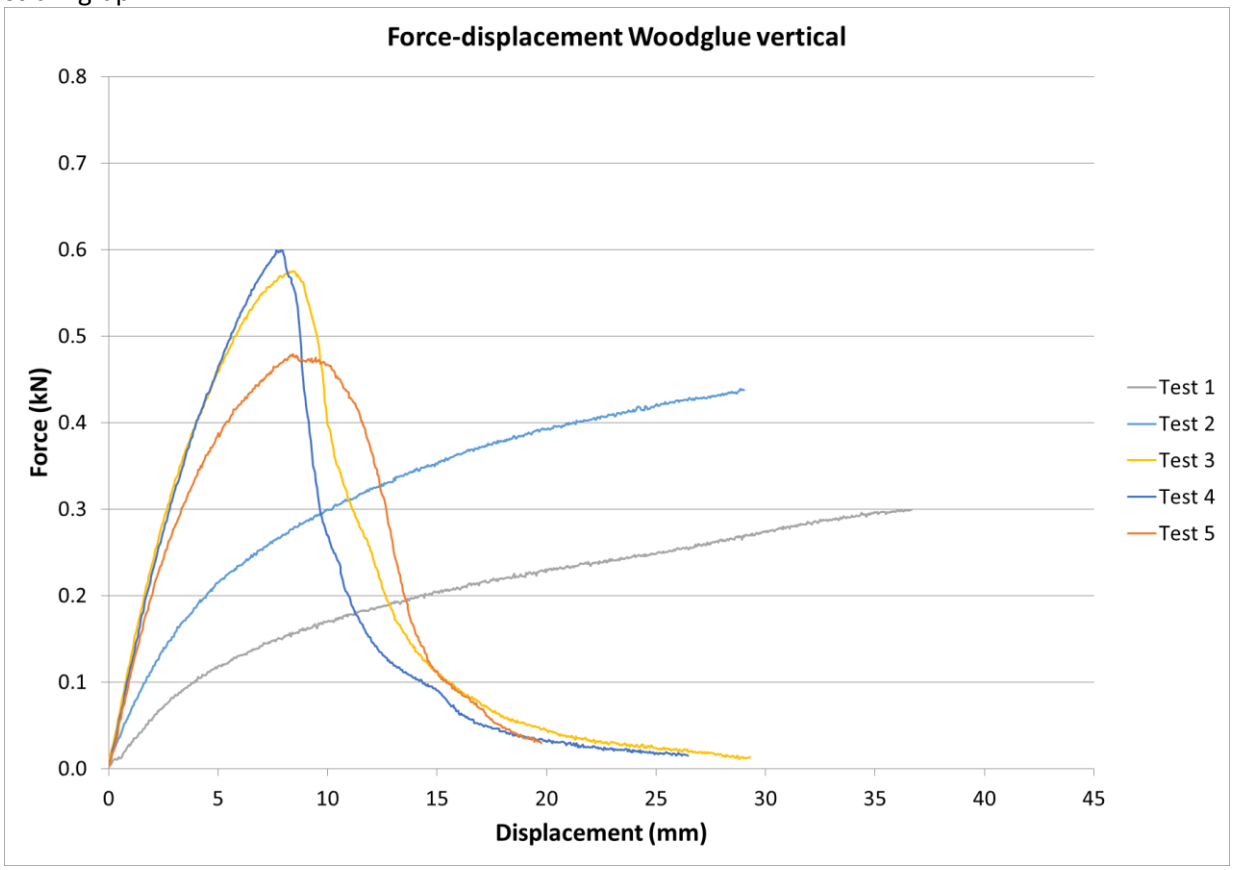


Figure F36. The force-displacement graph of all the wood glue flexural tests in the vertical orientation.

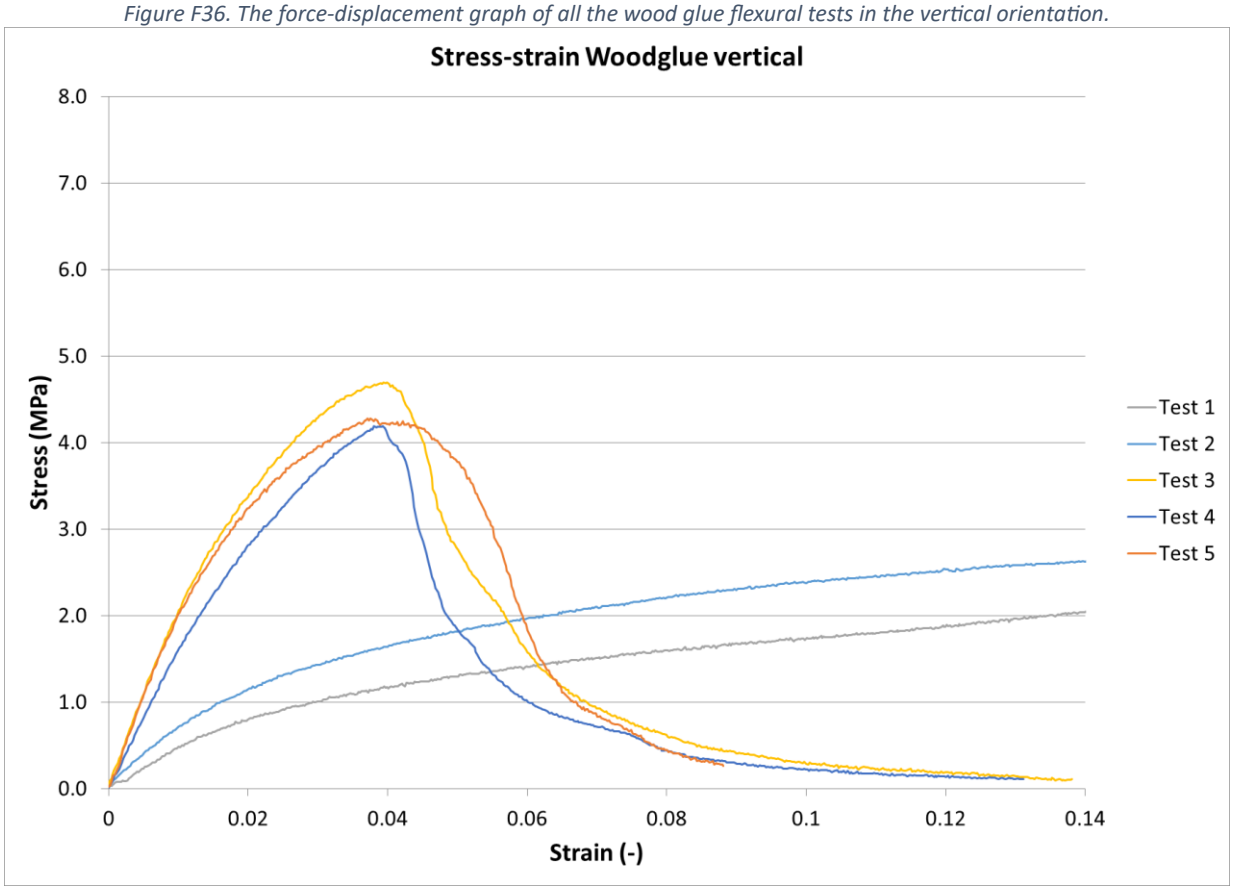


Figure F37. The stress-strain graph of all the wood glue flexural tests in the vertical orientation.

F.2.2 Bio-glue

F.2.2.1 Horizontal layer orientation

Figure F38 to Figure F58 show seven bio-glue tests with a horizontal layer orientation. Each test is accompanied with four photos during the test and two different graphs: the force-displacement and the stress-strain graph.

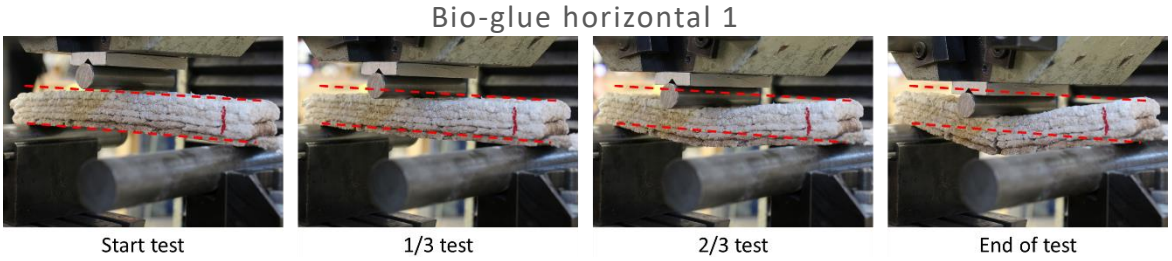


Figure F38. Four photos of process of the flexural test bio-glue horizontal 1. The red lines indicate the original position of the beam at the start of the test.

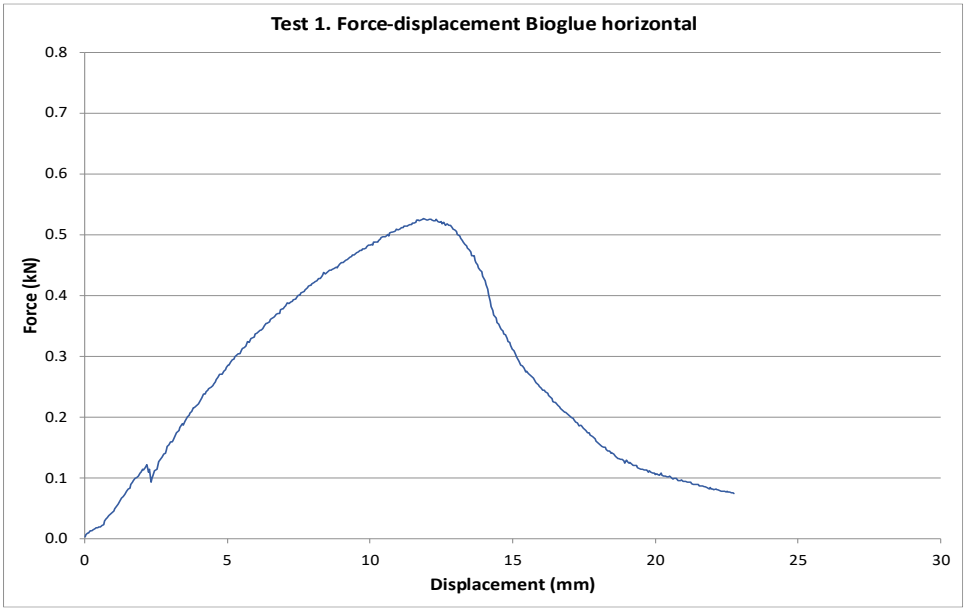


Figure F39. The force-displacement graph of flexural test bio-glue horizontal 1.

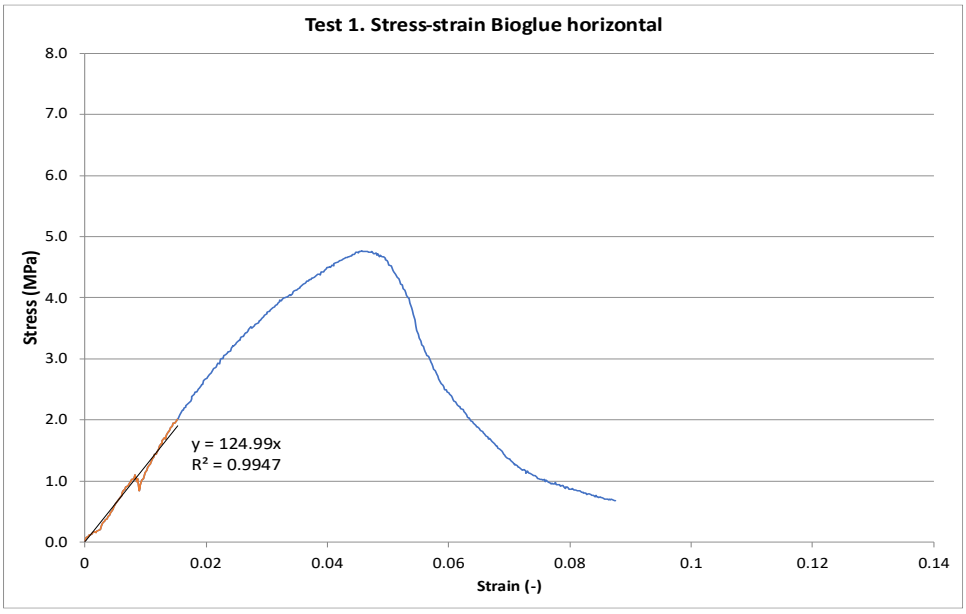


Figure F40. The stress-strain diagram of flexural test bio-glue horizontal 1.

Bio-glue horizontal 2

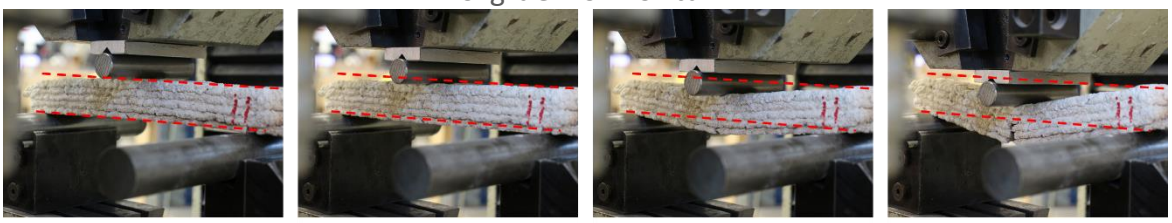


Figure F41. Four photos of the flexural test bio-glue horizontal 2. The red lines indicate the original position of the beam at the start of the test.

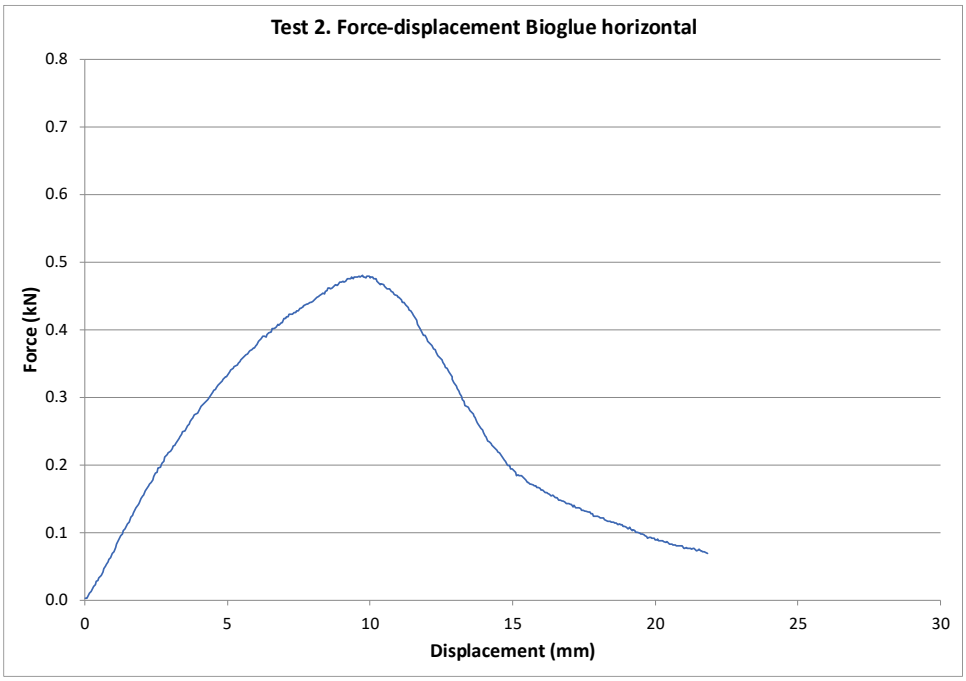


Figure F42. The force-displacement graph of flexural test bio-glue horizontal 2.

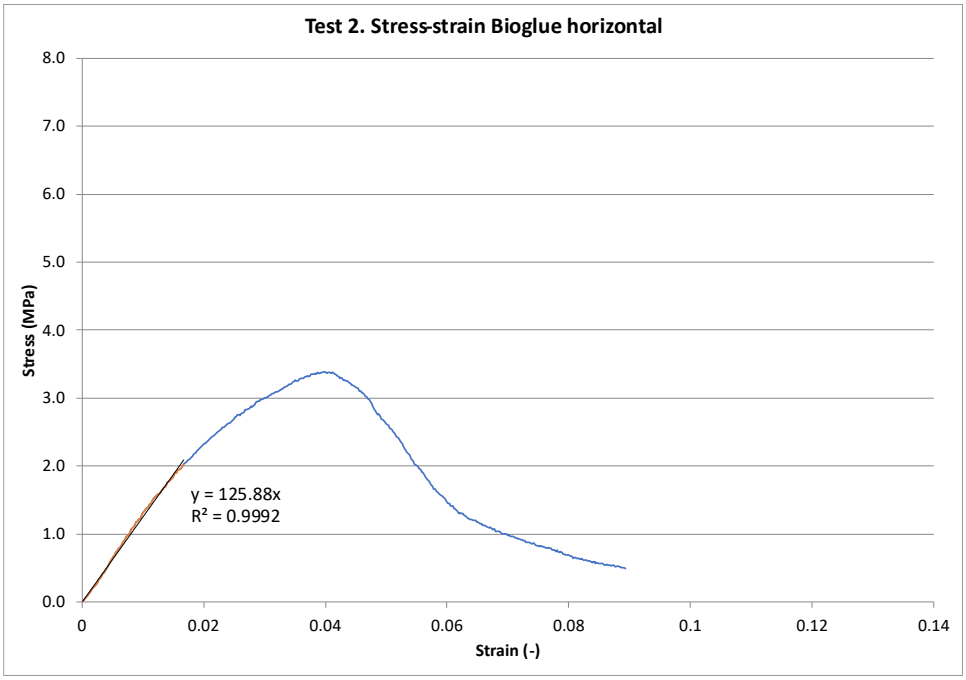


Figure F43. The stress-strain diagram of flexural test bio-glue horizontal 2.

Bio-glue horizontal 3

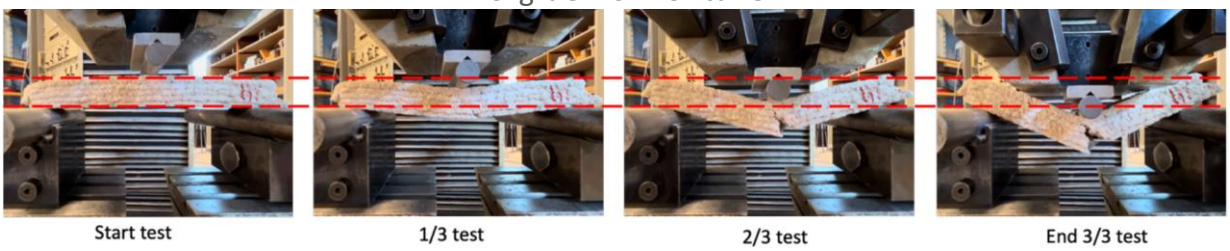


Figure F44. Four photos of the flexural test bio-glue horizontal 3. The red lines indicate the original position of the beam at the start of the test.

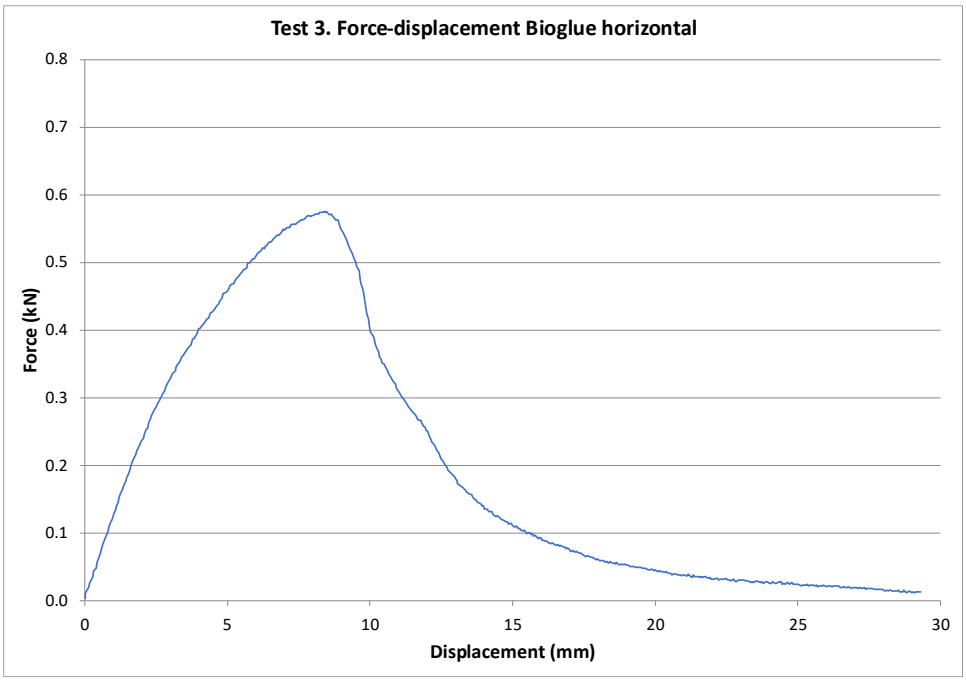


Figure F45. The force-displacement graph of flexural test bio-glue horizontal 3.

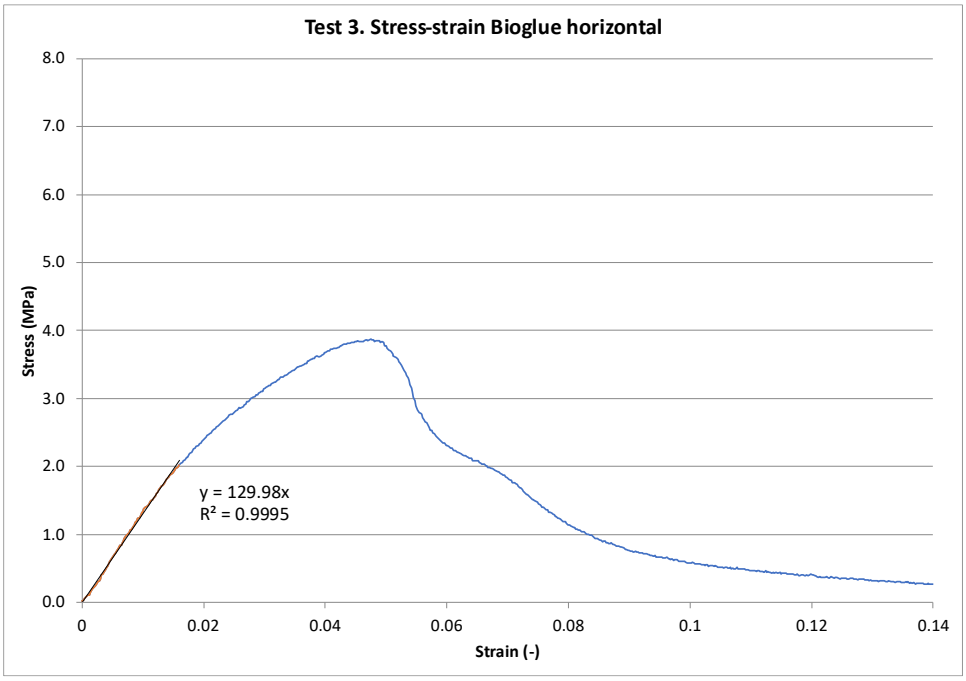


Figure F46. The stress-strain diagram of flexural test bio-glue horizontal 3.

Bio-glue horizontal 4

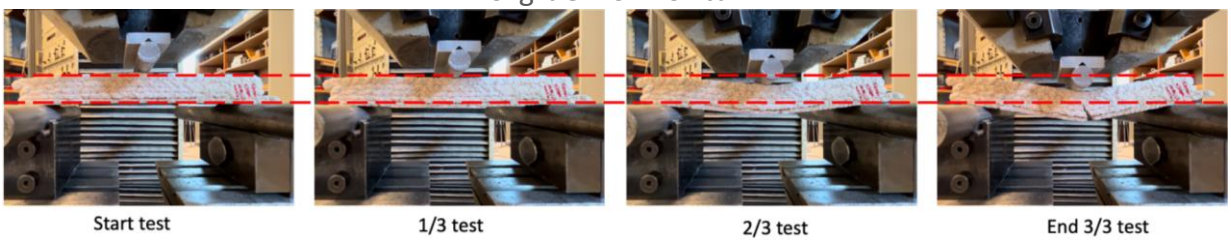


Figure F47. Four photos of the flexural test bio-glue horizontal 4. The red lines indicate the original position of the beam at the start of the test.

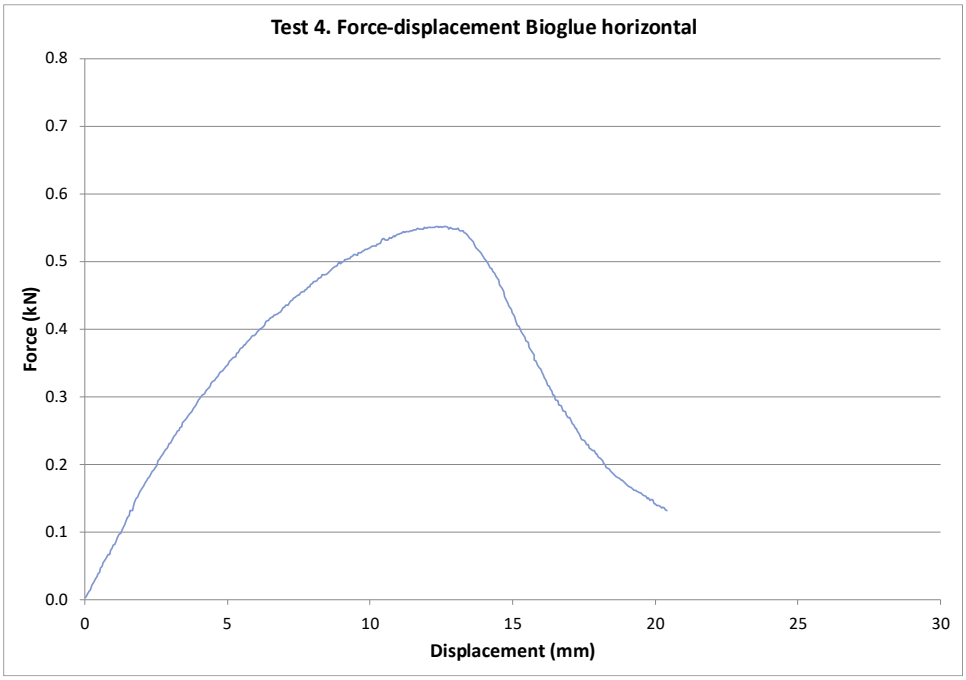


Figure F48. The force-displacement graph of flexural test bio-glue horizontal 4.

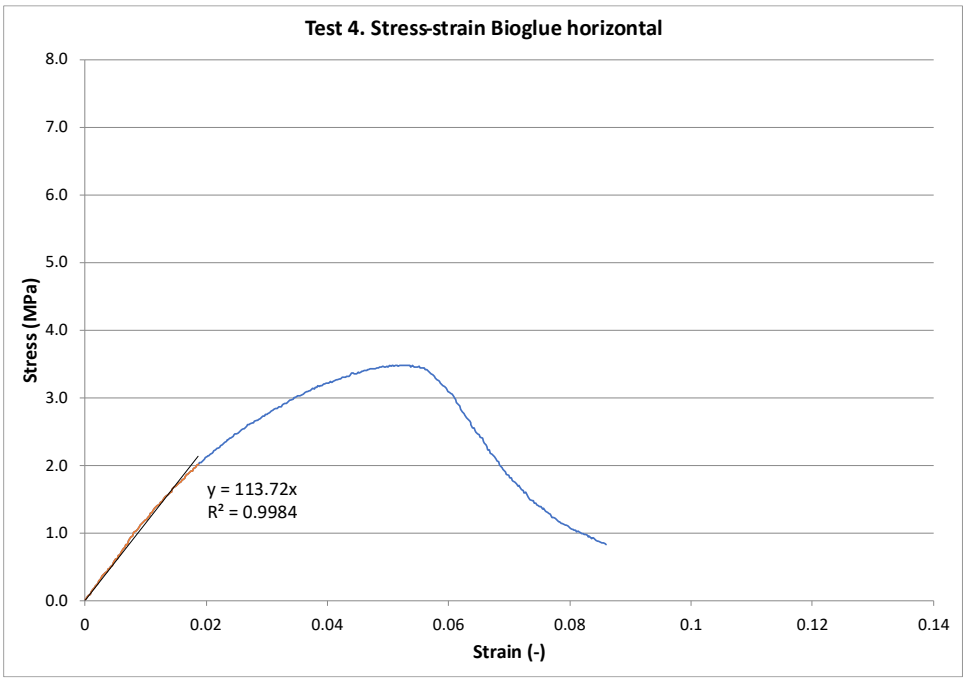


Figure F49. The stress-strain diagram of flexural test bio-glue horizontal 4.

Bio-glue horizontal 5

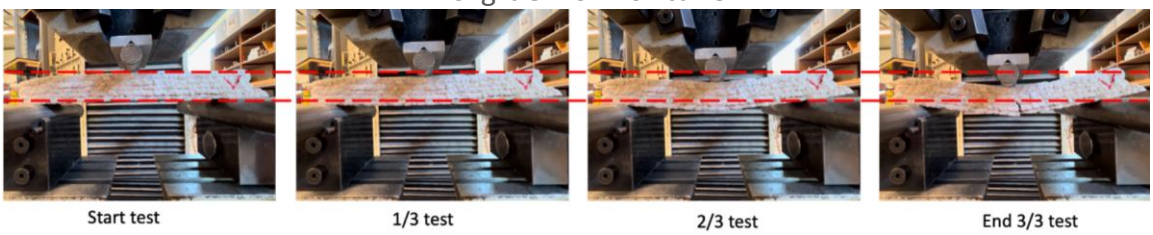


Figure F50. Four photos of the flexural test bio-glue horizontal 5. The red lines indicate the original position of the beam at the start of the test.

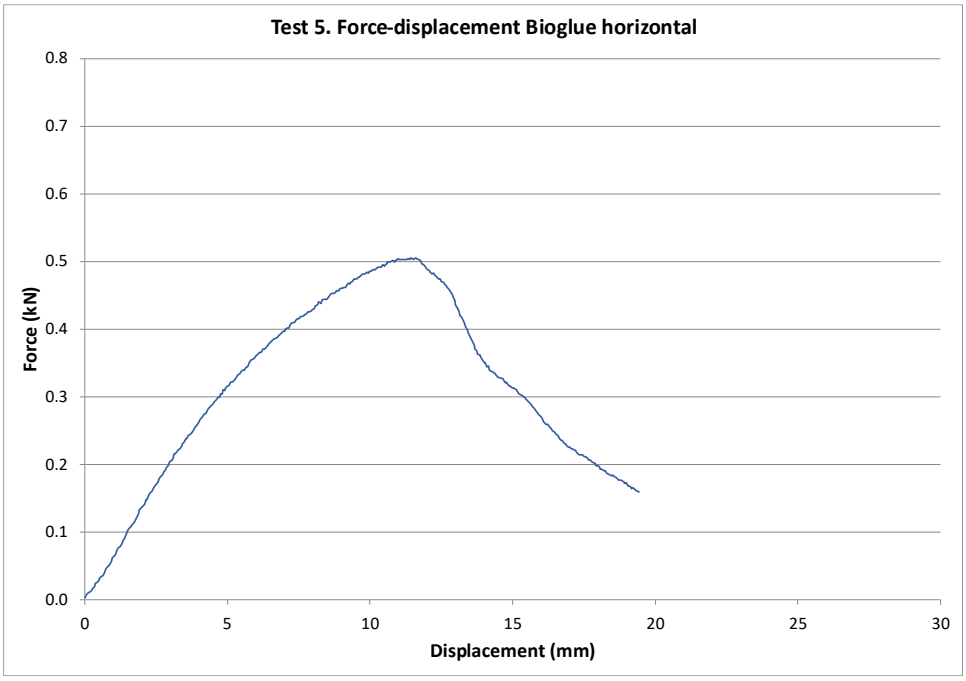


Figure F51. The force-displacement graph of flexural test bio-glue horizontal 5.

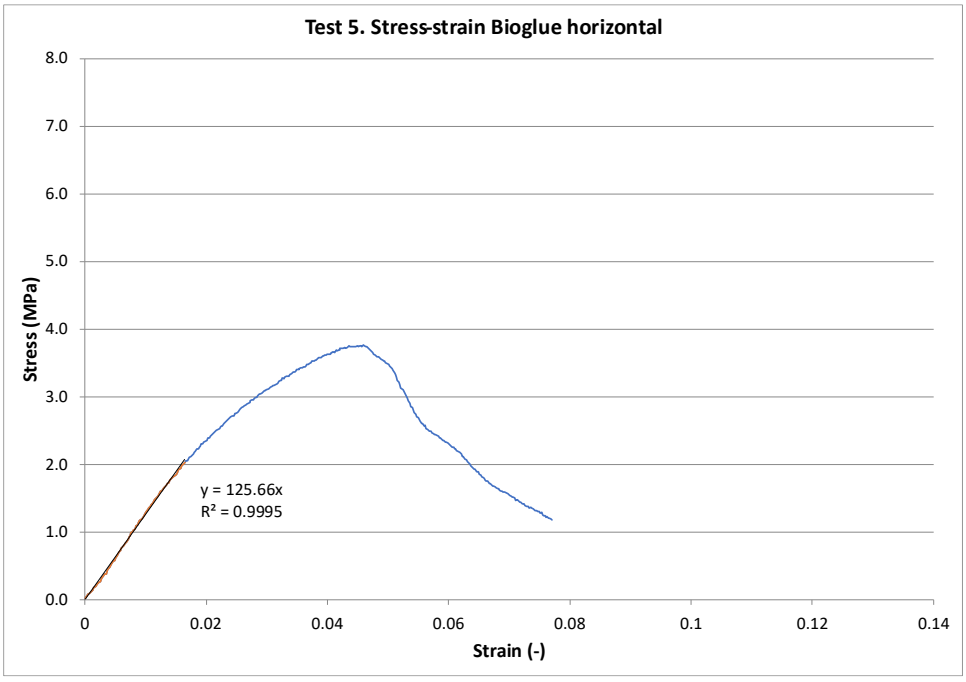


Figure F52. The stress-strain diagram of flexural test bio-glue horizontal 5.

Bio-glue horizontal 6

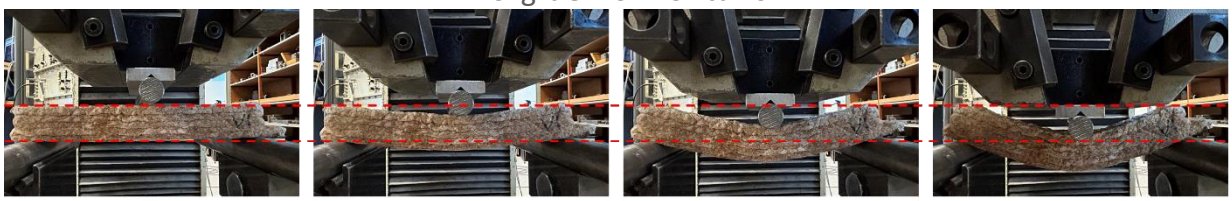


Figure F53. Four photos of the flexural test bio-glue horizontal 6. The red lines indicate the original position of the beam at the start of the test.

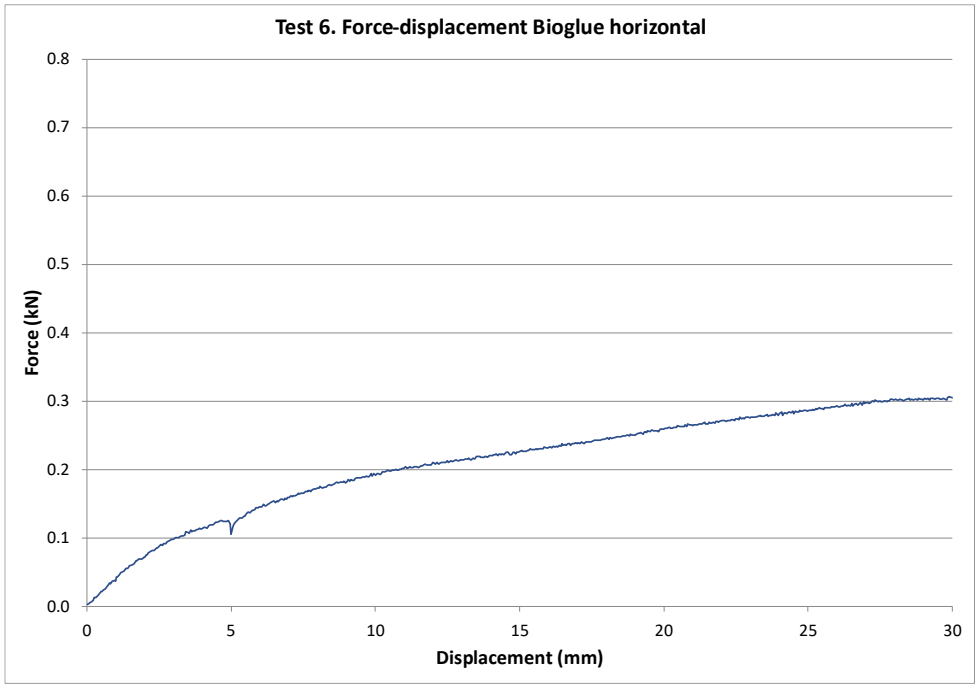


Figure F54. The force-displacement graph of flexural test bio-glue horizontal 6.

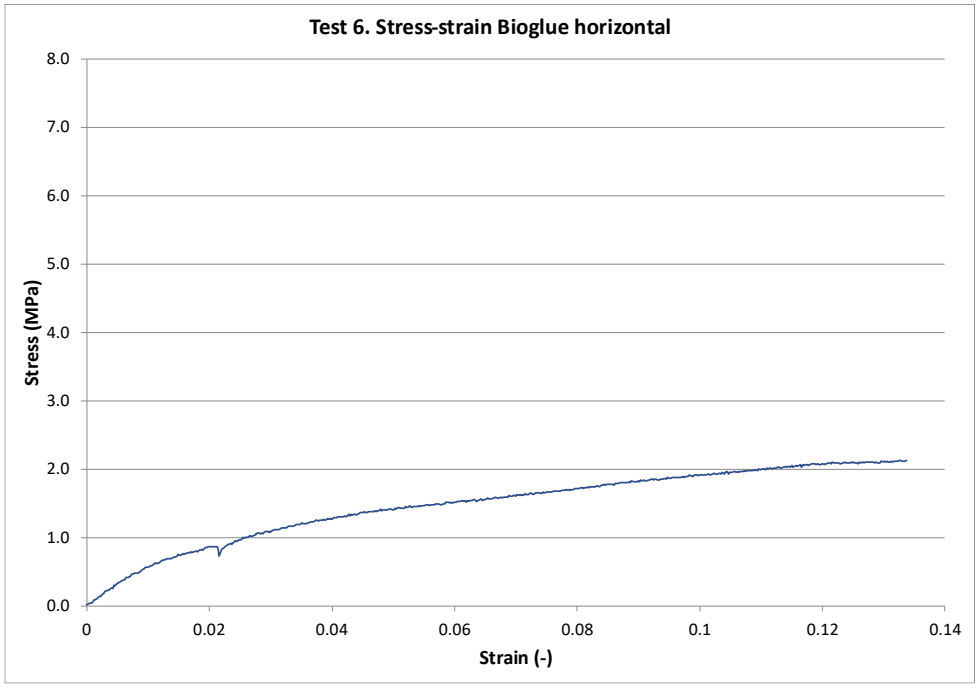


Figure F55. The stress-strain diagram of flexural test bio-glue horizontal 6.

Bio-glue horizontal 7

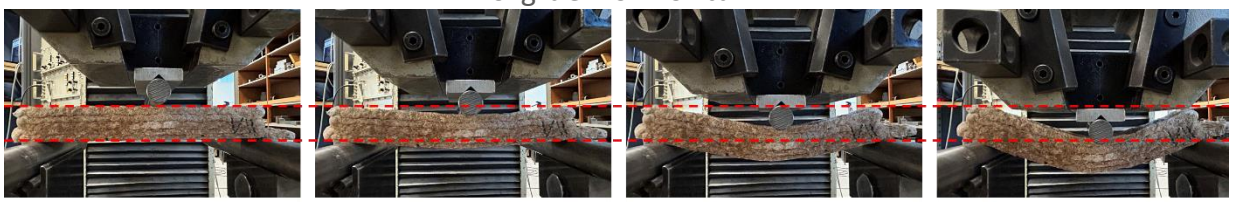


Figure F56. Four photos of the flexural test bio-glue horizontal. The red lines indicate the original position of the beam at the start of the test.

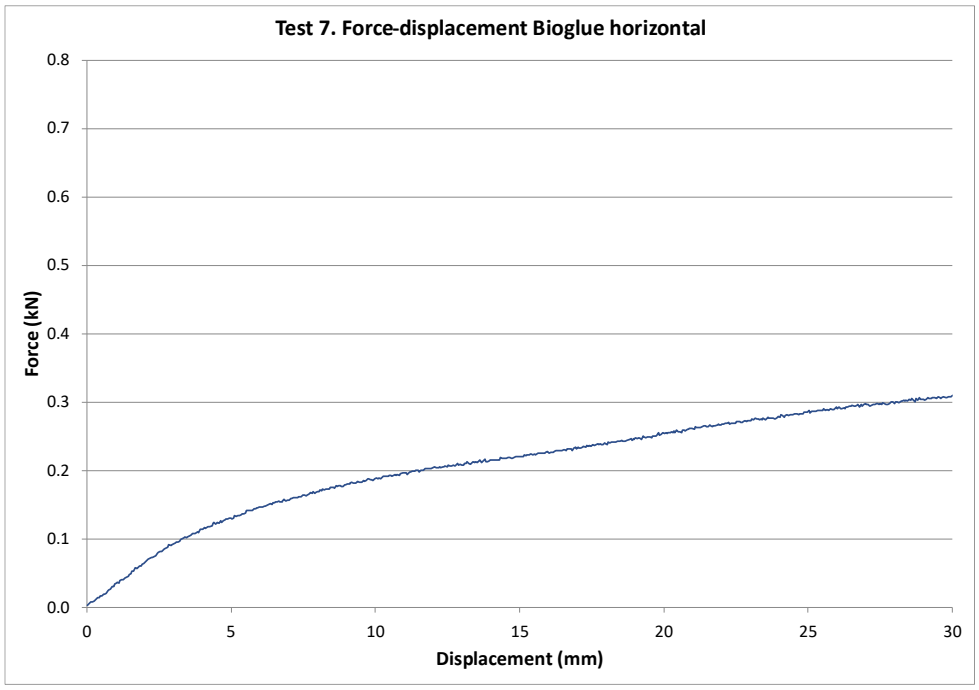


Figure F57. The force-displacement graph of flexural test bio-glue horizontal 7.

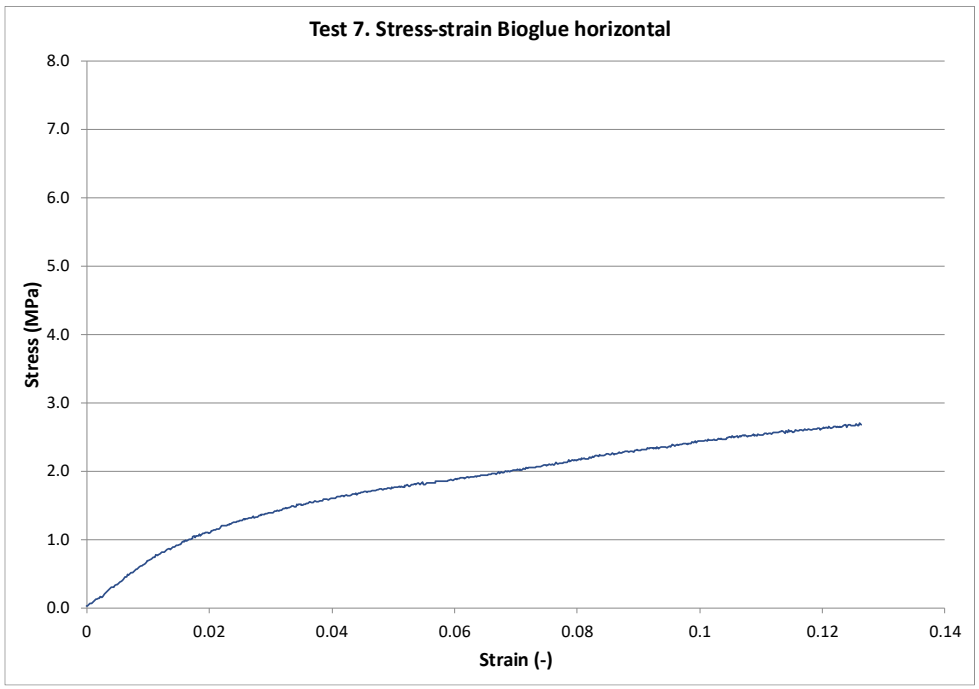


Figure F58. The stress-strain diagram of flexural test bio-glue horizontal 7.

Figure F59 and Figure F60 present all seven tests together in a force-displacement and a stress-strain graph.

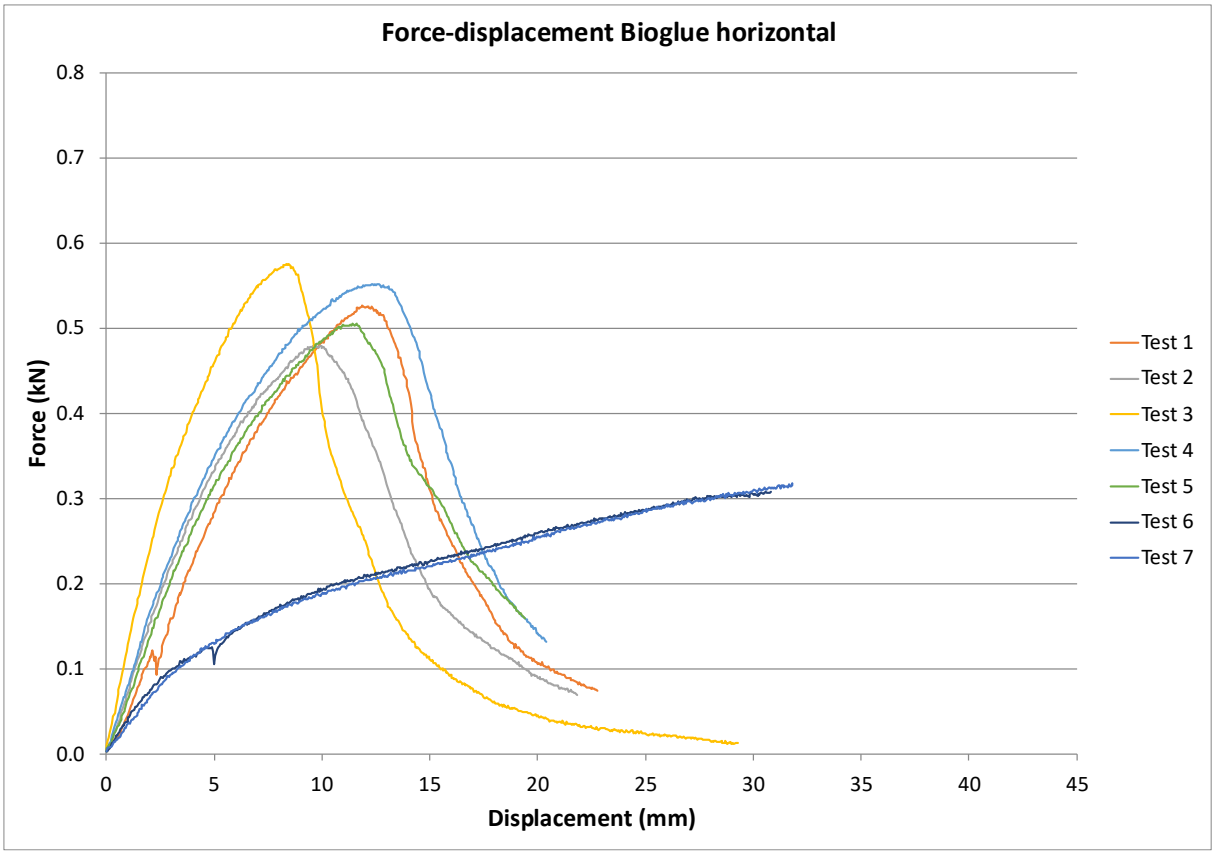


Figure F59. The force-displacement graph of all the bio-glue flexural tests in the horizontal orientation.

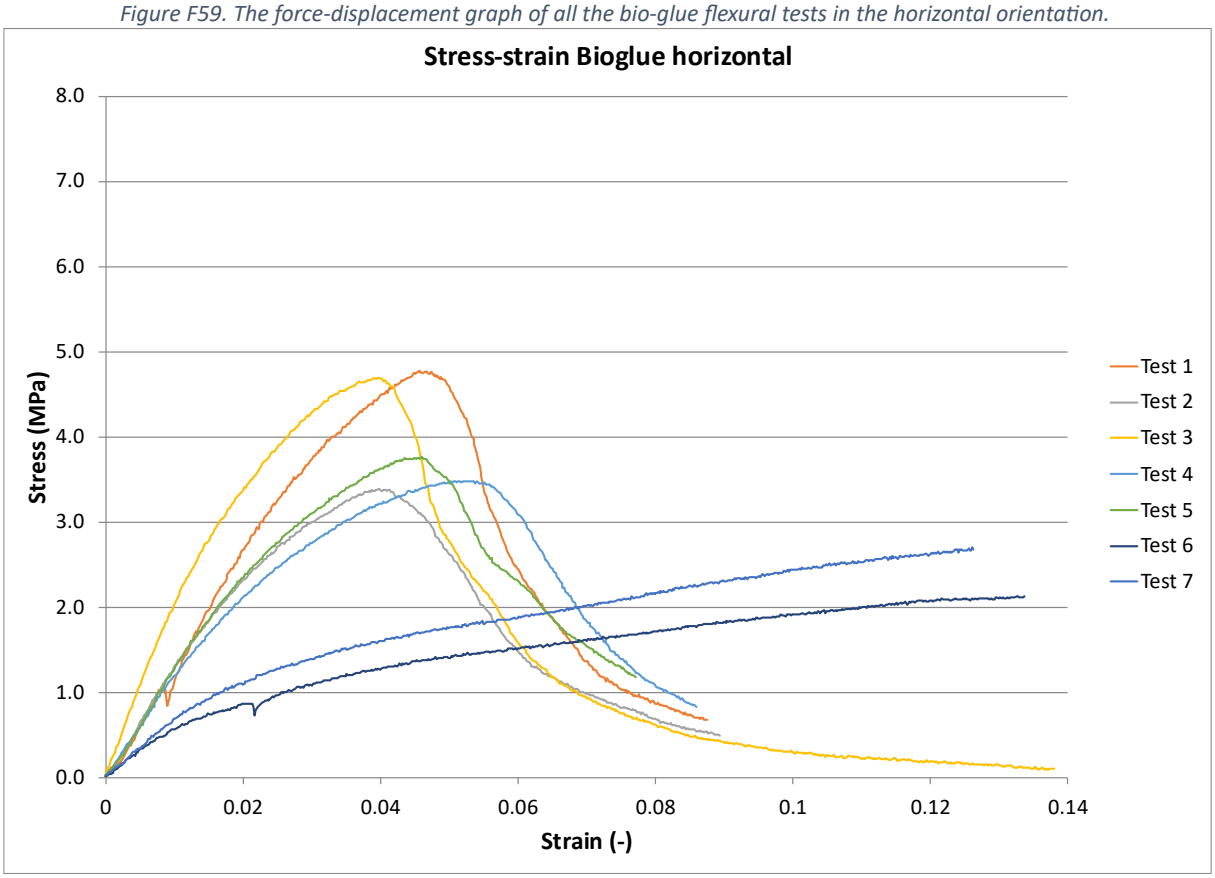


Figure F60. The stress-strain graph of all the bio-glue flexural tests in the horizontal orientation.

F.2.2.2 Vertical layer orientation

Figure F61 to Figure F77show six bio-glue tests with a vertical layer orientation. Each test is accompanied with four photos during the test and two different graphs: the force-displacement and the stress-strain graph.

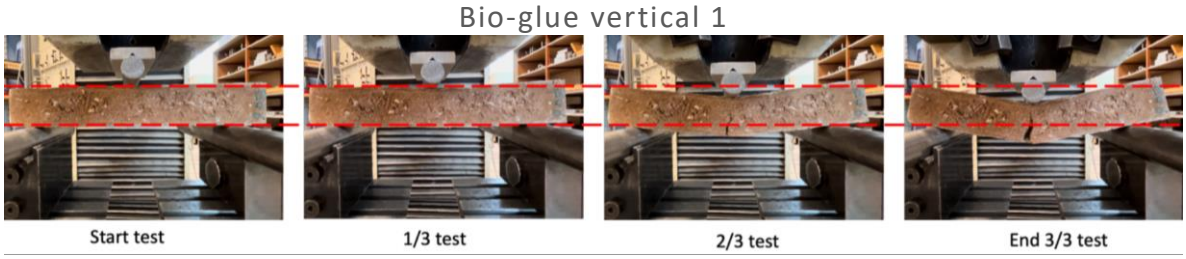


Figure F61. Four photos of process of the flexural test bio-glue vertical 1. The red lines indicate the original position of the beam at the start of the test.

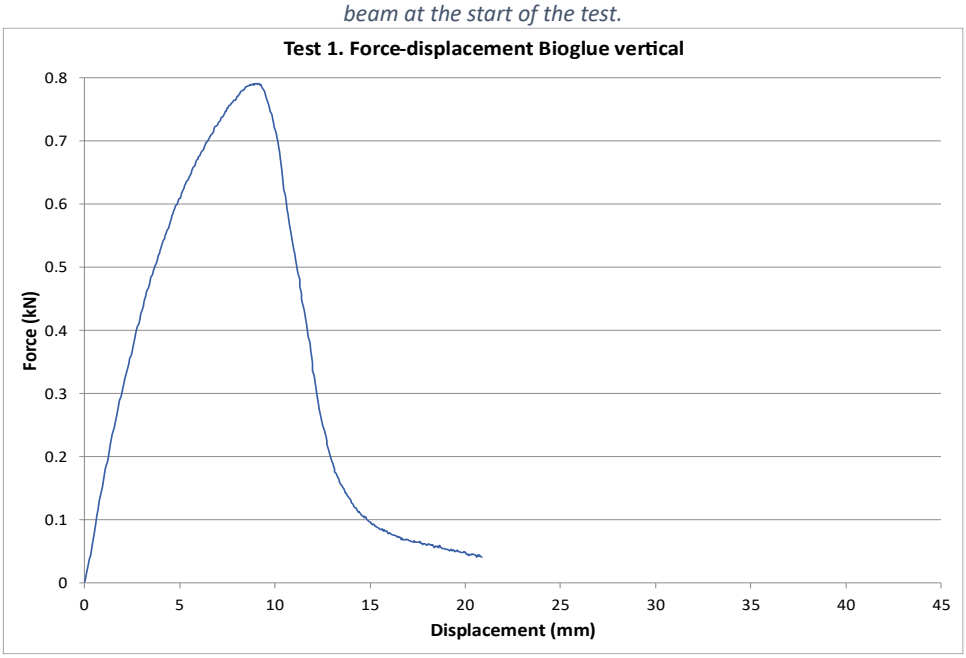


Figure F62. The force-displacement graph of flexural test bio-glue vertical 1.

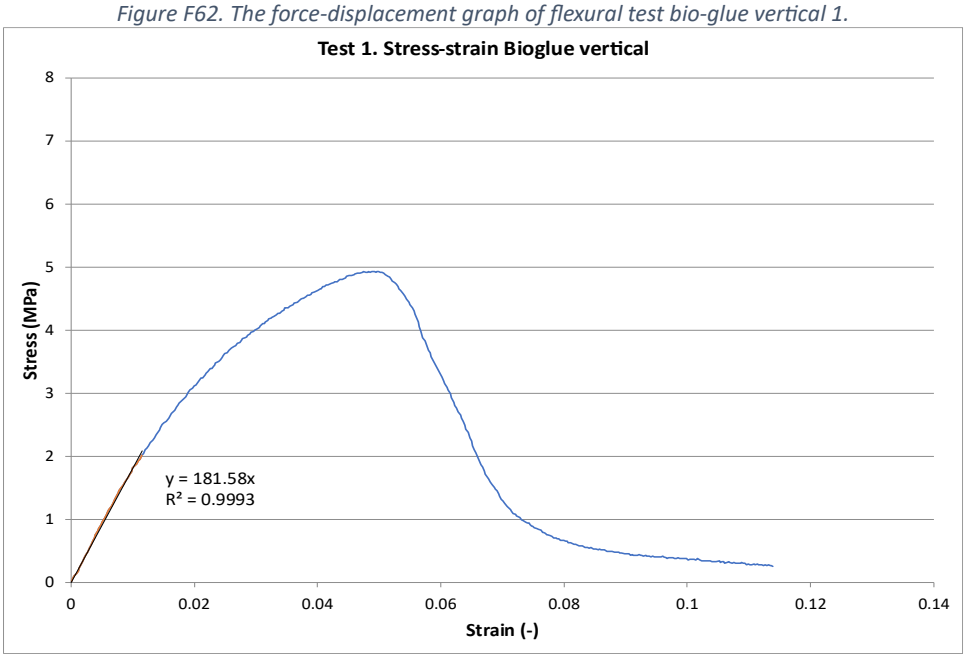


Figure F63. The stress-strain diagram of flexural test bio-glue vertical 1.

Bio-glue vertical 2

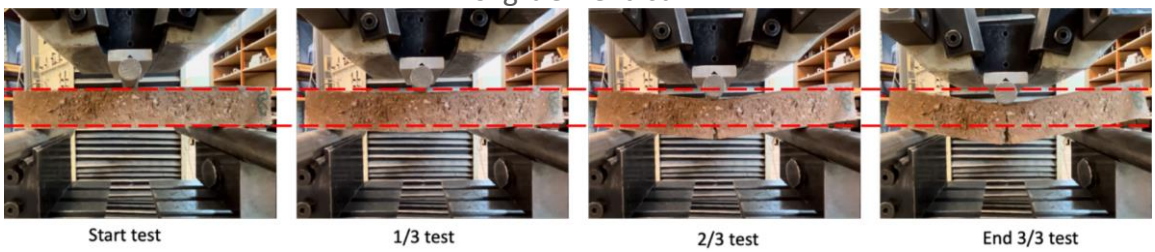


Figure F64. Four photos of the flexural test bio-glue vertical 2. The red lines indicate the original position of the beam at the start of the test.

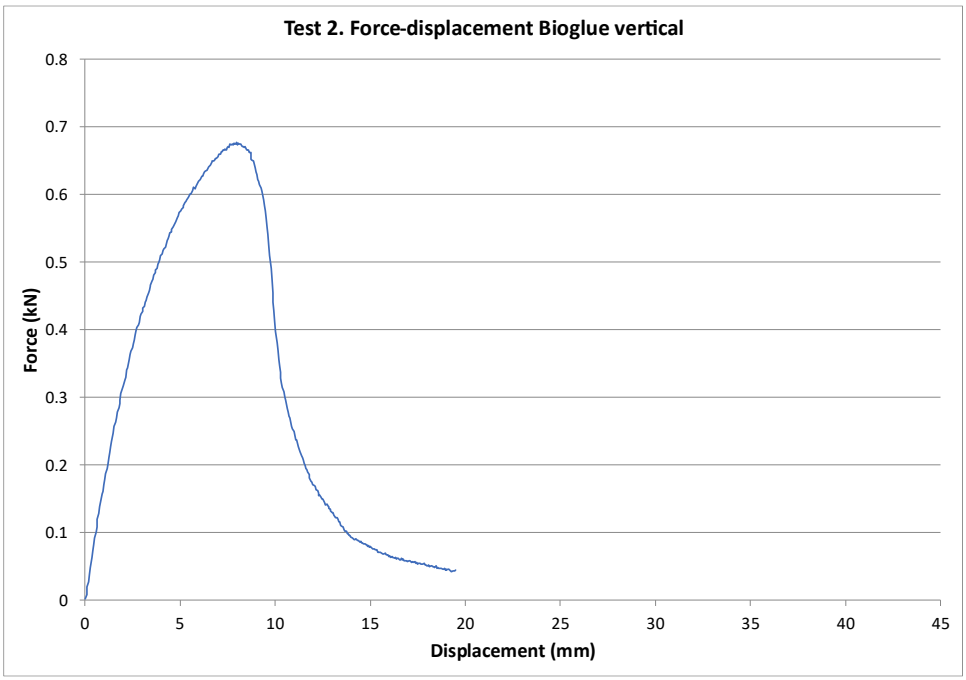


Figure F65. The force-displacement graph of flexural test bio-glue vertical 2.

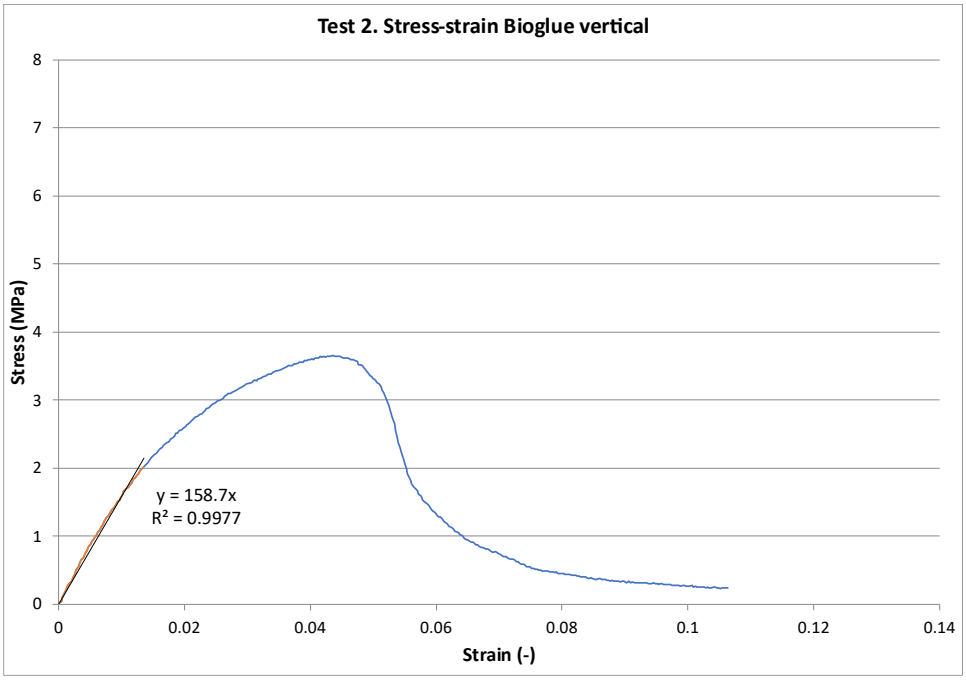


Figure F66. The stress-strain diagram of flexural test bio-glue vertical 2.

Bio-glue vertical 3



Start test | 1/3 test | 2/3 test | End of test

Figure F67. Four photos of the flexural test bio-glue vertical 3. The red lines indicate the original position of the beam at the start of the test.

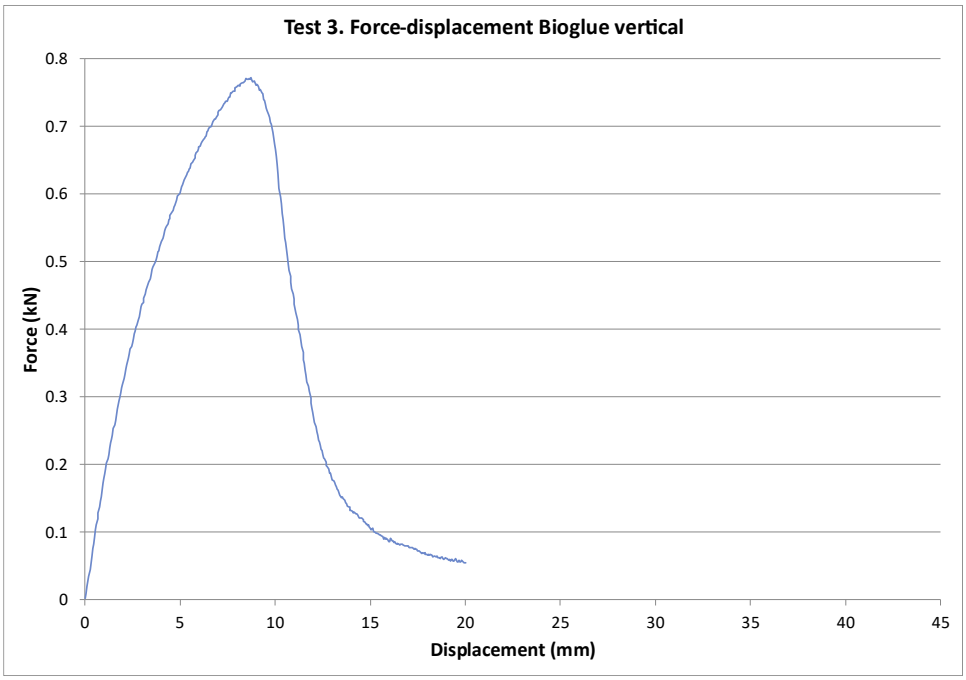


Figure F68. The force-displacement graph of flexural test bio-glue vertical 3.

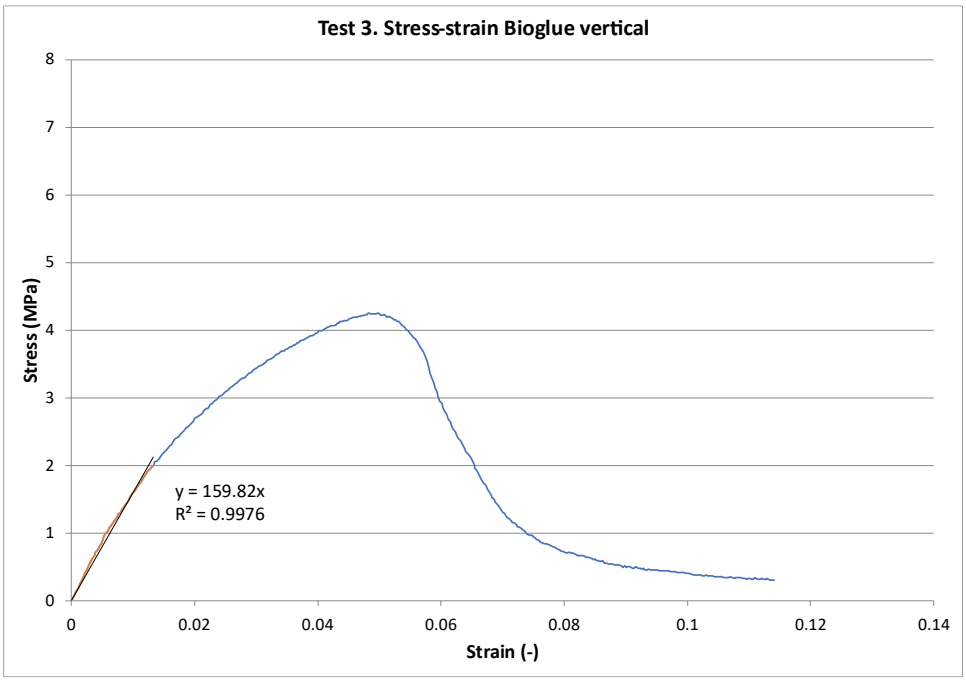


Figure F69. The stress-strain diagram of flexural test bio-glue vertical 3.

Bio-glue vertical 4

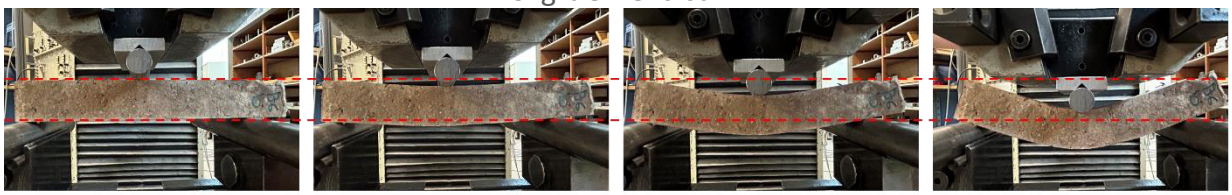


Figure F70. Four photos of the flexural test bio-glue vertical 4. The red lines indicate the original position of the beam at the start of the test.

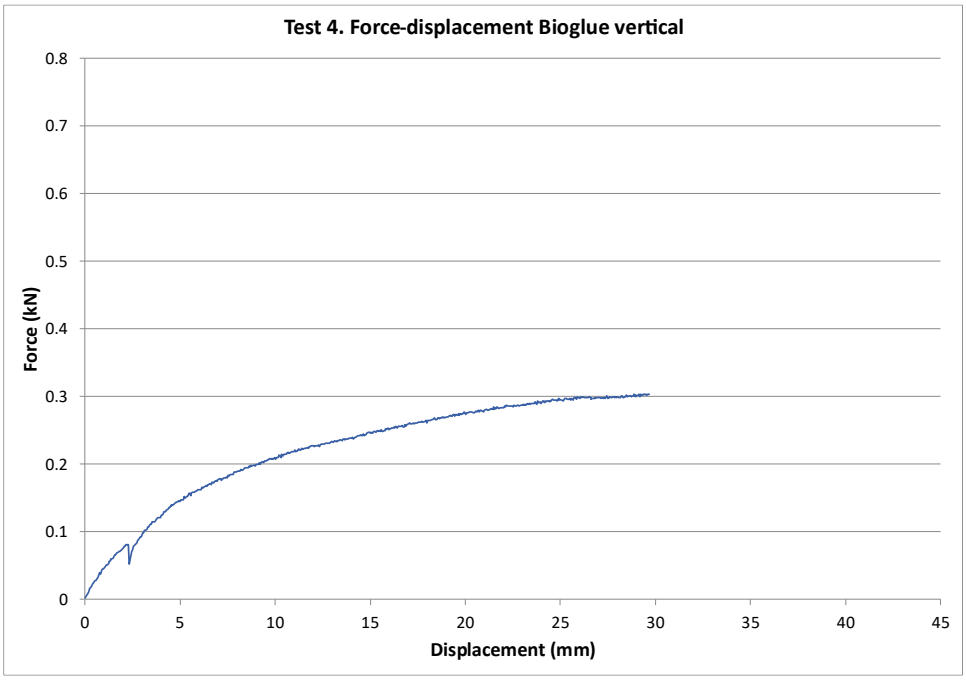


Figure F71. The force-displacement graph of flexural test bio-glue vertical 4.

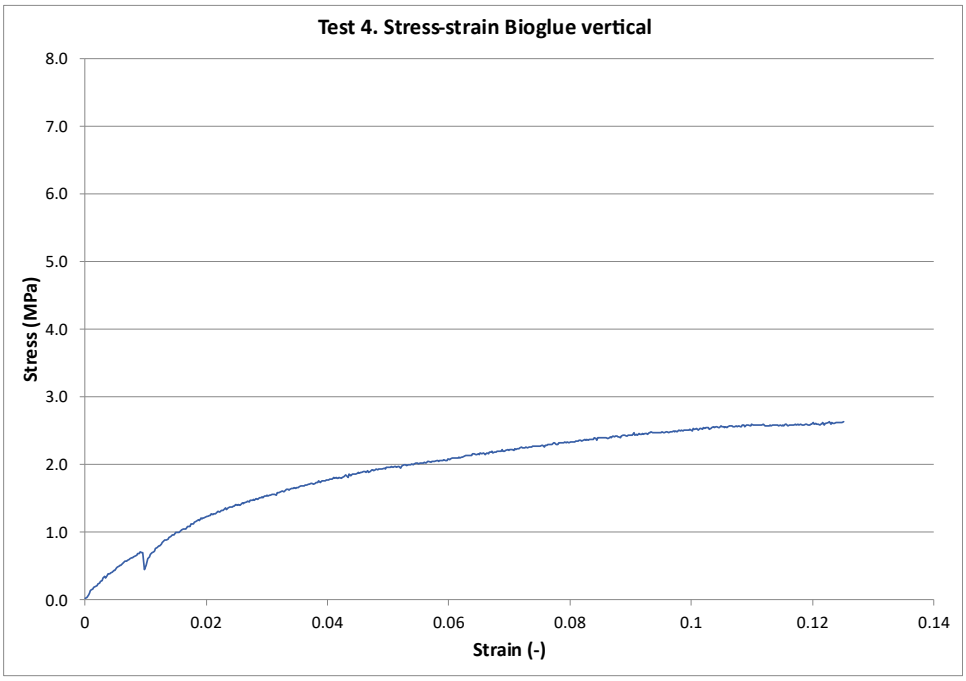


Figure F72. The stress-strain diagram of flexural test bio-glue vertical 4.

Bio-glue vertical 5

No pictures unfortunately

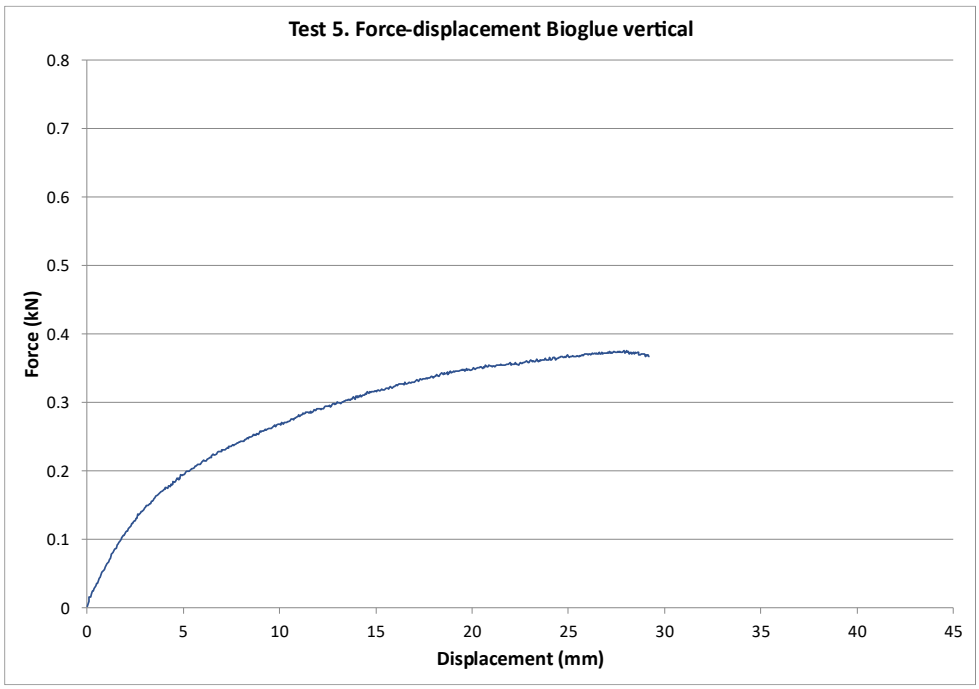


Figure F73. The force-displacement graph of flexural test bio-glue vertical 5.

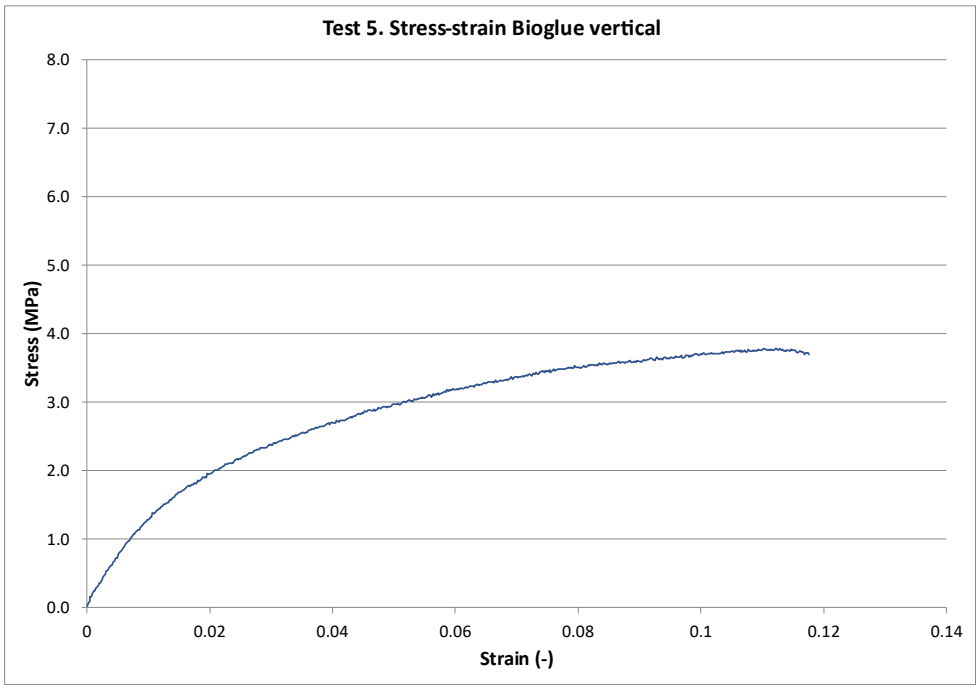


Figure F74. The stress-strain diagram of flexural test bio-glue vertical 5.

Bio-glue vertical 6



Figure F75. Four photos of the flexural test bio-glue vertical 6. The red lines indicate the original position of the beam at the start of the test.

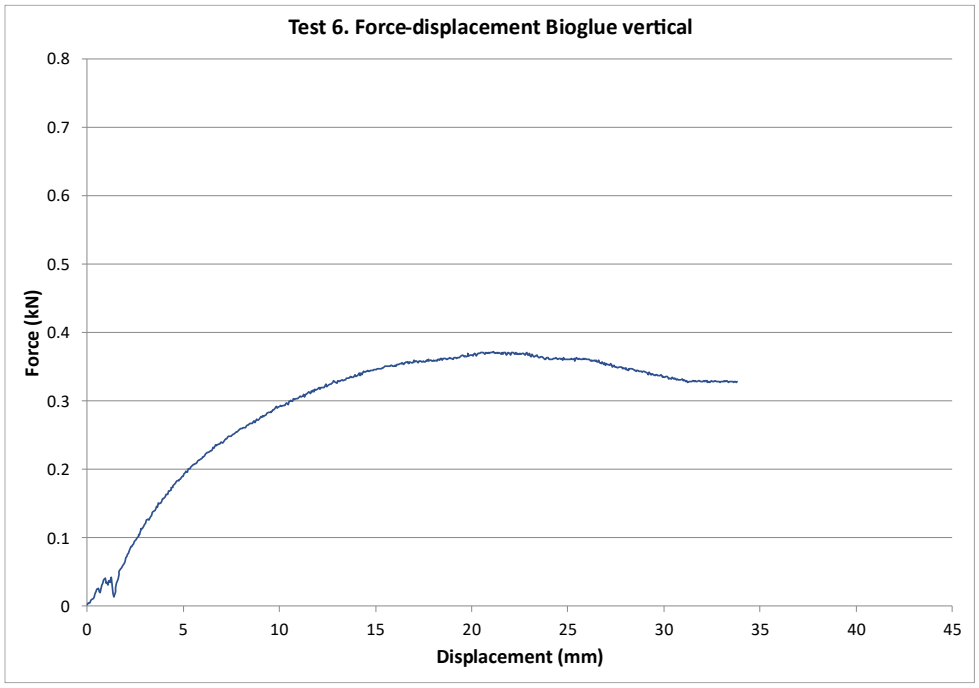


Figure F76. The force-displacement graph of flexural test bio-glue vertical 6.

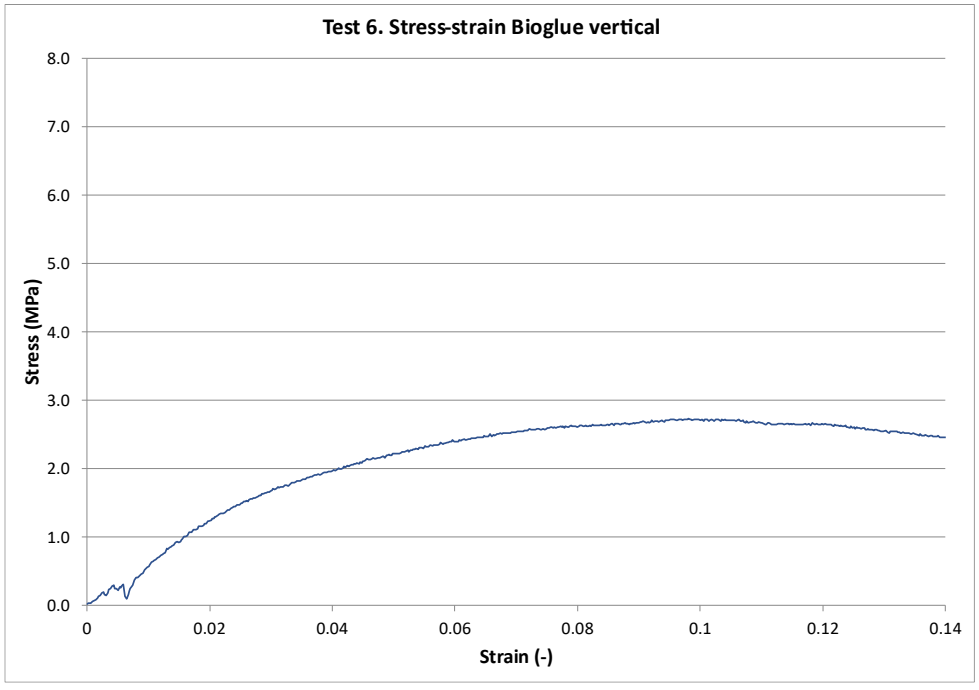


Figure F77. The stress-strain diagram of flexural test bio-glue vertical 6.

Figure F78 and Figure F79 present all six bio-glue tests together in a force-displacement and a stress-strain graph.

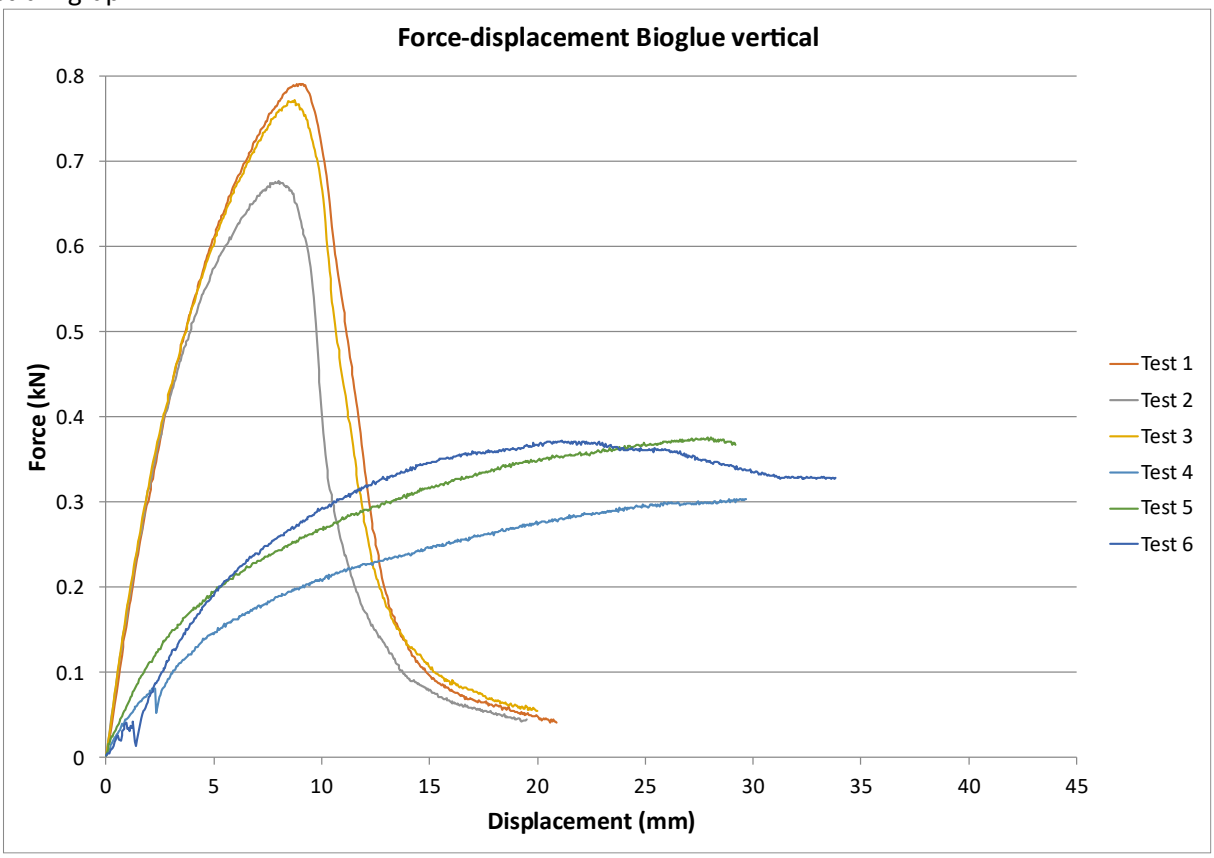


Figure F78. The force-displacement graph of all the bio-glue flexural tests in the vertical orientation.

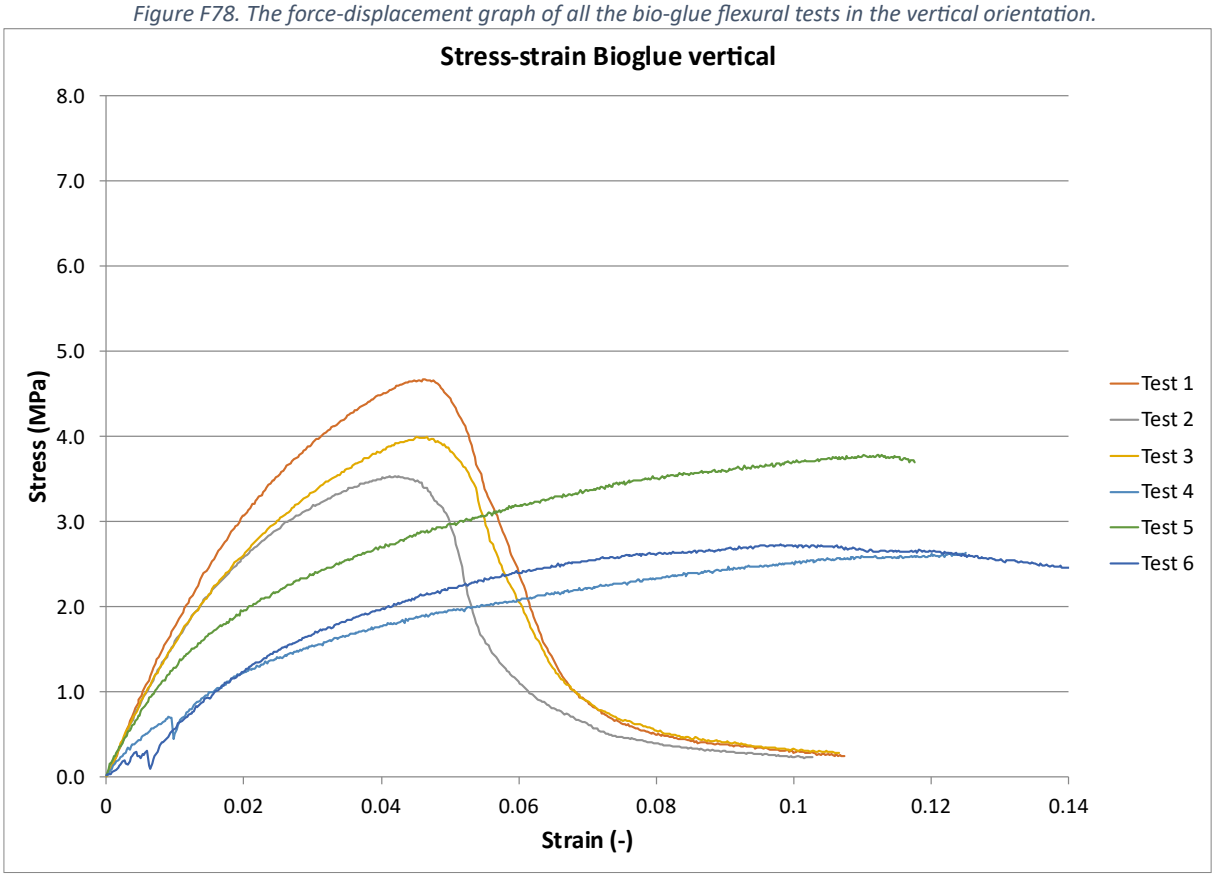


Figure F79. The stress-strain graph of all the bio-glue flexural tests in the vertical orientation.

F.2.3 Summary wood glue and bio-glue flexural test results

Table F11 to Table F14 present the results of the wood glue and bio-glue tests with both orientations.

Table F11. Results of flexural test wood glue with horizontal layer orientation.

Test	Beam	Days cured	Cross-sectional area [mm²]	Force [kN]	Displacement [mm]	Stress [MPa]	Strain [-]	Crack?	Flexural modulus [MPa]
1	1	42	1292.0	0.40	25.06	2.91	0.1056	No	-
2	2	42	1193.5	0.48	27.58	4.18	0.1060	No	-
3	3	42	1417.5	0.51	33.79	3.28	0.1466	No	-
4	5	37	1476.0	0.42	39.60	2.55	0.1767	No	-
5	6	37	1295.0	0.42	41.92	3.04	0.1819	No	-
6	13	38	1170.0	0.43	10.76	3.91	0.0400	Yes	149.29

Table F12. Results of flexural test wood glue with vertical layer orientation.

Test	Beam	Days cured	Cross-sectional area [mm²]	Force [kN]	Displacement [mm]	Stress [MPa]	Strain [-]	Crack?	Flexural modulus [MPa]
1	7	37	1260.0	0.30	36.66	2.18	0.1636	No	-
2	8	37	1360.0	0.44	28.84	2.66	0.1430	No	-
3	10	36	1064.0	0.58	8.37	4.70	0.0394	Yes	212.60
4	11	36	1180.0	0.60	7.67	4.19	0.0380	Yes	159.15
5	12	36	1026.0	0.48	8.41	4.28	0.0375	Yes	207.51

Table F13. Results of flexural test bio-glue with horizontal layer orientation.

Test	Beam	Days cured	Cross-sectional area [mm²]	Force [kN]	Displacement [mm]	Stress [MPa]	Strain [-]	Crack?	Flexural modulus [MPa]
1	1	41	1131.5	0.53	11.87	4.78	0.0456	Yes	124.99
2	2	41	1386.0	0.48	9.72	3.39	0.0398	Yes	125.88
3	3	42	1428.0	0.58	11.26	3.88	0.0475	Yes	129.98
4	4	41	1496.0	0.55	12.36	3.48	0.0521	Yes	113.72
5	5	41	1360.0	0.51	11.59	3.76	0.0460	Yes	125.66
6	12	37	1330.0	0.31	30.81	2.13	0.1337	No	-
7	14	37	1184.0	0.32	31.79	2.70	0.1261	No	-

Table F14. Results of flexural test bio-glue with vertical layer orientation.

Test	Beam	Days cured	Cross-sectional area [mm²]	Force [kN]	Displacement [mm]	Stress [MPa]	Strain [-]	Crack?	Flexural modulus [MPa]
1	6	41	1348.8	0.79	9.02	4.93	0.0492	Yes	181.58
2	7	41	1487.5	0.68	7.98	3.66	0.0435	Yes	158.70
3	8	41	1483.5	0.77	8.74	4.25	0.0498	Yes	159.82
4	10	43	1122.0	0.30	29.13	2.71	0.1264	No	-
5	11	35	1007.5	0.38	27.88	3.85	0.1140	No	-
6	13	37	1200.0	0.37	21.11	2.90	0.1047	No	-

F.3 Results bio-glue with additives

F.3.1 Bio-glue with bentonite

F.3.1.1 Horizontal layer orientation

Figure F80 to Figure F88 show three bio-glue with bentonite tests with a horizontal layer orientation. Each test is accompanied with three photos and two different graphs: the force-displacement and the stress-strain graph.

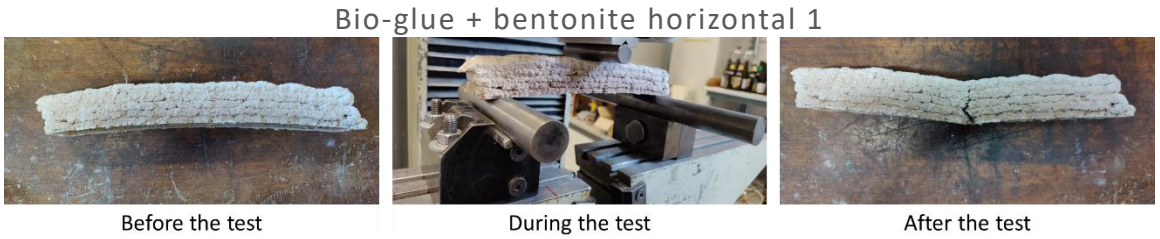


Figure F80. Three photos of the beam before, during and after the flexural test bio-glue + bentonite horizontal 1.

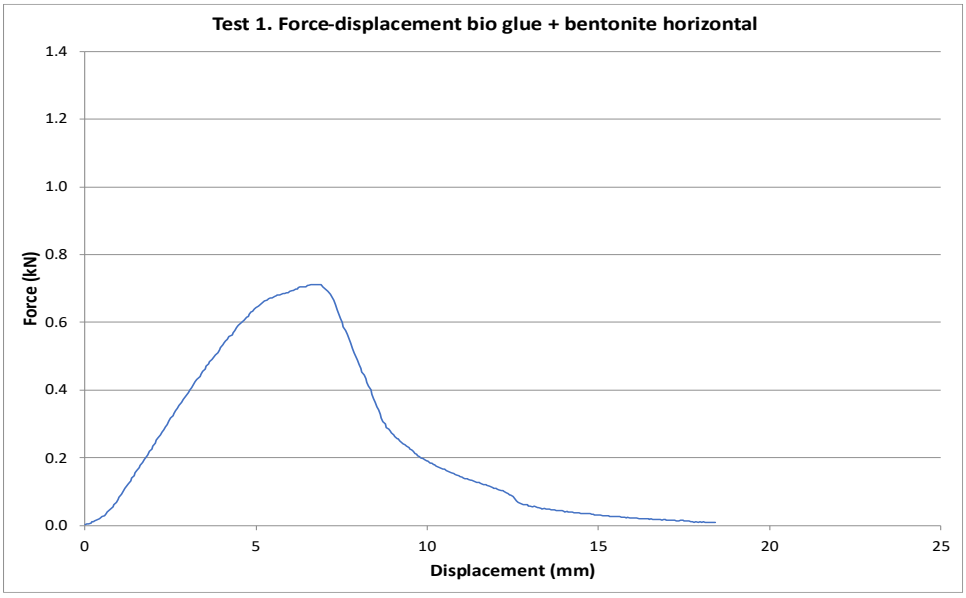


Figure F81. The force-displacement graph of flexural test bio-glue + bentonite horizontal 1.

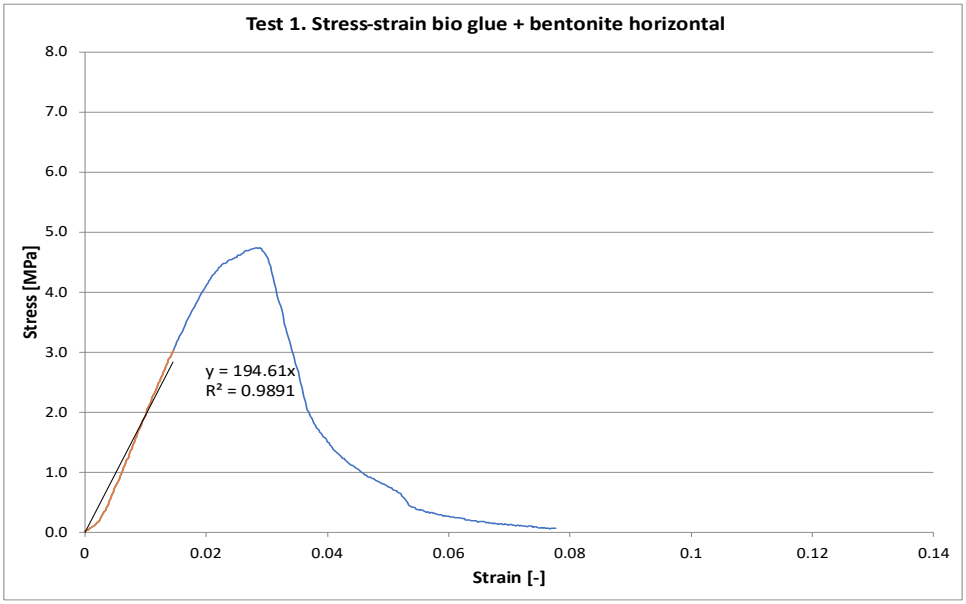


Figure F82. The stress-strain diagram of flexural test bio-glue + bentonite horizontal 1.

Bio-glue + bentonite horizontal 2



Before the test | During the test | After the test

Figure F83. Three photos of the beam before, during and after the flexural test bio-glue + bentonite horizontal 2.



Figure F84. The force-displacement graph of flexural test bio-glue + bentonite horizontal 2.

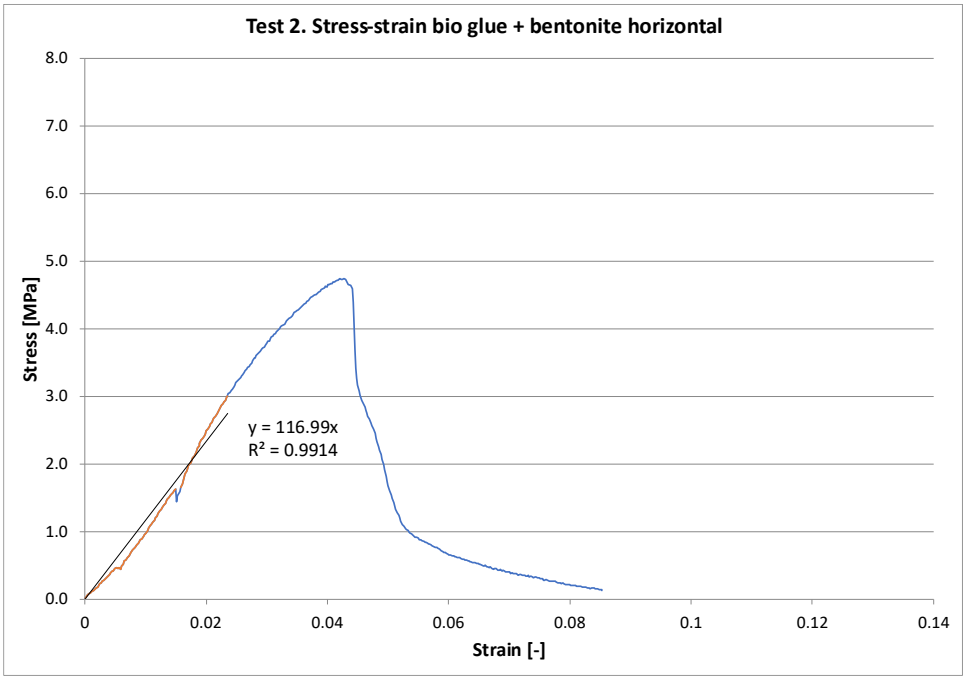
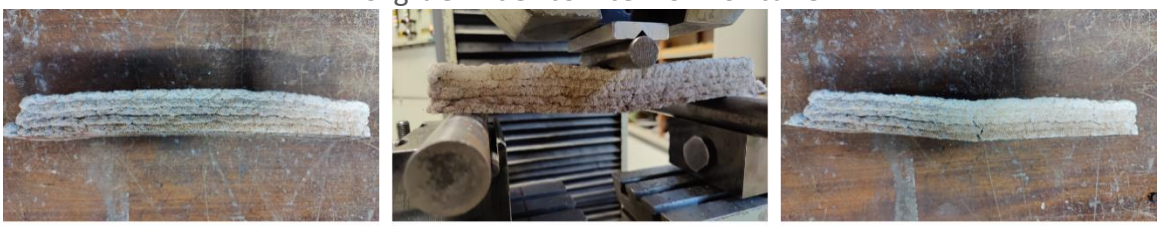


Figure F85. The stress-strain diagram of flexural test bio-glue + bentonite horizontal 2.

Bio-glue + bentonite horizontal 3



Before the test | During the test | After the test

Figure F86. Three photos of the beam before, during and after the flexural test bio-glue + bentonite horizontal 3.



Figure F87. The force-displacement graph of flexural test bio-glue + bentonite horizontal 3.

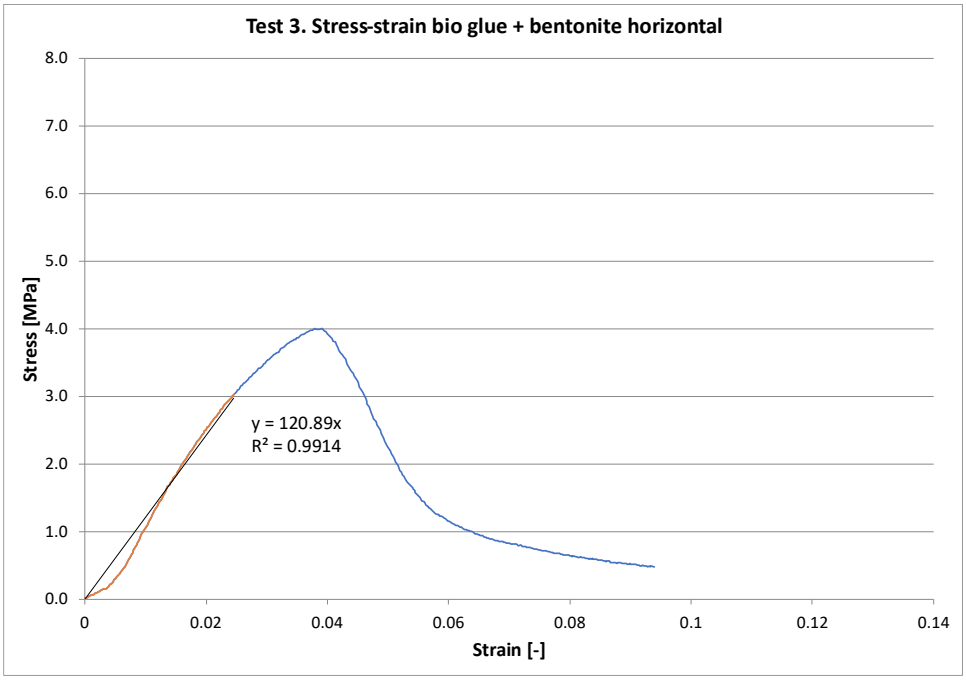


Figure F88. The stress-strain diagram of flexural test bio-glue + bentonite horizontal 3.

Figure F89 and Figure F90 present all three bio-glue with bentonite tests together in a force-displacement and a stress-strain graph.

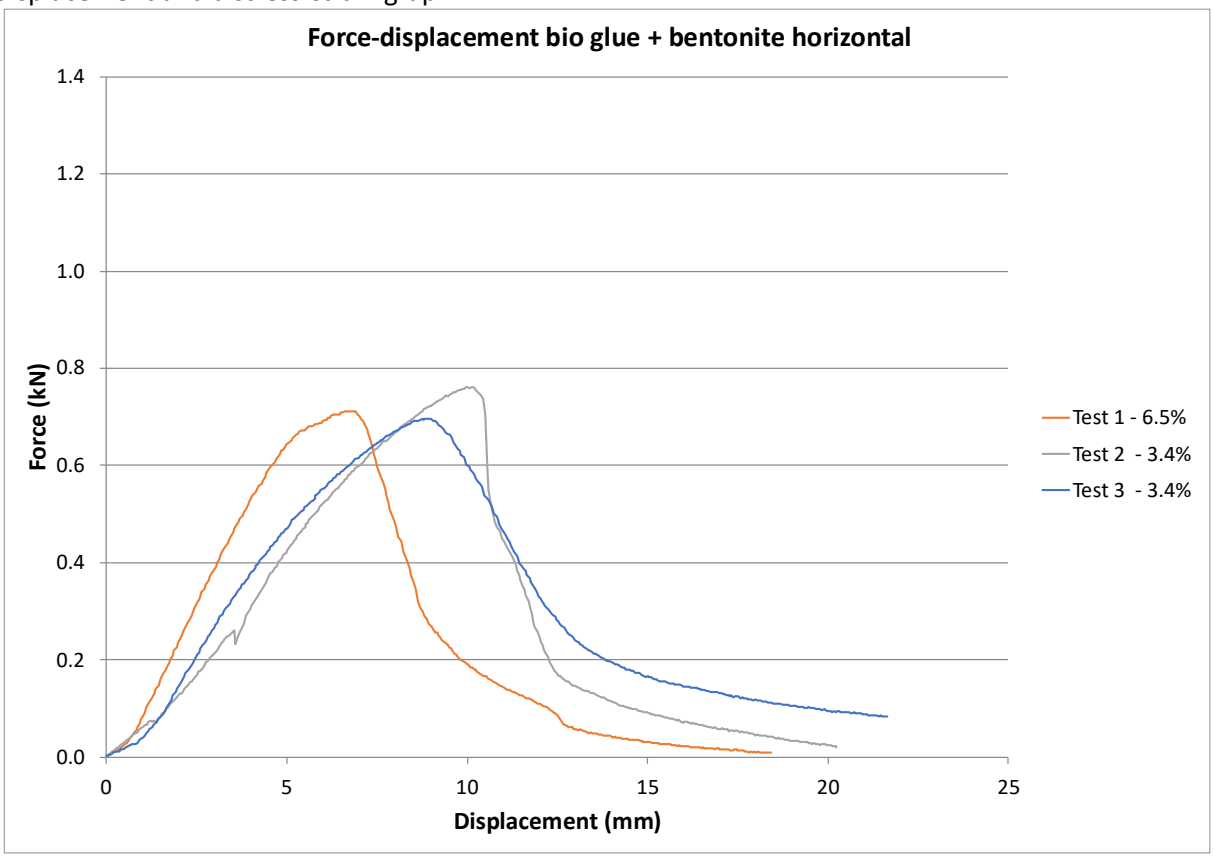


Figure F89. The force-displacement graph of all the bio-glue flexural tests in the horizontal orientation.

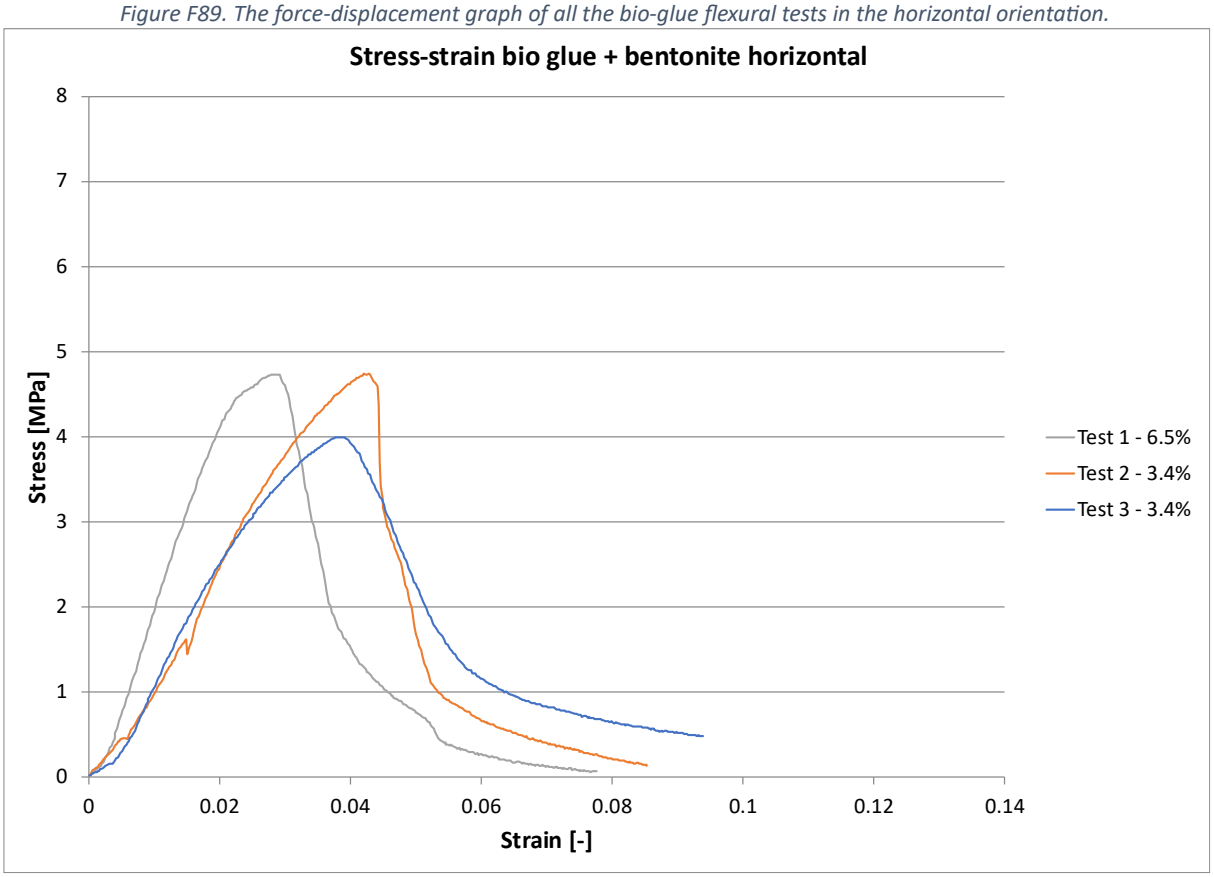


Figure F90. The stress-strain graph of all the bio-glue flexural tests in the horizontal orientation.

F.3.1.2 Vertical layer orientation

Figure F91 to Figure F102 show four bio-glue with bentonite tests with a vertical layer orientation. Each test is accompanied with three photos and two different graphs: the force-displacement and the stress-strain graph.



Figure F91. Three photos of the beam before, during and after the flexural test bio-glue + bentonite vertical 1.

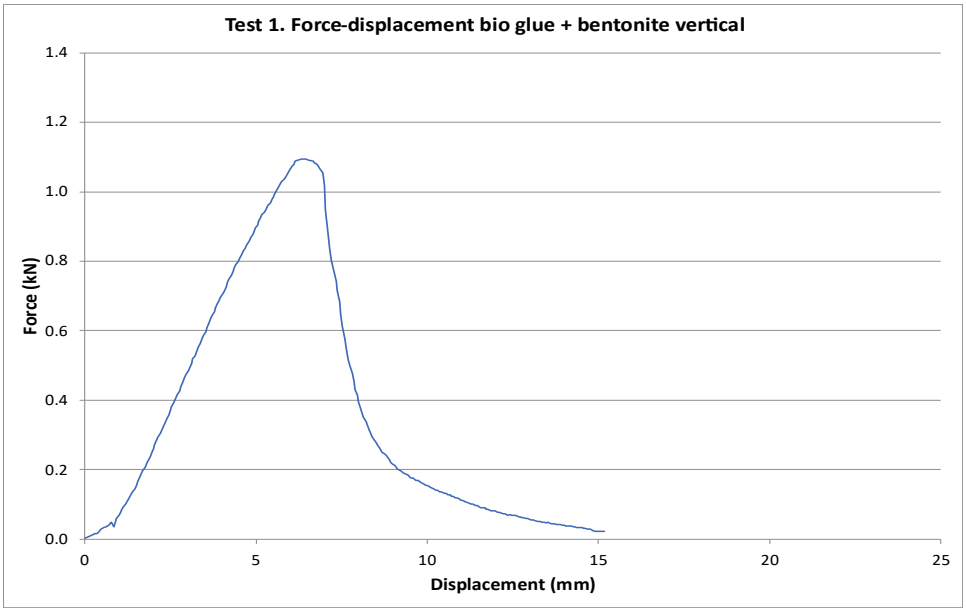


Figure F92. The force-displacement graph of flexural test bio-glue + bentonite vertical 1.

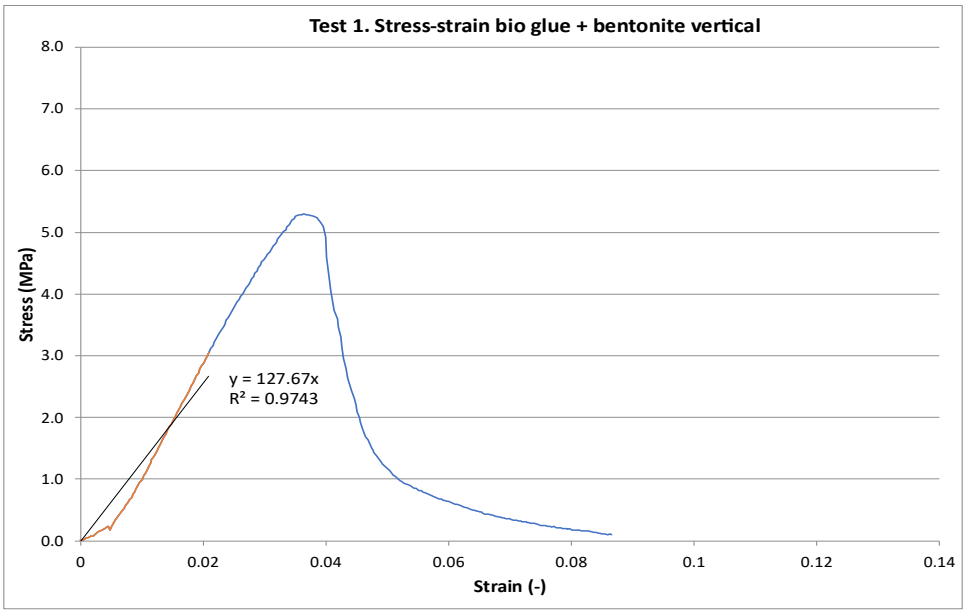


Figure F93. The stress-strain diagram of flexural test bio-glue + bentonite vertical 1.

Bio-glue + bentonite vertical 2



Before the test | During the test | After the test

Figure F94. Three photos of the beam before, during and after the flexural test bio-glue + bentonite vertical 2.

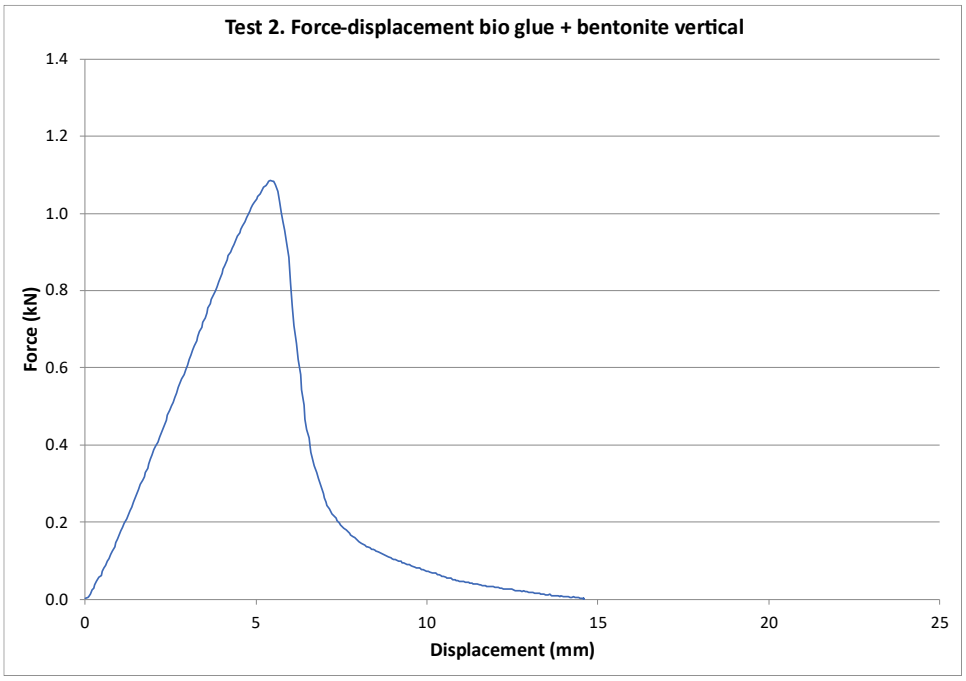


Figure F95. The force-displacement graph of flexural test bio-glue + bentonite vertical 2.

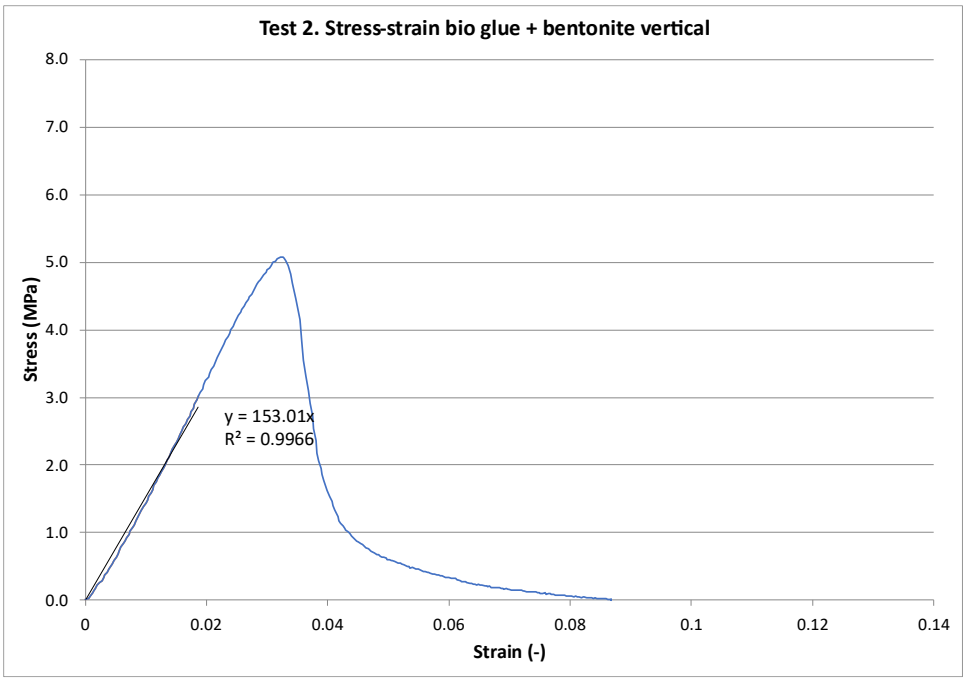


Figure F96. The stress-strain diagram of flexural test bio-glue + bentonite vertical 2.

Bio-glue + bentonite vertical 3



Before the test | During the test | After the test

Figure F97. Three photos of the beam before, during and after the flexural test bio-glue + bentonite vertical 3.

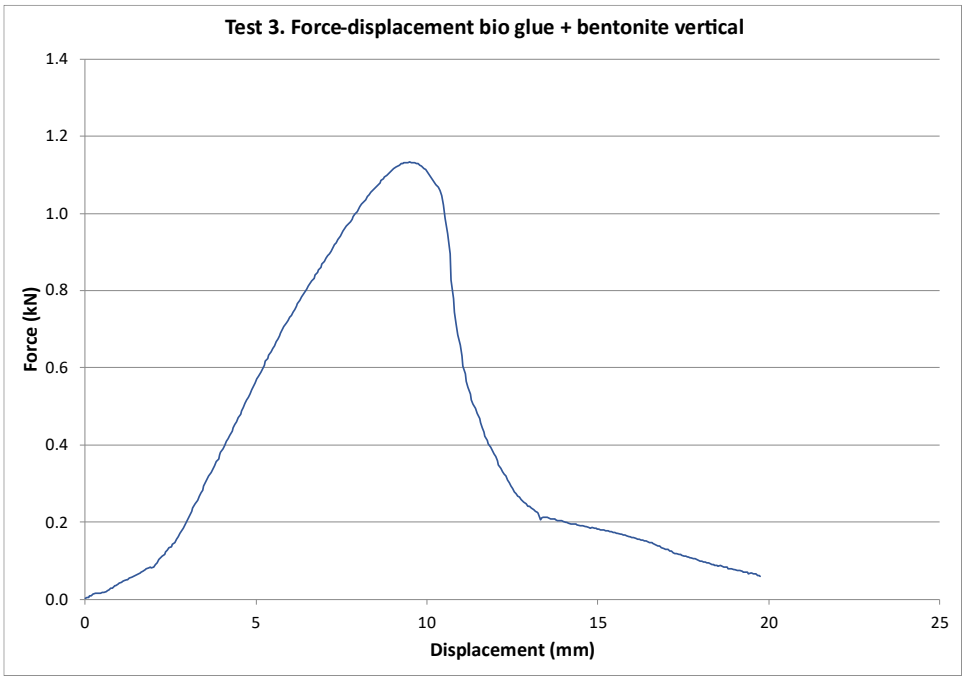


Figure F98. The force-displacement graph of flexural test bio-glue + bentonite vertical 3.

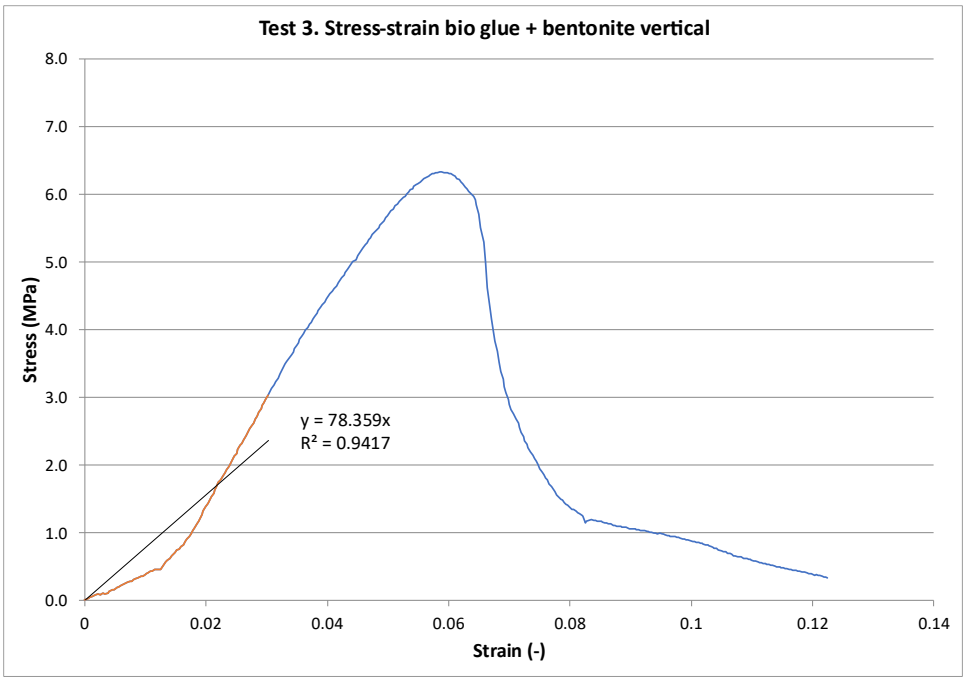


Figure F99. The stress-strain diagram of flexural test bio-glue + bentonite vertical 3.

Bio-glue + bentonite vertical 4



Before the test | During the test | After the test

Figure F100. Three photos of the beam before, during and after the flexural test bio-glue + bentonite vertical 4.

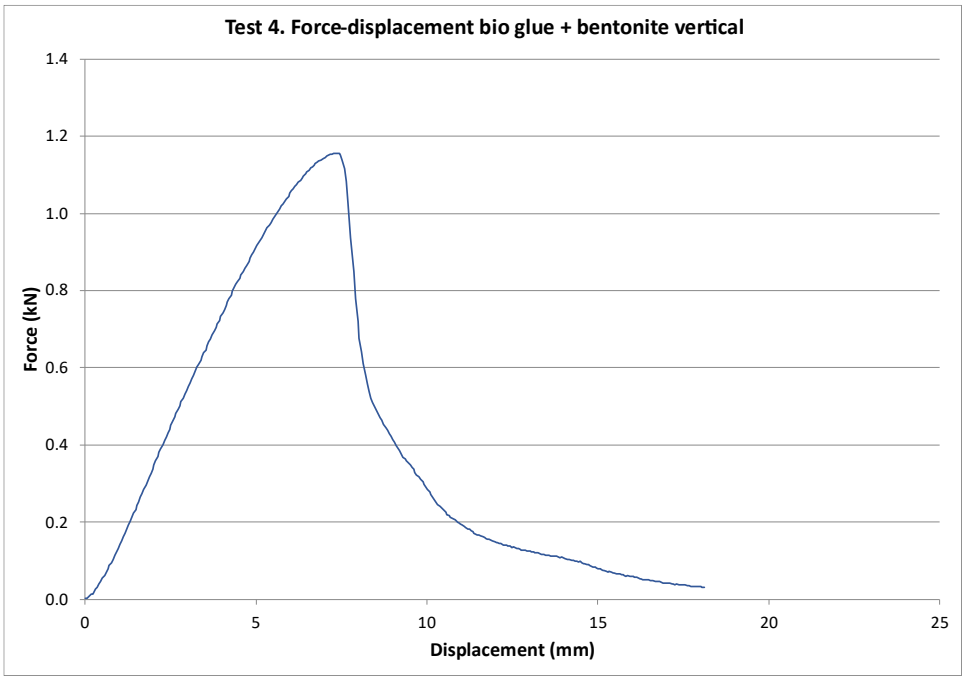


Figure F101. The force-displacement graph of flexural test bio-glue + bentonite vertical 4.

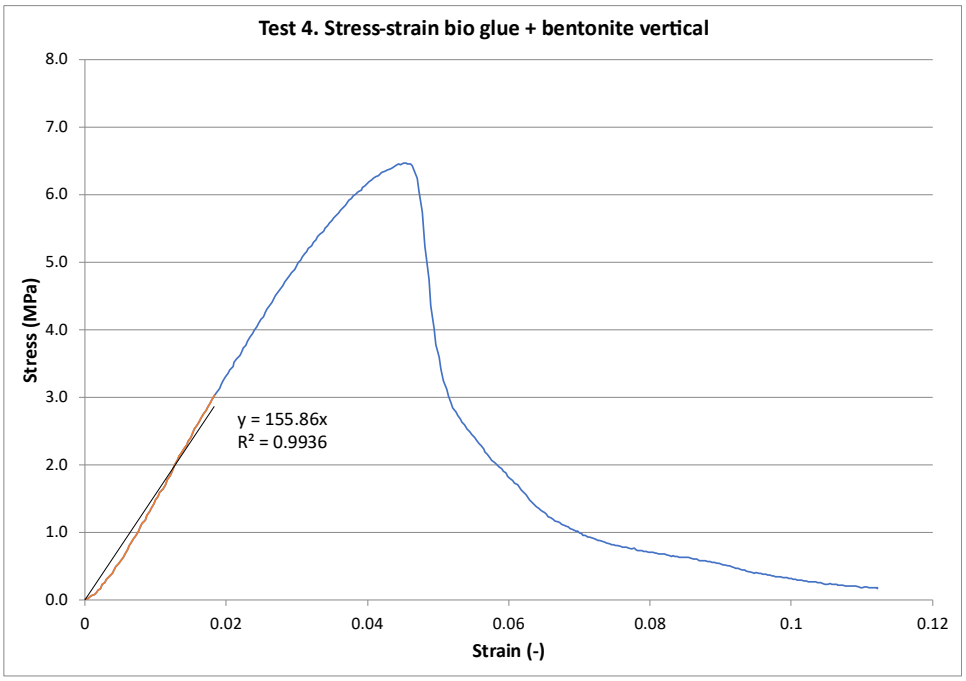


Figure F102. The stress-strain diagram of flexural test bio-glue + bentonite vertical 4.

Figure F103 and Figure F104 present all four bio-glue with bentonite tests together in a force-displacement and a stress-strain graph.

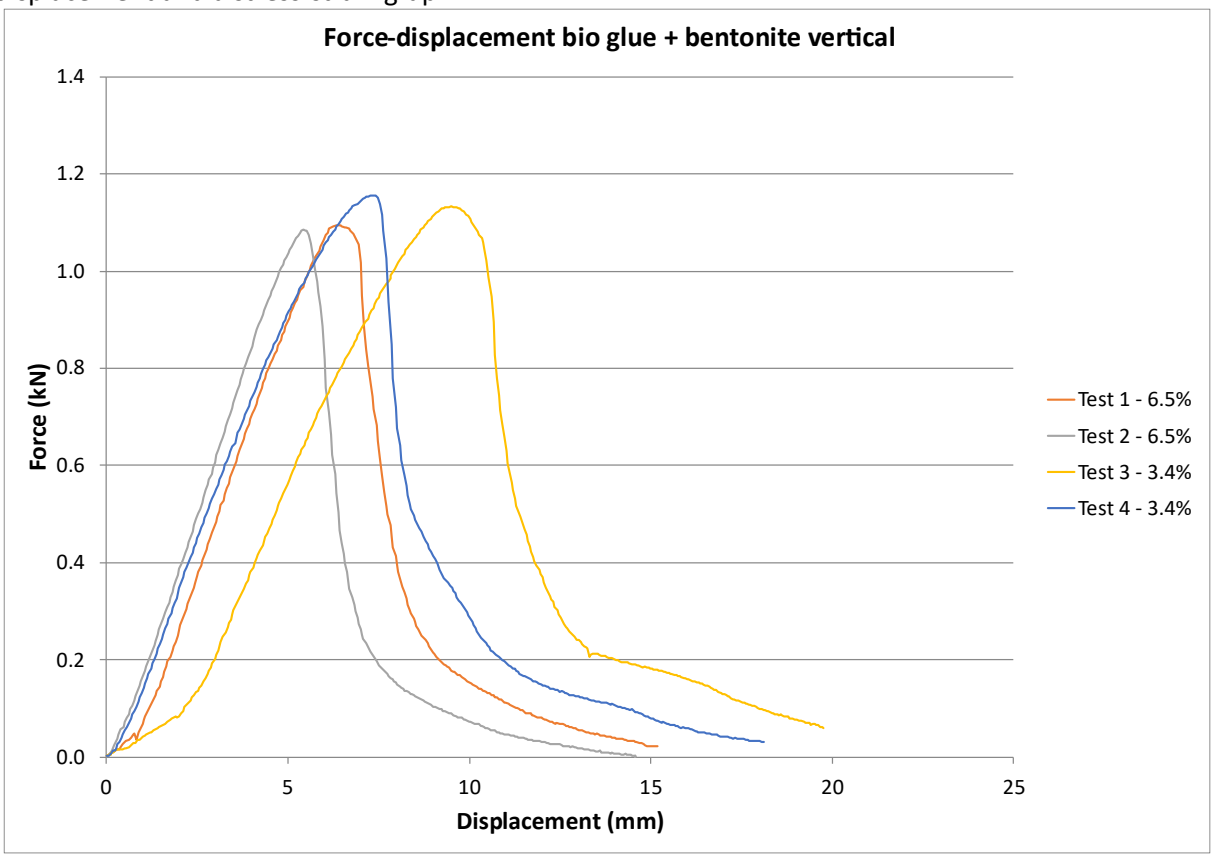


Figure F103. The force-displacement graph of all the bio-glue flexural tests in the vertical orientation.

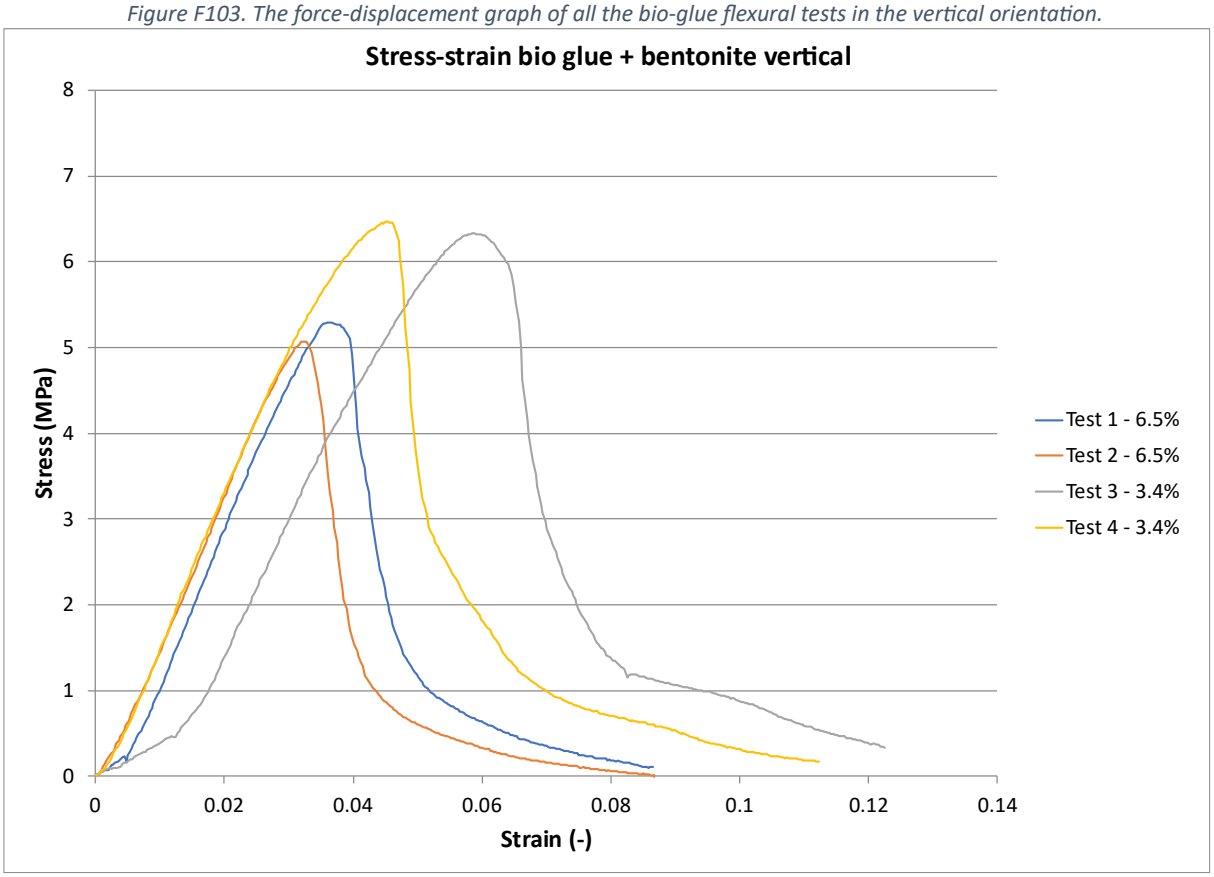


Figure F104. The stress-strain graph of all the bio-glue flexural tests in the vertical orientation.

F.3.2 Bio-glue with flax

F.3.2.1 Horizontal layer orientation

Figure F105 to Figure F113 show three bio-glue with flax tests with a horizontal layer orientation. Each test is accompanied with three photos and two different graphs: the force-displacement and the stress-strain graph.

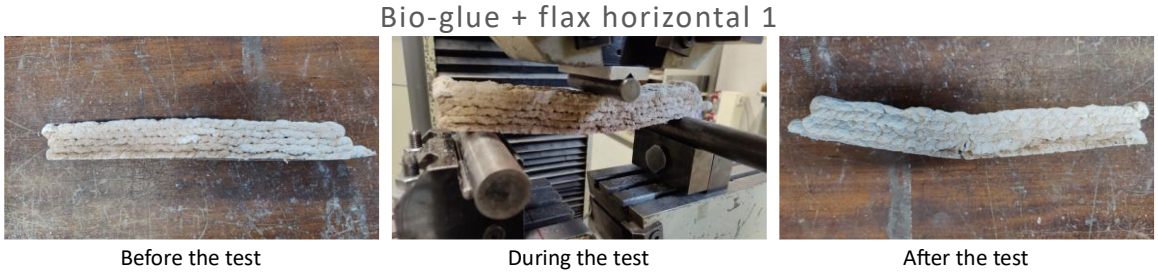


Figure F105. Three photos of the beam before, during and after the flexural test bio-glue + flax horizontal 1.

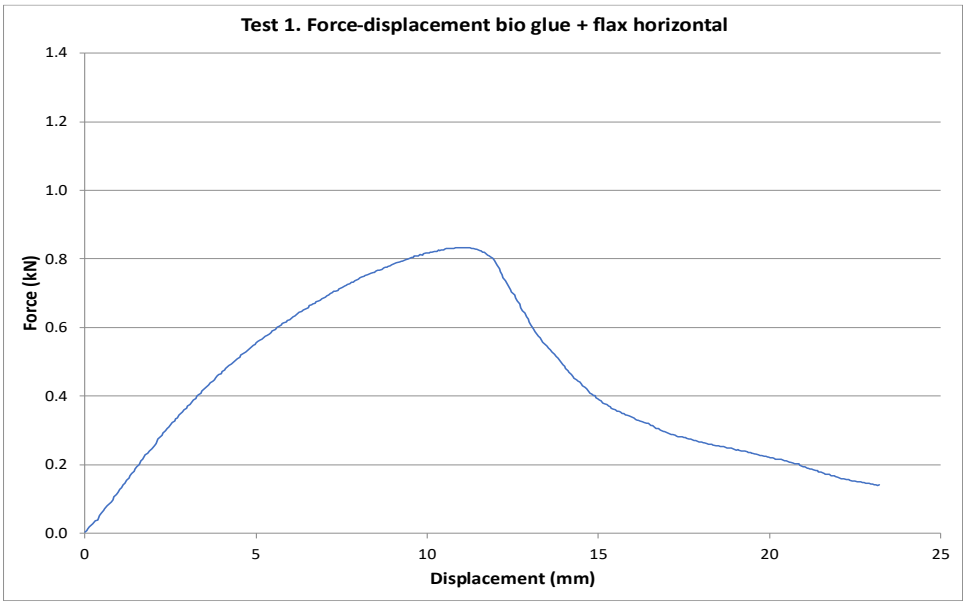


Figure F106. The force-displacement graph of flexural test bio-glue + flax horizontal 1.

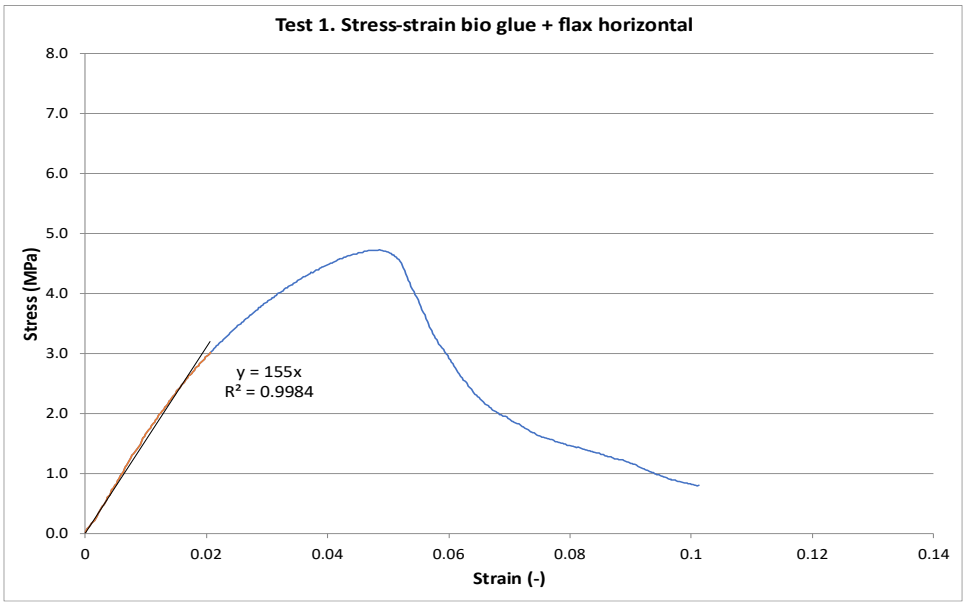
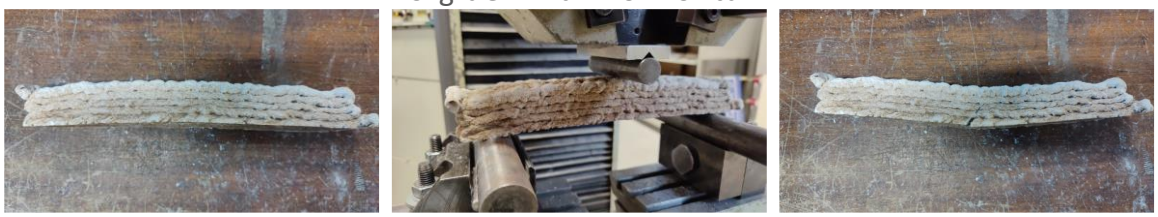


Figure F107. The stress-strain diagram of flexural test bio-glue + flax horizontal 1.

Bio-glue + flax horizontal 2



Before the test | During the test | After the test

Figure F108. Three photos of the beam before, during and after the flexural test bio-glue + flax horizontal 2.



Figure F109. The force-displacement graph of flexural test bio-glue + flax horizontal 2.

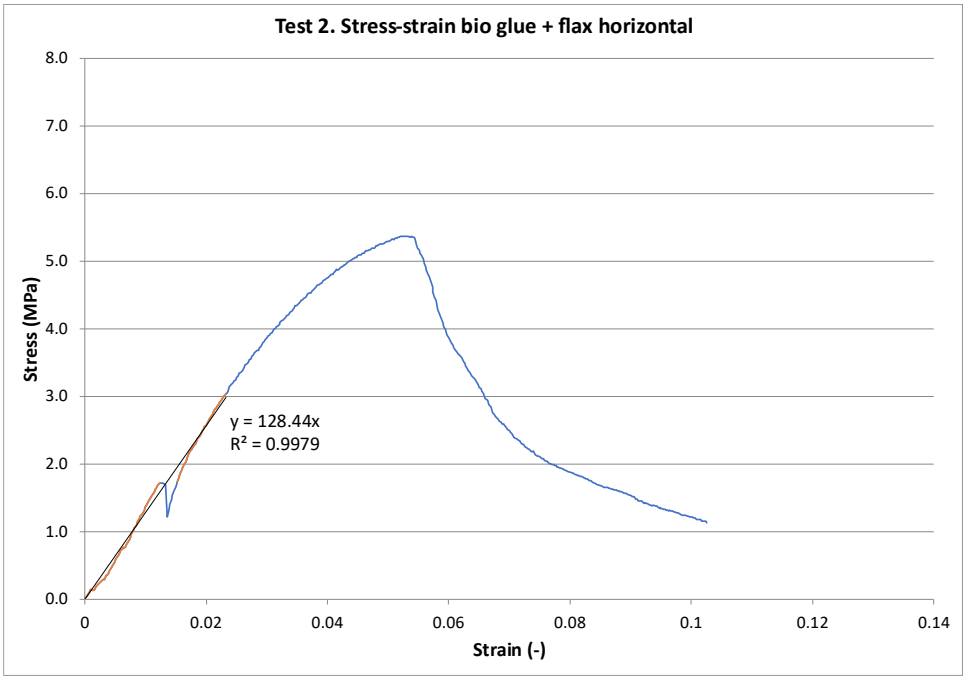


Figure F110. The stress-strain diagram of flexural test bio-glue + flax horizontal 2.

Bio-glue + flax horizontal 3



Before the test | During the test | After the test

Figure F111. Three photos of the beam before, during and after the flexural test bio-glue + flax horizontal 3.



Figure F112. The force-displacement graph of flexural test bio-glue + flax horizontal 3.

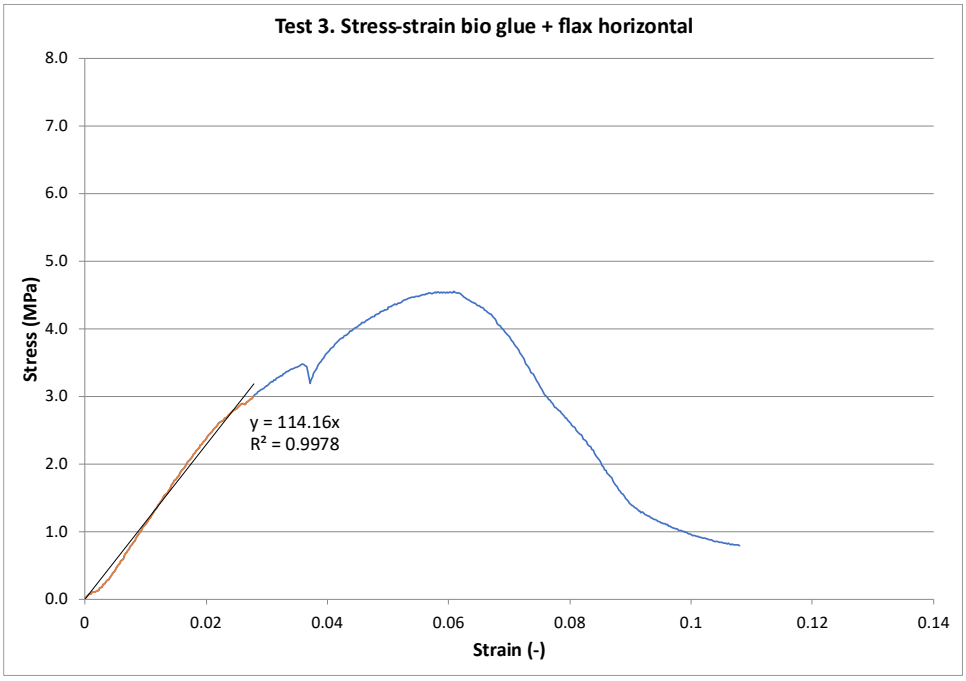


Figure F113. The stress-strain diagram of flexural test bio-glue + flax horizontal 3.

Figure F114 and Figure F115 present all three bio-glue with flax tests together in a force-displacement and a stress-strain graph.

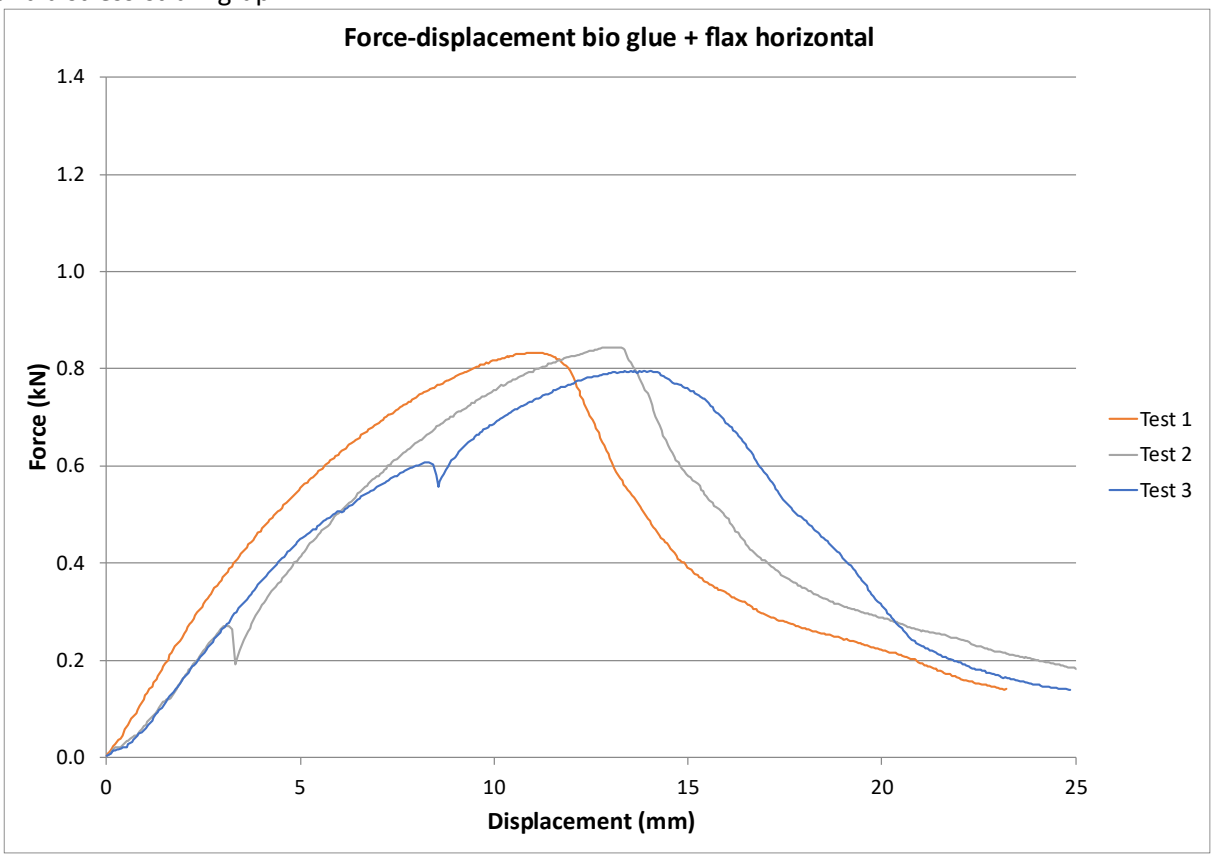


Figure F114. The force-displacement graph of all the bio-glue flexural tests in the horizontal orientation.

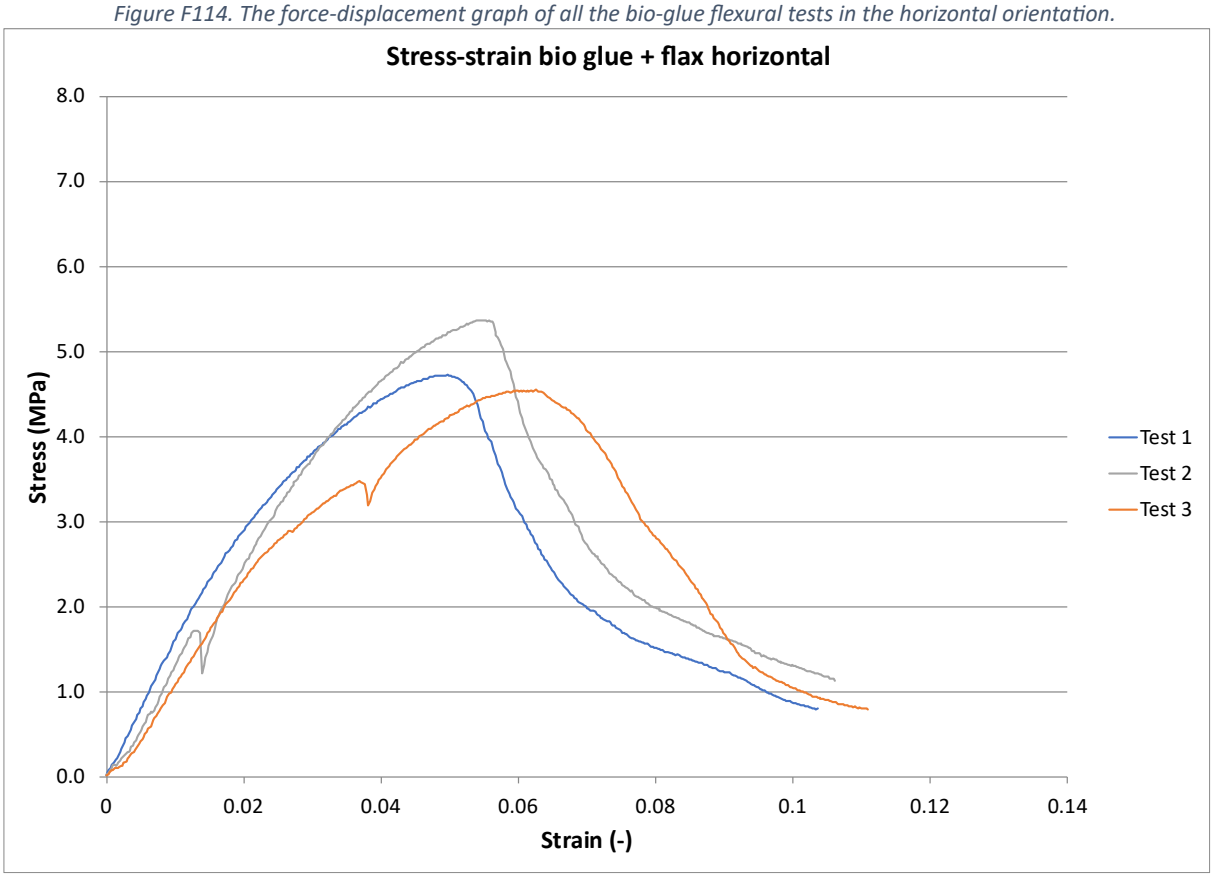


Figure F115. The stress-strain graph of all the bio-glue flexural tests in the horizontal orientation.

F.3.2.2 Vertical layer orientation

Figure F116 to Figure F124 show all three bio-glue with flax tests with a vertical layer orientation. Each test is accompanied with three photos and two different graphs: the force-displacement and the stress-strain graph.



Figure F116. Three photos of the beam before, during and after the flexural test bio-glue + flax vertical 1.

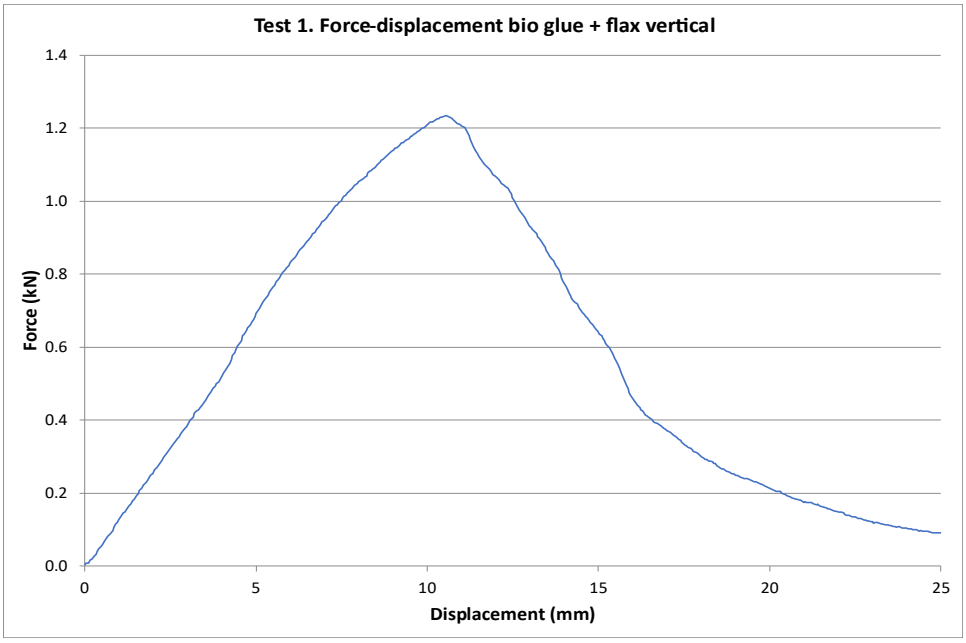


Figure F117. The force-displacement graph of flexural test bio-glue + flax vertical 1.

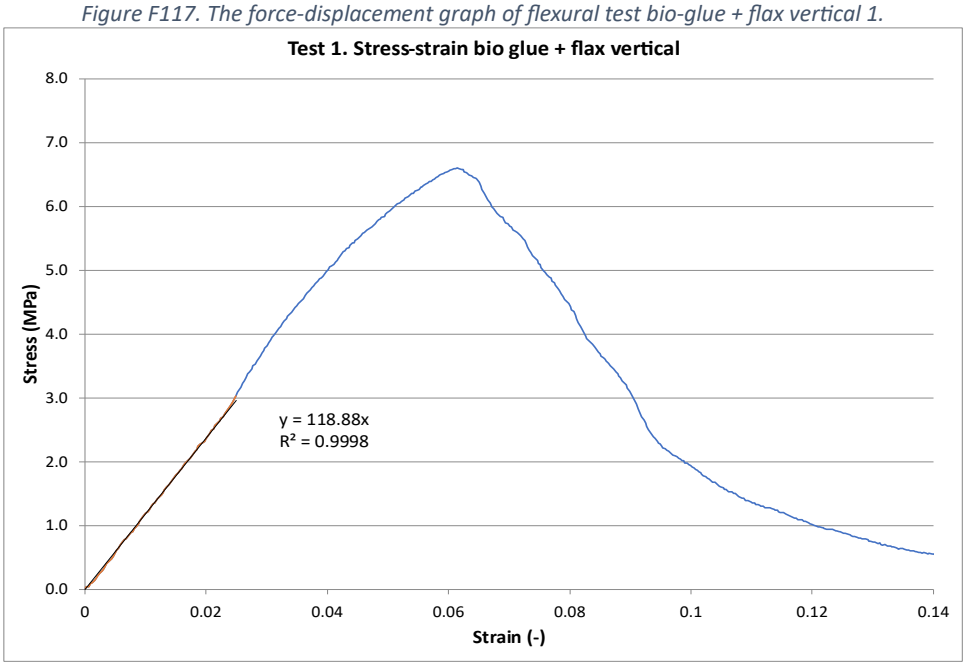


Figure F118. The stress-strain diagram of flexural test bio-glue + flax vertical 1.

Bio-glue + flax vertical 2



Before the test | During the test | After the test

Figure F119. Three photos of the beam before, during and after the flexural test bio-glue + flax vertical 2.

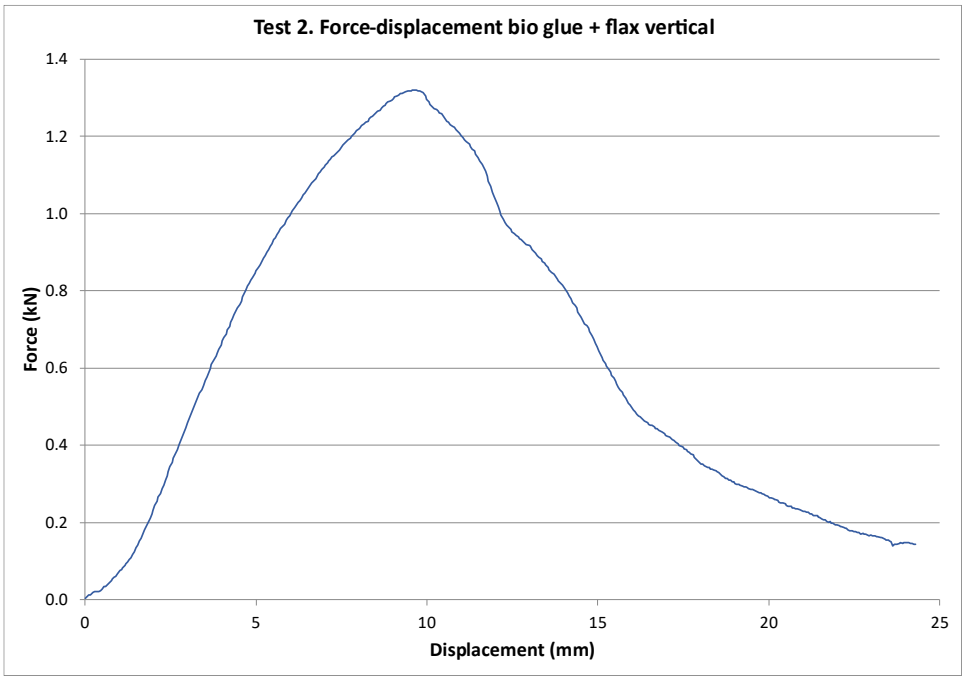


Figure F120. The force-displacement graph of flexural test bio-glue + flax vertical 2.

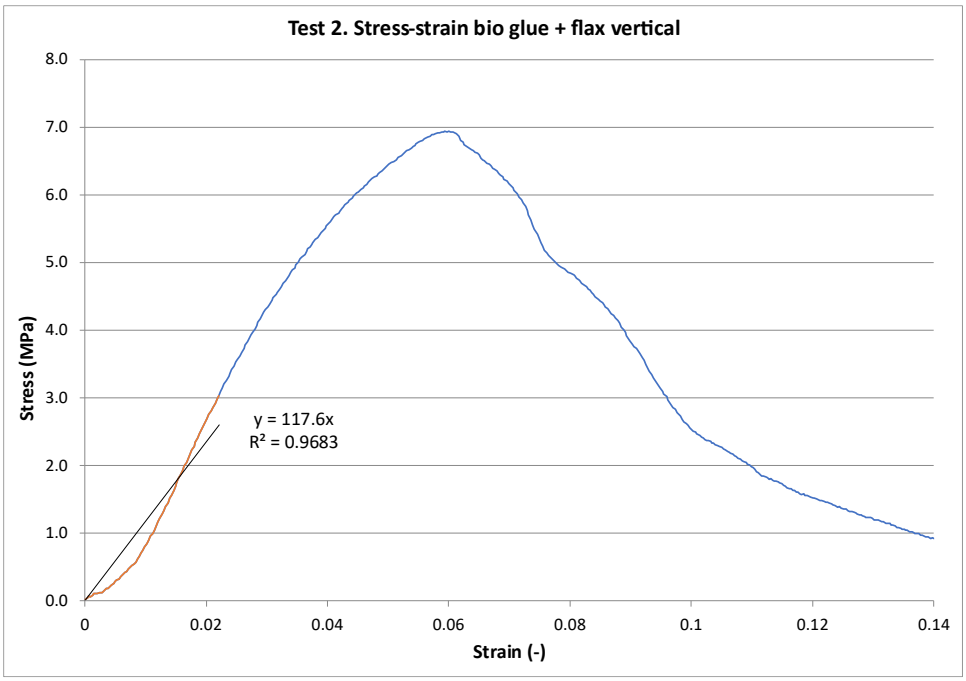


Figure F121. The stress-strain diagram of flexural test bio-glue + flax vertical 2.

Bio-glue + flax vertical 3



Before the test | During the test | After the test

Figure F122. Three photos of the beam before, during and after the flexural test bio-glue + flax vertical 3.

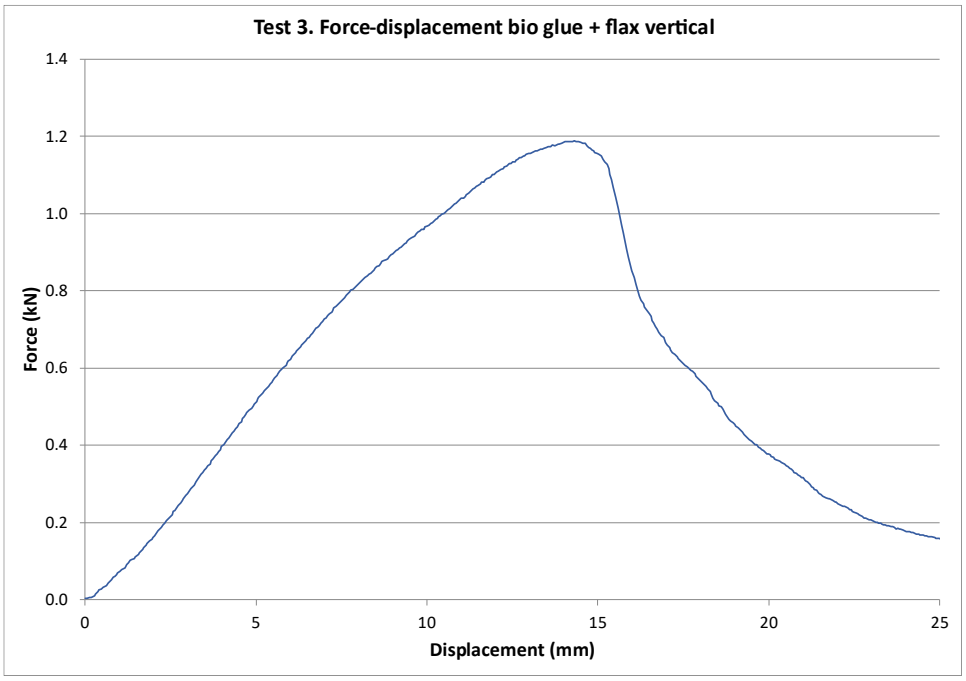


Figure F123. The force-displacement graph of flexural test bio-glue + flax vertical 3.

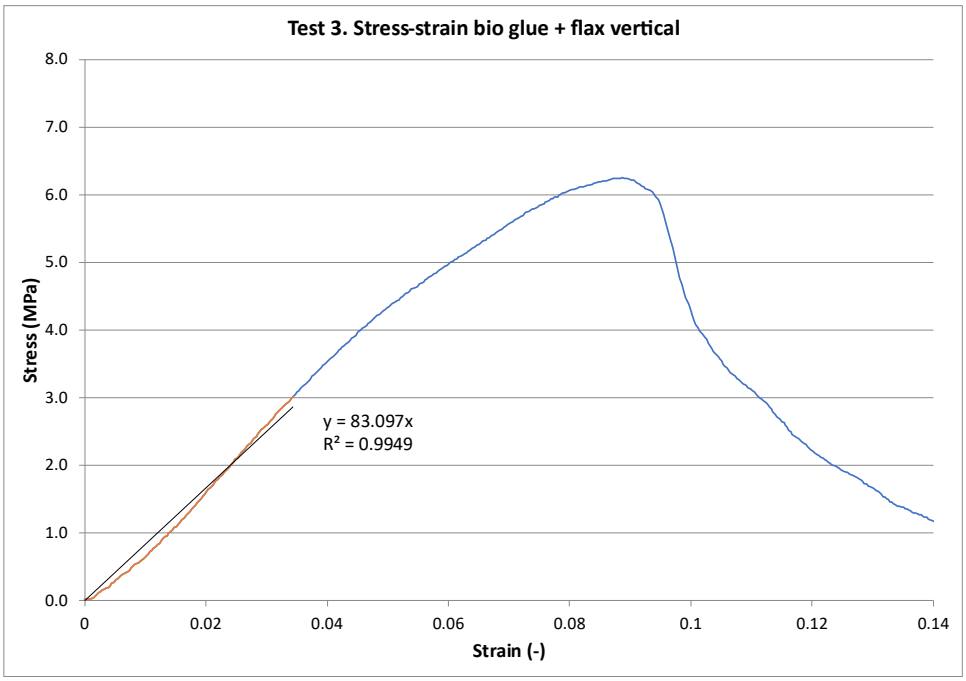


Figure F124. The stress-strain diagram of flexural test bio-glue + flax vertical 3.

Figure F125 and Figure F126 present all three bio-glue with flax tests together in a force-displacement and a stress-strain graph.

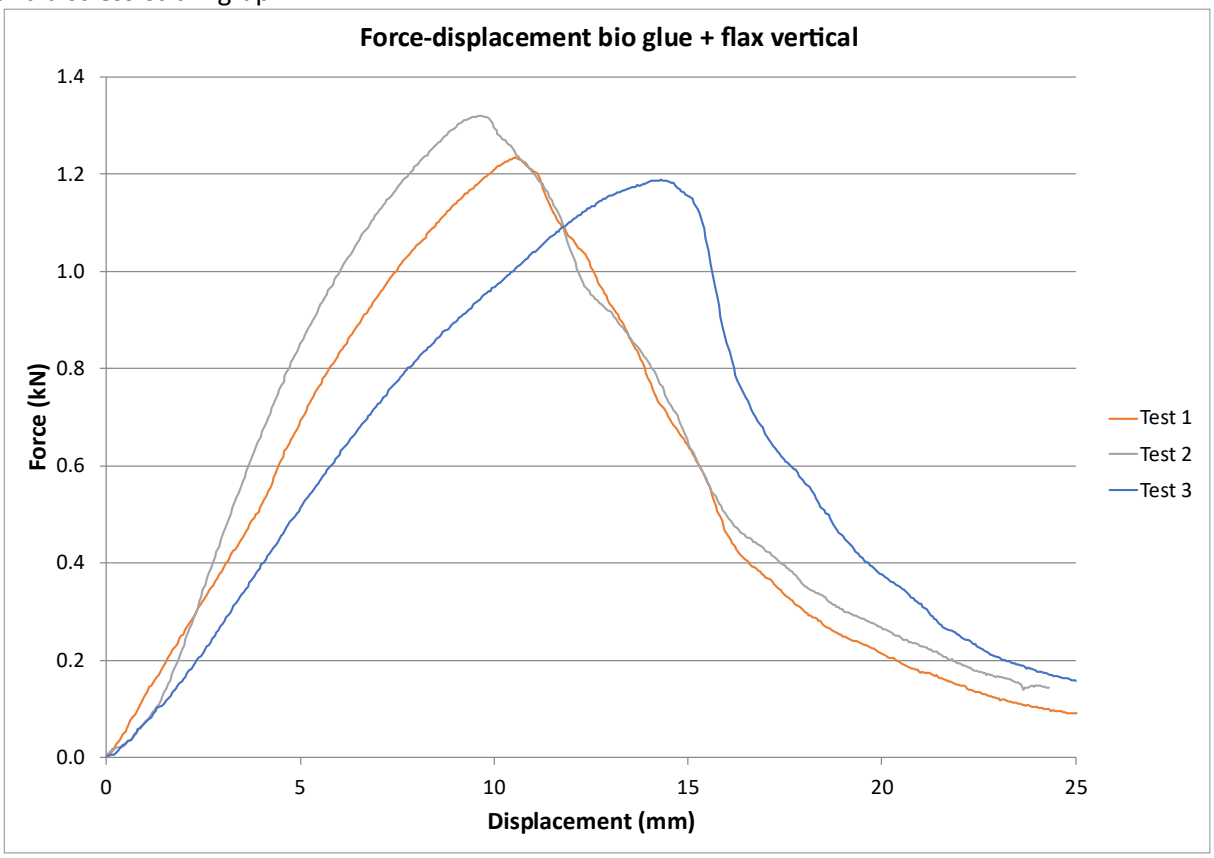


Figure F125. The force-displacement graph of all the bio-glue flexural tests in the vertical orientation.

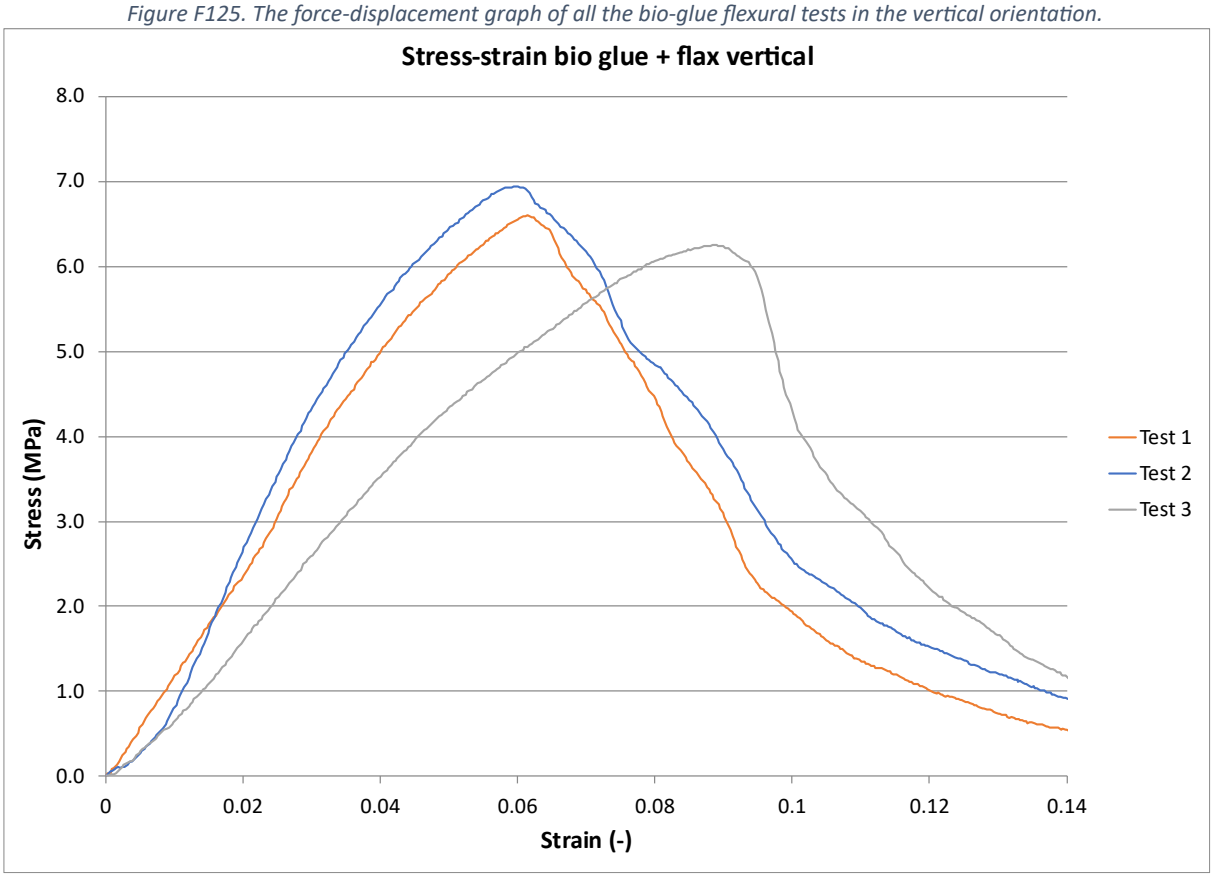


Figure F126. The stress-strain graph of all the bio-glue flexural tests in the vertical orientation.

F.3.3 Bio-glue with bentonite and flax

F.3.3.1 Horizontal layer orientation

Figure F127 to Figure F135 show three bio-glue with bentonite and flax tests with a horizontal layer orientation. Each test is accompanied with three photos and two different graphs: the force-displacement and the stress-strain graph.

Bio-glue + bentonite + flax horizontal 1



Before the test | During the test | After the test

Figure F127. Three photos of the beam before, during and after the flexural test bio-glue + bentonite + flax horizontal 1.

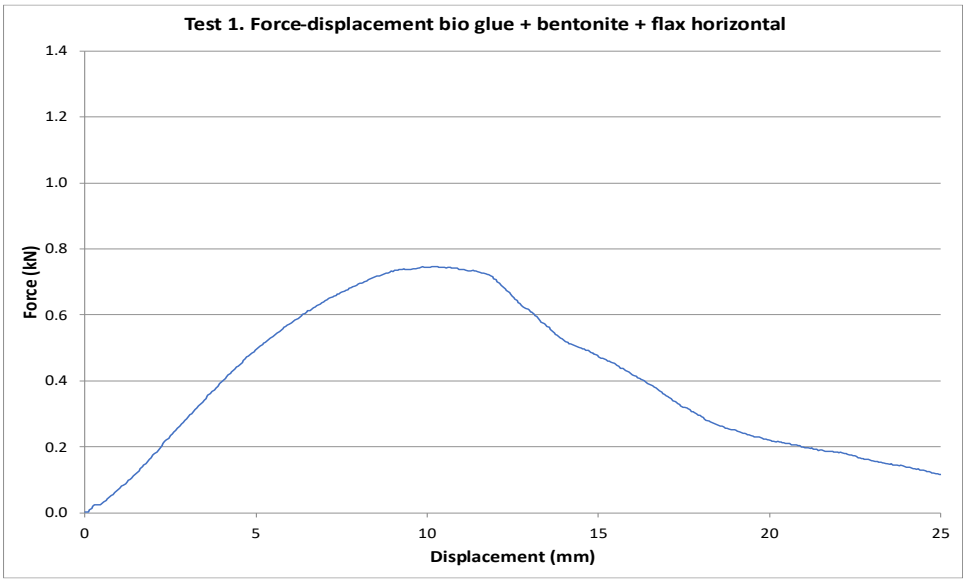


Figure F128. The force-displacement graph of flexural test bio-glue + bentonite + flax horizontal 1.

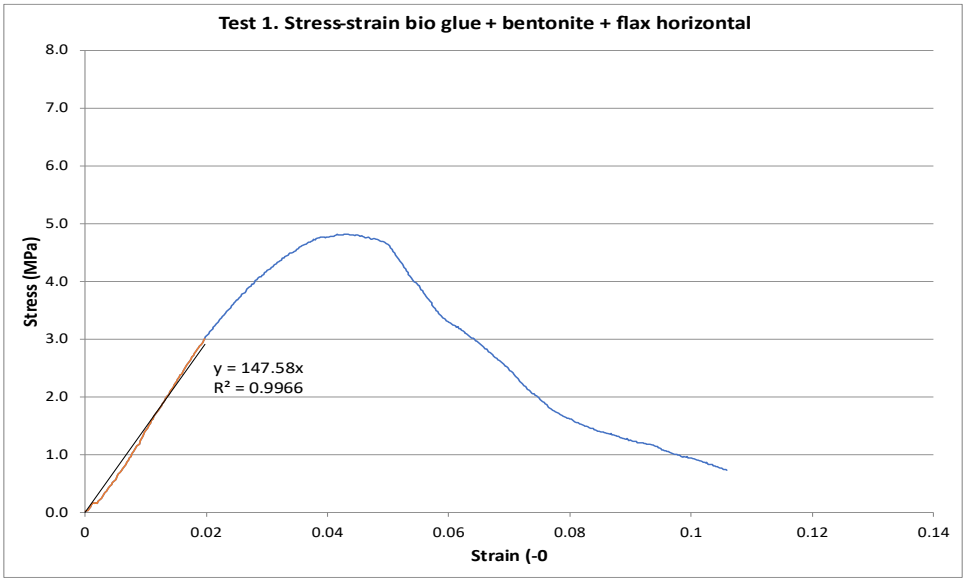


Figure F129. The stress-strain diagram of flexural test bio-glue + bentonite + flax horizontal 1.

Bio-glue + bentonite + flax horizontal 2



Before the test | During the test | After the test

Figure F130. Three photos of the beam before, during and after the flexural test bio-glue + bentonite + flax horizontal 2.

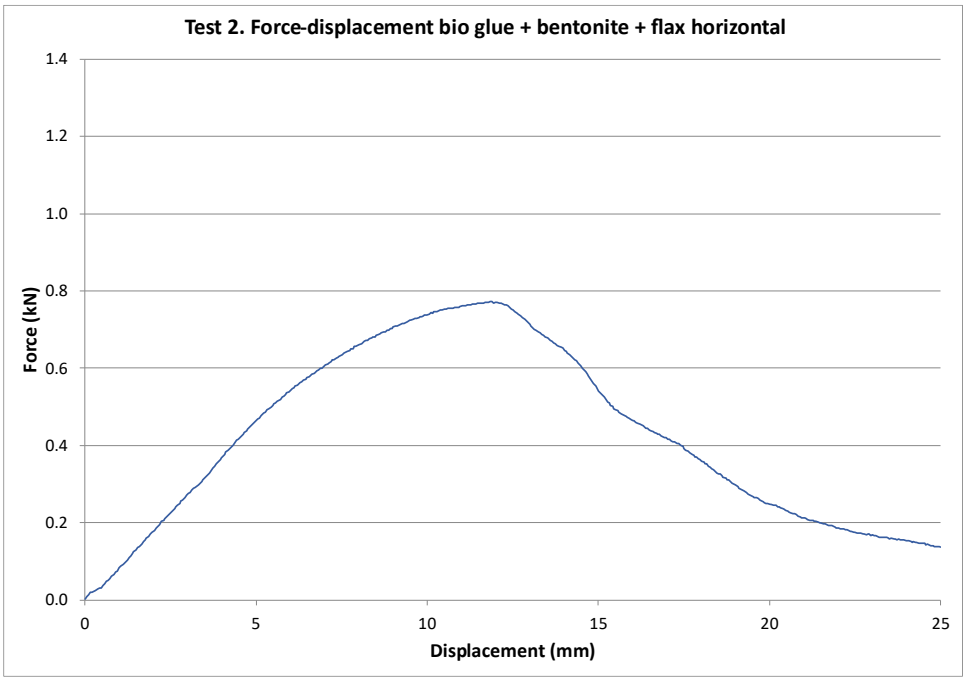


Figure F131. The force-displacement graph of flexural test bio-glue + bentonite + flax horizontal 2.

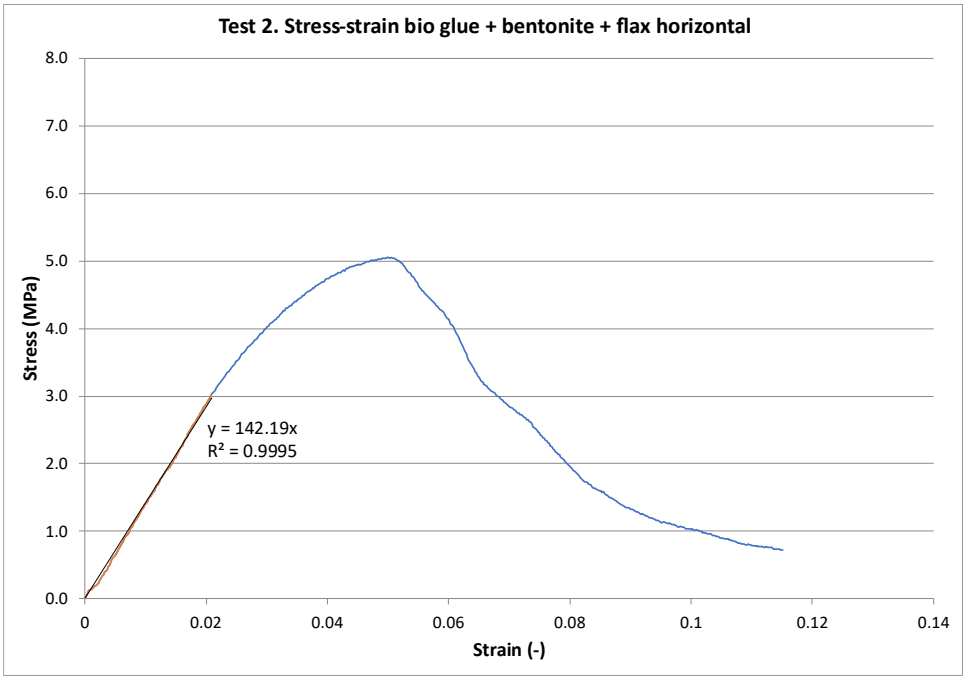


Figure F132. The stress-strain diagram of flexural test bio-glue + bentonite + flax horizontal 2.

Bio-glue + bentonite + flax horizontal 3



Before the test | During the test | After the test

Figure F133. Three photos of the beam before, during and after the flexural test bio-glue + bentonite + flax horizontal 3.

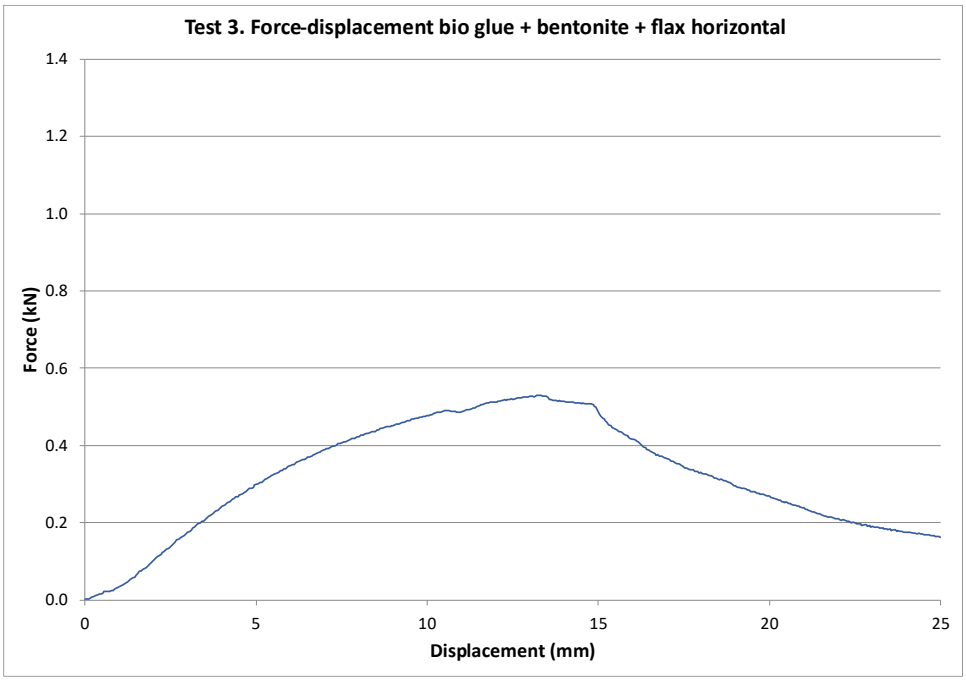


Figure F134. The force-displacement graph of flexural test bio-glue + bentonite + flax horizontal 3.

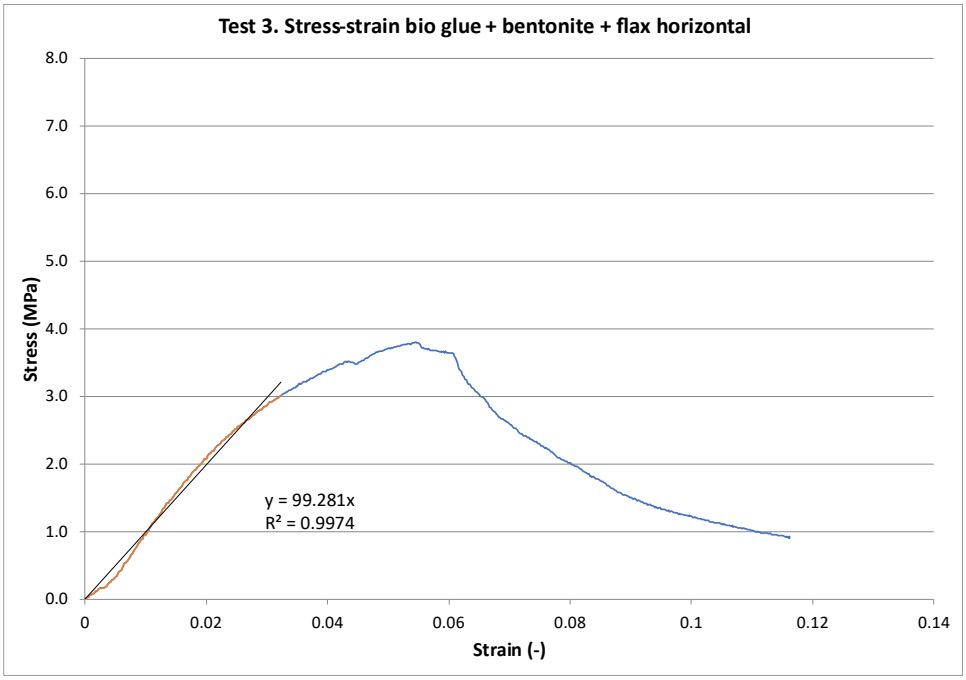


Figure F135. The stress-strain diagram of flexural test bio-glue + bentonite + flax horizontal 3.

Figure F136 and Figure F137 present all three bio-glue with bentonite and flax tests together in a force-displacement and a stress-strain graph.

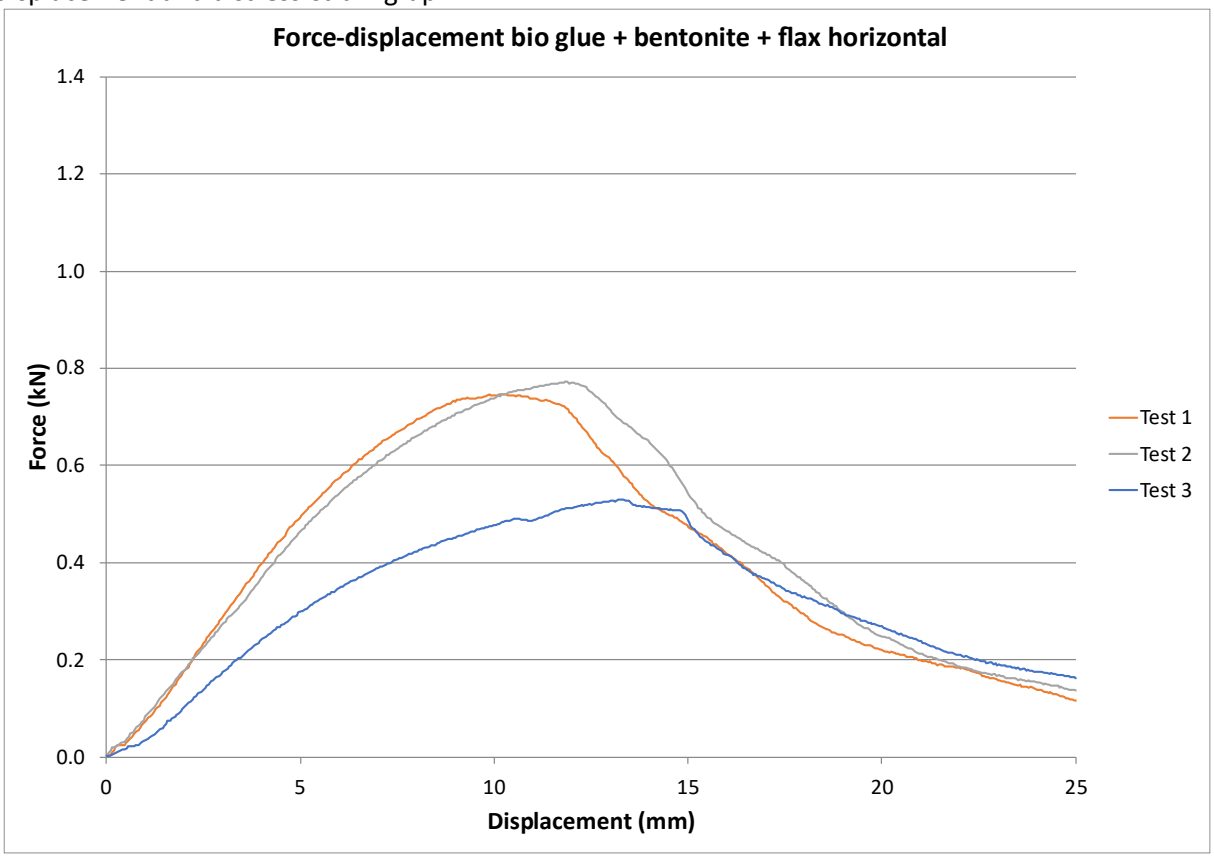


Figure F136. The force-displacement graph of all the bio-glue with bentonite and flax flexural tests in the horizontal orientation.

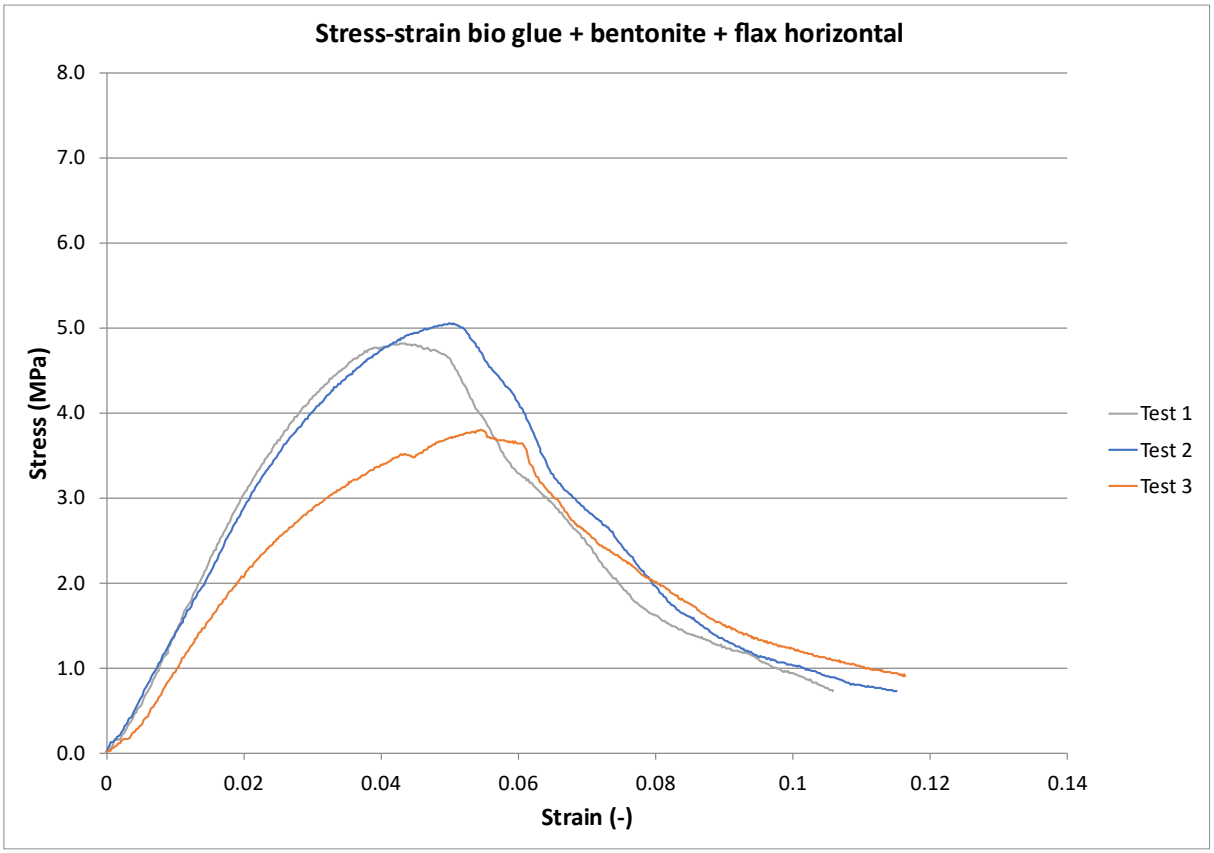


Figure F137. The stress-strain graph of all the bio-glue with bentonite and flax flexural tests in the horizontal orientation.

F.3.3.2 Vertical layer orientation

Figure F138 to Figure F146 show three bio-glue with bentonite and flax tests with a vertical layer orientation. Each test is accompanied with three photos and two different graphs: the force-displacement and the stress-strain graph.

Bio-glue + bentonite + flax vertical 1



Before the test | During the test | After the test

Figure F138. Three photos of the beam before, during and after the flexural test bio-glue + bentonite + flax vertical 1.

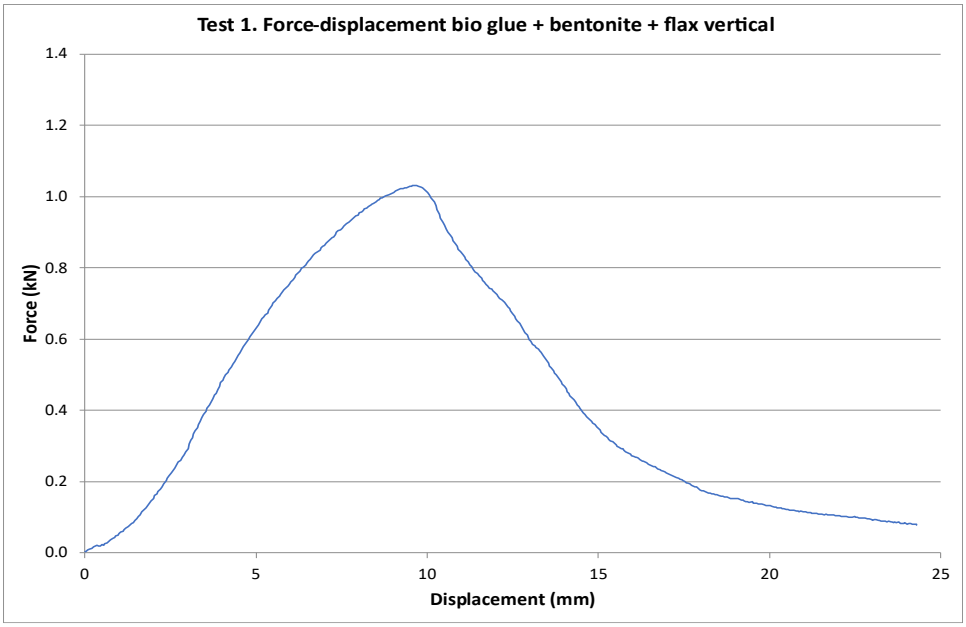


Figure F139. The force-displacement graph of flexural test bio-glue + bentonite + flax vertical 1

.

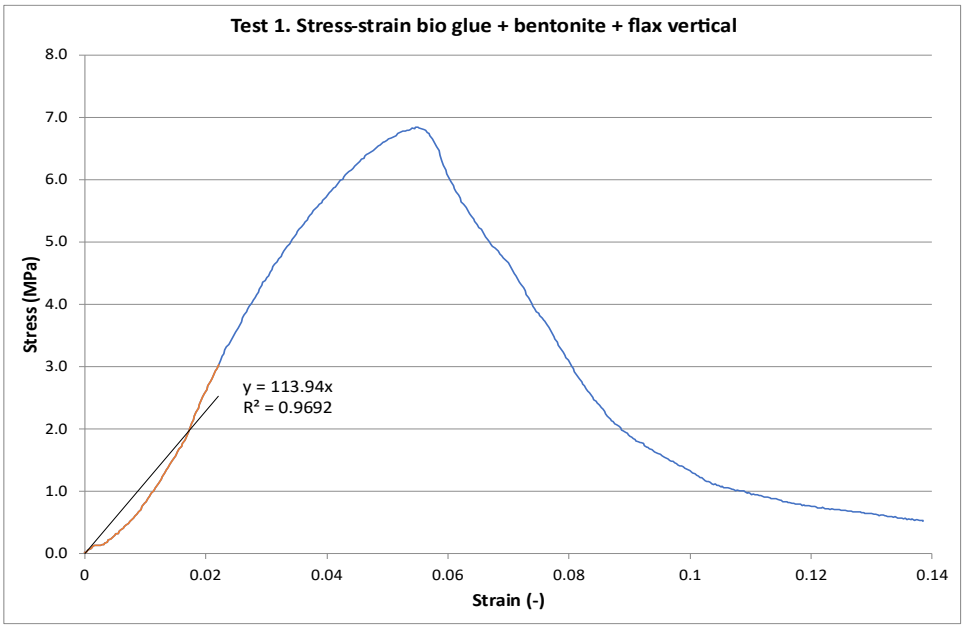


Figure F140. The stress-strain diagram of flexural test bio-glue + bentonite + flax vertical 1.

Bio-glue + bentonite + flax vertical 2



Before the test | During the test | After the test

Figure F141. Three photos of the beam before, during and after the flexural test bio-glue + bentonite + flax vertical 2.

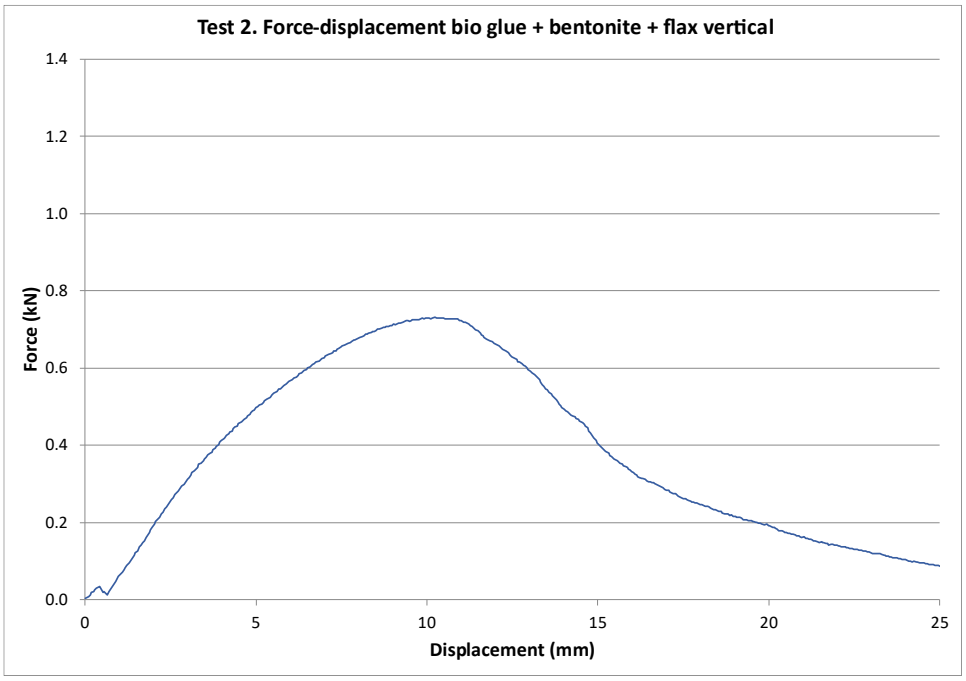


Figure F142. The force-displacement graph of flexural test bio-glue + bentonite + flax vertical 2.

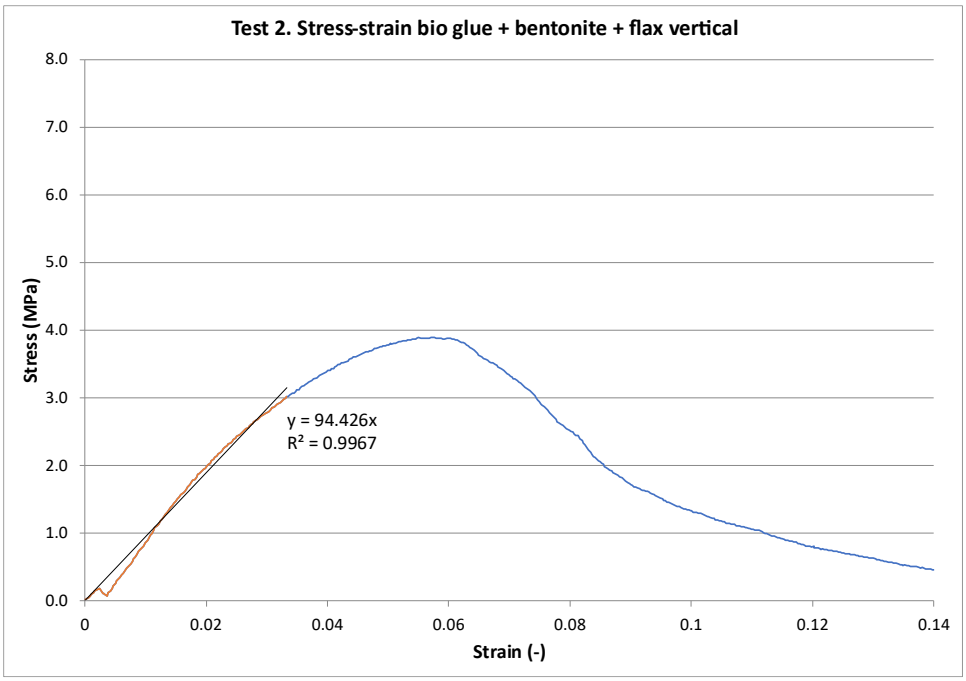


Figure F143. The stress-strain diagram of flexural test bio-glue + bentonite + flax vertical 2.

Bio-glue + bentonite + flax vertical 3



Before the test | During the test | After the test

Figure F144. Three photos of the beam before, during and after the flexural test bio-glue + bentonite + flax vertical 3.

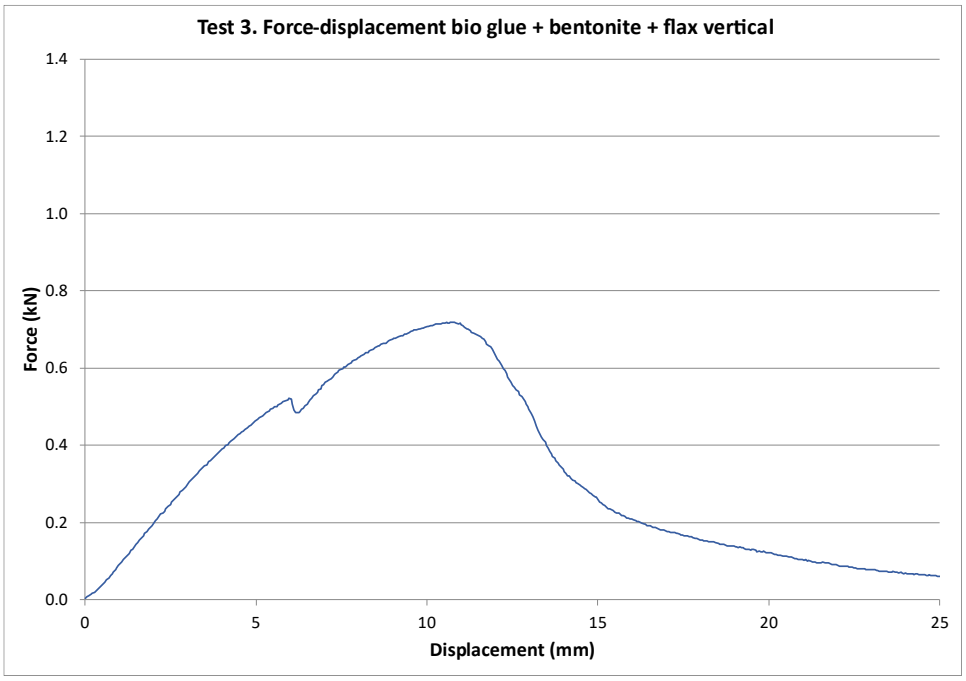


Figure F145. The force-displacement graph of flexural test bio-glue + bentonite + flax vertical 3.

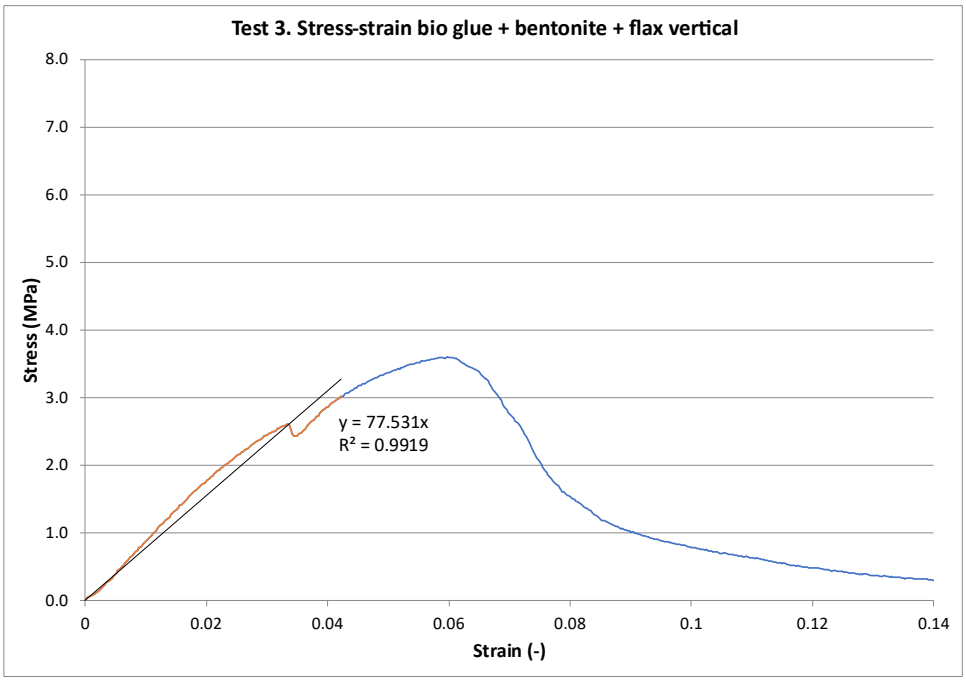


Figure F146. The stress-strain diagram of flexural test bio-glue + bentonite + flax vertical 3.

Figure F147 and Figure F148 present all three bio-glue with bentonite and flax tests together in a force-displacement and a stress-strain graph.

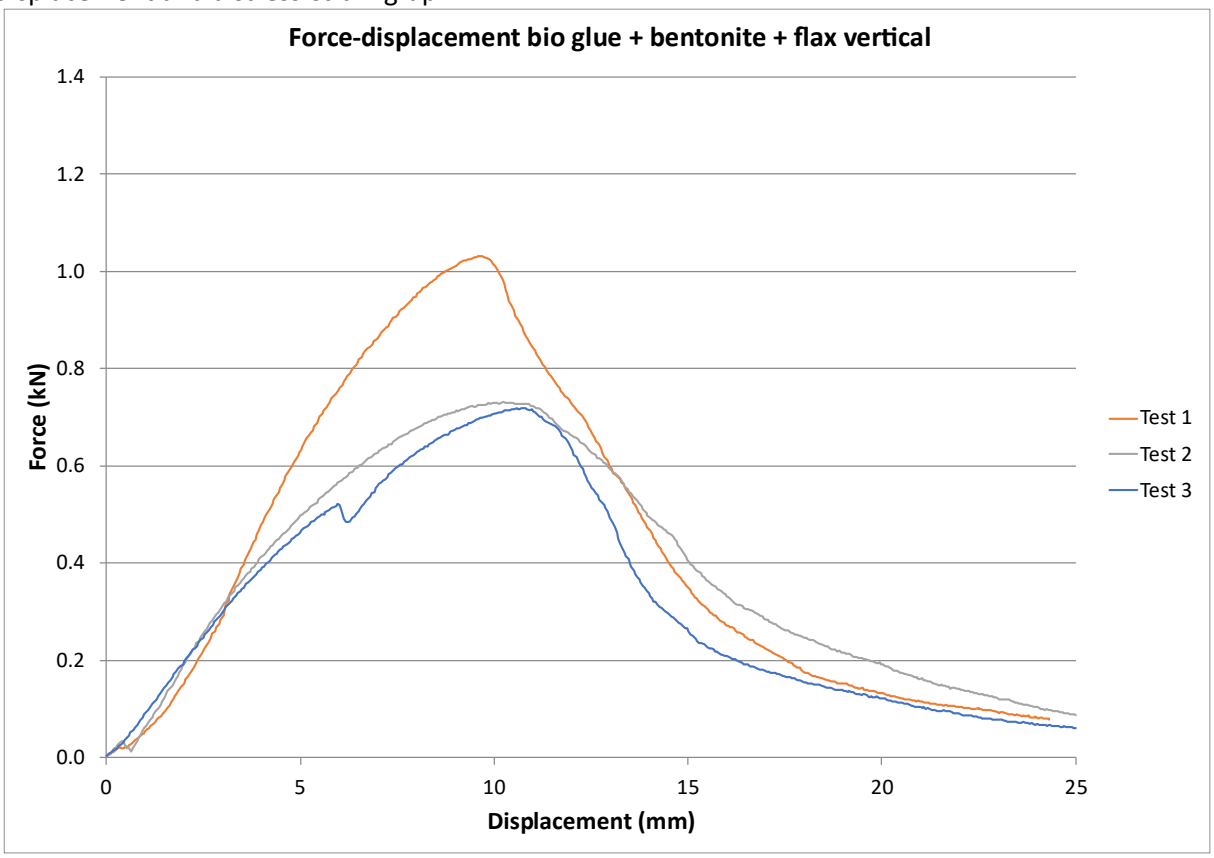


Figure F147. The force-displacement graph of all the bio-glue flexural tests in the vertical orientation.

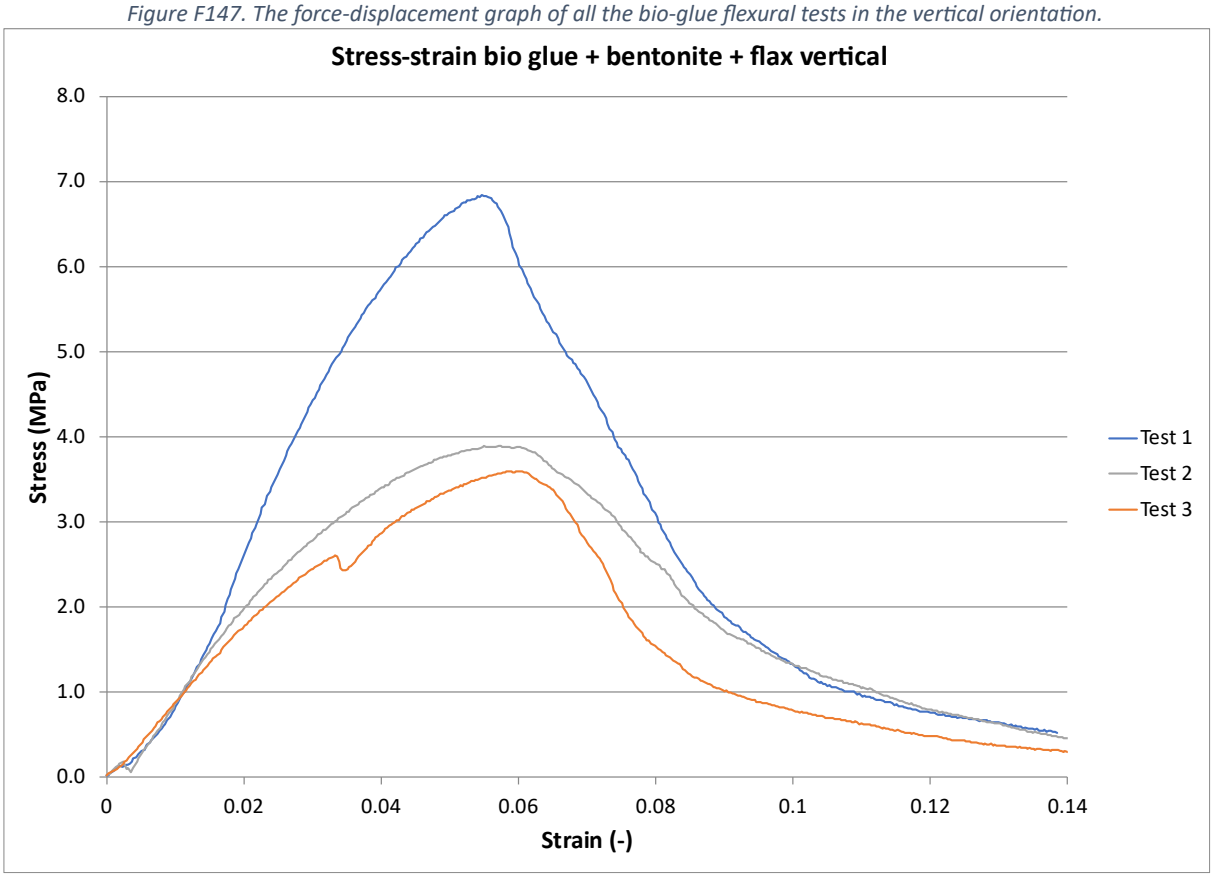


Figure F148. The stress-strain graph of all the bio-glue flexural tests in the vertical orientation.

F.3.4 Summary bio-glue + additives flexural test results

Table F15 to Table F20 present the results of the bio-glue with additives tests with both orientations.

Table F15. Results of flexural test bio-glue with bentonite with horizontal layer orientation.

Test	Beam	Curing time [days]	Cross-sectional area [mm²]	Max Force [kN]	Displacement [mm]	Stress [MPa]	Strain [-]	Crack?	Flexural modulus [MPa]
1	1	50	1411.0	0.71	6.83	4.74	0.0288	Yes	194.61
2	5	48	1513.0	0.76	10.15	4.74	0.0428	Yes	116.99
3	6	48	1592.5	0.70	8.76	4.00	0.0380	Yes	120.89

Table F16. Results of flexural test bio-glue with bentonite with vertical layer orientation.

Test	Beam	Curing time [days]	Cross-sectional area [mm²]	Max Force [kN]	Displacement [mm]	Stress [MPa]	Strain [-]	Crack?	Flexural modulus [MPa]
1	2	50	1653.0	1.10	6.35	5.30	0.0362	Yes	127.67
2	3	50	1665.0	1.08	5.42	5.07	0.0323	Yes	153.01
3	7	48	1468.5	1.13	9.49	6.34	0.0588	Yes	78.359
4	8	48	1468.5	1.16	7.27	6.46	0.0451	Yes	155.86

Table F17. Results of flexural test bio-glue with flax with horizontal layer orientation.

Test	Beam	Curing time [days]	Cross-sectional area [mm²]	Max Force [kN]	Displacement [mm]	Stress [MPa]	Strain [-]	Crack?	Flexural modulus [MPa]
1	1	49	1584.0	0.83	11.14	4.72	0.0497	Yes	151.48
2	2	49	1479.0	0.84	13.12	5.37	0.0553	Yes	124.01
3	3	49	1566.0	0.80	14.01	4.55	0.0625	Yes	111.10

Table F18. Results of flexural test bio-glue with flax with vertical layer orientation.

Test	Beam	Curing time [days]	Cross-sectional area [mm²]	Max Force [kN]	Displacement [mm]	Stress [MPa]	Strain [-]	Crack?	Flexural modulus [MPa]
1	4	50	1522.5	1.23	10.55	6.60	0.0615	Yes	118.88
2	5	50	1501.5	1.32	9.57	6.94	0.0593	Yes	117.60
3	7	49	1530.0	1.19	14.31	6.25	0.0887	Yes	83.10

Table F19. Results of flexural test bio-glue with bentonite and flax with horizontal layer orientation.

Test	Beam	Curing time [days]	Cross-sectional area [mm²]	Max Force [kN]	Displacement [mm]	Stress [MPa]	Strain [-]	Crack?	Flexural modulus [MPa]
1	1	47	1462.0	0.75	10.14	4.82	0.0427	Yes	147.58
2	3	47	1445.0	0.77	11.84	5.05	0.0499	Yes	142.19
3	4	33	1369.5	0.52	12.69	3.74	0.0519	Yes	99.28

Table F20. Results of flexural test bio-glue with bentonite and flax with vertical layer orientation.

Test	Beam	Curing time [days]	Cross-sectional area [mm²]	Max Force [kN]	Displacement [mm]	Stress [MPa]	Strain [-]	Crack?	Flexural modulus [MPa]
1	2	47	1400.0	1.03	9.58	6.84	0.0546	Yes	113.94
2	5	33	1505.0	0.73	10.23	3.89	0.0571	Yes	94.426
3	6	33	1566.0	0.70	9.60	3.49	0.0535	Yes	77.531

Appendix G – Topology optimisation

Bio-based 3D printing and testing of a digitally designed structural element

F.E. Pels Rijcken

Eindhoven,19-06-2025

Contents

G.1 Karamba3D components 1
G.1.1 Material properties 1
G.1.2 Calculation components 2
G.1.3 Determination of right inputs and components 3
G.1.3.1 Grasshopper script 3
G.1.3.2 Results of the Grasshopper beam analyses 4
G.1.3.3 Discussion and conclusion inputs and components 6
G.2 Topology optimization script 6
G.2.1 BESO for Shells component 10
G.3 Print path generation 13
G.4 Bibliography 14

G.1 Karamba3D components

Karamba is a finite element program which can be used to analyse structures, the plugin for Grasshopper is called Karamba3D [1]. In the following chapters the most important components needed for the topology optimization are addressed and at the end a Grasshopper script is used to determine which inputs and components are used for the topology optimization.

G.1.1 Material properties

The Karamba3D Grasshopper component for the material properties is displayed in Figure G1. Due to the limited material property research, it was assumed that the material is an isotropic material.
The input for the Young's modulus, the specific weight and the tensile and compressive strength are results from the tests in chapter 6. They only needed to be converted; the results of this conversion are provided in Table G1. The in-plane shear modulus, the transverse shear modulus and the strength hypothesis are unknown and have impact on the calculation results. These properties are discussed in the following sections.

Table G1. Material properties resulted from the bio glue with flax with a vertical layer orientation flexural tests.

Material properties				
Flexural modulus	106.53	MPa	10.653	kN/cm^2
Specific weight	923.73	kg/m^3	9.061	kN/m^3
Tensile strength	3.00	MPa	0.300	kN/cm^2
Compressive strength	-4.65	MPa	-0.465	kN/cm^2

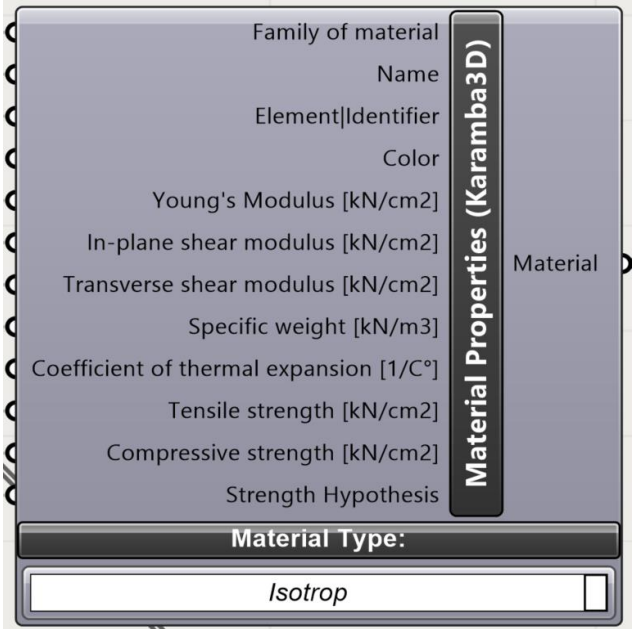


Figure G1. Karamba3D Grasshopper component for the material properties of an isotropic material [2].

In-plane and the transverse shear moduli

The in-plane and the transverse shear moduli directly affect the stresses and the displacement results of a structural analysis.
There are some conditions regarding the in-plane shear modulus: it should be larger than *E/3* and smaller than *E/2* (with *E* being the Young's modulus). In case this condition is not fulfilled, the structure may show strange behaviour. The transverse shear modulus has often the same value as the in-plane shear modulus, but can be chosen independently, for example with wood this may be significantly smaller than the in-plane shear modulus [2]. The values for these shear moduli are determined in chapter G.1.3.2.

Strength hypothesis

For the strength hypothesis there are three options: Von Mises, Tresca and Rankine. From the tests in chapter 6 can be seen that the material has a ductile failure behaviour, which means that there is a significant deformation before breaking. However, the compressive strength is higher than the tensile strength, which is often the case for brittle materials [3]. This means that there was no definitive/clear answer as to which criterion should be used when looking at the failure behaviour. The correct strength hypothesis is determined in chapter G.1.3.2.

G.1.2 Calculation components

AnalyzeThII

The calculation component AnalyzeThII, shown in Figure G2, executes a linear calculation and takes the second order effect into account through an iterative procedure. The useful output is the calculated model, from which the tensile and compressive stresses and the maximum displacement are calculated.

Analyze Nonlinear

The calculation component Analyze Nonlinear WIP is shown in Figure G3. It executes a nonlinear calculation, both material and geometric nonlinearity. The letters WIP in the component stand for "Work-In-Progress", indicating that the component is under development. In the case of a shell structure, the analysis may not converge, however, if a result is obtained, it is regarded as reliable [4]. The useful outputs are the calculated model, from which the tensile and compressive stresses are calculated, and the maximum displacement. There are three different options for the iterative solution algorithms: Dynamic Relaxation, Newton-Raphson Method and the Arc-Length Method. Table G2 gives simplified explanations of these algorithms. Given the differences, the Dynamic Relaxation method was used for the nonlinear calculations.

Table G2. Simplified explanations of the three different solution algorithms [4].

Dynamic Relaxation (DR)	Gives a reliable result but can need a large number of iterations.
Newton-Raphson Method	Is mostly the same as the DR algorithm, but it uses a stiffness matrix. This mean that less iterations are needed for a result, however this part of the component is still under development which could impact the results.
Arc-Length Method	This method is useful for thin plate and shell structures, it analyses the post-buckling behaviour.

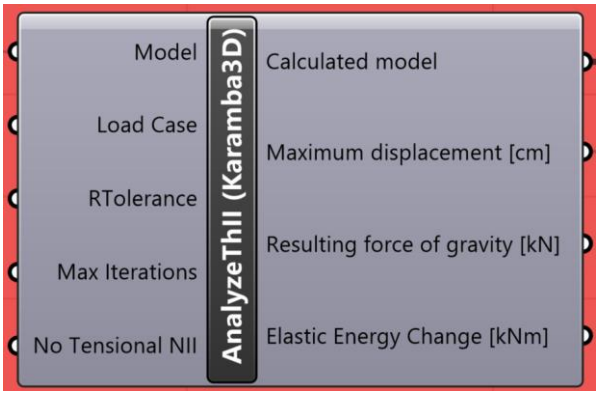


Figure G2. Karamba3D Grasshopper AnalyzeThII component [5].



Figure G3. Karamba3D Grasshopper Analyze Nonlinear WIP component [4].

G.1.3 Determination of right inputs and components

G.1.3.1 Grasshopper script

To find the right shear moduli values, the bio glue with flax with vertical layer orientation flexural tests were simulated using the Karamba3D components in Grasshopper. This script was also used to compare the two different calculation components.

In Figure G4 a screenshot of this script is shown. Each number indicates a part of the script:

1. Part of the script where the material properties can be entered, and a beam can be selected with a slider (see Figure G5 for a more detailed screenshot). The three different beams can be selected, or the average beam properties can be used as input.
2. The part of the script where the different beam and material properties are selected based on the slider. In this part the in-plane and the transverse shear moduli can be altered.
3. The part of the script where the line segments are made.
4. The part of the script where a beam is created with the “Line to beam (Karamba3D)” component.
5. The part of the script where the material properties are created using the “Material Properties (Karamba3D)” component.
6. The part of the script where a trapezoidal cross-section is created with the “Cross Section (Karamba3D)” component.
7. The part of the script where a point load in the middle of the beam, and the gravity load are created with the “Loads (Karamba3D)” component.
8. The part of the script where the supports are created with the “Support (Karamba3D)” component. On the left side of the beam a hinge support is created and on the right side a roller with hinge support is created.
9. The part of the script where all the different Karamba3D components together form one final model with the “Assemble Model (Karamba3D)” component. In Figure G6 the mechanical scheme of this model is displayed and in Figure G7 shows the whole geometry in Rhino.
10. The part of the script where the beam is calculated. The calculation is executed with two different Karamba3D components: AnalyzeThII and Analyze Nonlinear WIP.
11. The part of the script where the results of the calculations are extracted. These results include the maximum displacement and the maximum tensile stresses.
12. This is the part of the script where (un)deformed models are visualized.

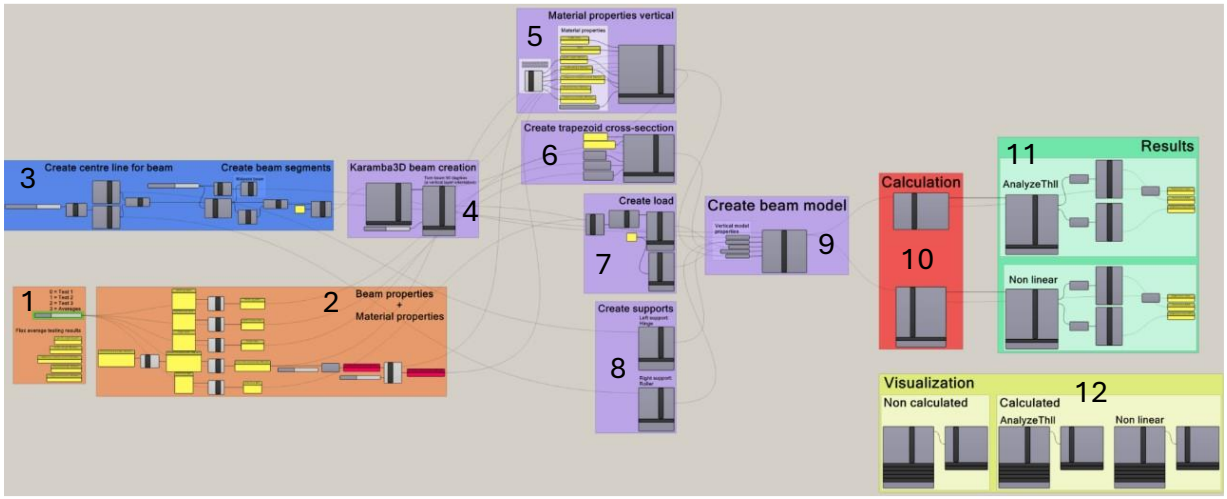


Figure G4. Screenshot of the script of the beam calculation in Grasshopper.

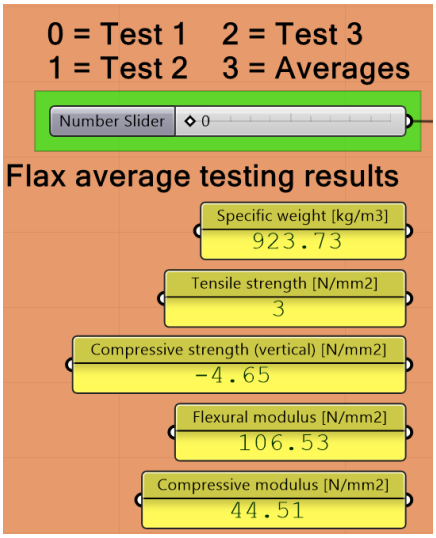


Figure G5. A screenshot of the slider that changes the beam that is analysed and the average testing results.

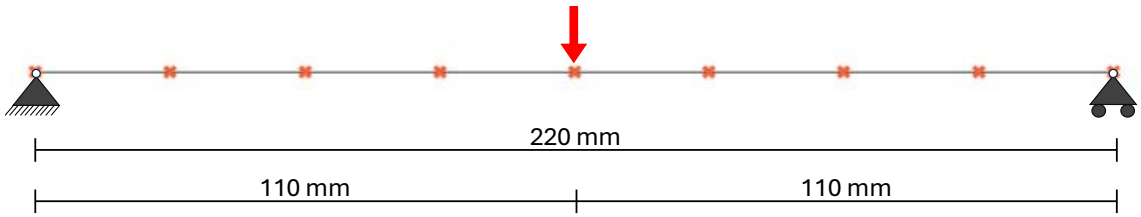


Figure G6. The mechanical scheme of the beams.

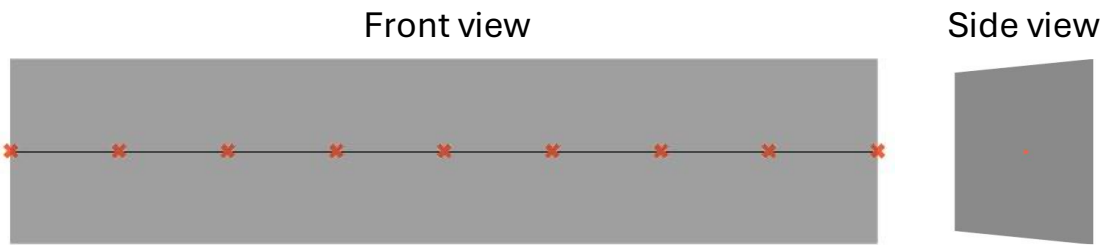


Figure G7. Two screenshots of an example of a beam geometry in Rhino.

G.1.3.2 Results of the Grasshopper beam analyses

Table G3 gives the inputs per beam option and the corresponding displacement and tensile stress results. The results of the script were compared to these results using the unit check in equation 1. If the results of the unity check are 1 the results are the same.

There were infinite options for the values of the in-plane and transverse shear modulus, so the values of these properties were determined by a trail-and-error analysis. Table G4 shows four different values of this trail-and-error analysis. The value of the in-plane shear modulus = *E/3* resulted too high results for both the displacements and tensile stresses, so only the values of *E/2* are displayed.

Table G5 to Table G8 give the results and the unity checks of both the calculation components for the four different tries given in Table G4.

Table G9 gives the average unity check calculations per try and some modifications of these unity checks.

$$Unity\ check = UC = \frac{Karamba3D\ results}{Test\ results} \qquad 1$$

Table G3. The important inputs for the script and the corresponding displacement and tensile stress results.

Beam	Young's modulus [kN/cm2]	Applied load [kN]	Displacement [mm]	Tensile stress [MPa]
1	11.888	1.23	10.55	6.60
2	11.760	1.32	9.57	6.94
3	8.310	1.19	14.31	6.25
Ave	10.653	1.25	11.48	6.60

Table G4. The in-plane shear modulus and the transverse shear modulus in relation to the Young's modulus E.

Try	In-plane shear modulus [kN/cm2]	Transverse shear modulus [kN/cm2]
1	E/2	E/2
2	E/2	E/2 *0.3
3	E/2	E/2 *0.8
4	E/2	E/2 *0.9

Table G5. Results of try 1.

TRY 1	Results				Unity check			
	AnalyzeThII		Nonlinear		AnalyzeThII		Nonlinear	
Beam	**Displacement** [mm]	**Tensile stress** [MPa]	**Displacement** [mm]	**Tensile stress** [MPa]	**Displacement**	**Tensile stress**	**Displacement**	**Tensile stress**
1	10.41	6.59	10.35	6.56	0.987	0.998	0.981	0.993
2	10.52	6.95	10.45	6.91	1.099	1.001	1.092	0.996
3	13.41	6.27	13.27	6.22	0.937	1.003	0.928	0.995
Ave	11.22	6.60	11.14	6.56	0.978	1.000	0.971	0.995
			Average unity check		1.000	1.000	0.993	0.995

Table G6. Results of try 2.

TRY 2	Results				Unity check			
	AnalyzeThII		Nonlinear		AnalyzeThII		Nonlinear	
Beam	**Displacement** [mm]	**Tensile stress** [MPa]	**Displacement** [mm]	**Tensile stress** [MPa]	**Displacement**	**Tensile stress**	**Displacement**	**Tensile stress**
1	12.507	6.587	12.402	6.544	1.185	0.998	1.175	0.991
2	12.826	6.947	12.714	6.899	1.340	1.001	1.328	0.994
3	16.297	6.268	16.070	6.199	1.139	1.003	1.123	0.992
Ave	13.599	6.601	13.466	6.549	1.185	1.000	1.173	0.993
			Average unity check		1.212	1.000	1.200	0.992

Table G7. Results of try 3.

TRY 3	Results				Unity check			
	AnalyzeThII		Nonlinear		AnalyzeThII		Nonlinear	
Beam	**Displacement** [mm]	**Tensile stress** [MPa]	**Displacement** [mm]	**Tensile stress** [MPa]	**Displacement**	**Tensile stress**	**Displacement**	**Tensile stress**
1	10.636	6.587	10.567	6.555	1.008	0.998	1.001	0.993
2	10.768	6.947	10.697	6.912	1.125	1.001	1.117	0.996
3	13.719	6.268	13.574	6.217	0.959	1.003	0.949	0.995
Ave	11.477	6.601	11.391	6.563	1.000	1.000	0.992	0.995
			Average unity check		1.023	1.000	1.015	0.994

Table G8. Results of try 4.

TRY 4	Results				Unity check			
	AnalyzeThII		Nonlinear		AnalyzeThII		Nonlinear	
Beam	**Displacement** [mm]	**Tensile stress** [MPa]	**Displacement** [mm]	**Tensile stress** [MPa]	**Displacement**	**Tensile stress**	**Displacement**	**Tensile stress**
1	10.511	6.587	10.444	6.555	0.996	0.998	0.990	0.993
2	10.630	6.947	10.562	6.912	1.110	1.001	1.103	0.996
3	13.548	6.268	13.406	6.218	0.947	1.003	0.937	0.995
Ave	11.336	6.601	11.252	6.564	0.988	1.000	0.980	0.995
			Average unity check		1.010	1.000	1.003	0.994

Table G9. The average unit checks, the total unity check and the difference with the test results per try and component.

Try	Average unity check				Total unity check[1]		Difference with test results[2]	
	AnalyzeThII		Nonlinear					
	Displacement	Tensile stress	Displacement	Tensile stress	AnalyzeThII	Nonlinear	AnalyzeThII	Nonlinear
1	1.000	1.000	0.993	0.995	2.0005	1.9872	0.0005	0.0128
2	1.212	1.000	1.200	0.992	2.2125	2.1921	0.2125	0.1921
3	1.023	1.000	1.015	0.994	2.0232	2.0093	0.0232	0.0093
4	1.010	1.000	1.003	0.994	2.0106	1.9971	0.0106	0.0029

[1] The unity checks of both the displacement and the tensile stresses are added.
[2] The difference of total unity check and the value 2. This indicates how much both results together differ from the test results of Table G3.

G.1.3.3 Discussion and conclusion inputs and components

With the script in Figure G4 several conclusions can be drawn:

- Calculation component: Comparing the two different calculation components shows that both components give results that are close to the test results. Changing the values of the in-plane and transverse shear moduli had different impacts on the results between the two components: the results of the AnalyzeThII component showed that the tensile stresses did not change when the moduli changed, it only impacted the displacement. With the Nonlinear component both the stresses and the displacement changed when the moduli changed.
  To be more accurate the Nonlinear component was used to determine the in-plane and transverse shear moduli.
- In-plane and transverse shear moduli: Looking at the final column in Table G9 shows that with try 4 the lowest difference was reached between the grasshopper results and the test results (0.0029). This means that the values for the in-plane and transverse shear moduli are *E/2* and *(E/2)*0.9* respectively.
- Strength hypothesis: The results of the beam analyses were analysed with the three different criteria as input. It showed no differences in the stresses or the displacements. So, for this specific material and calculation it did not matter which failure criterion was chosen.

G.2 Topology optimization script

In Figure G8 a screenshot of this script is shown. Each number indicates a part of the script (all the examples are generated with the variables input given in Table G10):

1. Part of the script where the material properties can be entered, and the element dimensions can be altered. Figure G9 shows a more detailed screenshot of this part.
2. The part of the script where the element is made into a 2D mesh. In order to reduce the calculation time and to ensure a fully symmetric structure at the end, only half of the element is simulated. The mesh is composed of quads, which can be modified with the U- and V-count sliders. The number of quads affects topology optimization: an increased number of quads results in a more accurate calculation of the mesh but also means a longer calculation time.
3. The part of the script where a shell element is created with the “Mesh to Shell (Karamba3D)” component, it converts all the quads to triangles.
4. The part of the script where the material properties are created using the “Material Properties (Karamba3D)” component. The values for the in-plane and transverse shear modulus are the one determined in chapter G.1.3.3.
5. The part of the script where a cross-section is created with the “Cross Section (Karamba3D)” component. The number of layers of part 1 alter the thickness of this cross-section.
6. The part of the script where a point load and the gravity load are created with the “Loads (Karamba3D)” component. For a full element, the point load is applied in the middle of the element, but with half the element this load acts on the right top corner.
7. The part of the script where the supports are created with the “Support (Karamba3D)” component. The full element has hinge support on one side and roller with hinge support on the

other side. For this mechanical scheme see Figure G10, converting this to only half the structure led to the mechanical scheme in Figure G11.

8. The part of the script where all the different Karamba3D components together form one final model with the “Assemble Model (Karamba3D)” component.
9. The part of the script where the model is calculated. The calculation is executed with the “Analyze Nonlinear WIP (Karamba3D)” component.
10. The part of the script where the topology optimization is executed using the “BESO for Shells (Karamba3D)” component. This component is explained with the help of this script in chapter G.2.1. The outcome from this part are all the different iterations and the final optimized shape. This shape is displayed in Rhino in a grey scale “figure”, the white parts indicate that those triangles do not have any thickness, and the grey/black colour indicate that those triangles have a certain thickness. Figure G12 shows an example of an optimized shape.
11. The part of the script where the triangles that have no thickness are deleted and the whole shape is mirrored to create a symmetrical element with smoothened edges, see Figure G13 and Figure G14.
12. This is the part of the script where the deformation, principal stresses and different iterations are visualized. This is to verify the optimization. In Figure G15 and Figure G16 examples of the two principal stress distributions are shown. Comparing these to the optimized model shows that material is placed where the higher stresses are located.

    The part of the script where the results of the calculations are extracted. These results include the maximum displacement and the maximum principal stresses.

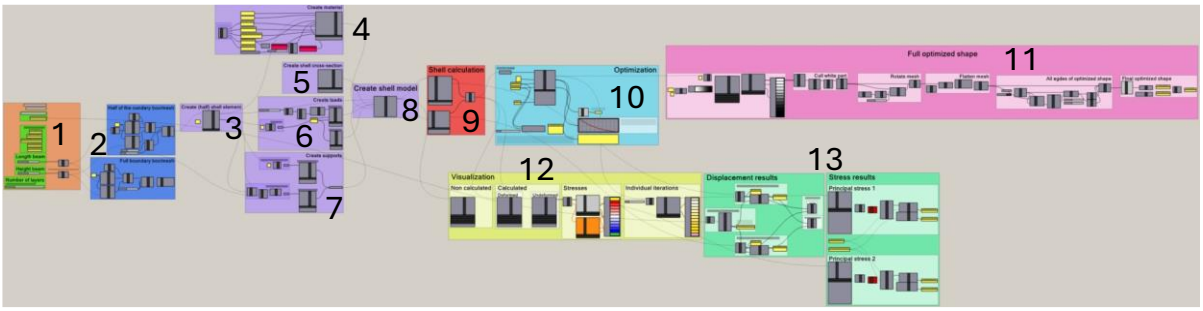


Figure G8. Screenshot of the script of the topology optimization in Grasshopper.

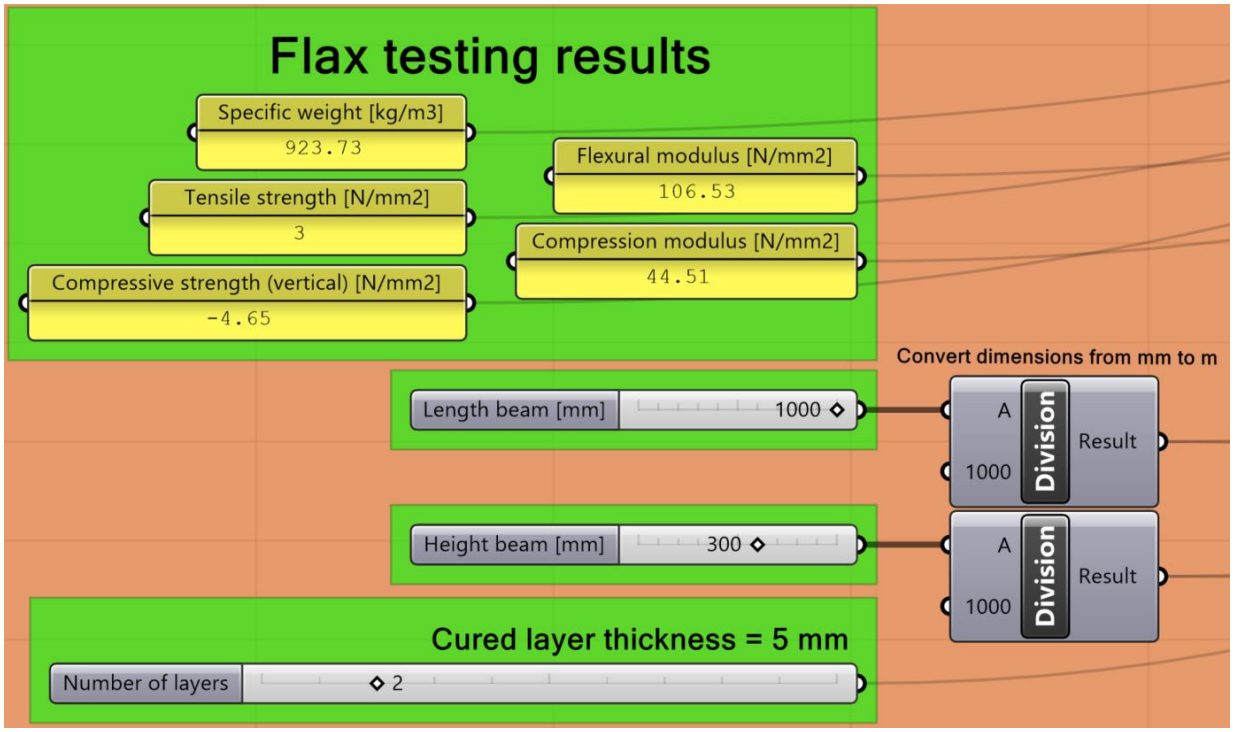


Figure G9. A screenshot of the part of the script where the material properties can be entered, and the element dimensions can be altered.

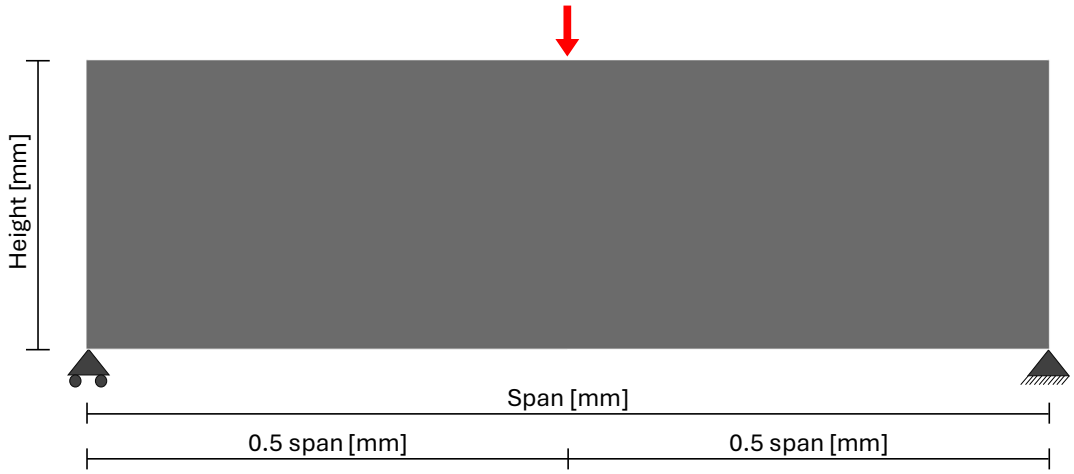


Figure G10. The mechanical scheme of the full element.

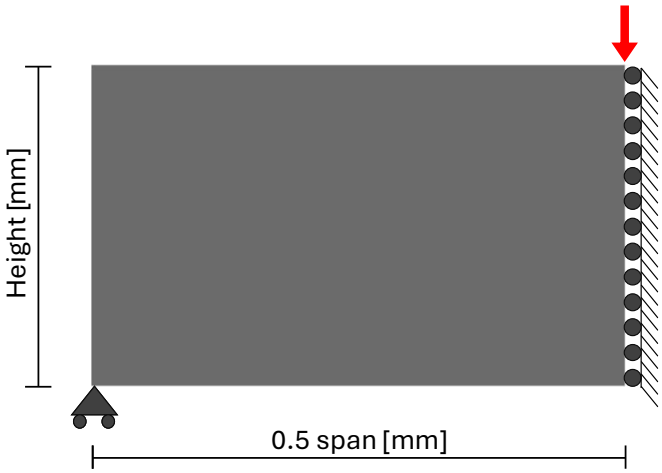


Figure G11. The mechanical scheme of only half the element.

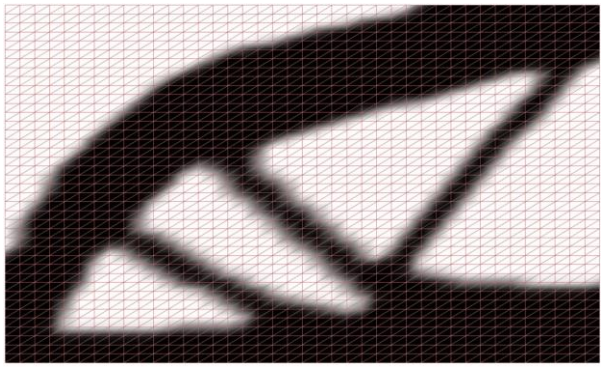


Figure G12. The original mesh in red lines with the grey scale "picture" of the optimized shape.

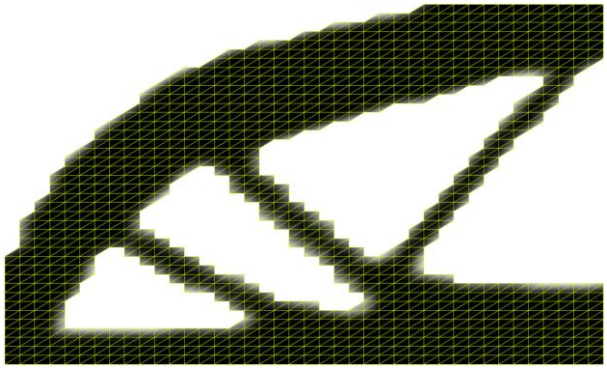


Figure G13. The cut shape with the cut mesh in yellow lines.

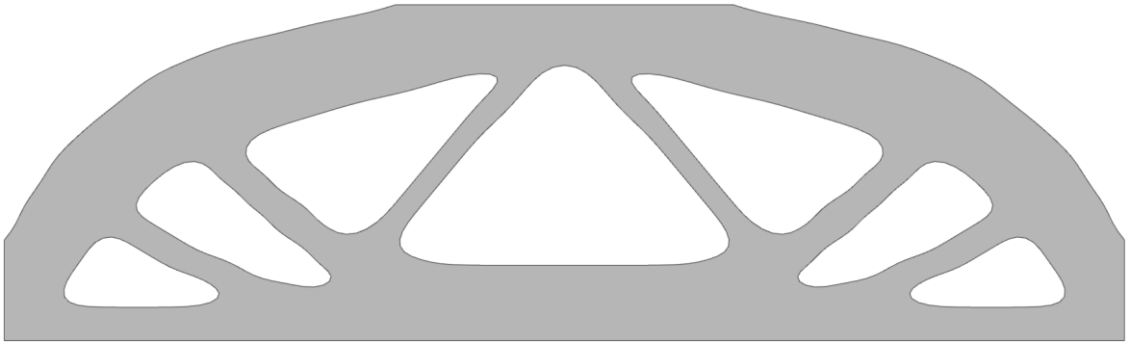


Figure G14. The final optimized element with smoothened edges.

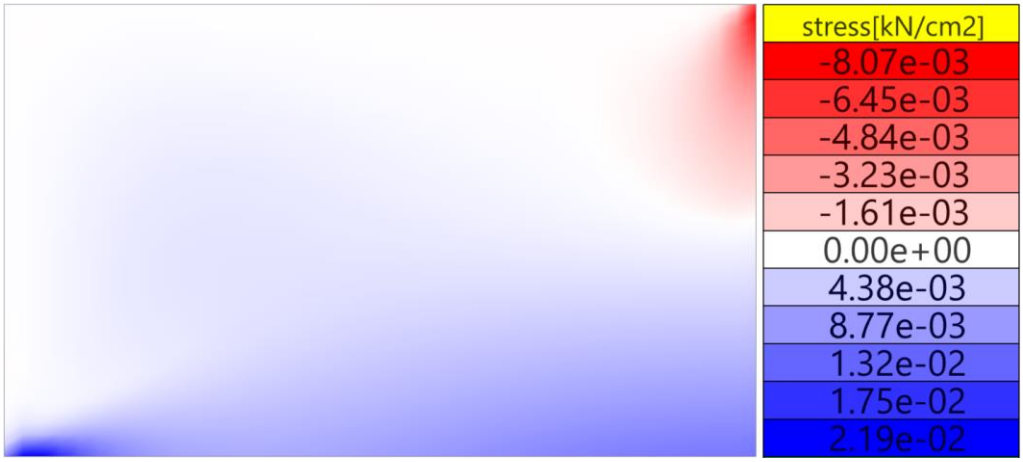


Figure G15. Principal stress 1 distribution.

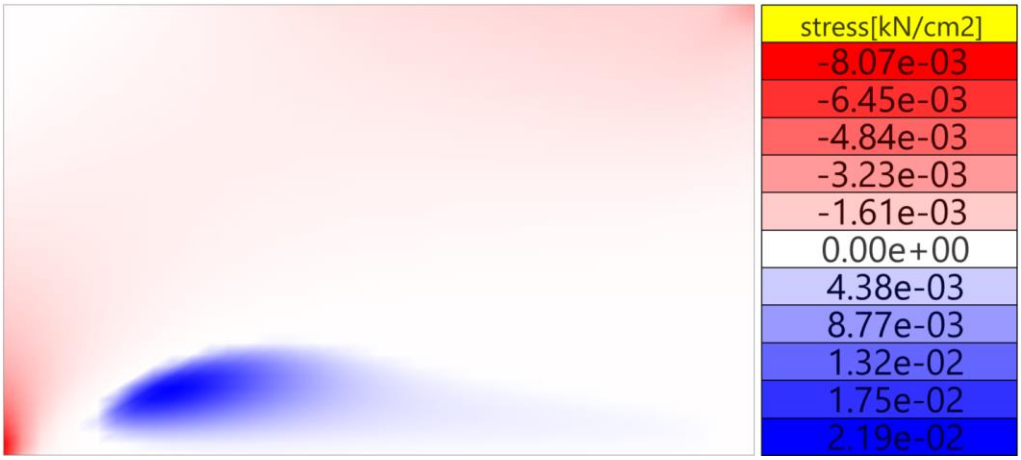


Figure G16. Principal stress 2 distribution

G.2.1 BESO for Shells component

The Karamba3D component "BESO for Shells" was used for the optimization process and is shown in Figure G17. It makes use of an evolutionary topology optimization algorithm to optimize an element [6]. The main input is the model described before and shown in Figure G11. Other important inputs are the target mass ratio (TargetRatio), the maximum number of iterations (MaxIter) and R_{exp}. To find the right values for these, the inputs for the model are fixed and given in Table G10.

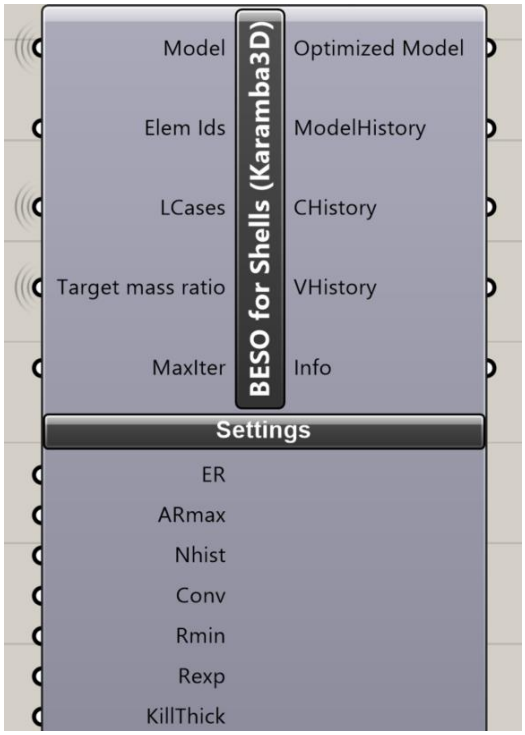


Figure G17. Karamba3D Grasshopper BESO for shells component [6].

The TargetRatio is the ratio of the final mass to the initial mass. However, this is only a target, depending on the model and loads it is not guaranteed that this ratio is achieved. For this model, a TargetRatio is kept at 0.3, to ensure as little material as possible is used for the final element.

The default setting for MaxIter is 10, however, this is not quite high enough and lead to not great optimizations. Setting this value to 500 gave better optimizations, with often using only around 20 to 40 iterations to get to the final optimization. Increasing this value even more led to slightly better optimizations but with longer calculations times.

The TargetRatio and MaxIter directly influence the evolutionary ratio with the equation given in Figure G18. (The value of AR_{max} is kept at the default value of 0.05.) However, the value of ER could also be chosen independently, but changing the ER value to a smaller value than the default (the result of the equation), did not lead to improved optimizations.
The input R_{exp} also influenced the final optimization. In Table G12 results are given of different R_{exp} values between 0.1 and 2. Based on these results it was decided to continue with R_{exp}=0.5.
Table G11 gives the final input values for the BESO component, the other inputs were kept to the default values.

Table G10. Input of the model variables.

Input whole model		
Length	1000	mm
Height	300	mm
Thickness	10	mm
Load	0.01	kN

Table G11. Input of the model variables and the input for the BESO component.

Input BESO component		
Target mass ratio	0.3	-
Max iterations	500	-
Rexp	0.5	-

"ER"	Is short for evolutionary ratio and defines the ratio between the volumes V_i and V_{i+1} of the optimized structure in two consecutive steps: $V_{i+1} = Vi \cdot (1 \pm ER)$. The sign of "ER" depends on whether elements shall be added or removed. In case that $ER < 0$ – which is the default –$ER$is set automatically: $ER = (1 - TargetRatio)/MaxIter + AR_{max}/2$. In case that **"ER"** is too small, the target mass of the optimized structure can not be reached within **"MaxIter"** steps.

Figure G18. Description of the evolutionary ratio input of the "BESO for Shells" Karamba3D component.

Table G12. Different optimization results with different inputs of R_{exp}.

R_{exp}	Volume ratio	
2	0.60875	
1.5	0.51	
1	0.564377	

0.5	0.524687	
0.1	0.499377	

G.3 Print path generation

After a density array was obtained, the next step was to create a print path. Ideally, the print path generation is automated in Grasshopper, however due to the time constraints of this project, it was decided to do this manually. The process up to step 2 is automated in Grasshopper, see Figure G14.

Figure G19 to Figure G23 have been sourced from the master's thesis of J. Versteege, and they show a simplified overview of the steps of the print path generation [7]:

- Step 1: Obtain a density array (Figure G19).
- Step 2: Convert the density array to a polygon with smoothened edges (Figure G20).
- Step 3: Find all the axes of the sections of the polygon and find the edges and nodes (Figure G21).
- Step 4: Determine the number of paths needed to create a section, this depends on the width of a print path and the width of an edge, this is also called a multigraph (Figure G22). In order to print the entire polygon in a single operation, each node needs to have an even number of paths.
- Step 5: Create a print path (Figure G23).

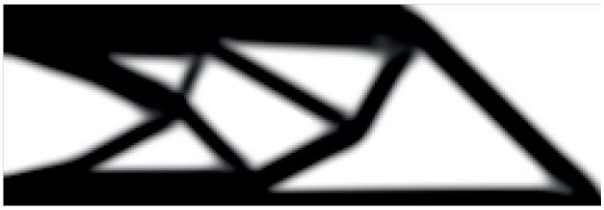


Figure G19. An example of a density array [7].

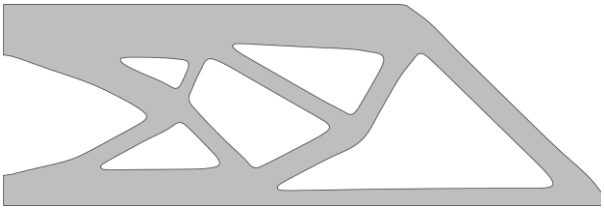


Figure G20. Results of the conversion of the density array to a polygon [7].

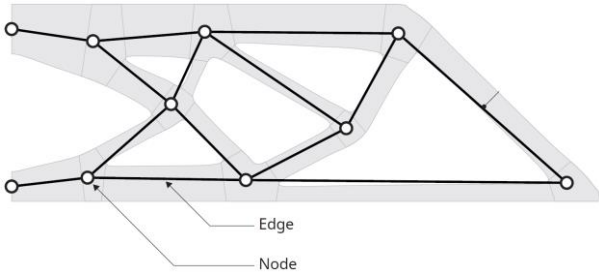


Figure G21. The defined edges and nodes of the polygon [7].

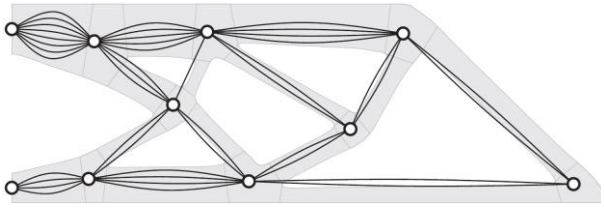


Figure G22. Example of a multigraph, representing the number of paths connected to each node [7].

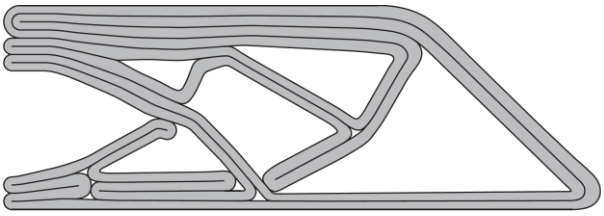


Figure G23 .An example of the print path geometry [7].

G.4 Bibliography

[1] Preisinger C. Linking Structure and Parametric Geometry. Lobe G, Tam M, editors. Vol. 83, Architectural Design. 2013. 110–113 p.

[2] Karamba3D. 3.5.1: Material Properties. In: Karamba3D Manual [Internet]. 2024 [cited 2024 Feb 28]. Available from: https://manual.karamba3d.com/3-in-depth-component-reference/3.4-material/3.4.1-material-properties

[3] Fidelis. Brittle and ductile failure theories in FEA – Which ones should we choose? [Internet]. Fidelis Engineering Associates. 2024 [cited 2024 Oct 15]. Available from: https://www.fidelisfea.com/post/brittle-and-ductile-failure-theories-in-fea-which-ones-should-we-choose

[4] Karamba3D. 3.6.3: Analyze Nonlinear WIP. In: Karamba3D Manual [Internet]. 2024 [cited 2024 Feb 28]. Available from: https://manual.karamba3d.com/3-in-depth-component-reference/3.5-algorithms/3.5.3-analyze-nonlinear-wip

[5] Karamba3D. 3.6.2: AnalyzeThII. In: Karamba3D Manual [Internet]. 2024 [cited 2024 Feb 28]. Available from: https://manual.karamba3d.com/3-in-depth-component-reference/3.5-algorithms/3.5.2-analyzethii

[6] Karamba3D. 3.6.10: BESO for Shells. In: Karamba3D Manual [Internet]. 2024 [cited 2024 Feb 28]. Available from: https://manual.karamba3d.com/3-in-depth-component-reference/3.5-algorithms/3.5.10-beso-for-shells

[7] Versteege J. An integrated approach for topology optimization and print path generation of cable-reinforced 3D printed concrete structures. [Eindhoven]: Eindhoven University of Technology; 2020.

Appendix H – Printability exploration with the bio glue with flax mixture

Bio-based 3D printing and testing of a digitally designed structural element



F.E. Pels Rijcken

Eindhoven, 19-06-2025

H.1 Full cartridge print 1
H.2 Adhesions tests 2
H.2.1 Path adhesion test 2
H.2.2 Corner adhesion test 2
H.3 Grasshopper scripts and RAPID codes 3
H.3.1 Full cartridge RAPID code 4
H.3.2 Path adhesion RAPID codes 7
H.3.3 Corner adhesion RAPID code 11

H.1 Full cartridge print

Figure H1 shows the full cartridge print. At the start of this test, the material didn't come out of the Makita when the Makita pressure was set on 1.1, so it was changed to 1.3. However, this resulted in the material to come out too quickly, leading to some excess material to bee extruded (see the excess material on the top right in Figure H1). This was followed by changing the Makita pressure to 1.2, which unfortunately resulted in a small gap in the print. After this the test went smoothly and the material came out consistently. However, as can be observed in Figure H1, as the test progressed, the path width gradually increased.



Figure H1. One full cartridge print, with Makita on 1.2 and the robot on 13 mm/min.

Table H1 lists the results after the full cartridge print. It was concluded that, with the Makita on 1.2 and the robot speed on 13 mm/min, a total length of around 4.2 meters was printed.
Table H2 provides the path width ranges, and the average path width was 19.6 mm.

Table H1. Results of the full cartridge test.

Path part	Length [mm]	Amount [-]	Total length [mm]
Straight parts	400	9.9	3960
Arcs	=11.5*π = 36.13	9	325.15

Total length	
[mm]	[m]
4285	4.28

Table H2. Widths per path of the full cartridge test.

Path	Path width range [mm]
1	14 - 15
2	16 - 18
3	17 - 20
4	17 - 20
5	18 - 21
6	17 - 21
7	19 - 23
8	19 - 24
9	21 - 24
10	23 - 25
Average path width	19.6

H.2 Adhesions tests

H.2.1 Path adhesion test

Table H3 shows the results of the overlap tests. The actual (average) path width was different than the width that was used to create these paths. Meaning that the actual overlap was calculated afterwards. From the freshly printed tests, the one with an overlap of -3.0 mm was deemed the best. This means that the centre to centre (C.T.C.) distance is 3.0 mm smaller that the path width.

Table H3. Results of the overlap tests

Test	Simulated path width [mm]	C.T.C distance [mm]	Simulated overlap [mm]	Average path width [mm]	Actual overlap [mm]
1	18	23	+5.0	19.0	+4.0
2	18	21	+3.0	19.0	+2.0
3	18	18	0.0	19.5	-1.5
4	18	16	-2.0	19.0	-3.0

H.2.2 Corner adhesion test

Table H4 gives the measured path width of the corner adhesion test and Table H5 provides the results of the corner adhesion test.

Table H4.Path widths of the corner adhesion test.

Path	Path width range [mm]	Average width per line [mm]
Start line	21.0 - 25.0	23.0
Straight line 1	19.0 - 24.0	21.5
Straight line 2	20.0 - 23.0	21.5
Straight line 3	20.0 - 25.0	22.5
Straight line 4	19.0 - 25.0	22.0
Straight line 5	19.0 - 21.0	20.0
Straight line 6	20.0 - 25.0	22.5
Straight line 7	23.0 - 27.0	25.0
End line	20.0 - 29.0	24.5
Average path width total	22.5	

Table H5. Results of the corner adhesions test.

Simulated path width [mm]	C.T.C distance [mm]	Simulated overlap [mm]	Average path width [mm]	Actual overlap [mm]
18	16	-2	22.5	-6.5

H.3 Grasshopper scripts and RAPID codes

In Figure H2 shows the script of the test prints in grasshopper. Each number indicates a part of the script:

1. The parameters that are changeable (see Figure H3 for a more detailed screenshot).
2. The part of the script where the main geometries are made.
3. The part of the script where the extra straight lines are added for the corner adhesion test.
4. The part of the script where the nozzle on the Makita is created.
5. The part of the script where the robot-setup is created.
6. The part of the script where the points for the targets are created.
7. The part of the script where the robot speed and configuration can be changed.
8. The parts of the script where the targets and robot movements for the full cartridge print and the path adhesion tests are finalized. 8a gives the targets that all are pointing towards the robot origin and 8b gives the targets that are to the global coordinate system.
9. The parts of the script where the targets and robot movements for the corner adhesions test are finalized. 9a gives the targets that all are pointing towards the robot origin and 9b gives the targets that are to the global coordinate system.
10. The part of the script where the print path and rapid code are generated.

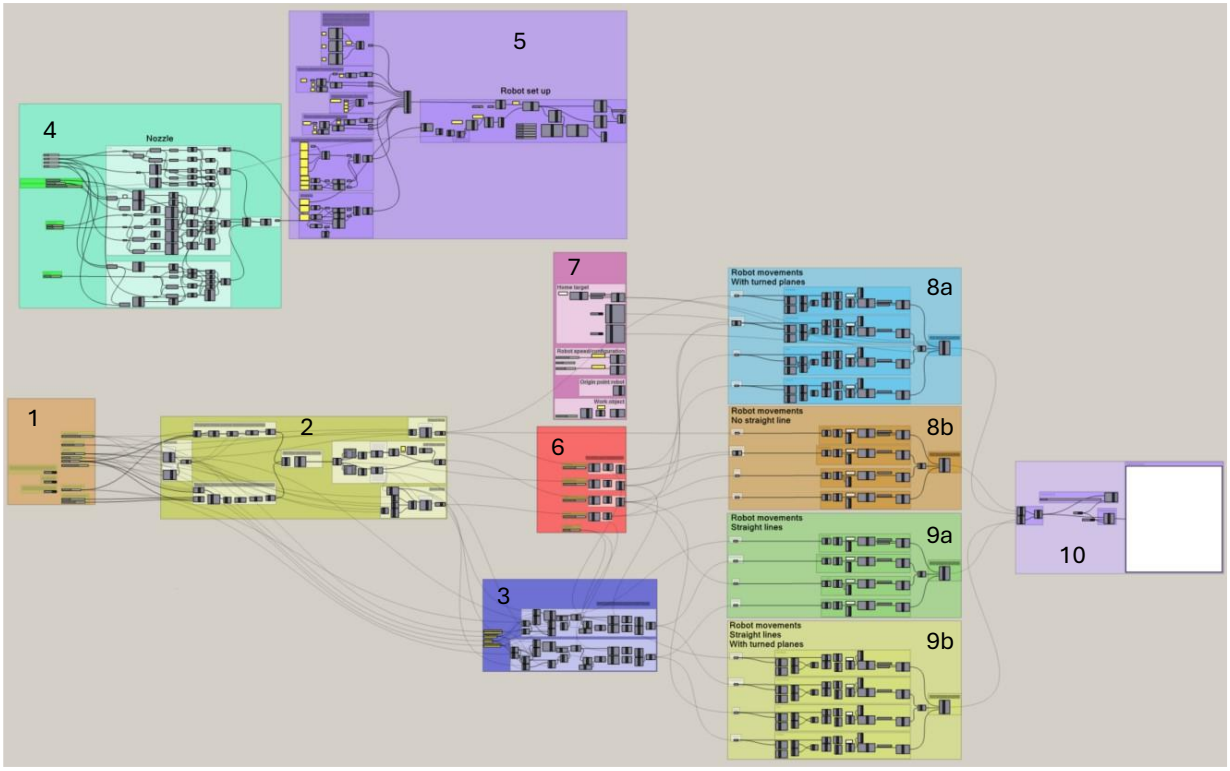


Figure H2. Screenshot of the full script of the test prints in grasshopper.

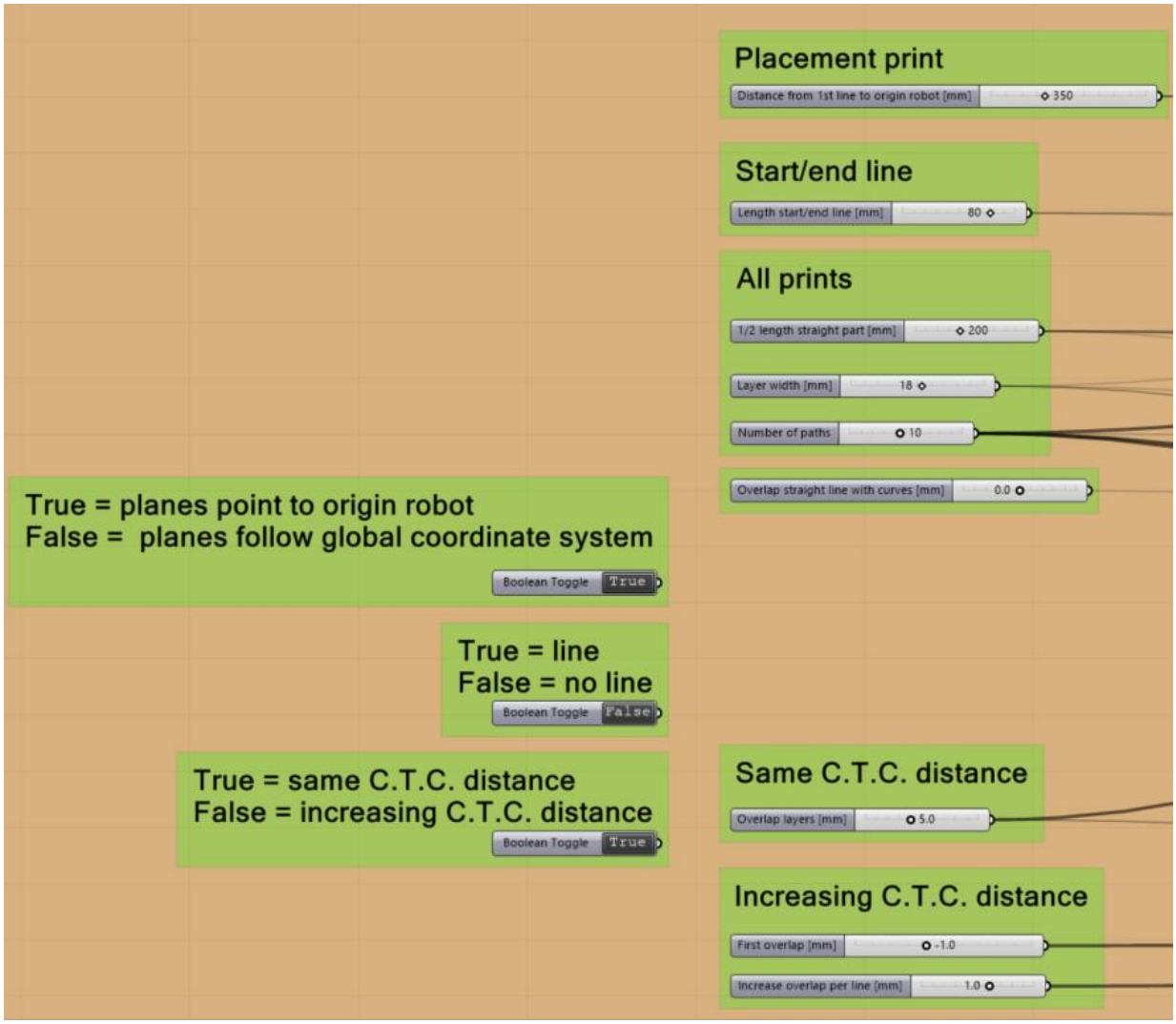


Figure H3. A screenshot the changeable parameters of the script in grasshopper.

The following subchapters provide the rapid codes for all the print tests. First, the rapid code for the full cartridge test is given, next the rapid codes for the four overlap tests are given, and finally the rapid code for the corner adhesion test.

H.3.1 Full cartridge RAPID code

```
MODULE MainModule

    ! This RAPID code was generated with RobotComponents v2.2.2 (GPL v3)
    ! Visit www.github.com/RobotComponents for more information

    ! User defined tooldata
    PERS tooldata Makita := [TRUE, [[-160, 0, 492.4], [1, 0, 0, 0]], [0.001, [0, 0, 0.001], [1, 0, 0, 0], 0, 0, 0]];

    ! User defined wobjdata
    PERS wobjdata Work_object := [FALSE, TRUE, "", [[0, 0, 0], [1, 0, 0, 0]], [[0, 0, 32.58], [1, 0, 0, 0]]];

    ! Declarations generated by Robot Components
    VAR jointtarget Home := [[0, 0, 0, 0, 0, 0], [9E9, 9E9, 9E9, 9E9, 9E9, 9E9]];
    VAR robtarget Arcs_3_0_0 := [[350.88, -204.4, 0], [0, 0.260696, 0.965421, 0], [0, 0, 0, 0], [9E9, 9E9, 9E9, 9E9, 9E9, 9E9]];
    VAR robtarget Arcs_3_0_1 := [[353.37, -208.13, 0], [0, 0.263013, 0.964792, 0], [0, 0, 0, 0], [9E9, 9E9, 9E9, 9E9, 9E9, 9E9]];
    VAR robtarget Arcs_3_0_2 := [[357.1, -210.62, 0], [0, 0.263309, 0.964712, 0], [0, 0, 0, 0], [9E9, 9E9, 9E9, 9E9, 9E9, 9E9]];
    VAR robtarget Arcs_3_0_3 := [[361.5, -211.5, 0], [0, 0.261602, 0.965176, 0], [0, 0, 0, 0], [9E9, 9E9, 9E9, 9E9, 9E9, 9E9]];
    VAR robtarget Arcs_3_0_4 := [[365.9, -210.62, 0], [0, 0.258197, 0.966092, 0], [0, 0, 0, 0], [9E9, 9E9, 9E9, 9E9, 9E9, 9E9]];
    VAR robtarget Arcs_3_0_5 := [[369.63, -208.13, 0], [0, 0.253614, 0.967306, 0], [0, 0, 0, 0], [9E9, 9E9, 9E9, 9E9, 9E9, 9E9]];
    VAR robtarget Arcs_3_0_6 := [[372.12, -204.4, 0], [0, 0.248514, 0.968628, 0], [0, 0, 0, 0], [9E9, 9E9, 9E9, 9E9, 9E9, 9E9]];
```

```
VAR robtarget Arcs_3_0_7 := [[373, -200, 0], [0, 0.243614, 0.969872, 0], [0, 0, 0, 0], [9E9, 9E9, 9E9, 9E9, 9E9, 9E9]];
VAR robtarget Arcs_3_1_0 := [[373.88, 204.4, 0], [0, -0.247555, 0.968874, 0], [0, 0, 0, 0], [9E9, 9E9, 9E9, 9E9, 9E9, 9E9]];
VAR robtarget Arcs_3_1_1 := [[376.37, 208.13, 0], [0, -0.249895, 0.968273, 0], [0, 0, 0, 0], [9E9, 9E9, 9E9, 9E9, 9E9, 9E9]];
VAR robtarget Arcs_3_1_2 := [[380.1, 210.62, 0], [0, -0.250314, 0.968165, 0], [0, 0, 0, 0], [9E9, 9E9, 9E9, 9E9, 9E9, 9E9]];
VAR robtarget Arcs_3_1_3 := [[384.5, 211.5, 0], [0, -0.248805, 0.968554, 0], [0, 0, 0, 0], [9E9, 9E9, 9E9, 9E9, 9E9, 9E9]];
VAR robtarget Arcs_3_1_4 := [[388.9, 210.62, 0], [0, -0.245642, 0.969361, 0], [0, 0, 0, 0], [9E9, 9E9, 9E9, 9E9, 9E9, 9E9]];
VAR robtarget Arcs_3_1_5 := [[392.63, 208.13, 0], [0, -0.24131, 0.970448, 0], [0, 0, 0, 0], [9E9, 9E9, 9E9, 9E9, 9E9, 9E9]];
VAR robtarget Arcs_3_1_6 := [[395.12, 204.4, 0], [0, -0.236438, 0.971646, 0], [0, 0, 0, 0], [9E9, 9E9, 9E9, 9E9, 9E9, 9E9]];
VAR robtarget Arcs_3_1_7 := [[396, 200, 0], [0, -0.231715, 0.972784, 0], [0, 0, 0, 0], [9E9, 9E9, 9E9, 9E9, 9E9, 9E9]];
VAR robtarget Arcs_3_2_0 := [[396.88, -204.4, 0], [0, 0.235563, 0.971859, 0], [0, 0, 0, 0], [9E9, 9E9, 9E9, 9E9, 9E9, 9E9]];
VAR robtarget Arcs_3_2_1 := [[399.37, -208.13, 0], [0, 0.23791, 0.971287, 0], [0, 0, 0, 0], [9E9, 9E9, 9E9, 9E9, 9E9, 9E9]];
VAR robtarget Arcs_3_2_2 := [[403.1, -210.62, 0], [0, 0.238429, 0.97116, 0], [0, 0, 0, 0], [9E9, 9E9, 9E9, 9E9, 9E9, 9E9]];
VAR robtarget Arcs_3_2_3 := [[407.5, -211.5, 0], [0, 0.237094, 0.971487, 0], [0, 0, 0, 0], [9E9, 9E9, 9E9, 9E9, 9E9, 9E9]];
VAR robtarget Arcs_3_2_4 := [[411.9, -210.62, 0], [0, 0.234148, 0.972201, 0], [0, 0, 0, 0], [9E9, 9E9, 9E9, 9E9, 9E9, 9E9]];
VAR robtarget Arcs_3_2_5 := [[415.63, -208.13, 0], [0, 0.230049, 0.973179, 0], [0, 0, 0, 0], [9E9, 9E9, 9E9, 9E9, 9E9, 9E9]];
VAR robtarget Arcs_3_2_6 := [[418.12, -204.4, 0], [0, 0.225391, 0.974268, 0], [0, 0, 0, 0], [9E9, 9E9, 9E9, 9E9, 9E9, 9E9]];
VAR robtarget Arcs_3_2_7 := [[419, -200, 0], [0, 0.220837, 0.975311, 0], [0, 0, 0, 0], [9E9, 9E9, 9E9, 9E9, 9E9, 9E9]];
VAR robtarget Arcs_3_3_0 := [[419.88, 204.4, 0], [0, -0.224589, 0.974454, 0], [0, 0, 0, 0], [9E9, 9E9, 9E9, 9E9, 9E9, 9E9]];
VAR robtarget Arcs_3_3_1 := [[422.37, 208.13, 0], [0, -0.22693, 0.973911, 0], [0, 0, 0, 0], [9E9, 9E9, 9E9, 9E9, 9E9, 9E9]];
VAR robtarget Arcs_3_3_2 := [[426.1, 210.62, 0], [0, -0.227532, 0.973771, 0], [0, 0, 0, 0], [9E9, 9E9, 9E9, 9E9, 9E9, 9E9]];
VAR robtarget Arcs_3_3_3 := [[430.5, 211.5, 0], [0, -0.226349, 0.974046, 0], [0, 0, 0, 0], [9E9, 9E9, 9E9, 9E9, 9E9, 9E9]];
VAR robtarget Arcs_3_3_4 := [[434.9, 210.62, 0], [0, -0.2236, 0.974681, 0], [0, 0, 0, 0], [9E9, 9E9, 9E9, 9E9, 9E9, 9E9]];
VAR robtarget Arcs_3_3_5 := [[438.63, 208.13, 0], [0, -0.219714, 0.975564, 0], [0, 0, 0, 0], [9E9, 9E9, 9E9, 9E9, 9E9, 9E9]];
VAR robtarget Arcs_3_3_6 := [[441.12, 204.4, 0], [0, -0.215257, 0.976557, 0], [0, 0, 0, 0], [9E9, 9E9, 9E9, 9E9, 9E9, 9E9]];
VAR robtarget Arcs_3_3_7 := [[442, 200, 0], [0, -0.210866, 0.977515, 0], [0, 0, 0, 0], [9E9, 9E9, 9E9, 9E9, 9E9, 9E9]];
VAR robtarget Arcs_3_4_0 := [[442.88, -204.4, 0], [0, 0.214521, 0.976719, 0], [0, 0, 0, 0], [9E9, 9E9, 9E9, 9E9, 9E9, 9E9]];
VAR robtarget Arcs_3_4_1 := [[445.37, -208.13, 0], [0, 0.216847, 0.976206, 0], [0, 0, 0, 0], [9E9, 9E9, 9E9, 9E9, 9E9, 9E9]];
VAR robtarget Arcs_3_4_2 := [[449.1, -210.62, 0], [0, 0.217515, 0.976057, 0], [0, 0, 0, 0], [9E9, 9E9, 9E9, 9E9, 9E9, 9E9]];
VAR robtarget Arcs_3_4_3 := [[453.5, -211.5, 0], [0, 0.216466, 0.97629, 0], [0, 0, 0, 0], [9E9, 9E9, 9E9, 9E9, 9E9, 9E9]];
VAR robtarget Arcs_3_4_4 := [[457.9, -210.62, 0], [0, 0.213895, 0.976857, 0], [0, 0, 0, 0], [9E9, 9E9, 9E9, 9E9, 9E9, 9E9]];
VAR robtarget Arcs_3_4_5 := [[461.63, -208.13, 0], [0, 0.210205, 0.977657, 0], [0, 0, 0, 0], [9E9, 9E9, 9E9, 9E9, 9E9, 9E9]];
VAR robtarget Arcs_3_4_6 := [[464.12, -204.4, 0], [0, 0.205937, 0.978565, 0], [0, 0, 0, 0], [9E9, 9E9, 9E9, 9E9, 9E9, 9E9]];
VAR robtarget Arcs_3_4_7 := [[465, -200, 0], [0, 0.201701, 0.979447, 0], [0, 0, 0, 0], [9E9, 9E9, 9E9, 9E9, 9E9, 9E9]];
VAR robtarget Arcs_3_5_0 := [[465.88, 204.4, 0], [0, -0.205258, 0.978708, 0], [0, 0, 0, 0], [9E9, 9E9, 9E9, 9E9, 9E9, 9E9]];
VAR robtarget Arcs_3_5_1 := [[468.37, 208.13, 0], [0, -0.207564, 0.978222, 0], [0, 0, 0, 0], [9E9, 9E9, 9E9, 9E9, 9E9, 9E9]];
VAR robtarget Arcs_3_5_2 := [[472.1, 210.62, 0], [0, -0.208286, 0.978068, 0], [0, 0, 0, 0], [9E9, 9E9, 9E9, 9E9, 9E9, 9E9]];
VAR robtarget Arcs_3_5_3 := [[476.5, 211.5, 0], [0, -0.207353, 0.978266, 0], [0, 0, 0, 0], [9E9, 9E9, 9E9, 9E9, 9E9, 9E9]];
VAR robtarget Arcs_3_5_4 := [[480.9, 210.62, 0], [0, -0.204944, 0.978774, 0], [0, 0, 0, 0], [9E9, 9E9, 9E9, 9E9, 9E9, 9E9]];
VAR robtarget Arcs_3_5_5 := [[484.63, 208.13, 0], [0, -0.201435, 0.979502, 0], [0, 0, 0, 0], [9E9, 9E9, 9E9, 9E9, 9E9, 9E9]];
VAR robtarget Arcs_3_5_6 := [[487.12, 204.4, 0], [0, -0.197343, 0.980334, 0], [0, 0, 0, 0], [9E9, 9E9, 9E9, 9E9, 9E9, 9E9]];
VAR robtarget Arcs_3_5_7 := [[488, 200, 0], [0, -0.193255, 0.981149, 0], [0, 0, 0, 0], [9E9, 9E9, 9E9, 9E9, 9E9, 9E9]];
VAR robtarget Arcs_3_6_0 := [[488.88, -204.4, 0], [0, 0.196716, 0.98046, 0], [0, 0, 0, 0], [9E9, 9E9, 9E9, 9E9, 9E9, 9E9]];
VAR robtarget Arcs_3_6_1 := [[491.37, -208.13, 0], [0, 0.198995, 0.980001, 0], [0, 0, 0, 0], [9E9, 9E9, 9E9, 9E9, 9E9, 9E9]];
VAR robtarget Arcs_3_6_2 := [[495.1, -210.62, 0], [0, 0.19976, 0.979845, 0], [0, 0, 0, 0], [9E9, 9E9, 9E9, 9E9, 9E9, 9E9]];
VAR robtarget Arcs_3_6_3 := [[499.5, -211.5, 0], [0, 0.198931, 0.980013, 0], [0, 0, 0, 0], [9E9, 9E9, 9E9, 9E9, 9E9, 9E9]];
VAR robtarget Arcs_3_6_4 := [[503.9, -210.62, 0], [0, 0.196668, 0.98047, 0], [0, 0, 0, 0], [9E9, 9E9, 9E9, 9E9, 9E9, 9E9]];
VAR robtarget Arcs_3_6_5 := [[507.63, -208.13, 0], [0, 0.193326, 0.981135, 0], [0, 0, 0, 0], [9E9, 9E9, 9E9, 9E9, 9E9, 9E9]];
VAR robtarget Arcs_3_6_6 := [[510.12, -204.4, 0], [0, 0.189399, 0.9819, 0], [0, 0, 0, 0], [9E9, 9E9, 9E9, 9E9, 9E9, 9E9]];
VAR robtarget Arcs_3_6_7 := [[511, -200, 0], [0, 0.185451, 0.982654, 0], [0, 0, 0, 0], [9E9, 9E9, 9E9, 9E9, 9E9, 9E9]];
VAR robtarget Arcs_3_7_0 := [[511.88, 204.4, 0], [0, -0.188819, 0.982012, 0], [0, 0, 0, 0], [9E9, 9E9, 9E9, 9E9, 9E9, 9E9]];
VAR robtarget Arcs_3_7_1 := [[514.37, 208.13, 0], [0, -0.191066, 0.981577, 0], [0, 0, 0, 0], [9E9, 9E9, 9E9, 9E9, 9E9, 9E9]];
VAR robtarget Arcs_3_7_2 := [[518.1, 210.62, 0], [0, -0.191866, 0.981421, 0], [0, 0, 0, 0], [9E9, 9E9, 9E9, 9E9, 9E9, 9E9]];
VAR robtarget Arcs_3_7_3 := [[522.5, 211.5, 0], [0, -0.191129, 0.981565, 0], [0, 0, 0, 0], [9E9, 9E9, 9E9, 9E9, 9E9, 9E9]];
VAR robtarget Arcs_3_7_4 := [[526.9, 210.62, 0], [0, -0.188998, 0.981977, 0], [0, 0, 0, 0], [9E9, 9E9, 9E9, 9E9, 9E9, 9E9]];
VAR robtarget Arcs_3_7_5 := [[530.63, 208.13, 0], [0, -0.185811, 0.982586, 0], [0, 0, 0, 0], [9E9, 9E9, 9E9, 9E9, 9E9, 9E9]];
VAR robtarget Arcs_3_7_6 := [[533.12, 204.4, 0], [0, -0.182037, 0.983292, 0], [0, 0, 0, 0], [9E9, 9E9, 9E9, 9E9, 9E9, 9E9]];
VAR robtarget Arcs_3_7_7 := [[534, 200, 0], [0, -0.178223, 0.98399, 0], [0, 0, 0, 0], [9E9, 9E9, 9E9, 9E9, 9E9, 9E9]];
VAR robtarget Arcs_3_8_0 := [[534.88, -204.4, 0], [0, 0.181499, 0.983391, 0], [0, 0, 0, 0], [9E9, 9E9, 9E9, 9E9, 9E9, 9E9]];
VAR robtarget Arcs_3_8_1 := [[537.37, -208.13, 0], [0, 0.183713, 0.98298, 0], [0, 0, 0, 0], [9E9, 9E9, 9E9, 9E9, 9E9, 9E9]];
VAR robtarget Arcs_3_8_2 := [[541.1, -210.62, 0], [0, 0.18454, 0.982825, 0], [0, 0, 0, 0], [9E9, 9E9, 9E9, 9E9, 9E9, 9E9]];
VAR robtarget Arcs_3_8_3 := [[545.5, -211.5, 0], [0, 0.183884, 0.982948, 0], [0, 0, 0, 0], [9E9, 9E9, 9E9, 9E9, 9E9, 9E9]];
VAR robtarget Arcs_3_8_4 := [[549.9, -210.62, 0], [0, 0.181875, 0.983322, 0], [0, 0, 0, 0], [9E9, 9E9, 9E9, 9E9, 9E9, 9E9]];
VAR robtarget Arcs_3_8_5 := [[553.63, -208.13, 0], [0, 0.17883, 0.98388, 0], [0, 0, 0, 0], [9E9, 9E9, 9E9, 9E9, 9E9, 9E9]];
VAR robtarget Arcs_3_8_6 := [[556.12, -204.4, 0], [0, 0.175201, 0.984533, 0], [0, 0, 0, 0], [9E9, 9E9, 9E9, 9E9, 9E9, 9E9]];
VAR robtarget Arcs_3_8_7 := [[557, -200, 0], [0, 0.171512, 0.985182, 0], [0, 0, 0, 0], [9E9, 9E9, 9E9, 9E9, 9E9, 9E9]];
VAR robtarget Pos3_3 := [[557, 280, 0], [0, -0.2308, 0.973001, 0], [0, 0, 0, 0], [9E9, 9E9, 9E9, 9E9, 9E9, 9E9]];
VAR robtarget Start_point_3 := [[350, 280, 0], [0, -0.331007, 0.943628, 0], [0, 0, 0, 0], [9E9, 9E9, 9E9, 9E9, 9E9, 9E9]];
VAR robtarget Straight_lines_3_0_0 := [[350, 200, 0], [0, -0.256668, 0.9665, 0], [0, 0, 0, 0], [9E9, 9E9, 9E9, 9E9, 9E9, 9E9]];
VAR robtarget Straight_lines_3_0_1 := [[350, 0, 0], [0, 0, 1, 0], [0, 0, 0, 0], [9E9, 9E9, 9E9, 9E9, 9E9, 9E9]];
VAR robtarget Straight_lines_3_0_2 := [[350, -200, 0], [0, 0.256668, 0.9665, 0], [0, 0, 0, 0], [9E9, 9E9, 9E9, 9E9, 9E9, 9E9]];
VAR robtarget Straight_lines_3_1_0 := [[373, 0, 0], [0, 0, 1, 0], [0, 0, 0, 0], [9E9, 9E9, 9E9, 9E9, 9E9, 9E9]];
```

```
VAR robtarget Straight_lines_3_1_1 := [[373, 200, 0], [0, -0.243614, 0.969872, 0], [0, 0, 0, 0], [9E9, 9E9, 9E9, 9E9, 9E9, 9E9]];
VAR robtarget Straight_lines_3_2_0 := [[396, 0, 0], [0, 0, 1, 0], [0, 0, 0, 0], [9E9, 9E9, 9E9, 9E9, 9E9, 9E9]];
VAR robtarget Straight_lines_3_2_1 := [[396, -200, 0], [0, 0.231715, 0.972784, 0], [0, 0, 0, 0], [9E9, 9E9, 9E9, 9E9, 9E9, 9E9]];
VAR robtarget Straight_lines_3_3_0 := [[419, 0, 0], [0, 0, 1, 0], [0, 0, 0, 0], [9E9, 9E9, 9E9, 9E9, 9E9, 9E9]];
VAR robtarget Straight_lines_3_3_1 := [[419, 200, 0], [0, -0.220837, 0.975311, 0], [0, 0, 0, 0], [9E9, 9E9, 9E9, 9E9, 9E9, 9E9]];
VAR robtarget Straight_lines_3_4_0 := [[442, 0, 0], [0, 0, 1, 0], [0, 0, 0, 0], [9E9, 9E9, 9E9, 9E9, 9E9, 9E9]];
VAR robtarget Straight_lines_3_4_1 := [[442, -200, 0], [0, 0.210866, 0.977515, 0], [0, 0, 0, 0], [9E9, 9E9, 9E9, 9E9, 9E9, 9E9]];
VAR robtarget Straight_lines_3_5_0 := [[465, 0, 0], [0, 0, 1, 0], [0, 0, 0, 0], [9E9, 9E9, 9E9, 9E9, 9E9, 9E9]];
VAR robtarget Straight_lines_3_5_1 := [[465, 200, 0], [0, -0.201701, 0.979447, 0], [0, 0, 0, 0], [9E9, 9E9, 9E9, 9E9, 9E9, 9E9]];
VAR robtarget Straight_lines_3_6_0 := [[488, 0, 0], [0, 0, 1, 0], [0, 0, 0, 0], [9E9, 9E9, 9E9, 9E9, 9E9, 9E9]];
VAR robtarget Straight_lines_3_6_1 := [[488, -200, 0], [0, 0.193255, 0.981149, 0], [0, 0, 0, 0], [9E9, 9E9, 9E9, 9E9, 9E9, 9E9]];
VAR robtarget Straight_lines_3_7_0 := [[511, 0, 0], [0, 0, 1, 0], [0, 0, 0, 0], [9E9, 9E9, 9E9, 9E9, 9E9, 9E9]];
VAR robtarget Straight_lines_3_7_1 := [[511, 200, 0], [0, -0.185451, 0.982654, 0], [0, 0, 0, 0], [9E9, 9E9, 9E9, 9E9, 9E9, 9E9]];
VAR robtarget Straight_lines_3_8_0 := [[534, 0, 0], [0, 0, 1, 0], [0, 0, 0, 0], [9E9, 9E9, 9E9, 9E9, 9E9, 9E9]];
VAR robtarget Straight_lines_3_8_1 := [[534, -200, 0], [0, 0.178223, 0.98399, 0], [0, 0, 0, 0], [9E9, 9E9, 9E9, 9E9, 9E9, 9E9]];
VAR robtarget Straight_lines_3_9_0 := [[557, 0, 0], [0, 0, 1, 0], [0, 0, 0, 0], [9E9, 9E9, 9E9, 9E9, 9E9, 9E9]];
VAR robtarget Straight_lines_3_9_1 := [[557, 200, 0], [0, -0.171512, 0.985182, 0], [0, 0, 0, 0], [9E9, 9E9, 9E9, 9E9, 9E9, 9E9]];
VAR speeddata Arc_speed := [13, 500, 5000, 1000];
VAR speeddata Straight_lines_speed := [13, 500, 5000, 1000];

PROC main()
  MoveAbsJ Home, v150, z0, Makita\WObj:=Work_object;
  ConfL\off;
  ConfJ\on;
  MoveJ Start_point_3, v150, z0, Makita\WObj:=Work_object;
  MoveL Straight_lines_3_0_0, Straight_lines_speed, z0, Makita\WObj:=Work_object;
  MoveL Straight_lines_3_0_1, Straight_lines_speed, z0, Makita\WObj:=Work_object;
  MoveL Straight_lines_3_0_2, Straight_lines_speed, z0, Makita\WObj:=Work_object;
  MoveL Arcs_3_0_0, Arc_speed, z0, Makita\WObj:=Work_object;
  MoveL Arcs_3_0_1, Arc_speed, z0, Makita\WObj:=Work_object;
  MoveL Arcs_3_0_2, Arc_speed, z0, Makita\WObj:=Work_object;
  MoveL Arcs_3_0_3, Arc_speed, z0, Makita\WObj:=Work_object;
  MoveL Arcs_3_0_4, Arc_speed, z0, Makita\WObj:=Work_object;
  MoveL Arcs_3_0_5, Arc_speed, z0, Makita\WObj:=Work_object;
  MoveL Arcs_3_0_6, Arc_speed, z0, Makita\WObj:=Work_object;
  MoveL Arcs_3_0_7, Arc_speed, z0, Makita\WObj:=Work_object;
  MoveL Straight_lines_3_1_0, Straight_lines_speed, z0, Makita\WObj:=Work_object;
  MoveL Straight_lines_3_1_1, Straight_lines_speed, z0, Makita\WObj:=Work_object;
  MoveL Arcs_3_1_0, Arc_speed, z0, Makita\WObj:=Work_object;
  MoveL Arcs_3_1_1, Arc_speed, z0, Makita\WObj:=Work_object;
  MoveL Arcs_3_1_2, Arc_speed, z0, Makita\WObj:=Work_object;
  MoveL Arcs_3_1_3, Arc_speed, z0, Makita\WObj:=Work_object;
  MoveL Arcs_3_1_4, Arc_speed, z0, Makita\WObj:=Work_object;
  MoveL Arcs_3_1_5, Arc_speed, z0, Makita\WObj:=Work_object;
  MoveL Arcs_3_1_6, Arc_speed, z0, Makita\WObj:=Work_object;
  MoveL Arcs_3_1_7, Arc_speed, z0, Makita\WObj:=Work_object;
  MoveL Straight_lines_3_2_0, Straight_lines_speed, z0, Makita\WObj:=Work_object;
  MoveL Straight_lines_3_2_1, Straight_lines_speed, z0, Makita\WObj:=Work_object;
  MoveL Arcs_3_2_0, Arc_speed, z0, Makita\WObj:=Work_object;
  MoveL Arcs_3_2_1, Arc_speed, z0, Makita\WObj:=Work_object;
  MoveL Arcs_3_2_2, Arc_speed, z0, Makita\WObj:=Work_object;
  MoveL Arcs_3_2_3, Arc_speed, z0, Makita\WObj:=Work_object;
  MoveL Arcs_3_2_4, Arc_speed, z0, Makita\WObj:=Work_object;
  MoveL Arcs_3_2_5, Arc_speed, z0, Makita\WObj:=Work_object;
  MoveL Arcs_3_2_6, Arc_speed, z0, Makita\WObj:=Work_object;
  MoveL Arcs_3_2_7, Arc_speed, z0, Makita\WObj:=Work_object;
  MoveL Straight_lines_3_3_0, Straight_lines_speed, z0, Makita\WObj:=Work_object;
  MoveL Straight_lines_3_3_1, Straight_lines_speed, z0, Makita\WObj:=Work_object;
  MoveL Arcs_3_3_0, Arc_speed, z0, Makita\WObj:=Work_object;
  MoveL Arcs_3_3_1, Arc_speed, z0, Makita\WObj:=Work_object;
  MoveL Arcs_3_3_2, Arc_speed, z0, Makita\WObj:=Work_object;
  MoveL Arcs_3_3_3, Arc_speed, z0, Makita\WObj:=Work_object;
  MoveL Arcs_3_3_4, Arc_speed, z0, Makita\WObj:=Work_object;
  MoveL Arcs_3_3_5, Arc_speed, z0, Makita\WObj:=Work_object;
  MoveL Arcs_3_3_6, Arc_speed, z0, Makita\WObj:=Work_object;
  MoveL Arcs_3_3_7, Arc_speed, z0, Makita\WObj:=Work_object;
  MoveL Straight_lines_3_4_0, Straight_lines_speed, z0, Makita\WObj:=Work_object;
  MoveL Straight_lines_3_4_1, Straight_lines_speed, z0, Makita\WObj:=Work_object;
  MoveL Arcs_3_4_0, Arc_speed, z0, Makita\WObj:=Work_object;
  MoveL Arcs_3_4_1, Arc_speed, z0, Makita\WObj:=Work_object;
  MoveL Arcs_3_4_2, Arc_speed, z0, Makita\WObj:=Work_object;
```

```
    MoveL Arcs_3_4_3, Arc_speed, z0, Makita\WObj:=Work_object;
    MoveL Arcs_3_4_4, Arc_speed, z0, Makita\WObj:=Work_object;
    MoveL Arcs_3_4_5, Arc_speed, z0, Makita\WObj:=Work_object;
    MoveL Arcs_3_4_6, Arc_speed, z0, Makita\WObj:=Work_object;
    MoveL Arcs_3_4_7, Arc_speed, z0, Makita\WObj:=Work_object;
    MoveL Straight_lines_3_5_0, Straight_lines_speed, z0, Makita\WObj:=Work_object;
    MoveL Straight_lines_3_5_1, Straight_lines_speed, z0, Makita\WObj:=Work_object;
    MoveL Arcs_3_5_0, Arc_speed, z0, Makita\WObj:=Work_object;
    MoveL Arcs_3_5_1, Arc_speed, z0, Makita\WObj:=Work_object;
    MoveL Arcs_3_5_2, Arc_speed, z0, Makita\WObj:=Work_object;
    MoveL Arcs_3_5_3, Arc_speed, z0, Makita\WObj:=Work_object;
    MoveL Arcs_3_5_4, Arc_speed, z0, Makita\WObj:=Work_object;
    MoveL Arcs_3_5_5, Arc_speed, z0, Makita\WObj:=Work_object;
    MoveL Arcs_3_5_6, Arc_speed, z0, Makita\WObj:=Work_object;
    MoveL Arcs_3_5_7, Arc_speed, z0, Makita\WObj:=Work_object;
    MoveL Straight_lines_3_6_0, Straight_lines_speed, z0, Makita\WObj:=Work_object;
    MoveL Straight_lines_3_6_1, Straight_lines_speed, z0, Makita\WObj:=Work_object;
    MoveL Arcs_3_6_0, Arc_speed, z0, Makita\WObj:=Work_object;
    MoveL Arcs_3_6_1, Arc_speed, z0, Makita\WObj:=Work_object;
    MoveL Arcs_3_6_2, Arc_speed, z0, Makita\WObj:=Work_object;
    MoveL Arcs_3_6_3, Arc_speed, z0, Makita\WObj:=Work_object;
    MoveL Arcs_3_6_4, Arc_speed, z0, Makita\WObj:=Work_object;
    MoveL Arcs_3_6_5, Arc_speed, z0, Makita\WObj:=Work_object;
    MoveL Arcs_3_6_6, Arc_speed, z0, Makita\WObj:=Work_object;
    MoveL Arcs_3_6_7, Arc_speed, z0, Makita\WObj:=Work_object;
    MoveL Straight_lines_3_7_0, Straight_lines_speed, z0, Makita\WObj:=Work_object;
    MoveL Straight_lines_3_7_1, Straight_lines_speed, z0, Makita\WObj:=Work_object;
    MoveL Arcs_3_7_0, Arc_speed, z0, Makita\WObj:=Work_object;
    MoveL Arcs_3_7_1, Arc_speed, z0, Makita\WObj:=Work_object;
    MoveL Arcs_3_7_2, Arc_speed, z0, Makita\WObj:=Work_object;
    MoveL Arcs_3_7_3, Arc_speed, z0, Makita\WObj:=Work_object;
    MoveL Arcs_3_7_4, Arc_speed, z0, Makita\WObj:=Work_object;
    MoveL Arcs_3_7_5, Arc_speed, z0, Makita\WObj:=Work_object;
    MoveL Arcs_3_7_6, Arc_speed, z0, Makita\WObj:=Work_object;
    MoveL Arcs_3_7_7, Arc_speed, z0, Makita\WObj:=Work_object;
    MoveL Straight_lines_3_8_0, Straight_lines_speed, z0, Makita\WObj:=Work_object;
    MoveL Straight_lines_3_8_1, Straight_lines_speed, z0, Makita\WObj:=Work_object;
    MoveL Arcs_3_8_0, Arc_speed, z0, Makita\WObj:=Work_object;
    MoveL Arcs_3_8_1, Arc_speed, z0, Makita\WObj:=Work_object;
    MoveL Arcs_3_8_2, Arc_speed, z0, Makita\WObj:=Work_object;
    MoveL Arcs_3_8_3, Arc_speed, z0, Makita\WObj:=Work_object;
    MoveL Arcs_3_8_4, Arc_speed, z0, Makita\WObj:=Work_object;
    MoveL Arcs_3_8_5, Arc_speed, z0, Makita\WObj:=Work_object;
    MoveL Arcs_3_8_6, Arc_speed, z0, Makita\WObj:=Work_object;
    MoveL Arcs_3_8_7, Arc_speed, z0, Makita\WObj:=Work_object;
    MoveL Straight_lines_3_9_0, Straight_lines_speed, z0, Makita\WObj:=Work_object;
    MoveL Straight_lines_3_9_1, Straight_lines_speed, z0, Makita\WObj:=Work_object;
    MoveL Pos3_3, Straight_lines_speed, z0, Makita\WObj:=Work_object;
    MoveAbsJ Home, v150, z0, Makita\WObj:=Work_object;
  ENDPROC

ENDMODULE
```

H.3.2 Path adhesion RAPID codes

H.3.2.1 5 mm overlap

```
MODULE MainModule

  ! This RAPID code was generated with RobotComponents v2.2.2 (GPL v3)
  ! Visit www.github.com/RobotComponents for more information

  ! User defined tooldata
  PERS tooldata Makita := [TRUE, [[-160, 0, 492.4], [1, 0, 0, 0]], [0.001, [0, 0, 0.001], [1, 0, 0, 0], 0, 0, 0]];

  ! User defined wobjdata
  PERS wobjdata Work_object := [FALSE, TRUE, "", [[0, 0, 0], [1, 0, 0, 0]], [[0, 0, 32.58], [1, 0, 0, 0]]];

  ! Declarations generated by Robot Components
  VAR jointtarget Home := [[0, 0, 0, 0, 0, 0], [9E9, 9E9, 9E9, 9E9, 9E9, 9E9]];
  VAR robtarget Arcs_0 := [[350.88, -84.4, 0], [0, 0, 1, 0], [0, 0, 0, 0], [9E9, 9E9, 9E9, 9E9, 9E9, 9E9]];
  VAR robtarget Arcs_1 := [[353.37, -88.13, 0], [0, 0, 1, 0], [0, 0, 0, 0], [9E9, 9E9, 9E9, 9E9, 9E9, 9E9]];
```

```
  VAR robtarget Arcs_2 := [[357.1, -90.62, 0], [0, 0, 1, 0], [0, 0, 0, 0], [9E9, 9E9, 9E9, 9E9, 9E9, 9E9]];
  VAR robtarget Arcs_3 := [[361.5, -91.5, 0], [0, 0, 1, 0], [0, 0, 0, 0], [9E9, 9E9, 9E9, 9E9, 9E9, 9E9]];
  VAR robtarget Arcs_4 := [[365.9, -90.62, 0], [0, 0, 1, 0], [0, 0, 0, 0], [9E9, 9E9, 9E9, 9E9, 9E9, 9E9]];
  VAR robtarget Arcs_5 := [[369.63, -88.13, 0], [0, 0, 1, 0], [0, 0, 0, 0], [9E9, 9E9, 9E9, 9E9, 9E9, 9E9]];
  VAR robtarget Arcs_6 := [[372.12, -84.4, 0], [0, 0, 1, 0], [0, 0, 0, 0], [9E9, 9E9, 9E9, 9E9, 9E9, 9E9]];
  VAR robtarget Arcs_7 := [[373, -80, 0], [0, 0, 1, 0], [0, 0, 0, 0], [9E9, 9E9, 9E9, 9E9, 9E9, 9E9]];
  VAR robtarget Pos3_0 := [[373, 106.67, 0], [0, 0, 1, 0], [0, 0, 0, 0], [9E9, 9E9, 9E9, 9E9, 9E9, 9E9]];
  VAR robtarget Pos3_1 := [[373, 133.33, 0], [0, 0, 1, 0], [0, 0, 0, 0], [9E9, 9E9, 9E9, 9E9, 9E9, 9E9]];
  VAR robtarget Pos3_2 := [[373, 160, 0], [0, 0, 1, 0], [0, 0, 0, 0], [9E9, 9E9, 9E9, 9E9, 9E9, 9E9]];
  VAR robtarget Start_point := [[350, 160, 0], [0, 0, 1, 0], [0, 0, 0, 0], [9E9, 9E9, 9E9, 9E9, 9E9, 9E9]];
  VAR robtarget Straight_lines_0_0 := [[350, 133.33, 0], [0, 0, 1, 0], [0, 0, 0, 0], [9E9, 9E9, 9E9, 9E9, 9E9, 9E9]];
  VAR robtarget Straight_lines_0_1 := [[350, 106.67, 0], [0, 0, 1, 0], [0, 0, 0, 0], [9E9, 9E9, 9E9, 9E9, 9E9, 9E9]];
  VAR robtarget Straight_lines_0_2 := [[350, 80, 0], [0, 0, 1, 0], [0, 0, 0, 0], [9E9, 9E9, 9E9, 9E9, 9E9, 9E9]];
  VAR robtarget Straight_lines_0_3 := [[350, 26.67, 0], [0, 0, 1, 0], [0, 0, 0, 0], [9E9, 9E9, 9E9, 9E9, 9E9, 9E9]];
  VAR robtarget Straight_lines_0_4 := [[350, -26.67, 0], [0, 0, 1, 0], [0, 0, 0, 0], [9E9, 9E9, 9E9, 9E9, 9E9, 9E9]];
  VAR robtarget Straight_lines_0_5 := [[350, -80, 0], [0, 0, 1, 0], [0, 0, 0, 0], [9E9, 9E9, 9E9, 9E9, 9E9, 9E9]];
  VAR robtarget Straight_lines_1_0 := [[373, -26.67, 0], [0, 0, 1, 0], [0, 0, 0, 0], [9E9, 9E9, 9E9, 9E9, 9E9, 9E9]];
  VAR robtarget Straight_lines_1_1 := [[373, 26.67, 0], [0, 0, 1, 0], [0, 0, 0, 0], [9E9, 9E9, 9E9, 9E9, 9E9, 9E9]];
  VAR robtarget Straight_lines_1_2 := [[373, 80, 0], [0, 0, 1, 0], [0, 0, 0, 0], [9E9, 9E9, 9E9, 9E9, 9E9, 9E9]];
  VAR speeddata Arc_speed := [13, 500, 5000, 1000];
  VAR speeddata Straight_lines_speed := [13, 500, 5000, 1000];

  PROC main()
    MoveAbsJ Home, v150, z0, Makita\WObj:=Work_object;
    ConfL\off;
    ConfJ\on;
    MoveJ Start_point, v150, z0, Makita\WObj:=Work_object;
    MoveL Straight_lines_0_0, Straight_lines_speed, z0, Makita\WObj:=Work_object;
    MoveL Straight_lines_0_1, Straight_lines_speed, z0, Makita\WObj:=Work_object;
    MoveL Straight_lines_0_2, Straight_lines_speed, z0, Makita\WObj:=Work_object;
    MoveL Straight_lines_0_3, Straight_lines_speed, z0, Makita\WObj:=Work_object;
    MoveL Straight_lines_0_4, Straight_lines_speed, z0, Makita\WObj:=Work_object;
    MoveL Straight_lines_0_5, Straight_lines_speed, z0, Makita\WObj:=Work_object;
    MoveL Arcs_0, Arc_speed, z0, Makita\WObj:=Work_object;
    MoveL Arcs_1, Arc_speed, z0, Makita\WObj:=Work_object;
    MoveL Arcs_2, Arc_speed, z0, Makita\WObj:=Work_object;
    MoveL Arcs_3, Arc_speed, z0, Makita\WObj:=Work_object;
    MoveL Arcs_4, Arc_speed, z0, Makita\WObj:=Work_object;
    MoveL Arcs_5, Arc_speed, z0, Makita\WObj:=Work_object;
    MoveL Arcs_6, Arc_speed, z0, Makita\WObj:=Work_object;
    MoveL Arcs_7, Arc_speed, z0, Makita\WObj:=Work_object;
    MoveL Straight_lines_1_0, Straight_lines_speed, z0, Makita\WObj:=Work_object;
    MoveL Straight_lines_1_1, Straight_lines_speed, z0, Makita\WObj:=Work_object;
    MoveL Straight_lines_1_2, Straight_lines_speed, z0, Makita\WObj:=Work_object;
    MoveL Pos3_0, Straight_lines_speed, z0, Makita\WObj:=Work_object;
    MoveL Pos3_1, Straight_lines_speed, z0, Makita\WObj:=Work_object;
    MoveL Pos3_2, Straight_lines_speed, z0, Makita\WObj:=Work_object;
    MoveAbsJ Home, v150, z0, Makita\WObj:=Work_object;
  ENDPROC

ENDMODULE
```

H.3.2.2 3 mm overlap

```
MODULE MainModule

  ! This RAPID code was generated with RobotComponents v2.2.2 (GPL v3)
  ! Visit www.github.com/RobotComponents for more information

  ! User defined tooldata
  PERS tooldata Makita := [TRUE, [[-160, 0, 492.4], [1, 0, 0, 0]], [0.001, [0, 0, 0.001], [1, 0, 0, 0], 0, 0, 0]];

  ! User defined wobjdata
  PERS wobjdata Work_object := [FALSE, TRUE, "", [[0, 0, 0], [1, 0, 0, 0]], [[0, 0, 32.58], [1, 0, 0, 0]]];

  ! Declarations generated by Robot Components
  VAR jointtarget Home := [[0, 0, 0, 0, 0, 0], [9E9, 9E9, 9E9, 9E9, 9E9, 9E9]];
  VAR robtarget Arcs_0 := [[350.8, -84.02, 0], [0, 0, 1, 0], [0, 0, 0, 0], [9E9, 9E9, 9E9, 9E9, 9E9, 9E9]];
  VAR robtarget Arcs_1 := [[353.08, -87.42, 0], [0, 0, 1, 0], [0, 0, 0, 0], [9E9, 9E9, 9E9, 9E9, 9E9, 9E9]];
  VAR robtarget Arcs_2 := [[356.48, -89.7, 0], [0, 0, 1, 0], [0, 0, 0, 0], [9E9, 9E9, 9E9, 9E9, 9E9, 9E9]];
  VAR robtarget Arcs_3 := [[360.5, -90.5, 0], [0, 0, 1, 0], [0, 0, 0, 0], [9E9, 9E9, 9E9, 9E9, 9E9, 9E9]];
  VAR robtarget Arcs_4 := [[364.52, -89.7, 0], [0, 0, 1, 0], [0, 0, 0, 0], [9E9, 9E9, 9E9, 9E9, 9E9, 9E9]];
```

```
  VAR robtarget Arcs_5 := [[367.92, -87.42, 0], [0, 0, 1, 0], [0, 0, 0, 0], [9E9, 9E9, 9E9, 9E9, 9E9, 9E9]];
  VAR robtarget Arcs_6 := [[370.2, -84.02, 0], [0, 0, 1, 0], [0, 0, 0, 0], [9E9, 9E9, 9E9, 9E9, 9E9, 9E9]];
  VAR robtarget Arcs_7 := [[371, -80, 0], [0, 0, 1, 0], [0, 0, 0, 0], [9E9, 9E9, 9E9, 9E9, 9E9, 9E9]];
  VAR robtarget Pos3_0 := [[371, 106.67, 0], [0, 0, 1, 0], [0, 0, 0, 0], [9E9, 9E9, 9E9, 9E9, 9E9, 9E9]];
  VAR robtarget Pos3_1 := [[371, 133.33, 0], [0, 0, 1, 0], [0, 0, 0, 0], [9E9, 9E9, 9E9, 9E9, 9E9, 9E9]];
  VAR robtarget Pos3_2 := [[371, 160, 0], [0, 0, 1, 0], [0, 0, 0, 0], [9E9, 9E9, 9E9, 9E9, 9E9, 9E9]];
  VAR robtarget Start_point := [[350, 160, 0], [0, 0, 1, 0], [0, 0, 0, 0], [9E9, 9E9, 9E9, 9E9, 9E9, 9E9]];
  VAR robtarget Straight_lines_0_0 := [[350, 133.33, 0], [0, 0, 1, 0], [0, 0, 0, 0], [9E9, 9E9, 9E9, 9E9, 9E9, 9E9]];
  VAR robtarget Straight_lines_0_1 := [[350, 106.67, 0], [0, 0, 1, 0], [0, 0, 0, 0], [9E9, 9E9, 9E9, 9E9, 9E9, 9E9]];
  VAR robtarget Straight_lines_0_2 := [[350, 80, 0], [0, 0, 1, 0], [0, 0, 0, 0], [9E9, 9E9, 9E9, 9E9, 9E9, 9E9]];
  VAR robtarget Straight_lines_0_3 := [[350, 26.67, 0], [0, 0, 1, 0], [0, 0, 0, 0], [9E9, 9E9, 9E9, 9E9, 9E9, 9E9]];
  VAR robtarget Straight_lines_0_4 := [[350, -26.67, 0], [0, 0, 1, 0], [0, 0, 0, 0], [9E9, 9E9, 9E9, 9E9, 9E9, 9E9]];
  VAR robtarget Straight_lines_0_5 := [[350, -80, 0], [0, 0, 1, 0], [0, 0, 0, 0], [9E9, 9E9, 9E9, 9E9, 9E9, 9E9]];
  VAR robtarget Straight_lines_1_0 := [[371, -26.67, 0], [0, 0, 1, 0], [0, 0, 0, 0], [9E9, 9E9, 9E9, 9E9, 9E9, 9E9]];
  VAR robtarget Straight_lines_1_1 := [[371, 26.67, 0], [0, 0, 1, 0], [0, 0, 0, 0], [9E9, 9E9, 9E9, 9E9, 9E9, 9E9]];
  VAR robtarget Straight_lines_1_2 := [[371, 80, 0], [0, 0, 1, 0], [0, 0, 0, 0], [9E9, 9E9, 9E9, 9E9, 9E9, 9E9]];
  VAR speeddata Arc_speed := [13, 500, 5000, 1000];
  VAR speeddata Straight_lines_speed := [13, 500, 5000, 1000];

  PROC main()
    MoveAbsJ Home, v150, z0, Makita\WObj:=Work_object;
    ConfL\off;
    ConfJ\on;
    MoveJ Start_point, v150, z0, Makita\WObj:=Work_object;
    MoveL Straight_lines_0_0, Straight_lines_speed, z0, Makita\WObj:=Work_object;
    MoveL Straight_lines_0_1, Straight_lines_speed, z0, Makita\WObj:=Work_object;
    MoveL Straight_lines_0_2, Straight_lines_speed, z0, Makita\WObj:=Work_object;
    MoveL Straight_lines_0_3, Straight_lines_speed, z0, Makita\WObj:=Work_object;
    MoveL Straight_lines_0_4, Straight_lines_speed, z0, Makita\WObj:=Work_object;
    MoveL Straight_lines_0_5, Straight_lines_speed, z0, Makita\WObj:=Work_object;
    MoveL Arcs_0, Arc_speed, z0, Makita\WObj:=Work_object;
    MoveL Arcs_1, Arc_speed, z0, Makita\WObj:=Work_object;
    MoveL Arcs_2, Arc_speed, z0, Makita\WObj:=Work_object;
    MoveL Arcs_3, Arc_speed, z0, Makita\WObj:=Work_object;
    MoveL Arcs_4, Arc_speed, z0, Makita\WObj:=Work_object;
    MoveL Arcs_5, Arc_speed, z0, Makita\WObj:=Work_object;
    MoveL Arcs_6, Arc_speed, z0, Makita\WObj:=Work_object;
    MoveL Arcs_7, Arc_speed, z0, Makita\WObj:=Work_object;
    MoveL Straight_lines_1_0, Straight_lines_speed, z0, Makita\WObj:=Work_object;
    MoveL Straight_lines_1_1, Straight_lines_speed, z0, Makita\WObj:=Work_object;
    MoveL Straight_lines_1_2, Straight_lines_speed, z0, Makita\WObj:=Work_object;
    MoveL Pos3_0, Straight_lines_speed, z0, Makita\WObj:=Work_object;
    MoveL Pos3_1, Straight_lines_speed, z0, Makita\WObj:=Work_object;
    MoveL Pos3_2, Straight_lines_speed, z0, Makita\WObj:=Work_object;
    MoveAbsJ Home, v150, z0, Makita\WObj:=Work_object;
  ENDPROC

ENDMODULE
```

H.3.2.3 0 mm overlap

```
MODULE MainModule

  ! This RAPID code was generated with RobotComponents v2.2.2 (GPL v3)
  ! Visit www.github.com/RobotComponents for more information

  ! User defined tooldata
  PERS tooldata Makita := [TRUE, [[-160, 0, 492.4], [1, 0, 0, 0]], [0.001, [0, 0, 0.001], [1, 0, 0, 0], 0, 0, 0]];

  ! User defined wobjdata
  PERS wobjdata Work_object := [FALSE, TRUE, "", [[0, 0, 0], [1, 0, 0, 0]], [[0, 0, 32.58], [1, 0, 0, 0]]];

  ! Declarations generated by Robot Components
  VAR jointtarget Home := [[0, 0, 0, 0, 0, 0], [9E9, 9E9, 9E9, 9E9, 9E9, 9E9]];
  VAR robtarget Arcs_0 := [[350.69, -83.44, 0], [0, 0, 1, 0], [0, 0, 0, 0], [9E9, 9E9, 9E9, 9E9, 9E9, 9E9]];
  VAR robtarget Arcs_1 := [[352.64, -86.36, 0], [0, 0, 1, 0], [0, 0, 0, 0], [9E9, 9E9, 9E9, 9E9, 9E9, 9E9]];
  VAR robtarget Arcs_2 := [[355.56, -88.31, 0], [0, 0, 1, 0], [0, 0, 0, 0], [9E9, 9E9, 9E9, 9E9, 9E9, 9E9]];
  VAR robtarget Arcs_3 := [[359, -89, 0], [0, 0, 1, 0], [0, 0, 0, 0], [9E9, 9E9, 9E9, 9E9, 9E9, 9E9]];
  VAR robtarget Arcs_4 := [[362.44, -88.31, 0], [0, 0, 1, 0], [0, 0, 0, 0], [9E9, 9E9, 9E9, 9E9, 9E9, 9E9]];
  VAR robtarget Arcs_5 := [[365.36, -86.36, 0], [0, 0, 1, 0], [0, 0, 0, 0], [9E9, 9E9, 9E9, 9E9, 9E9, 9E9]];
  VAR robtarget Arcs_6 := [[367.31, -83.44, 0], [0, 0, 1, 0], [0, 0, 0, 0], [9E9, 9E9, 9E9, 9E9, 9E9, 9E9]];
  VAR robtarget Arcs_7 := [[368, -80, 0], [0, 0, 1, 0], [0, 0, 0, 0], [9E9, 9E9, 9E9, 9E9, 9E9, 9E9]];
```

```
  VAR robtarget Pos3_0 := [[368, 106.67, 0], [0, 0, 1, 0], [0, 0, 0, 0], [9E9, 9E9, 9E9, 9E9, 9E9, 9E9]];
  VAR robtarget Pos3_1 := [[368, 133.33, 0], [0, 0, 1, 0], [0, 0, 0, 0], [9E9, 9E9, 9E9, 9E9, 9E9, 9E9]];
  VAR robtarget Pos3_2 := [[368, 160, 0], [0, 0, 1, 0], [0, 0, 0, 0], [9E9, 9E9, 9E9, 9E9, 9E9, 9E9]];
  VAR robtarget Start_point := [[350, 160, 0], [0, 0, 1, 0], [0, 0, 0, 0], [9E9, 9E9, 9E9, 9E9, 9E9, 9E9]];
  VAR robtarget Straight_lines_0_0 := [[350, 133.33, 0], [0, 0, 1, 0], [0, 0, 0, 0], [9E9, 9E9, 9E9, 9E9, 9E9, 9E9]];
  VAR robtarget Straight_lines_0_1 := [[350, 106.67, 0], [0, 0, 1, 0], [0, 0, 0, 0], [9E9, 9E9, 9E9, 9E9, 9E9, 9E9]];
  VAR robtarget Straight_lines_0_2 := [[350, 80, 0], [0, 0, 1, 0], [0, 0, 0, 0], [9E9, 9E9, 9E9, 9E9, 9E9, 9E9]];
  VAR robtarget Straight_lines_0_3 := [[350, 26.67, 0], [0, 0, 1, 0], [0, 0, 0, 0], [9E9, 9E9, 9E9, 9E9, 9E9, 9E9]];
  VAR robtarget Straight_lines_0_4 := [[350, -26.67, 0], [0, 0, 1, 0], [0, 0, 0, 0], [9E9, 9E9, 9E9, 9E9, 9E9, 9E9]];
  VAR robtarget Straight_lines_0_5 := [[350, -80, 0], [0, 0, 1, 0], [0, 0, 0, 0], [9E9, 9E9, 9E9, 9E9, 9E9, 9E9]];
  VAR robtarget Straight_lines_1_0 := [[368, -26.67, 0], [0, 0, 1, 0], [0, 0, 0, 0], [9E9, 9E9, 9E9, 9E9, 9E9, 9E9]];
  VAR robtarget Straight_lines_1_1 := [[368, 26.67, 0], [0, 0, 1, 0], [0, 0, 0, 0], [9E9, 9E9, 9E9, 9E9, 9E9, 9E9]];
  VAR robtarget Straight_lines_1_2 := [[368, 80, 0], [0, 0, 1, 0], [0, 0, 0, 0], [9E9, 9E9, 9E9, 9E9, 9E9, 9E9]];
  VAR speeddata Arc_speed := [13, 500, 5000, 1000];
  VAR speeddata Straight_lines_speed := [13, 500, 5000, 1000];

  PROC main()
    MoveAbsJ Home, v150, z0, Makita\WObj:=Work_object;
    ConfL\off;
    ConfJ\on;
    MoveJ Start_point, v150, z0, Makita\WObj:=Work_object;
    MoveL Straight_lines_0_0, Straight_lines_speed, z0, Makita\WObj:=Work_object;
    MoveL Straight_lines_0_1, Straight_lines_speed, z0, Makita\WObj:=Work_object;
    MoveL Straight_lines_0_2, Straight_lines_speed, z0, Makita\WObj:=Work_object;
    MoveL Straight_lines_0_3, Straight_lines_speed, z0, Makita\WObj:=Work_object;
    MoveL Straight_lines_0_4, Straight_lines_speed, z0, Makita\WObj:=Work_object;
    MoveL Straight_lines_0_5, Straight_lines_speed, z0, Makita\WObj:=Work_object;
    MoveL Arcs_0, Arc_speed, z0, Makita\WObj:=Work_object;
    MoveL Arcs_1, Arc_speed, z0, Makita\WObj:=Work_object;
    MoveL Arcs_2, Arc_speed, z0, Makita\WObj:=Work_object;
    MoveL Arcs_3, Arc_speed, z0, Makita\WObj:=Work_object;
    MoveL Arcs_4, Arc_speed, z0, Makita\WObj:=Work_object;
    MoveL Arcs_5, Arc_speed, z0, Makita\WObj:=Work_object;
    MoveL Arcs_6, Arc_speed, z0, Makita\WObj:=Work_object;
    MoveL Arcs_7, Arc_speed, z0, Makita\WObj:=Work_object;
    MoveL Straight_lines_1_0, Straight_lines_speed, z0, Makita\WObj:=Work_object;
    MoveL Straight_lines_1_1, Straight_lines_speed, z0, Makita\WObj:=Work_object;
    MoveL Straight_lines_1_2, Straight_lines_speed, z0, Makita\WObj:=Work_object;
    MoveL Pos3_0, Straight_lines_speed, z0, Makita\WObj:=Work_object;
    MoveL Pos3_1, Straight_lines_speed, z0, Makita\WObj:=Work_object;
    MoveL Pos3_2, Straight_lines_speed, z0, Makita\WObj:=Work_object;
    MoveAbsJ Home, v150, z0, Makita\WObj:=Work_object;
  ENDPROC

ENDMODULE
```

H.3.2.4 -2 mm overlap

```
MODULE MainModule

  ! This RAPID code was generated with RobotComponents v2.2.2 (GPL v3)
  ! Visit www.github.com/RobotComponents for more information

  ! User defined tooldata
  PERS tooldata Makita := [TRUE, [[-160, 0, 492.4], [1, 0, 0, 0]], [0.001, [0, 0, 0.001], [1, 0, 0, 0], 0, 0, 0]];

  ! User defined wobjdata
  PERS wobjdata Work_object := [FALSE, TRUE, "", [[0, 0, 0], [1, 0, 0, 0]], [[0, 0, 32.58], [1, 0, 0, 0]]];

  ! Declarations generated by Robot Components
  VAR jointtarget Home := [[0, 0, 0, 0, 0, 0], [9E9, 9E9, 9E9, 9E9, 9E9, 9E9]];
  VAR robtarget Arcs_0 := [[350.61, -83.06, 0], [0, 0, 1, 0], [0, 0, 0, 0], [9E9, 9E9, 9E9, 9E9, 9E9, 9E9]];
  VAR robtarget Arcs_1 := [[352.34, -85.66, 0], [0, 0, 1, 0], [0, 0, 0, 0], [9E9, 9E9, 9E9, 9E9, 9E9, 9E9]];
  VAR robtarget Arcs_2 := [[354.94, -87.39, 0], [0, 0, 1, 0], [0, 0, 0, 0], [9E9, 9E9, 9E9, 9E9, 9E9, 9E9]];
  VAR robtarget Arcs_3 := [[358, -88, 0], [0, 0, 1, 0], [0, 0, 0, 0], [9E9, 9E9, 9E9, 9E9, 9E9, 9E9]];
  VAR robtarget Arcs_4 := [[361.06, -87.39, 0], [0, 0, 1, 0], [0, 0, 0, 0], [9E9, 9E9, 9E9, 9E9, 9E9, 9E9]];
  VAR robtarget Arcs_5 := [[363.66, -85.66, 0], [0, 0, 1, 0], [0, 0, 0, 0], [9E9, 9E9, 9E9, 9E9, 9E9, 9E9]];
  VAR robtarget Arcs_6 := [[365.39, -83.06, 0], [0, 0, 1, 0], [0, 0, 0, 0], [9E9, 9E9, 9E9, 9E9, 9E9, 9E9]];
  VAR robtarget Arcs_7 := [[366, -80, 0], [0, 0, 1, 0], [0, 0, 0, 0], [9E9, 9E9, 9E9, 9E9, 9E9, 9E9]];
  VAR robtarget Pos3_0 := [[366, 106.67, 0], [0, 0, 1, 0], [0, 0, 0, 0], [9E9, 9E9, 9E9, 9E9, 9E9, 9E9]];
  VAR robtarget Pos3_1 := [[366, 133.33, 0], [0, 0, 1, 0], [0, 0, 0, 0], [9E9, 9E9, 9E9, 9E9, 9E9, 9E9]];
  VAR robtarget Pos3_2 := [[366, 160, 0], [0, 0, 1, 0], [0, 0, 0, 0], [9E9, 9E9, 9E9, 9E9, 9E9, 9E9]];
```

```
  VAR robtarget Start_point := [[350, 160, 0], [0, 0, 1, 0], [0, 0, 0, 0], [9E9, 9E9, 9E9, 9E9, 9E9, 9E9]];
  VAR robtarget Straight_lines_0_0 := [[350, 133.33, 0], [0, 0, 1, 0], [0, 0, 0, 0], [9E9, 9E9, 9E9, 9E9, 9E9, 9E9]];
  VAR robtarget Straight_lines_0_1 := [[350, 106.67, 0], [0, 0, 1, 0], [0, 0, 0, 0], [9E9, 9E9, 9E9, 9E9, 9E9, 9E9]];
  VAR robtarget Straight_lines_0_2 := [[350, 80, 0], [0, 0, 1, 0], [0, 0, 0, 0], [9E9, 9E9, 9E9, 9E9, 9E9, 9E9]];
  VAR robtarget Straight_lines_0_3 := [[350, 26.67, 0], [0, 0, 1, 0], [0, 0, 0, 0], [9E9, 9E9, 9E9, 9E9, 9E9, 9E9]];
  VAR robtarget Straight_lines_0_4 := [[350, -26.67, 0], [0, 0, 1, 0], [0, 0, 0, 0], [9E9, 9E9, 9E9, 9E9, 9E9, 9E9]];
  VAR robtarget Straight_lines_0_5 := [[350, -80, 0], [0, 0, 1, 0], [0, 0, 0, 0], [9E9, 9E9, 9E9, 9E9, 9E9, 9E9]];
  VAR robtarget Straight_lines_1_0 := [[366, -26.67, 0], [0, 0, 1, 0], [0, 0, 0, 0], [9E9, 9E9, 9E9, 9E9, 9E9, 9E9]];
  VAR robtarget Straight_lines_1_1 := [[366, 26.67, 0], [0, 0, 1, 0], [0, 0, 0, 0], [9E9, 9E9, 9E9, 9E9, 9E9, 9E9]];
  VAR robtarget Straight_lines_1_2 := [[366, 80, 0], [0, 0, 1, 0], [0, 0, 0, 0], [9E9, 9E9, 9E9, 9E9, 9E9, 9E9]];
  VAR speeddata Arc_speed := [13, 500, 5000, 1000];
  VAR speeddata Straight_lines_speed := [13, 500, 5000, 1000];

  PROC main()
    MoveAbsJ Home, v150, z0, Makita\WObj:=Work_object;
    ConfL\off;
    ConfJ\on;
    MoveJ Start_point, v150, z0, Makita\WObj:=Work_object;
    MoveL Straight_lines_0_0, Straight_lines_speed, z0, Makita\WObj:=Work_object;
    MoveL Straight_lines_0_1, Straight_lines_speed, z0, Makita\WObj:=Work_object;
    MoveL Straight_lines_0_2, Straight_lines_speed, z0, Makita\WObj:=Work_object;
    MoveL Straight_lines_0_3, Straight_lines_speed, z0, Makita\WObj:=Work_object;
    MoveL Straight_lines_0_4, Straight_lines_speed, z0, Makita\WObj:=Work_object;
    MoveL Straight_lines_0_5, Straight_lines_speed, z0, Makita\WObj:=Work_object;
    MoveL Arcs_0, Arc_speed, z0, Makita\WObj:=Work_object;
    MoveL Arcs_1, Arc_speed, z0, Makita\WObj:=Work_object;
    MoveL Arcs_2, Arc_speed, z0, Makita\WObj:=Work_object;
    MoveL Arcs_3, Arc_speed, z0, Makita\WObj:=Work_object;
    MoveL Arcs_4, Arc_speed, z0, Makita\WObj:=Work_object;
    MoveL Arcs_5, Arc_speed, z0, Makita\WObj:=Work_object;
    MoveL Arcs_6, Arc_speed, z0, Makita\WObj:=Work_object;
    MoveL Arcs_7, Arc_speed, z0, Makita\WObj:=Work_object;
    MoveL Straight_lines_1_0, Straight_lines_speed, z0, Makita\WObj:=Work_object;
    MoveL Straight_lines_1_1, Straight_lines_speed, z0, Makita\WObj:=Work_object;
    MoveL Straight_lines_1_2, Straight_lines_speed, z0, Makita\WObj:=Work_object;
    MoveL Pos3_0, Straight_lines_speed, z0, Makita\WObj:=Work_object;
    MoveL Pos3_1, Straight_lines_speed, z0, Makita\WObj:=Work_object;
    MoveL Pos3_2, Straight_lines_speed, z0, Makita\WObj:=Work_object;
    MoveAbsJ Home, v150, z0, Makita\WObj:=Work_object;
  ENDPROC

ENDMODULE
```

H.3.3 Corner adhesion RAPID code

```
MODULE MainModule

  ! This RAPID code was generated with RobotComponents v2.2.2 (GPL v3)
  ! Visit www.github.com/RobotComponents for more information

  ! User defined tooldata
  PERS tooldata Makita := [TRUE, [[-160, 0, 492.4], [1, 0, 0, 0]], [0.001, [0, 0, 0.001], [1, 0, 0, 0], 0, 0, 0]];

  ! User defined wobjdata
  PERS wobjdata Work_object := [FALSE, TRUE, "", [[0, 0, 0], [1, 0, 0, 0]], [[0, 0, 32.58], [1, 0, 0, 0]]];

  ! Declarations generated by Robot Components
  VAR jointtarget Home := [[0, 0, 0, 0, 0, 0], [9E9, 9E9, 9E9, 9E9, 9E9, 9E9]];
  VAR robtarget Arcs_2_0_0 := [[351.14, -85.74, 0], [0, 0, 1, 0], [0, 0, 0, 0], [9E9, 9E9, 9E9, 9E9, 9E9, 9E9]];
  VAR robtarget Arcs_2_0_1 := [[354.39, -90.61, 0], [0, 0, 1, 0], [0, 0, 0, 0], [9E9, 9E9, 9E9, 9E9, 9E9, 9E9]];
  VAR robtarget Arcs_2_0_2 := [[359.26, -93.86, 0], [0, 0, 1, 0], [0, 0, 0, 0], [9E9, 9E9, 9E9, 9E9, 9E9, 9E9]];
  VAR robtarget Arcs_2_0_3 := [[365, -95, 0], [0, 0, 1, 0], [0, 0, 0, 0], [9E9, 9E9, 9E9, 9E9, 9E9, 9E9]];
  VAR robtarget Arcs_2_0_4 := [[370.74, -93.86, 0], [0, 0, 1, 0], [0, 0, 0, 0], [9E9, 9E9, 9E9, 9E9, 9E9, 9E9]];
  VAR robtarget Arcs_2_0_5 := [[375.61, -90.61, 0], [0, 0, 1, 0], [0, 0, 0, 0], [9E9, 9E9, 9E9, 9E9, 9E9, 9E9]];
  VAR robtarget Arcs_2_0_6 := [[378.86, -85.74, 0], [0, 0, 1, 0], [0, 0, 0, 0], [9E9, 9E9, 9E9, 9E9, 9E9, 9E9]];
  VAR robtarget Arcs_2_0_7 := [[380, -80, 0], [0, 0, 1, 0], [0, 0, 0, 0], [9E9, 9E9, 9E9, 9E9, 9E9, 9E9]];
  VAR robtarget Arcs_2_1_0 := [[381.14, 85.74, 0], [0, 0, 1, 0], [0, 0, 0, 0], [9E9, 9E9, 9E9, 9E9, 9E9, 9E9]];
  VAR robtarget Arcs_2_1_1 := [[384.39, 90.61, 0], [0, 0, 1, 0], [0, 0, 0, 0], [9E9, 9E9, 9E9, 9E9, 9E9, 9E9]];
  VAR robtarget Arcs_2_1_2 := [[389.26, 93.86, 0], [0, 0, 1, 0], [0, 0, 0, 0], [9E9, 9E9, 9E9, 9E9, 9E9, 9E9]];
  VAR robtarget Arcs_2_1_3 := [[395, 95, 0], [0, 0, 1, 0], [0, 0, 0, 0], [9E9, 9E9, 9E9, 9E9, 9E9, 9E9]];
  VAR robtarget Arcs_2_1_4 := [[400.74, 93.86, 0], [0, 0, 1, 0], [0, 0, 0, 0], [9E9, 9E9, 9E9, 9E9, 9E9, 9E9]];
```

```
VAR robtarget Arcs_2_1_5 := [[405.61, 90.61, 0], [0, 0, 1, 0], [0, 0, 0, 0], [9E9, 9E9, 9E9, 9E9, 9E9, 9E9]];
VAR robtarget Arcs_2_1_6 := [[408.86, 85.74, 0], [0, 0, 1, 0], [0, 0, 0, 0], [9E9, 9E9, 9E9, 9E9, 9E9, 9E9]];
VAR robtarget Arcs_2_1_7 := [[410, 80, 0], [0, 0, 1, 0], [0, 0, 0, 0], [9E9, 9E9, 9E9, 9E9, 9E9, 9E9]];
VAR robtarget Arcs_2_2_0 := [[411.14, -85.74, 0], [0, 0, 1, 0], [0, 0, 0, 0], [9E9, 9E9, 9E9, 9E9, 9E9, 9E9]];
VAR robtarget Arcs_2_2_1 := [[414.39, -90.61, 0], [0, 0, 1, 0], [0, 0, 0, 0], [9E9, 9E9, 9E9, 9E9, 9E9, 9E9]];
VAR robtarget Arcs_2_2_2 := [[419.26, -93.86, 0], [0, 0, 1, 0], [0, 0, 0, 0], [9E9, 9E9, 9E9, 9E9, 9E9, 9E9]];
VAR robtarget Arcs_2_2_3 := [[425, -95, 0], [0, 0, 1, 0], [0, 0, 0, 0], [9E9, 9E9, 9E9, 9E9, 9E9, 9E9]];
VAR robtarget Arcs_2_2_4 := [[430.74, -93.86, 0], [0, 0, 1, 0], [0, 0, 0, 0], [9E9, 9E9, 9E9, 9E9, 9E9, 9E9]];
VAR robtarget Arcs_2_2_5 := [[435.61, -90.61, 0], [0, 0, 1, 0], [0, 0, 0, 0], [9E9, 9E9, 9E9, 9E9, 9E9, 9E9]];
VAR robtarget Arcs_2_2_6 := [[438.86, -85.74, 0], [0, 0, 1, 0], [0, 0, 0, 0], [9E9, 9E9, 9E9, 9E9, 9E9, 9E9]];
VAR robtarget Arcs_2_2_7 := [[440, -80, 0], [0, 0, 1, 0], [0, 0, 0, 0], [9E9, 9E9, 9E9, 9E9, 9E9, 9E9]];
VAR robtarget Arcs_2_3_0 := [[441.14, 85.74, 0], [0, 0, 1, 0], [0, 0, 0, 0], [9E9, 9E9, 9E9, 9E9, 9E9, 9E9]];
VAR robtarget Arcs_2_3_1 := [[444.39, 90.61, 0], [0, 0, 1, 0], [0, 0, 0, 0], [9E9, 9E9, 9E9, 9E9, 9E9, 9E9]];
VAR robtarget Arcs_2_3_2 := [[449.26, 93.86, 0], [0, 0, 1, 0], [0, 0, 0, 0], [9E9, 9E9, 9E9, 9E9, 9E9, 9E9]];
VAR robtarget Arcs_2_3_3 := [[455, 95, 0], [0, 0, 1, 0], [0, 0, 0, 0], [9E9, 9E9, 9E9, 9E9, 9E9, 9E9]];
VAR robtarget Arcs_2_3_4 := [[460.74, 93.86, 0], [0, 0, 1, 0], [0, 0, 0, 0], [9E9, 9E9, 9E9, 9E9, 9E9, 9E9]];
VAR robtarget Arcs_2_3_5 := [[465.61, 90.61, 0], [0, 0, 1, 0], [0, 0, 0, 0], [9E9, 9E9, 9E9, 9E9, 9E9, 9E9]];
VAR robtarget Arcs_2_3_6 := [[468.86, 85.74, 0], [0, 0, 1, 0], [0, 0, 0, 0], [9E9, 9E9, 9E9, 9E9, 9E9, 9E9]];
VAR robtarget Arcs_2_3_7 := [[470, 80, 0], [0, 0, 1, 0], [0, 0, 0, 0], [9E9, 9E9, 9E9, 9E9, 9E9, 9E9]];
VAR robtarget Arcs_2_4_0 := [[471.14, -85.74, 0], [0, 0, 1, 0], [0, 0, 0, 0], [9E9, 9E9, 9E9, 9E9, 9E9, 9E9]];
VAR robtarget Arcs_2_4_1 := [[474.39, -90.61, 0], [0, 0, 1, 0], [0, 0, 0, 0], [9E9, 9E9, 9E9, 9E9, 9E9, 9E9]];
VAR robtarget Arcs_2_4_2 := [[479.26, -93.86, 0], [0, 0, 1, 0], [0, 0, 0, 0], [9E9, 9E9, 9E9, 9E9, 9E9, 9E9]];
VAR robtarget Arcs_2_4_3 := [[485, -95, 0], [0, 0, 1, 0], [0, 0, 0, 0], [9E9, 9E9, 9E9, 9E9, 9E9, 9E9]];
VAR robtarget Arcs_2_4_4 := [[490.74, -93.86, 0], [0, 0, 1, 0], [0, 0, 0, 0], [9E9, 9E9, 9E9, 9E9, 9E9, 9E9]];
VAR robtarget Arcs_2_4_5 := [[495.61, -90.61, 0], [0, 0, 1, 0], [0, 0, 0, 0], [9E9, 9E9, 9E9, 9E9, 9E9, 9E9]];
VAR robtarget Arcs_2_4_6 := [[498.86, -85.74, 0], [0, 0, 1, 0], [0, 0, 0, 0], [9E9, 9E9, 9E9, 9E9, 9E9, 9E9]];
VAR robtarget Arcs_2_4_7 := [[500, -80, 0], [0, 0, 1, 0], [0, 0, 0, 0], [9E9, 9E9, 9E9, 9E9, 9E9, 9E9]];
VAR robtarget Arcs_2_5_0 := [[501.14, 85.74, 0], [0, 0, 1, 0], [0, 0, 0, 0], [9E9, 9E9, 9E9, 9E9, 9E9, 9E9]];
VAR robtarget Arcs_2_5_1 := [[504.39, 90.61, 0], [0, 0, 1, 0], [0, 0, 0, 0], [9E9, 9E9, 9E9, 9E9, 9E9, 9E9]];
VAR robtarget Arcs_2_5_2 := [[509.26, 93.86, 0], [0, 0, 1, 0], [0, 0, 0, 0], [9E9, 9E9, 9E9, 9E9, 9E9, 9E9]];
VAR robtarget Arcs_2_5_3 := [[515, 95, 0], [0, 0, 1, 0], [0, 0, 0, 0], [9E9, 9E9, 9E9, 9E9, 9E9, 9E9]];
VAR robtarget Arcs_2_5_4 := [[520.74, 93.86, 0], [0, 0, 1, 0], [0, 0, 0, 0], [9E9, 9E9, 9E9, 9E9, 9E9, 9E9]];
VAR robtarget Arcs_2_5_5 := [[525.61, 90.61, 0], [0, 0, 1, 0], [0, 0, 0, 0], [9E9, 9E9, 9E9, 9E9, 9E9, 9E9]];
VAR robtarget Arcs_2_5_6 := [[528.86, 85.74, 0], [0, 0, 1, 0], [0, 0, 0, 0], [9E9, 9E9, 9E9, 9E9, 9E9, 9E9]];
VAR robtarget Arcs_2_5_7 := [[530, 80, 0], [0, 0, 1, 0], [0, 0, 0, 0], [9E9, 9E9, 9E9, 9E9, 9E9, 9E9]];
VAR robtarget Pos3_2_0 := [[528.94, -88.02, 0], [0, 0, 1, 0], [0, 0, 0, 0], [9E9, 9E9, 9E9, 9E9, 9E9, 9E9]];
VAR robtarget Pos3_2_1 := [[525.85, -95.5, 0], [0, 0, 1, 0], [0, 0, 0, 0], [9E9, 9E9, 9E9, 9E9, 9E9, 9E9]];
VAR robtarget Pos3_2_10 := [[270, -111, 0], [0, 0, 1, 0], [0, 0, 0, 0], [9E9, 9E9, 9E9, 9E9, 9E9, 9E9]];
VAR robtarget Pos3_2_2 := [[520.92, -101.92, 0], [0, 0, 1, 0], [0, 0, 0, 0], [9E9, 9E9, 9E9, 9E9, 9E9, 9E9]];
VAR robtarget Pos3_2_3 := [[514.5, -106.85, 0], [0, 0, 1, 0], [0, 0, 0, 0], [9E9, 9E9, 9E9, 9E9, 9E9, 9E9]];
VAR robtarget Pos3_2_4 := [[507.02, -109.94, 0], [0, 0, 1, 0], [0, 0, 0, 0], [9E9, 9E9, 9E9, 9E9, 9E9, 9E9]];
VAR robtarget Pos3_2_5 := [[499, -111, 0], [0, 0, 1, 0], [0, 0, 0, 0], [9E9, 9E9, 9E9, 9E9, 9E9, 9E9]];
VAR robtarget Pos3_2_6 := [[453.2, -111, 0], [0, 0, 1, 0], [0, 0, 0, 0], [9E9, 9E9, 9E9, 9E9, 9E9, 9E9]];
VAR robtarget Pos3_2_7 := [[407.4, -111, 0], [0, 0, 1, 0], [0, 0, 0, 0], [9E9, 9E9, 9E9, 9E9, 9E9, 9E9]];
VAR robtarget Pos3_2_8 := [[361.6, -111, 0], [0, 0, 1, 0], [0, 0, 0, 0], [9E9, 9E9, 9E9, 9E9, 9E9, 9E9]];
VAR robtarget Pos3_2_9 := [[315.8, -111, 0], [0, 0, 1, 0], [0, 0, 0, 0], [9E9, 9E9, 9E9, 9E9, 9E9, 9E9]];
VAR robtarget Start_point_2 := [[610, 111, 0], [0, 0, 1, 0], [0, 0, 0, 0], [9E9, 9E9, 9E9, 9E9, 9E9, 9E9]];
VAR robtarget Straight_lines_2_0_0 := [[571.83, 111, 0], [0, 0, 1, 0], [0, 0, 0, 0], [9E9, 9E9, 9E9, 9E9, 9E9, 9E9]];
VAR robtarget Straight_lines_2_0_1 := [[533.67, 111, 0], [0, 0, 1, 0], [0, 0, 0, 0], [9E9, 9E9, 9E9, 9E9, 9E9, 9E9]];
VAR robtarget Straight_lines_2_0_10 := [[351.06, 88.02, 0], [0, 0, 1, 0], [0, 0, 0, 0], [9E9, 9E9, 9E9, 9E9, 9E9, 9E9]];
VAR robtarget Straight_lines_2_0_11 := [[350, 80, 0], [0, 0, 1, 0], [0, 0, 0, 0], [9E9, 9E9, 9E9, 9E9, 9E9, 9E9]];
VAR robtarget Straight_lines_2_0_12 := [[350, 48, 0], [0, 0, 1, 0], [0, 0, 0, 0], [9E9, 9E9, 9E9, 9E9, 9E9, 9E9]];
VAR robtarget Straight_lines_2_0_13 := [[350, 16, 0], [0, 0, 1, 0], [0, 0, 0, 0], [9E9, 9E9, 9E9, 9E9, 9E9, 9E9]];
VAR robtarget Straight_lines_2_0_14 := [[350, -16, 0], [0, 0, 1, 0], [0, 0, 0, 0], [9E9, 9E9, 9E9, 9E9, 9E9, 9E9]];
VAR robtarget Straight_lines_2_0_15 := [[350, -48, 0], [0, 0, 1, 0], [0, 0, 0, 0], [9E9, 9E9, 9E9, 9E9, 9E9, 9E9]];
VAR robtarget Straight_lines_2_0_16 := [[350, -80, 0], [0, 0, 1, 0], [0, 0, 0, 0], [9E9, 9E9, 9E9, 9E9, 9E9, 9E9]];
VAR robtarget Straight_lines_2_0_2 := [[495.5, 111, 0], [0, 0, 1, 0], [0, 0, 0, 0], [9E9, 9E9, 9E9, 9E9, 9E9, 9E9]];
VAR robtarget Straight_lines_2_0_3 := [[457.33, 111, 0], [0, 0, 1, 0], [0, 0, 0, 0], [9E9, 9E9, 9E9, 9E9, 9E9, 9E9]];
VAR robtarget Straight_lines_2_0_4 := [[419.17, 111, 0], [0, 0, 1, 0], [0, 0, 0, 0], [9E9, 9E9, 9E9, 9E9, 9E9, 9E9]];
VAR robtarget Straight_lines_2_0_5 := [[381, 111, 0], [0, 0, 1, 0], [0, 0, 0, 0], [9E9, 9E9, 9E9, 9E9, 9E9, 9E9]];
VAR robtarget Straight_lines_2_0_6 := [[372.98, 109.94, 0], [0, 0, 1, 0], [0, 0, 0, 0], [9E9, 9E9, 9E9, 9E9, 9E9, 9E9]];
VAR robtarget Straight_lines_2_0_7 := [[365.5, 106.85, 0], [0, 0, 1, 0], [0, 0, 0, 0], [9E9, 9E9, 9E9, 9E9, 9E9, 9E9]];
VAR robtarget Straight_lines_2_0_8 := [[359.08, 101.92, 0], [0, 0, 1, 0], [0, 0, 0, 0], [9E9, 9E9, 9E9, 9E9, 9E9, 9E9]];
VAR robtarget Straight_lines_2_0_9 := [[354.15, 95.5, 0], [0, 0, 1, 0], [0, 0, 0, 0], [9E9, 9E9, 9E9, 9E9, 9E9, 9E9]];
VAR robtarget Straight_lines_2_1_0 := [[380, -48, 0], [0, 0, 1, 0], [0, 0, 0, 0], [9E9, 9E9, 9E9, 9E9, 9E9, 9E9]];
VAR robtarget Straight_lines_2_1_1 := [[380, -16, 0], [0, 0, 1, 0], [0, 0, 0, 0], [9E9, 9E9, 9E9, 9E9, 9E9, 9E9]];
VAR robtarget Straight_lines_2_1_2 := [[380, 16, 0], [0, 0, 1, 0], [0, 0, 0, 0], [9E9, 9E9, 9E9, 9E9, 9E9, 9E9]];
VAR robtarget Straight_lines_2_1_3 := [[380, 48, 0], [0, 0, 1, 0], [0, 0, 0, 0], [9E9, 9E9, 9E9, 9E9, 9E9, 9E9]];
VAR robtarget Straight_lines_2_1_4 := [[380, 80, 0], [0, 0, 1, 0], [0, 0, 0, 0], [9E9, 9E9, 9E9, 9E9, 9E9, 9E9]];
VAR robtarget Straight_lines_2_2_0 := [[410, 48, 0], [0, 0, 1, 0], [0, 0, 0, 0], [9E9, 9E9, 9E9, 9E9, 9E9, 9E9]];
VAR robtarget Straight_lines_2_2_1 := [[410, 16, 0], [0, 0, 1, 0], [0, 0, 0, 0], [9E9, 9E9, 9E9, 9E9, 9E9, 9E9]];
```

```
VAR robtarget Straight_lines_2_2_2 := [[410, -16, 0], [0, 0, 1, 0], [0, 0, 0, 0], [9E9, 9E9, 9E9, 9E9, 9E9, 9E9]];
VAR robtarget Straight_lines_2_2_3 := [[410, -48, 0], [0, 0, 1, 0], [0, 0, 0, 0], [9E9, 9E9, 9E9, 9E9, 9E9, 9E9]];
VAR robtarget Straight_lines_2_2_4 := [[410, -80, 0], [0, 0, 1, 0], [0, 0, 0, 0], [9E9, 9E9, 9E9, 9E9, 9E9, 9E9]];
VAR robtarget Straight_lines_2_3_0 := [[440, -48, 0], [0, 0, 1, 0], [0, 0, 0, 0], [9E9, 9E9, 9E9, 9E9, 9E9, 9E9]];
VAR robtarget Straight_lines_2_3_1 := [[440, -16, 0], [0, 0, 1, 0], [0, 0, 0, 0], [9E9, 9E9, 9E9, 9E9, 9E9, 9E9]];
VAR robtarget Straight_lines_2_3_2 := [[440, 16, 0], [0, 0, 1, 0], [0, 0, 0, 0], [9E9, 9E9, 9E9, 9E9, 9E9, 9E9]];
VAR robtarget Straight_lines_2_3_3 := [[440, 48, 0], [0, 0, 1, 0], [0, 0, 0, 0], [9E9, 9E9, 9E9, 9E9, 9E9, 9E9]];
VAR robtarget Straight_lines_2_3_4 := [[440, 80, 0], [0, 0, 1, 0], [0, 0, 0, 0], [9E9, 9E9, 9E9, 9E9, 9E9, 9E9]];
VAR robtarget Straight_lines_2_4_0 := [[470, 48, 0], [0, 0, 1, 0], [0, 0, 0, 0], [9E9, 9E9, 9E9, 9E9, 9E9, 9E9]];
VAR robtarget Straight_lines_2_4_1 := [[470, 16, 0], [0, 0, 1, 0], [0, 0, 0, 0], [9E9, 9E9, 9E9, 9E9, 9E9, 9E9]];
VAR robtarget Straight_lines_2_4_2 := [[470, -16, 0], [0, 0, 1, 0], [0, 0, 0, 0], [9E9, 9E9, 9E9, 9E9, 9E9, 9E9]];
VAR robtarget Straight_lines_2_4_3 := [[470, -48, 0], [0, 0, 1, 0], [0, 0, 0, 0], [9E9, 9E9, 9E9, 9E9, 9E9, 9E9]];
VAR robtarget Straight_lines_2_4_4 := [[470, -80, 0], [0, 0, 1, 0], [0, 0, 0, 0], [9E9, 9E9, 9E9, 9E9, 9E9, 9E9]];
VAR robtarget Straight_lines_2_5_0 := [[500, -48, 0], [0, 0, 1, 0], [0, 0, 0, 0], [9E9, 9E9, 9E9, 9E9, 9E9, 9E9]];
VAR robtarget Straight_lines_2_5_1 := [[500, -16, 0], [0, 0, 1, 0], [0, 0, 0, 0], [9E9, 9E9, 9E9, 9E9, 9E9, 9E9]];
VAR robtarget Straight_lines_2_5_2 := [[500, 16, 0], [0, 0, 1, 0], [0, 0, 0, 0], [9E9, 9E9, 9E9, 9E9, 9E9, 9E9]];
VAR robtarget Straight_lines_2_5_3 := [[500, 48, 0], [0, 0, 1, 0], [0, 0, 0, 0], [9E9, 9E9, 9E9, 9E9, 9E9, 9E9]];
VAR robtarget Straight_lines_2_5_4 := [[500, 80, 0], [0, 0, 1, 0], [0, 0, 0, 0], [9E9, 9E9, 9E9, 9E9, 9E9, 9E9]];
VAR robtarget Straight_lines_2_6_0 := [[530, 48, 0], [0, 0, 1, 0], [0, 0, 0, 0], [9E9, 9E9, 9E9, 9E9, 9E9, 9E9]];
VAR robtarget Straight_lines_2_6_1 := [[530, 16, 0], [0, 0, 1, 0], [0, 0, 0, 0], [9E9, 9E9, 9E9, 9E9, 9E9, 9E9]];
VAR robtarget Straight_lines_2_6_2 := [[530, -16, 0], [0, 0, 1, 0], [0, 0, 0, 0], [9E9, 9E9, 9E9, 9E9, 9E9, 9E9]];
VAR robtarget Straight_lines_2_6_3 := [[530, -48, 0], [0, 0, 1, 0], [0, 0, 0, 0], [9E9, 9E9, 9E9, 9E9, 9E9, 9E9]];
VAR robtarget Straight_lines_2_6_4 := [[530, -80, 0], [0, 0, 1, 0], [0, 0, 0, 0], [9E9, 9E9, 9E9, 9E9, 9E9, 9E9]];
VAR speeddata Arc_speed := [13, 500, 5000, 1000];
VAR speeddata Straight_lines_speed := [13, 500, 5000, 1000];

PROC main()
  MoveAbsJ Home, v150, z0, Makita\WObj:=Work_object;
  ConfL\off;
  ConfJ\on;
  MoveJ Start_point_2, v150, z0, Makita\WObj:=Work_object;
  MoveL Straight_lines_2_0_0, Straight_lines_speed, z0, Makita\WObj:=Work_object;
  MoveL Straight_lines_2_0_1, Straight_lines_speed, z0, Makita\WObj:=Work_object;
  MoveL Straight_lines_2_0_2, Straight_lines_speed, z0, Makita\WObj:=Work_object;
  MoveL Straight_lines_2_0_3, Straight_lines_speed, z0, Makita\WObj:=Work_object;
  MoveL Straight_lines_2_0_4, Straight_lines_speed, z0, Makita\WObj:=Work_object;
  MoveL Straight_lines_2_0_5, Straight_lines_speed, z0, Makita\WObj:=Work_object;
  MoveL Straight_lines_2_0_6, Straight_lines_speed, z0, Makita\WObj:=Work_object;
  MoveL Straight_lines_2_0_7, Straight_lines_speed, z0, Makita\WObj:=Work_object;
  MoveL Straight_lines_2_0_8, Straight_lines_speed, z0, Makita\WObj:=Work_object;
  MoveL Straight_lines_2_0_9, Straight_lines_speed, z0, Makita\WObj:=Work_object;
  MoveL Straight_lines_2_0_10, Straight_lines_speed, z0, Makita\WObj:=Work_object;
  MoveL Straight_lines_2_0_11, Straight_lines_speed, z0, Makita\WObj:=Work_object;
  MoveL Straight_lines_2_0_12, Straight_lines_speed, z0, Makita\WObj:=Work_object;
  MoveL Straight_lines_2_0_13, Straight_lines_speed, z0, Makita\WObj:=Work_object;
  MoveL Straight_lines_2_0_14, Straight_lines_speed, z0, Makita\WObj:=Work_object;
  MoveL Straight_lines_2_0_15, Straight_lines_speed, z0, Makita\WObj:=Work_object;
  MoveL Straight_lines_2_0_16, Straight_lines_speed, z0, Makita\WObj:=Work_object;
  MoveL Arcs_2_0_0, Arc_speed, z0, Makita\WObj:=Work_object;
  MoveL Arcs_2_0_1, Arc_speed, z0, Makita\WObj:=Work_object;
  MoveL Arcs_2_0_2, Arc_speed, z0, Makita\WObj:=Work_object;
  MoveL Arcs_2_0_3, Arc_speed, z0, Makita\WObj:=Work_object;
  MoveL Arcs_2_0_4, Arc_speed, z0, Makita\WObj:=Work_object;
  MoveL Arcs_2_0_5, Arc_speed, z0, Makita\WObj:=Work_object;
  MoveL Arcs_2_0_6, Arc_speed, z0, Makita\WObj:=Work_object;
  MoveL Arcs_2_0_7, Arc_speed, z0, Makita\WObj:=Work_object;
  MoveL Straight_lines_2_1_0, Straight_lines_speed, z0, Makita\WObj:=Work_object;
  MoveL Straight_lines_2_1_1, Straight_lines_speed, z0, Makita\WObj:=Work_object;
  MoveL Straight_lines_2_1_2, Straight_lines_speed, z0, Makita\WObj:=Work_object;
  MoveL Straight_lines_2_1_3, Straight_lines_speed, z0, Makita\WObj:=Work_object;
  MoveL Straight_lines_2_1_4, Straight_lines_speed, z0, Makita\WObj:=Work_object;
  MoveL Arcs_2_1_0, Arc_speed, z0, Makita\WObj:=Work_object;
  MoveL Arcs_2_1_1, Arc_speed, z0, Makita\WObj:=Work_object;
  MoveL Arcs_2_1_2, Arc_speed, z0, Makita\WObj:=Work_object;
  MoveL Arcs_2_1_3, Arc_speed, z0, Makita\WObj:=Work_object;
  MoveL Arcs_2_1_4, Arc_speed, z0, Makita\WObj:=Work_object;
  MoveL Arcs_2_1_5, Arc_speed, z0, Makita\WObj:=Work_object;
  MoveL Arcs_2_1_6, Arc_speed, z0, Makita\WObj:=Work_object;
  MoveL Arcs_2_1_7, Arc_speed, z0, Makita\WObj:=Work_object;
  MoveL Straight_lines_2_2_0, Straight_lines_speed, z0, Makita\WObj:=Work_object;
  MoveL Straight_lines_2_2_1, Straight_lines_speed, z0, Makita\WObj:=Work_object;
```

```
    MoveL Straight_lines_2_2_2, Straight_lines_speed, z0, Makita\WObj:=Work_object;
    MoveL Straight_lines_2_2_3, Straight_lines_speed, z0, Makita\WObj:=Work_object;
    MoveL Straight_lines_2_2_4, Straight_lines_speed, z0, Makita\WObj:=Work_object;
    MoveL Arcs_2_2_0, Arc_speed, z0, Makita\WObj:=Work_object;
    MoveL Arcs_2_2_1, Arc_speed, z0, Makita\WObj:=Work_object;
    MoveL Arcs_2_2_2, Arc_speed, z0, Makita\WObj:=Work_object;
    MoveL Arcs_2_2_3, Arc_speed, z0, Makita\WObj:=Work_object;
    MoveL Arcs_2_2_4, Arc_speed, z0, Makita\WObj:=Work_object;
    MoveL Arcs_2_2_5, Arc_speed, z0, Makita\WObj:=Work_object;
    MoveL Arcs_2_2_6, Arc_speed, z0, Makita\WObj:=Work_object;
    MoveL Arcs_2_2_7, Arc_speed, z0, Makita\WObj:=Work_object;
    MoveL Straight_lines_2_3_0, Straight_lines_speed, z0, Makita\WObj:=Work_object;
    MoveL Straight_lines_2_3_1, Straight_lines_speed, z0, Makita\WObj:=Work_object;
    MoveL Straight_lines_2_3_2, Straight_lines_speed, z0, Makita\WObj:=Work_object;
    MoveL Straight_lines_2_3_3, Straight_lines_speed, z0, Makita\WObj:=Work_object;
    MoveL Straight_lines_2_3_4, Straight_lines_speed, z0, Makita\WObj:=Work_object;
    MoveL Arcs_2_3_0, Arc_speed, z0, Makita\WObj:=Work_object;
    MoveL Arcs_2_3_1, Arc_speed, z0, Makita\WObj:=Work_object;
    MoveL Arcs_2_3_2, Arc_speed, z0, Makita\WObj:=Work_object;
    MoveL Arcs_2_3_3, Arc_speed, z0, Makita\WObj:=Work_object;
    MoveL Arcs_2_3_4, Arc_speed, z0, Makita\WObj:=Work_object;
    MoveL Arcs_2_3_5, Arc_speed, z0, Makita\WObj:=Work_object;
    MoveL Arcs_2_3_6, Arc_speed, z0, Makita\WObj:=Work_object;
    MoveL Arcs_2_3_7, Arc_speed, z0, Makita\WObj:=Work_object;
    MoveL Straight_lines_2_4_0, Straight_lines_speed, z0, Makita\WObj:=Work_object;
    MoveL Straight_lines_2_4_1, Straight_lines_speed, z0, Makita\WObj:=Work_object;
    MoveL Straight_lines_2_4_2, Straight_lines_speed, z0, Makita\WObj:=Work_object;
    MoveL Straight_lines_2_4_3, Straight_lines_speed, z0, Makita\WObj:=Work_object;
    MoveL Straight_lines_2_4_4, Straight_lines_speed, z0, Makita\WObj:=Work_object;
    MoveL Arcs_2_4_0, Arc_speed, z0, Makita\WObj:=Work_object;
    MoveL Arcs_2_4_1, Arc_speed, z0, Makita\WObj:=Work_object;
    MoveL Arcs_2_4_2, Arc_speed, z0, Makita\WObj:=Work_object;
    MoveL Arcs_2_4_3, Arc_speed, z0, Makita\WObj:=Work_object;
    MoveL Arcs_2_4_4, Arc_speed, z0, Makita\WObj:=Work_object;
    MoveL Arcs_2_4_5, Arc_speed, z0, Makita\WObj:=Work_object;
    MoveL Arcs_2_4_6, Arc_speed, z0, Makita\WObj:=Work_object;
    MoveL Arcs_2_4_7, Arc_speed, z0, Makita\WObj:=Work_object;
    MoveL Straight_lines_2_5_0, Straight_lines_speed, z0, Makita\WObj:=Work_object;
    MoveL Straight_lines_2_5_1, Straight_lines_speed, z0, Makita\WObj:=Work_object;
    MoveL Straight_lines_2_5_2, Straight_lines_speed, z0, Makita\WObj:=Work_object;
    MoveL Straight_lines_2_5_3, Straight_lines_speed, z0, Makita\WObj:=Work_object;
    MoveL Straight_lines_2_5_4, Straight_lines_speed, z0, Makita\WObj:=Work_object;
    MoveL Arcs_2_5_0, Arc_speed, z0, Makita\WObj:=Work_object;
    MoveL Arcs_2_5_1, Arc_speed, z0, Makita\WObj:=Work_object;
    MoveL Arcs_2_5_2, Arc_speed, z0, Makita\WObj:=Work_object;
    MoveL Arcs_2_5_3, Arc_speed, z0, Makita\WObj:=Work_object;
    MoveL Arcs_2_5_4, Arc_speed, z0, Makita\WObj:=Work_object;
    MoveL Arcs_2_5_5, Arc_speed, z0, Makita\WObj:=Work_object;
    MoveL Arcs_2_5_6, Arc_speed, z0, Makita\WObj:=Work_object;
    MoveL Arcs_2_5_7, Arc_speed, z0, Makita\WObj:=Work_object;
    MoveL Straight_lines_2_6_0, Straight_lines_speed, z0, Makita\WObj:=Work_object;
    MoveL Straight_lines_2_6_1, Straight_lines_speed, z0, Makita\WObj:=Work_object;
    MoveL Straight_lines_2_6_2, Straight_lines_speed, z0, Makita\WObj:=Work_object;
    MoveL Straight_lines_2_6_3, Straight_lines_speed, z0, Makita\WObj:=Work_object;
    MoveL Straight_lines_2_6_4, Straight_lines_speed, z0, Makita\WObj:=Work_object;
    MoveL Pos3_2_0, Straight_lines_speed, z0, Makita\WObj:=Work_object;
    MoveL Pos3_2_1, Straight_lines_speed, z0, Makita\WObj:=Work_object;
    MoveL Pos3_2_2, Straight_lines_speed, z0, Makita\WObj:=Work_object;
    MoveL Pos3_2_3, Straight_lines_speed, z0, Makita\WObj:=Work_object;
    MoveL Pos3_2_4, Straight_lines_speed, z0, Makita\WObj:=Work_object;
    MoveL Pos3_2_5, Straight_lines_speed, z0, Makita\WObj:=Work_object;
    MoveL Pos3_2_6, Straight_lines_speed, z0, Makita\WObj:=Work_object;
    MoveL Pos3_2_7, Straight_lines_speed, z0, Makita\WObj:=Work_object;
    MoveL Pos3_2_8, Straight_lines_speed, z0, Makita\WObj:=Work_object;
    MoveL Pos3_2_9, Straight_lines_speed, z0, Makita\WObj:=Work_object;
    MoveL Pos3_2_10, Straight_lines_speed, z0, Makita\WObj:=Work_object;
    MoveAbsJ Home, v150, z0, Makita\WObj:=Work_object;
  ENDPROC

ENDMODULE
```

Appendix I – Script new shape

Bio-based 3D printing and testing of a digitally designed structural element



F.E. Pels Rijcken

Eindhoven, 19-06-2025

Script new shape

Figure I1 shows a screenshot of the script, of the new shape, in grasshopper. Each number indicated a part of the script:

1. The parameters that can be changed (see Figure I2 for a more detailed screenshot).
2. The part of the script where the main geometry is made (see Figure I3 for an example of the main geometry).
3. The part of the script where the main geometry converted to a print path (see Figure I4 for an example of such a print path).
4. The part of the script where the optimization takes place (see Figure I5 for a more detailed screenshot)
5. The part of the script where the nozzle on the Makita is created.
6. The part of the script where the robot-setup is created.
7. The part of the script where the points for the targets are created.
8. The part of the script where the robot speed and configuration can be changed.
9. The part of the script where the robot targets that are all pointing towards the robot origin are finalized (see Figure I6 for an example).
10. The part of the script where the robot targets that are all configured to the global coordinate system are finalized (see Figure I7 for an example).
11. The part of the script where the print path and rapid code are generated.

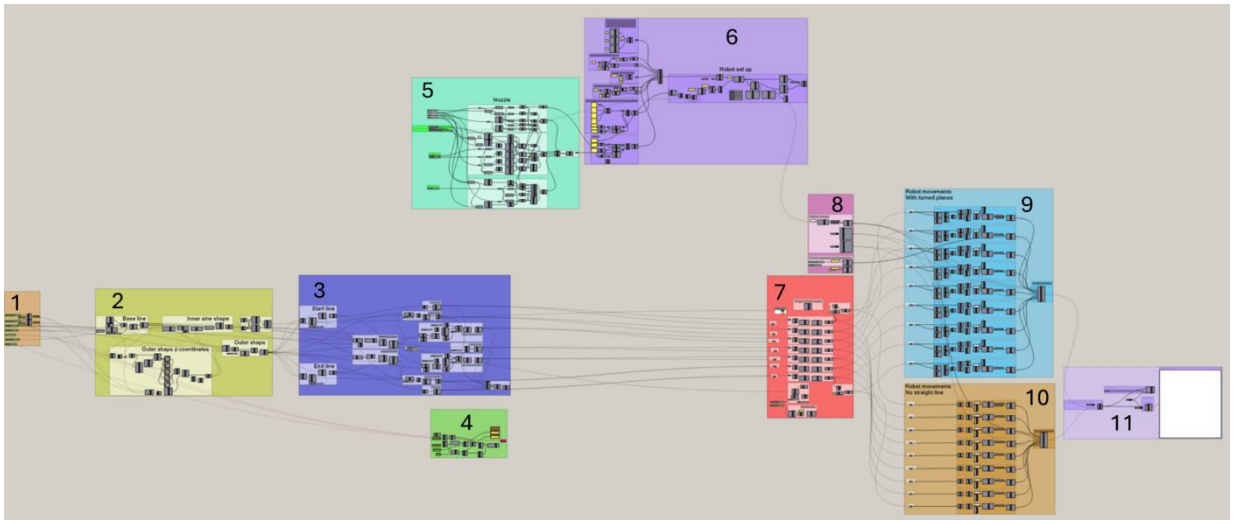


Figure I1. Screenshot of the full script of the new shape in grasshopper.

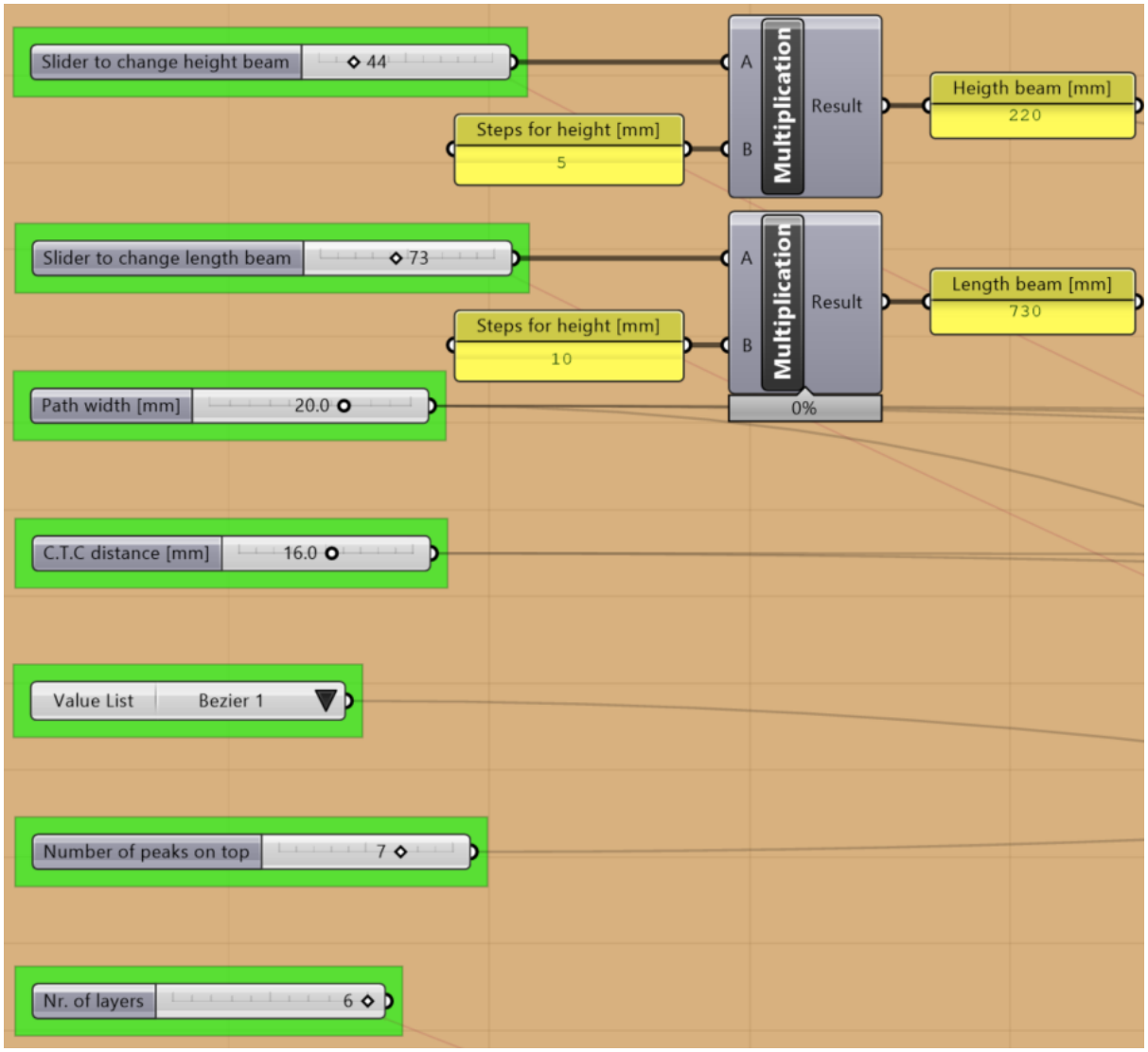


Figure I2. A screenshot of the changeable parameters of the script in grasshopper.

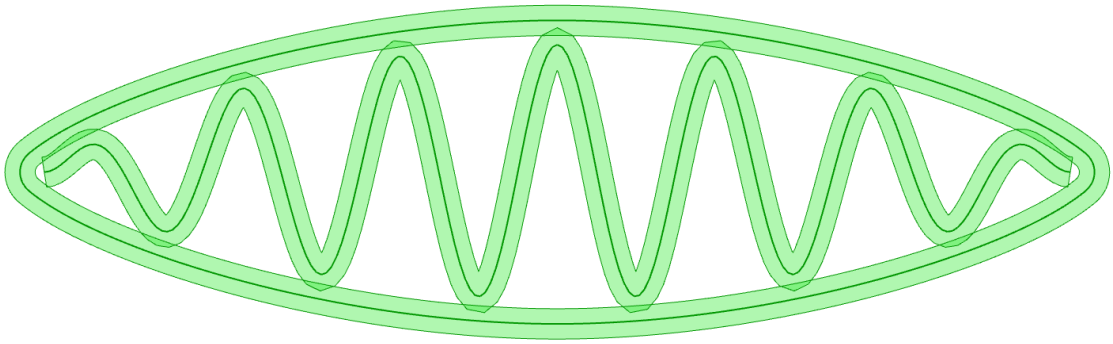


Figure I3. A screenshot of an example of the main geometry in Rhino.

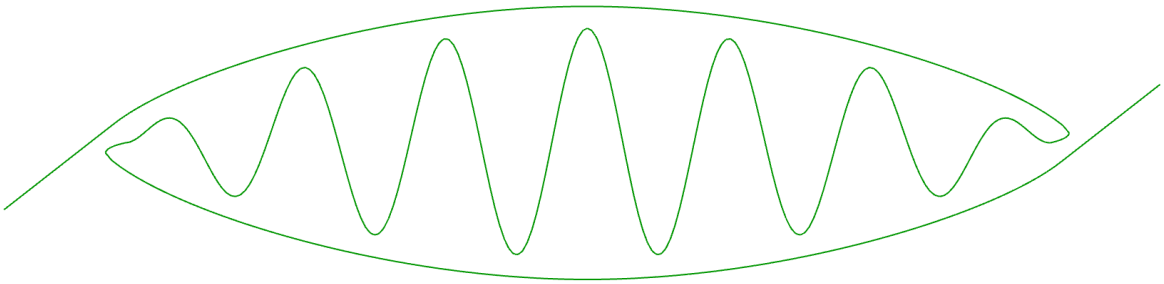


Figure I4. A screenshot of an example of a print path in Rhino.

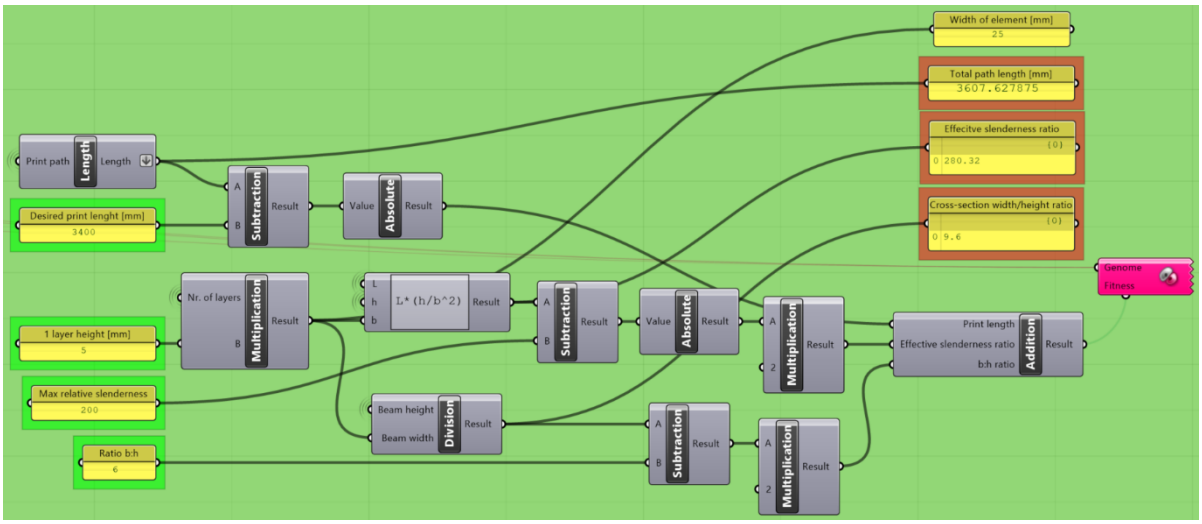


Figure I5. A screenshot of the optimization process in grasshopper.

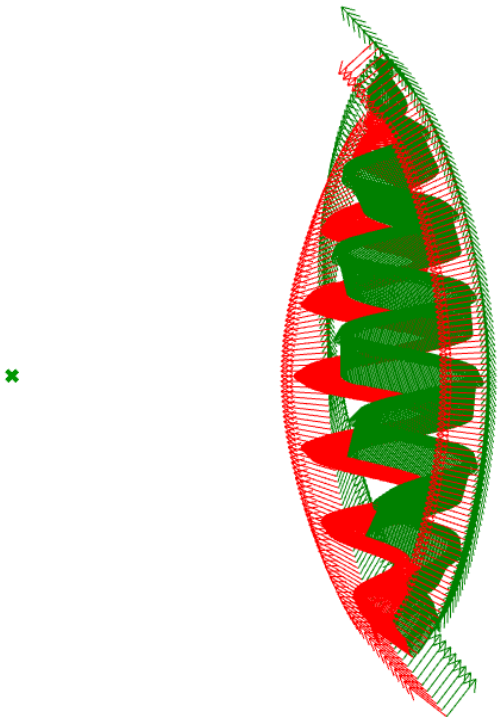


Figure I6. A screenshot of the targets pointing at the origin of the robot in Rhino.

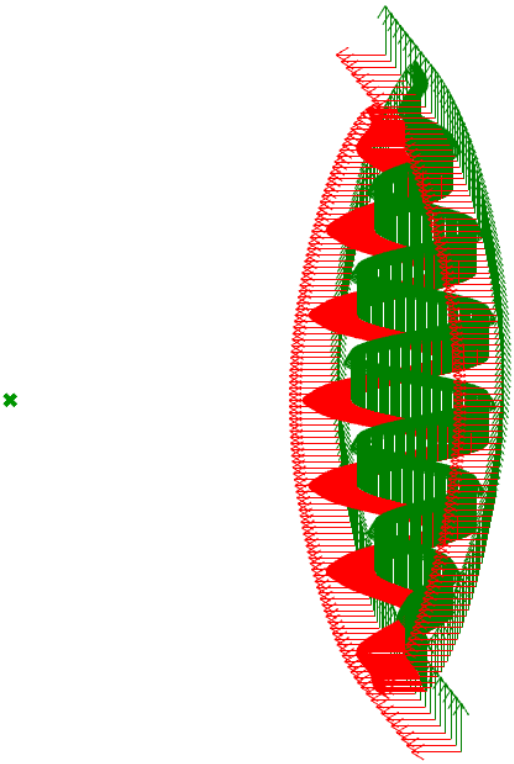


Figure I7. A screenshot of the targets configured to the global coordinate system in Rhino

Appendix J – Numerical models GSA

Bio-based 3D printing and testing of a digitally designed structural element



F.E. Pels Rijcken

Eindhoven, 19-06-2025

Contents

J.1 Sensitivity analyses 1
J.2 Results GSA analyses – outer shape 3
J.2.1 Shape 1 3
J.2.2 Shape 2 4
J.2.3 Shape 3 5
J.2.4 Shape 4 6
J.3 Results GSA analysis – infill 7
J.3.1 3 waves 7
J.3.2 5 waves 8
J.3.3 7 waves 9
J.4 Results GSA analyses – different setups 10
J.4.1 The first setup 10
J.4.2 The second setup 11
J.4.3 The first setup with an applied load of 1 kN 12
J.4.4 The second setup with an applied load of 1 kN 13
J.5 GSA mesh model 14
J.5.1 1 kN with same dimensions of line model 14
J.5.2 Applied load of 1.63 kN 16
J.5.3 GSA model broken wave model with 1 kN 19

J.1 Sensitivity analyses

To see if the default values of the poisson's ratio and the shear modulus are the right values for analysing the structures, sensitivity analyses need to be executed. This is done by changing only one value and comparing it to the standard results. For the sensitivity analyses shape 1 is used with the loads that are mentions earlier.

Poisson's ratio (ν)

When the poisson's ratio is changed, the shear modulus also changes due to the correlation between the two ($G = \frac{E}{2(1+\nu)}$). However, this correlation is disregarded for the first analysis, and the shear modulus is kept at 40.97 N/mm^2.

Table J1 gives the different values of the poisson's ratio (and the changed shear modulus for later analysis). Table J2 gives the results of the GSA analysis. These results indicate that changing the poisson's ratio to its extremes the results from the analysis do not change.

However, with the standard values of GSA, the shear modulus is dependent on the poisson's ratio, so the sensitivity analysis is also executed with this correlation taken into account. The results of this analysis can be found in Table J3. As can be observed, even when coupled, changing the poisson's ratio to the extremes did not have that much of an impact, with differences of smaller than 1% compared to the standard values.

Table J1. Values of the poisson's ratio for the sensitivity analysis of the poisson's ratio and the accompanying shear modulus.

	Lowered	**Standard**	**Higher**
Poisson's ratio [-]	0.1	0.3	0.49
Shear modulus [N/mm²]	48.42	40.97	35.75

Table J2. Results of the poisson's ratio sensitivity analysis.

				Combined stresses			
	U_z	**Axial stress**		**C1**		**C2**	
	[mm]	**[N/mm²]**		**[N/mm²]**		**[N/mm²]**	
Lowered	-2.503	0.2543	-0.2546	0.5565	-0.2172	0.2541	-0.7481
Standard	-2.503	0.2543	-0.2546	0.5565	-0.2172	0.2541	-0.7481
Higher	-2.503	0.2543	-0.2546	0.5565	-0.2172	0.2541	-0.7481

Table J3. Results of the poisson's ratio sensitivity analysis, with changing shear modulus.

				Combined stresses			
	U_z	**Axial stress**		**C1**		**C2**	
	[mm]	**[N/mm²]**		**[N/mm²]**		**[N/mm²]**	
Lowered	-2.489*	0.2543	-0.2546	0.5564**	-0.2170**	0.2540**	-0.7475**
Standard	-2.503	0.2543	-0.2546	0.5565	-0.2172	0.2541	-0.7481
Higher	-2.516*	0.2543	-0.2546	0.5565	-0.2172	0.2542**	-0.7487**

**) Difference of 0.05% or less*
***) Difference of 0.1% or less*

Shear modulus (G)

In Table J4 the extreme value of the shear modulus can be found; these values are used for the shear modulus sensitivity analysis. In Table J5 the results of this analysis. Changing the shear modulus has an impact on the results, but these differences are insignificant with a maximum difference of 1% or less compared to the standard results.

Table J4. Values of the shear modulus for the sensitivity analysis of the shear modulus.

	Lowered	**Standard**	**Lowered**
Shear modulus [N/mm²]	31.513	40.97	53.265

Table J5. Results of the shear modulus sensitivity analysis.

				Combined stresses			
	U_z [mm]	Axial stress [N/mm²]		C1 [N/mm²]		C2 [N/mm²]	
Lowered	-2.5170*	0.2543	-0.2546	0.5565	-0.2172	0.2542**	-0.7487**
Standard	-2.5030	0.2543	-0.2546	0.5565	-0.2172	0.2541	-0.7481
Higer	-2.4820*	0.2543	-0.2546	0.5564**	-0.2172	0.2540**	-0.7472**

**) Difference of 0.05% or less*
***) Difference of 0.1% or less*

The results of both sensitivity analyses show that changing the shear modulus has an impact on the results. However, these differences are insignificant leading to setting the shear modulus and the poisson's ratios to the GSA default settings.

J.2 Results GSA analyses – outer shape

J.2.1 Shape 1

Figure J1 to Figure J3 show the GSA analysis results of shape 1.

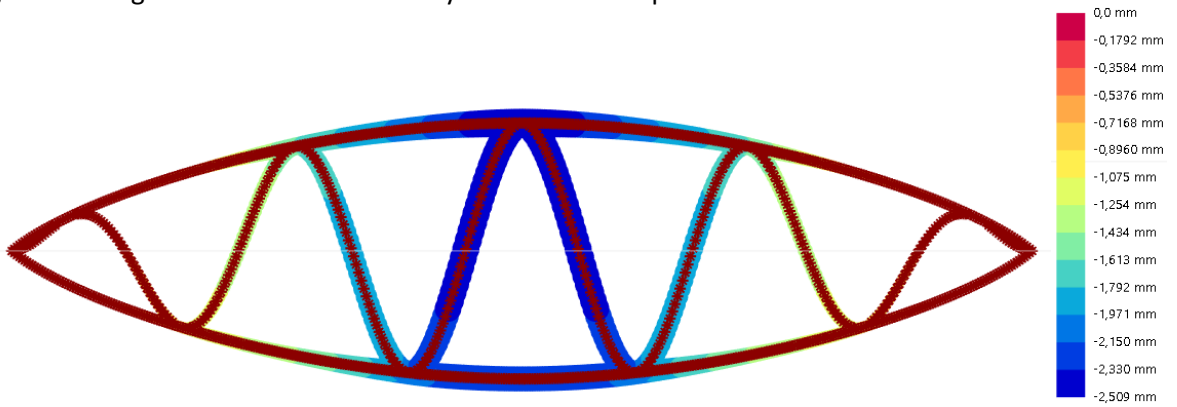


Figure J1. Translation (U_z) results shape 1 with an applied load of 0.1 kN.

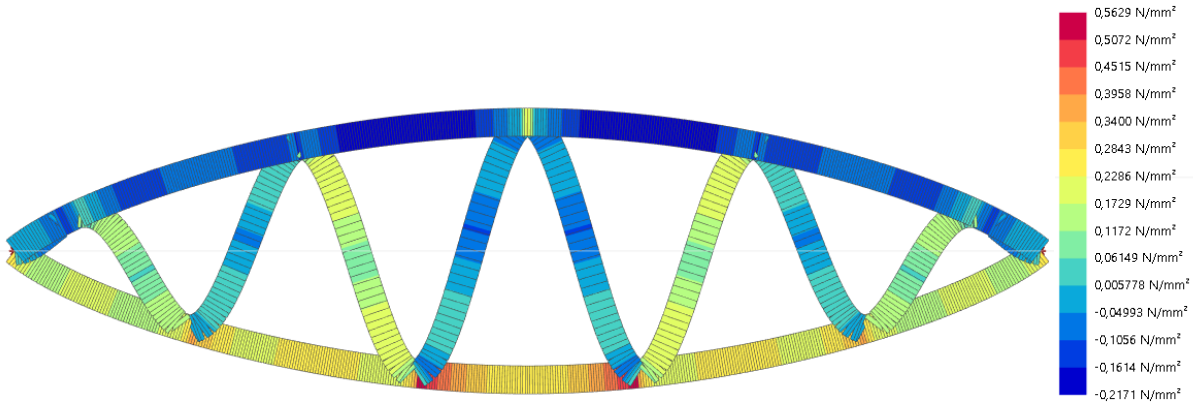


Figure J2. Combined stresses (C1) results shape 1 with an applied load of 0.1 kN.

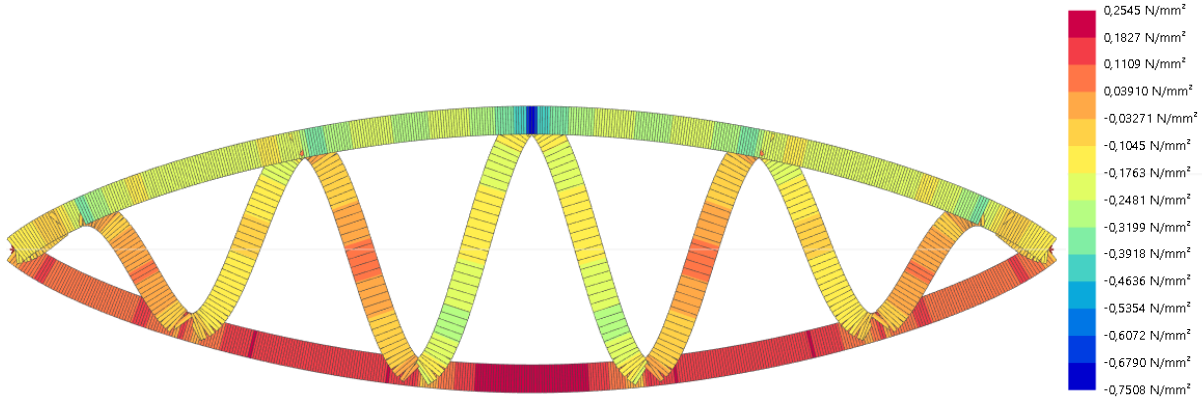


Figure J3. Combined stresses (C2) results shape 1 with an applied load of 0.1 kN.

J.2.2 Shape 2

Figure J4 to Figure J6 show the GSA analysis results of shape 2.

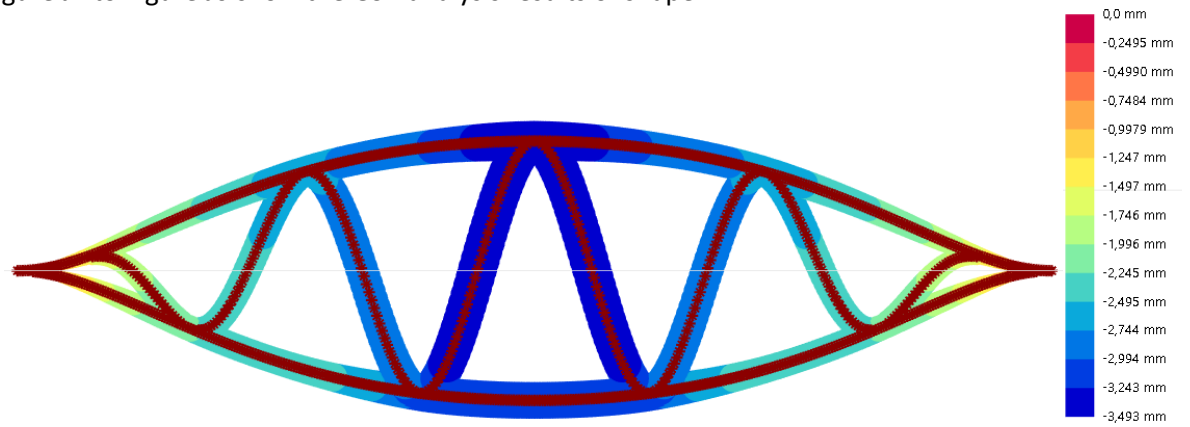


Figure J4. Translation (U_z) results shape 2 with an applied load of 0.1 kN.

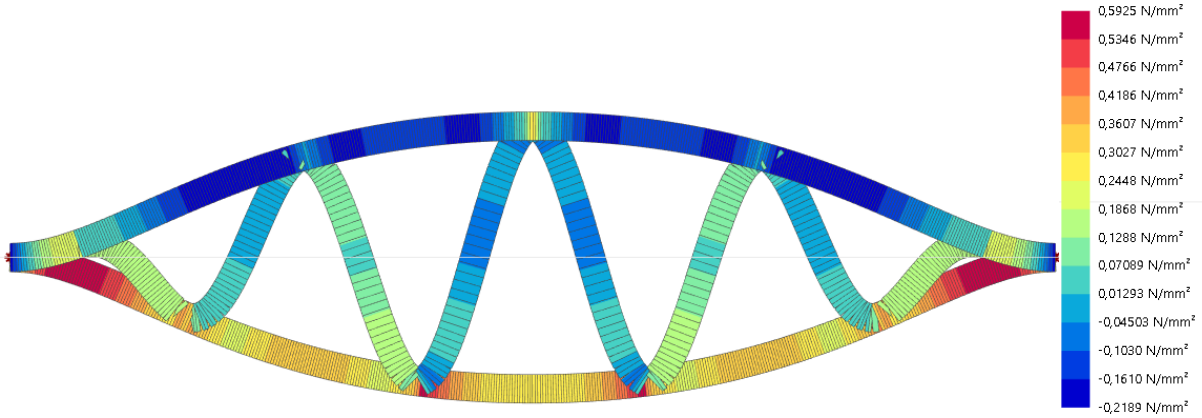


Figure J5. Combined stresses (C1) results shape 2 with an applied load of 0.1 kN.

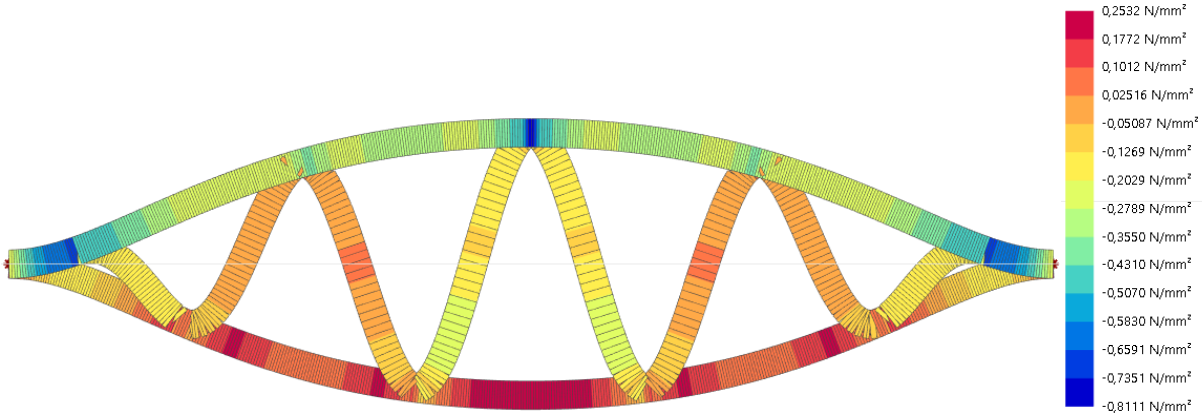


Figure J6. Combined stresses (C2) results shape 2 with an applied load of 0.1 kN.

J.2.3 Shape 3

Figure J7 to Figure J9 show the GSA analysis results of shape 3.

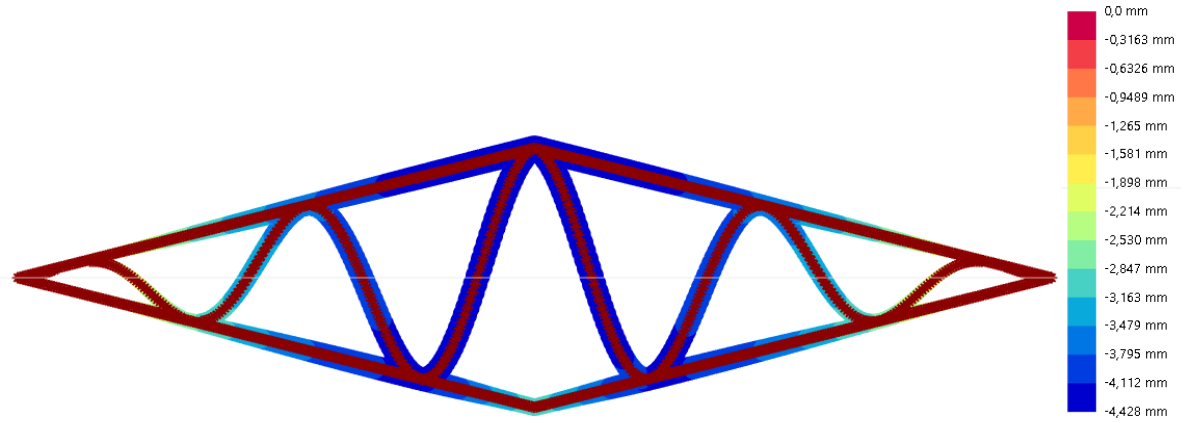


Figure J7. Translation (U_z) results shape 3 with an applied load of 0.1 kN.

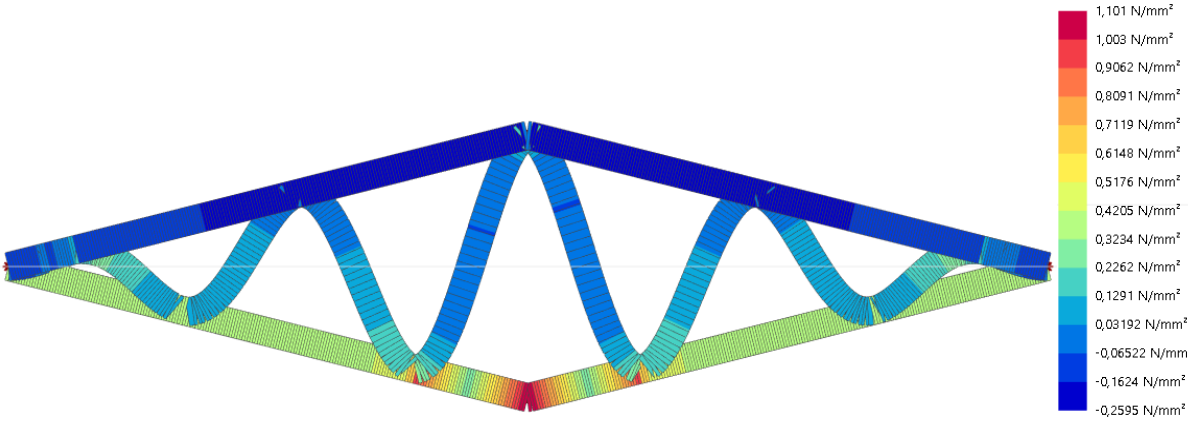


Figure J8. Combined stresses (C1) results shape 3 with an applied load of 0.1 kN.

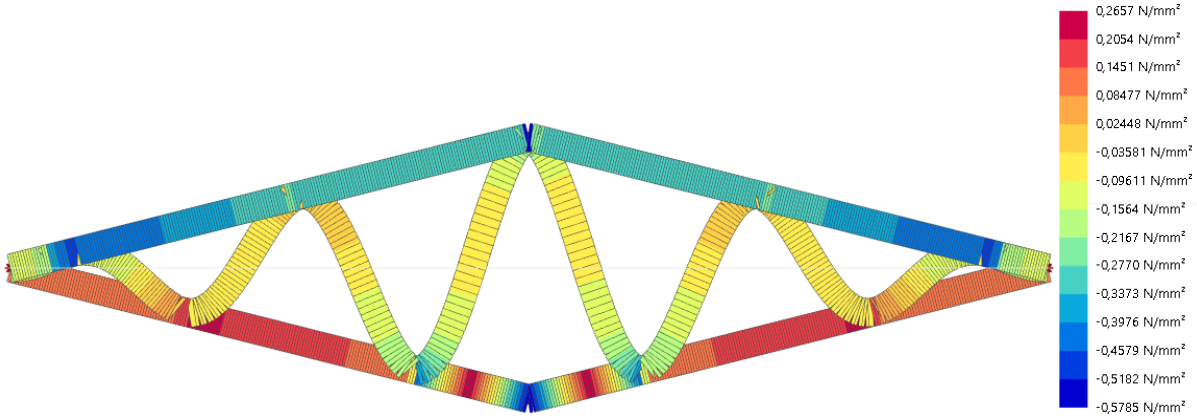


Figure J9. Combined stresses (C2) results shape 3 with an applied load of 0.1 kN.

J.2.4 Shape 4

In Figure J10 to Figure J12 the GSA analysis results of shape 4.

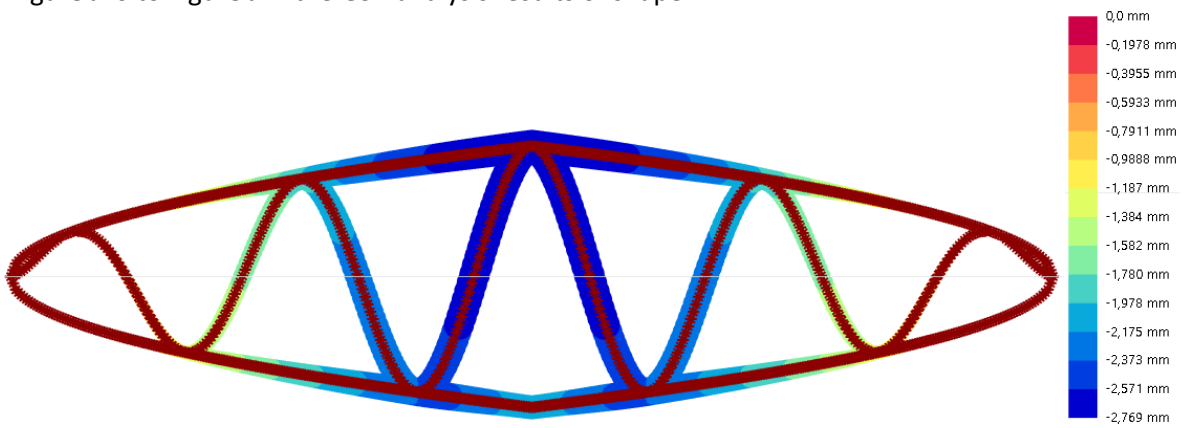


Figure J10. Translation (U_z) results shape 4 with an applied load of 0.1 kN.

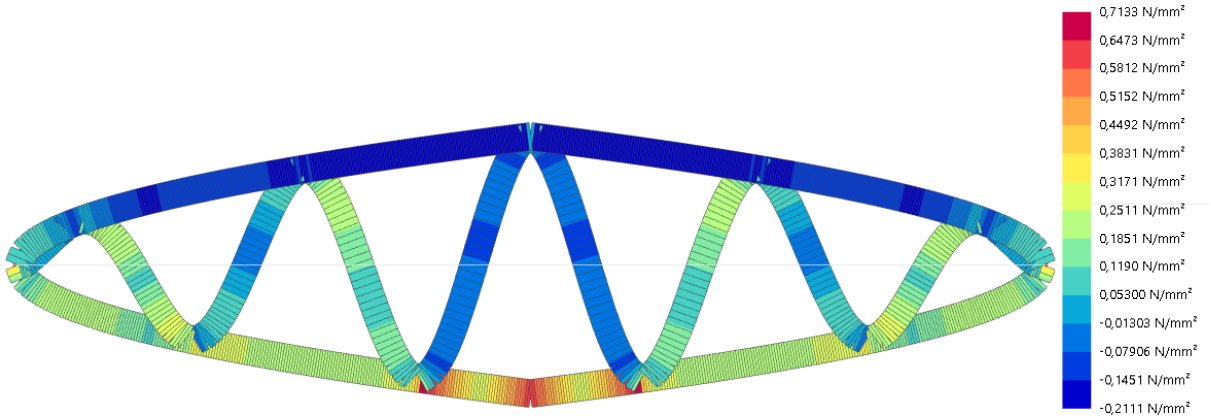


Figure J11. Combined stresses (C1) results shape 4 with an applied load of 0.1 kN.

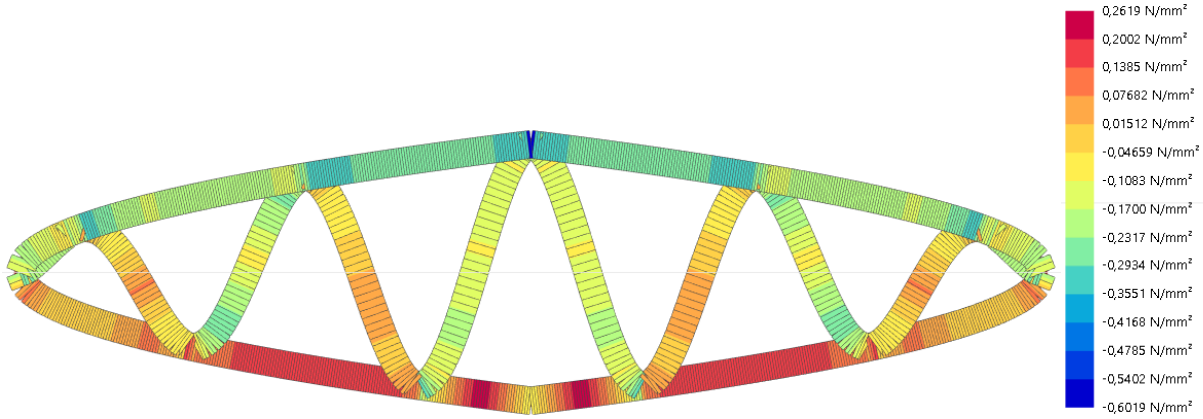


Figure J12. Combined stresses (C2) results shape 4 with an applied load of 0.1 kN.

J.3 Results GSA analysis – infill

J.3.1 3 waves

Figure J13 to Figure J15 show the GSA analysis results of the element with 3 waves.

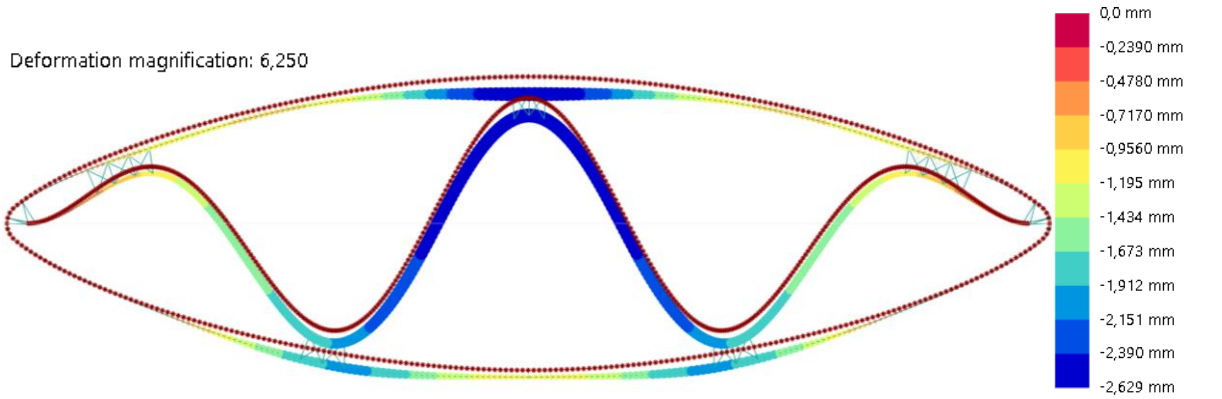


Figure J13. Deformation and translation (U_z) results 3 waves with an applied load of 0.1 kN (the red dotted line is the original shape).

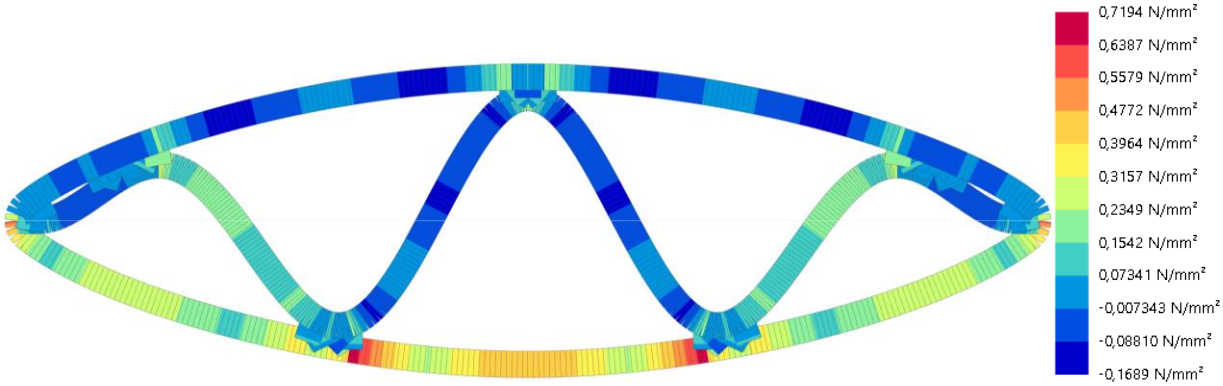


Figure J14. Combined stress (C1) results 3 waves with an applied load of 0.1 kN

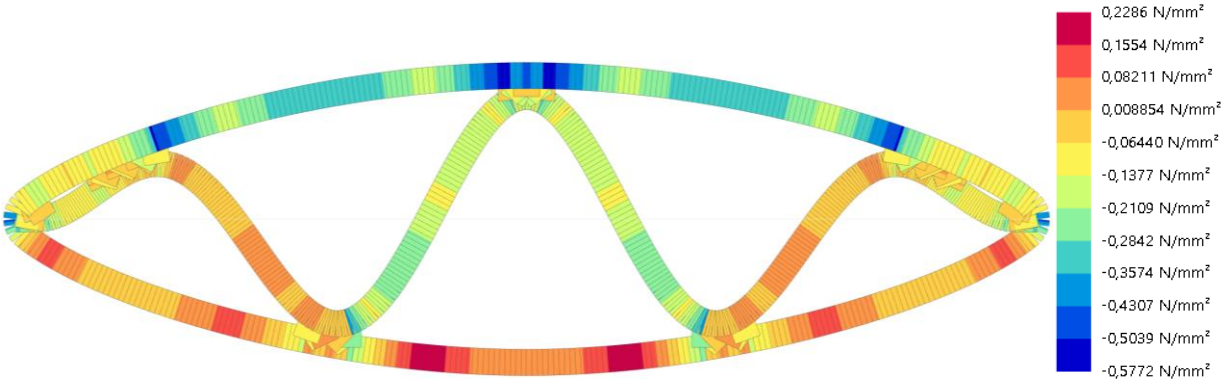


Figure J15. Combined stress (C2) results 3 waves with an applied load of 0.1 kN.

J.3.2 5 waves

Figure J16 to Figure J18 show the GSA analysis results of the element with 5 waves.

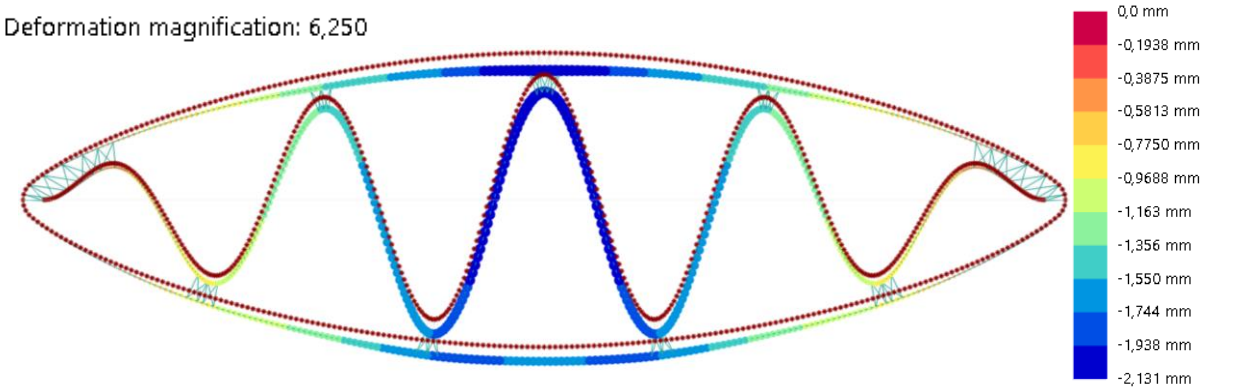


Figure J16. Deformation and translation (U_z) results 5 waves with an applied load of 0.1 kN (the red dotted line is the original shape).

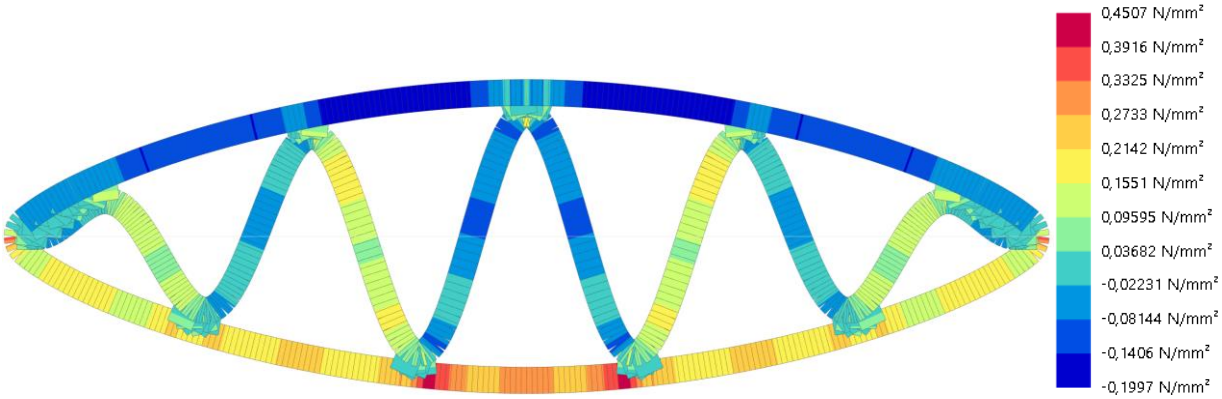


Figure J17. Combined stress (C1) results 5 waves with an applied load of 0.1 kN.

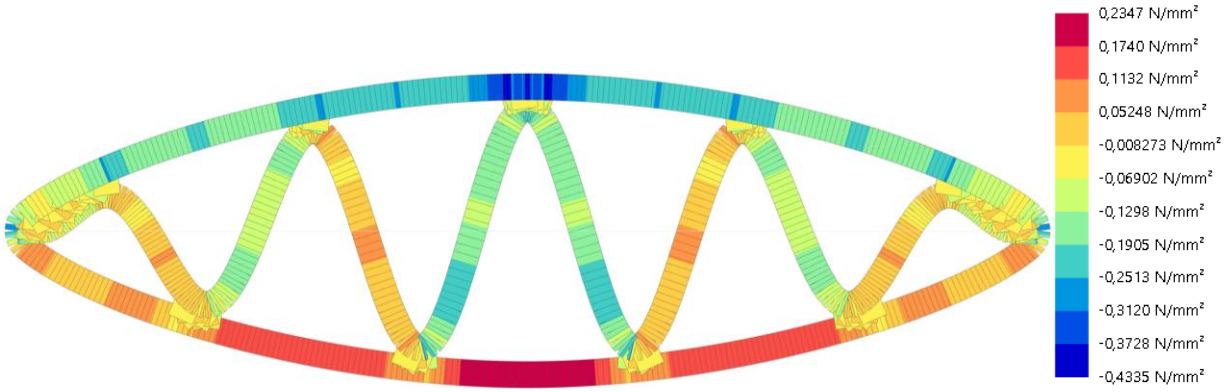


Figure J18. Combined stress (C2) results 5 waves with an applied load of 0.1 kN.

J.3.3 7 waves

Figure J19 to Figure J21 show the GSA analysis results of the element with 5 waves.

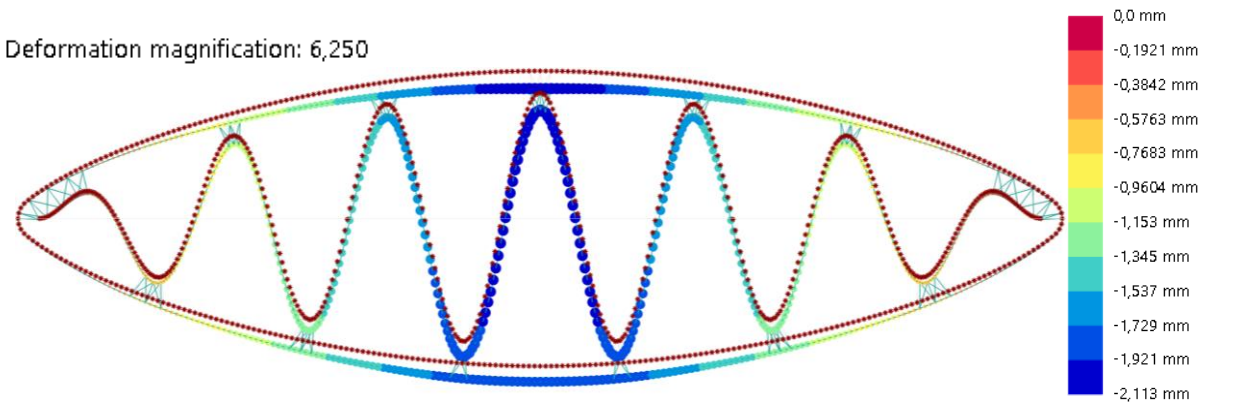


Figure J19. Deformation and translation (U_z) results 7 waves with an applied load of 0.1 kN (the red dotted line is the original shape).

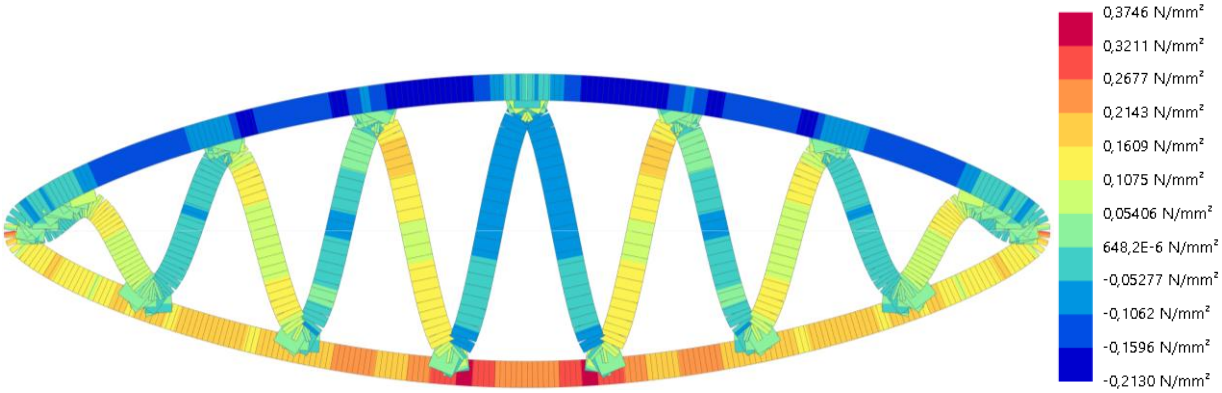


Figure J20. Combined stress (C1) results 7 waves with an applied load of 0.1 kN.

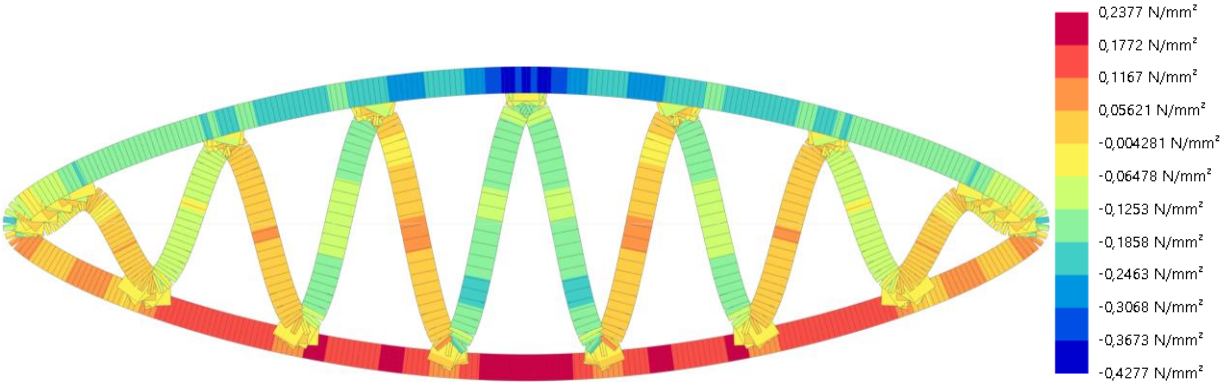


Figure J21. Combined stress (C2) results 7 waves with an applied load of 0.1 kN.

J.4 Results GSA analyses – different setups

J.4.1 The first setup

Figure J22 to Figure J24 show the GSA analysis results of the first setup.

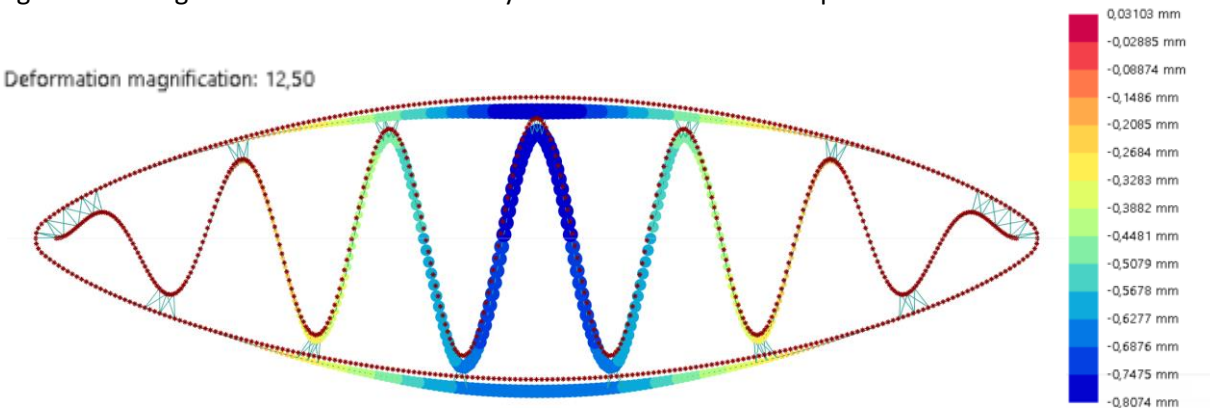


Figure J22. Translation (U_z) results of the first setup with an applied load of 0.1 kN.

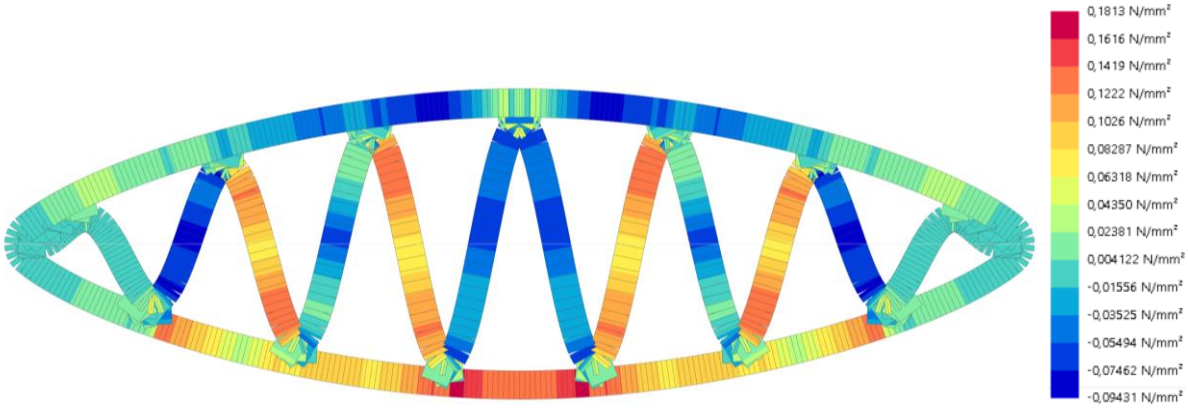


Figure J23. Combined stresses (C1) results of the first setup with an applied load of 0.1 kN.

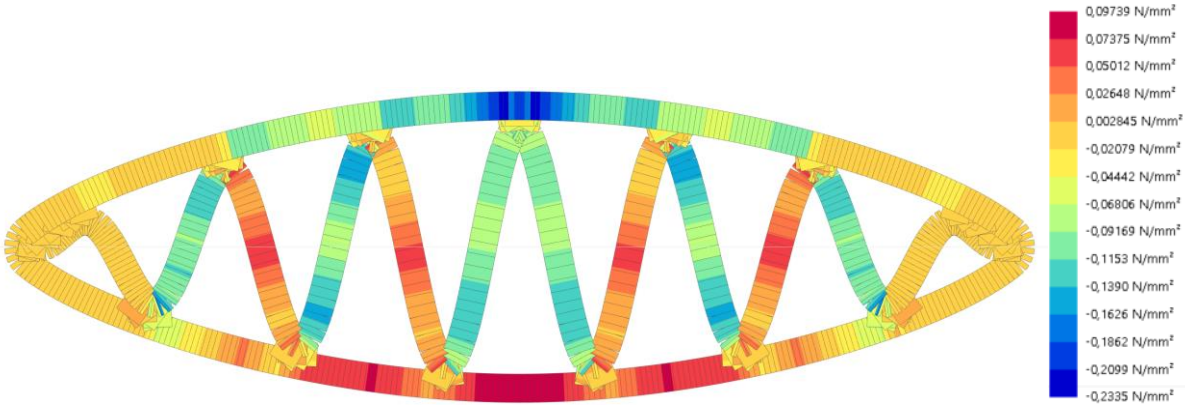


Figure J24. Combined stresses (C2) results of the first setup with an applied load of 0.1 kN.

J.4.2 The second setup

Figure J25 and Figure J27 show the GSA analysis results of the second setup.

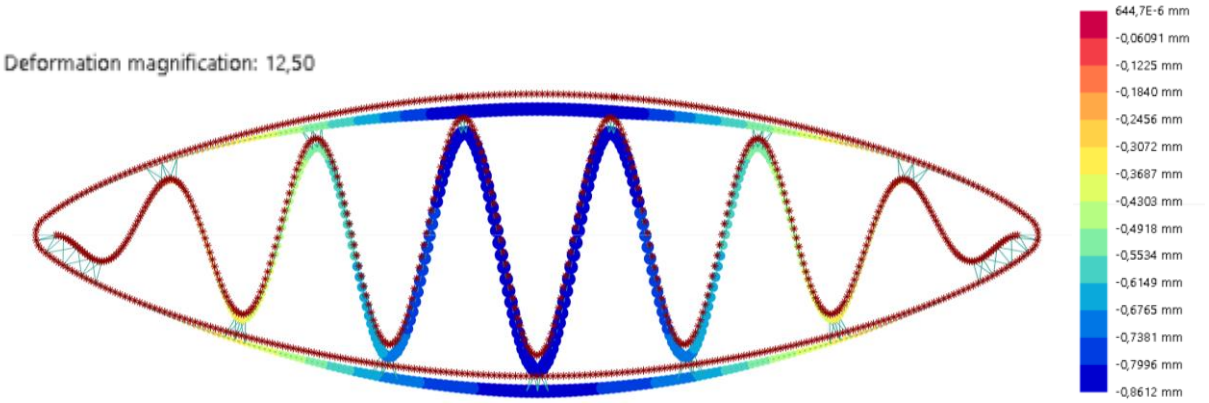


Figure J25. Translation (U_z) results of the second setup with an applied load of 0.1 kN.

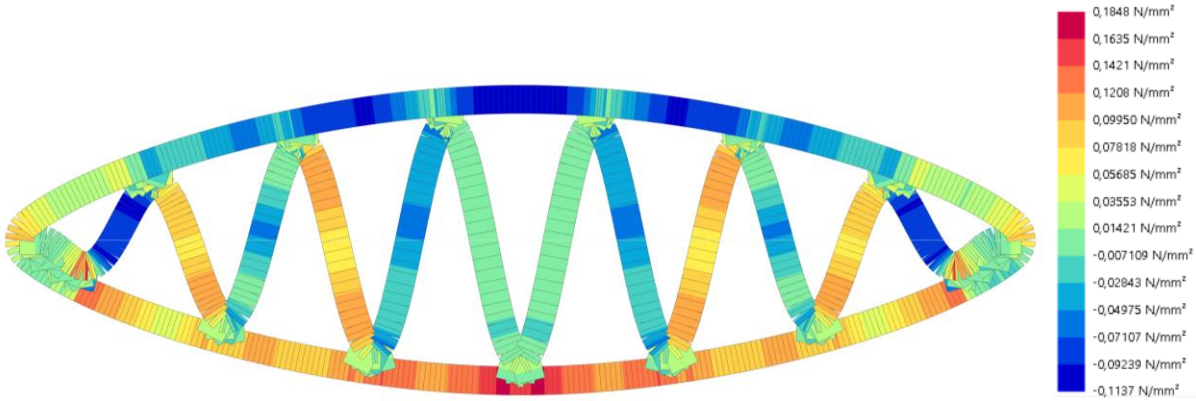


Figure J26. Combined stresses (C1) results of the second setup with an applied load of 0.1 kN.

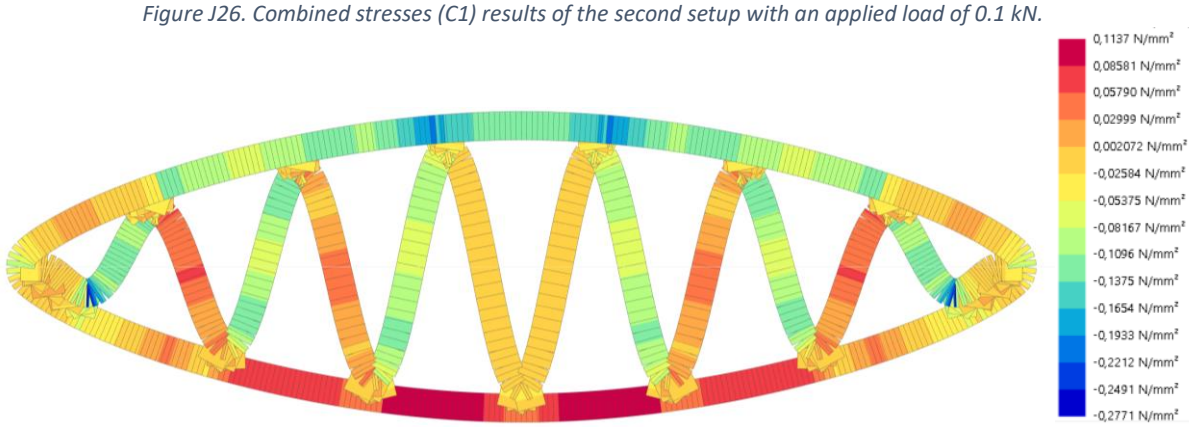


Figure J27. Combined stresses (C2) results of the second setup with an applied load of 0.1 kN.

J.4.3 The first setup with an applied load of 1 kN

Figure J28 and Figure J30 show the GSA analysis results of the first setup with an applied load of 1 kN.

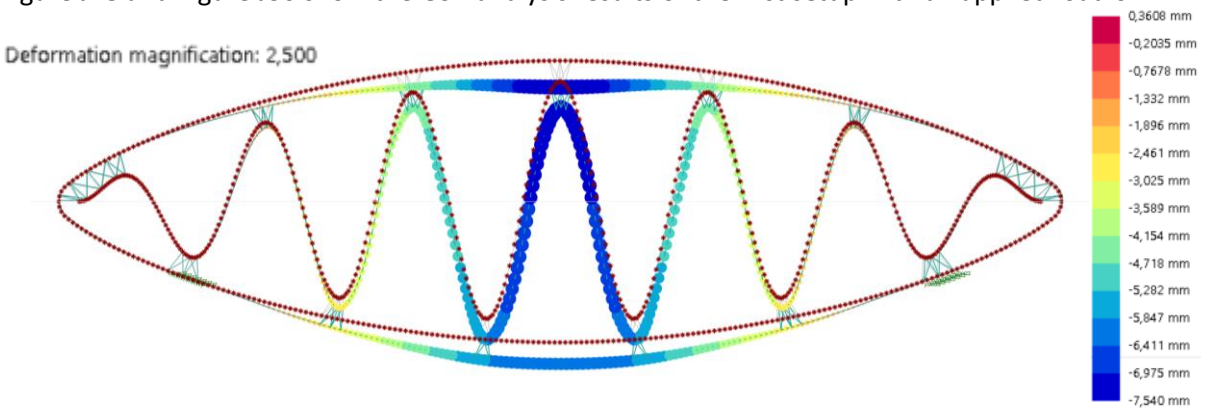


Figure J28. Translation (U_z) results of the first setup with an applied load of 1 kN.

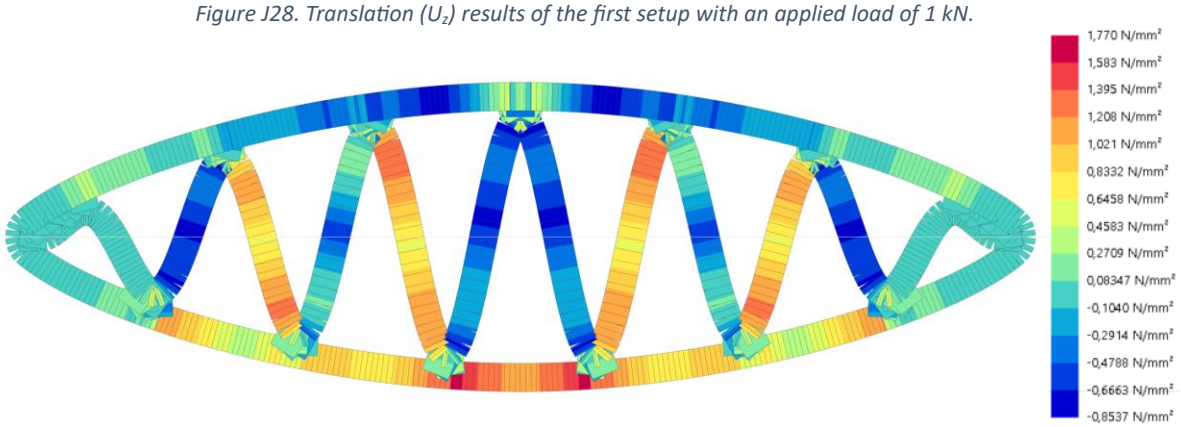


Figure J29. Combined stresses (C1) results of the first setup with an applied load of 1 kN.

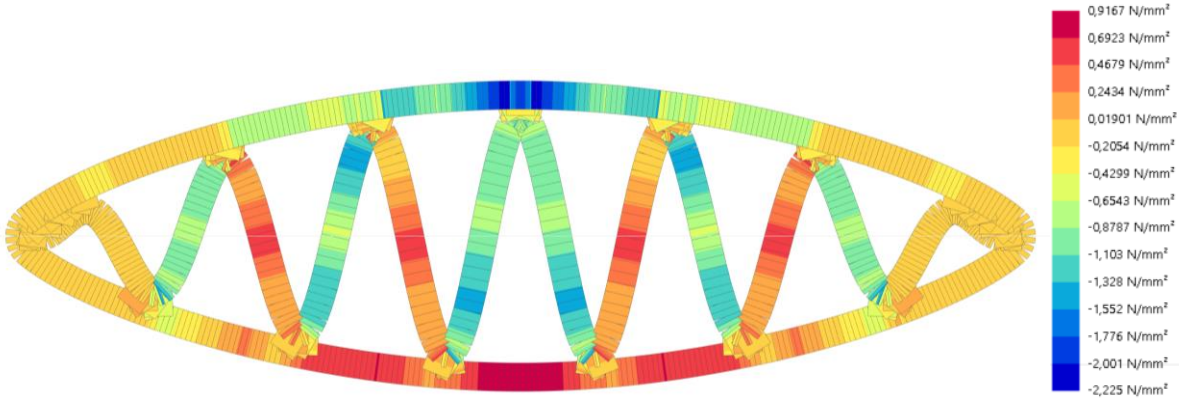


Figure J30. Combined stresses (C2) results of the first setup with an applied load of 1 kN.

J.4.4 The second setup with an applied load of 1 kN

Figure J31 and Figure J33 show the GSA analysis results of the second setup with an applied load of 1 kN.

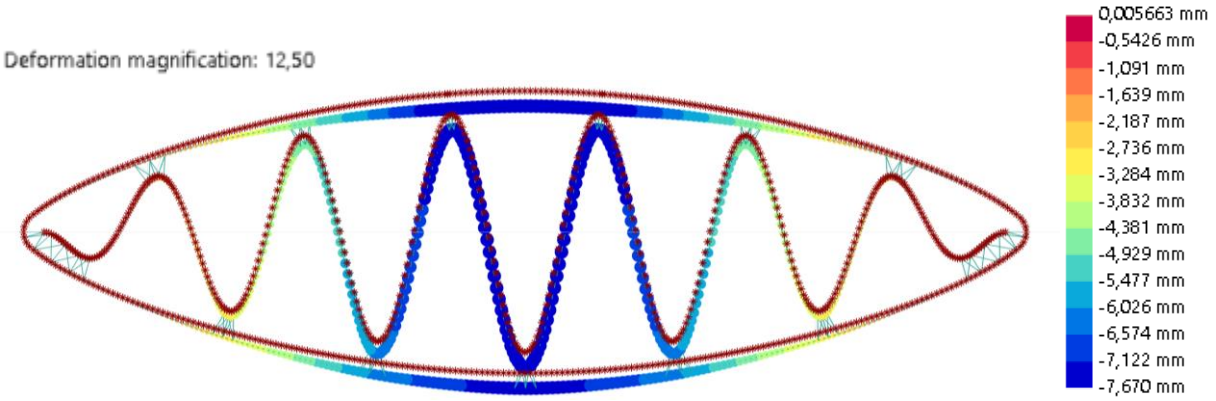


Figure J31. Translation (U_z) results of the second setup with an applied load of 1 kN.

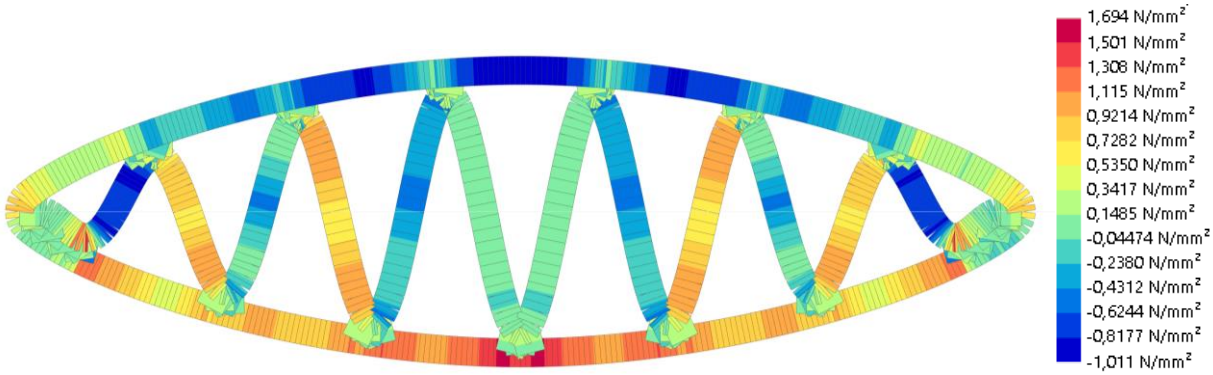


Figure J32. Combined stresses (C1) results of the second setup with an applied load of 1 kN.

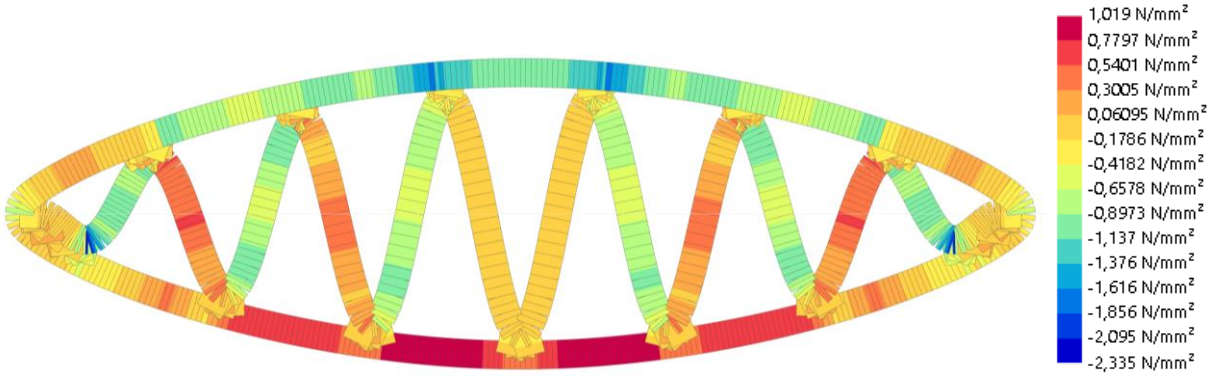


Figure J33. Combined stresses (C2) results of the second setup with an applied load of 1 kN.

J.5 GSA mesh model

J.5.1 1 kN with same dimensions of line model

In Figure J34 to Figure J36 the GSA analysis results of the mesh model with the same dimensions as the line model with setup 3 are displayed, with an applied load of 1 kN.

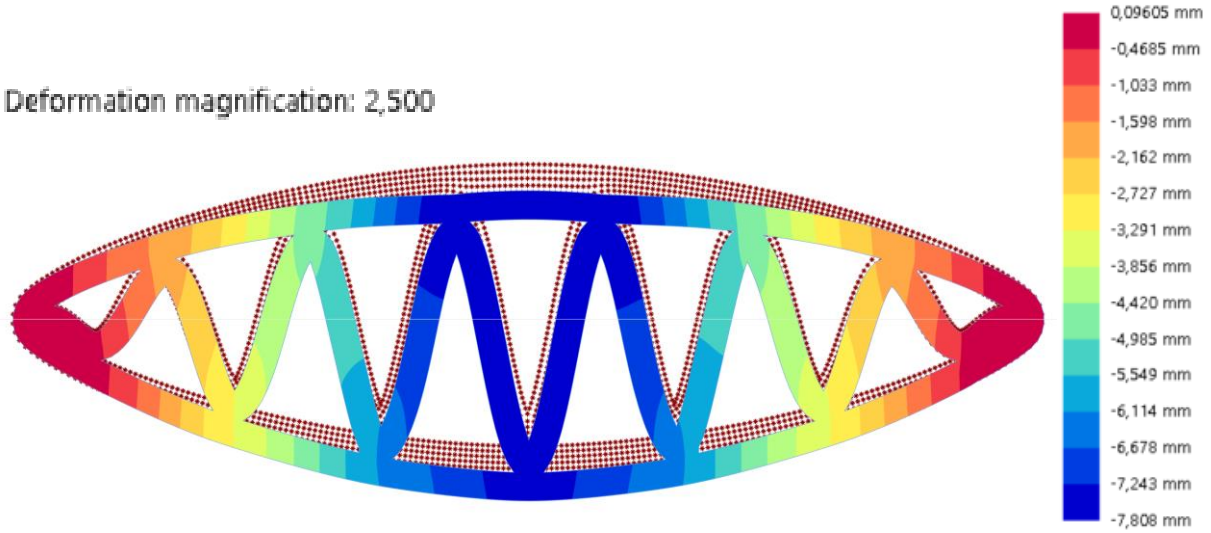


Figure J34. Translation (U_z) results of the mesh model with 1 kN as the applied load.

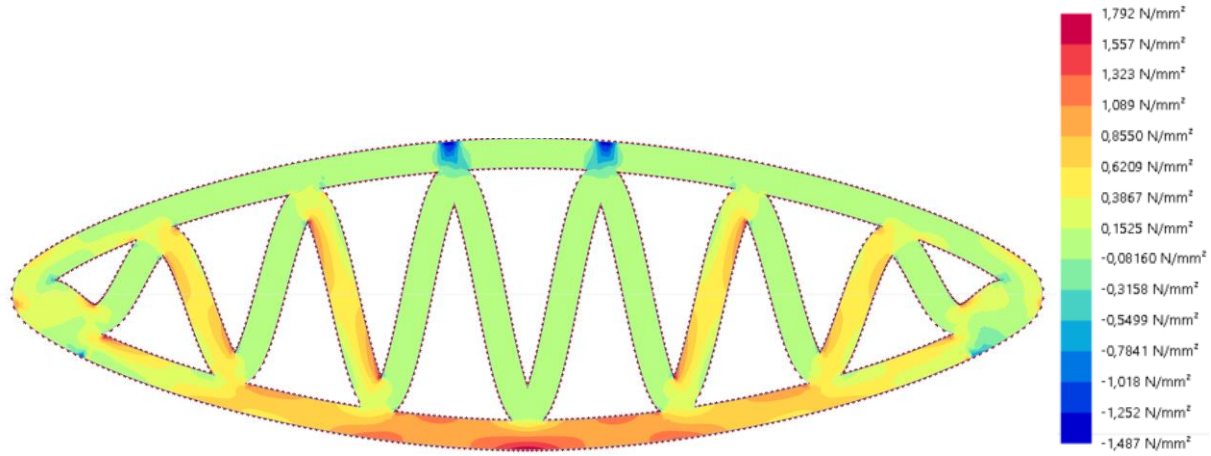


Figure J35. Maximum principal stresses (averaged at the nodes) results of the mesh model with 1 kN as the applied load.

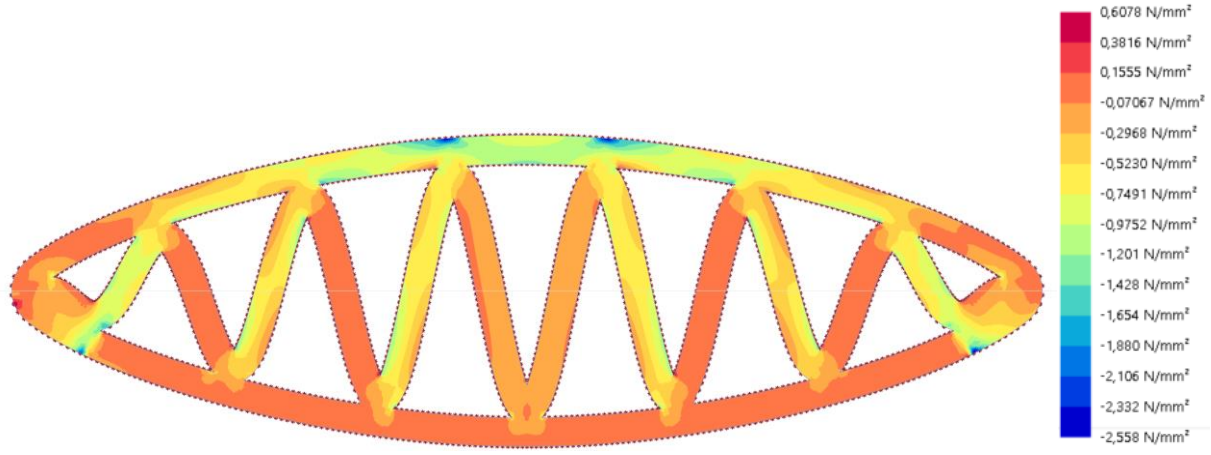


Figure J36. Minimum principal stresses (averaged at the nodes) results of the mesh model with 1 kN as the applied load.

The case with the applied load of 1 kN is compared to the line model with setup 2 of chapter J.4.4. This is done to verify the element, the supports and the load are correctly simulated. The results of the mesh model and the line model are presented in Table J6.
The results differ slightly, however, when the results in the bottom chord (displacement and stresses), these are relatively close to each other. So, it was concluded that this mesh model can be used to verify the final printed element.

Table J6. Summarized results of setup 2 and the mesh model in GSA.

Model	U_z		Principal stresses		
	Whole model [mm]	Bottom chord [mm]	Max [N/mm²]	Min [N/mm²]	Bottom chord [mm]
Line model setup 3	-7.670	-7.568	1.694	-2.335	1.694
Whole mesh model	-7.808	-7.526	1.792	-2.558	1.709

J.5.2 Applied load of 1.63 kN

Figure J37 to Figure J39 show the GSA analysis results of the mesh model with an applied load of 1.63 kN.

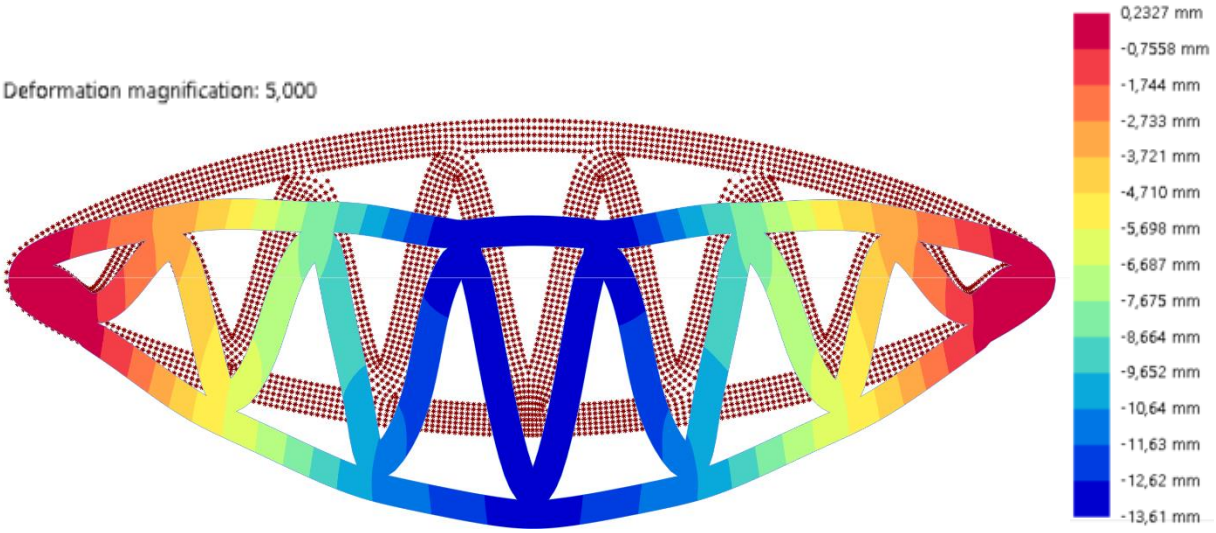


Figure J37. Translation (U_z) results of the mesh model with 1.63 kN as the applied load.

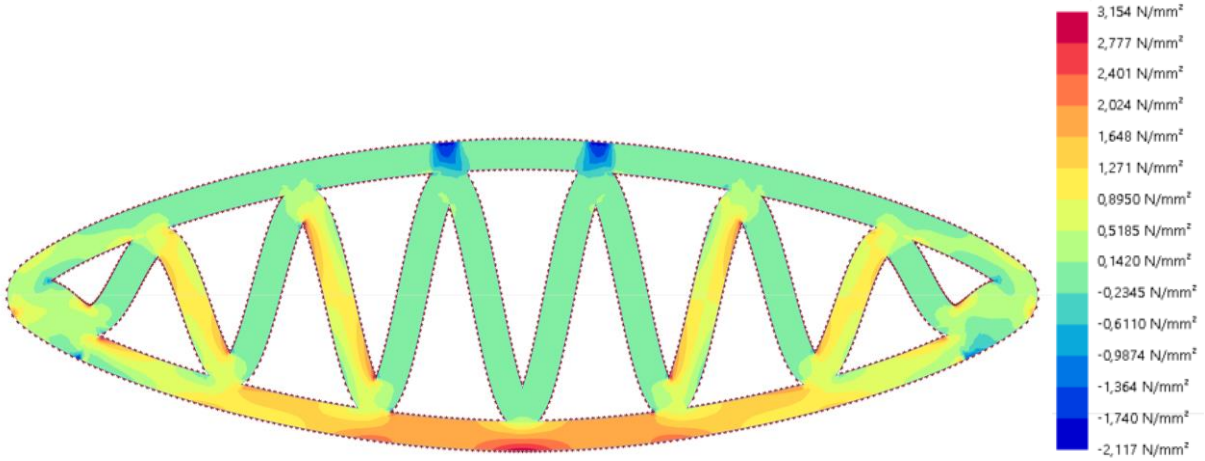


Figure J38. Maximum principal stresses (averaged at the nodes) results of the mesh model with 1.63 kN as the applied load.

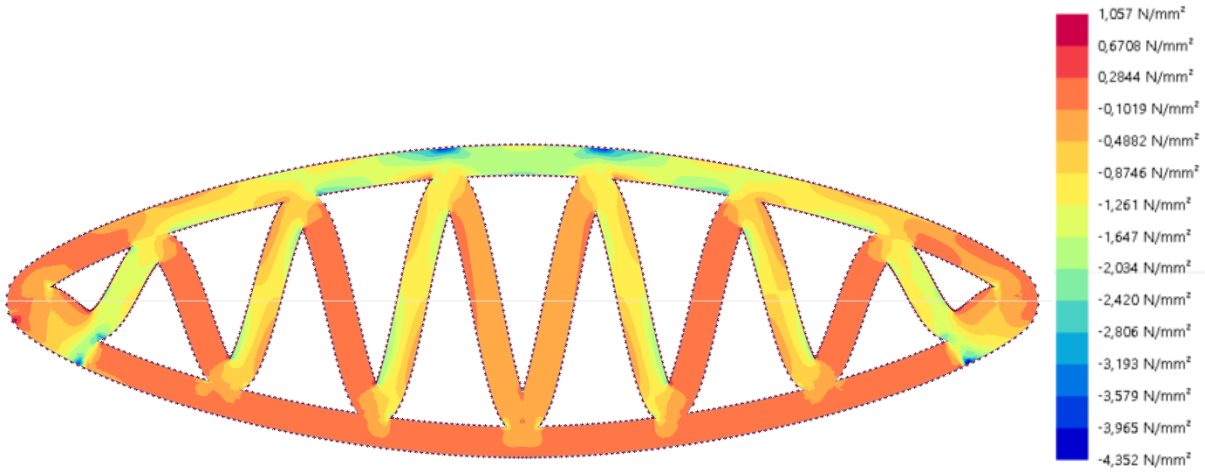


Figure J39. Minimum principal stresses (averaged at the nodes) results of the mesh model with 1.63 kN as the applied load.

These results show that there are quite a few local peak stresses occurring in the element. These peak stresses occur often at tight corners between the diagonals and the chords. In addition to that, peak stresses also occur at the location of the load and supports. The GSA model without the peak stresses is shown in Figure J40. The results of the model without the peak stress locations are shown in Figure J41 to Figure J43.

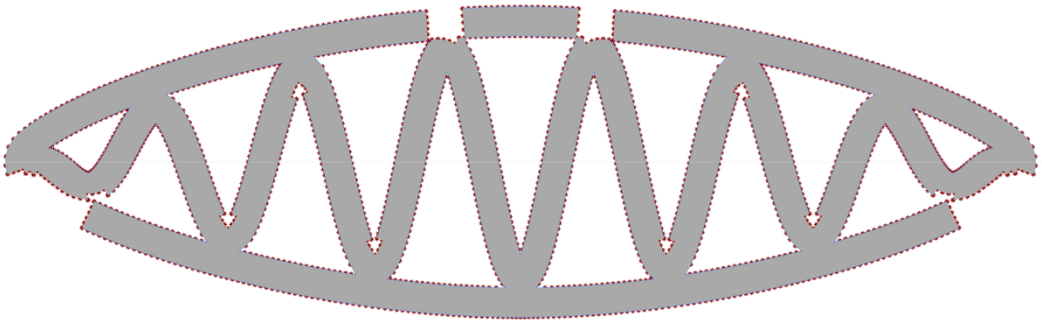


Figure J40. The GSA model without the local peak stresses and the locations of the loads and supports.

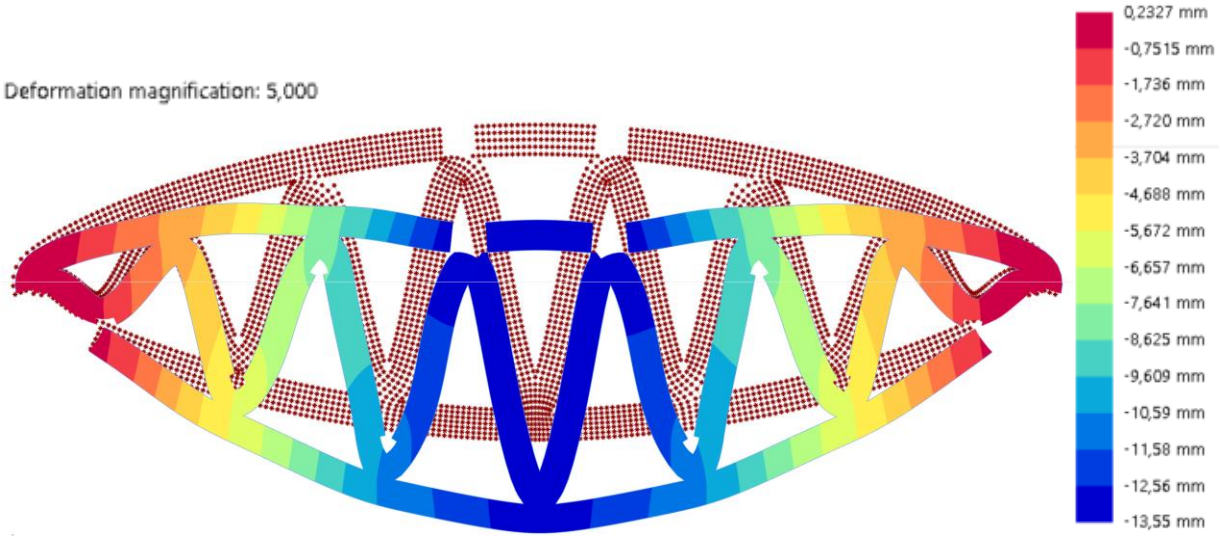


Figure J41. Translation (Uz) results of the mesh model without the local peak stresses.

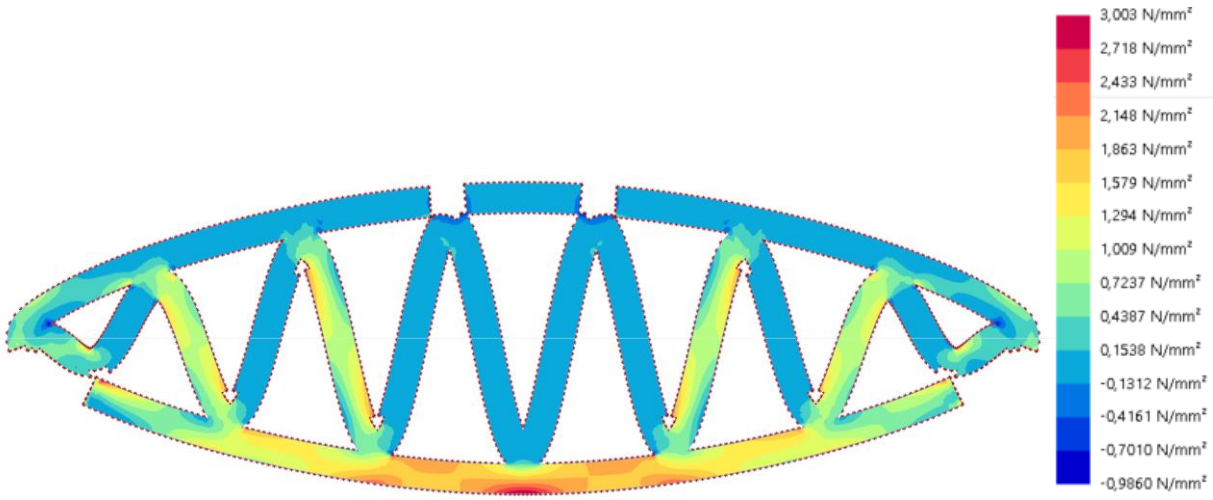


Figure J42. Maximum principal stresses (averaged at the nodes) results of the mesh model without the local peak stresses.

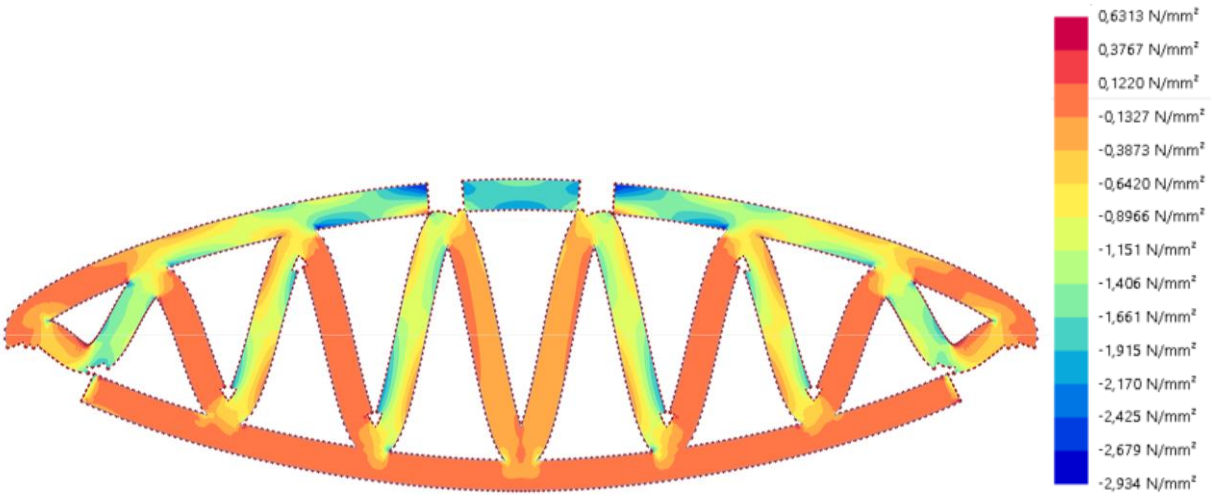


Figure J43. Minimum principal stresses (averaged at the nodes) results of the mesh model without the local peak stresses

Table J7. Summarized results with the applied load of 1.63 kN.

Model	U_z		Principal stresses		
	Whole model [mm]	Bottom chord [mm]	Max [N/mm²]	Min [N/mm²]	Bottom chord [mm]
Whole mesh model	-13.61	-13.10	3.154	-4.352	3.003
No local peak stresses	-13.55	-13.10	3.003	-2.934	3.003

J.5.3 GSA model broken wave model with 1 kN

Figure J44 shows the mesh model in GSA, with the red line indicating that there is no connection between the top of top 2 and the top chord.

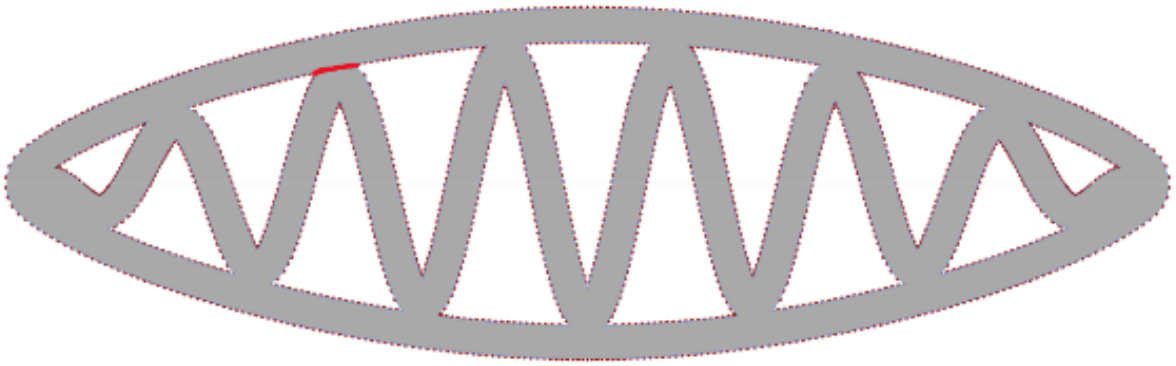


Figure J44. The GSA model without a connection between the top chord and the top 2.

Figure J45 to Figure J47 show the GSA analysis results of the "broken wave" mesh, a load of 1.0 kN is applied in these models.

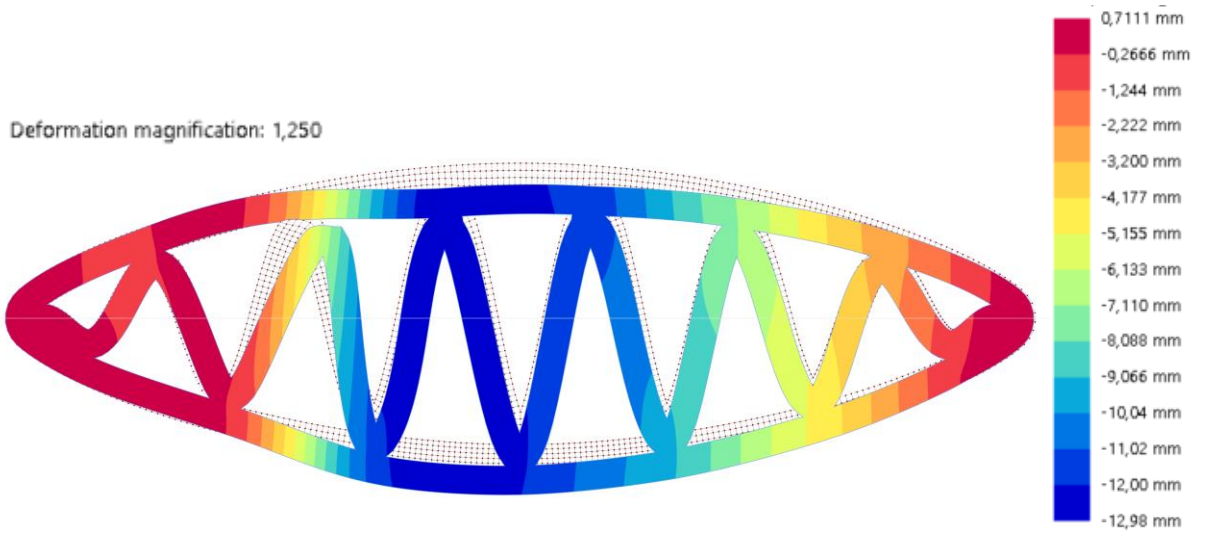


Figure J45. Translation (U_z) results of the broken wave model.

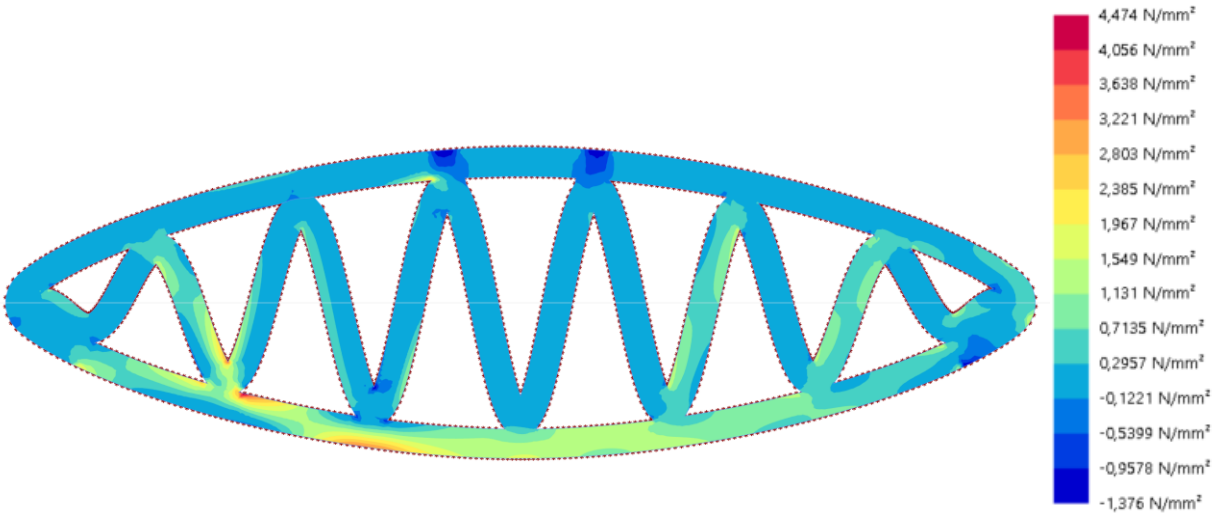


Figure J46. Maximum principal stresses (averaged at the nodes) results of the broken wave model.

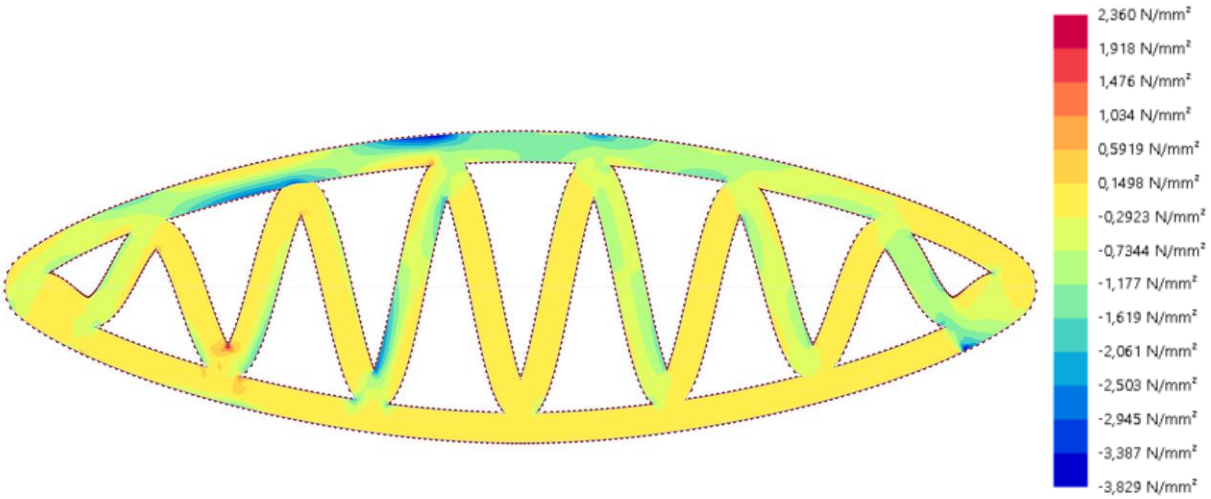


Figure J47. Minimum principal stresses (averaged at the nodes) results of the broken wave model.

Appendix K – Final prints

Bio-based 3D printing and testing of a digitally designed structural element



F.E. Pels Rijcken

Eindhoven, 19-06-2025

Contents

K.1 Printing 1
K.1.1 Print speed (re)test 1
K.1.2 Final element print 3
K.1.3 Test beam print 6
K.2 Curing conditions 7
K.3 Final element information 10
K.3.1 Freshly printed 10
K.3.2 Cured dimensions final element 11
K.4 Test beam information 12
K.4.1 Fresh and cured dimensions of the test beams 12
K.4.2 Shrinkage of the test beams 13

K.1 Printing

Before starting the print procedures, the right cartridges had to be selected. As mentioned in chapter 6.2.4 of the main thesis there was a cartridge in which a lot of the material stuck to the inside of cartridge. This could be a reason for the difference in path width during the print. Just to be sure that that occurrence was not playing a role in the print path width, the cartridge with which this occurred should be discarded. This was done by filling each cartridge (three cartridges) with the mix and pushing it out with the Makita. This process was executed twice to be sure that the right cartridges were selected. There was only one of the three cartridges where the material stuck to the insides, meaning that there were two cartridges available to print with.

After this faulty cartridge was discarded, a new print speed test was executed. After that the final element was printed and in the end a few test elements were printed.

K.1.1 Print speed (re)test

In Figure K1 a photograph of results of the first print speed test is shown. With this test the Makita pressure was set to 2 and the print speed of the straight parts changed during printing. Unfortunately, the speed in the corners was not altered, so the corners should be excluded from the analysis. The starting speed was set to 20 mm/s, and the speed was manually increased until a path of 20 mm was reached.

The fifth path width was small enough that the path next to it did not touch each other. This path was printed with a speed of 30 mm/s. The sixth and seventh straight paths were printed with a speed of 32.5 mm/s and the eight and nineth path were printed with a speed of 35 mm/s. From this print, it was concluded that the most optimal print speed was 32.5 mm/s.



Figure K1. Print speed test at final print day. Starting with a start print speed of 20 mm/s and ending with a speed 35 mm/s. The print started in the top right corner and ended in the bottom left corner.

Another full cartridge print was executed with the print speed kept at 32.5 mm/s for both the straight and the corner parts. The end result of this print is displayed in Figure K2 and is compared with the full cartridge print of chapter 6.2.2 of the main thesis. The first thing that can be noticed is that with the new full cartridge print, the path width does not differ significantly during the print. The path width stayed equal during the print and the average path width is provided in Table K1.

With the new Makita pressure and print speed a longer print could be achieved; the calculations of this print length can be found in Table K2.

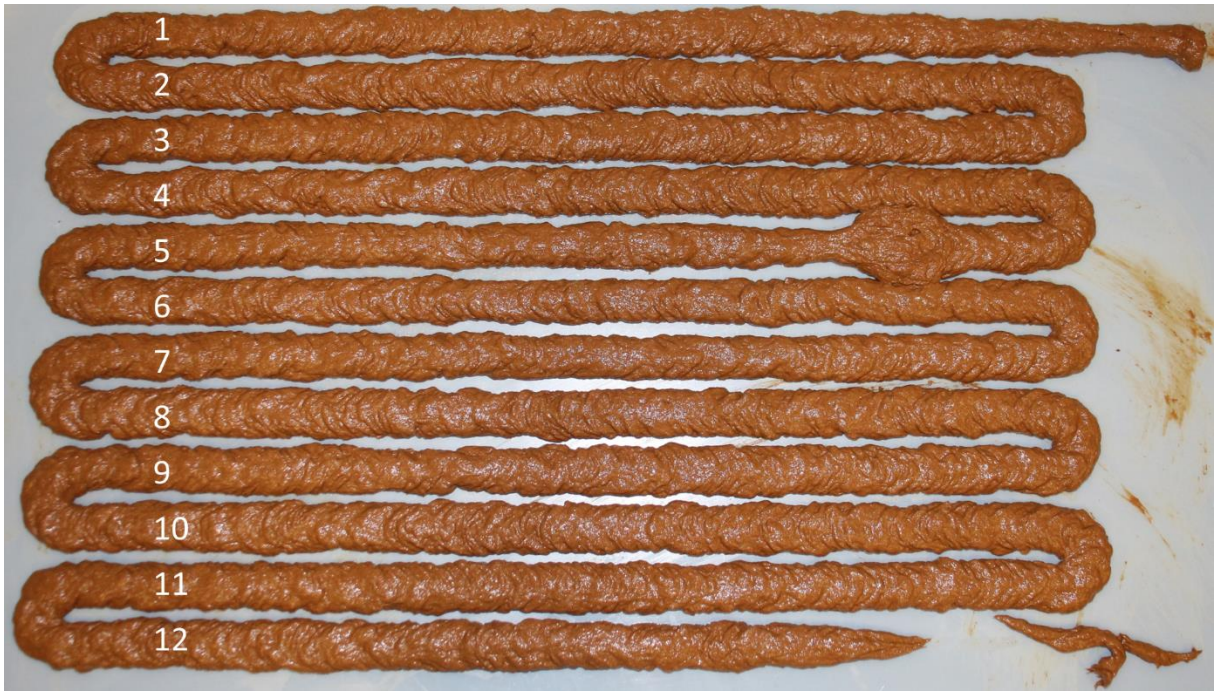


Figure K2. A full cartridge print with the Makita pressure at 2 at the robot speed at 32.5 mm/s.

Table K1. Widths per path of the full cartridge test.

Path	Path width [mm]
1	17 - 21
2	17 - 20
3	17 - 21
4	16 - 20
5	17 - 20
6	16 - 19
7	17 - 20
8	18 - 21
9	17 20
10	17 20
11	17 - 20
12	18 - 20
Average path width	18.7

Table K2. Print length results of the full cartridge test.

Path part	Length [mm]	Amount [-]	Total length [mm]
Straight parts	400	11.7	4680
Arcs	=11.5*π = 36.13	11	397.41

Total length [mm]	Total length [m]
5077.41	5.07

K.1.2 Final element print

The final element consists of six layers, each layer printed with one cartridge. Figure K3 to Figure K8 shows the print process, each photo is taken just after a new layer is finished printed

Printing the first layer went as expected, however printing the other five layers turned out to be a bit more difficult. The print path stayed the same for each layer, only the height of the nozzle was changed. Unfortunately, with the second and third layer the nozzle standoff distance was too high, with a theoretical distance of 10 mm. Usually this distance should be the same as the diameter of the nozzle, which in this case was 10 mm. However, this 10 mm turned out to be too much.

It was assumed that the height of a freshly printed layer was the same height as with Lucs final element [1], but the actual height turned out to be less than expected. This was only noticed after the third layer, so with the second and third layer the new layer just "dropped" onto the previous layer. This meant that the top layer was not perfectly placed on the existing layers, causing it to drop next to it and just "wiggle" on top of the existing layer. For an example of this "wiggling" of a layer see the highlighted part in Figure K9.

A reason for this difference in height of the fresh layer could be that in Lucs final mixture bentonite was used as additive instead of flax fibres. Bentonite gives the mixture more stiffness, which causes the mixture to keep its shape better compared to the mixture with flax fibres.

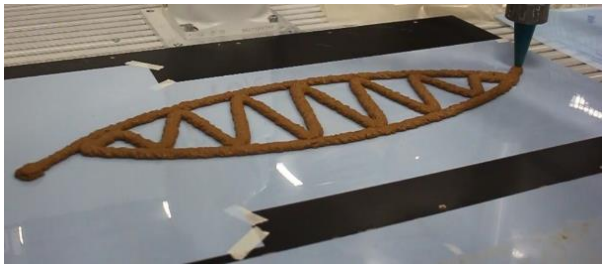


Figure K3. Photo of the first layer of the element just after printing the first layer.

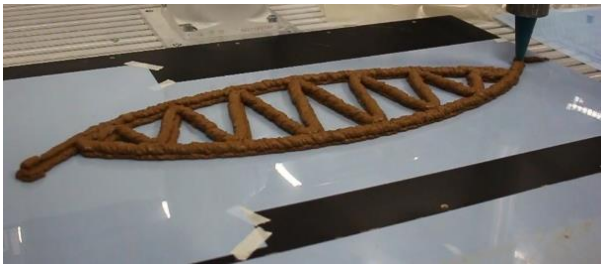


Figure K4. Photo of the first and second layer of the element just after printing the second layer.



Figure K5. Photo of the first, second and third layer of the element just after printing the third layer.



Figure K6. Photo of the first, second, third and fourth layer of the element just after printing the fourth layer.



Figure K7. Photo of the first, second, third, fourth and fifth layer of the element just after printing the fifth.



Figure K8. Photo of all six layers of the element just after printing the sixth layer.



Figure K9. The final element just after printing the third layer. With on the right the same photo but with the third layer highlighted in green.

From the fourth layer, the nozzle height increase was altered. Table K3 presents the increase, the Makita pressure and print speed per layer. When printing the fourth layer, it became apparent that this increase was still too much, leading to a too large the nozzle standoff distance. With the fifth and the sixth layer the nozzle was manually moved to a height that the standoff distances was around 5 to 6 mm. The height of the new nozzle placement was put into the script and next to adjusting the nozzle height, the print speed was increased to 33 mm/s for these two layers. Printing the last two layers went much better than layer two, three and four. However, due to that the previous layers did not lay perfect on top of each other, to two top layers still had many imperfections.

Table K3. The Makita pressure and print speed settings for the final element print

Layer	Makita pressure [-]	Print speed [mm/s]	Nozzle height* [mm]	Nozzle height increase** [mm]
1	2	32.5	9.5	-
2	2	32.5	19.5	10
3	2	32.5	29.5	10
4	2	32.5	36.41	6.91
5	2	33	38.41	2
6	2	33	41.91	3.5

** Measured from the top of the print bed*
*** Measured from the nozzle height of previous layer*

After printing layer 4, some adjustments were done by hand. At a few points the top layer caused the structure to tip over at a few places. The material was gently pushed back onto the layer(s) beneath them. Figure K10 shows the element just after printing the fourth layer and Figure K11 shows the element after the adjustments.



Figure K10. Photo taken right after printing the fourth layer. With the points where the structure is tipping over highlighted in the red circles.



Figure K11. Photo taken after the adjustments of the fourth layer. With the adjusted places highlighted in the red circles.

While printing the test elements, a part of the final element fell down (see the photo on the left in Figure K12). This fallen part was gently put back by hand and pushed onto the bottom layer and the corners of the waves. The photos in the middle and the right in Figure K12 show the element after the material was pushed back.



Figure K12. On the left: photo of the part of the final element that fell down. In the middle and on the right: photos of the part of the element that had fallen down but was pushed back up again.

K.1.3 Test beam print

With the material that remained after printing the final element, five test beams were printed (see Figure K13). The fresh dimensions are listed in Table K7 in chapter K.4.1



Figure K13. The five test elements directly after printing.

K.2 Curing conditions

After printing the element and the test beams were put into the climate room until they were tested. The climate room ensured that the temperature and the relative humidity was always constant during all the curing stages. The temperature in the climate room is always 20 °C and the average relative humidity (RH) is 60%.

Table K4 gives an overview of the different curing stages. Each stage is accompanied with a photo of the final and test elements. New to this curing process were the MDF planks and the weights. These planks and weight ensured that the elements did not warp (excessively) during the curing process.

Table K4. An overview of the different curing stages. The elements stayed in the climate room until testing

Date	Curing condition	Days cured	Figure
21/06/2024	Plastic cover	0	Figure K14
26/06/2024	Plastic cover and thin MDF plank	5	Figure K15
03/07/2024	Plastic cover removed	12	Figure K16
05/07/2024	MDF plank on top + small weights	14	Figure K17
10/07/2024	MDF plank removed	19	Figure K18
12/07/2024	Element turned upside down	21	Figure K19
15/07/2024	Element right side up, MDF plank+ larger weights	24	Figure K20
18/07/2024	Element upside down, MDF plank+ less larger weights	27	Figure K21
26/07/2024	Elements right side up	35	Figure K22
31/07/2024	Testing day	40	Figure K23



Figure K14. The test beams and the final element covered with plastic.



Figure K15. The test beams and the final element covered with plastic with a small MDF plank added on top.



Figure K16. The test beams and the final element without plastic.



Figure K17. The test beams and the final element without plastic and with the MDF planks and small weights.



Figure K18. The test beams and the final element without plastic or weights.



Figure K19. The test beams and the final element turned upside down.



Figure K20. The test beams and the final element turned right side up with large weights op top.



Figure K21. The test beams and the final element turned upside down with less large weights op top.



Figure K22. The test beams and the final element turned right side up.



Figure K23. The final element right before testing.

K.3 Final element information

K.3.1 Freshly printed

Figure K24 presents the 54 points where the full height of the element was measured. At these points the width of the top layer was also measured. These dimensions were measured five days after printing and in Table K5 provides these dimensions. The average height of the fresh element is 36.5 mm, and the average width of the sixth layer is 16.1 mm.



Figure K24. The 54 points on the final element where the full height and the width of the top layer were measured.

Table K5. The full height and width of the top layer of the final element measured at 54 different points in the element. Measured 5 days after printing.

Point	Height [mm]	Width [mm]	Point	Height [mm]	Width [mm]
1	37	13	**28**	38	20
2	35	15	**29**	36	14
3	35	16	**30**	39	19
4	37	17	**31**	35	16
5	38	19	**32**	38	20
6	38	18	**33**	35	14
7	37	16	**34**	38	16
8	38	14	**35**	34	15
9	35	15	**36**	37	18
10	36	15	**37**	34	16
11	33	15	**38**	37	17
12	36	14	**39**	39	16
13	35	16	**40**	36	17
14	36	15	**41**	36	18
15	36	16	**42**	37	18
16	36	15	**43**	38	19
17	37	18	**44**	38	17
18	38	18	**45**	38	13
19	36	18	**46**	39	17
20	36	15	**47**	36	17
21	35	14	**48**	37	16
22	36	19	**49**	36	16
23	37	16	**50**	36	15
24	36	15	**51**	37	14
25	36	16	**52**	37	14
26	37	18	**53**	36	15
27	35	14	**54**	37	15

	Height [mm]	Width [mm]
Average	36.5	16.1

K.3.2 Cured dimensions final element

Table K6 displays the cured dimensions of the final element. These dimensions were measured 35 days after printing. The widths were now measured in 24 different places, at three different heights: the top, the bottom and in the middle.

The average height of the cured element is 27.4 mm, and the average width is 20.4 mm.

Table K6. The height and width of the final element, measured at 54 different points in the element.

Point	Height	Width			Point	Height	Width		
		Top	Middle	Bottom			Top	Middle	Bottom
	[mm]	[mm]	[mm]	[mm]		[mm]	[mm]	[mm]	[mm]
1	27.7				**28**	25.2			
2	29.5				**29**	26.2	15.6	21.6	21.5
3	28.4	16.0	20.3	22.1	**30**	25.7			
4	29.1				**31**	28.4	16.1	24.2	22.8
5	28.9	22.4	23.6	21.2	**32**	25.5			
6	28.9				**33**	27.0	14.9	24.9	21.1
7	29.0	21.0	23.6	18.6	**34**	26.4			
8	28.9				**35**	27.2	15.4	21.3	19.3
9	30.2	16.5	23.4	21.1	**36**	26.3			
10	28.5				**37**	27.8	16.4	21.4	20.2
11	25.1	15.9	22.2	24.8	**38**	26.1			
12	28.8				**39**	27.8			
13	27.2	17.6	19.1	27.1	**40**	28.5			
14	29.3				**41**	28.0	18.5	24.5	19.2
15	28.2				**42**	27.5			
16	27.5				**43**	27.4	17.5	26.8	21.6
17	27.4	17.6	21.1	18.9	**44**	26.5			
18	25.4				**45**	28.0	18.4	25.4	21.1
19	27.4	18.9	23.1	21.3	**46**	27.4			
20	25.4				**47**	27.7	14.5	25.6	
21	26.8	15.8	23.3	19.8	**48**	26.7			
22	24.8				**49**	27.4	18.9	24.8	21.9
23	27.0	17.3	20.8	22.3	**50**	29.1			
24	25.2				**51**	27.5	15.5	23.4	20.0
25	26.3	13.8	22.6	22.6	**52**	27.8			
26	24.6				**53**	29.7	16.2	25.8	20.5
27	27.7	15.6	21.3	21.6	**54**	29.2			

	Height	Width
	[mm]	[mm]
Average	27.4	20.4

K.4 Test beam information

Table K7 presents information of each test beam. This includes the print speed, the important dates and what type of test was executed.

Table K7. Important information of the bio-glue with flax elements.

Print	Print speed [mm/s]	Dimension in Grasshopper [mm]	Printed [date]	Tested [date]	Test
1	18.5	210 x 40 x5 layers	21-6-2024	31-7-2024	Compression vertical 5 elements 3 mm/min
2	18.5	250 x 40 x5 layers	21-6-2024	31-7-2024	Bending vertical 3mm/min
3	18.5	250 x 40 x5 layers	21-6-2024	31-7-2024	Bending vertical 3mm/min
4	18.5	250 x 40 x5 layers	21-6-2024	31-7-2024	Bending vertical 3mm/min
5	18.5	250 x 40 x5 layers	21-6-2024	31-7-2024	Bending vertical 3mm/min

K.4.1 Fresh and cured dimensions of the test beams

Table K8 and Table K9 provides the dimensions of the beams. The fresh dimensions were measured were five days after printing (Table K8) and the cured dimensions were measured 40 days after printing (Table K9). Table K10 displays the volume, weight and density of each beam. The average density is 1106.6E-3 g/cm^3 = 1106.6 kg/m^3.

Table K8. Dimensions of the test beams, 5 days after curing.

Beam	Length [cm]	Height Left [cm]	Height Middle [cm]	Height Right [cm]	Width middle top [cm]
1	20.7	3.8	3.9	3.7	3.9
2	24.8	3.9	3.7	3.7	3.6
3	25.0	3.9	3.9	3.8	3.8
4	25.0	3.8	3.8	3.7	3.8
5	25.0	3.8	3.7	3.6	3.9

Table K9. Dimensions of cured printed bio-glue elements with flax. Measured 40 days after printing.

Beam	Length [cm]	Height Left [cm]	Height Middle [cm]	Height Right [cm]	Width middle top [cm]
1	-	-	-	-	-
2	24.0	2.4	2.5	2.6	3.2
3	23.9	2.5	2.5	2.6	3.6
4	23.9	2.4	2.6	2.7	3.5
5	24.1	2.3	3.0	2.7	3.4

Table K10. Volume, weight and density of the test beams and their averages.

Beam	Volume [cm^3]	Weight [g]	Density [gr/cm^3]
1	-	-	-
2	198.03	222.5	1123.6 E-3
3	213.94	242.5	1133.5 E-3
4	213.13	234.5	1100.3 E-3
5	223.84	239.3	1069.1 E-3
Average	212.23	234.7	1106.6 E-3

K.4.2 Shrinkage of the test beams

Table K11 presents the shrinkage of each test beam. The shrinkage was calculated as the difference in dimension; in absolute value [mm] and in percentage [%] compared to the freshly printed dimension.

Table K11. Shrinkage of the test beams.

Beam	Curing time	Shrinkage					
		Length		Height		Width at the top	
	[days]	[cm]	[%]*	[cm]	[%]*	[cm]	[%]*
1	40	-	-	-	-	-	-
2	40	0.8	3%	1.2	33%	0.4	11%
3	40	1.1	4%	1.3	35%	0.3	7%
4	40	1.1	4%	1.2	32%	0.4	10%
5	40	0.9	4%	1.0	28%	0.4	11%
Average	40	1.0	4%	1.2	32%	0.4	10%

**Shrinkage compared to the original dimensions of the freshly printed beam*.

Appendix L – Final testing

Bio-based 3D printing and testing of a digitally designed structural element



F.E. Pels Rijcken

Eindhoven, 19-06-2025

Contents

L.1 Test results of second flexural and compression elements 1
L.1.1 Compression 1
L.1.2 Flexural testing 8
L.2 Final element test results 13

L.1 Test results of second flexural and compression elements

L.1.1 Compression

Figure L1 to Figure L15 show all five compression tests of the second mix. Each test is accompanied with four photos during the test and two different graphs: the force-displacement and the stress-strain graph.

Test 1

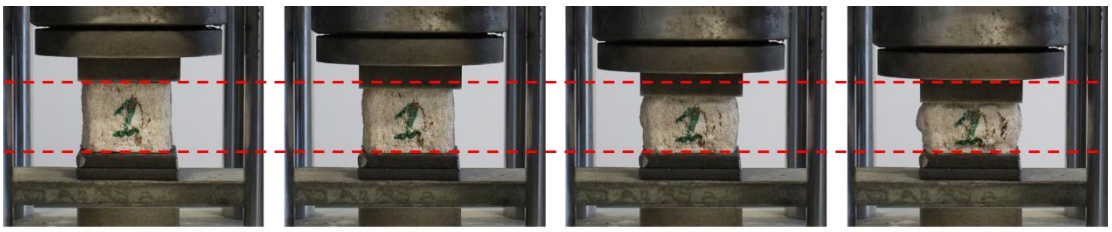


Figure L1. Four photos of compression test 4. One at the start of the test and one at the end of each cycle.

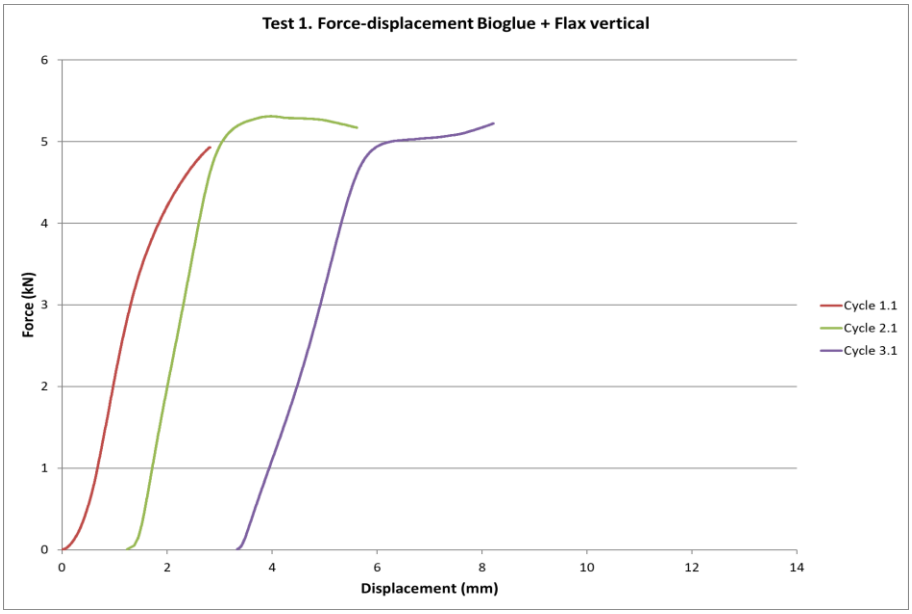


Figure L2. The force-displacement graph of compression test 1.

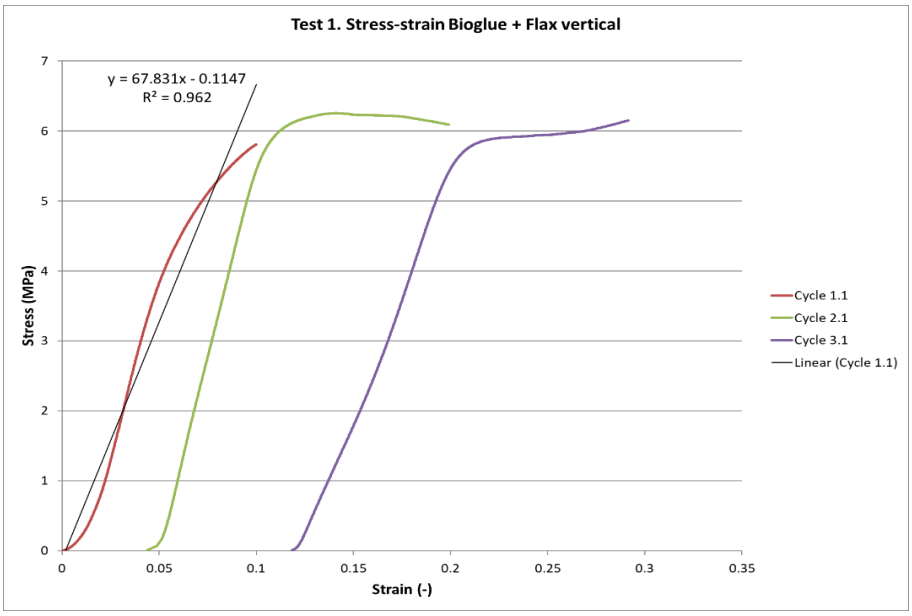


Figure L3. The stress-strain diagram of the three different cycles of compression test 1.

Test 2

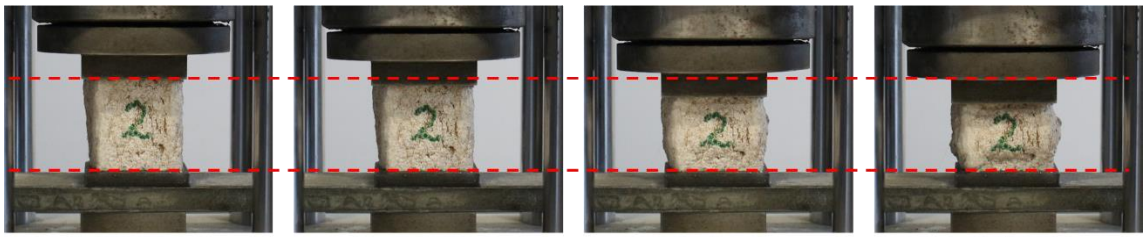


Figure L4. Four photos of compression test 2. One at the start of the test and one at the end of each cycle.

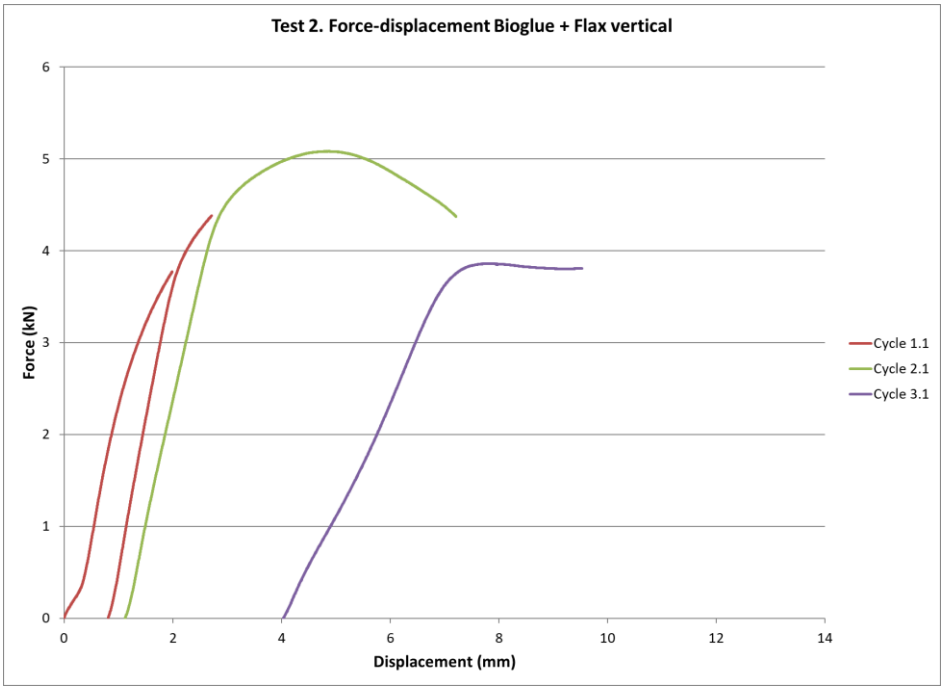


Figure L5. The force-displacement graph of compression test 2.

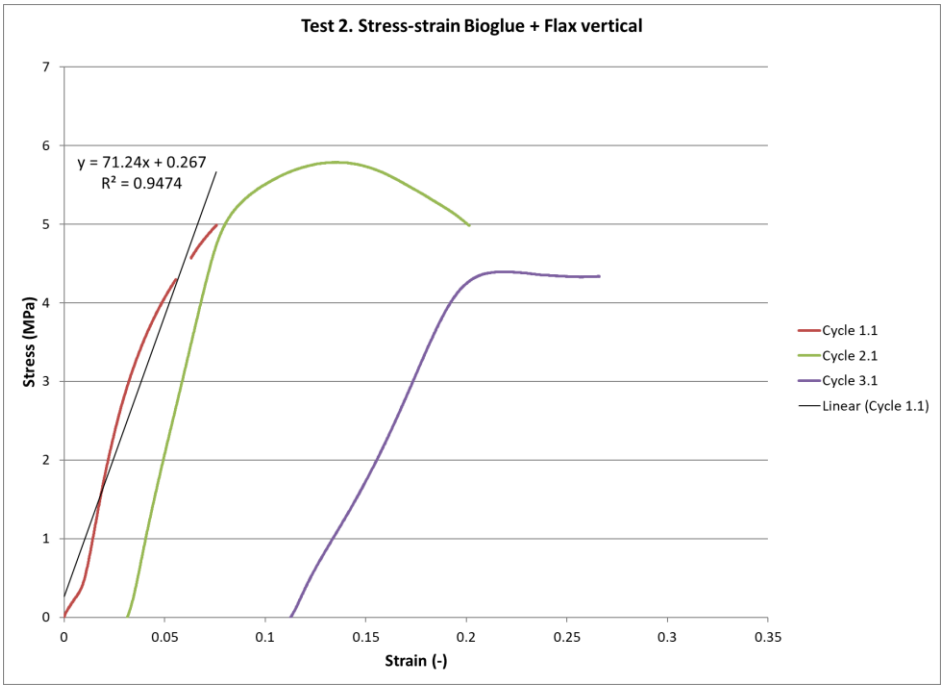


Figure L6. The stress-strain diagram of the three different cycles of compression test 2.

Test 3

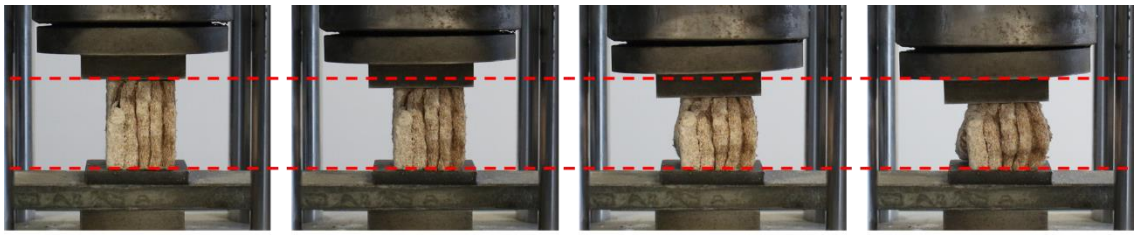


Figure L7. Four photos of compression test 3. One at the start of the test and one at the end of each cycle.

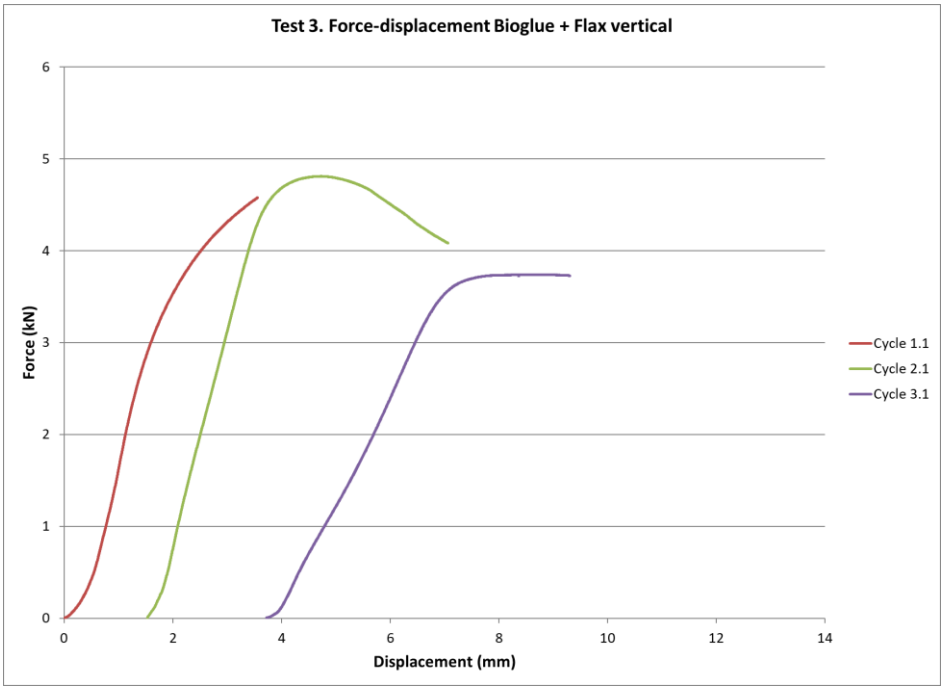


Figure L8. The force-displacement graph of compression test 3.

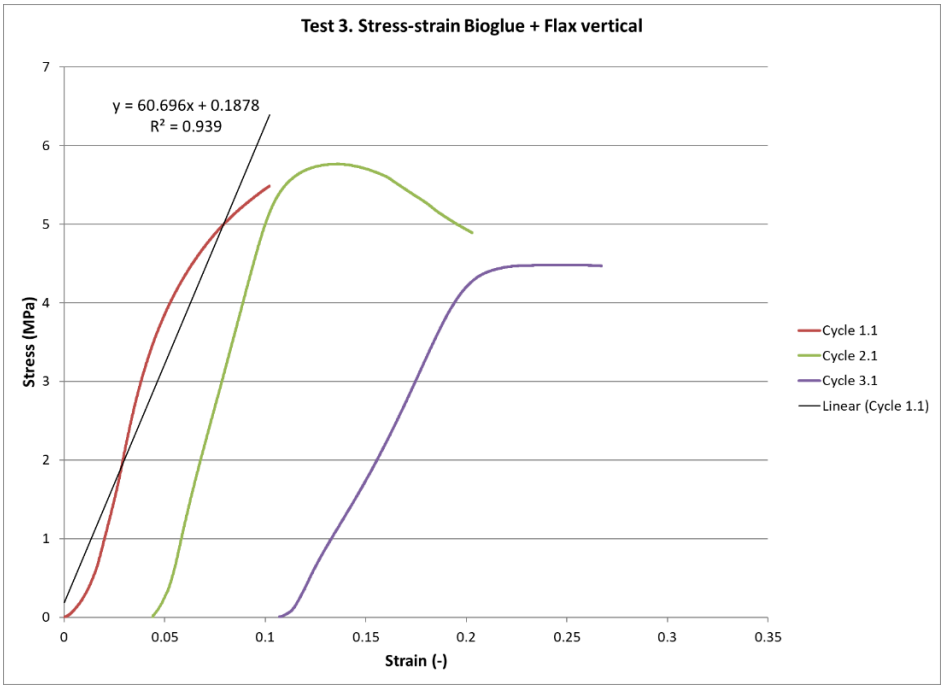


Figure L9. The stress-strain diagram of the three different cycles of compression test 3.

Test 4

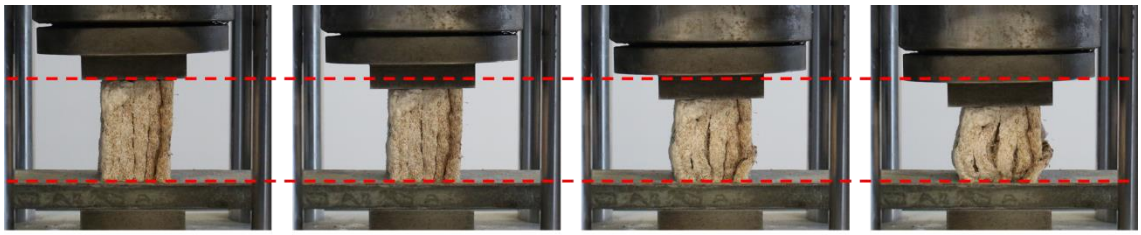


Figure L10. Four photos of compression test 4. One at the start of the test and one at the end of each cycle.

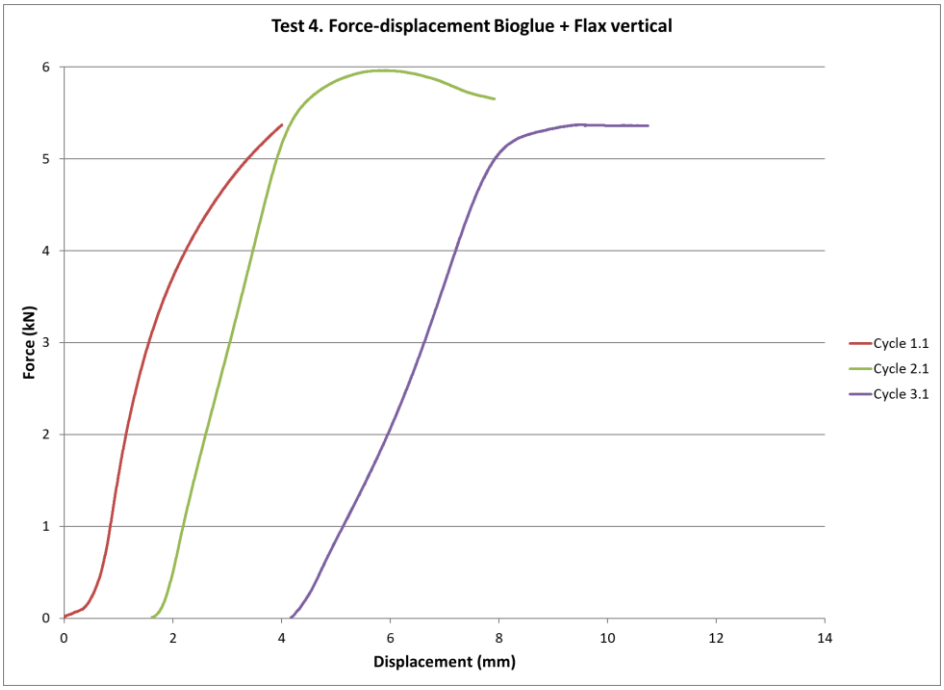


Figure L11. The force-displacement graph of compression test 4.

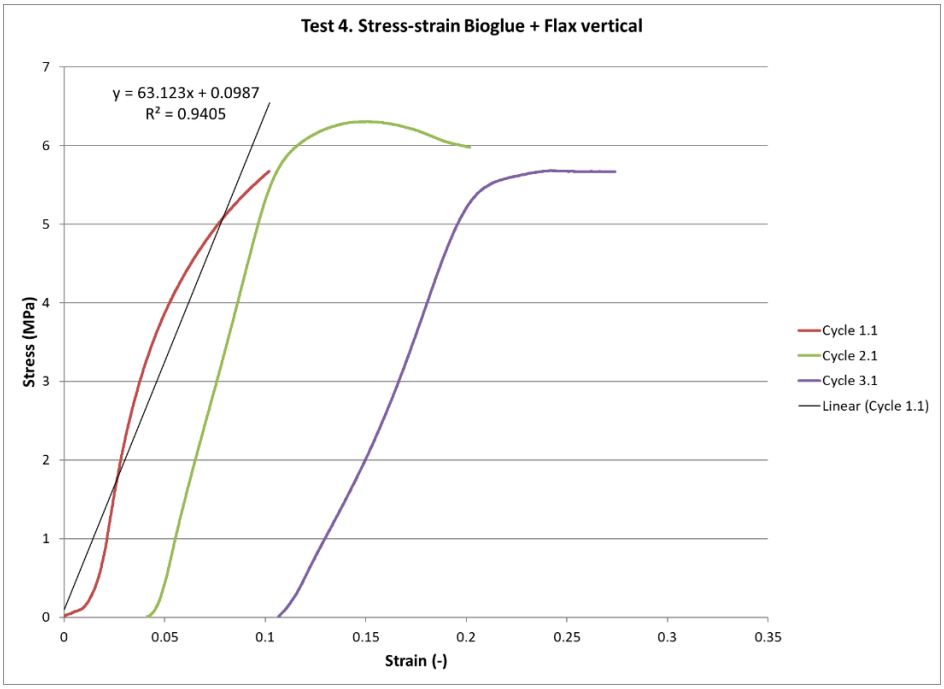


Figure L12. The stress-strain diagram of the three different cycles of compression test 4.

Test 5

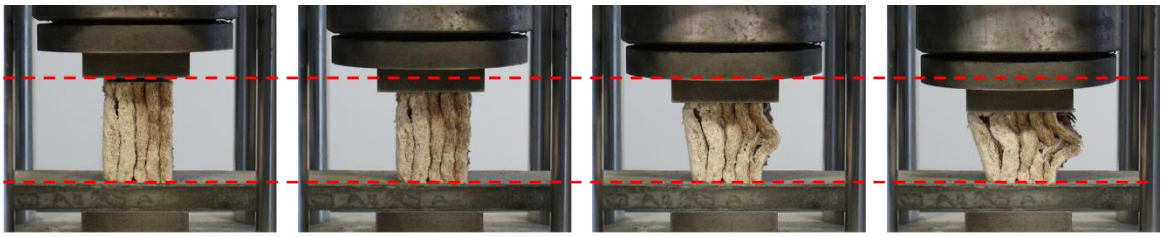


Figure L13. Four photos of compression test 5. One at the start of the test and one at the end of each cycle.

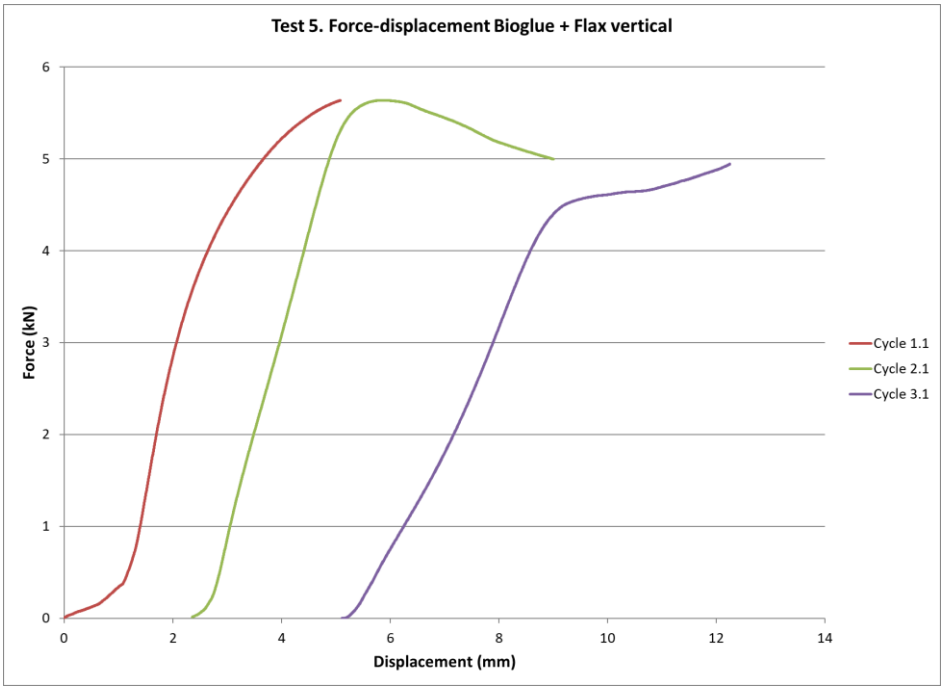


Figure L14. The force-displacement graph of compression test 4.

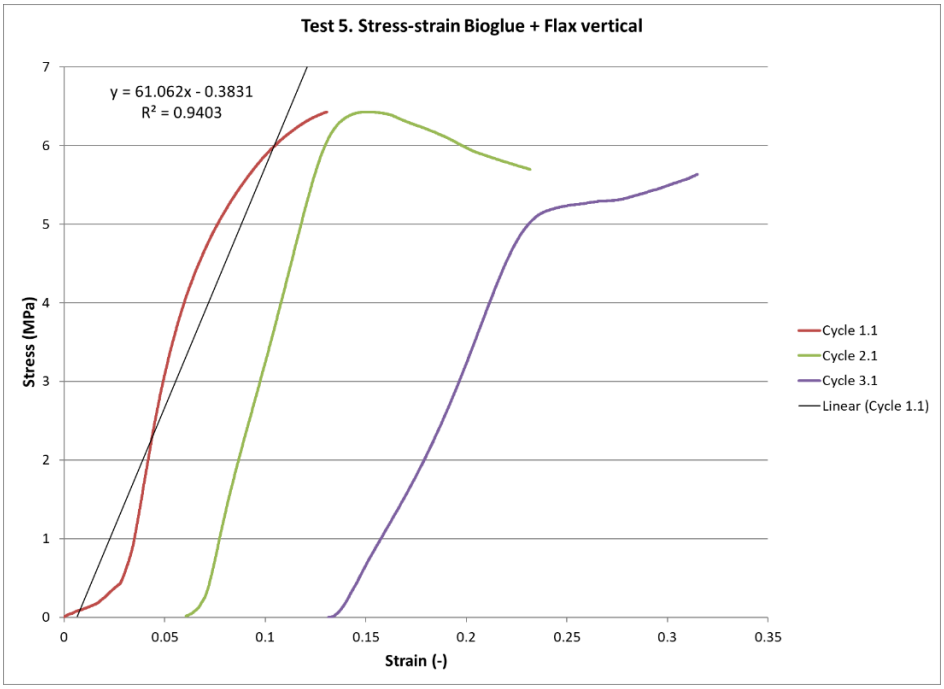


Figure L15. The stress-strain diagram of the three different cycles of compression test 5.

Figure L16 and Figure L17 present all four compression tests together in a force-displacement and a stress-strain graph.

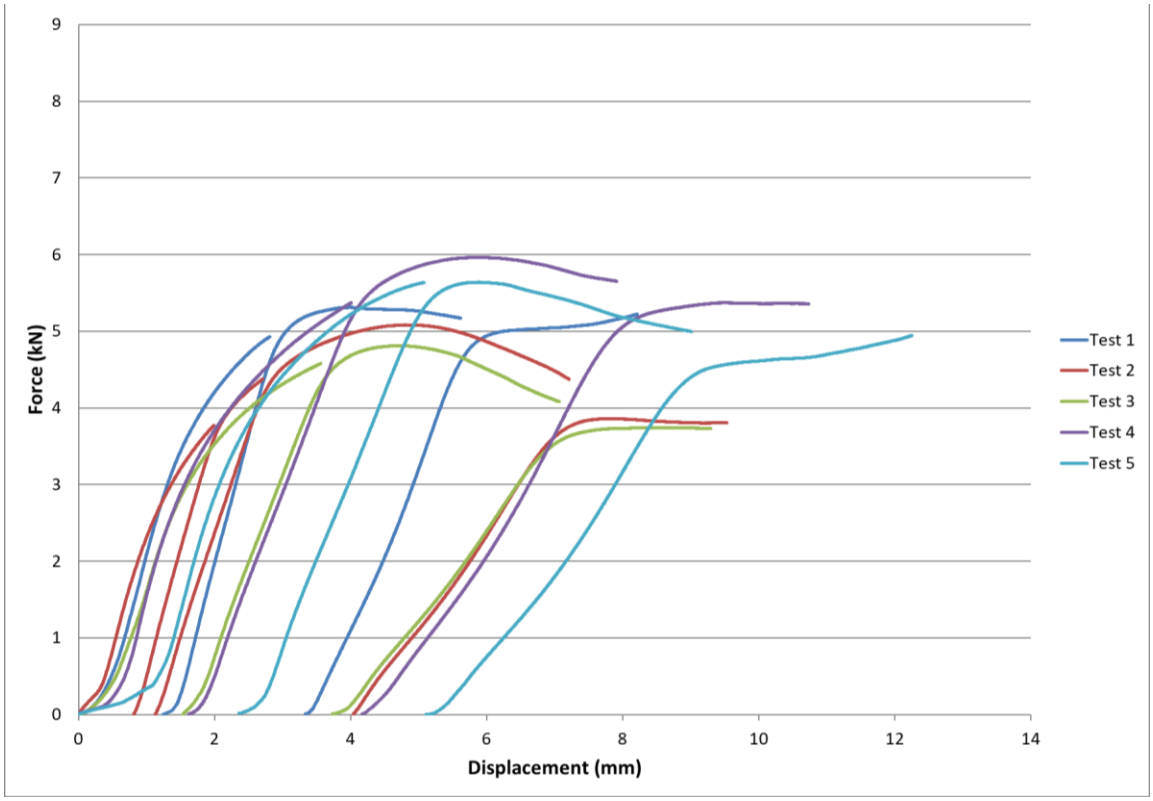


Figure L16. The force-displacement graph of the five compression tests with the second bio-glue and flax mix.

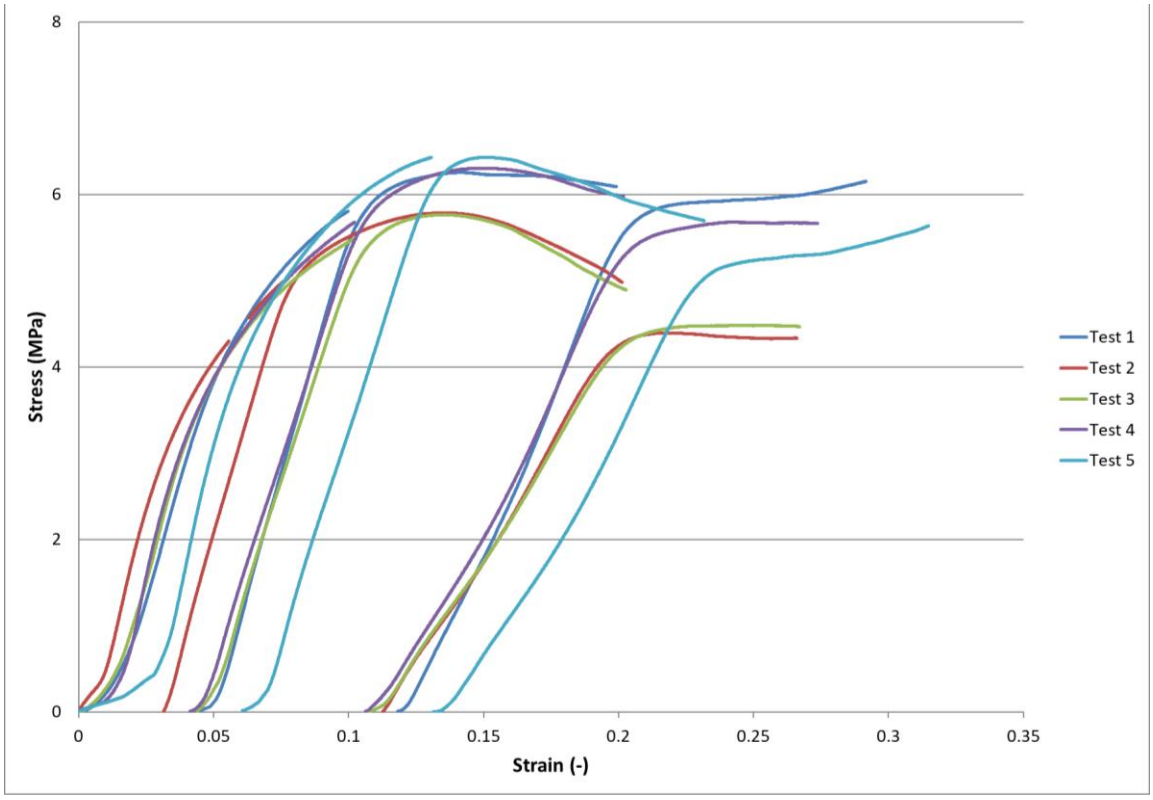


Figure L17. The stress-strain diagram of the five compression tests with the second bio-glue and flax mix.

Table L1 presents results of the results of the cycles 1.1, 2.1 and 3.1 of the five compression tests.

Table L1. The results of the three compression tests with the bio glue with bentonite mix with the horizontal layer orientation.

Test	Days cured	Cross-sectional area [mm²]	Cycle 1.1			Cycle 2.1			Cycle 3.1		
			Force [kN]	Stress [Mpa]	Strain [-]	Force [kN]	Stress [Mpa]	Strain [-]	Force [kN]	Stress [Mpa]	Strain [-]
1	40	849.00	4.93	5.81	0.10	5.31	6.26	0.14	5.22	6.15	0.29
2	40	878.16	4.38	4.99	0.08	5.08	5.79	0.13	3.81	4.33	0.27
3	40	834.34	4.58	5.49	0.10	4.81	5.77	0.20	3.73	4.47	0.27
4	40	945.66	5.37	5.68	0.10	5.96	6.30	0.20	5.36	5.67	0.27
5	40	876.80	5.64	6.43	0.13	5.64	6.43	0.23	5.64	5.64	0.31

L.1.2 Flexural testing

Figure L18 to Figure L29 show all four flexural tests of the second mix. Each test is accompanied with three photos during the test and two different graphs: the force-displacement and the stress-strain graph.

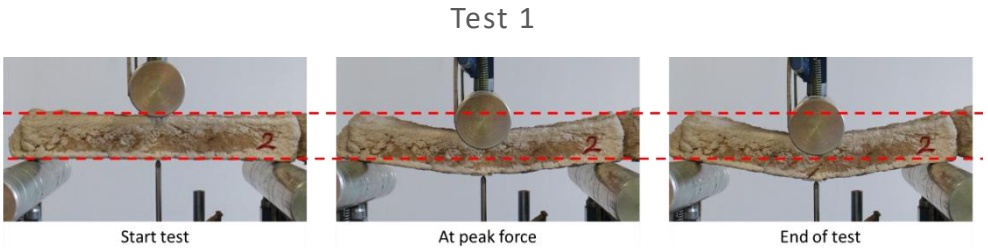


Figure L18. Three photos of flexural test 1. One at the start of the test, one at the peak force and one at the end of the test.

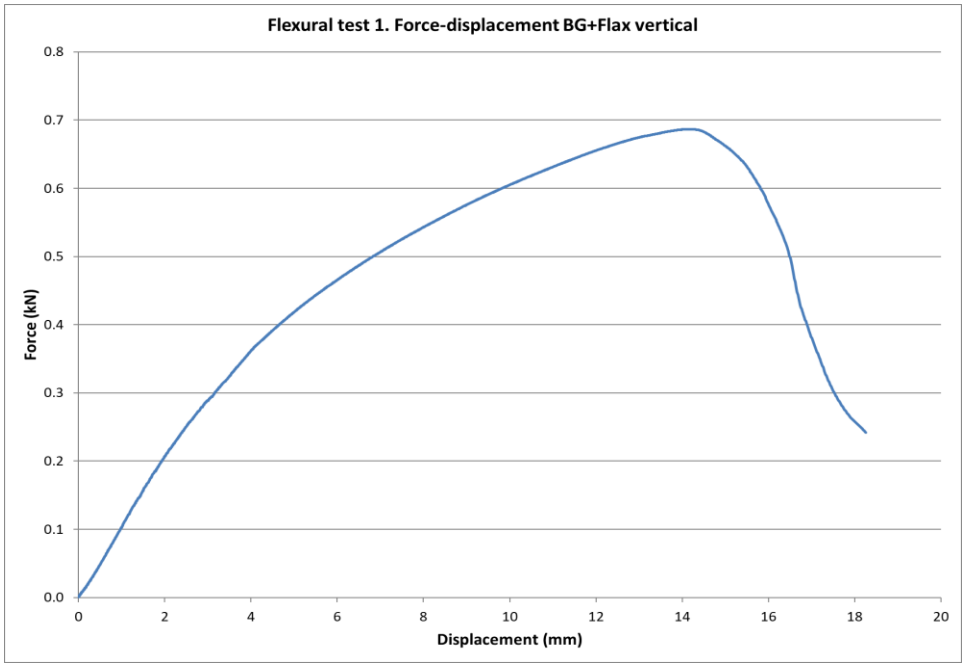


Figure L19. The force-displacement graph of flexural test 1.

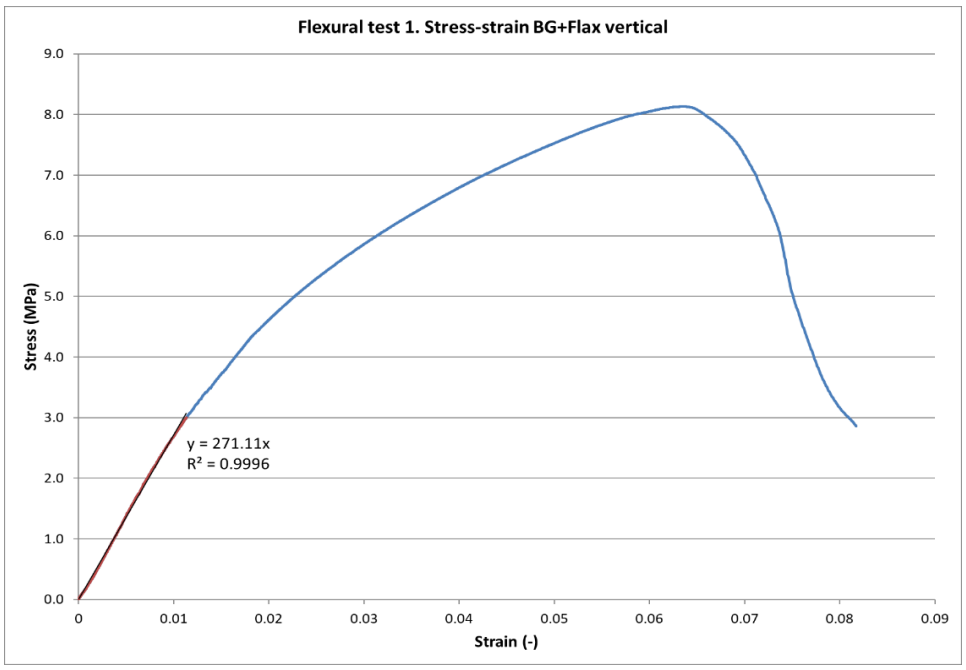


Figure L20. The stress-strain diagram of flexural test 1.

Test 2

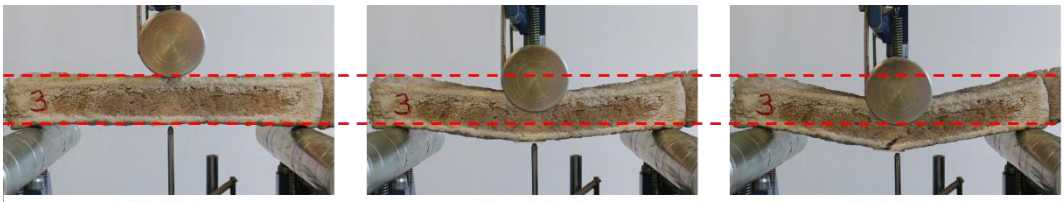


Figure L21. Three photos of flexural test 2. One at the start of the test, one at the peak force and one at the end of the test.

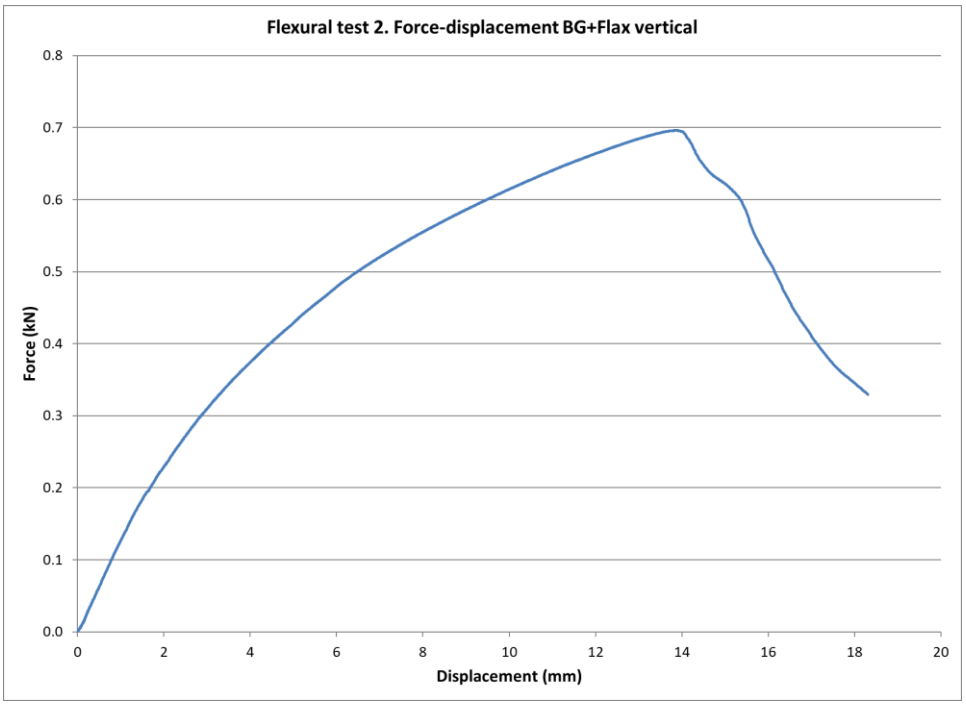


Figure L22. The force-displacement graph of flexural test 2.

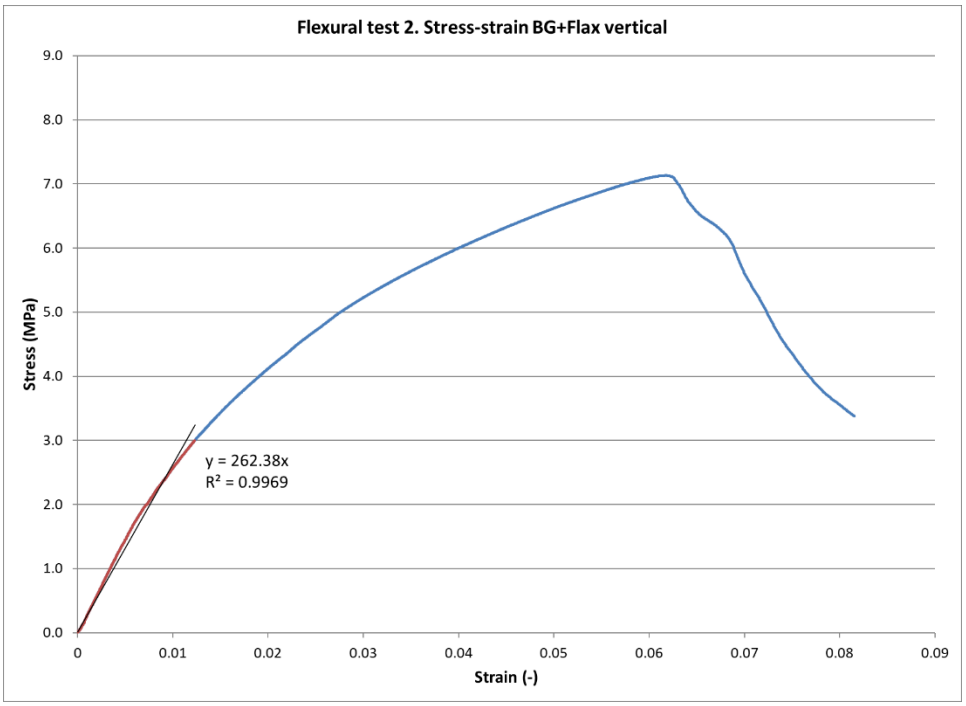


Figure L23. The stress-strain diagram of flexural test 2.

Test 3

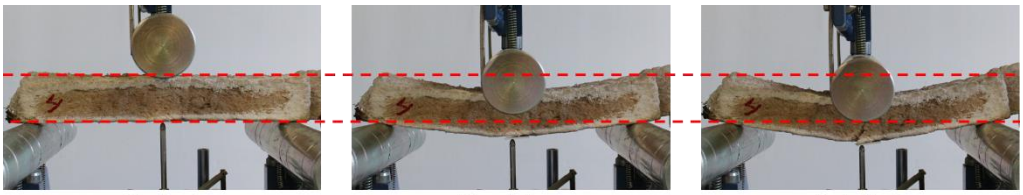


Figure L24. Three photos of flexural test 2. One at the start of the test, one at the peak force and one at the end of the test.

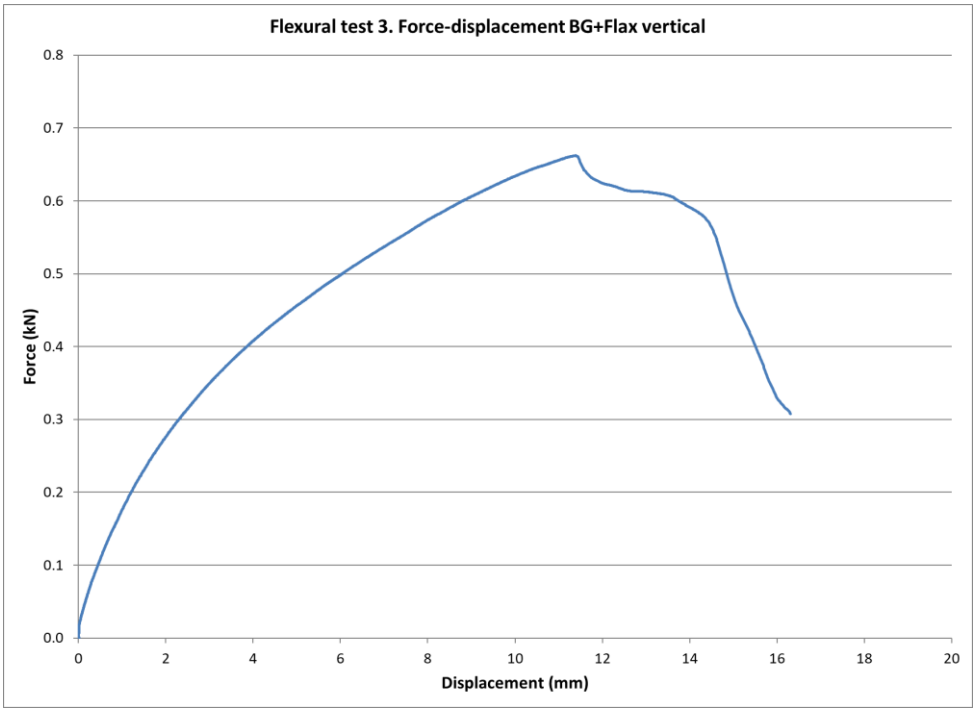


Figure L25. The force-displacement graph of flexural test 3.

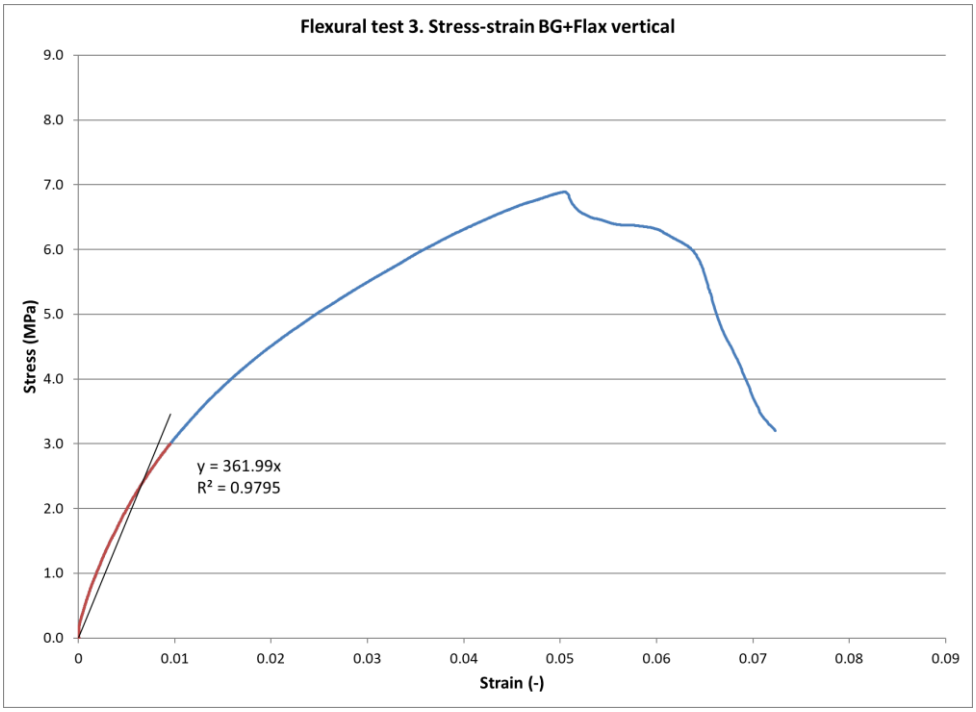


Figure L26. The stress-strain diagram of flexural test 3.

Test 4

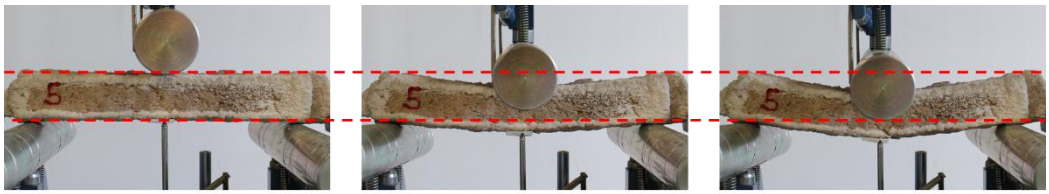


Figure L27. Three photos of flexural test 4. One at the start of the test, one at the peak force and one at the end of the test.

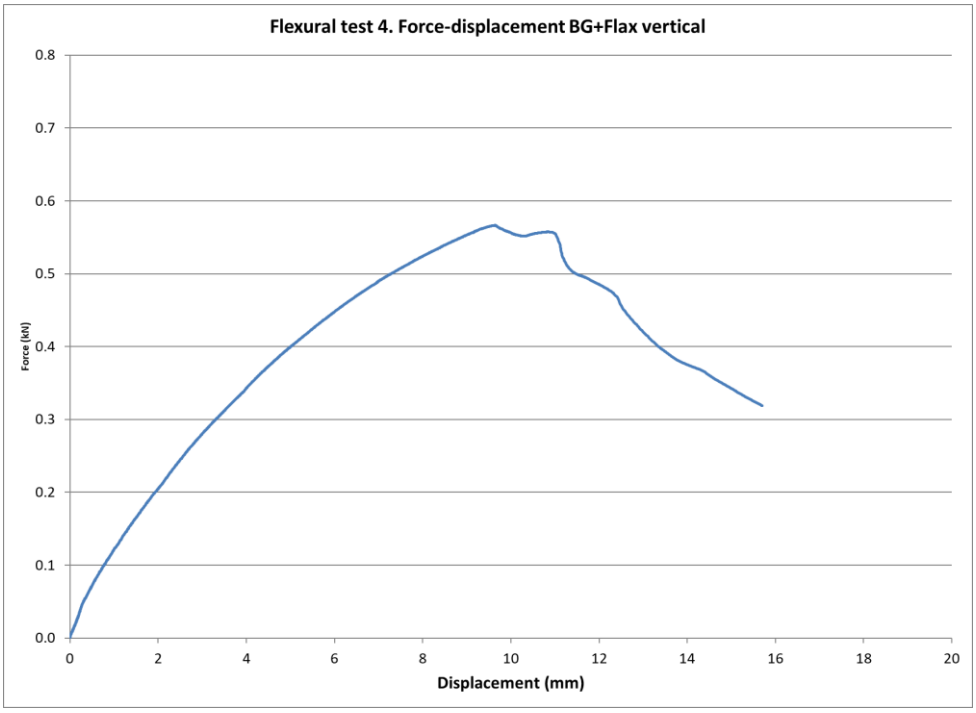


Figure L28. The force-displacement graph of flexural test 4.

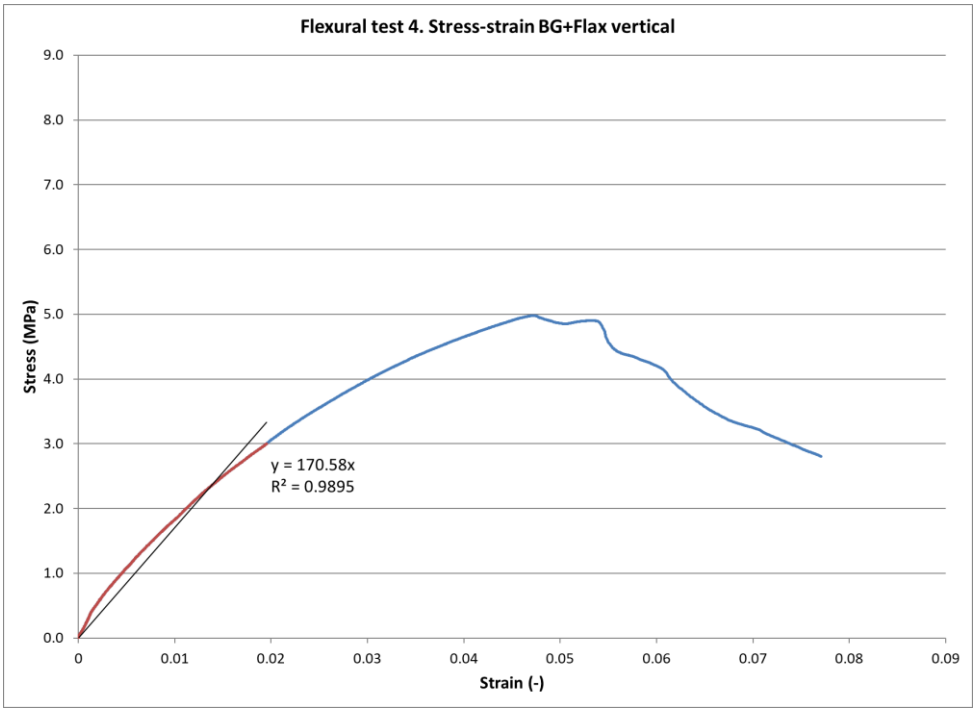


Figure L29. The stress-strain diagram of flexural test 4.

Figure L30 and Figure L31 present all four flexural tests together in a force-displacement and a stress-strain graph.

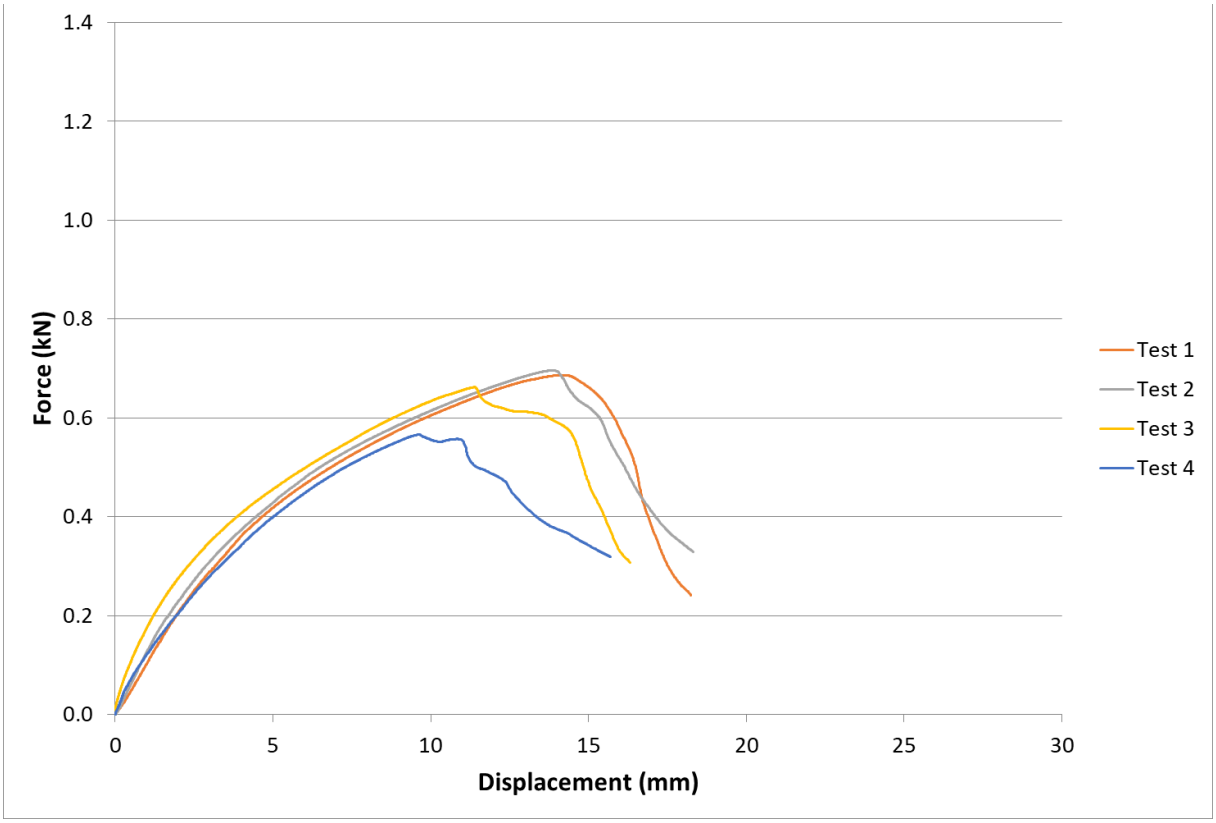


Figure L30. The force-displacement graph of the four flexural tests with the second bio-glue and flax mix.

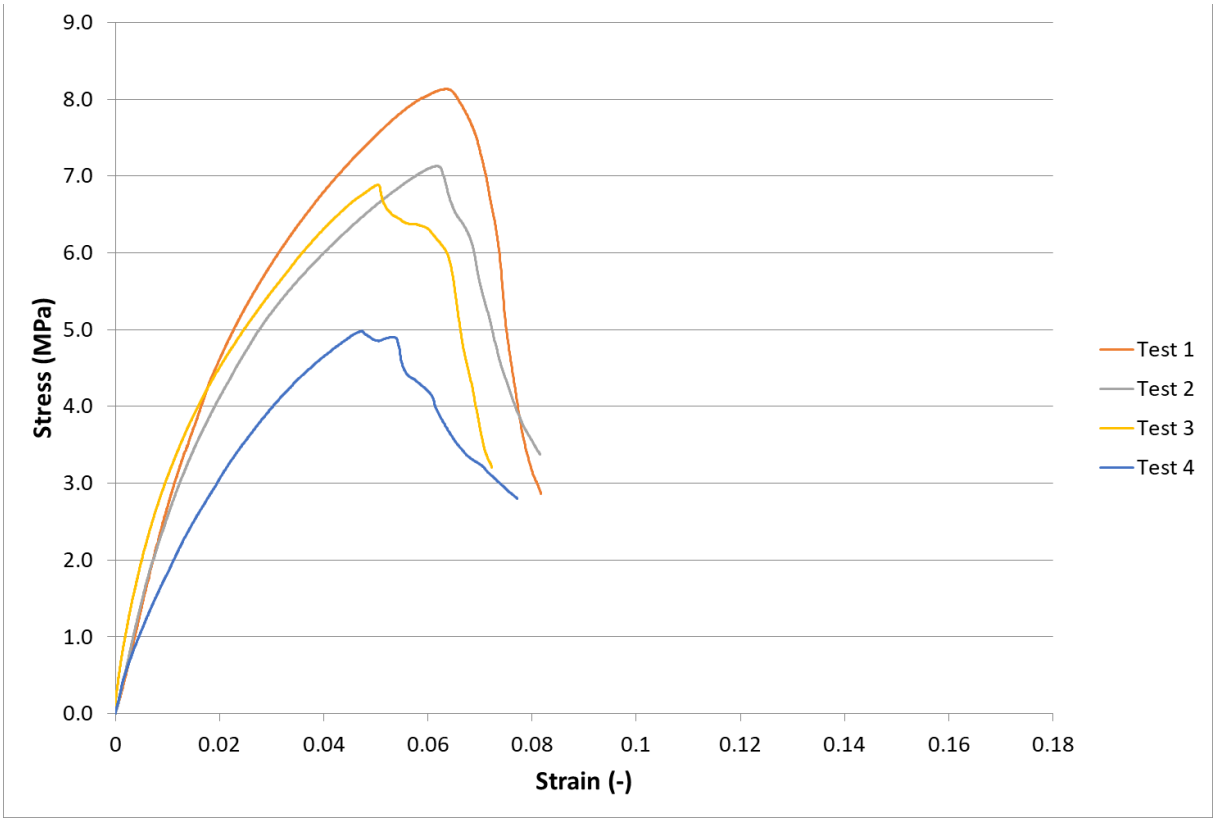


Figure L31. The stress-strain diagram of the four flexural tests with the second bio-glue and flax mix.

L.2 Final element test results

Figure L32 shows the force-displacement graph of the final element test and Figure L33 shows this graph with the numbers of the corresponding photos shown in Figure L34 to Figure L37. The numbers 1 to 4 are placed next to the moments during the test when they were taken. The red arrow indicates the moment when the test speeds was increased from 1 mm/min to 2 mm/min.
The red lines in the photos indicate the original position of the top and bottom chord.
Table L2 gives more information about the moment when photos 1 to 4 were taken. This information includes the force, displacement and a comment about the condition of the final element: if there are any cracks visible on the front or backside of the element.

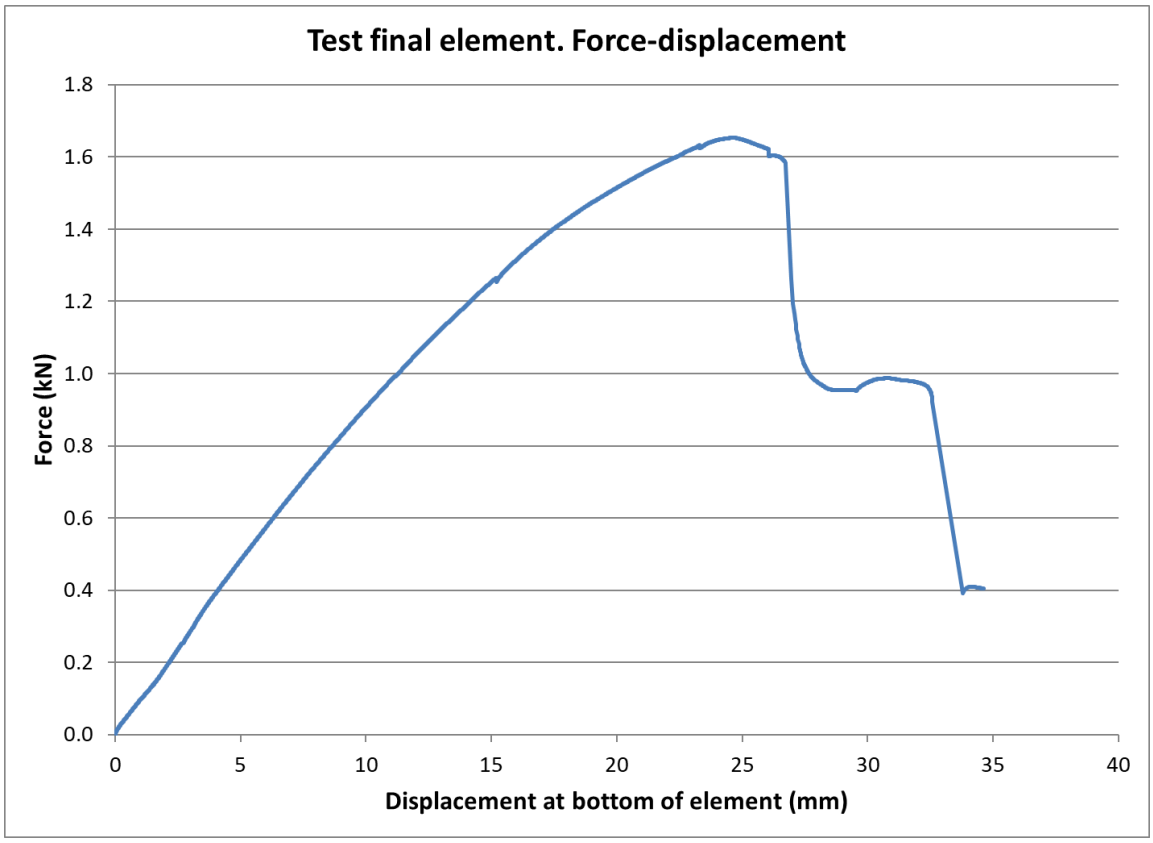


Figure L32. The force displacement graph of the final element test.

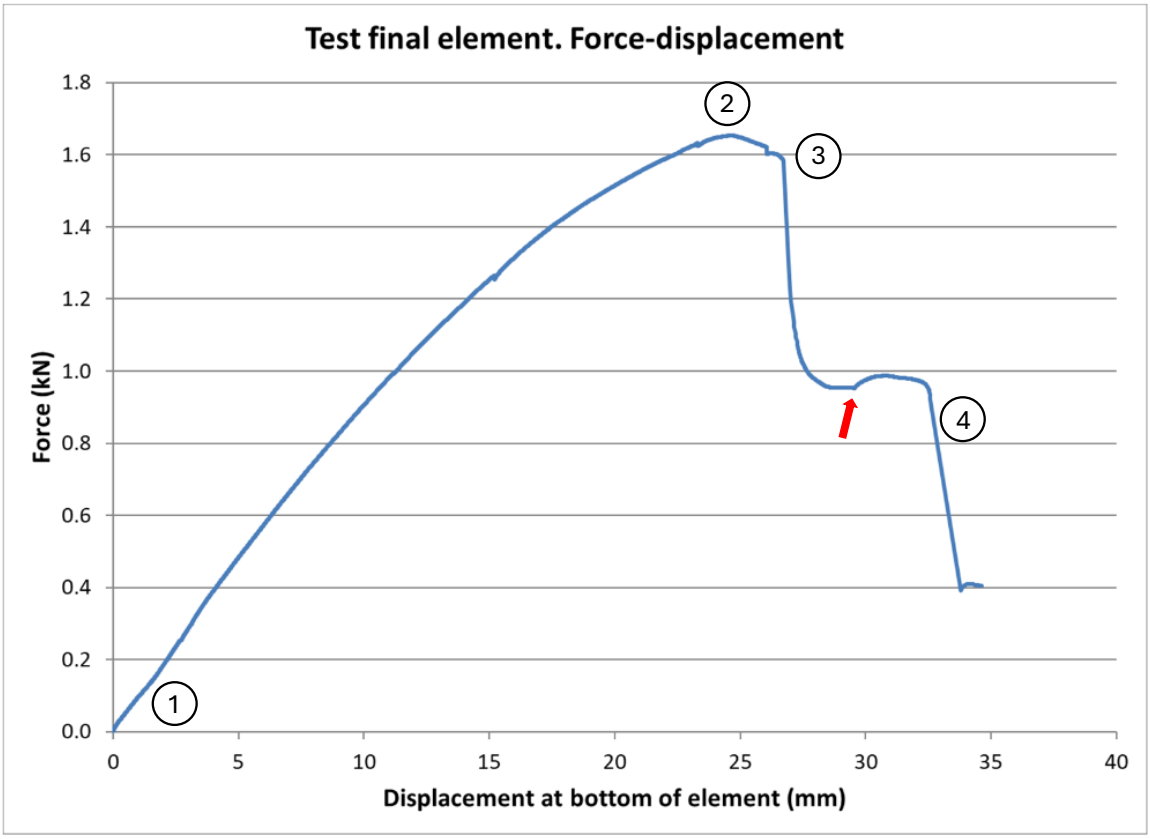


Figure L33. The force displacement graph of the final element test.

Table L2. The photo number with the corresponding force and displacement at the moment of taking and a comment has beed added of what is happening in the photo.

Photo	Force [kN]	Displacement [mm]	Comment
Photo 1	0	0	At the start of the test.
Photo 2	1.65	24.67	At the main peak. There are no visible cracks on the front as well as on the back of the element.
Photo 3	1.58	26.73	At the first big drop. The first wave on the left of the left load point has separated from the top chord and the top of that wave has moved to a little bit to the left.
Photo 4	0.93	32.58	At the second (and last) big drop. The bottom chord has been broken. And the wave that had separated has moved quite a bit to the left.

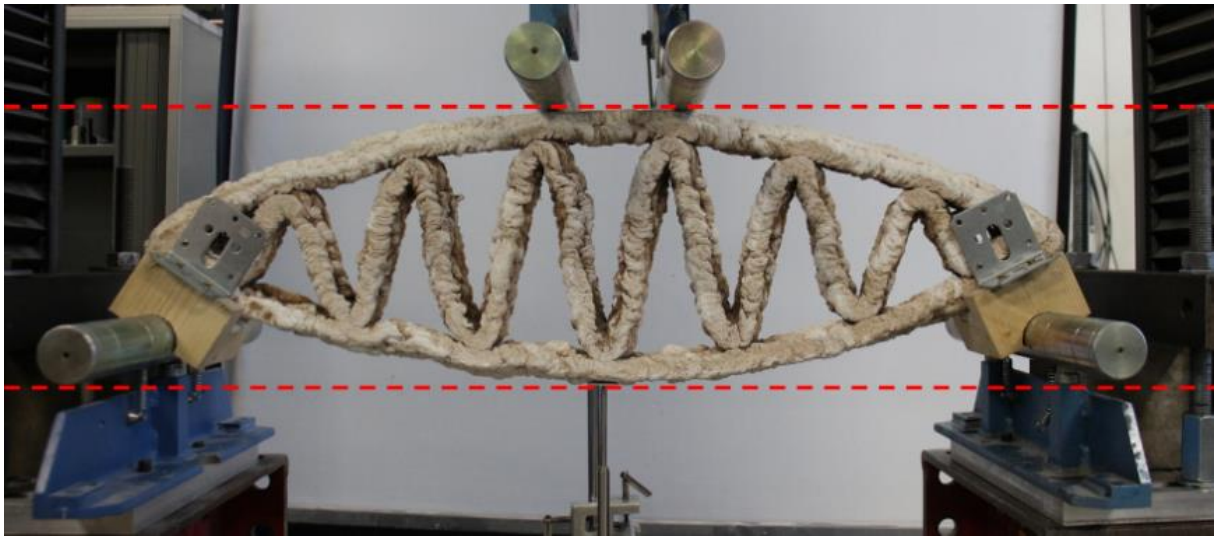


Figure L34. Photo 1.

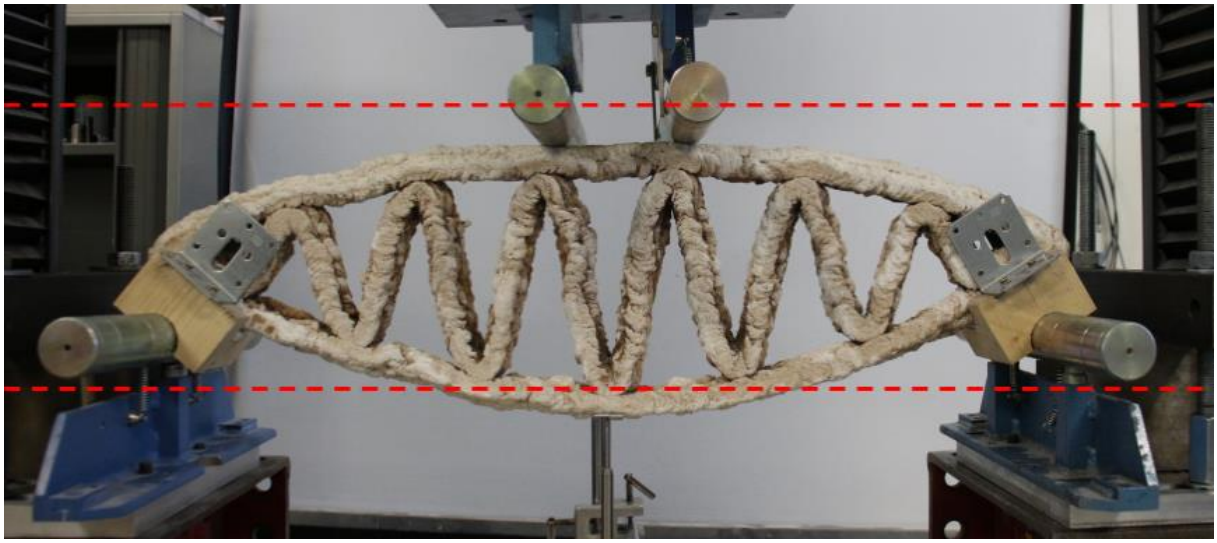


Figure L35. Photo 2.

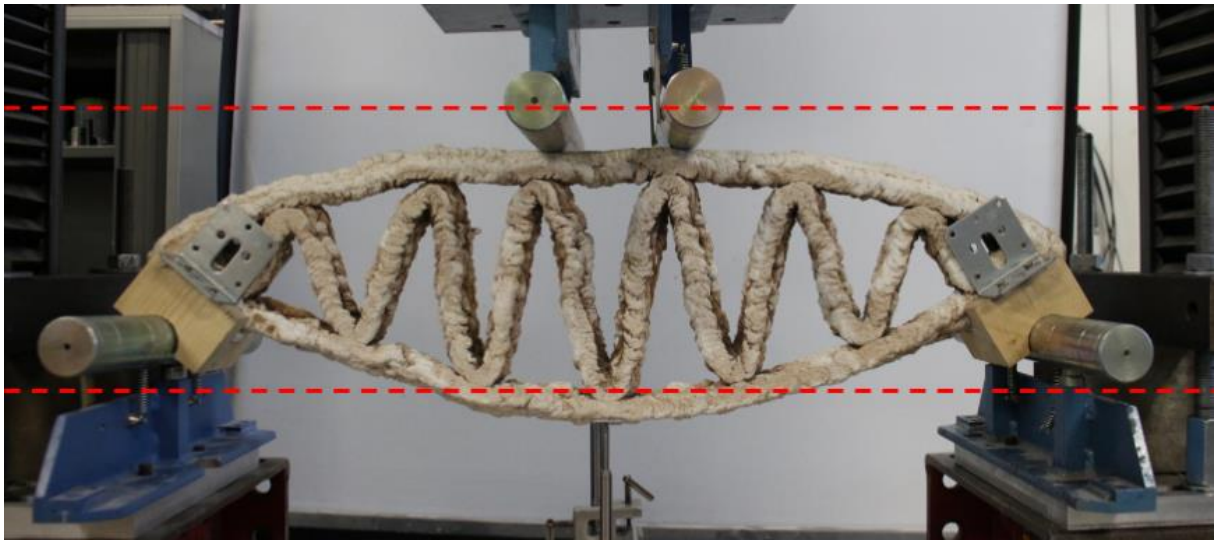


Figure L36. Photo 3.

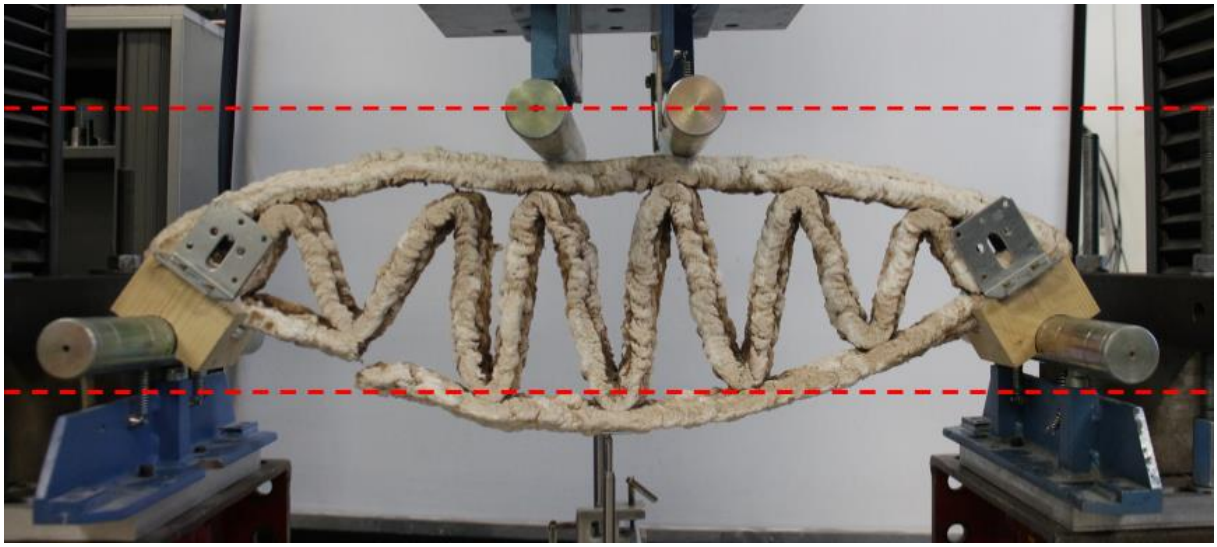


Figure L37. Photo 4